Vol. 18, No. 4, December, 2019
ISSN (Print): 0972-6268; ISSN (Online) : 2395-3454

NATURE ENVIRONMENT & POLLUTION TECHNOLOGY

A Multidisciplinary, International Journal on Diverse Aspects of Environment

Technoscience Publications
website: www.neptjournal.com

Technoscience Publications
A-504, Bliss Avenue, Balewadi,
Opp. SKP Campus, Pune-411 045
Maharashtra, India

www.neptjournal.com

Nature Environment and Pollution Technology

(An International Quarterly Scientific Research Journal)

Published by : Mrs. T. P. Goel, B-34, Dev Nagar, Tonk Road, Jaipur-302 018 Rajasthan, India

Managing Office : Technoscience Publications, A-504, Bliss Avenue, Balewadi, Pune-411 045, Maharashtra, India

E-mail : contact@neptjournal.com; operationst@neptjournal.com
journalnept@gmail.com

INSTRUCTIONS TO AUTHORS

Scope of the Journal

The Journal publishes original research/review papers covering almost all aspects of environment like monitoring, control and management of air, water, soil and noise pollution; solid waste management; industrial hygiene and occupational health hazards; biomedical aspects of pollution; conservation and management of resources; environmental laws and legal aspects of pollution; toxicology; radiation and recycling etc. Reports of important events, environmental news, environmental highlights and book reviews are also published in the journal.

Format of Manuscript

- The manuscript (*mss*) should be typed in double space leaving wide margins on both the sides.
- First page of mss should contain only the title of the paper, name(s) of author(s) and name and address of Organization(s) where the work has been carried out along with the affiliation of the authors.

Continued on back inner cover...

Nature Environment and Pollution Technology

Vol. 18, No. (4), December, 2019

CONTENTS

The Journal is Currently Abstracted and Indexed in:

- International Scientific Indexing (UAE) with Impact Factor 2.236 (2018)
- NAAS Rating of the Journal (2019) = 3.85
- Scopus®, SJR (0.146) 2018
- Index Copernicus (2016) = 109.45
- EI Compendex of Elsevier
- Indian Science Abstracts, New Delhi, India
- Chemical Abstracts, U.S.A.
- Elsevier Bibliographic Databases
- Pollution Abstracts, U.S.A.
- Paryavaran Abstract, New Delhi, India
- Zoological Records
- Indian Citation Index (ICI)
- Electronic Social and Science Citation Index (ESSCI)
- EBSCO: Environment Index™
- Zetoc
- Google Scholar
- ProQuest, U.K.
- J-Gate
- Environment Abstract, U.S.A.
- British Library
- Centre for Research Libraries
- WorldCat (OCLC)
- JournalSeek
- Connect Journals (India)
- CSA: Environmental Sciences and Pollution Management
- Research Bible (Japan)
- Indian Science
- Geobase
- Elektronische Zeitschriftenbibliothek (EZB)
- SHERPA/RoMEO
- Directory of Science
- CNKI Scholar (China National Knowledge Infrastructure)
- Access to Global Online Research in Agriculture (AGORA)
- AGRIS (UN-FAO)
- Full papers are available on the Journal's Website: www.neptjournal.com
- UDL-EDGE (Malaysia) Products like *i*-Journals, *i*-Focus and *i*-Future
- The journal is also included in the UGC CARE list of journals in India

www.neptjournal.com

Nature Environment and Pollution Technology

Nature Environment and Pollution Technology
An International Quarterly Scientific Journal

p-ISSN: 0972-6268
e-ISSN: 2395-3454

Vol. 18 | No. 4 | pp. 1083-1094 | 2019

Original Research Paper | Open Access

3D Simulation Model of Tidal, Internal Mixing and Turbulent Kinetic Energy of Palu Bay

Sabhan*†, Alan Frendy Koropitan, Mulia Purba*** and Widodo Setiyo Pranowo******

*Marine Science, Postgraduate Study Program, IPB University/Department of Physics, Faculty of Mathematical and Natural Sciences, Tadulako University, Indonesia, Perumahan Bumi Mallantan Rezkita Blok C2/1, Jl Roviega, Tondo, Palu City, Central Sulawesi, Indonesia

**Department of Marine Science and Technology, Faculty of Fisheries and Marine Science, IPB University, Jl.Raya Dramaga, Bogor 16680, West Java, Indonesia

***Department of Marine Science and Technology, Faculty of Fisheries and Marine Science, IPB University, Jl.Raya Dramaga, Bogor 16680, West Java, Indonesia

****Department of Hydrography, Indonesian Naval Postgraduate School (STTAL)/Researcher at Marine Research Center, Indonesian Ministry of Marine Affairs & Fisheries, Indonesia

† Corresponding author: Sabhan

Nat. Env. & Poll. Tech.
Website: www.neptjournal.com

Received: 18-02-2019
Accepted: 22-05-2019

Key Words:
3D simulation model
Tidal simulation models
Turbulent kinetic energy
Palu bay

ABSTRACT

The tidal simulation models and internal mixing were constructed using finite volume method to simulate diurnal tide (K1) constituent and semidiurnal tide (M2) constituent, the mixing level model using General Ocean Turbulence Model (GOTM). Tidal elevation amplitude of the model K1 ranges from 19.27 to 19.31 cm, high tidal amplitude at the point near the mouth of the Palu River, low tidal amplitude at the open boundary of the model that leads to the Makassar Strait. The amplitude range by M2 tidal constituents is 55.55-55.75 cm, high tidal amplitude at the mouth of Palu Bay and the end of Palu Bay and the slope area. The tidal current of the K1 constituent strengthens at the open boundary of the model and weakens into Palu Bay, which then undergoes strengthening near the mouth of the Palu River which experiences extreme siltation, tidal currents strengthen in the mouth area of Palu Bay and the tip of Palu Bay is caused by the tidal constituent propagation M2 and also the slope of the area along the coast of Palu Bay. Bottom Ekman layer which is caused by K1 constituent can reach 11 meters while the M2 constituent reaches 7 meters. In the slope area, are also found the buoyancy frequency with the order of 10-5 which is at a depth of 75-150 m. Kinetic energy in Palu Bay stands at O (10-5-10-3) with high kinetic energy around rough topography in the order of 10-3 around the mouth of Palu Bay.

INTRODUCTION

Palu Bay is administratively located in Donggala Regency, Palu City of Central Sulawesi Province. The position of Palu Bay is facing north with the bay mouth leading to the Makassar Strait, which is the main line of Indonesian Throughflow. The circulation of Palu Bay as semi-closed waters is strongly influenced by tides. Palu Bay has a unique morphology with a high depth degradation at a distance of 2000 meters from the coast, which can reach the depth of 300 meters or a slope of 25%. It is very potential for the occurrence of internal mixing on the slope. The process of seawater circulation is important to detect areas that have robust internal mixing in the management of the marine environment.

The depth of 450 meters in the mouth of Palu Bay allows the potential of Arlindo flow to affect the circulation in Palu Bay. At the end of the Palu Bay there is a major river that flows with an average discharge of 83.6 m^3/s with a maximum discharge of 423 m^3/s which is possible to carry sediment of 0.42244 kg/s/m (Rusdin et al. 2014) from the upstream which are intensely experiencing land clearing for new agriculture land. This high level of discharge enables the potential nutrient transport into the Palu Bay.

Research on the 2D tidal circulation model in the bay area has been conducted by Carbajal & Backhaus (1998) with the semi-implicit method showing that tidal energy dissipation is found very strong in the delta. A 3D model study conducted by Koropitan & Ikeda (2008) with a larger scale on the Java Sea shows that the mixing is dominant by the K1 tidal constituent. Pichon & Correard (2006) modelled internal tides using a spring tidal constituent of daily tidal, showing that the vertical distribution of internal tidal amplitude is related to baroclinic propagations. Kartadikaria et al. (2011) conducted research in the Indonesian Sea using POM with (1/36)° resolution showing that vertical

mixing increased due to the effects of baroclinic pairs and increased horizontal mixing with the presence of barotropic tidal movements. Increased mixing has a role in eliminating high salinity water masses from the Pacific Ocean. Robertson & Field (2005) stated that in the Indonesian Sea significant M2 values of baroclinic tides were found on slope and rough topography, especially in the strait.

Tidal circulation modelling is an essential step to apply as it is being the main cause of internal mixing in the slope that occurs by reflection of M2 internal waves (Nash et al. 2004). Strong internal mixing indicates high primary productivity, although the internal mixing has insignificant contribution (10% to 25%) to primary productivity (Schafstall et al. 2010). Internal mixing causes nutrients to be mixed in the sediment so that they enter the upper water column which is then utilized by phytoplankton which is characterized by increased chlorophyll-*a* (McGowan & Hayward 1978, Pingree & Mardell 1981). Internal mixing is a mechanism for lifting nutrients to the surface in increasing primary productivity (Sharples et al. 2001, Holt et al. 2012). In the previous study, the focus was on regional areas, while this study focused on more detailed areas with a grid size of 100 m so that small degradation could be clearly identified.

This research simulates hydrodynamics in 3D, which is driven by wind and tides by using numerical models of finite volume. The result is verified by using measurements of currents and tides. This study investigates significant tidal constituents and its role to the mixing level. The total turbulent kinetic energy and dissipation in the domain model area are also computed.

MATERIALS AND METHODS

Description of the study sites: This research was conducted in Palu Bay, Central Sulawesi Province, Indonesia. Palu Bay is located on the Arlindo line in the Makassar Strait and the input of the Palu River is large during the rainy season. Rainfall patterns in the Palu bay fall into the category of Local Rain Patterns with only one (unimodal) peak season with an average annual rainfall of 547 mm, the lowest in all of Indonesia with the peak of the rainy season in June (Bayong 1999). Palu Bay provides environmental quality with human activities as the central government of Central Sulawesi Province (Fig. 1).

Hydrodynamic model, turbulent and validation: Hydrodynamic modelling in Palu Bay using 3D MOHID uses a finite volume approach to discretize equations (Neves 2007). MOHID 3D is a hydrodynamic model based on the Navier-Stokes equation with a Boussinesq and hydrostat-

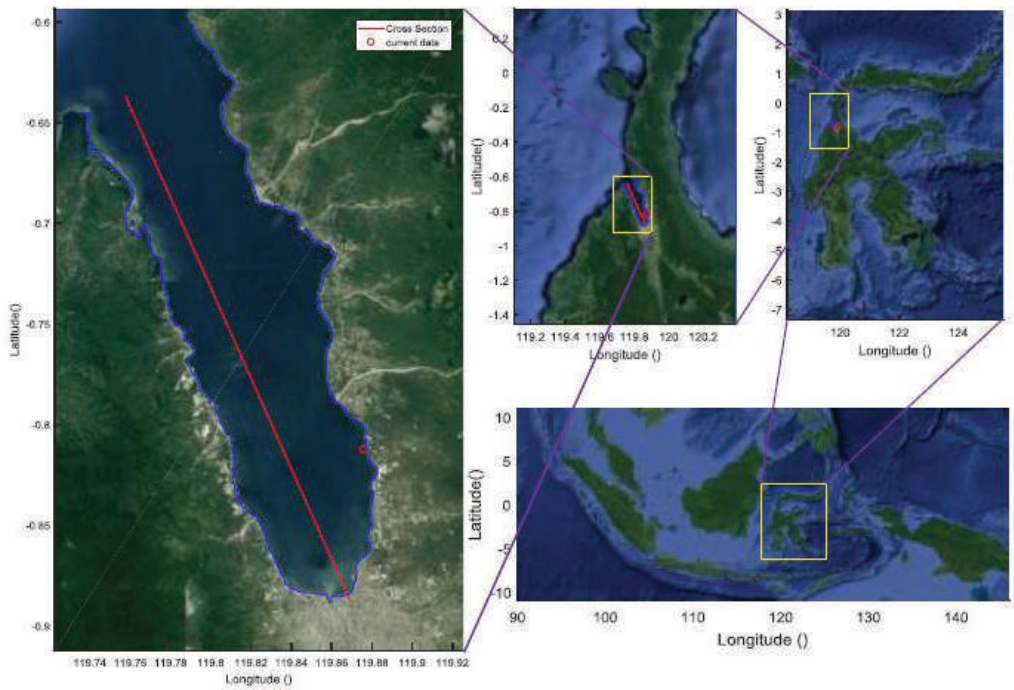

Fig. 1: the location of Teluk Palu, Central Sulawesi Province, Indonesia.

ic approach. 3D MOHID is formulated in a volume up to vertical discretization approach using sigma coordinates (Neves 2007). The open boundary of the model which is the generator input point for the tidal mouth model of Palu Bay leading to the Makassar Strait uses tidal constituents from FES2004. The study was carried out in Palu Bay (Fig. 1) by building a model that covers the entire water body of the Palu Bay. Turbulence modelling was carried out using a module (GOTM) which has been integrated with MOHID (Baumert et al. 2005) using the κ-$\in$ model approach (Versteeg & Malalasekera 2007).

Horizontal turbulence is calculated using a Smagorinsky turbulence model based on grid size and local derivative:

$$v_H = \Delta x \Delta y \sqrt{\left(\frac{\partial u}{\partial x}\right)^2 + \left(\frac{\partial v}{\partial y}\right)^2 + \frac{1}{2}\left(\frac{\partial u}{\partial x} + \frac{\partial v}{\partial y}\right)} \quad \ldots(1)$$

Equation (1) in MOHID has an expression in the form (Marín et al. 2013):

$$v_H = Horcon \times \Delta x \times \Delta y \sqrt{\left(\frac{\partial u}{\partial x}\right)^2 + \left(\frac{\partial v}{\partial y}\right)^2 + \frac{1}{2}\left(\frac{\partial u}{\partial x} + \frac{\partial v}{\partial y}\right)} \quad \ldots(2)$$

Where, Horcon = 2.5 (Marín et al. 2013), is a dimensionless calibration constant.

Turbulence parameters in the form of vertical eddy diffusion by internal waves are calculated by the following equation (Gargett & Holloway 1984):

$$K_z = \frac{R_f}{1 - R_f} \frac{\varepsilon}{N^2} \quad \ldots(3)$$

Where, R_f is the Richardson number flux (0.20). Vertical displacement is obtained from the equation (Wang et al. 2018):

$$APE = \frac{g\rho'}{2\rho_c N^2} \quad \ldots(4)$$

Where, g is gravity acceleration, ρ is the perturbation density, ρ_c is the reference density, and N is the buoyancy frequency.

The grid cell size is 0.001° × 0.001°. As many as 14 main constituents of tidal (Mf, Mm, Msqm, Mtm, O1, P1, Q1, K1, M2, K2, 2N2, N2, S2 and M4) are used as tidal generators at the open boundary, and these constituents are derived from the tide model FES2004 global tide (Lyard et al. 2006). Tidal data were also obtained from the Pantoloan Port station operated by the Geospatial Information Agency (BIG). Bathymetry data were obtained from the Navy Base (Lanal) Palu with a grid of 20 × 20 meters (not accommodating bathymetry changes by the 2018 earthquake and tsunami incident).

***Model Analysis*:** Characteristics of water level by tides and tidal currents resulting from the model based on the tidal harmonic constants of the two dominant tidal constituents (M2 and K1) were analysed with T_TIDE program (Pawlowicz et al. 2002).

RESULTS

Validation of model: The model was run for 30 days and validated with the results of tidal measurements from the Geospatial Information Agency (BIG) in Pantoloan Port for January (Table 1), the velocity of the model results was validated with the results of measurements at Donggala Beach (Fig. 2). K1 tidal constituent has the greatest contribution to the occurrence of discrepancies between the results of observation (Fig. 2) and results of model with the difference in amplitude and phase respectively 2.41 cm and -12.17 (Table 1).

Tidal Simulation

***Tidal constituent K1*:** The amplitude, phase, and tidal currents of the K1 constituent are calculated for each 5 grids. Co-amplitude, co-phase and elliptical tidal currents of the K1 constituent are shown in Fig. 3a. The co-amplitude pattern and co-phase show a high tidal amplitude pattern at the end of the bay compared to the mouth of Palu Bay, while the phase propagates from the bay mouth who experience resonance in the middle of the bay due to the reflection of the wave returning from the end of the bay. The tidal eleva-

Table 1: Comparison of amplitude and phase between data from BIG and model results.

	Amplitudes (cm)			Phase (°)		
Constituent	Model	BIG Data	ΔH	Model	BIG Data	ΔHO1
ΔHO1	15.48	16.35	-0.87	128.09	131.57	-3.48
K1	19.06	21.47	-2.41	138	150.17	-12.17
M2	54.38	55.1	-0.72	284.09	282.38	1.71
S2	42.97	42.05	0.92	337.83	332.74	5.09

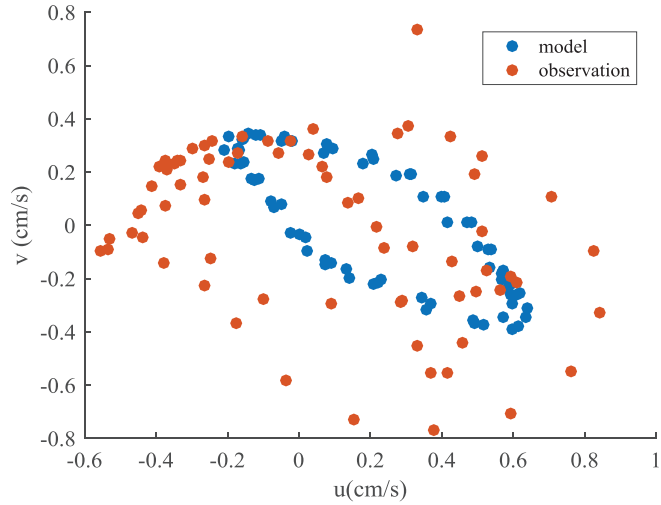

Fig. 2: Zonal and meridional current velocity plots between tidal currents of observation results (red) and model results (blue).

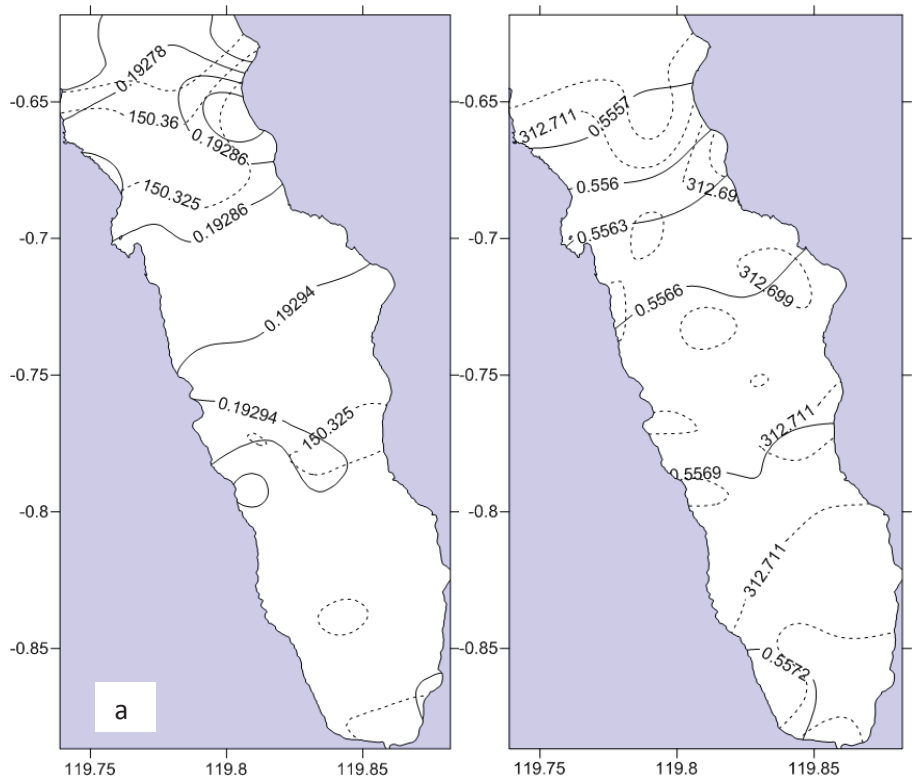

Fig. 3: Co-amplitude (cm) and Co-phase (°) (a) tidal constituent of K1, (b) tidal constituent of M2, amplitude (solid line) co-phase (dashed line).

tion amplitude of the K1 model results ranged from 19.27 to 19.31 cm high amplitude at points close to the mouth of the Palu River and low at the open boundary of the model leading to the Makassar Strait.

Co-phase model results show that the tidal wave propagates from the open boundary of the model in the Makassar Strait entering the bay until it reaches the end of the bay at the Palu river mouth with tidal co-phase from 150.3-150.42°.

Tidal current constituent K1 is presented from the model results for the surface (Fig. 4b) and bottom (Fig. 4a) of the waters in Palu Bay. The pattern of velocity of tidal currents of the K1 constituent strengthens at the open boundary of the model and weakens into the Palu Bay, which then undergoes strengthening at a certain point near the estuary which experiences extreme silting, the pattern between the speed on the surface and the bottom of the waters resembles only the 25% stronger surface compared to velocity at the bottom.

The average current velocity of the K1 constituent model results shows that there was a fairly strong current heading north near the east coast of the bay with a velocity of about 0.5 m/s in January 2016, the same as the research conducted by Sabhan et al. (2019). A strong K1 constituent velocity is also found in the area near the mouth of the Palu Bay in a shallow topographic area (Fig. 6a).

***Tidal constituent M2*:** Elliptical parameters of tidal currents by tidal constituents M2 was calculated for every 10 grids. Co-tidal is shown in Fig. 3b, referring that the M2 constituent fluctuates from the open boundary of the model at the mouth of Palu Bay then strengthens at the mouth of the Palu River at the end of the bay so that the co-amplitude is low in the centre of the bay, the amplitude range of M2 tidal constituents are 55.55 - 55.75 cm. Fig. 3b shows that the high amplitude in the bay mouth area, at the bay end and the slope areas which are close to the beach.

The velocity of the tidal current represented by the tidal current ellipse by the M2 constituent shows the same pattern between the surface and the bottom of the waters, but at the latter is weakened due to friction with the bottom of the waters (Fig. 5a). Tidal currents strengthened in the bay mouth area and the gulf tip (Fig. 5b) by the M2 tidal constituent propagation and the slope areas along the coast of Palu Bay. That corresponds to the results of research on the Hawaiian Sea backs that experienced siltation (Merrifield & Holloway 2002). Because Palu Bay only opens towards the Makassar Strait, the tidal propagation of M2 constituents comes from the Makassar Strait.

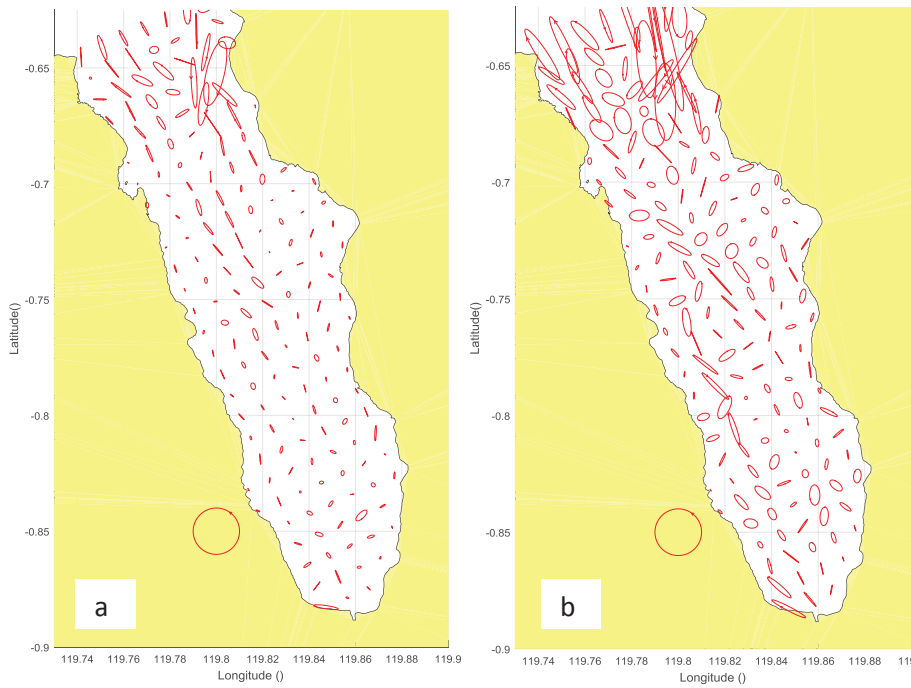

Fig. 4: Tidal current ellipses for K1 constituent (a) bottom (b) Surface.

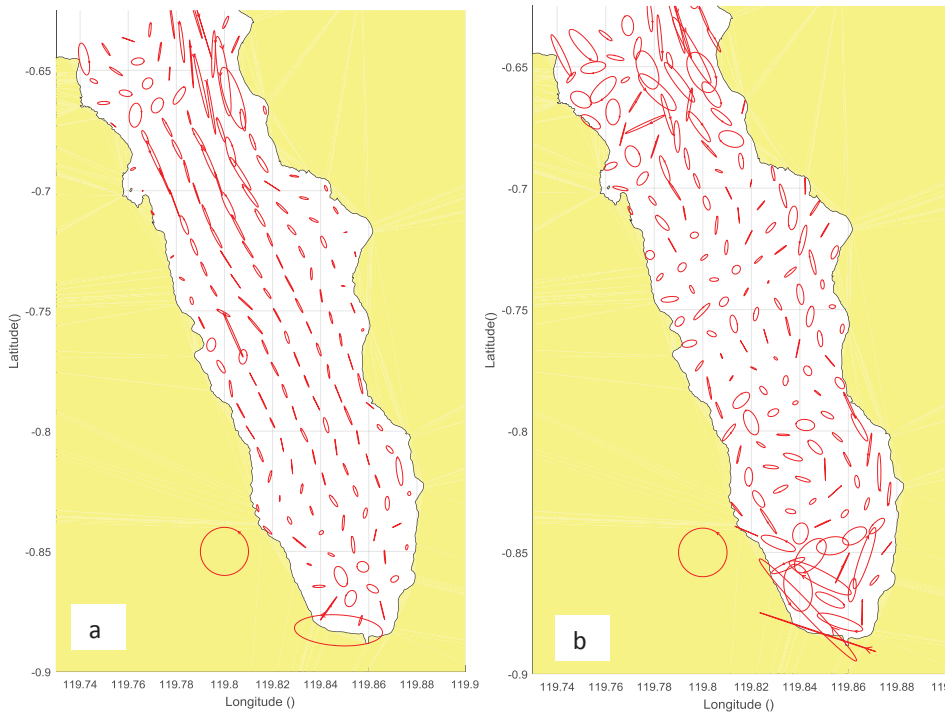

Fig. 5: Tidal current ellipses for M2 constituent (a) bottom, (b) Surface.

A strong M2 constituent velocity was also found in the area near the estuary of Palu Bay in a shallow topographical area (Fig. 6b). The M2 constituent pattern is almost the same as the K1 constituent pattern but the M2 constituent is stronger than the K1 constituent. Besides that, it is found that a fairly strong average current velocity reaching 1 m/s near the Palu River estuary is occurring in an area with low depth. Robertson & Field (2005) found that in the Indonesian Sea strong M2 baroclinic tides were present on the slope and rough topography especially in the strait.

Turbulent Models

***Buoyancy frequency*:** The results of the model show that the buoyancy frequency (Brunt-Väisälä frequency) is in order (10^{-1}-10^{-9}) s^{-2}. The cross section intersecting the y axis that passes through the end of Palu Bay (estuary of Palu River) to the mouth of Palu Bay (Makassar Strait) shows that the frequency of buoyancy is high in the bay area, which is close to the river mouth, where the input of high river water forms a strong stratification by difference density. This result corresponds to the results of the study by Hordoir et al. (2018) which states that high buoyancy frequency values are present under strong stratification conditions. In the slope area also found areas with the order 10^{-5} which are at a depth of 75-150 m with a depth of about 25 m from the bottom of the waters (Fig. 11a), this occurs because the slope area is a region with high friction (Wunsch 1968).

***Turbulent dissipation*:** Fig. 10a shows the turbulent dissipation distribution pattern near the bottom in the Palu Bay. Fig. 11b shows that turbulent dissipation in the slope area is at O (10^{-5}-10^{-4}), whereas in areas with rough topography there is a turbulent dissipation area that is small, but higher one to two orders from the surrounding environment. These results are consistent with the results of the model conducted by Nikurashin et al. (2013) which states that in the absence of rough topography, internal turbulent mixing will decrease. As for the ocean with small tidal currents, internal wave friction is the dominant cause of turbulent dissipation (Ledwell et al. 2000, Jayne & St Laurent 2001).

***Eddy diffusivity*:** Vertical slice of vertical eddy diffusivity on the y = 33 axis (Fig. 11c) has a fairly wide order with (10^{0}-10^{-9}), areas that have high eddy diffusivity in areas close to coarse topography with O (10^{-3}-10^{-2}) and the surface area, in the mouth area of the Bay found a high diffusivity area with first order where the incoming tidal currents hit the rough topography. According to the results of the study (Toole et al. 1994), increased dissipation was

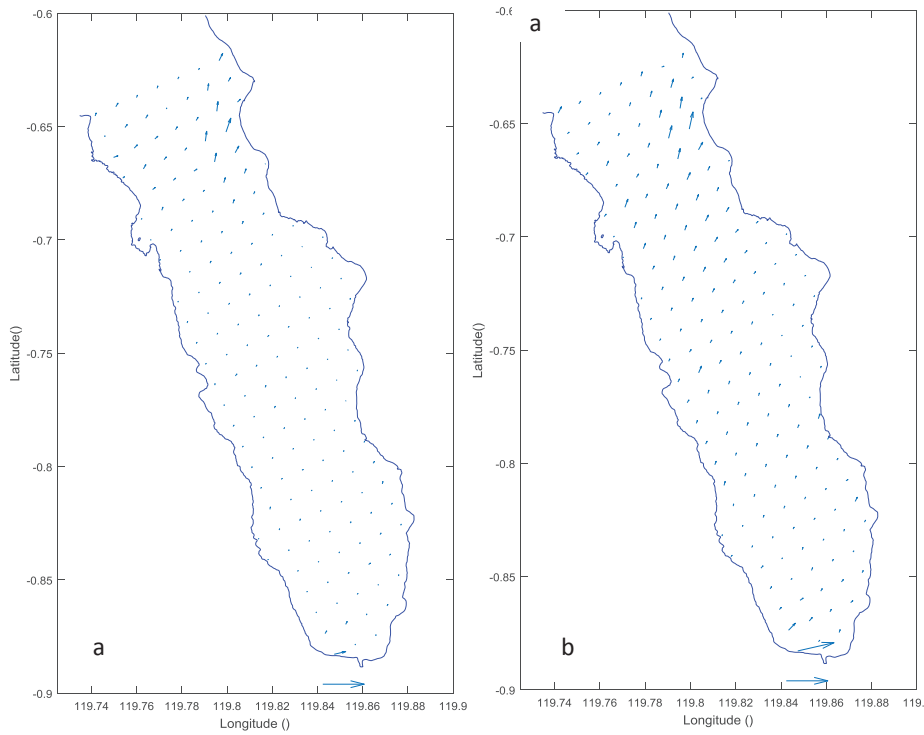

Fig. 6: The average velocity vector of (a) K1 constituent, (b) M2 constituent.

observed in the areas near steep boundaries (eddy diffusivity >10^{-4} square meters per second).

***Bottom friction velocity*:** Bottom friction velocity was calculated using equations (Zhurbas et al. 2018):

$$u^* = \left(\tau/\rho\right)^{0.5} \quad \ldots(5)$$

$$\tau = \rho C_d u^2 \quad \ldots(6)$$

Where, τ is the basic shear stress, ρ is the density of seawater. Fig. 8, the bottom friction velocity distribution for the tidal K1 and M2 constituents shows that the basic friction velocity of K1 constituent (Fig. 8a) has increased at a point where there is a rough topography, but is rapidly weakened, while the M2 constituent (Fig. 8b) speeds up from the bay mouth until reach the middle of the bay. High velocity is also found at the end of the bay due to silting or slope plus the flow of the river at the mouth of the Palu River. Sea threshold topography causes constriction, increasing the velocity of basic friction, this implies an increase in mixing on the other side of the sea threshold topography (Xing & Davies 2009).

***Delta Ekman layer*:** Delta Ekman layer is calculated using equation (He & Weisberg 2002):

$$\delta = \frac{cu^*}{\sigma + f} \quad \ldots(7)$$

Where, c = 0.2-0.4, σ is the tidal frequency and f is the tidal parameter. The M2 tidal frequency for Palu Bay is 2 times the frequency of the coriolis parameter so that the Ekman layer for the tidal constituent of M2 becomes: $\delta = \frac{cu^*}{3f}$. Fig. 9 shows that the Ekman layer by the K1 constituent (Fig. 9a) can reach 11 meters, while the M2 constituent (Fig. 9b) reaches 7 meters. The point undergoes a high layer Ekman on the rough topography of the north side of the mouth of Palu Bay. But what is effective in mixing is in the slope section where the sea is getting shallow and the layer Ekman is getting bigger so that the mixed layer from the base is getting higher, in the next study this area has the potential to supply nutrients to the water column.

Energy flux is calculated using the equation:

$$\left(E_x, E_y\right) = \frac{\rho_0}{T}\int_0^T\int_{-h}^{\eta}(u,v)\left[g\eta + \frac{u^2+v^2}{2}\right]dzdt \quad \ldots(8)$$

Where, E_x and E_y are each flux energy of the constituent vector x and y, (u, v) is the vector of horizontal velocity,

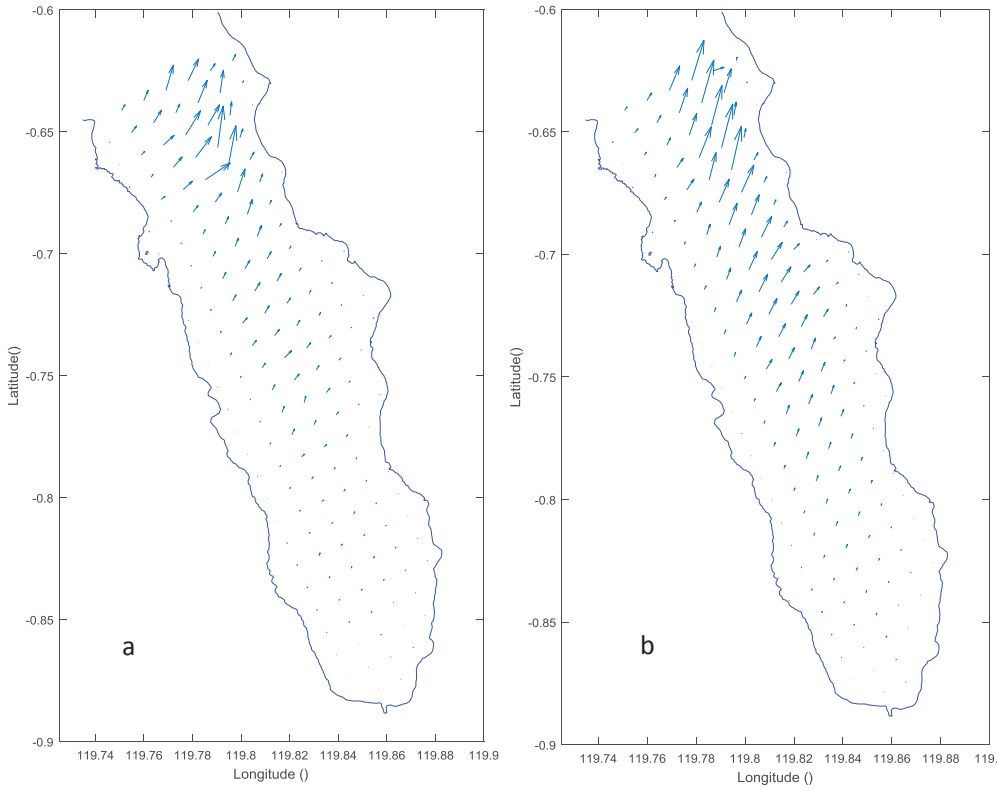

Fig. 7: Energy flux of Palu Bay by (a) tidal constituent K1, (b) tidal constituent M2.

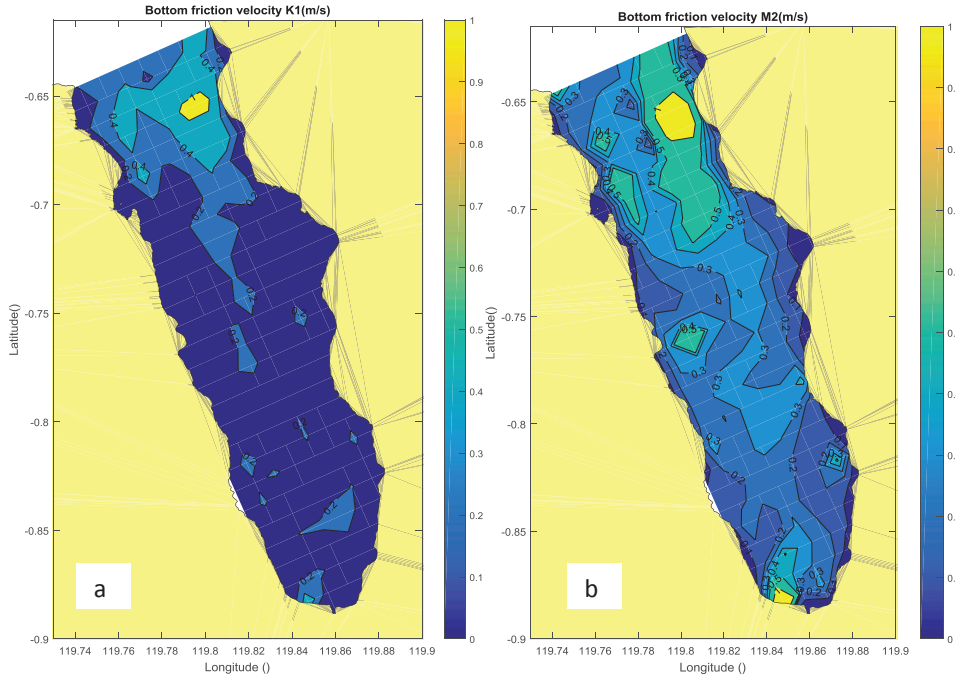

Fig. 8: Bottom friction velocity by (a) tidal constituent of K1, (b) tidal constituent of M2.

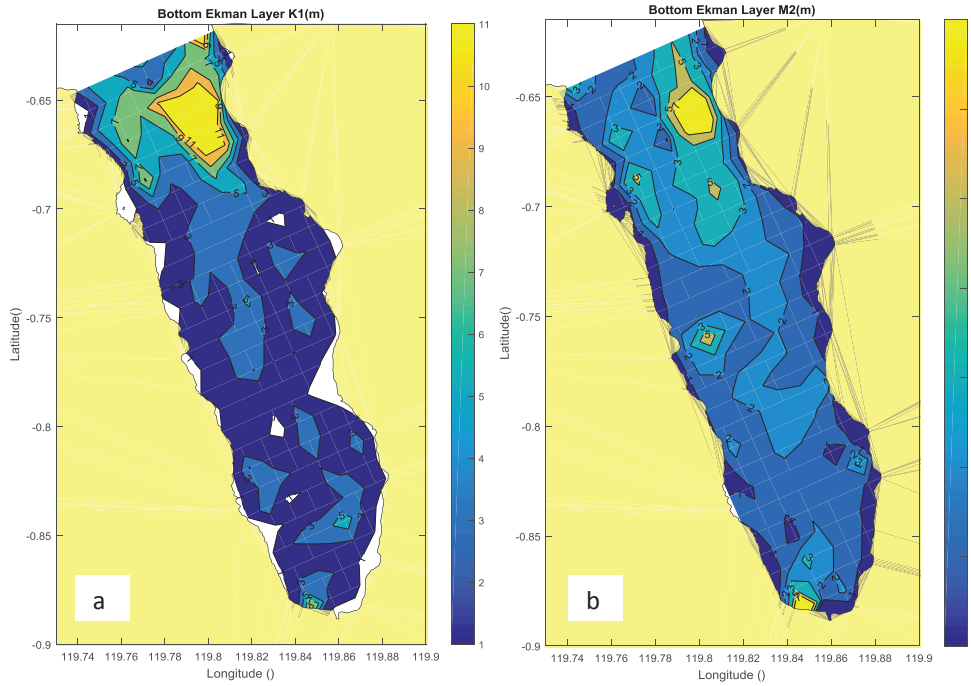

Fig. 9: Bottom Ekman layer by (a) Tidal constituent of K1, and (b) Tidal constituent of M2.

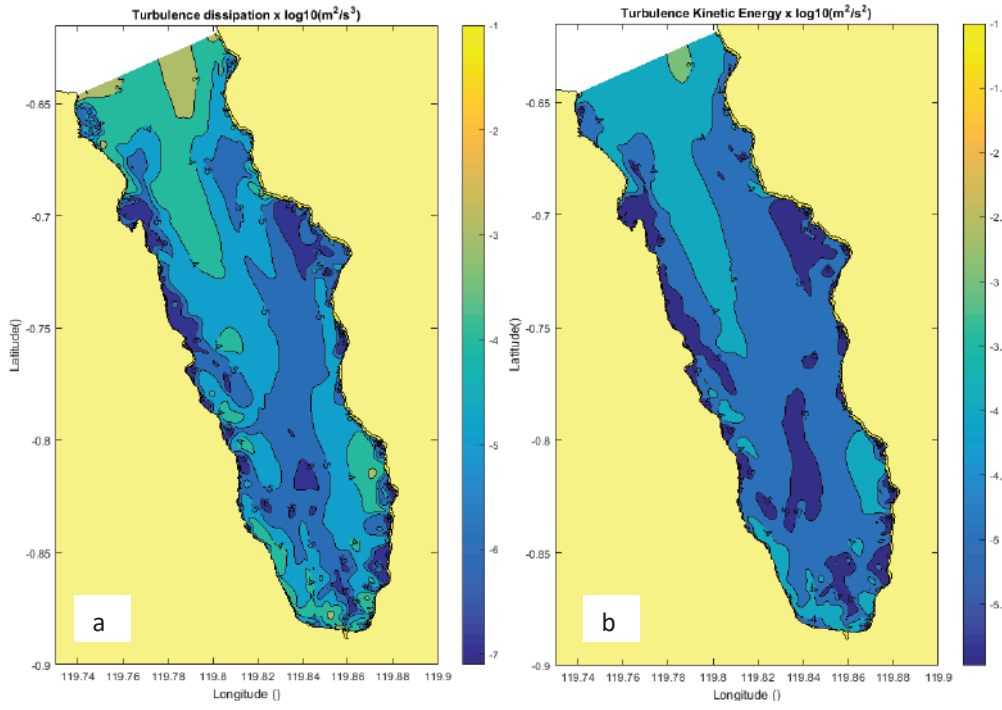

Fig. 10 (a): Turbulent dissipation (ε) (b) turbulent kinetic energy Palu Bay.

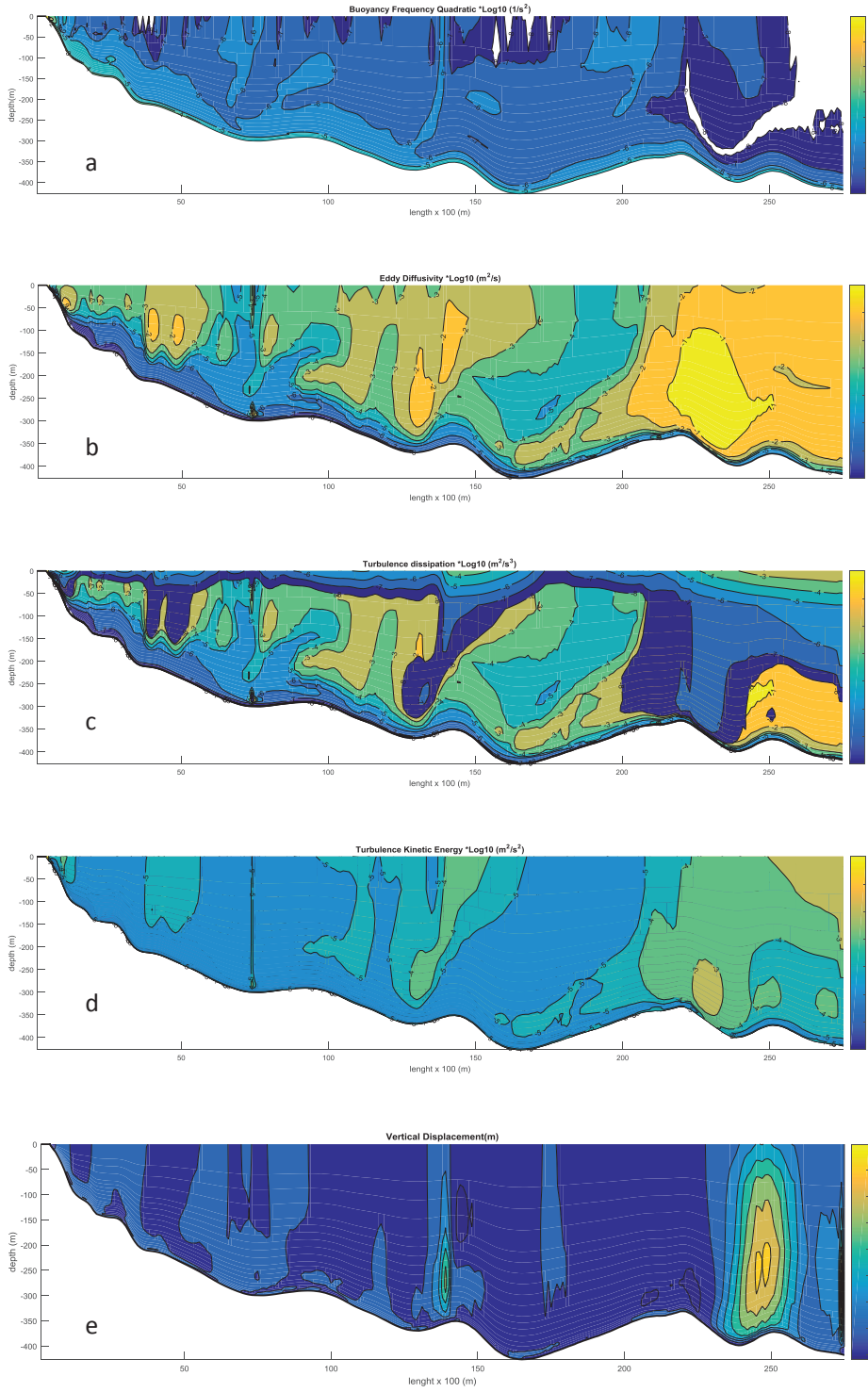

Fig. 11: Vertical slice of (a) buoyancy frequency, (b) eddy diffusivity, (c) turbulent dissipation, (d) turbulent kinetic energy, (e) vertical displacement in the waters of Palu Bay.

"η" is the elevation of the water level, "g" is acceleration of gravity, "h" is the depth of seawater, "T" is the period of tides, r_0 density of seawater. The results of the model show that M2 kinetic energy of turbulent (Fig. 7b) is greater than K1 (Fig. 7a) with the dominant energy vector to the north with large on the right side of Palu Bay.

***Turbulent kinetic energy*:** The kinetic energy in Palu Bay is at O (10^{-5}-10^{-3}) with high kinetic energy found around the rough topography in the 10^{-3} order around the mouth of Palu Bay (Fig. 11d), the roughness effect tends to lower the average velocity distribution and increase turbulent kinetic energy within the boundary layer (Rachman et al. 2011).

CONCLUSION

The tidal elevation amplitude of the model K1 ranges from 19.27 to 19.31 cm, high tidal amplitude at the point near the mouth of the Palu River, and low tidal amplitude at the open boundary of the model that leads to the Makassar Strait. The amplitude range of M2 tidal constituents is 55.55 - 55.75 cm, high tidal amplitude at the mouth of Palu Bay and the end of Palu Bay and the slope area. The tidal current of the K1 constituent is strengthened at the open boundary of the model and weakened when it enters Palu Bay which then amplify near the mouth of the Palu River because of its extreme siltation. Tidal currents strengthen in the mouth area and the tip of Palu Bay by propagation of the tidal constituent M2 and the area in the slope along the coast of Palu Bay. The basic Ekman layer by the K1 constituent can reach 11 meters while the M2 constituent reaches 7 meters. In the slope area also found the buoyancy frequency with the order of 10^{-5} which is at a depth of 75-150 m. The kinetic energy in Palu Bay stands at O (10^{-5}-10^{-3}) with the highest kinetic energy found in the rough topography of the mouth of Palu Bay in the order of 10^{-3}.

REFERENCES

Baumert, H.Z., Simpson, J. and Sündermann, J. 2005. Marine Turbulence: Theories, Observations, and Models. Cambridge University Press.

Bayong T. 1999. Klimatologi Umum. Penerbit ITB Bandung.

Carbajal, N. and Backhaus, J. 1998. Simulation of tides, residual flow and energy budget in the Gulf of California. Oceanologica Acta., 21(3): 429-446.

Fortin, W.F., Holbrook, W.S. and Schmitt RW. 2016. Mapping turbulent diffusivity associated with oceanic internal lee waves offshore Costa Rica. Ocean Sci., 12: 601-612.

Gargett, A.E. and Holloway, G. 1984. Dissipation and diffusion by internal wave breaking. Journal of Marine Research, 42(1):15-27.

He, R. and Weisberg, R.H. 2002. Tides on the west Florida shelf. J. of Physical Oceanography, 32(12): 3455-3473.

Holt, J., Butenschon M., Wakelin S., Artioli Y. and Allen J. 2012. Oceanic controls on the primary production of the northwest European continental shelf: Model experiments under recent past conditions and a potential future scenario. Biogeosciences, 9: 97-117.

Hordoir, R., Höglund, A., Pemberton, P. and Schimanke, S. 2018. Sensitivity of the overturning circulation of the Baltic Sea to climate change, a numerical experiment. Climate Dynamics, 50(3-4): 1425-1437.

Jayne, S.R. and St Laurent, L.C. 2001. Parameterizing tidal dissipation over rough topography. Geophysical Research Letters, 28(5): 811-814.

Kartadikaria, A., Miyazawa, Y., Varlamov, S. and Nadaoka, K. 2011. Ocean circulation for the Indonesian seas driven by tides and atmospheric forcings: Comparison to observational data. Journal of Geophysical Research: Oceans, 116(C9).

Koropitan, A.F. and Ikeda, M. 2008. Three-dimensional modelling of tidal circulation and mixing over the Java Sea. Journal of Oceanography, 64(1): 61-80.

Ledwell, J., Montgomery, E., Polzin, K., Laurent, L.S., Schmitt, R. and Toole, J. 2000 Evidence for enhanced mixing over rough topography in the abyssal ocean. Nature, 403(6766): 179.

Lyard, F., Lefevre, F., Letellier, T. and Francis, O. 2006. Modelling the global ocean tides: Modern insights from FES2004. Ocean Dynamics, 56(5-6): 394-415.

Marín, V.H., Tironi, A., Paredes, M.A. and Contreras, M. 2013. Modelling suspended solids in a Northern Chilean Patagonia glacier-fed fjord: GLOF scenarios under climate change conditions. Ecological Modelling, 264: 7-16.

McGowan, J.A. and Hayward, T.L. 1978. Mixing and oceanic productivity. Deep Sea Research, 25(9): 771-793.

Merrifield, M.A. and Holloway, P.E. 2002. Model estimates of M2 internal tide energetics at the Hawaiian Ridge. Journal of Geophysical Research: Oceans, 107(C8): 5-1-5-12.

Nagai, T. and Hibiya, T. 2015. Internal tides and associated vertical mixing in the Indonesian Archipelago. Journal of Geophysical Research: Oceans, 120(5): 3373-3390.

Nash, J.D., Kunze, E., Toole, J.M. and Schmitt, R.W. 2004. Internal tide reflection and turbulent mixing on the continental slope. Journal of Physical Oceanography, 34(5): 1117-1134.

Neves, R. 2007. Numerical models as decision support tools in coastal areas. In: Di Dalam (ed.) Assessment of the Fate and Effects of Toxic Agents on Water Resources, Springer, pp. 171-195.

Nikurashin, M., Vallis, G.K. and Adcroft, A. 2013. Routes to energy dissipation for geostrophic flows in the Southern Ocean. Nature Geoscience, 6(1): 48.

Pawlowicz, R., Beardsley, B. and Lentz, S. 2002. Classical tidal harmonic analysis including error estimates in MATLAB using T_TIDE. Computers & Geosciences, 28(8): 929-937.

Pichon, A. and Correard, S. 2006. Internal tides modelling in the Bay of Biscay. Comparisons with observations. Scientia Marina, 70(S1): 65-88.

Pingree, R.D. and Mardell, G. 1981. Slope turbulence, internal waves and phytoplankton growth at the Celtic Sea shelf-break. Phil. Trans. R. Soc. Lond. A., 302(1472): 663-682.

Rachman, T., Suntoyo, S., Sambodho, K., Armono, H.D. and Yusroni, E. 2011. Numerical modelling of turbulent bottom boundary layer over rough bed under irregular waves. IPTEK The Journal for Technology and Science, 22(4): 177-189.

Robertson, R. and Ffield, A. 2005. M2 Baroclinic tides in the Indonesian seas. Oceanography-Washington Dc-Oceanography Society, 18(4): 62.

Rusdin, A., Abu, A., R. Kalawawo, P. 2014. Effect of debit on Palu River based sediment movements. National Civil Engineering Conference.

Sabhan, Koropitan A. F., Purba M., Pranowo W. S., Rusydi M. 2019 Numerical model of ocean currents, sediment transport, and geomorphology due to reclamation planning in Palu Bay. AES Bioflux 11(2): 87-96.

Schafstall, J., Dengler, M., Brandt, P. and Bange, H. 2010. Tidal-induced mixing and diapycnal nutrient fluxes in the Mauritanian upwelling region. Journal of Geophysical Research: Oceans, 115(C10).

Sharples, J., Moore, C.M. and Abraham, E.R. 2001. Internal tide dissipation, mixing, and vertical nitrate flux at the shelf edge of NE New Zealand. Journal of Geophysical Research: Oceans, 106(C7): 14069-14081.

Toole, J.M., Schmitt, R.W. and Polzin, K.L. 1994. Estimates of diapycnal mixing in the abyssal ocean. Science, 264(5162): 1120-1123.

Versteeg, H.K. and Malalasekera, W. 2007. An Introduction to Computational Fluid Dynamics: The Finite Volume Method. Pearson Education, Pearson Education Limited

Wunsch, C. 1968. On the propagation of internal waves up a slope. Deep Sea Research and Oceanographic, 15: 251-258.

Xing, J. and Davies, A.M. 2009. Influence of bottom frictional effects in sill regions upon lee wave generation and implications for internal mixing. Ocean Dynamics, 59(6): 837-861.

Zhurbas, V., Väli, G., Golenko, M. and Paka, V. 2018. Variability of bottom friction velocity along the inflow water pathway in the Baltic Sea. Journal of Marine Systems, 184: 50-58.

Nature Environment and Pollution Technology
An International Quarterly Scientific Journal

p-ISSN: 0972-6268
e-ISSN: 2395-3454

Vol. 18 | No. 4 | pp. 1095-1106 | 2019

Original Research Paper | Open Access

Mapping of Terrestrial Gamma Radiation in Soil Samples at Baghdad Governorate (Karakh Side), Using GIS Technology

Ali Abid Abojassim and Leith Hani Rasheed
University of Kufa, Faculty of Science, Department of Physics, Al-Najaf, Iraq

Nat. Env. & Poll. Tech.
Website: www.neptjournal.com

Received: 14-02-2019
Accepted: 30-04-2019

Key Words:
Terrestrial radiation
Gamma ray
GIS
NaI(Tl)
Baghdad Governorate

ABSTRACT

The radioactive field is one of the most important areas in human health. It must be studied to see the changes in the doses of human exposure. In this study, 46 soil samples were collected from different locations of Karakh side at Baghdad Governorate. The specific activity of natural radionuclides (terrestrial gamma radiation) ^{238}U, ^{232}Th and ^{40}K for soil samples were measured using gamma-ray spectroscopy with NaI(Tl) ("3×3") detector in low-background. Moreover, ten radiological hazard parameters, which include radium equivalent activity (Ra_{eq}), absorbed gamma dose rate (Dγ), external hazard index (H_{ext}), internal hazard index (H_{int}), representative gamma index ($I_{γr}$), annual effective dose equivalent (AEDE) that includes the indoor and outdoor effective dose rate, and ELCR were calculated. It has also used GIS technology for mapping specific activity and radiological radiation parameters for all the samples under study. The results show that, the average value of specific activity of terrestrial gamma radiation ^{238}U, ^{232}Th, ^{40}K, ^{238}U+^{232}Th+^{40}K and ^{235}U were 16.47±0.94 Bq/kg, 9.72±0.43 Bq/kg, 367.95±11.13 Bq/kg, 394.15±11.90 Bq/kg and 0.76±0.043 Bq/kg respectively. While, the average value of radiological radiation parameters such as Ra_{eq}, H_{ex}, H_{in}, $I_{γr}$, $I_{α}$, Exposure, D_r, AGED, $AEDE_{indoor}$, $AEDE_{outdoor}$, $AEDE_{total}$, and ELCR in present study were 58.7183±2.017 Bq/kg, 0.1586±0.00546, 0.2032±0.00768, 0.4523±0.0151, 0.08237±0.0046, 3.367±0.113 μR/h, 28.8309±0.968 nGy/h, 207.1078±6.86 mSv/y, 0.1415±0.00475 mSv/y, 0.03541±0.00119 mSv/y, 0.177±0.00594 mSv/y and 0.6192 ±0.0208 respectively. The results indicate that the effective dose from terrestrial gamma radiation is everywhere across the area within the acceptable level, subject to the inherent spatial averaging of the measurements.

INTRODUCTION

The annual exposure of human population to radioactive radiations from all natural and artificial sources is regularly evaluated in the world. Natural radioactivity arises mainly from primordial radionuclides, such as ^{40}K and the nuclides from the ^{232}Th, ^{238}U series and their decay products, which occur at trace levels in all ground formations on the earth (Spinks et al. 1990). The study of natural radioactivity is important because naturally occurring radioactive materials (NORM) can serve as good biochemical and geochemical tracers in environment in case of geological events such as earthquakes and eruptions volcanic (Cherry et al. 2012). Gamma radiation emitted from natural radioactive isotopes, such as ^{238}U and ^{232}Th series and decomposition products and ^{40}K, which are found in trace levels in all land configurations, is the main external source of radiation to the human body. Gamma-ray emissions externally cause the risk exposure and internally cause inhalation of radon (Ting 2010, Clavensjö & Åkerblom 1992). Natural radioactivity and associated external exposure due to gamma radiation depend mainly on the local geographical and geological conditions that appear on different levels in every region of the world. The rate of natural gamma dose is an important contributor to the medium dose that the world's population receives (Eisenbud & Gesell 1997, White & Pharoah 2014). This terrestrial component arises due to primordial radionuclides that were synthesized during the creation of the planet, and has always accompanied life on the Earth. Both, humans and biota are exposed to an annual dose rate. Since, the natural flux is largely determined by soil and associated parent geological material, personal annual exposure to terrestrial gamma radiation is determined by the home location, the localities visited and the amount of time spent indoors and outdoors within a geological framework. Terrestrial gamma dose rates largely reflect the natural variation of potassium, uranium and thorium across the environment. The data sets provide a basis for studies of dose rates derived from both NORMs (naturally occurring radioactive materials) and TENORMs (technologically enhanced naturally occurring radioactive materials) (Bauer & Westfall 2011). The soil is one of the main contributors to background radiation. It is very interesting to know the radioactivity content of the soil over the world (Hayde 1994). Therefore, the knowl-

edge of natural radioactivity of soil evaluation of radiation risks is important. Measurement of natural radioactivity in the soil is of great importance to many researchers all over the world, which led to a worldwide national survey in the past two decades. The measurement of natural radioactivity in the soil is very significant to determine the amount of changes in the natural background activity with due time or radioactivity leak (Sroor et al. 2001). Geostatistical techniques are useful components of GIS applications that are frequently applied. Geostatistics involves the analysis and estimation techniques which have been used to obtain the value of a variable dispersed in time and location. Many research and mappings have been done at different locations of countries in the world for natural radioactivity in soil samples using GIS technology (Doğan 2010, Hassan 2012, Yang et al. 2017, Çam et al. 2012, Einas et al. 2012). For this reason, the main purpose of this work is to evaluate the terrestrial gamma radiation in soil samples from most districts of Karakh side at Baghdad Governorate as well as to assess the health risks from background radiation through evaluating the ten radiological radiation parameters. Finally, it is drawn to establish the radiological map to be a reference for the next studies using GIS technical.

GEOLOGY OF BAGHDAD SOIL

Baghdad is located in central Iraq at coordinates latitude 33°18'03.56''N, longitude 44°25'07.11''E, which is located between the coordinates latitude 33°31'53.29''N, longitude 44°20'14.12''E at the entrance of the Tigris River from the north, and coordinate latitude 33°5'74.43''N, longitude 44°31'45.44''E at the exit of the Tigris River from the south. The range of height above sea level of Baghdad is 29-44m. Generally, the soil of Baghdad area has been derived from around areas especially Mesopotamian plain and the desert (Hatab et al. 1986). Most soils of Baghdad area are therefore secondary soils (residual soils) derived from the above regions, transported from the place of weathering and accumulated as a result of sedimentation. Besides, Baghdad soil strata are affected by river course changes during previous decades leading to coarse silt deposits and giving different depositional stratigraphy every few meters. Thus, Baghdad strata are erratic, somewhat nonhomogeneous with a water table near ground. This soil, generally, is alkaline with poor permeability (Albusoda 2016). Baghdad soil is characterized by its high salinity due to dryness, rainfall scarcity and evaporation leading to groundwater upward movement and causing fluctuation of groundwater levels in the area (Hatab et al. 1986). Baghdad lies in the middle of Iraq within the Mesopotamian Plain. The Tigris River passes through the city dividing it into two parts; Karkh and Rasafa. The study area is restricted to Karkh area which it is located at latitudes (33°19'-33°31'N) and longitudes (44°24'-44°40'E) with an area of about 1350km^2 approximately (Fig. 1). Karkh is historically the name of the western half of Baghdad, Iraq, or alternatively, the western shore of the Tigris River as it ran through Baghdad. In a more limited sense, Karkh is one of nine administrative districts in Baghdad, with Mansour district to the west, Kadhimiya district to the northwest, and the Tigris to the north, east and south. The Green Zone (International Zone) is in this district.

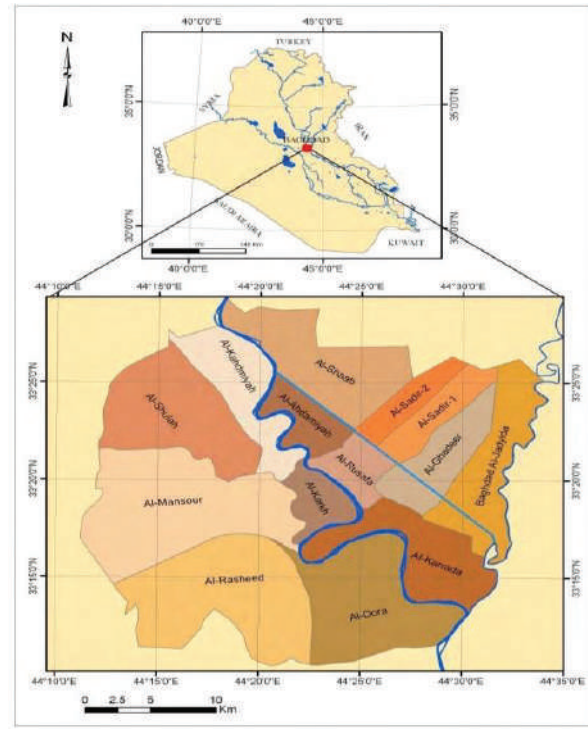

Fig. 1: Location map of the study area.

MATERIALS AND METHODS

Sample Collection and Preparation

In this study, 46 samples of soil were collected from 46 areas of Karakh side from Baghdad governorate. The collected samples were transferred to labelled closed polyethylene bags and taken to the laboratory of radiation detection and measurement in the Physics Department, Faculty of Science, University of Kufa. The sample codes, locations, and coordinates by GPS are given in Table1 .

The samples with the mean weight of 1kg were collected at the depth of 15cm from the upper layer using a plastic cup and then put in plastic bags. Prior to the analysis, the samples were dried, crushed and homogenized. Thereafter, before subjecting the samples to gamma spectrometer,

Table 1: Location name, sample codes, and coordinates.

No.	Location name	Sample code	Coordinates (° ' ")	
1	Aamiriya	K1	33 18 09.9 N	44 17 03.0 E
2	Shuala	K2	33 22 03.7	44 16 30.3
3	AL- Jamaah	K3	33 19 06.3	44 19 08.1
4	Near halib biladi	K4	33 19 32.9	44 10 06.8
5	Near Taji gas	K5	33 26 17.4	44 16 13.1
6	Al- washash	K6	33 19 32.2	44 21 10.4
7	Tarmiyah	K7	33 40 22.5	44 23 56.8
8	College of Agriculture – Abu Ghraib	K8	33 18 36.0	44 12 52.8
9	Sabaa Al Bour	K9	33 27 46.0	44 09 09.9
10	Jhazaliya	K10	33 20 31.8	44 16 36.0
11	Tajyat	K11	33 22 33.5	44 24 47.8
12	Shurtah 4^{th}	K12	33 14 48.5	44 18 34.9
13	Kadhimiya	K13	33 22 12.2	44 20 38.5
14	Khan Dhari	K14	33 17 54.1	44 03 31.1
15	Dora Refinry	K15	33 15 41.5	44 25 10.3
16	Shuhada Al Sydia	K16	33 14 06.3	44 21 07.3
17	Latifiya	K17	32 57 47.8	44 21 20.1
18	AL-Rasheed	K18	33 07 00.8	44 22 03.2
19	Abu Disher	K19	33 12 33.2	44 22 58.8
20	Al Alam	K20	33 14 50.6	44 20 38.3
21	Shati Tajiyat	K21	33 24 10.1	44 19 33.6
22	AL- Taifiya	K22	33 21 09.9	44 21 53.1
23	Quirish	K23	33 10 57.8	44 21 50.6
24	AL- Aamel	K24	33 16 42.2	44 19 28.6
25	Abu Ghraib	K25	33 18 12.8	44 10 08.4
26	Allawi	K26	33 19 37.3	44 23 03.3
27	Toma	K27	33 15 18.0	44 23 36.5
28	Qadissiya	K28	33 16 51.2	44 21 24.8
29	AL-Raay	K29	33 13 54.8	44 19 23.8
30	Mansour	K30	33 18 53.2	44 20 48.7
31	Harthiya	K31	33 18 12.6	44 21 54.6
32	AL- Jihad	K32	33 16 18.5	44 17 17.9
33	Shaqaq AL- Salam	K33	33 15 49.9	44 18 52.2
34	Suwaib	K34	33 13 18.6	44 17 44.2
35	Manshaet Nasr (Taji)	K35	33 35 17.9	44 13 56.3
36	Project 14 Ramadan	K36	33 44 48.2	44 19 23.3
37	Shuhada Abu Ghraib	K37	33 18 17.6	44 07 33.8
38	Hurriya	K38	33 21 14.7	44 19 07.3
39	Malef	K39	33 12 53.3	44 19 29.6
40	AL- Mekanek	K40	33 13 41.8	44 24 22.7
41	Mahmudiyah	K41	33 03 14.8	44 21 27.0
42	AL- Sahaa	K42	33 13 31.9	44 23 42.3
43	Rahmaniya	K43	33 20 34.3	44 22 19.8
44	Bayaa	K44	33 16 23.1	44 20 43.3
45	Saidya	K45	33 15 34.9	44 21 09.7
46	Al Radwan Company	K46	33 19 33.9	44 01 30.7

the containers were sealed for a month to ensure the secular equilibrium between ^{226}Ra, ^{232}Th, and their progenies (Al-Hamidawi 2014).

Gamma Radiation Measurement

The samples were placed directly on the NaI(Tl) detector (3"×3") crystal dimension and the supplier of the company (Alpha Spectra, Inc.-12I12/3) for the gamma analysis. The exposure time for each sample to the detector was 5 hours (Al-Hamidawi 2014, Abojassim et al. 2016, Mirza et al. 2017). Three types of calibrations including energy, resolution, and efficiency calibrations were performed for gamma spectrometer**.** The ^{152}Eu, ^{137}Cs, ^{60}Co, ^{22}Na and ^{54}Mn standard sources were used for efficiency calibration which was produced in Amersham International Plc. (U.K.). The parallel measurements of the International Atomic Energy Agency (IAEA) intercomparison sediment samples (IAEA-300 and IAEA-315) were used for checking the precision and accuracy. An empty polyethylene container with the same geometry and measuring conditions as those used for the samples to determine the background due to the existence of natural radionuclides in the environment. The uncertainties in the calibration of the peak areas of these photopeaks were ±2% (Harb 2004). The specific activity of the samples adopted on the Bismuth (^{214}Bi) at energy 1764.5keV is equivalent to the specific activity of Uranium (^{238}U). While the specific activity adopted on the Thallium (^{208}Tl) at energy 2614keV is equivalent to the specific activity of Thorium (^{232}Th). The specific activity concentrations of radionuclides ^{40}K have been calculated by using the energy 1460.80keV (Mirza et al. 2017, Abojassim 2017).

CALCULATIONS

Specific Activity (A): The specific activity (activity concentration) of the gamma-emitting radionuclides in the sample can be calculated from the following equation (Al-Hamidawi 2014, Abojassim et al. 2016, Mirza et al. 2017):

$$A\left(\frac{Bq}{kg}\right)=\frac{N}{I_\gamma\,\varepsilon\,M\,T} \qquad \ldots(1)$$

Where, A is the specific activity of the radionuclide in the sample, N is the net area under photopeak, I_γ is the probability of gamma decay, ε is the efficiency of the gamma-ray detector, M is the weight of the measured sample in Kg, and T is the life time for collecting the spectrum in seconds. But, the specific activity of ^{235}U was calculated by (Harb 2004, Abojassim 2017):

$$A_{235_U}=\frac{A_U}{21.7} \qquad \ldots(2)$$

External hazard index (H_{ex}): The external hazard index for samples under investigation is given by the following equation (Krieger 1981):

$$H_{ex}=\frac{A_U}{370}+\frac{A_{Th}}{259}+\frac{A_K}{4810} \qquad \ldots(3)$$

Where, A_U, A_{Th} and A_k are the specific activity of ^{238}U, ^{232}Th and ^{40}K, respectively.

Internal hazard index (H_{in}): Internal exposure to ^{222}Rn and its radioactive progeny is controlled by the internal hazard index. It can be calculated according to the following equation (Venturini & Nisti 1997):

$$H_{in}=\frac{A_U}{185}+\frac{A_{Th}}{259}+\frac{A_K}{4810} \qquad \ldots(4)$$

Representative Level Index (I_γ): Radiation hazards due to the specified radionuclides of ^{238}U(^{226}Ra), ^{232}Th and ^{40}K were assessed by another index called representative level index ($I_{\gamma r}$), The following equation can be used to calculate $I_{\gamma r}$ for soil samples under the study (Abojassim 2017).

$$I_{\gamma r}=\left(\frac{1}{150}\right)A_U+\left(\frac{1}{100}\right)A_{Th}+\left(\frac{1}{1500}\right)A_K \qquad \ldots(5)$$

Alpha index (Iα**)**: Alpha index has been developed to assess the excess alpha radiation due to the radon inhalation originating from building materials. The alpha-indexes were determined using the equation below (Krieger 1981):

$$I_\alpha=\frac{A_U}{200\left(\frac{Bq}{kg}\right)} \qquad \ldots(6)$$

Radium Equivalent Activity (Ra_{eq}): The radiological hazard associated with samples contained radionuclides, namely ^{238}U, ^{232}Th, and ^{40}K, can be assessed using a common radiological index, called radium equivalent activity. It can be expressed mathematically as (Abojassim et al. 2017):

$$Ra_{eq}\left(\frac{Bq}{kg}\right)=A_U+1.43\,A_{Th}+0.077\,A_K \qquad \ldots(7)$$

Exposure rate ($\dot{X}$) : The gamma ray exposure rate in air, at 1 m above an infinitely extended and thick slab, due to ^{238}U, ^{232}Th series and ^{40}K uniformly distributed in the material, is given by (Kahn et al. 1983, Venturini & Nisti 1997):

$$\dot{X}\left(\frac{\mu R}{h}\right)=1.90\,A_U+2.82\,A_{Th}+0.197\,A_K \qquad \ldots(8)$$

Where, $\dot{X}$ is the exposure rate (μR/h), the activity concentrations are given in pCi/g. The constants on the right-

hand side of Equation 8 are related to the average gamma ray energies for each radionuclide or series.

Absorbed Dose Rate in Air (D_r): The main contribution to the absorbed dose rate in the air comes from terrestrial gamma-ray radionuclides present in trace amounts in the soil, the measurements of dose rate depend on measurements of specific activity concentrations of radionuclides, mainly ^{238}U, ^{232}Th and ^{40}K. The UNSCEAR 2008 report explains that the absorbed dose rate in air 1 meter above the ground surface can be given by (UNSCEAR 2008):

$$D_r\left(\frac{nGy}{h}\right) = 0.462\,A_U + 0.604\,A_{Th} + 0.0417A_K \quad \ldots(9)$$

Annual gonadal equivalent dose (AGED): According to UNSCEAR (1988), the gonads are considered as the organs of the interest. However, the annual gonadal equivalent dose (AGED) for the residents in the study area due to the specific activities of ^{238}U, ^{232}Th and ^{40}K was calculated using Equation 10 given by Arafa (2004) and Okogbue & Nweke (2018) as:

$$AGED\left(\frac{mSv}{y}\right) = 3.09\,A_U + 4.18\,A_{Th} + 0.314A_K \quad \ldots(10)$$

Annual Effective Dose Equivalent (AEDE): The annual effective dose equivalent (AEDE) can be calculated from the absorbed dose by applying the dose conversion factor of 0.7 (Sv/Gy) with an outdoor occupancy factor of 0.2 and 0.8 for indoor (UNSCEAR 1993, UNSCEAR 2000).

$$AEDE_{outdoor}\left(\frac{mSv}{y}\right) = \left[D_r\,(mGy/hr)\times 8760\,hr\times 0.2\times 0.7Sv/Gy\right]\times 10^{-6} \quad \ldots(11)$$

$$AEDE_{indoor}\left(\frac{mSv}{y}\right) = \left[D_r\,(mGy/hr)\times 8760\,hr\times 0.8\times 0.7Sv/Gy\right]\times 10^{-6} \quad \ldots(12)$$

Excess Lifetime Cancer Risk (ELCR): This gives the probability of developing cancer over a lifetime at a given exposure level, considering 70 years as the average duration of life for human being. It is given as (Al-Hamidawi 2014, Abojassim et al. 2017):

$$ELCR = AEDE\times DL\times RF \quad \ldots(13)$$

Where, AEDE is the total of Annual Effective Dose Equivalent ($AEDE_{outdoor}$ + $AEDE_{indoor}$), DL is the average Duration of Life (estimated to be 70 years) and RF is the Risk Factor (Sv), i.e. fatal cancer risk per Sievert. For stochastic effects, ICRP uses RF as 0.05 for the public.

RESULTS AND DISCUSSION

The specific activities of radionuclides ^{238}U, ^{232}Th, ^{40}K and ^{235}U were measured in selected soil samples from different locations of Karakh side from Baghdad governorate and their radiation hazard parameters are listed in Table 2. The comparison between the specific activity in Bq/kg for all the samples is shown in Fig. 2, which is drawn by GIS technology. From Table 2, the specific activity of ^{238}U ranged from 3.16±0.31 Bq/kg in sample K15 to 33.33±0.92 Bq/kg in sample K28 with the mean value of 16.47±0.94 Bq/kg. However, the specific activity of ^{232}Th varied from 2.41±0.16 Bq/kg in sample K19 to 15.92±0.39 Bq/kg in sample K38 with the mean value of 9.72±0.43. In addition, the values of ^{40}K were 171.50±2.35 Bq/kg in sample K16 and 496.78±3.71 in sample K43 with the mean value of 367.95±11.13, while for ^{235}U were ranged 0.15-1.54 Bq/kg with the mean value of 0.76±0.043. In general, the activity concentrations indicate that $^{40}K > ^{238}U > ^{232}Th$. This agrees that the association among the radionuclides may be because uranium and thorium decay series come from the same origin and exist together in nature. Whereas potassium is from a different origin (Tanaskovic et al. 2012). The errors as noted in the table include the statistical uncertainty in the peak area, calibration and counting errors. The UNSCEAR recommended standard indicate that the worlds average specific activity of ^{238}U, ^{232}Th and ^{40}K are 33 Bq/kg, 45 Bq/kg and 420 Bq/kg respectively (UNSCEAR 2008). It was found that all the values of ^{238}U specific activities were lower than the world's average activity recommended by UNSCEAR (2008) as shown in Fig. 3. Also, as shown in Fig. 3, which is drawn by GIS technology, all values of specific activity of ^{232}Th were within the UNSCEAR (2008) report. While, for ^{40}K, it is clear that the specific activities, with the exception of K7, K21, K25, K26, K28, K31, K32, K35, K36, K38, K43 and K44 samples were only found to be higher than the worldwide average, as shown in Fig. 4 which is drawn by GIS technology. In some samples, the values are more than the highest allowable concentration in the region because of the increase in the concentration of potassium nuclide in some areas of the region which is due to the existence of agricultural land and areas containing phosphate fertilizers in which the focus increasingly peer-potassium (^{40}K). The values obtained for radium equivalent activity (Ra_{eq}), external hazard index (H_{ex}), internal hazard index (H_{in}), representative level index ($I_{\gamma r}$) and alpha index (I_{α}) are presented in Table 3. As can be seen from Table 2, the radium equivalent activity (Ra_{eq}) values for soil samples varied from 24.95 to 86.46 Bq/kg with an average 58.7183 ±2.017 Bq/kg. All the values are lower than 370 Bq/kg (OECD 1979). It may be concluded that

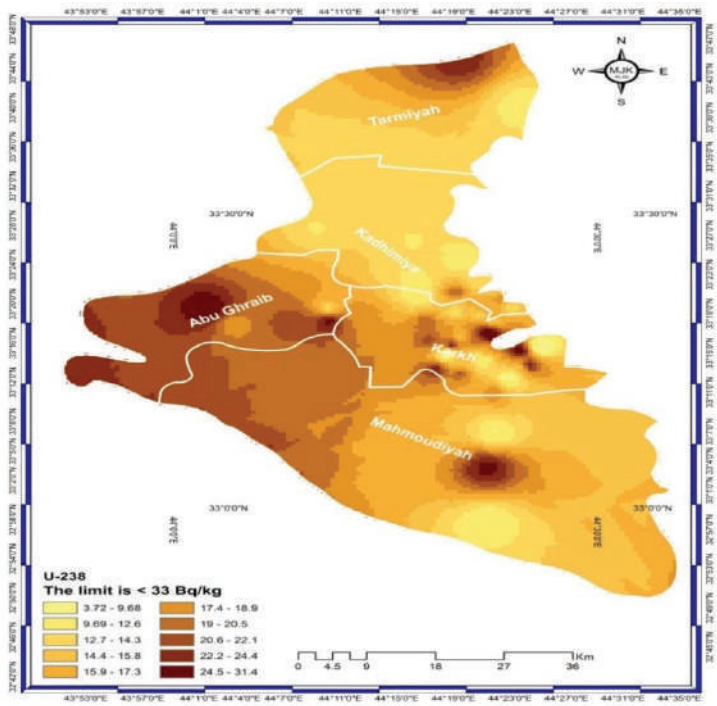

Fig. 2: The choropleth maps of the values of specific activity of ^{238}U and comparison of the results with word average activity UNSCEAR (2008).

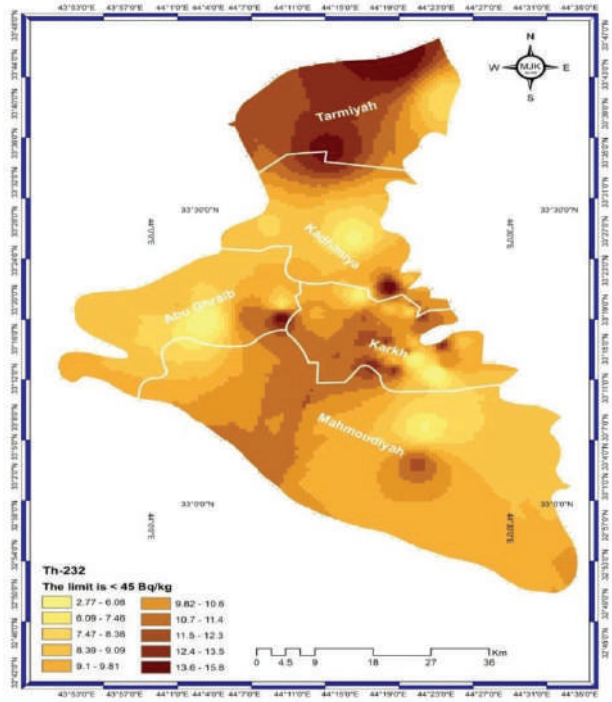

Fig. 3: The choropleth maps of the values of specific activity of ^{232}Th and comparison of the result with word average activity UNSCEAR (2008).

Table 2: Specific Activity of ^{238}U, ^{232}Th, ^{40}K and ^{235}U with their uncertainties.

Sample code	Specific Activity in (Bq/kg)				
	^{238}U	^{232}Th	^{40}K	$^{238}U + ^{233}Th + ^{40}K$	^{235}U
K1	20.44±0.78	11.48±0.35	367.45±3.44	399.37	0.94
K2	10.91±0.57	9.66±0.32	379.70±3.50	400.27	0.50
K3	12.46±0.61	8.69±0.31	312.56±3.17	333.71	0.57
K4	13.80±0.64	7.17±0.28	325.62±3.24	346.59	0.64
K5	12.49±0.61	5.60±0.25	346.32±3.34	364.41	0.58
K6	17.04±0.71	11.26±0.35	360.03±3.41	388.33	0.79
K7	11.23±0.58	7.51±0.29	440.26±3.77	459	0.52
K8	17.70±0.73	9.66±0.32	319.49±3.21	346.85	0.82
K9	12.46±0.61	8.21±0.30	401.50±3.60	422.17	0.57
K10	10.04±0.55	5.54±0.25	318.85±3.21	334.43	0.46
K11	11.38±0.58	6.22±0.26	347.55±3.35	365.15	0.52
K12	5.87±0.42	9.44±0.32	320.78±3.22	336.09	0.27
K13	12.93±0.62	8.64±0.31	343.32±3.33	364.89	0.60
K14	17.79±0.73	4.15±0.21	290.60±3.06	312.54	0.82
K15	3.16±0.31	8.58±0.31	339.45±3.31	351.19	0.15
K16	9.68±0.54	3.58±0.20	171.50±2.35	184.76	0.45
K17	10.16±0.55	9.73±0.33	285.15±3.03	305.04	0.47
K18	9.59±0.53	5.89±0.25	263.35±2.91	278.83	0.44
K19	6.59±0.44	2.41±0.16	193.72±2.50	202.72	0.30
K20	12.34±0.61	11.23±0.35	298.21±3.10	321.75	0.57
K21	10.46±0.56	9.34±0.32	475.93±3.92	495.73	0.48
K22	15.20±0.67	9.37±0.32	367.51±3.44	392.08	0.70
K23	18.65±0.75	8.65±0.31	377.70±3.49	405	0.86
K24	15.11±0.67	10.50±0.34	402.95±3.60	428.56	0.70
K25	25.33±0.87	14.30±0.39	442.55±3.78	482.18	1.17
K26	12.96±0.62	10.42±0.34	465.81±3.88	489.19	0.60
K27	27.75±0.84	12.66±0.35	416.81±3.40	457.22	1.28
K28	33.33±0.92	11.48±0.33	476.84±3.64	521.65	1.54
K29	14.98±0.62	8.83±0.29	310.89±2.94	334.7	0.69
K30	13.50±0.59	7.32±0.26	217.10±2.46	237.92	0.62
K31	14.88±0.62	12.38±0.34	461.65±3.58	488.91	0.69
K32	21.48±0.74	12.07±0.34	430.25±3.46	463.8	0.99
K33	22.73±0.76	12.39±0.34	388.96±3.29	424.08	1.05
K34	24.23±0.79	13.39±0.36	412.12±3.38	449.74	1.12
K35	13.76±0.59	14.10±0.36	425.14±3.44	453	0.63
K36	23.77±0.78	15.53±0.38	461.29±3.58	500.59	1.10
K37	21.71±0.74	11.35±0.33	395.77±3.31	428.83	1.00
K38	20.28±0.72	15.92±0.39	454.60±3.55	490.8	0.93
K39	21.07±0.73	12.69±0.35	412.79±3.39	446.55	0.97
K40	23.80±0.78	10.24±0.31	263.46±2.70	297.5	1.10
K41	25.45±0.81	11.73±0.33	345.23±3.10	382.41	1.17
K42	15.42±0.63	10.46±0.31	385.22±3.27	411.1	0.71
K43	19.26±0.70	10.23±0.31	496.78±3.71	526.27	0.89
K44	20.31±0.72	9.64±0.30	421.45±3.42	451.4	0.94
K45	16.84±0.66	8.77±0.29	403.18±3.35	428.79	0.78
K46	27.49±0.84	9.11±0.29	388.41±3.28	425.01	1.27
Mean ± S.E.	16.47±0.94	9.72±0.43	367.95±11.13	394.15±11.90	0.76±0.043

the high activity concentration of Ra_{aq} is still in the range of the permissible level. The results of H_{ex}, H_{in}, $I_{\gamma r}$ and I_{α} (see Table 3) ranged from 0.067 to 0.234 with an average value of 0.1586 ±0.00546, from 0.085 to 0.239 with an average 0.2032 ±0.00768, from 0.197 to 0.655 with an average 0.4523±0.0151 and from 0.167 to 0.016 with an average 0.08237 ±0.0046 respectively. The results of hazard indexes (H_{ex}, H_{in}, $I_{\gamma r}$ and I_{α}) of all values for all the samples studied in this work are less than one which is the maximum value of the permissible safety limit recommended (EC1999). The results of exposure rate ($\dot{X}$), absorbed dose rate in air (D_r), annual gonadal equivalent dose (AGED), annual effective dose equivalent indoor, outdoor and total ($AEDE_{indoor}$, $AEDE_{outdoor}$, $AEDE_{total}$), excess lifetime cancer risk (ELCR) are listed in Table 4. The $\dot{X}$ found is the minimum values in sample K19 1.46 μR/h and the maximum values in sample K28 4.89 μR/h, with an average value of 3.367 ±0.113μR/h. The results of D_r ranges from 12.58nGy/h to 42.217nGy/h with an average value of 28.8309 ±0.968nGy/h. The values of D_r were smaller than the value of the world average, which is equal to 55 nGy/h according to UNSCEAR (2000). The values of AGED as given in Table 4 have ranged from 91.26 mSv/y to 300.70 mSv/y with an average of 207.1078 ±6.86mSv/y. The annual gonadal equivalent dose values are lower than when compared with the world average permissible limit of ≤ 300 mSv/y, as relates to radiation (Okogbue & Nweke 2018), except sample k28. The calculated values of $AEDE_{indoor}$, $AEDE_{outdoor}$ and $AEDE_{total}$ in this study ranged from 0.062mSv/y to 0.207mSv/y, with an average of 0.1415 ±0.00475mSv/y, from 0.015mSv/y to 0.052mSv/y with an average of 0.03541 ±0.00119mSv/y and from 0.077mSv/y to 0.259mSv/y with an average of 0.177 ±0.00594mSv/y respectively. Since, all the values of $AEDE_{indoor}$, $AEDE_{outdoor}$ and $AEDE_{total}$ are lower than the corresponding worldwide values of 0.42, 0.08 and 0.50 mSv/y respectively (ICRP 1993). The calculated excess lifetime cancer risk of this location is given in Table 4. These values vary from 0.270×10^{-3} to 0.907×10^{-3} with an average of $0.465\pm0.019\times10^{-3}$. According to these results, the values of ELCR are very less, therefore, it may be decided that the risk of cancer is negligible. The results of specific activity in natural radionuclides for the studied samples were lower than the world's average according to UNSCEAR (2008). As well as, the average specific activity of ^{238}U, ^{232}Th and ^{40}K in soil samples in Baghdad governorate (Karakh side) were compared with those from similar investigations in other countries and summary results are given in Table 5.

CONCLUSION

Geostatistical tools of ArcGIS software analysed terrestrial gamma radiation in soil samples at Baghdad Governorate (Karakh Side) pollution by element mapping. It was

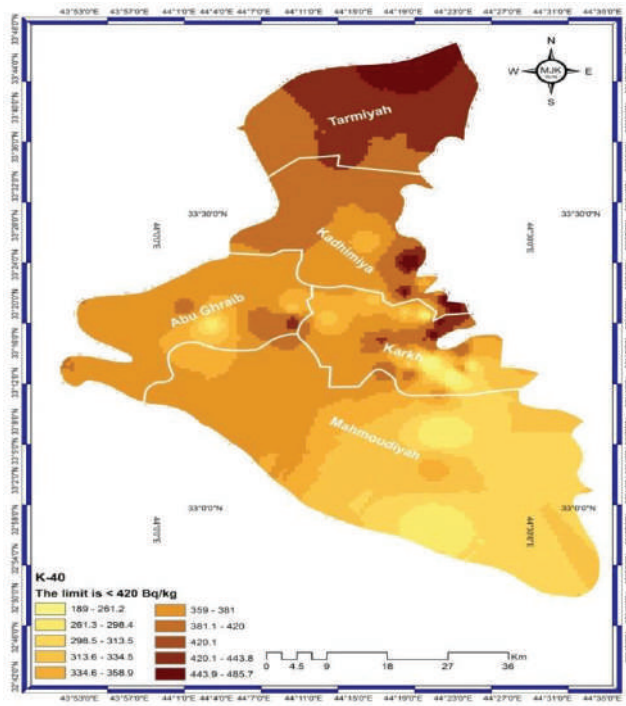

Fig. 4: The choropleth maps of the values of specific activity of ^{40}K and comparison of the results with word average activity UNSCEAR (2008).

Table 3: Results of Ra_{eq}, H_{ex}, H_{in}, $I_{\gamma r}$ and I_{α} in the present study.

Sample code	Ra eq (Bq/kg)	H_{ex}	H_{in}	$I_{\gamma r}$	$I_{\alpha\gamma}$
K1	65.15	0.176	0.231	0.496	0.102
K2	53.96	0.146	0.175	0.422	0.055
K3	48.95	0.132	0.166	0.378	0.062
K4	49.13	0.133	0.170	0.381	0.069
K5	47.16	0.127	0.161	0.370	0.062
K6	60.86	0.164	0.210	0.466	0.085
K7	55.87	0.151	0.181	0.443	0.056
K8	56.11	0.152	0.199	0.428	0.089
K9	55.12	0.149	0.183	0.433	0.062
K10	42.51	0.115	0.142	0.335	0.050
K11	47.04	0.127	0.158	0.370	0.057
K12	44.07	0.119	0.135	0.347	0.029
K13	51.72	0.140	0.175	0.401	0.065
K14	46.10	0.125	0.173	0.354	0.089
K15	41.57	0.112	0.121	0.333	0.016
K16	28.00	0.076	0.102	0.215	0.048
K17	46.03	0.124	0.152	0.355	0.051
K18	38.29	0.103	0.129	0.298	0.048
K19	24.95	0.067	0.085	0.197	0.033
K20	51.36	0.139	0.172	0.393	0.062
K21	60.46	0.163	0.192	0.480	0.052
K22	56.90	0.154	0.195	0.440	0.076
K23	60.10	0.162	0.213	0.463	0.093
K24	61.15	0.165	0.206	0.474	0.076
K25	79.86	0.216	0.284	0.607	0.127
K26	63.73	0.172	0.207	0.501	0.065
K27	77.95	0.211	0.286	0.589	0.139
K28	86.46	0.234	0.324	0.655	0.167
K29	51.55	0.139	0.180	0.395	0.075
K30	40.68	0.110	0.146	0.308	0.068
K31	68.13	0.184	0.224	0.531	0.074
K32	71.87	0.194	0.252	0.551	0.107
K33	70.40	0.190	0.252	0.535	0.114
K34	75.11	0.203	0.268	0.570	0.121
K35	66.66	0.180	0.217	0.516	0.069
K36	81.50	0.220	0.284	0.621	0.119
K37	68.41	0.185	0.243	0.522	0.109
K38	78.05	0.211	0.266	0.597	0.101

Table cont....

Sample code	Ra eq (Bq/kg)	H_{ex}	H_{in}	$I_{\gamma r}$	$I_{\alpha\gamma}$
K39	71.00	0.192	0.249	0.543	0.105
K40	58.73	0.159	0.223	0.437	0.119
K41	68.81	0.186	0.255	0.517	0.127
K42	60.04	0.162	0.204	0.464	0.077
K43	72.14	0.195	0.247	0.562	0.096
K44	66.55	0.180	0.235	0.513	0.102
K45	60.43	0.163	0.209	0.469	0.084
K46	70.42	0.190	0.265	0.533	0.137
Mean ± S.E.	58.71 ±2.01	0.158 ±0.005	0.203 ±0.007	0.45 ±0.01	0.082 ±0.004

Table 4: Results of D_r, Exposure, AGED, $AEDE_{indoor}$, $AEDE_{outdoor}$, $AEDE_{total}$, ELCR in the present study.

Sample code	Exposure (μR/h)	D_r (nGy/h)	AGED (mSv/y)	$AEDE_{indoor}$ (mSv/y)	$AEDE_{outdoor}$ (mSv/y)	AEDE (mSv/y)	ELCR×10^{-3}
K1	3.70	31.70	226.53	0.156	0.039	0.195	0.681
K2	3.13	26.71	193.32	0.131	0.033	0.164	0.574
K3	2.81	24.04	172.97	0.118	0.030	0.148	0.516
K4	2.83	24.28	174.86	0.119	0.030	0.149	0.522
K5	2.74	23.59	170.75	0.116	0.029	0.145	0.507
K6	3.47	29.69	212.77	0.146	0.036	0.182	0.638
K7	3.28	28.08	204.33	0.138	0.034	0.172	0.603
K8	3.19	27.33	195.39	0.134	0.034	0.168	0.587
K9	3.21	27.46	198.89	0.135	0.034	0.168	0.590
K10	2.48	21.28	154.30	0.104	0.026	0.131	0.457
K11	2.74	23.51	170.29	0.115	0.029	0.144	0.505
K12	2.57	21.79	158.32	0.107	0.027	0.134	0.468
K13	2.98	25.51	183.87	0.125	0.031	0.157	0.548
K14	2.64	22.84	163.57	0.112	0.028	0.140	0.491
K15	2.46	20.80	152.22	0.102	0.026	0.128	0.447
K16	1.60	13.79	98.73	0.068	0.017	0.085	0.296
K17	2.64	22.46	161.60	0.110	0.028	0.138	0.482
K18	2.22	18.97	136.95	0.093	0.023	0.116	0.407
K19	1.46	12.58	91.26	0.062	0.015	0.077	0.270
K20	2.93	24.92	178.71	0.122	0.031	0.153	0.535
K21	3.55	30.32	220.80	0.149	0.037	0.186	0.651
K22	3.27	28.01	201.53	0.137	0.034	0.172	0.601
K23	3.44	29.59	212.38	0.145	0.036	0.182	0.636
K24	3.53	30.13	217.11	0.148	0.037	0.185	0.647
K25	4.53	38.79	277.00	0.190	0.048	0.238	0.833
K26	3.71	31.71	229.87	0.156	0.039	0.195	0.681

Table cont....

Sample code	Exposure (μR/h)	D_r (nGy/h)	AGED (mSv/y)	$AEDE_{indoor}$ (mSv/y)	$AEDE_{outdoor}$ (mSv/y)	AEDE (mSv/y)	ELCR×10^{-3}
K27	4.41	37.848	269.54	0.186	0.046	0.232	0.813
K28	4.89	42.217	300.70	0.207	0.052	0.259	0.907
K29	2.95	25.218	180.82	0.124	0.031	0.155	0.542
K30	2.30	19.711	140.48	0.097	0.024	0.121	0.423
K31	3.94	33.603	242.69	0.165	0.041	0.206	0.722
K32	4.10	35.155	251.92	0.173	0.043	0.216	0.755
K33	3.99	34.204	244.16	0.168	0.042	0.210	0.735
K34	4.26	36.467	260.25	0.179	0.045	0.224	0.783
K35	3.84	32.602	234.95	0.160	0.040	0.200	0.700
K36	4.64	39.598	283.21	0.194	0.049	0.243	0.850
K37	3.89	33.389	238.80	0.164	0.041	0.205	0.717
K38	4.45	37.942	271.96	0.186	0.047	0.233	0.815
K39	4.05	34.612	247.77	0.170	0.042	0.212	0.743
K40	3.28	28.167	199.07	0.138	0.035	0.173	0.605
K41	3.87	33.239	236.07	0.163	0.041	0.204	0.714
K42	3.45	29.506	212.33	0.145	0.036	0.181	0.634
K43	4.17	35.793	258.26	0.176	0.044	0.220	0.769
K44	3.82	32.780	235.39	0.161	0.040	0.201	0.704
K45	3.48	29.890	215.29	0.147	0.037	0.183	0.642
K46	3.99	34.400	244.98	0.169	0.042	0.211	0.739
Mean ± S.E.	3.36 ±0.11	28.83 ±0.96	207.1078 ±6.86	0.141 ±0.004	0.035 ±0.001	0.177 ±0.005	0.61 ±0.02

Table 5: Comparison of the specific activity of soil samples under investigation with other countries.

Country	specific activity in Bq/kg			Reference
	^{238}U	^{232}Th	^{40}K	
Egypt	27	31.4	427.5	(El Mamoney & Khater 2004)
Iran	23	31	453	(Saleh 2017)
Saudi Arabia	11.68	6.21	169.40	(El-Taher et al. 2018)
Libya	7.5	4.2	27.5	(El-Kameesy et al. 2008)
World average (soil)	33	45	420	(UNSCEAR 2008)
Iraq (Baghdad-Karakh side)	16.47	9.72	367.95	Present study

seen that terrestrial gamma radiation map resembled with uranium-238, thorium-232 and potassium-40 maps. The level of naturally occurring radioactivity in soil samples at Baghdad Governorate (Karakh Side) was evaluated using NaI(Tl) gamma-ray spectrometry. The obtained results revealed that the level of measured radioactivity could not pose any radiological threat to the people living near it, also the obtained values when compared to the worlds permissible values were below the acceptable value standard and hence risk of developing cancer by the people will be low.

REFERENCES

Abojassim, A. A. 2017. Estimation of human radiation exposure from natural radioactivity and radon concentrations in soil samples at green zone in Al-Najaf, Iraq. Iranian Journal of Energy and Environment, 8(3): 239-248.

Abojassim, A. A., Oleiwi, M. H. and Hassan, M. 2016. Natural radioactivity and radiological effects in soil samples of the main electrical stations at Babylon Governorate. Nuclear Physics and Atomic Energy

17(3): 308-315.
Albusoda, B.S. 2016. Engineering assessments of liquefaction potential Baghdad soil under dynamic loading. Journal of Engineering and Sustainable Development, 20(1): 59-76.
Al-Hamidawi, A. 2014. Assessment of radiation hazard indices and excess life time cancer risk due to dust storm for Al-Najaf, Iraq. WSEAS Trans. Environ. Dev., 10: 312.
Arafa, W. 2004. Specific activity and hazards of granite samples collected from the eastern desert of Egypt. Journal of Environmental Radioactivity, 75(3): 315-327.
Bauer, W. and Westfall, G.D., 2011. University Physics with Modern Physics. New York: McGraw-Hill.
Çam, N. F., Özken, I and Yaprak, G. 2012. A survey of natural radiation levels in soils and rocks from Aliaγa-Foça region in Izmir, Turkey. Radiation Protection Dosimetry, 155(2): 169-180.
Cherry, S.R., Sorenson, J.A. and Phelps, M.E. 2012. Physics in Nuclear Medicine E-Book. Elsevier Health Sciences.
Clavensjö, B. and Åkerblom, G. 1992. The Radon Book. Measures Against Radon (No. BFR-T--5-92). Swedish Council for Building Research.
Doγan, M., Meriç, N., Kadioγlu, Y. K. and Samet, R. 2010. GIS approach to radioactive contamination around Seyitömer thermic powerhouse. Gazi University Journal of Science, 23(2): 137-148.
Einas H.O., Salih, I. and Khatri A. Sam 2012. GIS mapping and assessment of terrestrial gamma radiation in Northern state. J. Radiation Protection Dosimetry, 151(3): 1-11.
Eisenbud, M. and Gesell, T.F. 1997. Environmental Radioactivity from Natural, Industrial and Military Sources: From Natural, Industrial and Military Sources. Elsevier.
El Mamoney, M. H. and Khater, A. E. 2004. Environmental characterization and radio-ecological impacts of non-nuclear industries on the Red Sea coast. Journal of Environmental Radioactivity, 73(2): 151-168.
El-Kameesy, S.U., El-Ghany, S.A., El-Minyawi, S.M., Miligy, Z. and El-Mabrouk, E.M. 2008. Natural radioactivity of beach sand samples in the Tripoli Region, Northwest Libya. Turkish Journal of Engineering and Environmental Sciences, 32(4): 245-251.
El-Taher, A., Alshahri, F. and Elsaman, R. 2018. Environmental impacts of heavy metals, rare earth elements and natural radionuclides in marine sediment from Ras Tanura, Saudi Arabia along the Arabian Gulf. Applied Radiation and Isotopes, 132, 95-104.
Harb, S. R. M. 2004. On the human radiation exposure as derived from the analysis of natural and man-made radionuclides in soils, Doctoral dissertation, Verlag nicht ermittelbar).
Hassan, N.S. 2012. Assessment and GIS mapping of terrestrial Gamma radiation in Elfao area in Elgedaref states. Thesis of Master of Nuclear Science and Technology, Sudan Academy of Sciences, Atomic Energy Council.
Hatab, T.N., Kachachy, G.A. and Taiseer, S. 1986. A study of the engineering soil characteristics of Baghdad area. Report for National Center for Construction Laboratories, 39: 82.
Heyde, K. 2004. Basic Ideas and Concepts in Nuclear Physics: An Introductory Approach. CRC Press.
ICRP 1993. ICRP Publication 63: Principles for Intervention for Protection of the Public in a Radiological Emergency (Vol. 63). Elsevier Health Sciences.
Kahn, B., Eichholz, G.G. and Clarke, F.J. 1983. Search for building materials as sources of elevated radiation dose. Health Physics, 45(2): 349-361.
Krieger, R. 1981. Radioactivity of Construction Materials. Betonwerk Fertigteil Techn, 47(468).
Mirza, A.A., Al-Gazaly, H.H. and Abojassim, A.A. 2017. Radioactivity levels and radiological risk assessment in soil samples of Nasiriyah thermal power station, Iraq. Poll. Res., 36(4): 39-44
OECD 1979. Exposure to radiation from the natural radioactivity in building materials. Nuclear Energy Agency Report.
Okogbue, C. and Nweke, M. 2018. The 226Ra, 232Th and 40K contents in the Abakaliki baked shale construction materials and their potential radiological risk to public health, southeastern Nigeria. Journal of Environmental Geology, 2(1).
Saleh Kotahi, M. 2017. Estimation of natural radioactivity and radiation exposure in environmental soil samples of Golestan, Iran. Iranian Journal of Medical Physics, 14(2): 98-103.
Spinks, J.W.T. and Woods, R.J. 1990. An Introduction to Radiation Chemistry. J. Wiley and Sons, New York
Sroor, A., El-Bahi, S. M., Ahmed, F. and Abdel-Haleem, A.S. 2001. Natural radioactivity and radon exhalation rate of soil in southern Egypt. Applied Radiation and Isotopes, 55(6): 873-879.
Tanaskoviγ, I., Golobocanin, D. and Miljeviγ, N. 2012. Multivariate statistical analysis of hydrochemical and radiological data of Serbian spa waters. Journal of Geochemical Exploration, 112: 226-234.
Ting, D.S.K. 2010. WHO Handbook on Indoor Radon: A Public Health Perspective. World Health Organization, Geneva.
UNSCEAR, A. 1988. Sources, effects and risks of ionizing radiation. United Nations, New York.
UNSCEAR (United Nations Sources and Effects of Ionizing Radiation) 1993. Report to the General Assembly, with Scientific Annexes. New York: United Nations.
UNSCEAR (United Nations Scientific Committee on the Effects of Atomic Radiation). 2000. Sources and effects of ionizing radiation. UNSCEAR Report to the General Assembly, Volume I: Sources.
UNSCEAR (United Nations Scientific Committee on the Effects of Atomic Radiation). 2008. Sources and effects of ionizing radiation. UNSCEAR Report to the General Assembly, Volume I: Sources.
Venturini, L. and Nisti, M.B. 1997. Natural radioactivity of some Brazilian building materials. Radiation Protection Dosimetry, 71(3): 227-229.
White, S.C. and Pharoah, M.J., 2014. Oral Radiology-E-Book: Principles and Interpretation. Elsevier Health Sciences.
Yang, Z., Zhuo, W. and Chen, B. 2017. Mapping the baseline of terrestrial gamma radiation in China. Radiation Environment and Medicine: Covering a Broad Scope of Topics Relevant to Environmental and Medical Radiation Research, 6(1): 29-33.

Nature Environment and Pollution Technology
An International Quarterly Scientific Journal

p-ISSN: 0972-6268
e-ISSN: 2395-3454

Vol. 18 | No. 4 | pp. 1107-1118 | 2019

Original Research Paper | Open Access

Impacts of Human Disturbances on Riparian Herbaceous Communities in a Chinese Karst River

Yuan Ren*, Dongmei Wang*† and Xiaochen Li**
*School of Soil and Water Conservation, Beijing Forestry University, Beijing, 100083, China
**China Sino-Water Water Science & Technology Institute Co. Ltd., Beijing, 100053, China
†Correspondence: Dongmei Wang

Nat. Env. & Poll. Tech.
Website: www.neptjournal.com

Received: 04-02-2019
Accepted: 25-04-2019

Key Words:
Anthropogenic disturbance
Community diversity
Ecological degradation
Riparian communities
Hydrological effect

ABSTRACT

Riparian zones suffer from increased human disturbances and the plant communities change unpredictably in response to altered conditions. It is important to understand the effects of human activities on plant communities for rational tourism development and ecological protection programs. We sampled 14 and 27 sites in nearly natural and human-influenced landscapes along the Lijiang River in southwest China, respectively, to detect human impacts on the ecosystem. We set three survey lines, based on a submersion gradient, at each site to determine whether herbaceous species richness increased with distance from the river, and we examined the effects of disturbance on herbaceous distribution. The landscapes shared 101 common species, and unique species in the human-influenced landscape were partly synanthropic. The species richness and diversity indices of the nearly natural landscape were significantly higher than those of the human-influenced landscape ($P < 0.01$). Species richness increased with distance from the river in the nearly natural landscape, and a significant difference was detected among the variances of survey lines ($P < 0.05$) in the human-influenced landscape. In the nearly natural landscape, species richness increased with fewer hydrological effects, and a stable community was maintained. However, human disturbances led to community variability and fragmented riparian habitats, resulting in species extinction and ecological degradation. We suggest that appropriate dam and reservoir regulations, prohibition of soil destructions, and a long-term research program for ecosystem protection may help in improving the monitoring of human influences and sustainable management in riparian zones of tourist rivers.

INTRODUCTION

People tend to live in areas adjacent to rivers to meet transportation, power production, food, and waste disposal needs (Naiman & Decamps 1997). Rivers and associated dependent territories, namely riparian zones, have increasingly suffered because of anthropogenic activities. Riparian zones sustain numerous plant and animal communities, maintain a range of ecosystem services (Coroi et al. 2004), and provide vital freshwater resources (Allan 1995). Riparian vegetation is currently rooted in the most vulnerable and threatened ecosystem in the world, and its conservation is thus of immense importance (Tockner & Stanford 2002). However, areas with riparian vegetation lack adequate protection, especially in third world countries that emphasize development. Plant communities are changing faster, and becoming more unpredictable in response to human disturbances and increased abiotic and biotic pressures (Parmesan & Yohe 2003, Root et al. 2003, Walther 2010). These changes have been particularly pronounced, as evidenced by shifts in composition and changes in diversity and distribution in forests at different elevations (Klanderud & Birks 2003, Lesica & McCune 2004, Pauli et al. 2007, Randin et al. 2009, Sproull et al. 2015) and in different watersheds (Méndez-Toribio et al. 2014, Pennington et al. 2010, Sunil et al. 2016).

Several studies that focused on forest composition and diversity only minimally addressed the herbaceous layer, probably because it comprises a minuscule proportion of the forest biomass. However, the herbaceous layer can contain greater than 90% of the plant species in a forest, and contributes up to 20% of the foliar litter on the forest floor (Gilliam 2007). Furthermore, the herbaceous layer can become intricately linked with canopy species by competing with tree seedlings for energy and nutrients (Graves et al. 2006, George & Bazzaz 2003, Lyon & Sharpe 2003), which mitigates the potential loss of nutrients that are essential to trees (Gilliam 2007). Karst landforms are generally characterized by extensive outcropping of soluble rocks and thin soil layers (Li et al. 2015), and frequent hydrological processes render the riparian ecosystem even more vulnerable, leading to the dominance of water-tolerant herbs. There-

fore, herbaceous plants are crucial to the structure and function of riparian ecosystems. Moreover, knowledge of the composition and distribution of local natural vegetation is needed for improved restoration, because the most successful restoration methods mimic the processes of natural ecosystems (Fries et al. 1997). As water tolerance thresholds narrow, acclimation potential diminishes and productivity is limited to unsubmerged growing periods. These sensitivities provide unique circumstances for observations of the long-term effects of hydrology and the biotic interactions between herbaceous community processes and patterns. The Lijiang River riparian community is influenced by frequent hydrological fluctuations and consequent soil factors, and this influence decreases as distance from the river increases. Therefore, we hypothesized that, in a natural circumstance, herbaceous species richness and soil nutrient increase as the distance from the river increases (H1).

There are likely multiple drivers of change in the herbaceous layer (Sproull et al. 2015) and global warming, biotic interactions, and disturbances often work in concert, making it difficult to disentangle the contribution of each factor (Schweiger et al. 2010, Walther et al. 2009). Nevertheless, most short-term local changes are not caused by climate change but by land-use changes and natural fluctuations of species abundance and distribution (Parmesan & Yohe 2003). Site conditions affect local resource availability and can be important drivers of plant species diversity (Bartels & Chen 2010, Chipman & Johnson 2002, Roberts & Gilliam 1995). Although canopy tree species richness appears to be predominantly controlled by the availability of energy and climatic water, total plant species richness, which is primarily composed of understorey plants, is mainly controlled by soil conditions (Zhang et al. 2014). Other studies also found that local site conditions may have a stronger influence than regional climate on understorey plant species (Chipman & Johnson 2002, Oberle et al. 2009).

The conditions at the Lijiang River site have changed in recent years because of increased tourism interest in its scenic karst landscape, and human disturbances have subtly differentiated riparian land use. Some researchers are concerned that ecological degradation has occurred in the human-influenced landscape, and that this may cause species extinction and decreased species diversity. However, other researchers suggested that intermediate disturbances result in high species diversity in these communities. For instance, they cite the intermediate disturbance hypothesis (IDH) (Connell 1978), which predicts that high disturbance frequencies lead to the dominance of disturbance-adapted pioneer species, low disturbance frequencies lead to low-diversity communities of competitive-dominant species, and intermediate disturbance frequencies result in a mixture of both the species groups, thus resulting in peak plant diversity via succession (Chen & Taylor 2012, Connell & Slatyer 1977, Taylor & Chen 2011). In consideration of the moderate disturbance frequencies and appropriate water and temperature condition of Lijiang River, we hypothesized that in the human-influenced landscape, the species diversity may remain at a level similar to that of the nearly natural landscape, but that featured species might exhibit greater variability in areas with human disturbance (H2).

This study evaluated human disturbances in riparian herbaceous communities in the riparian zone of the Lijiang River. Here, we compared herbaceous composition and soil conditions in nearly natural and human-influenced landscape to assess changes under anthropogenic disturbances. In our analysis, we examined discrepancies in species diversity and lateral herbaceous distribution. We also built longitudinal species richness patterns to measure the effect of human disturbance. Our study aimed to determine whether the ecosystem had degraded and to identify the most vulnerable zones under present anthropogenic disturbances. We addressed the two hypotheses by analysing the differences in the patterns of herbaceous species richness and soil nutrient with the decreased hydrological effects from the river, exploring the differences in species diversity, and detecting the variability of its featured species between the nearly natural and the human-influenced landscapes.

METHODS

Study Area

The Lijiang River refers to the upper reaches of a second-order stream that drains into Pearl River. It is located in the northeast part of the Guangxi Zhuang Autonomous Region which is characterized by average annual precipitation of 1500-2600 mm (Qin et al. 2017), of which 40% occurs during the summer. This region is a subtropical monsoon climate zone, and the low-latitude study area (24°46'N-25°38'N, 110°17'E-110°31'E, (Fig. 1) contains abundant energy and illumination as well as a warm average annual temperature of 17.8-19.1°C (Qin et al. 2017). The Lijiang River has been the focus of anthropogenic service activities, including orchard picking, local catering, modern infrastructure development, and riverbank protection measures that have been constructed for tourist convenience and safety. However, the riparian zone faces increasing disturbances because of the convenient activities that occur close to the water, and riparian vegetation has been forced to adapt to transforming local land conditions. However, there are two natural reserve areas, Qingshitan Reservoir Natural Reserve and Maoershan Natural Reserve, in the northern upper and middle reaches of the Lijiang River. In

addition, with the obstruction of karst clustered mountains, some lower reaches also remain undeveloped. These artificially or naturally protected areas have few inhabitants, and with the exception of some human activities, the ecosystem exhibits original species succession and remains relatively unchanged. The changes in other lands provide special circumstances for the study of anthropogenic disturbance in riparian communities.

Canopy species are sparsely distributed in riparian zones, and the species differ between the nearly natural landscape and the human-influenced landscape. *Pterocarya stenoptera* C. DC. is the most dominant tree, and it occurs along the entire length of the Lijiang River. Furthermore, *Bambusa multiplex* (Lour.) Raeusch. ex Schult. & Schult. f. is common because it was planted within riparian communities during the middle of the last century because of its well-developed roots, which can aid dyke strengthening and prevent soil erosion along banks. Nevertheless, the nearly natural riparian communities share diverse dominant species, including *Cinnamomum camphora* (L.) J. Presl, *Triadica sebifera* (L.) Small, *Salix rosthornii* Seemen, and *P. stenoptera*. Forest belts occur close to the riparian zone, and these zones are intermittent because they have been replaced with other land use types (e.g., paddy fields, gardens, and urban infrastructures).

Strips of Riparian Zone

Regarding the condition of the site, the riparian zone can be divided into four strips that are influenced by hydrological fluctuations: floodplain (7-8 months of submersion), riverside slope (5-6 months of submersion), midslope terrace (3-4 months of submersion), and upland side slope (1-2 months of submersion). This division is based on a preliminary study similar to that of Zenner et al. (2013). The floodplain strip failed to grow vegetation, with the exception of sporadic aquatic plants, because the area is full of cobblestones. Furthermore, the floodplain strip contains few fine soil particles because of drastic scouring. However, from the riverside slope strip to the upland side slope strip, gravel with a relatively higher fine soil content nourishes several herbaceous plants. The aforementioned bank protection measures were constructed exactly midway between the riverside slope and the midslope terrace along the 'golden travel reach', which can be used as a waterside pavilion after the 3-4 month wet season.

Sampling

In total, 41 sites were sampled (Fig. 1), including 14 in nearly natural landscapes and 27 in human-influenced landscapes. We constrained the sites to those that could be reached by wading, including areas without steeps and

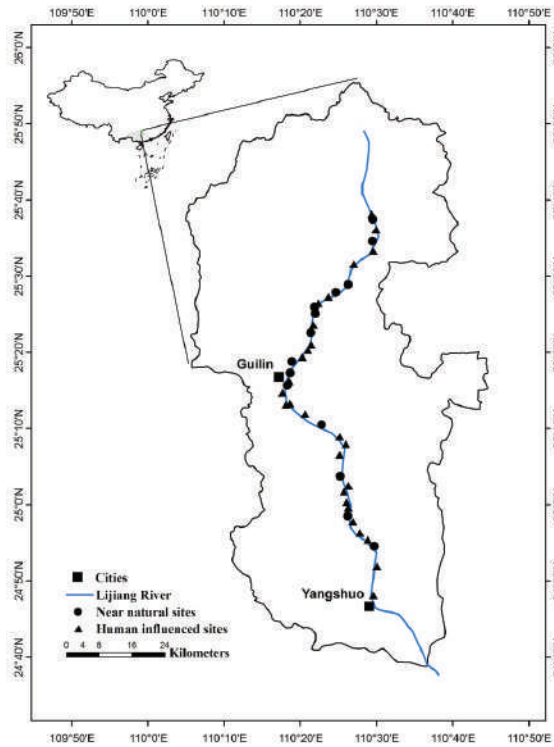

Fig. 1: Location of the study area and sampling sites.

those without appreciable channel manipulation (Jackson et al. 2015) such as revetments constructed within two to three years. Hence, sites associated with each landscape type were randomly set at a variable distance on both sides of the river, depending on specific circumstances. At each of the sites, one survey line was set in the riverside slope, midslope terrace, and upland side slope strips. Survey lines were 45 m long, and 100 × 100 cm quadrats (five per line) were systematically located 10 m apart along each survey line. Therefore, 15 plots were surveyed for species composition, richness, and diversity at each site. All species (including herbs, lianas, and shrubs under 50 cm and woody saplings under 100 cm) rooted within the confines of the plot were recorded to determine richness and composition (Sproull 2015). Cover estimates (Biswas & Mallik 2010, Coroi et al. 2004, Rheault et al. 2015) were scored by the same observer looking down at a 1 m height, and plot species presence/absence counts were summed to determine the frequency. Soil samples were collected in every 100 × 100 cm quadrats and analysed in Key Laboratory of Soil and Water Conservation and Desertification Combating, Ministry of Education, Beijing Forestry University. Species accumulation curves were used to estimate the validity of the sample sizes (27 and 14 sample sites in nearly natural and human-impacted landscapes, respectively).

From March to May of 2015, the 41 sites were surveyed, and species with different life-history characteristics were accounted for each month. Most species were identified in the field, uncommon species were verified at the College of Life Science, Guangxi Normal University (Guilin, China), and a few species were unidentified.

Data Analyses

We calculated bootstrap and abundance cover estimator (ACE) values using the statistical software program Estimates (v8.2; http://viceroy.eeb.uconn.edu/estimates), and frequency data (percentage of plots per site in which each species was present) were used to accurately gauge our sampling efforts. ACE values are used to estimate richness with a focus on species abundance and rare species, whereas bootstrapping is a more traditional randomization-based estimation method (Sproull 2015). Bootstrap and ACE values were plotted alongside one another to compare species accumulation in each landscape based on the survey data.

To compare the herbaceous composition and to test species diversity differences between human-influenced and nearly natural regions, we examined landscape scales. We used importance values for riparian herbaceous species to describe the composition differences between the two landscape types. The importance value index (IVI) was calculated by summing the relative density, relative frequency, and relative cover, and the sum was then divided by three. To estimate species diversity, we used richness (number of species at each site), the Shannon-Wiener diversity index, the Simpson diversity index, and the evenness index (Magurran 2004). We also used regression analyses, following the River Continuum Concept (Vannote et al. 1980), to reveal the longitudinal richness distribution pattern, which could reflect riparian habitat availability and physical heterogeneity in different river reach types (more habitat availability should host more richness); then, we used a general linear model to measure the effect of human disturbance on riparian diversity.

To test the hypothesis that herbaceous species richness and soil nutrient increased as the distance from the river increased, we counted the species (number of species in each strip) and computed the average of soil data at the survey line scale, and then analysed the differences among the three strips that represented different distances. The standard deviation of species richness was calculated for each strip from the five plots. The standard deviations were then used to determine whether species richness exhibited greater variability in human-influenced landscapes that were subjected to various degrees of anthropogenic disturbance among the three strips. We used an analysis of variance (ANOVA) to examine the differences in the mean species richness standard deviations across the three riparian strips that were subjected to human disturbances. For further understanding of different kinds of human disturbance on soil condition, we also used an ANOVA to analyse the differences of soil data between nearly natural landscape and tourism, grazing, and sand mining landscapes which were most common disturbances in Lijiang River riparian zone.

A two-tailed *t*-test was used to compare species diversity indices for each categorized landscape, and a one-way ANOVA was used to compare soil data and species richness and its variability among strips. Fisher's least significant difference (LSD) and Tamhane's T2 significant difference (if equal variance not assumed) were calculated from the ANOVA results. All data analyses were conducted using Excel 2010 and IBM SPSS Statistics 20.

RESULTS

Bootstrap and ACE data exhibited saturation at the high end, indicating that almost all species present in each landscape were captured during this survey. The result confirmed that our sample sizes (n = 27 in human-influenced landscape; n = 14 in nearly natural landscape) were adequate (Fig. 2). Regarding the two landscapes, 175 species belonging to 55 families were recorded, and most genera were represented by a single species. Nearly natural landscapes harbored a

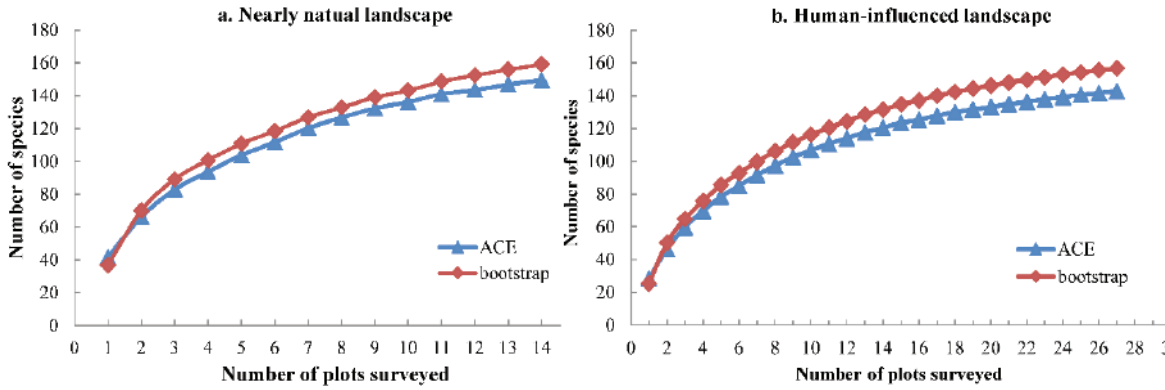

Fig. 2: Species accumulation curves illustrating bootstrap and ACE values calculated from the frequency survey data from the two landscapes. Frequency data were calculated as the percentage of plots per site in which a species was present.

higher number of species (144 species from 52 families) than that in the human-influenced landscape (132 species from 48 families). Furthermore, the mean species number for each site in the nearly natural landscape (35.07) was significantly higher ($P < 0.01$) than that of the human-influenced landscape (25.44). The two landscapes shared 101 common species, which accounted for 70.14% and 76.52% of species from the nearly natural and human-influenced landscapes, respectively (Table 1).

Table 1: Herbaceous characteristics in nearly natural and human-influenced landscapes.

Variables	Nearly natural landscape	Human-influenced landscape	Total
Species numbers	144	132	175
Genera numbers	123	106	130
Family numbers	52	48	55
Unique species	43	31	74
Mean number of species/site	35.07 ± 9.55a	25.44 ± 8.40b	-

Unidentified species were included in the species numbers of the two landscapes, but excluded from genera and family numbers. The mean species number per site (±standard deviation) was the average of the amount surveyed at each site, and different letters denote significant differences between landscapes (two-tailed *t*-test; $P < 0.01$).

The importance value index (IVI) indicated that all the dominant species belonged to the 101 most common species, and the IVI of the top 20 species accounted for 65.35 and 74.99 (100 total) in nearly natural and human-influenced landscapes, respectively. Furthermore, 14 of these top 20 species were common, indicating their dominance in the Lijiang River riparian zone (Table 2). The IVI ranges for unique species were 0.02-0.95 and 0.02-0.37 for nearly natural and human-influenced landscapes, respectively. Although the association seemed negligible, we identified the following synanthropic species that were highly associated with the human-influenced landscape: the planted fruits *Vitis vinifera* L., *Garcinia tetralata* C.Y. Wu ex Y.H. Li, and *Citrullus lanatus* (Thunb.) Matsum. & Nakai; the local delicacy *Colocasia esculenta* (L.) Schott; and greening and beautification plants *Styphnolobium japonicum* (L.) Schott, *Senna sophera* (L.) Roxb., and *Clerodendrum japonicum* (Thunb.) Sweet. However, unique species in the nearly natural landscape were not common, with the exception of *Impatiens macrovexilla* Y.L. Chen, which was cultivated and originated in Guilin.

The nearly natural landscape had higher and more significant Shannon-Weiner and Simpson indices than the human-influenced landscape (two-tailed *t*-test, $P < 0.01$), whereas the Pielou evenness indices from the two landscapes did not differ significantly. The high Simpson and evenness indices indicated high levels of sample diversity and low levels of species dominance in both the landscapes (Fig. 3).

In lateral herbaceous distribution, the mean species richness increased from the riverside slope to the upland side slope, and a significant difference between the means (Fisher's LSD, $P < 0.05$) was detected in the nearly natural landscape. However, the data resembled a hump-shaped pattern in the human-influenced landscape, and a significant difference was only detected between the riverside slope and the midslope terrace (Fisher's LSD, $P < 0.05$, Fig. 4). In longitudinal species richness patterns, Pearson correlation coefficients showed that mean plot-level species richness was strongly associated and increased with site distance (curve length along the river of each site to the northernmost site, the same below) in both the landscapes (0.893/0.673 in nearly natural and human-influenced landscapes, respectively, $P < 0.001$), and the slope of regression line was significantly higher in the nearly natural landscape than in the human-influenced landscape ($P < 0.01$). This discrepancy

Table 2: Importance value index (IVI) for some of the common species in the two landscapes.

Nearly natural landscape species	IVI	Human-influenced landscape species	IVI
Arthraxon hispidus (Thunb.) Makino	7.60	*Arthraxon hispidus*	14.86
Oplismenus hirtellus (L.) P. Beauv. subsp. undulatifolius (Ard.) U. Scholz	7.20	*Murdannia triquetra*	7.21
Trachelospermum jasminoides(Lindl.) Lem.	4.69	*Cynodon dactylon*	5.48
Achyranthes aspera L.	4.58	*Oplismenus hirtellus* subsp. *undulatifolius*	5.29
Glechoma longituba (Nakai) Kuprian.	4.20	*Achyranthes aspera*	5.07
Murdannia triquetra (Wall. ex C.B. Clarke) G. Brükn.	4.03	*Glechoma longituba*	5.01
Persicaria hydropiper (L.) Spach	3.45	*Humulus japonicus*	3.74
Aster tataricus L. f.	3.17	*Persicaria hydropiper*	3.33
Persicaria barbata (L.) H. Hara	2.94	*Oxalis debilis* var. *corymbosa*	3.22
Humulus japonicus Siebold &Zucc.	2.71	*Clinopodium chinense*	2.59
Kalimeris indica (L.) Sch. Bip.	2.70	*Trachelospermum jasminoides*	2.49
Rubus rosifolius Sm.	2.70	*Persicaria barbata*	2.31
Cynodon dactylon (L.) Pers.	2.62	*Persicaria chinensis* (L.) H. Gross	2.26
Paederia foetida L.	2.38	*Aster tataricus*	2.24
Urena lobata L.	1.86	*Setaria plicata*	2.14
Salvia prionitis Hance	1.86	*Cyperus cyperoides* (L.) Kuntze	1.93
Ageratum conyzoides L.	1.85	*Perilla frutescens* (L.) Britton	1.81
Oxalis debilis Kunth var. *corymbosa* (DC.) Lourteig	1.78	*Kalimeris indica*	1.35
Setaria plicata (Lam.) T. Cooke	1.60	*Alternanthera philoxeroides* (Mart.) Griseb.	1.35
Clinopodium chinense (Benth.) Kuntze	1.45	*Bidens pilosa* L.	1.33
Total	65.35	Total	74.99

All dominant species were common species surveyed in the two landscapes. Only the top 20 are shown in descending order, and 14 of these species were common. The IVI values of other common species ranged from 0.03 to 1.24 in the nearly natural landscape and from 0.12 to 1.28 in the human-influenced landscape.

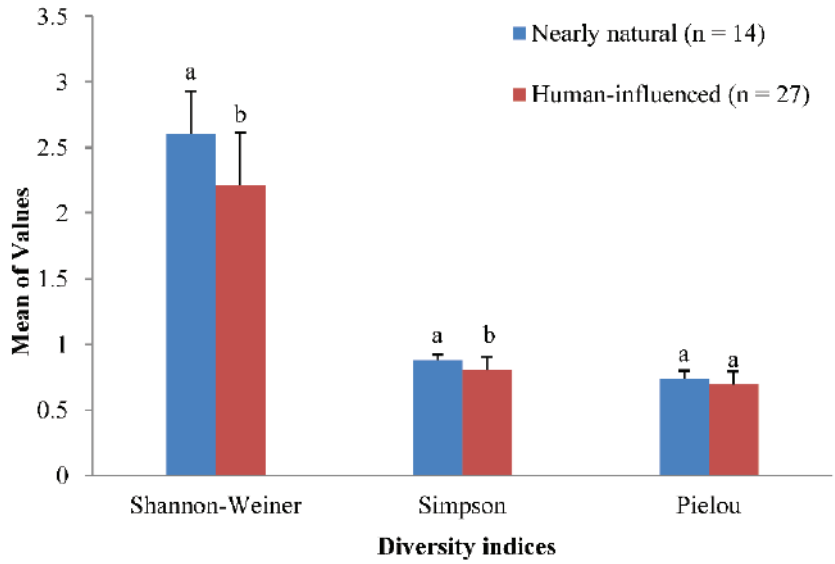

Fig. 3: Mean diversity indices between the two landscapes. Bars represent one standard deviation. Columns with a different letter are significantly different at the $P < 0.01$ level using a two-tailed t test.

indicates that human disturbance had a negative effect on riparian species richness (Fig. 5). Furthermore, the standard deviation of species richness within the survey lines ranged from 0.707 to 2.510 in the nearly natural landscape, and no significant difference was detected. However, the standard deviations of species richness were significantly different and much higher for the midslope terrace and the upland side slope than for the riverside slope in the human-influenced landscape (Fisher's LSD, $P < 0.05$). This result indicated greater variability associated with disturbance in the human-influenced landscape (Fig. 6).

Soil organic matter, available nitrogen, available phosphorus, and clay particle content increased from the riverside slope to the upland side slope in nearly natural landscape, however no significant difference showed in grazing and sand mining landscape except clay particle content in

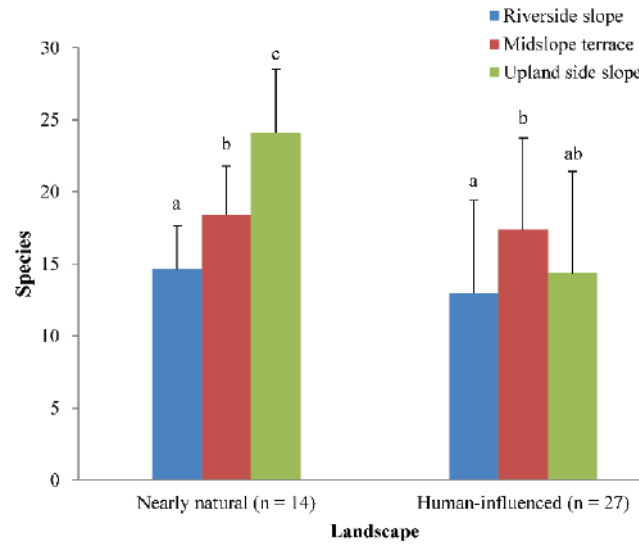

Fig. 4: Mean species richness among strips in the two landscapes. Bars represent one standard deviation. Columns sharing a common letter are not significantly different at the $P < 0.05$ level using Fisher's LSD.

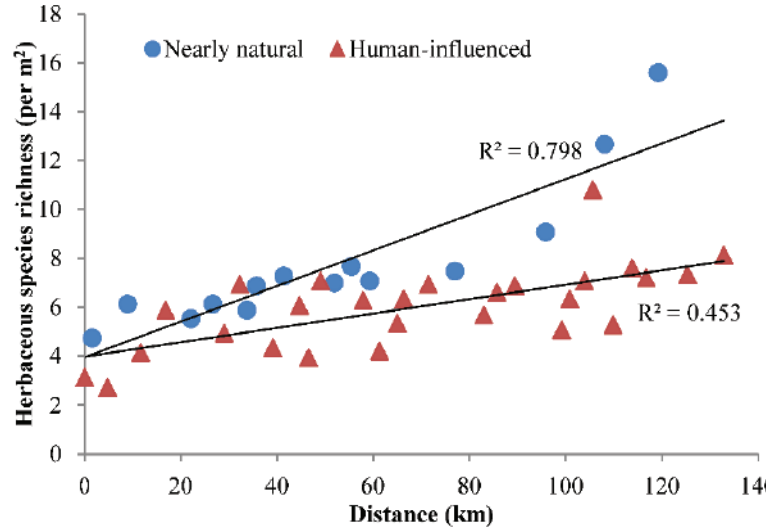

Fig. 5: Mean herbaceous species richness within the Lijiang River riparian zone, in relation to distance of 14/27 sites (nearly natural and human-influenced respectively). Distance represents the curve length along the river of each site to the northernmost site.

sand mining landscape. What's more, the soil indices in tourism landscape was significantly higher in midslope terrace and upland side slope than in riverside slope (Fig. 7).

DISCUSSION

Species Composition and Distribution

We found the plant species in the herbaceous community of Lijiang River riparian zone to have more competitive/ruderal strategies, thus providing greater ecosystem resilience (López et al. 2013). This is because the nearly natural landscape and human-influenced landscape shared a substantial proportion of species and exhibited no absolute predominant species (top 20 species with a total IVI of 65.35%/74.99%, respectively), which was confirmed by a high Pielou evenness index (Table 2, Fig. 3). Indeed, most of the common

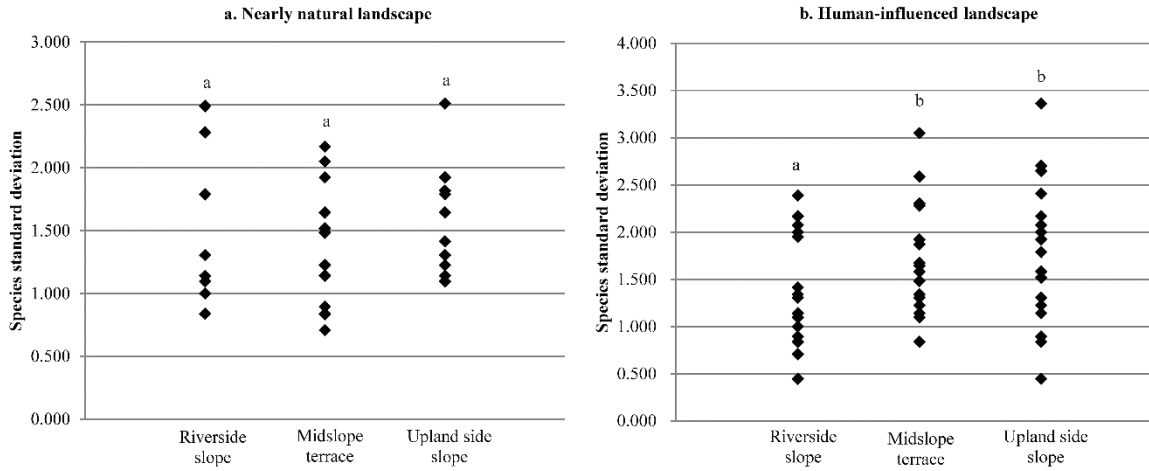

Fig. 6: Distribution of the standard deviation of species richness, by survey lines, for the two landscapes. Distributions that do not share a letter have different mean standard deviations of species richness according to Fisher's LDS at the P < 0.05 level.

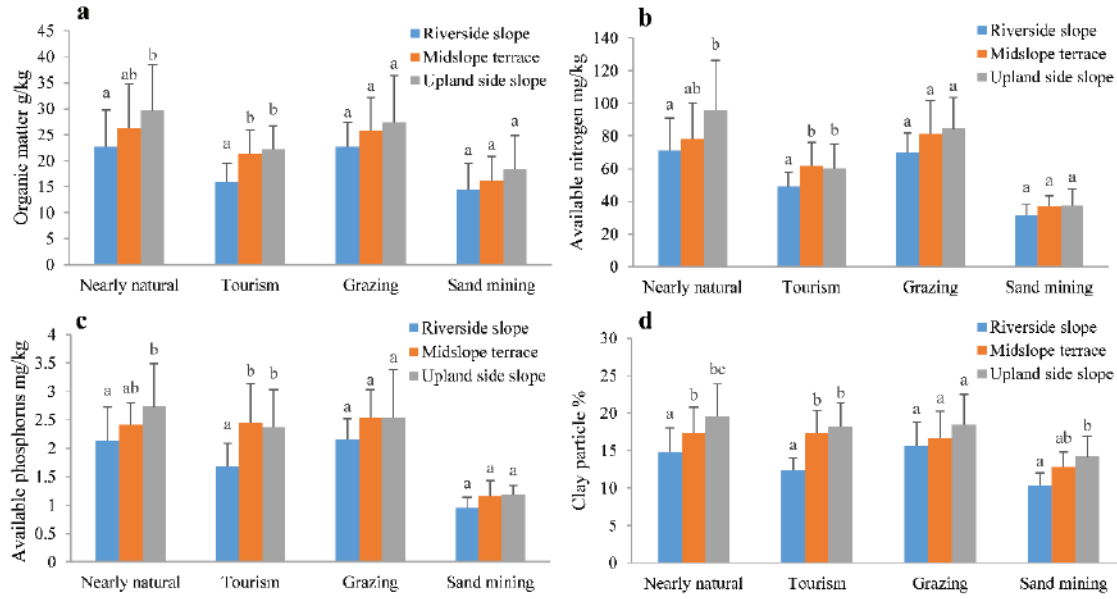

Fig. 7: Mean soil organic matter, available nitrogen, available phosphorus, and clay particle content among strips in the nearly natural landscape and tourism-influence, grazing-influenced, and sand-mining-influenced landscapes. Bars represent one standard deviation. Columns sharing a common letter are not significantly different at the P < 0.05 level.

species were perennials with a branched rhizome or exhibited higher relative cover, which implied an elevated leaf canopy and capacity for extensive spread, i.e., competitive strategies (Grime 1974). In contrast, although the 3-4 month wet season had disastrous floods, the abundant energy, illumination, and precipitation as well as the warm temperature of the Lijiang River provided appropriate growing conditions for annuals or short-lived perennials that had a characteristic of rapid growth, i.e. ruderal strategies (Grime 1974). The unique species showed the same strategies in the nearly natural landscape but exhibited more human-related sapling shrubs or trees in the human-influenced landscape, which reflects the impacts of human activity on herbaceous composition. In the human-influenced landscape, picking orchards, featured restaurants, and greening and beautification projects exist to attract tourists. Many fruits (e.g., *Vitis vinifera* and *Garcinia tetralata*), vegetables (e.g., *Colocasia esculenta*), flowers, and trees (e.g., *Styphnolobium japonicum*, *Senna sophera* and *Clerodendrum japonicum*) were planted in gardens, and these species might disperse to adjacent lands (Moran 1984), including riparian zones used for human activities (e.g., picnics or barbecues in the wild with fresh fruits and vegetables). In fact, exotic species could easily end up in undisturbed areas without human activities within 2-4 years (Gomes et al. 2014). Thus, these synanthropic species might change the species composition of Lijiang Riparian zone by intruding to other human-influenced and even natural landscapes under further tourism.

Our results confirmed the hypothesis (H1) that herbaceous species richness increased with distance from the river (Fig. 4). This result contradicted that of Coroi et al. (2004) in that the restrictive factors in their study area were light, water and soil nutrients, which declined in the farther streamside forest, thus leading to lower species richness. In our study area, the vegetation of riparian zones was frequently removed or covered with alluvia following floods, and the terrain left after water withdrawal was subsequently colonized by pioneer species, as is typical (Coroi et al. 2014). Thus, the nearly natural landscape species were mainly affected by hydrological factors and consequent soil factors, because the canopy species are sparsely distributed in riparian zones and other factors were not restricted (e.g., abundant energy, sufficient illumination, and a warm average annual temperature in the study area). As the water tolerance thresholds declined, reduced scour in the upper riparian zones retained fine soil particles that provided a better environment for growth. Herbaceous species richness also increased from the upper reaches to the lower reaches because of more complex natural conditions. In natural riparian zones, reaches with higher riparian habitat availability and physical heterogeneity are thought to support greater species richness (Bruno et al. 2014). Our data showed a monotonically increasing species richness pattern from upper reaches to lower reaches in both the landscapes; this implies a natural higher riparian habitat availability and physical heterogeneity in the lower reaches of Lijiang River because of its more peculiar pinnacles in 'golden travel reach', which may lead to a wider range of illumination and temperature. Under these conditions, optimum illumination or temperature will occur for a larger number of species.

Effects on Herbaceous Community

Although the herbaceous composition and distribution are highly structured by hydrological processes and habitat availability under natural circumstances, the land-use variables can be more important for explaining riparian vegetation patterns under anthropogenic pressure (Tabacchi et al. 1996, Ferreira & Moreira 1999). Sand mining observed in the riverside slope of the landscape might pose a threat to native species because it can obstruct the flow of surface water (Sunil et al. 2016, Nagler et al. 2008), leaving pits that are always full of rainwater, and make the clay particle be washed away easier (Fig. 7), therefore, the germination and establishment ability of species would be diminished. Defecation behavior by grazing animals seemed to be beneficial to nutrition, but the study did not reveal a significant increase in nutrients associated with restored floodplain dynamics and inundations, which have been documented for other rivers (Schaich et al. 2010). Furthermore, grazing can also play a vital role in influencing the vegetation and topsoil structure, including the preference and trampling of specific herbs by cattle. Therefore, grazing can change the habitat fitness (Sagar et al. 2003) and influence competitive interactions between species, and the destruction of the topsoil structure can also lead to low-nutrient conditions under strong hydrological effects that promote the colonization of a few stress-tolerant species (Gomes & Asaeda 2009, Doležal et al. 2013). Traditional revetments are generally constructed with concrete and have extremely low conductivity (Li et al. 2015), which obstructs the substance and energy exchange between the riverside slope strip and upper strips. On the one hand, when lacking supplements from upper lands, species in lower lands may face an inferior growing environment (Fig. 7). On the other hand, the interception of nutrients or pollutants makes upper lands uncertain for nourishing plants. Tourism activities add additional complication factors to riparian zones, and these factors may have positive or negative effects on species diversity. However, uncontrolled tourism activities can exert immense pressure on the riparian zones, leading to declines of typical riparian species, and consequently affecting the biodiversity of a river (Sunil et al. 2016).

The human disturbances associated with these land-use practices existing in the riparian zone of Lijiang River could easily cause habitat fragmentation, which could drive species to local extinction (Gilliam 2007). For example, the unique species and non-dominant common species appeared negligible with little importance, but these sparsely distributed species played a crucial role along the riparian zone. The absence of these species resulted from fragmentation that could lead to the decline of native species over time (Tabarelli et al. 1999). Although there is often a lag time before inevitable extinction occurs (Gilliam 2007), we believe that these human-induced factors have already combined to induce ecological degradation in the human-influenced landscape even it is not as optimistic as our H2, because the species richness and diversity of the nearly natural landscape were significantly higher than those of the human-influenced landscape (Table 1, Fig. 3). The results also showed a significant higher slope for the regression line in the nearly natural landscape and a higher standard deviation of richness among strips in the human-influenced landscape (Figs. 5 & 6), thus confirming that human disturbances had caused negative effects on the riparian diversity and made the midslope terrace and upland side slope strips more variable. However, the average Simpson diversity of the human-influenced landscape remained high (0.804). This result is attributed to greater ecosystem resilience and implies that the human-influenced riparian zone encountered relatively low or moderate disturbance intensities at the present stage. The theory of "intermediate disturbance" suggests that in some ecosystems with low or moderate disturbance intensities, a species diversity increase might occur (López et al. 2013). Additionally, the increased standard deviation of species richness in the human-influenced landscape was similar to that in former studies, which showed an increased standard deviation of structure variables between transects under intensive grazing near water sources; these results also agreed with the theory of "intermediate disturbance" (Adler et al. 2001, Cingolani et al. 2005).

Implications

Generally, an equilibrium steady state ecosystem is elastic and resistant to disturbance factors, and high-resilience communities may initially have minimal change (Morecroft et al. 2016). However, with higher climate or human disturbance, once a tipping point or critical threshold is reached, there may be a sudden change in community which is associated with a loss of ecosystem functional integrity (López et al. 2013, Morecroft et al. 2016). In this study, although a significant decrease of diversity was found in the human-influenced landscape, the diversity remained high, and a substantial proportion of species remained the same as in the nearly natural landscape. Preventing the crossing of a tipping point or critical threshold is crucial for sustainable management. As the vegetation distribution is highly structured by hydrological factors and consequent soil factors, and changing these environmental conditions can drastically alter community richness (Looy et al. 2016), we suggest the prevention of extensive intervention on water level and direct damage on soil. For example, dam and reservoir regulations should put an emphasis on flood peak cutting so as to not cooperate in deepening of the waterbed to better serve sightseeing boats during the dry season, which may lower the water level and intensify the competitive interactions. Sand mining should be forbidden as it directly destroys the structure of thin surface soils that are easily washed away by frequent hydrological process, consequently leading to difficulties associated with vegetation nourishment. A long-term research program is also needed to thoroughly evaluate community organization and stability and to explore mechanisms and how confounding human-induced factors influence the species community in the Lijiang River riparian zones. By analysing the changes in riparian community composition during the long-term research program, we can also infer community assembly mechanisms of resilience (Looy et al. 2016). Such information might help in the prevention of crossing a tipping point or critical threshold and be used for sustainable management of tourist rivers.

CONCLUSIONS

In the Lijiang River riparian zones, the nearly natural landscape and the human-influenced landscape shared a substantial proportion of herbaceous layer species, but human activities are changing the species composition by dispersing synanthropic species. These human activities affect biodiversity in various forms and have led to decreased species diversity, especially in the upper riparian sides. The herbaceous community is highly structured by the hydrological process and habitat availability in the natural riparian zone of the Lijiang River, but human activities have altered the natural species distributions and fragmented riparian habitats. The differentiated riparian land-use practices may have driven species to local extinction, and might have led to a more variable community. Our hypotheses were mostly supported by our study, although the significantly different diversity between nearly natural landscape and human-influenced landscape did not support H2. The disturbances to the riparian zone are not lethal at the present stage, and we found the greater ecosystem resilience maintained a high level of Simpson diversity in human-influenced landscape because of the competitive/ruderal strategies of herbaceous

community. To prevent crossing a tipping point or critical threshold which may drastically decrease community richness, we suggest appropriate dams and reservoirs regulations, prohibition of soil destructions, and a long-term research program for better understanding of mechanisms in plant community to human disturbances.

In this study, we started by analysing the species composition, i.e., the stability of the community itself, for which less attention has been paid and few empirical studies exist. We revealed the species distribution mechanism, and then pointed out the most vulnerable district of the riparian zone and proposed protection strategies. This information may improve the monitoring of human influences on riparian zones of tourist rivers, especially in developing countries, which are keen on benefits that may limit ecological protections. Our findings can also be used as a reference to reconcile conflicts between tourism development and ecosystem stability for sustainable management.

ACKNOWLEDGMENTS

This work was supported by the National Science and Technology Pillar Program during the Twelfth Five-Year Plan Period (grant number 2012BAC16B03).

REFERENCES

Adler, P., Raff, D. and Lauenroth, W. 2001. The effect of grazing on the spatial heterogeneity of vegetation. Oecologia, 128: 465-479.

Allan J.D. and Castillo M.M. (ed.) 2007. Stream Ecology: Structure and Function of Running Water, 2nd ed., Springer: Dordrecht, Netherlands, pp. 13-31.

Bartels, S.F. and Chen, H.Y.H. 2010. Is understory plant species diversity driven by resource quantity or resource heterogeneity? Ecology, 91: 1931-1938.

Biswas, S.R. and Mallik A.U. 2010. Disturbance effects on species diversity and functional diversity in riparian and upland plant communities. Ecology, 91: 28-35.

Bruno, D., Belmar, O., Sánchez-Fernández, D. and Velasco, J. 2014. Environmental determinants of woody and herbaceous riparian vegetation patterns in a semi-arid mediterranean basin. Hydrobiologia, 730: 45-57.

Chen, H.Y.H. and Taylor, A.R. 2012. A test of ecological succession hypotheses using 55-year time-series data for 361 boreal forest stands. Global Ecol. Biogeogr., 21: 441-454.

Chipman, S.J. and Johnson, E.A. 2002. Understory vascular plant species diversity in the mixed wood boreal forest of western Canada. Ecol. Appl., 12: 588-601.

Cingolani, A. M., Noy-Meir, I. and Díaz, S. 2005. Grazing effects on rangeland diversity: a synthesis of contemporary models. Ecol. Appl., 773-757 :15.

Connell, J.H. 1978. Diversity in tropical rainforest and coral reefs. Science, 199: 1302-1310.

Connell, J.H. and Slatyer, R.O. 1977. Mechanisms of succession in natural communities and their role in community stability and organization. Am. Nat., 111: 1119-1144.

Coroi, M., Skeffington, M.S., Giller, P., Smith, C., Gormally, M. and O'Donovan, G. 2004. Vegetation diversity and stand structure in streamside forests in the south of Ireland. Forest Ecol. Manag., 202: 39-57.

Doležal, J., Yakubov, V. and Hara, T. 2013. Plant diversity changes and succession along resource availability and disturbance gradients in Kamchatka. Plant Ecol., 214: 477-488.

Ferreira, M.T. and Moreira, I.S. 1999. River plants from an Iberian basin and environmental factors influencing their distribution. Hydrobiologia, 415: 101-107.

Fries, C., Johansson, O., Pettersson, B. and Simonsson, P. 1997. Silvicultural models to maintain and restore natural stand structures in Swedish boreal forest. Forest Ecol. Manag., 94: 89-103.

George, L.O. and Bazzaz, F.A. 2014. The herbaceous layer as a filter determining spatial pattern in forest tree regeneration. In: Herbaceous Layer in Forests of Eastern North America, 2nd ed., Gilliam F.S., (eds.), Oxford University Press: New York, United States of America, pp. 340-355.

Gilliam, F. S. 2007. The ecological significance of the herbaceous layer in temperate forest ecosystems. BioScience, 57: 845-858.

Gomes, P.I., Wai, O.W., Kularatne, R.K.A., Priyankara, T.D.P., Anojika, K.G.M.S. and Kumari, G.M.N.R. 2014. Relationships among anthropogenic disturbances representative riparian and non-riparian herbaceous indicators (biomass and diversity), land use, and lotic water quality: implications on rehabilitation of lotic waters. Water Air Soil Pollut., 225: 2060.

Gomes, P.I.A. and Asaeda, T. 2009. Spatial and temporal heterogeneity of *Eragrostis curvula* in the downstream flood meadow of a regulated river. Ann. Limnol. Int. J. Lim., 45: 181-193.

Graves, J.H., Peet, P.K. and White, P.S. 2006. The influence of carbon-nutrient balance on herb and woody plant abundance in temperate forest understories. J. Veg. Sci., 17: 217-226.

Grime, J.P. 1974. Vegetation classification by reference to strategies. Nature, 250: 26-31.

Jackson, C.R., Leigh, D.S., Scarbrough, S.L. and Chamblee, J.F. 2015. Herbaceous versus forested riparian vegetation: Narrow and simple versus wide, woody and diverse stream habitat. River Res. Appl., 31: 847-857.

Klanderud, K. and Birks, H.J.B. 2003. Recent increases in species richness and shifts in altitudinal distributions of Norwegian mountain plants. Holocene, 13: 1-6.

Lesica, P. and McCune, B. 2004. Decline of arctic-alpine plants at the southern margin of their range following a decade of climatic warming. J. Veg. Sci., 15: 679-690.

Li, Y., Šimůnek, J., Zhang, Z., Huang, M., Ni, L., Zhu, L., Hua, J. and Chen, Y. 2015. Water flow and nitrate transport through a lakeshore with different revetment materials. J. Hydrol., 520: 123-133.

Looy, K.V., Lejeune, M. and Verbeke, W. 2016. Indicators and mechanisms of stability and resilience to climatic and landscape changes in a remnant calcareous grassland. Ecol. Indic., 70: 498-506.

López, D.R., Brizuela, M.A., Willems, P., Aguiar, M.R., Siffredi, G. and Bran, D. 2013. Linking ecosystem resistance, resilience, and stability in steppes of North Patagonia. Ecol. Indic., 24: 1-11.

Lyon, J. and Sharpe, W.E. 2003. Impacts of hay-scented fern on nutrition of northern red oak seedlings. J. Plant Nutr., 26: 487-502.

Magurran A.E. (ed.) 2004. Measuring Biological Diversity. Blackwell Science: Oxford, United Kingdom, pp.107-115.

Méndez-Toribio, M., Zermeño-Hernández, I. and Ibarra-Manríquez, G. 2014. Effect of land use on the structure and diversity of riparian vegetation in the Duero river watershed in Michoacán, Mexico. Plant Ecol., 215: 285-296.

Moran, M.A. 1984. Influence of adjacent land use on understory vegetation of New York forests. Urban Ecol., 8: 329-340.

Morecroft, M.D., Bealey, C.E., Scott, W.A. and Taylor, M.E. 2016. Interannual variability, stability and resilience in UK plant communities. Ecol. Indic., 68: 63-72.

Nagler, P.L., Glenn, E.P., Hinojosa-Huerta, O., Zamora, F. and Howard, K. 2008. Riparian vegetation dynamics and evapotranspiration in the riparian corridor in the delta of the Colorado River, Mexico. J. Environ. Manage., 88: 864-874.

Naiman, R.J. and Decamps, H. 1997. The ecology of interfaces: Riparian zones. Annu. Rev. Ecol. Evol. Syst., 28: 621-658.

Oberle, B., Grace, J.B. and Chase, J.M. 2009. Beneath the veil: Plant growth form influences the strength of species richness- productivity relationships in forests. Global Ecol. Biogeogr., 18: 416-425.

Parmesan, C. and Yohe, G. 2003. A globally coherent fingerprint of climate change impacts across natural systems. Nature, 421: 37-42.

Pauli, H., Gottfried, M., Reiter, K., Klettner, C. and Grabherr, G. 2007. Signals of range expansions and contractions of vascular plants in the high Alps: observations (1994-2004) at the GLORIA* master site Schrankogel, Tyrol, Austria. Global Change Biol., 13: 147-156.

Pennington, D.N., Hansel, J.R. and Gorchov, D.L. 2010. Urbanization and riparian forest woody communities: Diversity, composition, and structure within a metropolitan landscape. Biol. Conserv., 143:182-194.

Qin, Y., Xin, Z., Wang, D. and Xiao, Y. 2017. Soil organic carbon storage and its influencing factors in the riparian woodlands of a Chinese karst area. Catena, 153: 21-29.

Randin, C.F., Engler, R., Normand, S., Zappa, M., Zimmermann, N.E., Pearman, P.B., Vittoz, P., Thuiller, W. and Guisan, A. 2009. Climate change and plant distribution: local models predict high-elevation persistence. Global Change Biol., 15: 1557-1569.

Rheault, G., Proulx, R. and Bonin, L. 2015. Plant species richness prolongs the growing season of freely assembled riparian herbaceous communities under dry climatic conditions. Agric. Ecosyst. Environ., 200: 71-78.

Roberts, M.R. and Gilliam, F.S. 1995. Patterns and mechanisms of plant diversity in forested ecosystems-implications for forest management. Ecol. App., 5: 969-977.

Root, T.L., Price, J.T., Hall, K.R., Schneider, S.H., Rosenzweig, C. and Pounds, J.A. 2003. Fingerprints of global warming on wild animals and plants. Nature, 421: 57-60.

Sagar, R., Raghubanshi, A.S. and Singh, J.S. 2003. Tree species composition, dispersion and diversity along a disturbance gradient in a dry tropical forest region of India. For. Ecol. Manage., 186: 61-71.

Schaich, H., Rudner, M. and Konold, W. 2010. Short-term impact of river restoration and grazing on floodplain vegetation in Luxembourg. Agric. Ecosyst. Environ., 139: 142-149.

Schweiger, O., Biesmeijer, J.C., Bommarco, R., Hickler, T., Hulme, P.E., Klotz, S., Kühn, I., Moora, M., Nielsen, A., Ohlemüller, R. and Petanidou, T. 2010. Multiple stressors on biotic interactions: how climate change and alien species interact to affect pollination. Biol. Rev. Camb. Philos. Soc., 85: 777-795.

Sproull, G.J., Quigley, M.F., Sher, A. and González, E. 2015. Long-term changes in composition, diversity and distribution patterns in four herbaceous plant communities along an elevational gradient. J. Veg. Sci., 26: 552-563.

Sunil, C., Somashekar, R.K. and Nagaraja, B.C. 2016. Diversity and composition of riparian vegetation across forest and agroecosystem landscapes of river Cauvery, southern India. Trop. Ecol., 57: 343-354.

Tabacchi, E., Planty-Tabacchi, A.M., Salinas, M.J. and Décamps H. 1996. Landscape structure and diversity in riparian plant communities: A longitudinal comparative study. Regulated Rivers: Research and Management, 390-367 :12.

Tabarelli, M., Mantovani, W. and Peres, C.C. 1999. Effects of habitat fragmentation on plant guild structure in the montane Atlantic forest of southeastern Brazil. Biol. Conserv., 91: 119-127.

Taylor, A.R. and Chen, H.Y.H. 2011. Multiple successional pathways of boreal forest stands in central Canada. Ecography, 34: 208-219.

Tockner, K. and Stanford, J.A. 2002. Riverine flood plains: present state and future trends. Environ. Conserv., 29: 308-330.

Vannote, R.L., Minshall, G.W., Cummins, K.W., Sedell, J.R. and Cushing, C.E. 1980. The river continuum concept. Can. J. Fish. Aquat. Sci., 37: 130-137.

Walther, G.R. 2010. Community and ecosystem responses to recent climate change. Phil. Trans. R. Soc. B., 365: 2019-2024.

Walther, G.R., Roques, A., Hulme, P.E., Sykes, M.T., Pyšek, P., Kühn, I., Zobel, M., Bacher, S., Botta-Dukát, Z., Bugmann, H., Czúcz, B., Dauber, J., Hickler, T., Jarosík, V., Kenis, M., Klotz, S., Minchin, D., Moora, M,, Nentwig, W., Ott, J., Panov, V.E., Reineking, B., Robinet, C., Semenchenko, V., Solarz, W., Thuiller, W., Vilà, M., Vohland, K. and Settele, J. 2009. Alien species in a warmer world: risks and opportunities. Trends Ecol. Evol., 24: 686-693.

Zenner, E.K., Martin, M.A., Palik, B.J., Peck, J.E. and Blinn, C.R. 2013. Response of herbaceous plant community diversity and composition to overstorey harvest within riparian management zones in Northern Hardwoods. Forestry, 86: 111-118.

Zhang, Y., Chen, H.Y.H. and Taylor, A. 2014. Multiple drivers of plant diversity in forest ecosystems. Global Ecol. Biogeogr., 23: 885-893.

Nature Environment and Pollution Technology
An International Quarterly Scientific Journal

p-ISSN: 0972-6268
e-ISSN: 2395-3454

Vol. 18 | No. 4 | pp. 1119-1129 | 2019

Original Research Paper | Open Access

Biosorption of Chromium by *Bacillus subtilis* Isolated from Ganga River

Vani Sharma and Padma Singh
Department of Microbiology, Kanya Gurukul Campus, Gurukul Kangri Vishwavidhyalaya, Haridwar-249407, India
Corresponding author: Vani Sharma

Nat. Env. & Poll. Tech.
Website: www.neptjournal.com

Received: 27-03-2019
Accepted: 31-05-2019

Key Words:
Biosorption
Chromium
Bacillus subtilis
River Ganga

ABSTRACT

Water pollution by heavy metals due to discharge of industrial and anthropogenic waste leads to serious environmental and health problems as most of these heavy metals are carcinogenic in nature. In the present study chromium biosorption capacity of live and dead biomass of bacterial strain HGB1 isolated from Ganga River in Haridwar, which was examined as *Bacillus subtilis*, following 16S rDNA sequence analysis, was examined for different physical parameters such as pH, time of incubation and temperature. Experimental results indicate that the *Bacillius subtilis* has maximum tolerance capacity up to 1000 mg.L^{-1} with highest metal uptake of 95.64%, 97.25% and 97.11% at pH 3, 60 minutes, 2.5 mg/mL biomass respectively in case of dead biomass. In case of living biomass, highest metal uptake was 81.64%, 96.79 % and 95.89% at pH 7, 72hr and 32°C respectively. The surface chemical functional groups of *Bacillus subtilis* identified by FTIR were amino, carboxyl, hydroxyl and carbonyl groups. The morphological changes were examined by SEM analysis.

INTRODUCTION

Metals naturally occur in earth crust and remain distributed in environment according to their properties and the environmental factors (Khlifi & Hamzachaffai 2010). Notably out of 92 naturally occurring elements, approximately 30 metals are toxic to humans (Sharma & Singh 2015), which basically comprise of heavy metals. In recent decades, heavy metals are widespread in environment and cause water, air and soil pollution (Simly & Sumithra 2017). Heavy metals refer to all those metals and metalloids with atomic density greater than 4 g/cm^3 or 5 times or more than water (Huton & Symon 1986, Battarbee et al. 1988, Nriagu et al. 1995, Hawkes 1997). Out of these heavy metals chromium contamination in aquatic system is of great concern as it is 7^{th} most abundant element in the earth crust (Mohanty & Kumar 2013). Chromium enters into various environmental grids, i.e. air, water and soil through various anthropogenic and industrial wastes (Mondal et al. 2017, Sharma & Singh 2018). In aqueous environment two forms of chromium exist, which are trivalent and tetravalent chromium. The trivalent chromium [Cr(III)] is considered as essential trace elements, which plays role in metabolism of mammals whereas tetravalent chromium [Cr(IV)] is considered as toxic and carcinogenic for mammals (Puentes-Cardenes et al. 2012). The toxic effects of chromium from environmental samples can be treated by the methodologies such as ion-exchange, electrochemical treatment, chemical reduction, etc. but all these techniques are highly expensive, labor intensive, and also generate secondary wastes, which are difficult to be managed, and also these methods are not applicable when the concentration of heavy metals are low (Rakhunde et al. 2012). In recent years a great attention was paid for the use of biological matters as biosorbent for the removal of heavy metals from the environment (Aravindhan et al. 2012). These biosorbents are readily available, cheap and possess high biosorption efficiency. Both live and dead biomass can be used as biosorbent (Saha & Orvig 2010, Samuel et al. 2015). In the present study, live and dead biomass of *Bacillus subtilis* was used as biosorbent for the biosorption of chromium from the aqueous solution. *Bacillus subtilis* is a Gram positive bacteria mainly composed of peptidoglycan and teichoic acid. Peptidoglycan is a polymer of acetyl glucosamine and acetyl muramic acid which displace carboxyl and hydroxyl functional groups. On the other hand, teichoic acid is composed of copyranosyl glycerol phosphate and it displace phosphate and hydroxyl functional groups. These functional groups play main role in forming the bonds between metals and biomass (Sivaprakash et al. 2009). The experimental data were analyzed using kinetics and adsorption isotherms, while Fourier Transform Infrared (FT-IR) spectroscopy was used for the identification of functional groups and SEM was used for the analysis of surface changes present on chromium unloaded and chromium loaded biomass.

MATERIALS AND METHODS

Bacterial isolation from Ganga samples: Bacterial isolates were isolated from Ganga river through serial dilution

method (Waksman & Fred 1922). The 1 mL of water sample was suspended in 9 mL of sterile distilled water blanks and diluted up to 10^{-3} dilution; 0.1 mL of suspension was spreaded on nutrient agar plates and incubated at 30±2°C.

Selection of chromium tolerant bacterial isolate: Ability of 18 bacterial isolates to tolerate chromium was determined by well diffusion method (Hemambika et al. 2011). Chromium salt solution of different concentrations, i.e. 20, 40, 60, 80 and 100 mg/L were prepared and 0.1 mL of these chromium solutions were added in 8mm well prepared nutrient agar plates that were spread with 24 hours old culture of bacterial isolates and then were incubated at 30±2°C for 24 hours and after that incubation zone of inhibition was measured.

Molecular identification of chromium resistant bacteria: The partial sequencing of 16S rDNA of chromium tolerant bacteria was carried out commercially by Eurofins Genomics India Private Limited. Later to accurately identify the strain by software program Clustal W. Distance matrix was generated and the phylogenetic tree was constructed using MEGA 7.

Metal solution preparation: A stock solution of 1000 mg/L concentration was prepared by dissolving potassium dichromate ($K_2Cr_2O_7$) known quantity in double distilled water and stored in refrigerator (Hussein et al. 2004).

Biosorbent Preparation

(a) Preparation of live biomass: Selected and identified *Bacillus subtilis* strain was grown and maintained on the nutrient agar slants and a loopful pure culture was transferred in sterile nutrient broth and incubated at 30 ± 2°C in a shaker incubator for overnight and used as live biomass.

(b) Preparation of dead biomass: *Bacillus subtilis* culture was grown in nutrient broth at 30±2°C for 24 hours and harvested by centrifuging at 10000 rpm for 10 min at 4°C. Cell pellets, thus obtained, was washed twice with distilled water to make sure that no media remain attached to pellets and then they are dried for 6 hours at 80°C in hot air oven.

Biosorption experiments: The biosorption experiment were conducted during different physical parameters in 100 mL Erlenmeyer flasks containing 50 mL of 100 $mg.L^{-1}$ chromium salt solution; biosorption studies were performed using 0.5 to 2.5 $g.L^{-1}$ of died and living biomass (Aravindhan et al. 2011). The flasks with test solutions were agitated at 120 rpm using a shaker incubator at room temperature for different time intervals, i.e. 20, 40, 60, 80 and 100 minutes for dead biomass and 24, 48, 72, 96 and 120 hours for live biomass and different pH such as 3, 5, 7, 9 and 11 (Congeevaram et al. 2007). The batch biosorption experiments were also done at different temperatures for biosorption. The change in metal concentration after biosorption was determined by AAS technique. For isotherm study cell weight was kept constant, i.e. 1 mg/mL (Gelagutashvili 2013).

Kinetics studies: To study biosorption kinetics, varying biosorbent dose, i.e. 0.5, 1.0, 1.5, 2.0 and 2.5 g was used for the biosorption of 100 mg/L chromium in aqueous solution. Pseudo first order and Pseudo second order were used to determine the biosorption kinetics of *Bacillus subtilis* biosorption. First order rate expression was given by Lagergren (Namasivayam & Kanchana 1993).

$$\log(q_e - q) = \log q_e - \frac{K_1}{2.303} \quad \ldots(1)$$

Where, q_e is amount of chromium absorbed at equilibrium, q is amount of chromium absorbed while *t* is time in minutes in which Cr absorbed, k_t and q_e were first order rate constant and these are determined by slopes and intercepts of plots of log (q_e –q) versus t at different biomass dosages.

Second order kinetics was given by (Ho & McKay 1999).

$$\frac{t}{q_t} = \frac{1}{k_2 q_e^2} + \frac{1}{q_e t} \quad \ldots(2)$$

Where, k_2 and q_e were determined by the intercept of the slope of plot obtained by plotting *t/qt* versus time *t*.

Biosorption Characterization Through Surface Studies

Fourier transforms infrared (FT-IR) spectroscopy: FT-IR was used for the analysis of chemical nature of biosorbent surface before and after chromium loading. For FT-IR analysis chromium unloaded and loaded pellets of *Bacillus subtilis* were obtained and oven dried at 80°C for 2 hours, and 0.1 g of finely grounded biomass pellets were mixed with KBr for analysis (Rezaei 2013).

Scanning electron microscopy: For SEM analysis culture of *Bacillus subtilis* was centrifuged at 6000 rpm for 15 minutes, the supernatant was discarded and bacterial pellets were washed 3-4 times with 0.1M phosphate buffer (pH 7.2) after which pellets were fixed in 2.5% glutaraldehyde and dehydrated with 30-90% ethanol and finally dehydrated with 100% ethanol for 8-10 minutes. Chromium loaded and non-loaded samples were coated with gold 90 Å thick layer under vacuum to improve the quality of the image (Michalak et al. 2014).

RESULTS AND DISCUSSION

Total of 15 bacterial isolates were isolated from Ganga water samples. All these isolates were now screened for chro-

Table 1: Ability of bacterial isolates to tolerate chromium (average of triplicates).

Isolates	Chromium tolerance ability (± SE)					
	10 mg/L	20 mg/L	40 mg/L	60 mg/L	80 mg/L	100 mg/L
HGB1	-	-	-	-	-	-
HGB2	-	3.6±0.3	5.2±0.1	6.6±0.3	6.8±0.05	7.7±0.1
HGB3	-	-	-	-	-	4.4±0.05
HGB4	-	-	-	-	-	-
HGB5	-	4.3±0.3	5.6±0.2	6.8±0.02	8.6±0.3	10.8±0.02
HGB6	-	-	-	-	-	13.1±0.01
HGB7	-	-	-	-	6.5±0.01	7.9±0.01
HGB8	-	-	4.9±0.03	6.6±0.06	7.6±0.1	9.6±0.1
HGB9	-	-	6.3±0.33	6.9± 0.01	8.8±0.01	10.5± 0.5
HGB10	-	-	-	-	-	-
HGB11	-	-	-	5.1±0.05	8.3±0.66	10.3±0.66
HGB12	-	-	-	-	-	-
HGB13	-	3.3±0.3	4.6±0.33	5±0.01	6.4± 0.02	7.8±0.01
HGB14	-	-	-	-	-	-
HGB15	-	-	-	-	-	-

mium tolerance capacity through well diffusion method (Table 1). The growth of isolate, which is chromium resistant, will show no or very less zone of inhibition.

From the results (Table 1), it was found that HGB1 isolate shows no zone of inhibition up to 100 mg/L concentration of chromium, further on the basis of 16S rDNA sequencing HGB1 was found to be *Bacillus subtilis* (Fig. 1).

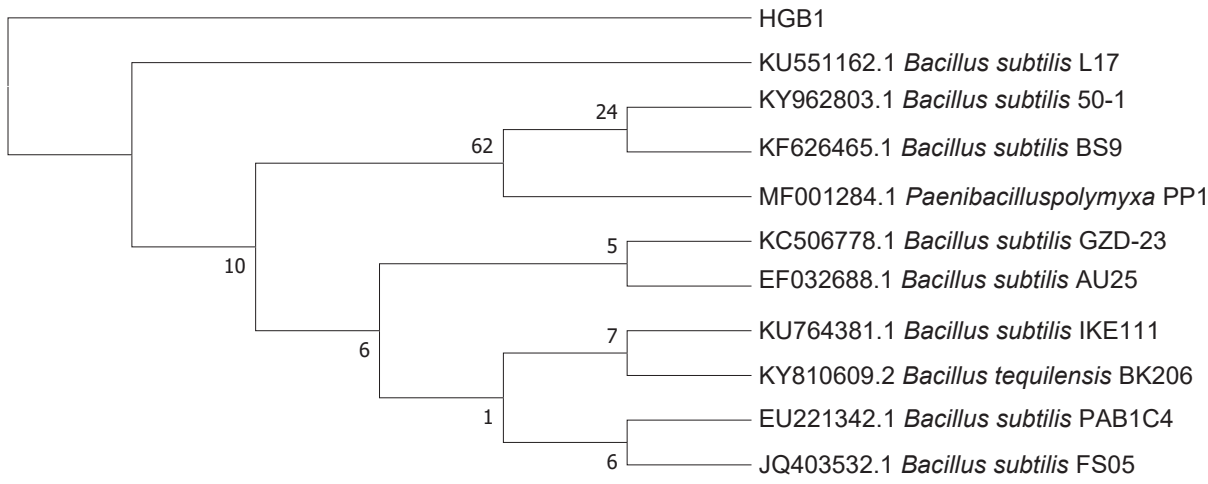

Fig. 1: Phylogenetic tree showing the relationship on the basis of 16S rDNA gene sequencing.

Table 2: Biosorption assay at different physical parameters.

Heavy metals	Microorganisms	Initial Concentration (mg/L)	Parameters	% of Removal		
			pH	**Dead**	**Live**	
Chromium (Cr)	*Bacillus subtilis*	100	3	81.89	2.06	
			5	92.65	19.89	
			7	83.09	91.34	
			9	74.78	22.40	
			11	34.99	3.68	
			Temp., °C	**Dead**	**Live**	
Chromium (Cr)	*Bacillus subtilis*	100	25	80.31	69.92	
			30	91.94	87.27	
			35	95.91	93.61	
			40	86.11	73.93	
			45	66.44	67.02	
			Time (min)	**Dead**	**Time (Hours)**	**Live**
Chromium (Cr)	*Bacillus subtilis*	100	20	79.72	24	61.48
			40	88.92	48	87.12
			60	97.25	72	94.02
			80	98.80	96	95.01
			100	98.95	120	95.97
			Biomass dose (mg/mL)	**Dead**	**Live**	
Chromium (Cr)	*Bacillus subtilis*	100	0.5	83.34	38.02	
			1.0	89.79	53.87	
			1.5	92.78	79.92	
			2.0	94.89	87.22	
			2.5	97.11	95.71	

Effect of pH change: The pH of the solution had a significant role in the removal of chromium; at particular pH the adsorption becomes maximum, below or above that pH the biosorption rate decreases (Zhou & Kiff 1991). In the present study the effect of pH on biosorption was determined by varying pH from 3 to 11, and it was found that in case of dead and live biomass at pH 5 and pH 7 biosorption was maximum, i.e. 92.65 % and 91.34 % respectively (Fig. 2). Aravindhan et al. (2011), Garcia et al. (2016) and Sukumar et al. (2014) also studied the effect of pH on biosorption of chromium by *Bacillus subtilis* and they also found that pH 2, 4.5 and 6 and are optimum for the biosorption (Table 2). Sethuraman & Balasubramanian (2010) studied the effect of pH on live biomass of *Bacillus subtilis* biosorption capacity and found that pH 7 was optimum. The possible reason for this might be that pH may affect the ionization state of the chemical functional groups such as carboxyl, amino and hydroxyl that are responsible for the binding of heavy metals (carry a positive charge). On low pH these functional groups become protonated and increase positive charge on the biosorbent and decrease the attachment of metal ions on biosorbent. On the other hand at high pH value, functional group becomes deprotonated and hence increase negative charge on the biosorbent, that is why more and more metal ions get attached to the surface of biosorbent (Comte et al. 2008 and Krishnani et al. 2008).

Effect of time of incubation: The incubation time was one of the important parameters that affect biosorption efficiency. In present study, the effect of time on 100 mg/L concentration of chromium was examined, and observed that 60 minutes and 72 hours was optimum for dead and live biomass and they show 95.91% and 93.61% removal of chromium respectively (Figs. 3 & 4). The similar study made by Murthy et al. (2012) showed 75.6% biosorption at

Fig. 2: Effect of pH on biosorption of chromium by dead and live biomass.

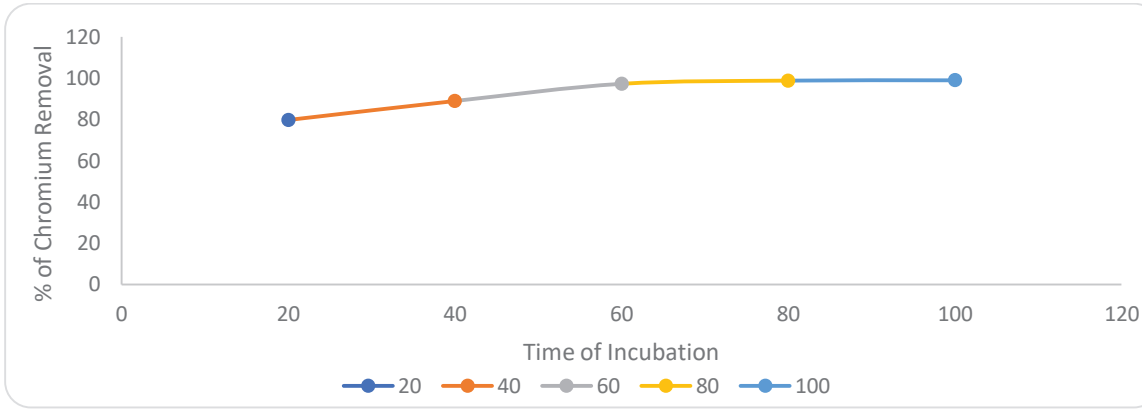

Fig. 3: Effect of time of incubation on the metal uptake capacity of dead biomass.

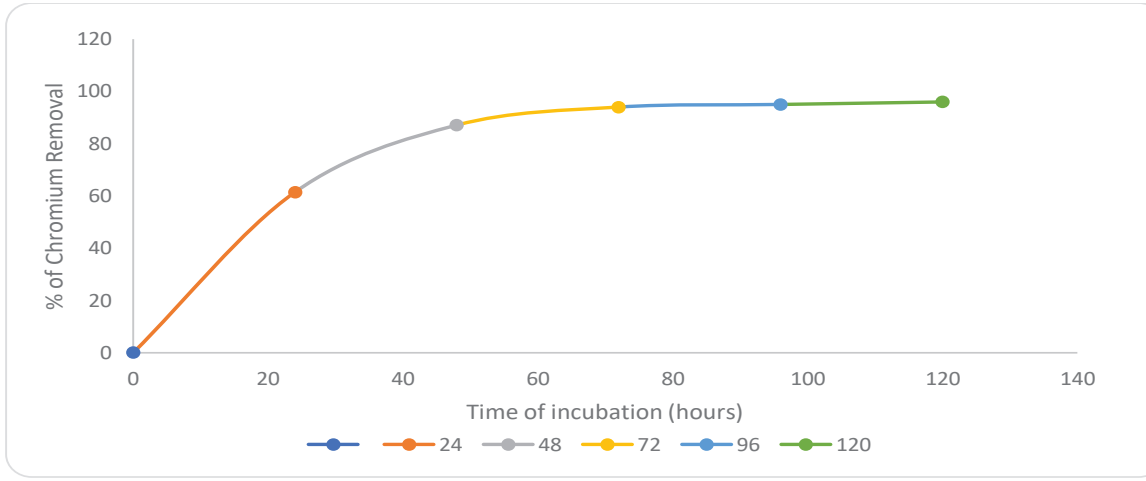

Fig. 4: Effect of time of incubation on the metal uptake capacity of live biomass.

72 hours to be optimum while studying biosorption of 200 mg/L lead by *Bacillus cereus*. Giri (2012) studied biosorption capability of living *Bacillus cereus* for 50 mg/L Pb and Cd and found 50.11% reduction in 48 hours.

Effects of temperature: To study the effects of temperature on the biosorption of 100 mg/L chromium by *Bacillus subtilis,* we carried our experiment on temperature ranging from 25°C to 45°C. It was found that the maximum biosorption was attained at 35°C, i.e. 95.91% and 93.61% for dead and live biomass respectively, which kept on slightly increasing with further increase in temperature (Fig. 5). These results indicate that the process of metal uptake was endothermic in nature. Similar results were also observed by Congeevaram et al. (2007) when they studied biosorption of Cr(VI) and Ni by *Micrococcus* sp. Aravindhan et al. (2012) studied the effect of temperature on the biosorption of Cr(III) using *Bacillus subtilis* biomass and found that at 30°C, biosorbent achieved maximum biosorption of Cr, i.e. 71.69%. Similar results were also obtained by Murthy et al. (2012), Ahmed & Kibret (2013), Kareem et al. (2014), Verma (2017) supporting the present study.

Effect of biomass dose: To study the effect of biomass dos-

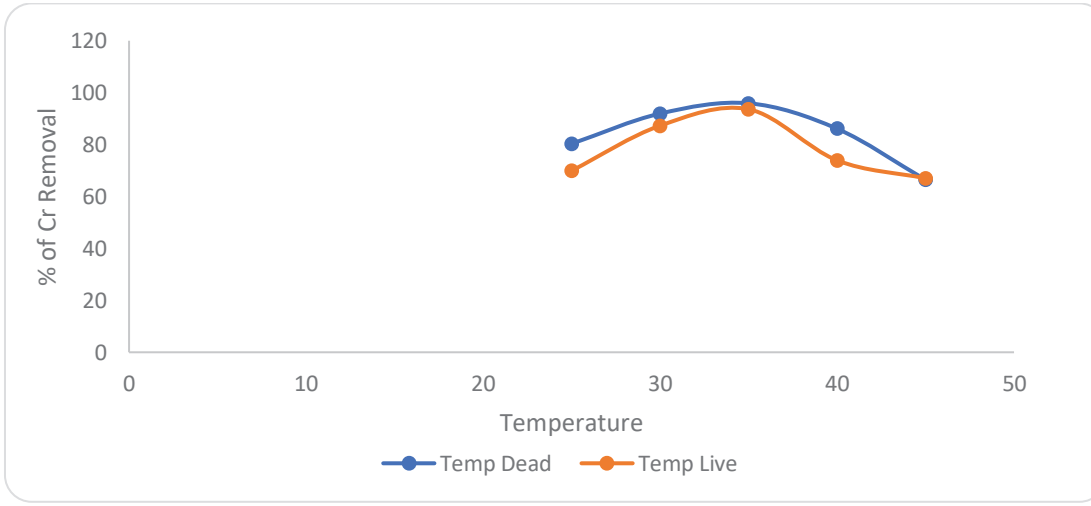

Fig. 5: Effect of temperature on metal uptake capacity of dead and live biomass.

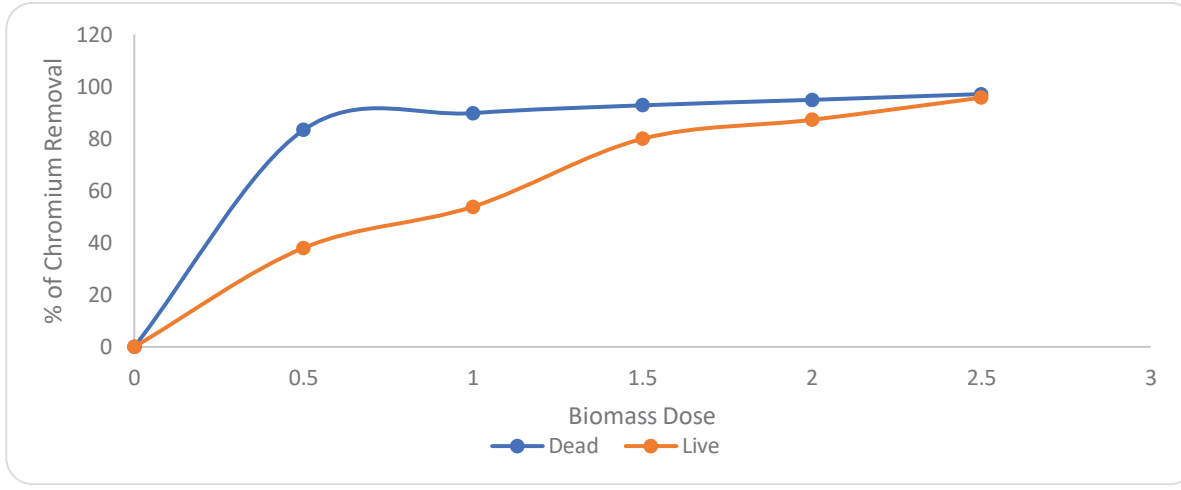

Fig. 6: Effect of biomass dose on metal uptake capacity of dead and live biomass.

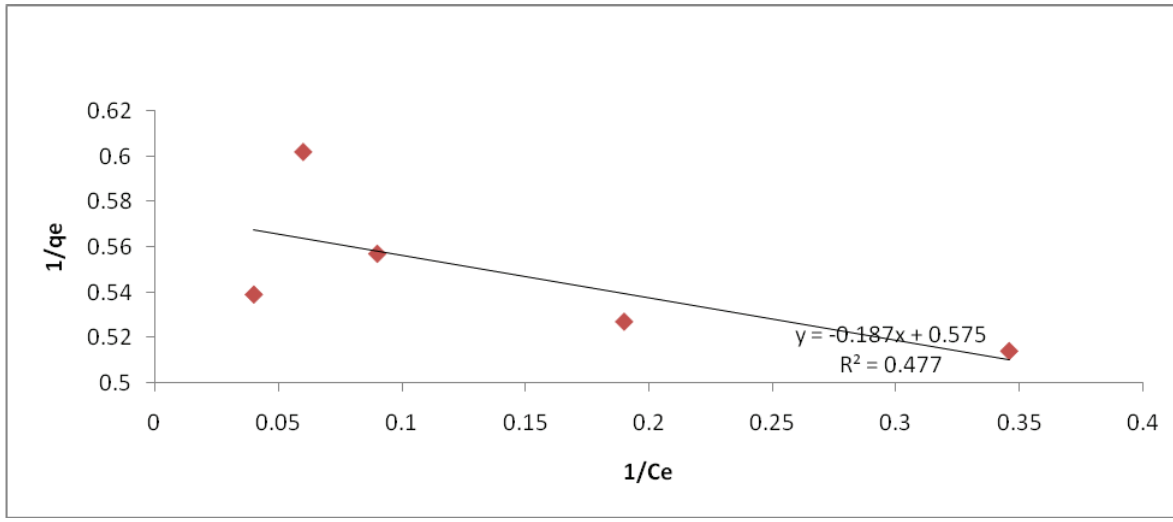

Fig. 7: Langmiur isotherm for chromium by *Bacillus subtilis* at pH 5, 60 min, 350°C temperature.

age on 100 mg/L heavy metals aqueous solution, 0.5, 1.0, 1.5, 2.0 and 2.5 mg/mL of biomass dosage were considered, and it was found that the percentage uptake increased with increase in biomass (Fig. 6). During the study with *Bacillus subtilis*, % biosorption increases to 97.11% for dead biomass and 95.71% for live biomass. The same was observed by Aravindhan et al. (2011) and Bala-Kumaran et al. (2013).

Isotherm Analysis

Langmuir isotherm: The data obtained in the study of 100 mg/L aqueous solution of chromium showed the value of R^2 (Langmuir) as 0.004 (Fig. 7) and R^2 (Freundlich) as 0.909 (Fig.8) for *Bacillus subtilis* (Table 3). The value of 1/n further supports the Freundlich equation. Thus, equilibrium experimental results of chromium ions have been

Table 3: Parameters of isotherm models for chromium.

Biosorbent	Langmuir Isotherm			Freundlich Isotherms		
	q^o	B	R^2	r^2	K_f	n
Bacillus subtilis	2.89	1.019	0.477	0.921	2.15	0.4

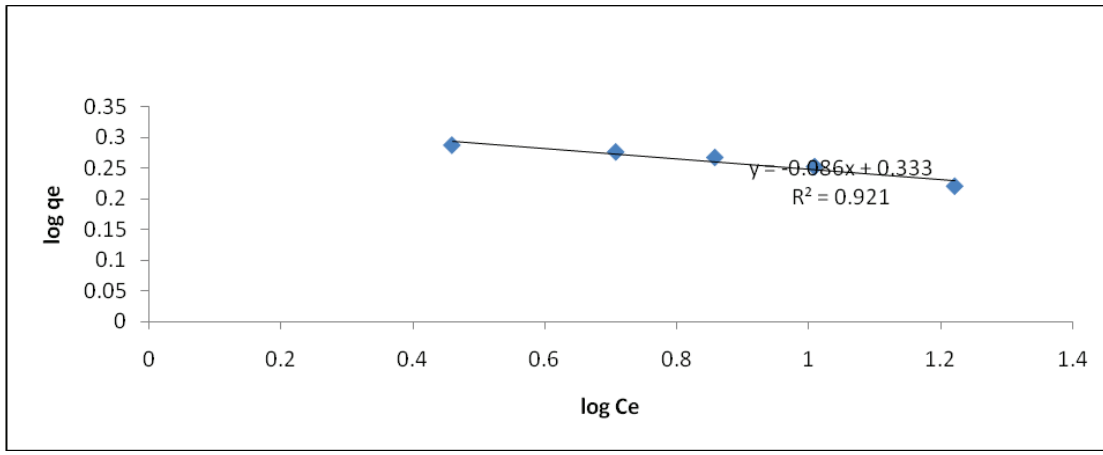

Fig. 8: Freundlich isotherm for chromium by *Bacillus subtilis* at pH 5, 60 min, 35°C temperature.

fitted in Langmuir and Freundlich models according to the Vijaykumar et al. (2012). If the value of the coefficient is less than 1, absorption is favorable. Similar pattern was also observed by Wierzba (2015).

Kinetic analysis: To calculate a suitable kinetic model, metal uptake data were plotted against time. The linear line shows the favorable biosorption process. In the present study, the results fitted in second-order kinetics (Table 4, Figs. 9 & 10).

FT-IR analysis: The spectra that were obtained during FT-IR analysis of chromium unloaded biomass (Fig. 11) show a broad and strong peak at 3447.82 cm^{-1} indicating the presence of hydroxyl groups. Another peak 2928 cm^{-1} lies in the range of 2930-2925 cm^{-1} which was considered for the presence of C-H group. The strong peak occurring at 1636 cm^{-1} indicates the presence of amino (N-H) group. Peaks at 1384.55 and 1056.80 cm^{-1} lie in the range of 1430-1280 cm^{-1} and 1.350-900 cm^{-1}, which represent the presence of

Table 4: Parameters of pseudo kinetics for chromium.

Biosorbent	Pseudo first order			Pseudo second order		
	K_1	q_e	R^2	K_2	q_e	R^2
Bacillus subtilis	0.0004	1.945	0.773	0.00041	2.75	0.999

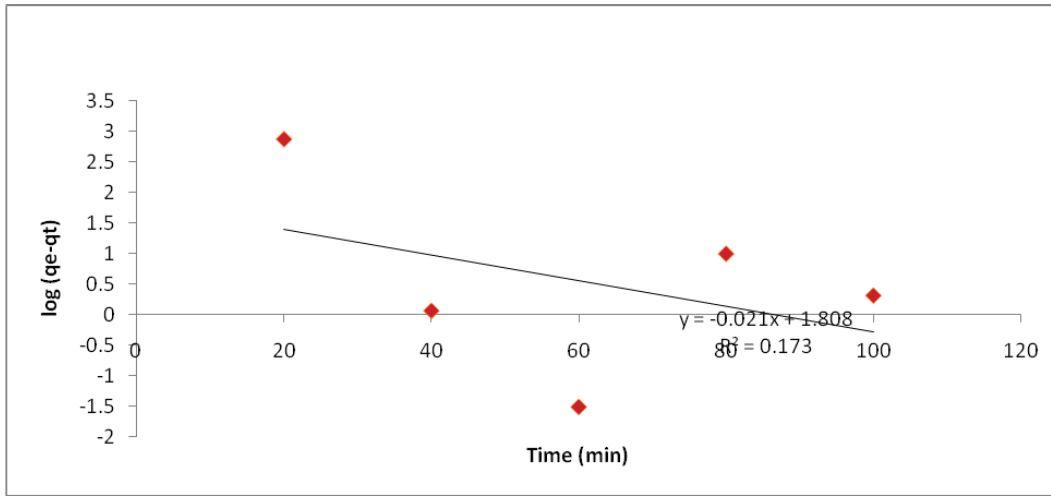

Fig. 9: First order kinetics for chromium by *Bacillus subtilis* at 60 min, pH 5, 35°C temperature.

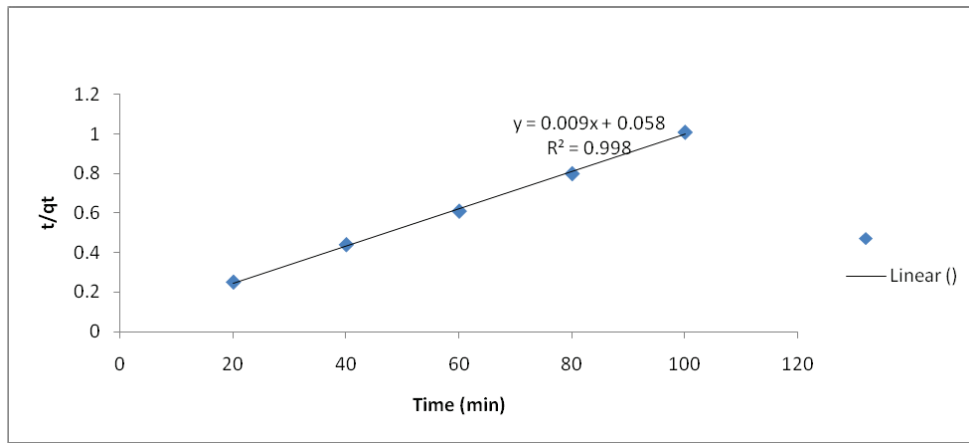

Fig. 10: Second order kinetics for chromium by *Bacillus subtilis* at 1 mg/mL biomass concentration, pH 5, 30°C.

O-H and C-N stretching respectively (Jaafar et al. 2015 and Yun et al. 2001). A peak at 680 cm^{-1} may be assigned to OH variation (Coates 2000). On the study of chromium loaded biomass (Fig. 12) peak of O-H group changes from 3469.68 cm^{-1} to 3447.82 cm^{-1}.

SEM analysis: Scanning electron microscopy (SEM) of *Bacillus subtilis* before and after biosorption of chromium clearly revealed the surface texture difference before and after biosorption (Fig. 13).

CONCLUSION

The present study has demonstrated the ability of *Bacillus subtilis,* isolated from Ganga river, as biosorbent for the removal of chromium ions from aqueous solution. Its biosorption ability was depend upon various factors, i.e. pH, temperature and time of incubation. Kinetics and equilibrium data also fitted with pseudo first and second order and Langmuir isotherm model; these models provide the information that the present process was favorable process-

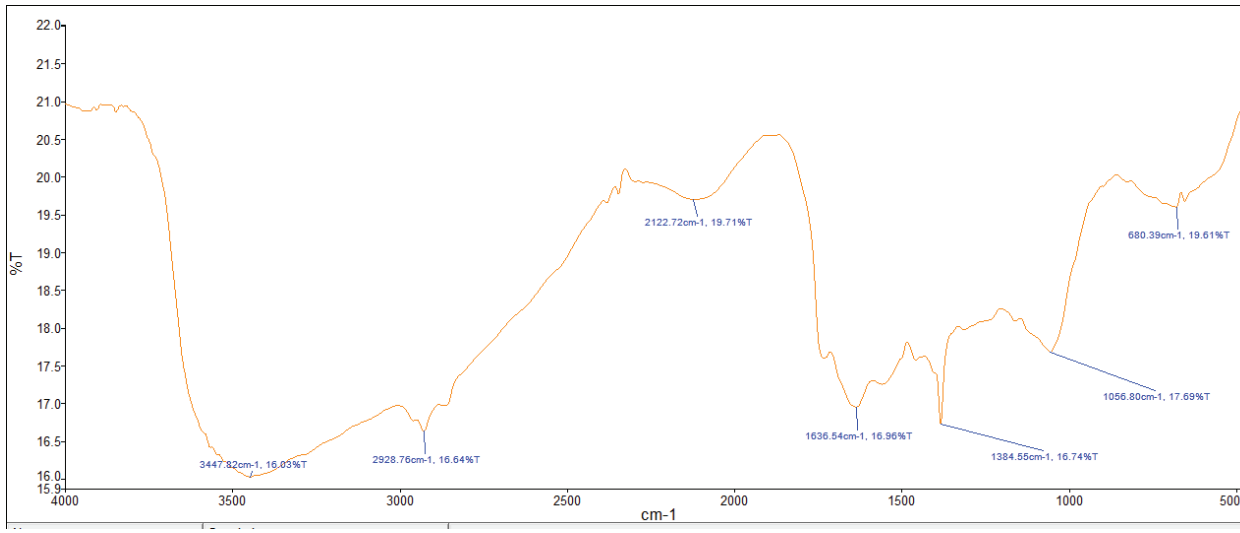

Fig. 11: FT-IR analysis of chromium unloaded *Bacillus subtilis*.

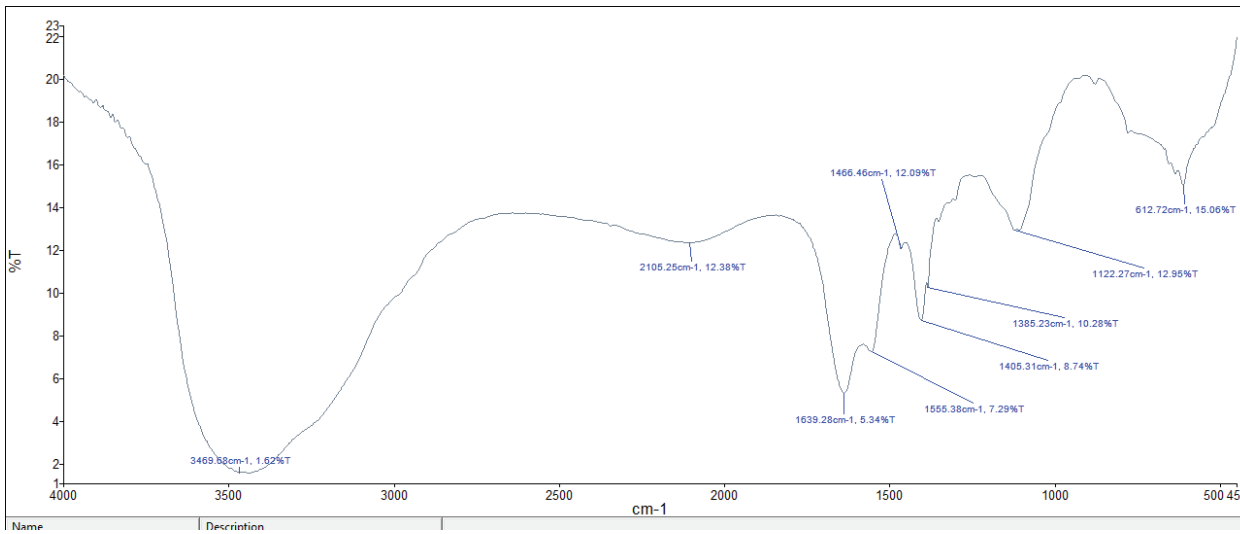

Fig. 12: FT-IR analysis of chromium loaded *Bacillus subtilis*.

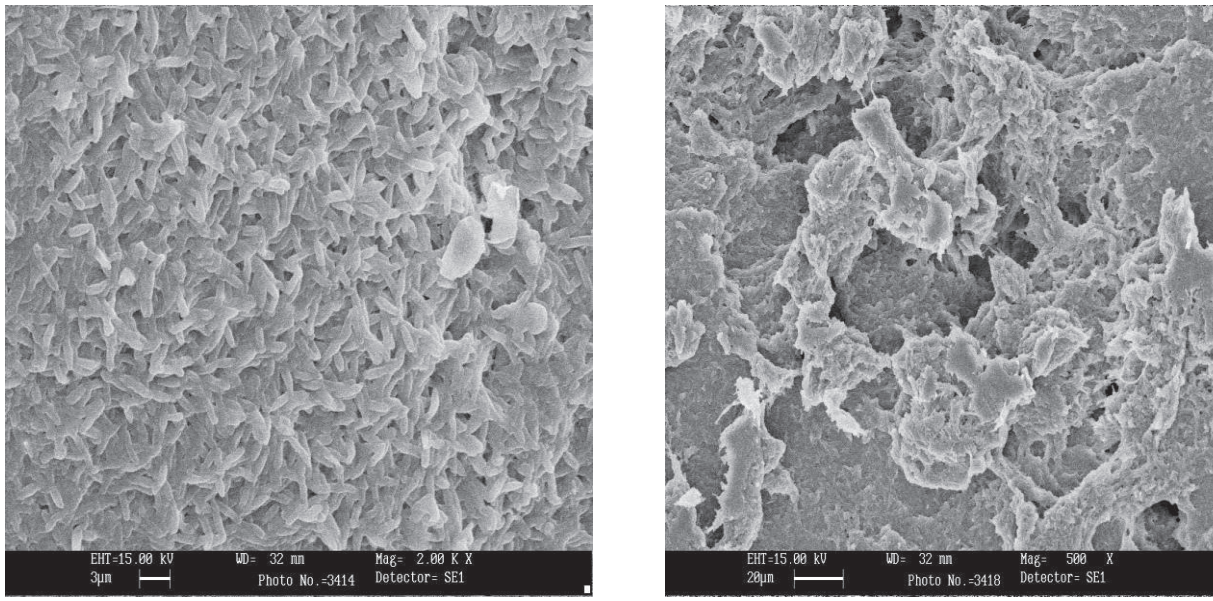

(a) (b)

Fig. 13: Scanning electron microscopy (SEM) micrographs of *Bacillus subtilis* before (a) and after (b) of biosorption.

es. The proposed biosorption process can be successfully applied for the treatment of the waste that contains chromium ions.

ACKNOWLEDGEMENT

We owe our sincere gratitude to Gurukul library for finding literature on our work; we also wish to acknowledge DST for providing the financial support by providing INSPIRES fellowship.

REFERENCES

Arvindhan, R., Fathima, A., Selvamurugan, M., Rao, J.R., and Balachandran, U.N. 2012. Adsorption, desorption and Kinetic study on Cr (III) removal from aqueous solution using *Bacillus subtilis* biomass. Clean Technol. Environ. Policy, 14: 727-735.

Battarbee, R.W., Anderson, N.J., Appleby, P.G., Flower, R.J., Fritz, S.C., Haworth, E.Y., Higgitti,S., Jones, V.J., Kreiser, A., Munro, M.A.R., Natkanshi, J., Oldfeild, F., Patrick, S.T., Richard-son, N.G., Rippey, B. and Stevenson, A.C. 1988. Lake Acidification in United Kingdom. ENSIS, London.

Coates, J. 2000. Interpretation of infrared spectra, a practical approach. In: Meyers, R.A. (Ed), Encyclopedia of Analytical Chemistry. John Wiley and Sons Ltd, Chichester, pp. 10815-10837.

Comte, S., Guibaud, G. and Baudu, M. 2008. Biosorption properties of extracellular polymeric substances (EPS) towards Cd, Cu and Pb for different pH values. J. Hazard Master, 151: 185-193.

Congeevaram, S., Dhanarani, S., Park, J., Dexillin, M. and Thamaraiselvi, K. 2007. Biosorption of chromium and nickel by heavy metals resistant fungal and bacterial isolates. Journal of Hazardous Material, 146: 270-277.

Garcia, R., Campas, J., Cruz, J. A., Calderon, M. E., Raynal, M. E. and Buitron, Y. G. 2016. Biosorption of Cd, Cr, Mn and Pb from aqueous solutions by *Bacillus* sp. strains isolated from industrial waste activate sludge. TIP Rev. Esp. Ciene. Quim. Biol., 19(1): 5-14.

Gelagutashvili, E. 2013. Comparative study on heavy metals biosorption by different types of bacteria. Open Journal of Metal, 3: 62-67.

Giri, A.K. 2012. Removal of arsenic (III) and chromium (IV) from the water using phytoremediation and bioremediation technique. PhD Thesis, Odisha, India.

Hawkes, J.S. 1997. Heavy metals. J. Chem. Educ., 74(11): 1374.

Hemambika, B., Johmcy, M.R. and Kannan, V.R. 2011. Biosorption of heavy metals by immobilized and dead fungal cells: A comparative assessment. Journal of Ecology and the Natural Environment, 3(5): 168-175.

Hussein, H., Ibrahim, S. F., Kandeel, K. and Hassan, M. 2004. Biosorption of heavy metals from waste water using *Pseudomonas* sp. Electronic Journal of Biotechnology, 7(1).

Hutton, M. and Symon, C. 1986. The quantities of cadmium, lead, arsenic entering the U.K. environment from human activities. Science of the Total Environment, 16: 1677-1700.

Jaafar, Sulami, A. A., Taee, A. A. and Aldoghachi, F. 2015. Biosorption of some heavy metals by metals by metal resistant *Bacillus thuringiensis* isolated from soil in Basra Government, Iraq. Journal of Biology, Agriculture and Healthcare, 5: 106-114.

Khilfi, R. and Hamza-chaffai, A. 2010. Head and neck cancer due to heavy metals exposure via tobacco smoking and professional exposure. A review. Toxicology and Applied Pharmacology, 248: 71-88.

Krishnani, K.K., Meng, X.G., Christodoulatos, C. and Boddu, V.M. 2008. Biosorption mechanism of nine different heavy metals onto biomatrix from rice husk. J. Hazard Mater., 153: 1222-1234.

Kumar, R., Bishnoi, N. R. and Garima, Bishnoi, K. 2008. Biosorption of chromium (VI) from aqueous solution and electroplating wastewater using fungal biomass. Chemical Engineering Journal, 135: 202-208.

Michalak, J., Wolowiee, P. and Chojnacka, K. 2014. Determination of

exposure to lead of subjects from South-Western Poland by human hair analysis. Environmental Monitoring and Assessment, 186: 1259-2267.

Mohanty, M. and Kumar, P.H. 2013. Effect of ionic and chelate assisted hexavalent chromium on mung bean seedlings (Vigna Radiata. Wilczek Ark- 351) during seedling growth. JSPB, 9(2): 232-241.

Mondal, N.K., Samanta, A., Dutta, S. and Chattoraj S. 2017. Optimization of Cr (VI) biosorption onto Aspergillus niger using 3- level Box Behnken design, equilibrium, kinetic, thermodynamic and regeneration studies. Journal of Genetic Engineering and Biotechnology, 24: 65-71.

Namasivayam, C. and Kanchana, N. 1993. Removal of congo red from aqueous solutions by waste banana pith. Pertanika, 1: 32-42.

Puentes-Cardenas, I.J., Pedroza- Rodriguez,A.M., Navarrete-lopez, M., Villegas-Garrido, T. L. and Cristiani-Urbina, E. 2012. Biosorption of trivalent chromium from aqueous solutions by *Pleurotus ostreatus* biomass. Environ. Eng. Manag. J., 11: 1741-52.

Rakhunde, R., Deshpande, L. and Juneja, H.D. 2012. Chemical speciation of chromium in water: A review. Crit. Rev. Environ. Sci. Technol., 42(7): 776-810.

Rezaei, H. 2013. Biosorption of chromium by using *Spirulina* sp. Arabian Journal of Chemistry, 9(6): 846-853.

Saha, B. and Orvig, C. 2010. Biosorbent of hexavalent chromium elimination from industrial and municipal effluents. Coord. Chem. Rev., 254: 2959-2972.

Sahin, Y. and Ozturk. 2005. Biosorption of Chromium (IV) ions from aqueous solution by the bacterium *Bacillus thuringiensis*. Process Biochem., 40: 1895-1901.

Samuel, M. S., Abigail, M. E.A. and Ramalingam, C. 2015. Biosorption of Cr (VI) by *Ceratocystis paradoxa* MSR2 using isotherm modeling, kinetic study and optimization of batch parameters using response surface methodology. PLOS one, 10(3).

Sethuraman, P. and Balasubramanian, N. 2010. Removal of Cr (IV) from aqueous solution using *Bacillus subtilis, Pseudomonas aeruginosa* and *Enterobacter cloacae*. International Journal of Engineering Science and Technology, 2(6): 1811-1825.

Sharma, V. and Singh, P. 2015. Heavy metals pollution and its effect on environment and human health. International Journal of Recent Scientific Research, 6(10): 7752-7755.

Sharma, V. and Singh, P. 2018. Correlation study on physico-chemical parameters of river Ganga, during different seasons in Haridwar. International Journal of Research in Advent Technology, 6(9): 2261-2272.

Sivaprakash, A., Aravindhan, R., Rao, J. R. and Nair, B.U. 2009. Kinetics and equilibrium studies on the biosorption of hexavalent chromium from aqueous solutions using *Bacillus subtilis* biomass. Appl. Ecol. Environ. Res., 7: 45-57.

Smily, J.R.M.B. and Sumithra, P.A. 2017. Optimization of chromium biosorption by fungal adsorbent, *Trichoderma* sp. BSCR02 and its desorption studies. Hayati Journal of Biosciences, 24(2): 65-71.

Sukumar, C., Janaki, V., Kannan, S.K. and Shanti, K. 2014. Biosorption of chromium (VI) using *Bacillus subtilis* SS-1 isolated from soil samples of electroplating industry. Clean Technologies and Environmental Policy, 16(2): 405- 413.

Vijaykumar, G., Tamilarsan, R. and Dharmendira kumar, M. 2012. Adsorption, kinetic, equilibrium and thermodynamic studies on the removal of basic dye Rhodamine-B from aqueous solution by the use of natural adsorbent perlite. Journal of Material Environmental Science, 3(1): 157-170.

Waksman, S.A. and Fred, E.B. 1922. A tentative outline of the plate method for determining the number of microorganisms in the soil. Soil Sci., 14: 27-28.

Wierzba, S. 2015. Biosorption of lead (II), zinc (II) and nickel (II) from industrial wastewater by *Strenotrophomonas maltophilia* and *Bacillus subtilis*. Polish Journal of Chemical Technology, 17(1): 79-87.

Yun, Y.S., Park, J.M. and Volesky, B. 2001. Biosorption of trivalent chromium on the brown seaweeds biomass. Environ. Sci. Technol., 35: 4353-4358.

Zhou, J.L. and Kiff, R.J. 1991. The uptake of copper from aqueous solution by immobilized fungal biomass. J. Chem. Technol. Biotechnol., 52: 317- 340.

Nature Environment and Pollution Technology
An International Quarterly Scientific Journal

p-ISSN: 0972-6268
e-ISSN: 2395-3454

Vol. 18 | No. 4 | pp. 1131-1141 | 2019

Original Research Paper | Open Access

Nano-porous Membrane Process for Brackish Groundwater Treatment: Efficiency Analysis Using Response Surface Methodology

Yuzheng Lv*, Jihao Zhou, Zhengjun Mai** and Jie Liu**†**

*Research Institute for National Defense Engineering for Academy of Military Science PLA, Beijing, 100085, China
**Department of Military Facilities, Army Logistics University, Chongqing, 401331, China
†Corresponding author: Jie Liu

Nat. Env. & Poll. Tech.
Website: www.neptjournal.com

Received: 30-07-2018
Accepted: 21-09-2018

Key Words:
Nanofiltration
Groundwater
Desalination
Response surface methodology (RSM)

ABSTRACT

Excessively high concentration of inorganic salts in the groundwater is the main threat for residents to drink directly in the remote areas of northwestern China. In this paper, nano-porous membrane process was proposed to removal of diverse ions in such raw water. Through the response surface methodology (RSM), the effects of multiple factors on permeate flux and ion rejection rates were analysed, and the application scope of nanofiltration for various water resource was evaluated. It was found that the factors affecting permeate flux, chloride removal and nitrate removal (response value) followed some typical sequences, and the operating pressure was always the most influential factor. Besides, nano-porous membrane process showed predominant performance in the removal of sulphate, chloride and fluoride; the rejection rates were over 99%, 97% and 95%, respectively, and the produced water could completely satisfy the relevant national standards for drinking water. However, nitrate removal rate was seldom over 80%, and it reduced obviously with the increasing initial concentration of nitrate, thus the nitrate content of raw water should be controlled within 40 mg.L^{-1}.

INTRODUCTION

Compared with traditional surface water, the groundwater resource is considered more abundant in most remote rural areas in northwest China. However, the groundwater is often not suitable for residents to drink directly due to its excessive levels of inorganic salts (Greenlee et al. 2010). It is necessary to desalt this brackish groundwater so that it can be utilized without threats from the high salinity. Conventional brackish groundwater treatment methods include ion exchange (Fox et al. 2014), adsorption (Zhang et al. 2016), electrodialysis (Onorato et al. 2017), distillation (Plattner et al. 2017) and reverse osmosis (Pérez-González et al. 2012), which have several disadvantages such as high investments and operation costs, low efficiency and recontamination problems (Pangarkar et al. 2011).

In the northwest rural areas of China, the phenomena that inorganic salt concentration among groundwater outnumber the standard are mainly embodied in indicators like sulphate, chloride, fluoride, nitrate and hardness. Compared with the seawater, salt concentration is lower in the groundwater, but both the ratios of $m_{SO_4^{2-}}/m_{TDS}$ and $m_{Ca^{2+}}/m_{TDS}$ are higher. Thus, these water quality characteristics make nanofiltration an alternative method for brackish groundwater desalination and purification. With a nominal pore size of 1~2 nm, nanofiltration falls between reverse osmosis and ultrafiltration in its separation characterization and becomes a new type of separation technology in recent years. Sieving and Donnan repulsion are the two main separation mechanisms for nanofiltration, they are separation of uncharged solutes due to size effects and separation of charged species like ions because of electrical repulsion, respectively (Bouranene et al. 2008). Possessing the advantages of high permeate flux, high divalent ion removal efficiency, low operating pressure and low investment, nanofiltration technology is gradually being applied in the fields of desalination of groundwater, softening of seawater, reuse and treatment of wastewater. At present, the reverse osmosis process with the separation feature of broad-spectrum has been partly applied in the northwest of China for brackish groundwater desalination. However, the shortcomings of low recovery rate, high energy consumption and strict pretreatment originate from the reverse osmosis process have a serious impact on the economics for the groundwater treatment systems. Compared with reverse osmosis, choosing nanofiltration cannot only avoid these defects, but also obtain a satisfactory desalting effect with some elements retained which are beneficial to the human body (Strathmann 2010). In addition, low operating pressure is the further superiority to promote the application of nanofiltration at remote locations with limited electrical supply (Padilla & Saitua 2010).

Nowadays, it has been confirmed that the groundwater source with higher pollutant concentrations may exist in the remote areas of Northwest China (Ma et al. 2011). Howev-

er, the application scope of raw water and the competitive relationship of ions removal during nano-porous membrane process are not completely understood. In this way, there is seldom a completely theoretical model to accurately describe the dynamic process for inorganic salts removing in brackish groundwater through nanofiltration membrane. The purification efficiency of the nanofiltration membrane is mainly measured by the water flux and ion rejection rate. A large number of studies have shown that the main factors affecting the water purification efficiency of nanofiltration are the raw water quality (the initial concentration of pollutants) and operating conditions (operating pressure and the inlet flow) (Han et al. 2013, Diawara 2008).

This work investigated the efficiency of nano-porous membrane as a potential technique for groundwater advanced treatment by satisfying the standard for drinking water quality of GB5749-2006. The aim of this study was to better understand the purification mechanism for removing inorganic salts in the brackish groundwater by nanofiltration, and to analyse various factors that influence the membrane flux and ion rejection rate, thus to evaluate the application scope of raw water quality based on the produced water quality. Response surface methodology (RSM), a critical tool for experimental design and parameters optimization, was utilized in this research, and the results obtained could provide technical support for the practical demonstration projects in the remote areas of Northwest China.

MATERIALS AND METHODS

Raw Water and Membrane

With reference to the characteristics of groundwater quality in all regions of Northwest China, the raw water was prepared by mixing the tap water and inorganic salts. The tap water was allowed to stand still for about 24 h so that most of the residual chlorine could be removed, which ensured that it had met the inflow chlorine control standards before the membrane treatment. According to the measured data from five representative sampling points (Table 1), the test raw water quality parameters are given in Table 2. Meanwhile, NF90 (The Dow Chemical Company. USA), a commercial nano-porous membrane, was selected as the experimental membrane in the nanofiltration process. The main characteristic parameters of the membrane NF90 are given in Table 3.

Experimental Method and Procedure

Aiming at the groundwater with excessive salt content, a desalination process with the core technology of nanofiltration was constructed. The schematic diagram of the experimental filtration setup is shown in Fig. 1. It is a cross-flow membrane system, which mainly includes the water tank (1000L), the security filter, the pump unit, the membrane module and the ancillary equipment. The test raw water passes through the security filter first and then enters into

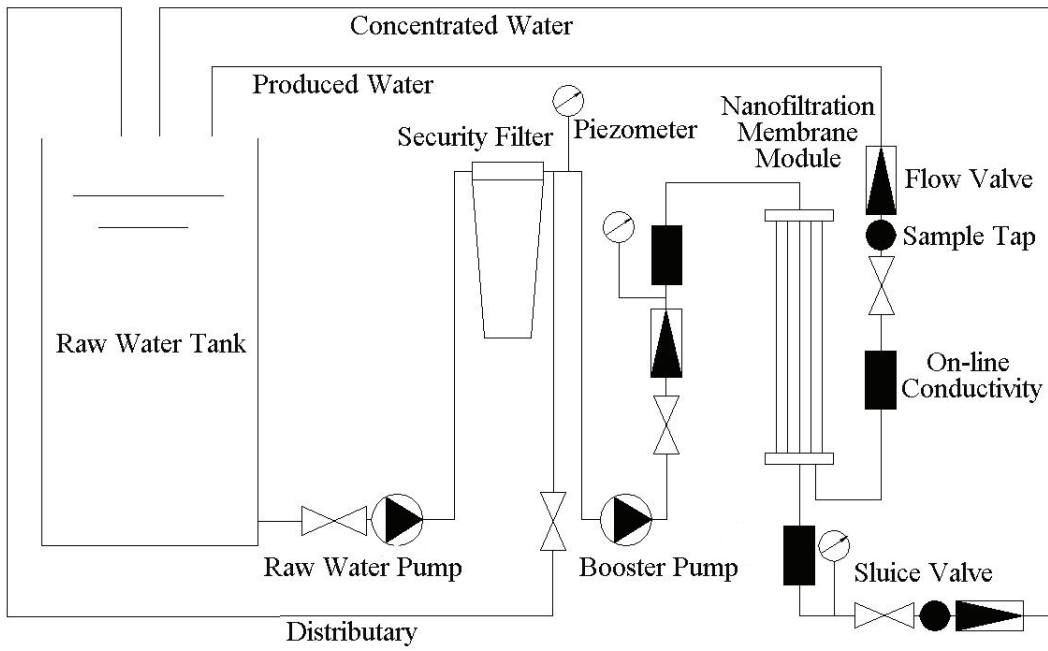

Fig. 1: The schematic diagram of the experimental filtration setup.

Table 1: The quality data of typical water samples.

Sampling points	Mass concentration, $mg \cdot L^{-1}$			
	SO_4^{2-}	Cl^-	F^-	NO_3^-
P1	622.03±8.35	70.97±2.14	0.36±0.09	2.69±0.08
P2	145.01±3.41	104.93±2.56	0.25±0.04	23.09±1.12
P3	464.66±5.27	103.61±1.98	0.99±0.03	3.32±0.17
P4	460.91±6.38	100.58±2.77	0.82±0.08	3.64±0.75
P5	25.10±1.36	28.07±0.69	2.03±0.04	2.68±0.30

Table 2: The main quality parameters of raw water.

Parameter		Unit	Value
Temperature		°C	19.5±1.0
pH		-	8.00+0.05
Redox Potential		mV	110~150
Mass Concentration	TDS	$mg \cdot L^{-1}$	1351~1372
	Ca^-	$mg \cdot L^{-1}$	136.17~142.21
	Mg^{2+}	$mg \cdot L^{-1}$	58.55~60.76
	Na^-	$mg \cdot L^{-1}$	184.04~191.85
	K^-	$mg \cdot L^{-1}$	31.67~33.32
	HCO_3^-	$mg \cdot L^{-1}$	187.90~208.41
	SO_4^{2-}	$mg \cdot L^{-1}$	611.86~629.35
	NO_3^-	$mg \cdot L^{-1}$	25.83~26.71
	F^-	$mg \cdot L^{-1}$	2.13~2.18
	Cl^-	$mg \cdot L^{-1}$	96.67~101.03
	CO_3^{2-}	$mg \cdot L^{-1}$	1.03~1.15

Table 3: The main characteristics of the test membrane NF90.

Material	Molecular Cut Off (Da)	Effective Area (m^2)	Zeta Potential (pH=7，mV)	Surface Roughness (nm)	Highest Temperature (°C)	Applicable pH	Highest Pressure (MPa)
polyamide	200	2.6	-30	70~129	40	2~11	4.1

the nanofiltration membrane module for desalination treatment. In this experiment, a permeate full circulation mode of operation was used, which required all the producing water and the concentrated water to flow back into the raw water tank. The rate of inflow and operating pressure were adjusted by simultaneously changing the valves for both inlet and the concentrated water outlet. The water samples under a special working condition were detected when a steady on-line conductivity value corresponding to the produced and concentrated water was observed respectively.

Analytical Methods

The mass concentration of TDS, and pH were determined by Hach portable multi-spectrometer (HQ 40d). The concentrations of cations (Ca^{2+}, Mg^{2+}, Na^+, K^+) in water were determined by ICP-OES (Agilent 715 model), and the concentrations of anions (SO_4^{2-}, Cl^-, F^-, NO_3^-) were determined by ion chromatography (Metrohm 881 Compact IC pro). The concentrations of HCO_3^- and CO_3^{2-} were calculated via the law of electric charge conservation and the ionization balance formula.

Design of Experiments by RSM Model

In the current study, RSM has been used for the determination of the relation between the input variables and output responses over numerous experimental processes (Salahi et al. 2013; Maher et al. 2014). The Design-Expert 8.0.6 software was used in this study to design experiment schemes, analyse experimental data and plot. There were six independent variables considered in the process of NF90 nanofiltration for the brackish groundwater treatment, which included operating pressure, inlet flow, and the concentrations of sulphate, chloride, fluoride and nitrate. According to the results of the pre-experiments and the possible groundwater quality conditions, the selected level-value of each factor is given in Table 4. These six factors were coded at three levels between -1 and +1, where -1 corresponded to the minimum and +1 corresponded to the maximum value of each variable. The response values used for results analysis included permeate flux, removal rates of chloride as well as nitrate. Besides, the sulphate and fluoride removal rates were measured at the same time. Afterwards, 52 groups of related experiments (Table 5) were designed through RSM based on the central composite design (CCD).

RESULTS AND DISCUSSION

Response Surface Analysis with Permeate Flux as the Response Value

A quadratic regression model was constructed by means of Design-Expert 8.0.6 software with regarding permeate flux as the response value. The results of Anova in this model are

Table 4: The selected level-value of each factor.

Factor	Unit	Level-value		
		Minimum（-1）	Central Point（0）	Maximum（1）
Operating pressure（X_1）	MPa	0.3	0.5	0.7
Inlet Flow（X_2）	$L{\cdot}h^{-1}$	300	400	500
Sulfate Concentration（X_3）	$mg{\cdot}L^{-1}$	500	750	1000
Chloride Concentration（X_4）	$mg{\cdot}L^{-1}$	100	250	400
Fluoride Concentration（X_5）	$mg{\cdot}L^{-1}$	2	4	6
Nitrate Concentration（X_6）	$mg{\cdot}L^{-1}$	20	35	50

Table 5: Experimental design and response values.

No.	Factor						Response Value				
							Permeate Flux（$L{\cdot}h^{-1}{\cdot}m^{-2}$） X_2	Ion Rejection Rate（%）		SO_4^{2-} Rejection Rate（%）	F^- Rejection Rate%）
	X_1		X_3	X_4	X5	X_6		Cl^-	NO_3^-		
1	0.5	400	500	250	4	35	33.3	95.8	78.2	99.91	98.3
2	0.7	500	500	100	6	50	54.1	97.3	81.7	99.93	98.8
3	0.5	400	1000	250	4	35	29.9	96.2	78.0	99.90	98.6
4	0.5	400	750	250	4	20	32.2	96.3	79.8	99.92	98.5
5	0.7	300	1000	400	2	50	39.7	96.7	79.2	99.99	97.8
6	0.7	400	750	250	4	35	46.5	96.8	81.5	99.93	98.6
7	0.3	300	1000	100	6	20	14.5	94.6	72.3	99.67	95.1
8	0.3	500	500	100	6	20	19.6	94.9	71.5	99.89	98.0
9	0.7	300	500	400	6	50	48.3	96.1	76.2	99.91	98.6
10	0.7	500	500	400	2	50	44.5	97.5	84.3	99.92	98.9
11	0.5	400	750	250	4	35	31.1	96.2	78.0	99.92	98.4
12	0.5	400	750	250	2	35	31.2	95.6	76.4	99.92	97.3
13	0.5	400	750	250	4	35	31.1	96.2	78.0	99.92	98.6

Table Cont....

No.	Factor						Response Value				
							Permeate Flux ($L \cdot h^{-1} \cdot m^{-2}$) X_2	Ion Rejection Rate (%)		SO_4^{2-} Rejection Rate (%)	F^- Rejection Rate%
	X_1		X_3	X_4	X5	X_6		Cl^-	NO_3^-		
14	0.3	500	500	400	6	50	16.4	93.3	60.4	99.90	97.8
15	0.3	500	1000	400	6	20	12.5	93.9	63.4	99.86	97.8
16	0.3	300	500	100	6	50	18.5	94.3	61.6	99.89	97.9
17	0.5	400	750	250	4	35	31.1	96.2	78.0	99.92	98.6
18	0.5	400	750	250	4	35	31.1	96.2	78.0	99.92	98.6
19	0.7	500	1000	100	2	50	44.5	97.1	83.0	99.92	98.4
20	0.3	500	1000	100	6	50	14.7	94.2	64.9	99.87	98.1
21	0.5	300	750	250	4	35	31.1	95.4	74.7	99.89	98.3
22	0.7	500	1000	400	2	20	37.9	98.0	87.8	99.93	98.7
23	0.7	300	1000	400	6	20	39.7	96.5	80.3	99.59	98.3
24	0.3	300	500	100	2	20	19.1	93.3	65.8	99.59	99.7
25	0.7	500	500	100	2	20	56.6	97.1	83.4	99.92	98.6
26	0.3	300	1000	100	2	50	12.4	92.5	54.3	99.81	97.5
27	0.5	400	750	250	4	35	31.1	96.2	78.0	99.92	98.6
28	0.7	300	1000	100	2	20	40.8	97.4	83.5	99.91	97.9
29	0.7	300	500	100	6	20	53.9	96.5	80.8	99.91	98.6
30	0.3	300	500	400	2	50	14.1	93.9	62.6	99.85	97.6
31	0.3	300	1000	400	2	20	11.4	94.3	67.9	99.81	97.3
32	0.5	400	750	250	4	35	31.1	96.2	78.0	99.92	98.6
33	0.3	400	750	250	4	35	15.5	93.3	63.9	99.88	97.9
34	0.7	500	1000	400	6	50	45.4	96.5	78.0	99.94	98.6
35	0.7	500	1000	100	6	20	42.2	98.2	88.3	99.94	99.0
36	0.7	300	500	400	2	20	45.3	96.9	84.0	99.81	98.4
37	0.5	500	750	250	4	35	31.7	96.4	79.3	99.94	98.6
38	0.3	500	1000	400	2	50	12.3	93.5	60.2	99.87	97.6
39	0.5	400	750	250	4	50	31.2	95.9	75.7	99.92	90.6
40	0.5	400	750	100	4	35	33.1	96.7	79.8	99.92	98.1
41	0.3	500	1000	100	2	20	15.2	95.9	73.6	99.89	97.8
42	0.5	400	750	400	4	35	30.5	95.5	76.5	99.91	98.0
43	0.5	400	750	250	4	35	31.1	96.2	78.0	99.92	98.6
44	0.7	300	1000	100	6	50	41.9	96.4	79.3	99.82	98.7
45	0.3	500	500	400	2	20	15.4	94.6	72.1	99.87	97.5
46	0.3	500	500	100	2	50	17.2	95.2	71.8	99.87	97.9
47	0.7	500	500	400	6	20	45.0	97.6	84.9	99.89	98.9
48	0.7	300	500	100	2	50	46.9	96.4	82.2	99.66	98.4
49	0.3	300	500	400	6	20	14.3	94.4	66.4	99.83	97.8
50	0.5	400	750	250	4	35	31.1	96.2	78.0	99.92	98.6
51	0.5	400	750	250	6	35	31.1	96.2	77.2	99.92	98.5
52	0.3	300	1000	400	6	50	13.7	90.6	45.3	99.87	97.2

given in Table 6. Meanwhile, combined with the analysis results from Design-Expert 8.0.6, it could be found that the P-value was less than 0.0001, the determination coefficient (R^2) was 99.54%, and the correction coefficient (Adj R^2) was 99.01%, all of which indicated that the model is very significant. In addition, the coefficient of variation (C.V.) of the model was 4.16%, which was less than 10%, indicating that the model possessed high accuracy and reliability. The signal-to-noise ratio (Adeq-Precision), which was 46.498 (greater than 4), suggested that the model's precision was reasonable.

Through the software Design-Expert 8.0.6, the P-value of each factor was investigated. According to the significance level, three factors influencing permeate flux (operating pressure, sulphate concentration and chloride concentration) were selected. Taking permeate flux as the response value, the response surface diagrams revealing the influences by each factor are presented in Fig. 2. As can be seen from Fig. 2a, under the condition of a constant concentration of sulphate ions at inflow, permeate flux increased linearly with the increase of operating pressure. In the experiment, when the operating pressure increased from 0.3 to 0.7MPa, permeate flux increased from 17.44 to 49.66 $L \cdot h^{-1} \cdot m^{-2}$ at the influent sulphate concentration of

Table 6: The results of Anova for permeate flux.

Item	Sum of Squares	Degrees of Freedom	Mean Square	F-value	Prob > F
Model	8366.49	27	309.87	190.63	< 0.0001
Residual	39.01	24	1.63	-	-
Lack of Fit	38.55	17	2.27	34.62	< 0.0001
Pure Error	0.46	7	0.066	-	-
Cor Total	8405.50	51	-	-	-

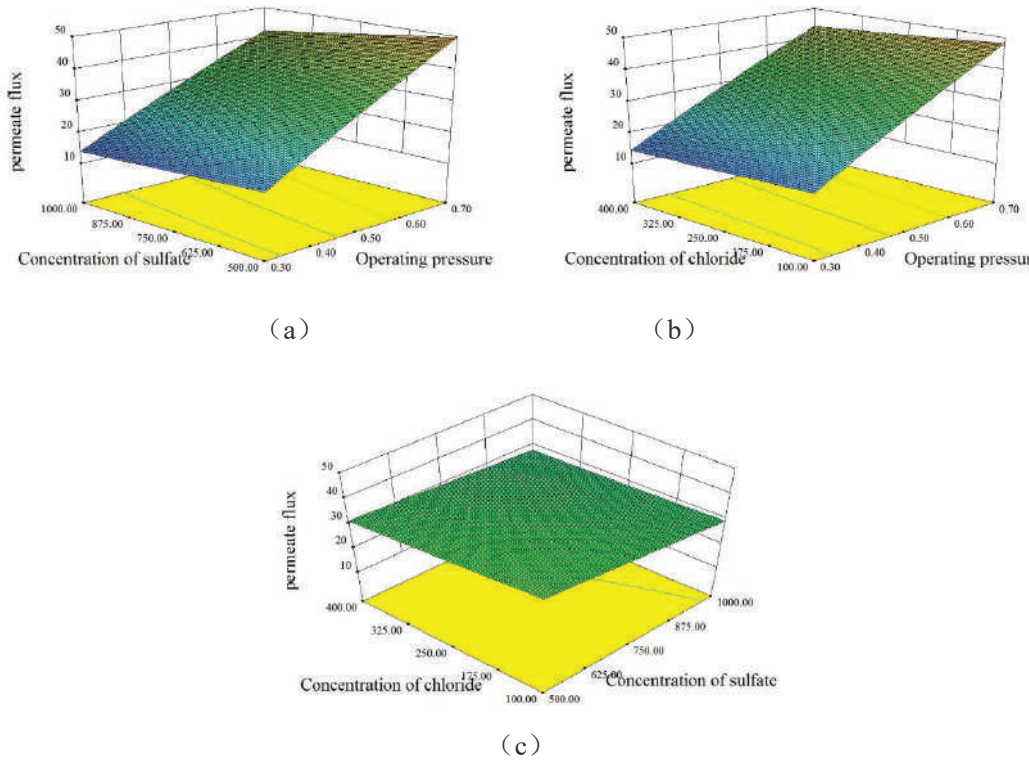

Fig. 2: Analysis of each factor's influence on permeate flux by RSM: (a) concentration of sulphate and operating pressure; (b) concentration of chloride and operating pressure; (c) concentration of chloride and sulphate.

500 mg·L^{-1}. In contrast, the permeate flux increased from 14.06 to 42.00 L·h^{-1}·m^{-2} when the influent sulphate concentration became 1000 mg·L^{-1}. This showed that under low salinity influent conditions, the effect of operating pressure on permeate flux was more pronounced, and the increase of permeate flux could be more dramatic. The same variation trend between permeation flux and operating pressure could also be seen in Fig. 2b, which may be explained by the non-equilibrium thermodynamic model. This is, under conditions of constant water quality, the net driving pressure on both sides of the nanofiltration membrane increased linearly with increasing inlet pressure. In addition, under low operating pressure conditions, permeate flux was less affected by changes in ion concentration in the influent water than under high operating pressure conditions (Figs. 2a, 2b). A comprehensive analysis of Fig. 2 showed that operating pressure, initial sulphate concentration and chloride concentration all affected permeate flux in the nanofiltration process, and the effect of these factors were operating pressure, initial sulphate concentration, initial chloride concentration in turn.

Response Surface Analysis with Chloride Rejection Rate as the Response Value

A quadratic regression model was also constructed with regard to removal rate of chloride as the response value, and results of the Anova are presented in Table 7. It indicated that the P-value was less than 0.0001, the R^2 was 96.02%, and the Adj R^2 was 91.54%, all of which indicated that the model is very significant. In addition, the C.V. of 0.46% (less than 10%) indicated that the model possessed high accuracy and reliability. The Adeq-Precision of 23.163 (greater than 4) suggested that the model's precision was reasonable.

Table 7: The results of Anova for chloride rejection.

Item	Sum of Squares	Degrees of Freedom	Mean Square	F-value	Prob > F
Model	111.00	27	4.11	21.45	< 0.0001
Residual	4.60	24	0.19	-	-
Lack of Fit	4.58	17	0.27	101.89	< 0.0001
Pure Error	0.019	7	2.645×10^{-3}	-	-
Cor Total	115.60	51	-	-	-

Chloride removal rate was used as the response value. Analysis by Design-Expert 8.0.6 software found that the P-values of the five factors of operating pressure, inlet flow, sulphate concentration, chloride concentration, and nitrate concentration were all less than 0.01. Therefore, it could be considered that all these five factors had a significant effect on the removal of chloride. The influence of each factor on chloride removal rate is shown in Fig. 3. It could be seen that the rejection of chloride increased continually as the operating pressure increased from 0.3MPa to 0.6MPa under a certain influent quality (Figs. 3a, 3b). However, when the operating pressure exceeded 0.6MPa, the chloride rejection did not increase and remained substantially constant. As shown in Figs. 3a and 3e, the increase of the initial sulphate concentration could reduce the removal rate of chloride because of the competitive relationship between the two coexisting ions. A similar situation occurred in Fig. 3b, with the increase of the initial concentration of chloride, the rejection rate of chloride also decreased slightly. But when the system was under a higher operating pressure condition, the influence of the initial chloride concentration on chloride rejection in produced water significantly reduced. Figs. 3c, 3d indicated that the increase of inlet flow rate was conducive to the removal of chloride. When the operating condition was kept at the centre point, the chloride rejection rate increased from 95.56% to 96.46% within the inflow range of 300-500 L/h, though the growth rate was relatively slow. The influence of initial nitrate concentration on chloride removal rate is shown in Figs. 3d, 3f. When the influent nitrate concentration was increased from 20 to 50 mg·L^{-1}, the chloride rejection rate decreased from 96.44% to 95.95%, which suggested that the increase of nitrate concentration was not conducive to the removal of chloride. A comprehensive analysis of Fig. 3 showed that these five factors affecting the removal of chloride were as follows: operating pressure, inlet flow, initial sulphate concentration, initial nitrate concentration, initial chloride concentration.

Response Surface Analysis with Nitrate Rejection Rate as the Response Value

With regard to removal rate of nitrate as the response value, the quadratic regression model was constructed. As given in Table 8, the Anova results indicated that the P-value was less than 0.0001, the R^2 was 97.67%, and the Adj R^2 was 95.05%, all of which indicated that the model is very significant. Meanwhile, the C.V. was less than 10%, which showed high accuracy and reliability. The Adeq-Precision (reached 29.386 and exceed 4) suggested that the model's precision was reasonable.

Taking the nitrate removal rate as the response value, analysis found that the operating pressure, inlet flow, sulphate concentration, chloride concentration, and nitrate concentration all had significant effects on nitrate rejection. The effects of each factor on nitrate removal is presented in

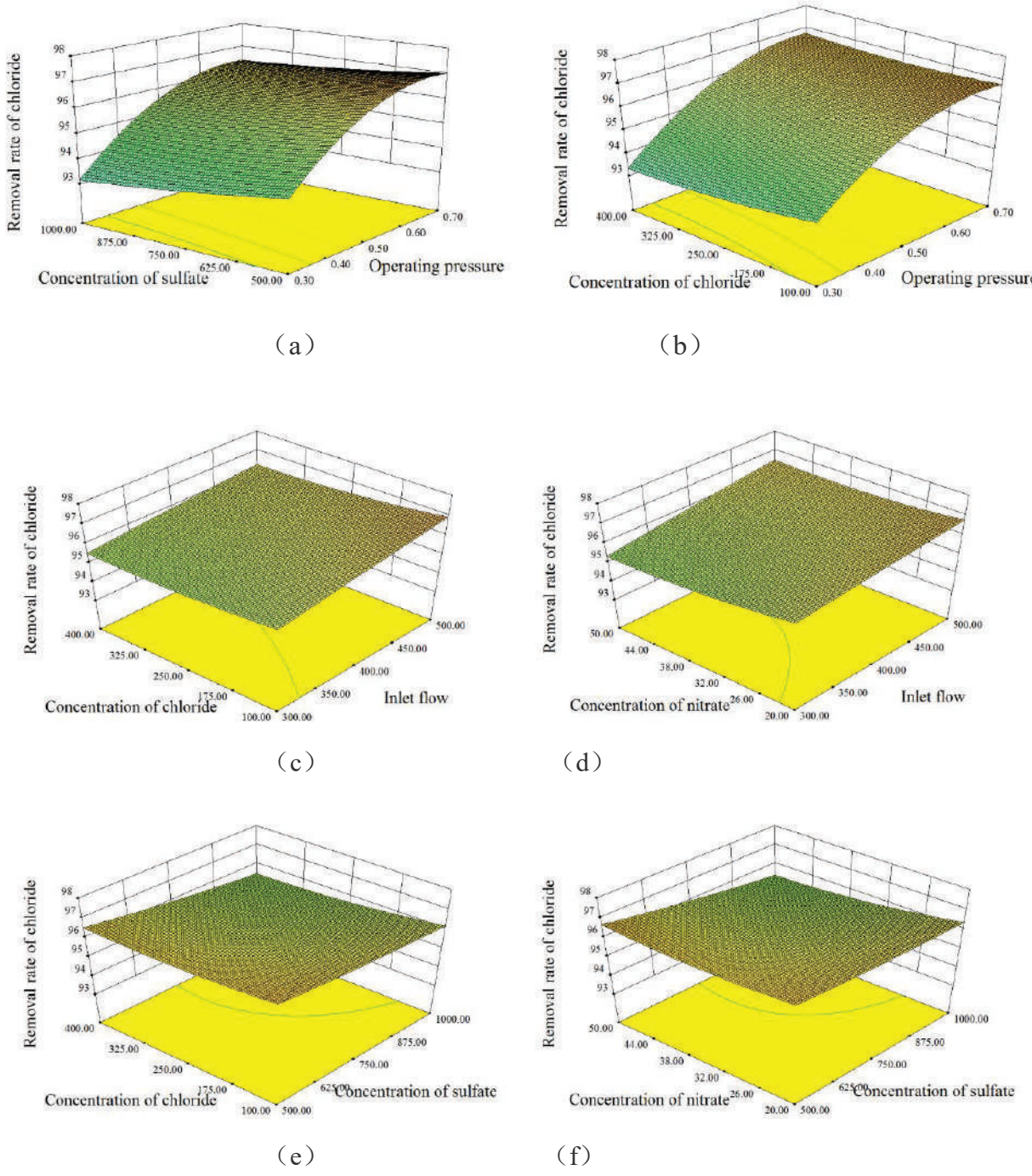

Fig. 3: Analysis of each factor's influence on the chloride rejection by RSM: (a) concentration of sulphate and operating pressure; (b) concentration of chloride and operating pressure; (c)concentration of chloride and inlet flow; (d) concentration of nitrate and inlet flow; (e)concentration of sulphate and chloride; (f) concentration of nitrate and sulphate.

Table 8: The results of Anova for nitrate rejection.

Item	Sum of Squares	Degrees of Freedom	Mean Square	F-value	Prob > F
Model	3819.43	27	141.46	37.26	< 0.0001
Residual	91.11	24	3.80	-	-
Lack of Fit	90.28	17	5.31	44.56	< 0.0001
Pure Error	0.83	7	0.12	-	-
Cor Total	3910.54	51	-	-	-

Fig. 4. In general, nitrate removal was affected more than other ions removal. From Figs. 4a, 4d and 4e, it could be seen that the increase of the initial concentration of influent sulphate would cause the decrease of nitrate reject rate. Taking Fig. 4d as an example, in the range of the initial sulphate concentration of 500 to 1000 mg·L^{-1}, the nitrate rejection rate decreased from 79.14% to 77.49%. Figs. 4b, 4d illustrated the influence of initial concentration of influent chloride on nitrate rejection rate, that is, the increase of the initial chloride concentration hindered the removal

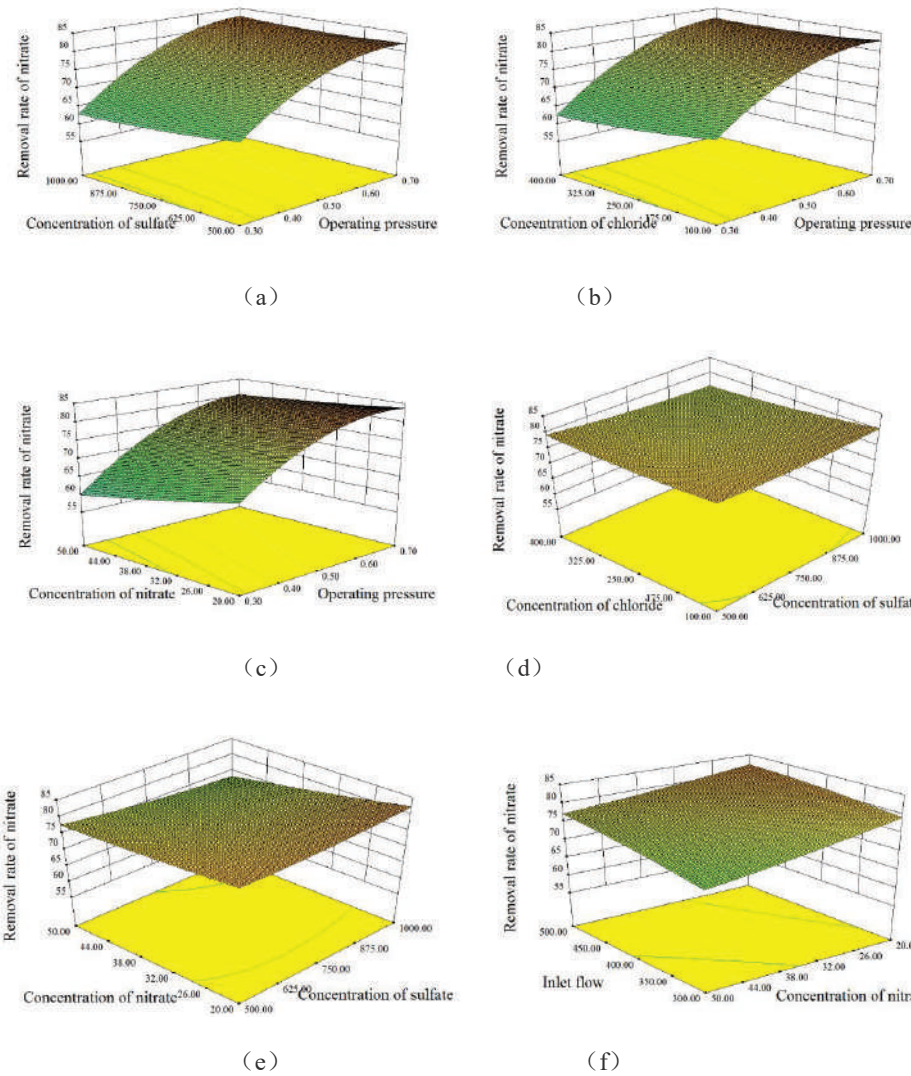

Fig. 4: Analysis of each factor's influence on the nitrate rejection by RSM: (a) concentration of sulphate and operating pressure; (b) concentration of chloride and operating pressure; (c) concentration of nitrate and operating pressure; (d) concentration of chloride and sulphate; (e) concentration of sulphate and nitrate; (f) concentration of nitrate and inlet flow.

of nitrate. Meanwhile, it could be seen from Fig. 4f that the increase of inlet flow would promote the rejection of nitrate. In the range of 300 to 500 L/h, the rejection rate increased from 76.11% to 79.69%. In addition, a major factor affecting nitrate removal was the initial nitrate concentration in the inflow water. As Figs. 4c, 4e and 4f illustrated, nitrate removal was greatly affected by the change of its own initial concentration. Taking Fig. 4e as an example, when the initial nitrate concentration was increased from 20 to 50 mg·L^{-1}, the rejection rate decreased from 81.01% to 75.05%. According to the saliency analysis by software, the factors affecting the nitrate removal were operating pressure, concentration of nitrate, inlet flow, concentration of sulphate and concentration of chloride in turn.

Evaluation of the Application Scope of Nanofiltration for Various Raw Waters

Combined with the previous experimental design and results, in the NF90 nanofiltration membrane system, variation laws of the ion concentration at outlet with the inlet concentration changing are shown in Fig. 5. As shown in Fig. 5a, sulphate rejection was less affected by the initial concentration in raw water, increasing initial sulphate concentration from 500 to 1000 mg·L^{-1} only caused a small increase in sulphate in the produced water. During the whole process of NF90 nanofiltration membrane system, sulphate removal rates were all over 99.9%, but the concentrations were all below 1.5 mg·L^{-1}, which were far below the standard limit of 250 mg·L^{-1}. Fig. 5b showed that increasing initial chloride concentration decreased the rejection rate. Chloride concentration increased from 3.3 to 18 mg·L^{-1} as the initial ion concentration increased from 100 to 400 mg·L^{-1}, the quality parameter chloride content always met the standard limit of 250 mg·L^{-1}. For the fluoride ion from Fig. 5c, it could be seen that the rejection rate increased first and then slightly reduced with increasing the initial fluoride concentration from 2 to 6 mg·L^{-1}. During this process, the fluoride concentration in outlet increased from 0.05 to 0.09 mg·L^{-1} and the rejection rate was all above 97.3%, which completely met the standard limit of 1.0 mg·L^{-1}. Therefore, it is feasible to use nanofiltration membrane process for purifying brackish groundwater with sulphate, chloride and fluoride exceeding the standard in northwest China, and the produced water can completely satisfy the drinking water hygiene standard of GB5749-2006. Fig. 5d showed the same trends for nitrate rejection, when the concentration

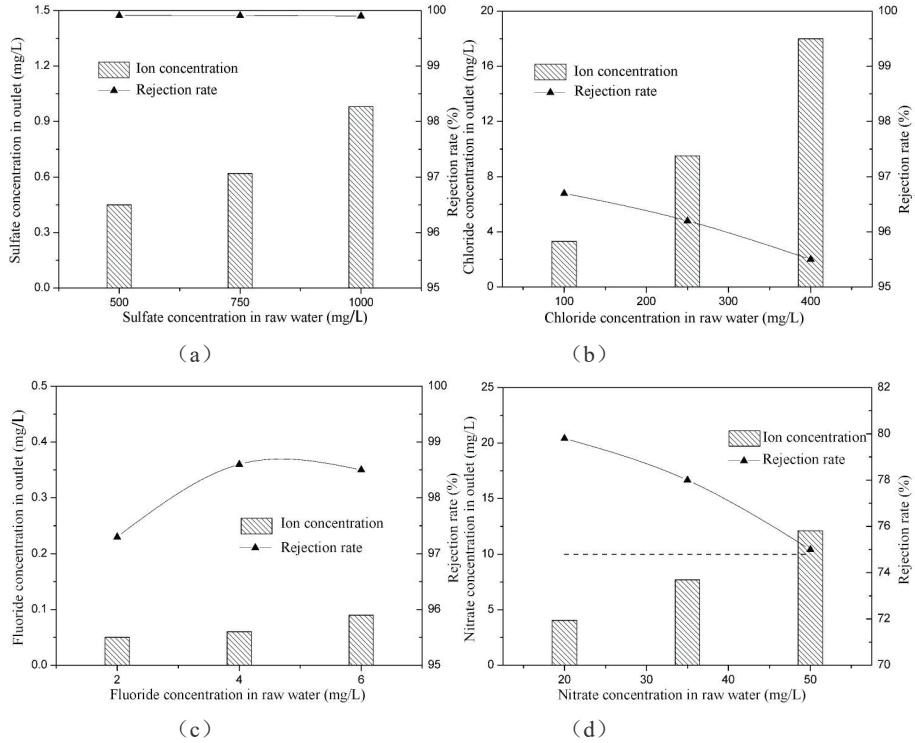

Fig. 5: The variation of ion concentration in outlet in the NF90 nanofiltration membrane system: (a) SO_4^{2-}, (b) Cl^-, (c) F^- and (d) NO_3^-.

of nitrate in raw water increased from 20 to 50 $mg \cdot L^{-1}$, the concentration in outlet increased from 4.05 to 12.1 $mg \cdot L^{-1}$, and the rejection rate decreased from 79.8% to 75%. It suggested that the produced water cannot meet the standard limit of 10 $mg \cdot L^{-1}$ in the case where the raw water possesses a high level of nitrate concentration. Thus, the nitrate concentration in raw water should be controlled within 40 $mg \cdot L^{-1}$ to ensure a safe residual.

CONCLUSION

In view of the possible existence of anion pollution for groundwater resource in the remote areas of northwestern China, through RSM, the effects of various factors on flux and ion rejection rates in the nano-porous membrane process were analysed, and its application scope for diverse water resource was evaluated. Under the test parameters, the main factors influencing permeate flux are operating pressure, initial sulphate concentration as well as chloride concentration, and the effect of operating pressure on membrane flux is most obvious. Secondly, chloride rejection affects in the order of operating pressure, inlet flow, initial sulphate concentration, initial nitrate concentration, initial chloride concentration. On the other hand, the factors affecting the nitrate removal are operating pressure, concentration of nitrate, inlet flow, concentration of sulphate, concentration of chloride in turn. In the aspect of evaluation in water quality adaptability, nano-porous membrane process puts up predominant performance in the removal of sulphate, chloride and fluoride, and the residual can abundantly satisfy the national standard (GB5749-2006) for drinking water. In particular, the nitrate content of raw water should be controlled within 40 $mg \cdot L^{-1}$. In summary, it appears that nanofiltration can be very promising in producing ion-free safe drinking water with a wide range of water quality adaptation. This study is expected to raise scale up confidence in the backdrop of rare implementation of nano-porous membrane process in removing diverse ions from brackish groundwater at an affordable cost in the vast affected areas.

ACKNOWLEDGEMENT

This research was supported by the Graduate Scientific Research and Innovation Foundation of Chongqing, China (Grant No. CYB18127).

REFERENCES

Bouranene, S., Fievet, P., Szymczyk, A., Samar, M. E. H. and Vidonne, A. 2008. Influence of operating conditions on the rejection of cobalt and lead ions in aqueous solutions by a nanofiltration polyamide membrane. Journal of Membrane Science, 325(1): 150-157.

Diawara, C. K. 2008. Nanofiltration process efficiency in water desalination. Separation & Purification Reviews, 37(3): 302-324.

Fox, S., Oren, Y., Ronen, Z. and Gilron, J. 2014. Ion exchange membrane bioreactor for treating groundwater contaminated with high perchlorate concentrations. Journal of Hazardous Materials, 264: 552-559.

Greenlee, L.F., Testa, F., Lawler, D.F., Freeman, B.D. and Moulin, P. 2010. Effect of antiscalants on precipitation of an RO concentrate: Metals precipitated and particle characteristics for several water compositions. Water Research, 44(8): 2672-2684.

Han, Y., Xu, Z. and Gao, C. 2013. Ultrathin graphene nanofiltration membrane for water purification. Advanced Functional Materials, 23(29): 3693-3700.

Ma, Y., Zhang, J., Zhang, H., Tian, H. and Xue, Y. 2011. Investigation on safety and health status of domestic drinking water in the remote areas in Xinjiang. Journal of Environment and Health, 28(9): 820-821.

Onorato, C., Banasiak, L.J. and Schäfer, A.I. 2017. Inorganic trace contaminant removal from real brackish groundwater using electrodialysis. Separation and Purification Technology, 187: 426-435.

Padilla, A.P. and Saitua, H. 2010. Performance of simultaneous arsenic, fluoride and alkalinity (bicarbonate) rejection by pilot-scale nanofiltration. Desalination, 257(1-3): 16-21.

Pangarkar, B.L., Sane, M.G. and Guddad, M. 2011. Reverse osmosis and membrane distillation for desalination of groundwater: A review. ISRN Materials Science, pp. 1-9.

Pérez-González, A., Urtiaga, A.M., Ibáñez, R. and Ortiz, I. 2012. State of the art and review on the treatment technologies of water reverse osmosis concentrates. Water Research, 46(2): 267-283.

Plattner, J., Naidu, G., Wintgens, T., Vigneswaran, S. and Kazner, C. 2017 Fluoride removal from groundwater using direct contact membrane distillation (DCMD) and vacuum enhanced DCMD (VEDCMD). Separation and Purification Technology, 180: 125-132.

Strathmann, H. 2010 Electrodialysis, a mature technology with a multitude of new applications. Desalination, 264(3): 268-288.

Zhang, S., Lyu, Y., Su, X., Bian, Y., Yu, B. and Zhang, Y. 2016. Removal of fluoride ion from groundwater by adsorption on lanthanum and aluminum loaded clay adsorbent. Environmental Earth Sciences, 75(5): 401.

Nature Environment and Pollution Technology
An International Quarterly Scientific Journal

p-ISSN: 0972-6268
e-ISSN: 2395-3454

Vol. 18 | No. 4 | pp. 1143-1155 | 2019

Original Research Paper

Open Access

Calculation of Water Volume for Sediment Transport in the Sediment-laden River of the Main Stream of Liaohe River, Northern China

Xin Yu*, Haoming Fan(***), Liquan Liu**** and Jing Chen*†**

*School of Hydraulic Engineering, Faculty of Infrastructure Engineering, Dalian University of Technology, Dalian, 116024, China

**Liaoning Shuangtai Estuary Wetland Ecosystem Research Station, Nanjingzi Village, Panjin, 124000, China

***Liaoning Key Laboratory of Soil Erosion Prevention and Ecological Restoration, Shenyang, 110866, China

****Water and Soil Conservation Bureau of Liaoning Province, Shenyang, 110003, China

†Corresponding author: Jing Chen

Nat. Env. & Poll. Tech.
Website: www.neptjournal.com

Received: 03-06-2019
Accepted: 24-07-2019

Key Words:
Water volume
Sediment transport
Liaohe river
Sediment-laden river

ABSTRACT

The water volume for sediment transport affects the distribution of sediments in rivers and offers important guidance for river dredging, management and remediation. In this paper, with daily water and sediment data of major hydrological stations of main stream of Liaohe River from 1988 to 2010, we calculated the average water volume and unit water volume for sediment transport of the year with the methods of sediment discharge, sediment concentration and erosion and silting ratio correction that are based on net water volume method. We analyzed the relations between change process of water volume for sediment transport and its impact factors to identify the critical water volume for sediment transport for non-scouring and non-silting situation. The results showed that (1) according to the calculation with the hydrological data from the major hydrological stations in Tongjiangkou, Tieling, Mahushan, Ping'anpu and Liujianfang, the average water volume and the unit water volume for sediment transport during the flood season of the year were $13.88\times10^8 m^3$ and $1136.62 m^3/t$ respectively; (2) According to the theoretical calculation, the water demand model for hydraulic sediment dredging in the major reaches of the main stream of Liaohe River was determined and there was linear function relationship between the sediment discharge and the water demand. When the channel kept the sediment from silting, the water demand at Tieling was $\geq18.73\times10^8 m^3$, $\geq5.49\times10^8 m^3$ at Mahushan, $\geq2.90\times10^8 m^3$ at Ping'anpu and $\geq10.97\times10^8 m^3$ at Liaozhong. In a word, net water volume method can accurately calculate the amount of sediment transport in sediment-laden rivers with a prospect of broad application.

INTRODUCTION

As the largest river in the southern part of Northeast China, Liaohe River extends its catchment to nearly 20 cities with its downstream reaching as far as the most industrially and economically developed areas in China. The Liaohe River has a large sediment concentration, second only to the Yellow River and Haihe River, and is the third in China. The sand-laden Liaohe River suffers severe soil erosion as there are large hilly and semi-desert areas and sparse vegetation along the western part of its catchment. The heavy rains and floods in the Liaohe River are rapid in speed and repetitive in scouring and silting and often have a significant sediment-carrying capacity. Between 1985 and 1996, large floods occurred many times, resulting in dramatic erosion and siltation (Xiong et al. 2005). Currently, the main stream of the Liaohe River is still characteristic of having wide bench land but a narrow groove in the river channel, being shallow and curved and slow water flow. In order to strengthen the management and planning and utilization of the Liaohe River, it is urgent to identify the reasonable sediment transport volume of the Liaohe River.

So far, many scholars around the world have studied the relationship between water volume and sediment. Based on the fundamental formula of "the more is the incoming sediment, the more the sediment discharged", Wu et al. (2015) proposed a general expression of sediment discharge. And with measured water and sediment data of the Inner Mongolian section of the Yellow River from 1953 to 2010, they fitted for the annual sediment discharge formula of the Sanhukou and Toudaoguai reaches and then further figured out the year-by-year scouring and silting amount of major reaches by sediment transport rate method. After analysing the calculation results with the collected hydrological data from the stations at Xiaolangdi, Huayuankou etc., Zhao et al. (2017) found that the water volume for sediment transport generally increases as the runoff, the flow and incoming sediment go up and decreases and tends to be stable as the sediment concentration and incoming sediment coefficient fall and that the proportion of water volume for sedi-

ment transport in the runoff increases and tends to be stable as the sediment concentration and incoming sediment coefficient rise. In the lower reaches of the Yellow River, the amount of sediment transported during the flood season is relatively stable with the sediment transport volume being small and the sediment transport efficiency being high. Yan et al. (2013) set up a generalized movable bed model for the lower reaches of the Yellow River by summarizing the relevant results of the sediment transport efficiency in the lower Yellow River and simulated the sediment transport process of the lower Yellow River channel under different fluctuating flows after water and sediment adjustment at Xiaolangdi. They found that with the standard deviation of 4.03 L/s in the model experiment (i.e., the fluctuation ratio was 0.375), the 1 hour period water-sediment process witnessed the highest sediment transport efficiency. Shao-lei et al. (2015) used physical model tests to predict the trend of erosion and siltation in the lower Yellow River. Based on the water and sediment data from the lower reaches of the Yellow River from 1960 to 2012, statistical methods were used to analyse the sediment transport in the lower reaches of the Yellow River in the situations of different flows and different sediment concentrations. They found that reasonable water and sediment regulation is a necessary measure to avoid later siltation. And the discharge and sediment concentration in the Huayuankou section should change within the ranges of 3000 $m^3/s < Q < 4000$ m^3/s and 20 $kg/m^3 < S < 60$ kg/m^3 respectively, so that the equilibrium sediment transport can be achieved. Tu et al. (2017) applied coupling models constructed with two-dimensional hydrodynamic sediment transport and morphology to evaluate the effects of different watershed management strategies on flood inundation, sediment transport dynamics and morphological changes in different extreme flood events.

Water and sediment are very important elements for the good regulation or operation of the natural rivers or reservoirs. Watershed management requires accurate discharge and sediment predictions (Fasikaw et al. 2018). So far many researches have been conducted with regard to the relationship between water demand or volume and sediment. Toffolon & Vignoli (2007) used to discuss the limitations of the depth-averaged approach for suspended sediment transport. Castro et al. (2008) researched on the numerical approximation of bed-load sediment transport because of the shallow layer flows on unstructured meshes, and proposed the technique that gave expression to several empirical bed-load formulas in the form of grass Model with a complex bed-load coefficient. Many scholars have conducted researches on the problem of sedimentation in the lower Yellow River based on water-sediment regulation. Hu et al. (2012) and Liu et al. (2016) summarized that the average annual erosion rates vary from 5000 to 10000 Mg $km^{-2}yr^{-1}$. Arabkhedri et al. (2010) resorted to sediment rating curves for the estimation of sediment load. Some ancillary data like time-weighted SSC, suspended sediment load, stream data, instantaneous flow discharge, and erosivity density as per Kinnell et al. (2010) and Panagos et al. (2016, 2015, 2017), were either obtained or calculated based on the available data. Jothiprakash & Garg (2010) used BPNN, the back propagation neural network to evaluate sediment trap efficiency in a reservoir and found that the BPNN model shows better accuracy in results compared to that by regression analysis. Han (2011) and Peng (2011) found that the equilibrium sediment transport is more viable than balanced sediment transport in the lower reaches of the Yellow River. Benkhaldoun & Seaïd (2011) came up with a new numerical method to solve the equations of coupled sediment transport and bed morphology by free-surface water flows. As reported by Chao et al. (2012) in the inflow of supplemental sand-laden river water, the supplement water flow renders the key factor in the determination of the sediment load into lakes, and it brings influences to the lake hydrodynamics and sediment transport. Yesuf et al. (2014) proposed that models are necessarily in need if wanting to predict reliable quantity and sediment transport rate from land surface into streams, rivers and water bodies, to identify erosion problem areas within a watershed and to propose the best management practices to reduce erosion impact. Zhao et al. (2011) applied a three-dimensional numerical model to make a simulation of sediment transport in water bodies influenced by wind-induced currents and waves in shallow oxbow lakes. Kisi et al. (2015) proposed that river sediment transport can be put into model either by physical modelling, which required several efforts and information or conceptually using intelligence models. Benjankar & Yager (2012) made a comparison between the sediment transport model simulated suspended sediment concentrations (SSCs) and measured concentrations at a gage station. Erosion and deposition processes were simulated with two sediment transport equations and five hydrograph scenarios as a function of high and low SSC. Yaseen et al. (2015) came to the conclusion that intelligence models have been found an appeal in accordance to their advantages (e.g., accurate models, simplicity, less time consuming and less required information). A three-dimensional hydrodynamic and suspended sediment transport model was established by Liu et al. (2016) in order to simulate temporal and spatial variations in suspended sediment in a subalpine lake. Chiang & Hsiao (2011) found if correctly removed from the transport equation of the diffusion term, the Courant number boundary value can be exceeded. The grain saltation was used to perform the essential role in initiating the

motion of sediment (Bialik & Czernuszenko 2015). Cavalli et al. (2013) applied the spatially explicit modelling of the watershed via sediment connectivity models and found its potential to reflect the actual three-dimensional landscape to clarify concentrated pathways of sediment transport and zones of active erosion. Climate change impact on water and sediment regulation has also been touched upon. Leong & Donner (2015) evaluated climate change impacts on annual flow, centroid of flow, and timing of spring runoff at a station downstream of oil-sands region of the ARB, including impacts on low-flow frequency. Adem et al. (2016) discovered a synergetic response of increases in temperature and precipitation on mean annual sediment yield in the Upper Gilgel Abay catchment, Blue Nile Basin, in Ethiopia. However, Rodríguez-Blanco et al. (2016) found non-linear responses between changes in climatic variables and sediment concentrations in the Corbeira catchment, Spain as a result of complex interactions between atmospheric carbon dioxide level, climatic forcing, water yield, streamflow, and biomass. Milhous (2005) studied the relationship between the climate change and the corresponding changes in sediment transport capacity in the Colorado Plateau. Yang (2005, 2007) made an analysis of the sediment transport capacity in rivers and the correlations between the total sediment discharge and hydraulic parameters of various conditions.

Among the researches that have been conducted so far, there is generally no differentiation made between the water volume for sediment transport and the net water volume (the net volume of water left with the sediment volume removed from net flow of water), and it is not clear how much water from the total water volume is used to transport the sediment. With the actual water and sediment data (flow, sediment transport, sediment concentration, etc.) measured by the main hydrological stations of the main stream of Liaohe River from 1988 to 2010, this paper used sediment transport method, sediment concentration method and erosion and sedimentation ratio correction method to calculate the amount of sediment transport in different periods of Tongjiangkou, Tieling, Ping'anbao and Liujianfang, and figured out critical water volume for sediment transport in the non-scouring and no-silting situation, attempting to provide some reference for the production practices such as river dredging and management remediation.

SURVEY OF STUDY AREA

The Liaohe River is located between 117°00′-125°30′ east longitude and 40°30′-45°10′ north latitude. It is one of the seven major rivers in China with many tributaries. The Liaohe River originates from the Guangtou Mountain in the Qilaotu Mountain Range in Hebei Province. The upstream is named the Laoha River. It flows northward through Dayushu bordered on with the city of Chifeng and the city of Tongliao in Inner Mongolia and is named the West Liaohe River. The West Liaohe River flows eastward and the Dongliao River flows in Liaoning. After the confluence of the Fudedian in Changtu County, Tieling City, it was named Liaohe River. The Liaohe River flows through cities of Tieling, Shenyang, Anshanand and Panjin in Liaoning Province, and flows into Bohai Sea from Dayi County in the city of Panjin. Fig. 1 shows the map of Liaohe River basin (Qiang et al. 2019).

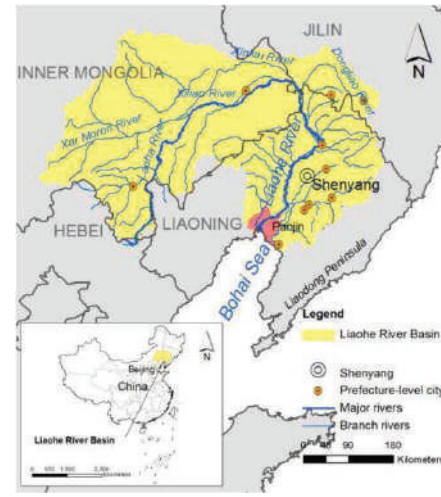

Fig. 1: Map of Liaohe River Basin.

Liaohe River has a high concentration of sediment, ranking the third highest sediment concentration river in China and only next to the Yellow River and Haihe River. As measured by the hydrological station in Tieling reach of Liaohe River, the average annual sediment discharge from 1954 to 2000 was 13.8 million tons and the average annual sediment concentration was 3.09 kg/m^3. The measurement data of the hydrological station in the Zhujiafang reach of Liaohe River shows its average annual sediment discharge was 6.94 million tons from 1969 to 2000 and the average annual sediment concentration is 2.19 kg/m^3. The main stream of Liaohe River is generally categorized as sediment-laden river with less runoff and too much sediment.

IDENTIFICATION OF WATER VOLUME FOR SEDIMENT TRANSPORT USING NET WATER VOLUME METHOD

Calculation Formula

From the correlation between sediment transport efficiency and water volume for sediment transport, following

equation is used to calculate the water volume for sediment transport:

$$W' = \eta^{\alpha} \cdot W\omega \text{, in which } W\omega = W - W_s / \gamma_s \quad \ldots(1)$$

In the equation, W′ is the water volume for sediment transport (m^3), η is sediment transport efficiency, α is exponent (decided by η), W_ω is net water volume (m^3), W is the runoff (m^3), W_S is sediment discharge(10^8t), γ_S is sediment volume-weight (usually taken as 2.65t/ m^3).

Here, the calculation method of water volume for sediment transport can be divided into sediment transport method, sediment concentration method and erosion and silting ratio correction method. The sediment transport efficiency η and coefficient α can be determined according to sediment transport method, sediment concentration method and erosion and silting ratio correction method.

The sediment transport efficiency η_1 in the sediment transport method and the sediment transport efficiency η_2 in the sediment concentration method can be expressed by the following formulas:

$$\eta_1 = W_{s;entrance} / W_{s;exit} \quad \ldots(2)$$

$$\eta_2 = S_{entrance} / S_{exit} \quad \ldots(3)$$

In which, $W_{s;\,entrance}$ and $W_{s;\,exit}$ are sediment discharge at the river entrance and exit (t), $S_{entrance}$ and S_{exit} are sediment concentration at the river entrance and exit (kg/m^3). When η_1<1, the sediment discharge of the river entrance $W_{s;entrance}$ being less than that of river exit $W_{s;exit}$, the river reach was scoured and α=1; when $\eta_1 \geq 1$, sediment transport of river entrance $W_{s;entrance}$ being more than or equivalent to that of river exit $W_{s;exit}$, it came to the sedimentation or scouring and silting balance at the river reach and α=0. When η_2<1, sediment concentration of river entrance being less than that of river exit, the river reach was scoured and α=1; when $\eta_2 \geq 1$, sediment concentration of river entrance being more than or equivalent to that of river exit, the river reach saw the sedimentation or scouring and silting balance and α=0.

The balance of scouring and silting is a range, which is generally difficult to accurately grasp. So, for the silting channel in the lower reaches of the Liaohe River, the requirements for the equilibrium state between scouring and silting can be appropriately relaxed. For example, if the sediment deposition ratio is equal to 0.1 or 0.2 and the river channel is approximately in equilibrium state between the scouring and silting (that is, $\eta'_{critical}$ = 0.1 or 0.2), and the correction coefficient A of the scouring-silting ratio associated with the $\eta'_{critical}$ is introduced, and the water volume for sediment transport at different sediment deposition ratios can be calculated by the following formula:

$$W' = (A \cdot \eta)^a \cdot W_\omega \text{, in which } A = 1 - \eta'_{critical} \quad \ldots(4)$$

The net water volume W_ω and sediment transport efficiency in the scouring-silting ratio correction method can be calculated by formula (2) and formula (3), sediment deposition ratio η′ can be obtained through the following formula:

$$\eta' = \Delta W_s / W_{s;\text{entrance}} = (W_{s;entrance} \cdot W_{s;exit}) / W_{s;entrance} \quad \ldots(5)$$

In which, $W_{s;\text{entrance}}$ is sediment transport volume of river entrance (t), $W_{s;\,exit}$ is sediment transport volume of river exit (t). The correlation between the scouring-silting ratio η′ and sediment transport efficiency η can be found as follows:

$$\eta = 1 / (1 - \eta') \quad \ldots(6)$$

When the critical value of η′ is taken as 0.1, according to formula (6), $\eta_{critical}$ equals to 1.11. When η_1<1.11, α=1; when $\eta_1 \geq 1.11$, α=0. When the critical value of η′ is taken as 0.2, according to formula (6), $\eta_{critical}$ = 1.25, when η_1<1.25, α stands as 1; when $\eta_1 \geq 1.25$, α = 0.

Similarly, the unit water volume for sediment transport is calculated based on the amount of water required for every-ton sediment discharge and the computation expression is as follows:

$$q' = W / W_s \quad \ldots(7)$$

In which, q′ is unit water volume for sediment transport (m^3/t), W′ is water volume for sediment transport (m^3), W_S is sediment discharge (t). Corresponding with the calculation method of water volume for sediment transport, that of unit water volume for sediment transport is also divided into sediment transport volume method, sediment concentration method, and scouring-silting ratio correction method. In the sediment transport method, the calculation of the sediment transport efficiency η is expressed further as follows:

$$\eta = \frac{W_{s;\text{entrance}}}{W_{s;exit}} = \sum_{i=1}^{n} \left[\frac{(Q_{entrance;i} \cdot S_{entrance;i} \cdot t_i) /}{(Q_{exit;i} \cdot S_{entrance;i} \cdot t_i)} \right] \quad \ldots(8)$$

In which, $W_{s;entrance}$ is the sediment discharge of the entrance station (t); $W_{s;exit}$ is the sediment discharge of exit station (t); i is period unit serial number; $Q_{entrance}$ and $Q_{exit;.i}$ are in-flow rate and out-flow rate (m^3/s); $S_{entrance;i}$ and $S_{exit;i}$ are the sediment concentration of entrance station and exit station (kg^3/m); t_i is the time duration of the first period (s).

Data Sources and Application

According to the collected water and sediment data (flow, sediment transport amount, sediment concentration, etc.) from the five major hydrological stations of the main stream

in the Liaohe from 1988 to 2010, the formula (2) was used to calculate the net water volume at each station. With the measured water and sediment data, the relationship can be obtained between water volume for sediment transport and unit water volume for sediment transport at each hydrological station of the main steam of Liaohe River and the average flow rate, average sediment concentration and the incoming sediment coefficient from the Fudedian station.

According to the analysis of the measured water and sediment data in the river channel, the average sediment concentration range during the flood seasons of the Liaohe River in different periods of time can be obtained. The sediment transport amount of each station can be calculated with runoff data of the main hydrological stations.

RESULTS AND ANALYSIS

Correlation Analysis of Water Volume for Sediment Transport of the Year and its Impact Factors

Water volume for sediment transport is defined as the volume of water used to transport certain amount of sediment to next reach of river under certain conditions of water, sediment and river boundary. There is water volume for sediment transport as long as there is transport of sediment, the former refers to the amount of water used for sediment transport in the net water, and the former is a part or the whole of the latter at a ratio closely related to water and sediment conditions as well as sediment transport efficiency. If the entire reach is scoured, the former is less than the latter; if there is a balance of scouring and silting for the reach, the former equals to the latter for all the net water is used for sediment transport.

Water Volume for Sediment Transport of the Year

The results of periodical water volumes for sediment transport at major hydrological stations in the lower reaches of Liaohe River are given in Table 1.

It can be seen from the Table 1 that the average annual water volumes for sediment transport of hydrological stations of Tongjiangkou, Tieling, Mahushan, Ping'anpu and Liujianfang during the flood seasons from 1988 to 2010 were 6.9, 11, 17.6, 16.2 and 17.7×10^8 m^3, respectively; the water volumes for sediment transport during the non-flood seasons were 3, 3.9, 7.5, 5.3 and 9×10^8 m^3, and the annual water volumes for sediment transport were 9.9, 14.9, 25, 21.4 and 26.7×10^8 m^3. The ratios of net water volume to runoff during the flood seasons were 74.3%, 64%, 95.2%, 79.55% and 84.2%, respectively. The ratios of net water volume to runoff during the non-flood seasons were 89.2%, 58.5%, 98.8%, 69.86% and 83.7%; and the ratios of net water volume to runoff on the annual basis were 78.22%, 62.5%, 96.3%, 76.95% and 93.6%, respectively.

From 1988 to 2010, the water volumes for sediment transport recorded by the hydrological stations in the lower reaches of the Liaohe River in the flood seasons, non-flood season and on the whole year basis showed a downward trend with the passage of time. Especially after 1996, the reduction level was significant. From the statistical results of water volumes for sediment transport by periods, since 2000, the period of 2000 to 2005 and 2006 to 2010 witnessed high water volumes for sediment transport and their annual average water volumes for sediment transport varied significantly.

The changes of water volumes for sediment transport of different periods of in lower reaches of Liaohe River were as follows: The Fudedian-Mahushan section had an increasing trend; and the Mahushan-Liujianfang section had a smaller trend along the way. Among them, water volumes for sediment transport during the non-flood season had the most significant increase along the river, and the water volumes for sediment transport on the whole year basis went second and the water volumes for sediment transport in the flood season had a relatively small change along the river.

Table 1: Periodical water volumes for sediment transport at major hydrological stations in the lower reaches of Liaohe River (sediment transport method).

Year	W' Flood Seasons/$10^8 m^3$					W' Non-Flood Periods/$10^8 m^3$					W' Whole Year Periods/$10^8 m^3$				
	Tongjiangkou	Tieling	Mahushan	Ping'anpu	Liu Jianfang	Tongjiangkou	Tieling	Mahushan	Ping'anpu	Liu Jianfang	Tongjiangkou	Tieling	Mahushan	Ping'anpu	Liu Jianfang
1988~1993	10.7	15.7	19.8	18.7	20.6	5.5	7.6	9.8	7.6	10.2	16.2	23.3	29.6	26.3	30.8
1994~1999	13.6	22.6	60.4	61.8	30.4	3.4	2.5	14.0	13.6	14.1	17.0	25.1	74.3	75.4	44.5
2000~2005	0.5	2.7	6.9	5.4	7.8	0.2	1.2	2.2	0.9	3.3	0.7	3.8	9.1	6.3	11.1
2006~2010	3.5	3.9	16.9	14.9	13.2	1.3	2.2	8.7	4.9	5.7	4.8	6.1	25.6	19.8	18.9
1988~2010	6.9	11.0	17.6	16.2	17.7	3.0	3.9	7.5	5.2	9.0	9.9	14.9	25.0	21.4	26.7

Correlation of Water Volume for Sediment Transport in the Flood Seasons of the Year and its Impact Factors

Fig. 2 shows the correlation between the water volume for sediment transport at the hydrological stations in the lower reaches of the Liaohe River and the incoming sediment at Fudedian station based on the measured water and sediment data. It can be seen from the figure that the water volumes for water transport at the stations during the flood seasons, non-flood periods and whole year periods were exponential with the average flows of the Fudedian station; the water volumes for sediment transport at the hydrological stations increased with the increase of sediment concentration, and decreased with the increase of the incoming sediment coefficient. When the average sediment concentration is greater than 1kg/m^3 or the incoming sediment coefficient is bigger than 0.06, the water volumes for sediment transport at each station during the flood seasons were relatively stable at about 10×10^8m^3.

In Fig. 2, the correlation between water volumes for sediment transport at the hydrological stations and the incoming sediment of Fudedian station can be expressed by the following formula:

$$w=-4.9\ln S/Q+2.201 \quad \ldots(9)$$

In which, W' is water volumes for sediment transport at the hydrological stations (10^8m^3); Q is the average flow at Fudedian station during the flood seasons (m^3/s); S is the average sediment concentration at Fudedian station during

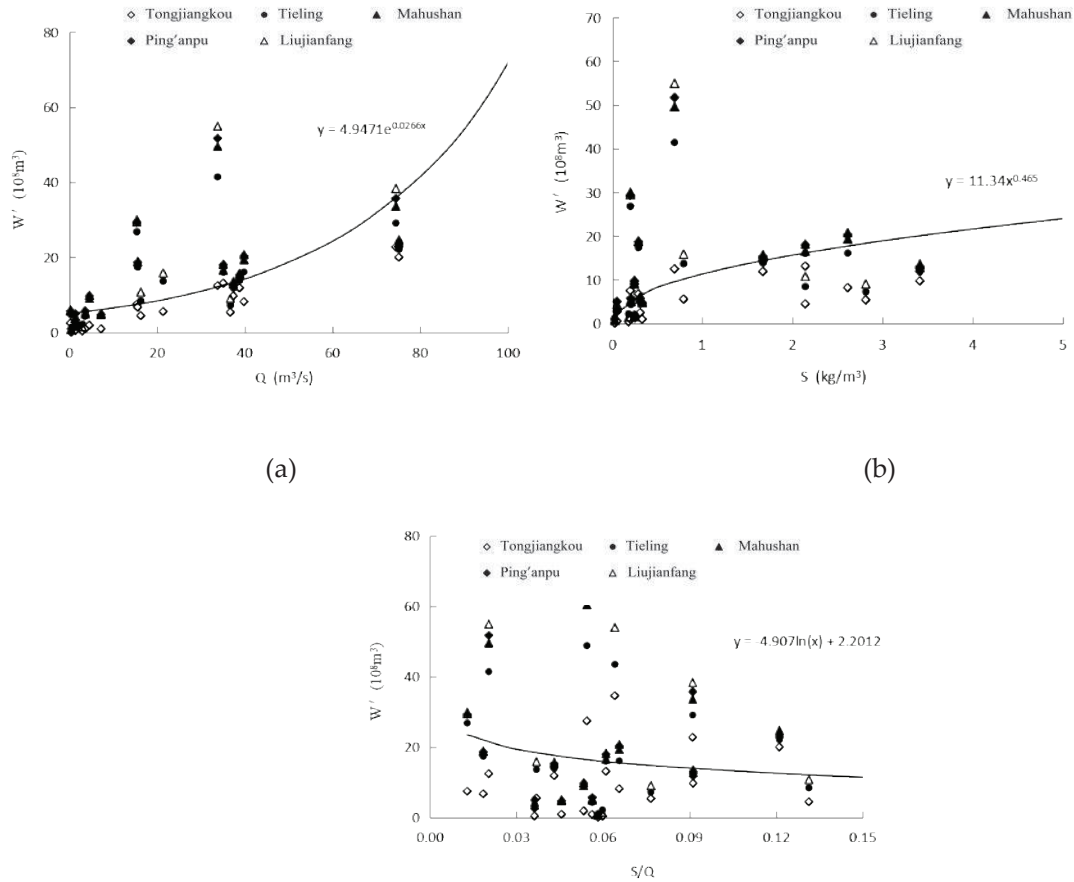

Fig. 2: The correlation between water volume for sediment transport at the hydrological stations along the lower reaches of Liaohe river and the incoming sediment of Fudedian station from 1988 to 2010: (a) The correlation between water volume for sediment transport and the average flow; (b) The correlation between water volume for water transport and the average sediment concentration; (c) The correlation between water volume for sediment transport and incoming sediment coefficient

the flood seasons (kg/m^3); S/Q is the incoming sediment coefficient at Fudedian station during the flood seasons.

The annual average unit net water volume of the stations of Tongjiangkou, Tieling, Mahushan Ping'anpu and Liujianfang between 1988 and 2010 were 1780.7, 2098.8, 2183, 1534.1 and 1563.4m^3/t in flood seasons, and 6653.9, 4581.5, 6154.6, 1801.4 and 3130m^3/t in non-flood seasons, and 1242.8, 2274.9, 2740.4, 1325.7 and 1541.5m^3/t on the whole year basis. The change of unit net water volume of each station in the flood season, non-flood period and on the whole year basis corresponded with the change law of the average sediment concentration in their corresponding periods. Generally, the lowest happened in the flood seasons; the highest took place in the non-flood period and the change on the whole year basis was between them. The year-on-year changes did not show a significant increased or decreased trend.

Correlation Analysis of Unit Water Volume for Sediment Transport and its Impact Factors

Unit water volume for sediment transport is defined as the volume of water used to transport unit amount of sediment to next reach of river under certain conditions of water, sediment and river boundary, which is directly related to water volume for sediment transport and volume of sediment transport, as well as sediment transport efficiency and net water volume per unit. Because water volume for sediment transport is influenced by many factors, such as volume of runoff, sediment transport, average runoff volume, average sediment concentration, coefficient of incoming sediment, sediment quantity of scour-silt, volume and ratio of scouring and silting, sediment transport efficiency, fluvial facies coefficient, and grain composition, etc., especially with a close relationship with runoff volume. Under natural circumstances, runoff volume of the same reach changes a lot at different times, therefore water volume for sediment transport often fluctuates greatly, by contrast, unit water volume for sediment transport is relatively stable which reflects the relationship between water volume for sediment transport and volume of sediment transport and is more capable of reflecting the sediment transport features of the reach.

Unit Water Volume for Sediment Transport

The result of periodical unit water volumes for sediment transport at major hydrological stations in the lower reaches of Liaohe River (sediment transport method) are given in Table 2.

Sediment transport at major hydrological stations in the lower reaches of Liaohe River by sediment transport method (Table 2), it can be found that: The annual average unit water volume for sediment transport of stations at Tongjiangkou, Tieling, Mahushan Ping'anpu and Liujianfang from 1988 to 2010 were 935.5, 776.4, 1870.6, 1001.5 and 1099.1m^3/t in flood seasons; 2970.6, 1984.2, 5140.8, 907.7 and 2830.7m^3/t in non-flood periods; and 772.1, 899.9, 2551.5, 809.5 and 1310.9m^3/t in unit year. The proportion of the annual average unit water volumes for sediment transport to the unit net water volumes at each of the hydrological stations from 1988 to 2010 were 52.53%, 36.99%, 85.69%, 65.28% and 70.3% in flood seasons; 44.64%, 43.31%, 83.53%, 50.39% and 90.44% in non-flood seasons and 62.12%, 39.56%, 93.11%, 61.06% and 85.04% on the whole year basis.

The unit water volumes for sediment transport at each station along the lower reaches of the Liaohe River from 1988 to 2010 displayed an increasing trend with the passage of time in the flood seasons, non-flood seasons as well as on the whole year basis. The increase turned more significant after 2002.

The unit water volumes for sediment transport at the low-

Table 2: Periodical unit water volumes for sediment transport at major hydrological stations in the lower reaches of Liaohe River (sediment transport method).

Year	q' Flood Seasons (m^3/t)					q' Non-Flood Periods (m^3/t)					q' Whole Year Periods (m^3/t)				
	Tongjiangkou	Tieling	Mahushan	Ping'anpu	Liu Jianfang	Tongjiangkou	Tieling	Mahushan	Ping'anpu	Liu Jianfang	Tongjiangkou	Tieling	Mahushan	Ping'anpu	Liu Jianfang
1988-1993	199	239	400	310	479	902	784	1503	420	1172	201	334	506	374	496
1994-1999	382	636	2003	1127	710	534	554	735	1053	2088	373	516	351	477	766
2000-2005	1386	1626	1714	851	1566	6326	6005	11736	690	10209	629	1592	3899	510	2271
2006-2010	1902	825	3666	1861	1750	4718	1066	6868	1580	1869	2029	1132	4368	1637	1630
1988-2010	935	776	1871	1002	1099	2971	1984	5141	908	2831	772	900	2551	810	1311

er reaches of Liaohe River showed little change in different time periods along the river. There was a slight increasing trend for unit water volume for sediment transport in flood seasons, non-flood seasons and on the whole year basis, with Mahushan station showing the more significant change than others, thus indicating a stronger river sediment transport capacity in the lower reaches of Liaohe River.

Correlation of Unit Water Volume for Sediment Transport in the Flood Seasons and its Impact Factors

Fig. 3 shows the correlation between water volumes for sediment transport at the hydrological stations during flood seasons and the incoming sediment of Fudedian station based on the measured water and sediment data. It can be found that the water volumes for water transport at the stations during the flood seasons, non-flood periods and whole year periods were logarithmically related to the average flow of Fudedian station in the flood seasons. The water volumes for sediment transport decreased with the increase of incoming sediment coefficient and that trend was most significant in terms of unit water volume for sediment transport and the corresponding incoming sediment coefficient. When the average sediment concentration at the Fudedian station was less than 4 or incoming sediment coefficient was less than 0.15, there was a smaller value range for unit water volume for sediment transport at the hydrological stations and the point group was more concentrated. When the average sediment concentration of Fudedian station was larger than 40kg/m^3, the water volumes for sediment transport at each station during the flood season remained relatively stable, and the value was about 450m^3/t.

As shown in Fig. 3, the correlation between the unit water volumes for sediment transport at the stations during the flood seasons and the average flow, average sediment concentration and incoming sediment of Fudedian station can be expressed by following formulas respectively:

$$q' = -189\ln(Q) + 1025 \quad \ldots(10)$$

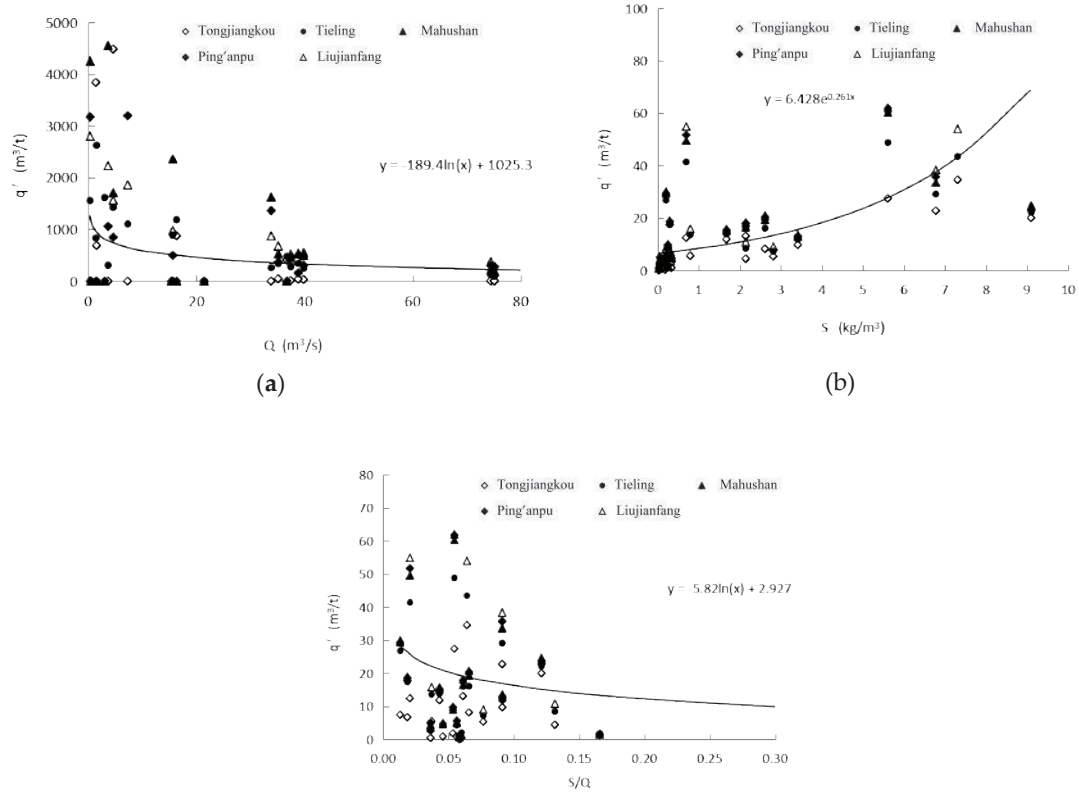

(a) (b) (c)

Fig. 3: The correlation between water volumes for sediment transport at the hydrological stations during flood seasons and the incoming sediment of Fudedian station based on the measured water and sediment data from 1988 to 2010: (a) The correlation between water volume for sediment transport and average flow; (b)The correlation between water volume for sediment transport and average sediment concentration; (c) The correlation between water volume for sediment transport and incoming sediment coefficient.

$$q' = 6.428e^{0.261S} \quad \ldots(11)$$

$$q' = -5.82\ln(S/Q) + 2.927 \quad \ldots(12)$$

In which, q is water volume for sediment transport at the stations during the flood seasons (m^3/t); Q is the average flow of Fudedian station during flood seasons (m^3/s); S is the average sediment concentration of Fudedian station during flood seasons (kg/m^3); S/Q is the incoming sediment coefficient of Fudedian station during the flood seasons.

Non-Scouring and Non-Silting Critical Water Volume for Sediment Transport of Typical Reaches of the Main Stream of Liaohe River

There are many factors influencing the sediments in the main stream of Liaohe River. As the main source of sand in the downstream of Liaohe River, Liuhe River's sand is not only large in amount but also coarse in size, which constitutes the major reason for the main stream being sand-laden and sediments in the river channel. Therefore, we prioritize our research on the influence of afflux of Liuhe River on sediments in the river channel and referred to the nearby 4 hydrological stations: Tieliang, Mahushan, Ping'anpu and Liaozhong for data (Fig. 4 for the major hydrological stations in the main stream of Liaohe River). Using the sediment discharge and runoff data of each station, we applied the knowledge on water volume for sediment transport and sediment transport efficiency to calculate the sediment discharge of the four hydrological stations with relevant formulas. The four stations' water volumes for sediment transport were worked out by calculation with diameters. We also established the relationship between scouring and silting volume and water volume for sediment transport and determined the critical points of water volume for sediment transport in the non-scouring and non-silting situation. When the water volume is equitable to or more than the value, the sediment will not be deposited. The result can provide some reference for the work of river channel dredging.

The correlation between the annual scouring and silting amount and water volume for sediment transport measured at the four hydrological stations is given in Table 3. Table 4 shows the regression equations established through linear fitting and the squared value of the relevant coefficients.

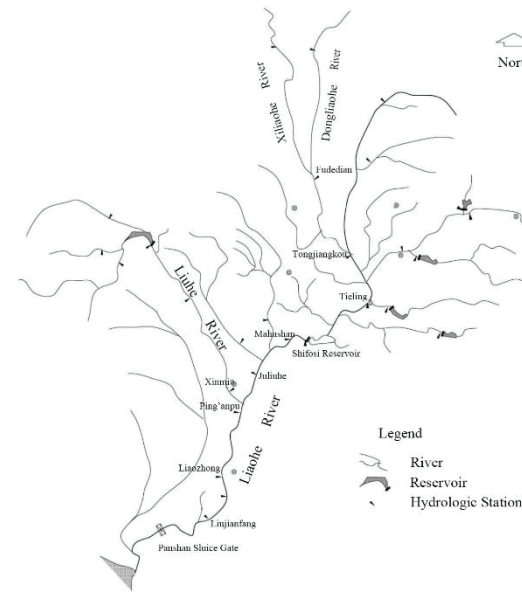

Fig. 4: Distribution diagram of the major hydrological stations in the main stream of Liaohe River.

Sediment discharge method was used to calculate the annual scouring and silting amount of each hydrological station, the relations between water volume for sediment transport and scouring and silting amount are shown in Fig. 5. The formula of the linear fitting for Fig. 5 is:

$$Dep = aQ - b \quad \ldots(13)$$

In which Dep is sediment discharge; Q is water volume for sediment transport; a, b are positive constants. Through differential on the two ends of the formula, the following was obtained:

$$dDep/dQ = a \quad \ldots(14)$$

The a in the formula represents the quantity of sediment transported by the water volume for sediment transport.

As is shown in Fig. 5, each regression line has an intersection with the straight line Dep=0, and water volume for sediment transport corresponding to the intersection makes the scouring and silting amount be zero. The intersection point can be regarded as the critical point of scouring and silting, and the corresponding water volume for sediment

Table 3: Water volume for sediment transport of the hydrological stations in the main stream of Liaohe River after the afflux of Liuhe River (in 10^8m^3).

Year	Annual Water Volume for Sediment Transport (10^8m^3)			
	Tieling	Mahushan	Ping'anpu	Liaozhong
1988-1999	24.18	36.02	34.72	36.13
2000-2007	3.61	10.32	12.17	7.02
1988-2007	15.95	23.17	23.45	25.41

transport is the critical water volume for sediment transport. When the amount of the incoming water to transport sediment is more than the critical water volume for sediment transport, the river channel is seen as scoured, i.e. the sediment storage is reduced; when the amount of incoming water to transport sediment is less than the critical water volume for sediment transport, there is a silting in the river channel, i.e. the sediment storage increases. When letting the left end of the formula (13) be 0, the formula can work out the water volumes for sediment transport at the critical points of sediment storage and discharge as:

$$Q = b/a \tag{15}$$

Using the above method, we figured out the scouring and silting amount of per ton sediment and the critical water volume for sediment transport, i.e. non-scouring and non-silting critical water volume for sediment transport (Table 4).

Based on the net water volume method to calculate the amount of water required for sediment transport as above-mentioned and according to the hydrological characteristics of different reaches of the river, we proposed the corresponding hydraulic sediment dredging model as guidance for practical projects of hydraulic sediment dredging. The core of the technology is to use the years of data on sediment transport to work out the critical water volume for sediment transport with which the water amount required for hydraulic sediment transport can be determined. When the incoming water volume for sediment transport is larger than the critical water volume for sediment transport, the river channel is scoured, i.e. the storage of sediment decreased in the channel. When the incoming water volume for sediment transport is less than the critical water volume for sediment transport, the river channel is silted, i.e. there is an increase of sediment storage in the channel.

According to the analysis, floods of Liuhe River, which

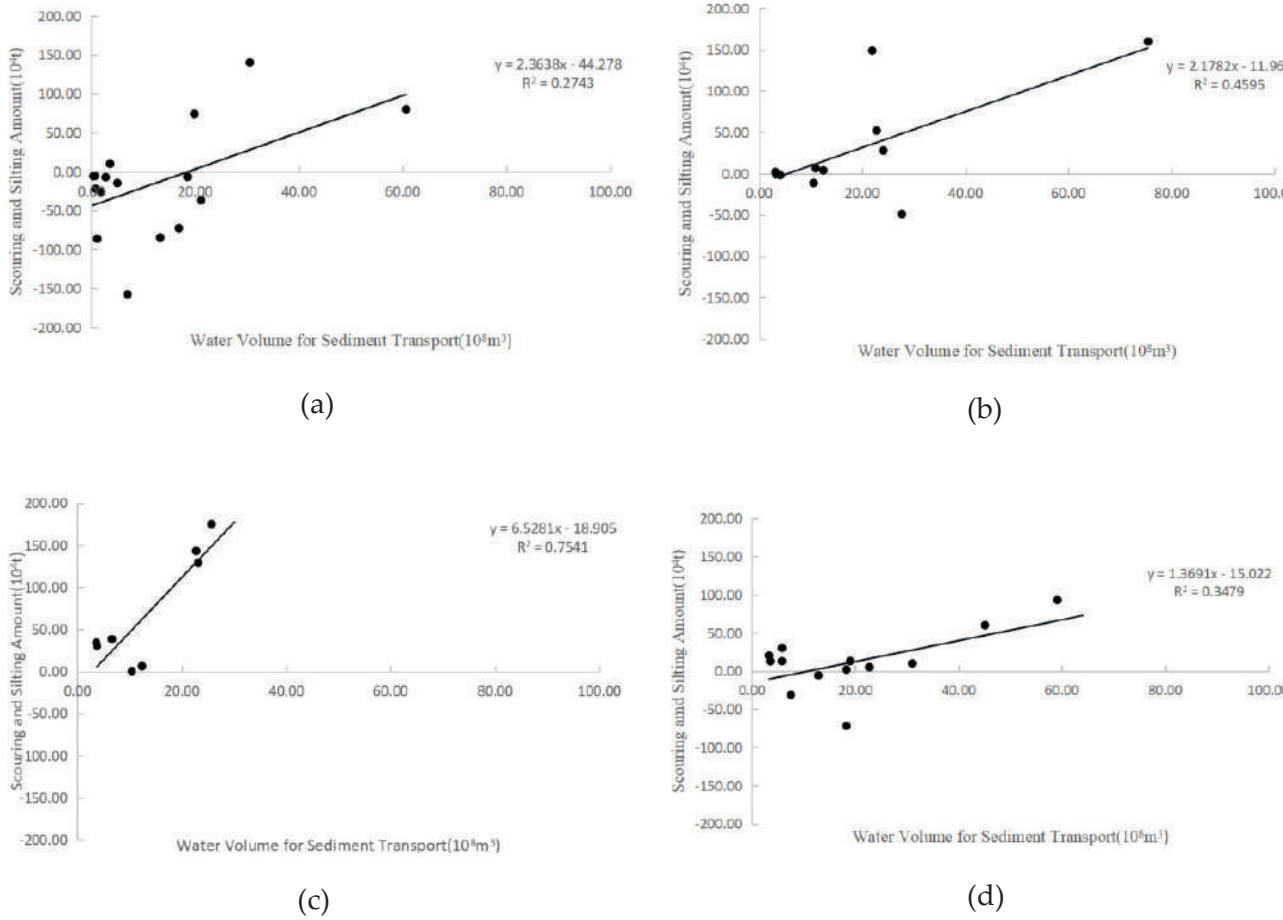

Fig. 5: The relationship between the water volume for sediment transport and scouring and silting amount in each hydrological station: (a) Tieling station; (b) Mahushan station; (c) Ping'anpu Station; (d) Liaozhong Station

Note: The positive value of the ordinate in each figure is the amount of sedimentation, Negative value is the amount of flushing.

Table 4: Model of water demand for hydraulic sediment dredging in the major reaches of the main stream of Liaohe River.

Reach	Regression Equation	Squared Value of Relevant Coefficient, r^2	Non-scouring and Non-Silting Critical Water Volume for Sediment Transport (10^8m^3)	Sediment Discharge by Unit Water Volume for Sediment Transport (10^4t)
Tieling	y=2.364x-44.278	0.274	18.73	2.364
Mahushan	y=2.178x-11.967	0.460	5.49	2.178
Ping'anpu	y=6.258x-18.905	0.754	2.90	6.528
Liaozhong	y=1.369x-15.022	0.348	10.97	1.369

Note: The function in the table indicates the relationship between the sediment deposition of per ton incoming sand and the critical water demand for sediment transport.

are highest in sediment concentration, normally would not meet with the floods of the upstream. The sand of Liuhe River going into Liaohe River often clogged the river channel. Though the sand could be washed away afterwards by the floods of the main stream, it would often silt up the Liaohe River channel at the upstream and downstream of Liuhe River mouth. According to the theoretical calculation, the water demand model for hydraulic sediment dredging in the major reaches of the main stream of Liaohe River was determined and there is linear function relationship between the sediment discharge and the water demand. Specifically, when the water amount in the Tieling reach is more than $18.73\times10^8m^3$, in the Mahushan reach more than $5.49\times10^8m^3$, in the Ping'anpu reach more than $2.90\times10^8m^3$, and in Liaozhong reach more than $10.97\times10^8m^3$, the channel can keep sediment from silting.

DISCUSSION

The water volume for sediment transport of Liaohe River, a sediment-laden river, is influenced by various factors, such as its sediment discharge, rainfall and stream discharge and so forth. The average water volume for sediment transport during flood seasons for Liaohe river from 1988 to 2010 is $13.88\times10^8m^3$, and that during non-flood seasons is $5.74\times10^8m^3$. The research of Yan et al. (2004) showed that the average water volume for sediment transport in downstream of the Yellow River during flood seasons from 1950-2000 is $182.37\times10^8m^3$, and that during non-flood seasons is $107.84\times10^8m^3$. There is a difference in water volume for sediment transport of the two rivers with a method of net water volume, indicating that the results are influenced by rivers' sediment concentration. Meanwhile, both of the water volumes for sediment transport of the two rivers during flood seasons is higher than that during non-flood seasons, indicating that water volume for sediment transport is influenced by rainfall. The annual precipitation in downstream of the Yellow River is around 435mm (Wu et al. 2000), while that of Liaohe River is 700mm, the comparison of water volume for sediment transport of the two rivers shows that the water volume for sediment transport of the Yellow River during flood seasons is 10 times as much as that of Liaohe River, and 20 times during non-flood seasons, indicating that the water volume for sediment transport is influenced by rainfall, and is related to the fact of higher sediment concentration and greater gravity of stream.

By calculation, there is an exponential relationship between the annual water volume for sediment transport in main stream of Liaohe River no matter in flood or non-flood seasons and the average water discharge in Fudedian station in flood seasons, and a logarithmic relationship for unit water volume for sediment transport. Yan et al. (2004) took the same method and drew the conclusion that there is an obvious linear relationship between the annual water volume for sediment transport as well as unit water volume for sediment transport of the Yellow River no matter in flood or non-flood seasons and the average water discharge in Xiaolangdi station in flood seasons. Therefore, we can conclude that there is a different relationship with the same method being applied to different rivers, and the different results are caused by rivers' sediment concentration and other features.

The average annual unit water volume for sediment transport is a good indicator of river sediment conditions. By calculation, it is $1136.62m^3/t$ in Liaohe River during flood seasons and $2766.8m^3/t$ during non-flood seasons, while $28.90m^3/t$ and $84.89m^3/t$ in the Yellow River respectively. The study of Yan et al. (2004) shows that the unit water volume for sediment transport of the Yellow River is 40 times as much as that in Liaohe River, because the Yellow River carries a great volume of sediment which ranks the top of the world, with an annual sediment discharge of $37.8kg/m^3$, and an average annual volume for sediment transport up to 16×10^8t (http://www.waterpub.com.cn/jhdb/DetailRiver.asp?ID=8, 2015). Meanwhile, the average sediment concentration in the main stream of Liaohe River is $3.6kg/m^3$, the annual sediment transport volume

is 2.1×10^7t (http://www.yellowriver.gov.cn/hhyl/hhgk/qh/szyl/201108/t20110814_103518.html, 2011), the results show that there is quite a higher sediment concentration in the Yellow River. Silt carrying stream has a better sediment carrying capacity than clean stream, the above mentioned results also confirm that the net water volume method is applicable to the calculation of sediment transport volume in sediment-laden rivers.

CONCLUSIONS

The calculation results using the net water flow method show that:

1. According to the hydrological data of the hydrological stations of Tongjiangkou, Tieling, Mahushan, Ping'anbao and Liujianfang from 1988 to 2010, the annual average water volume for sediment transport and unit water volume for sediment transport of the main stream of Liaohe River are calculated to be $13.88\times10^8m^3$ and 1136.62 m^3/t respectively.
2. From 1988 to 2010, the unit water volume for sediment transport of the main stream of the Liaohe River in the flood season, non-flood period and whole year showed an increasing trend with time, and it was logarithmically related to the mean flow of the Fudedian station in the flood season. The water volume for sediment transport decreases with increase of the average water flow and coefficient of incoming sediment and increases with the increase of sediment concentration.
3. When the average sediment concentration in the Fudedian station is less than 4 kg/m^3 or the incoming sediment coefficient is less than 0.15, the unit sediment water volume for sediment transport has a smaller value range. When the average sediment concentration is more than 40kg/m^3, the water volume for sediment transport of each station is relatively stable during the flood seasons, and the value was about 450m^3/t.
4. According to the model of water demand for dredging of the main reaches of the main stream of the Liaohe River, there was a functional relationship between sediment transport volume and its water demand. If the river keeps sediment from silting, the water demand of the Tieling section needs to be larger than $18.73\times10^8m^3$. And the number needs to be larger than $5.49\times10^8m^3$ at Mahushan reach, larger than $2.90\times10^8m^3$ at Ping'anpu reach, and larger than $10.97\times10^8m^3$ at Liaozhong reach.

ACKNOWLEDGEMENTS

The authors would like to thank the financial support of the National Natural Science Foundation of China (No. 31570706). We also thank the work of many people in data collection and processing. Our thanks also go to the editor and referees for their invaluable suggestions.

REFERENCES

Adem, A.A. 2016. Climate change impact on sediment yield in the Upper Gilgel Abay Catchment, Blue Nile Basin, Ethiopia. In: Assefa M. Melesse, Wossenu Abtew, (Eds.) Landscape Dynamics, Soils and Hydrological Processes in Varied Climates, Springer, Cham, Switzerland, pp. 615-644.

Arabkhedri, M., Lai F. S., Ibrahim, N. A. and Kasim, M.R.M. 2010. The effect of adaptive cluster sampling design on accuracy of sediment rating curve estimation. J. Hydrol. Eng., 15: 142-151.

Benjankar, Rohan and Yager, Elowyn M. 2012. The impact of different sediment concentrations and sediment transport formulas on the simulated floodplain processes, J. Hydrol., 450-451: 230-243.

Benkhaldoun, F. and Seaïd, M. 2011. Combined characteristics and finite volume methods for sediment transport and bed morphology in surface water flows. Mathematics and Computers in Simulation, 81: 2073-2086.

Bialik, R.J. and Czernuszenko, W. 2015 On the numerical analysis of bedload transport of saltating grains. Int. J. Sediment Res., 28(3): 413-420.

Cavalli, M., Trevisni, S., Comiti, F. and Marchi, L. 2013. Geomorphometric assessment of spatial sediment connectivity in small Alpine catchments. Geomorphology, 188: 31-41.

Chao, X., Jia, Y., Wang, S.Y. and Azadhossain, A.K.M. 2012. Numerical modelling of surface flow and transport phenomena with applications to Lake Pontchartrain. Lake Reserv. Manage., 28(1): 31-45.

Chiang, Y. Ch., and Hsiao, S.S. 2011. Coastal morphological modelling. In: A.J. Manning (Ed.) Sediment Transport in Aquatic Environments, In-Tech: Shanghai, pp. 203-230.

Díaz, M.C., Fernández-Nieto, E.D. and Ferreiro, A.M. 2008. Sediment transport models in shallow water equations and numerical approach by high order finite volume methods. Comput. Fluids, 37(3): 299-316.

Fasikaw, A. Z., Moges, M.A., Alemu, M.L., Ayana, E.K., Demissie, S.S., Tilahun, S.A. and Steenhuis, T.S. 2018. Budgeting suspended sediment fluxes in tropical monsoonal watersheds with limited data: the Lake Tana basin. J. Hydrol. Hydromech., 66(1): 65-78.

Guo, S.L., Sun, D.P., Jiang, E.H. and Li, P. 2015. Equilibrium sediment transport in lower Yellow River during later sediment-retaining period of Xiaolangdi Reservoir. Water Science and Engineering, 8(1): 78-84.

Han, Q.W. 2011. Equilibrium trend of sediment transportation and river morphology. J. Sediment Res., 4: 1-14 (in Chinese).

http://www.yellowriver.gov.cn/hhyl/hhgk/qh/szyl/201108/t20110814_103518.html, August 14, 2011.

http://www.waterpub.com.cn/jhdb/DetailRiver.asp?ID=8, December 15, 2015.

Hu, C.H., Chen, J.G. and Guo, Q.C. 2012. Shaping and maintaining a medium-sized main channel in the Lower Yellow River. Int. J. Sediment Res., 27(3): 259-270.

Jothiprakash, V. and Garg, G. 2010. Reservoir sedimentation estimation using artificial neural network. J. Hydrol. Eng., 14: 1035-1040.

Kinnell, P.I.A. 2010. Event soil loss, runoff and the universal soil loss equation family of models: a review. J. Hydrol., 385: 384-397.

Kisi, O., Sanikhani, H., Zounemat-Kermani, M. and Niazi, F. 2015. Long-term monthly evapotranspiration modelling by several data-driven methods without climatic data. Comput. Electron. Agric., 115: 66-77.

Leong, D.N.S. and Donner, S.D. 2015. Climate change impacts on streamflow availability for the Athabasca oil sands. Clim. Chang., 133(4): 651-663.

Liu, F., Zhang, G.H., Sun, L. and Wang, H. 2016. Effects of biological soil crusts on soil detachment process by overland flow in the loess plateau of china. Earth Surf. Proc. Land, 41(7): 875-883.

Milhous, R T. 2005. Climate change and changes in sediment transport capacity in the Colorado Plateau, USA. Sediment Budgets, 2(292): 271-278.

Panagos, P., Ballabio, C., Borrelli, P. and Meusburger, K. 2016. Spatio-temporal analysis of rainfall erosivity and erosivity density in Greece. Catena, 137: 161-172.

Panagos, P., Ballabio, C., Borrelli, P., Meusburger, K., Klik, A., Rousseva, S., Tadić M.P., Michaelides, S., Hrabalíková, M., Olsen, P. and Aalto, J. 2015. Rainfall erosivity in Europe. Sci. Total Environ, 511: 801-814.

Panagos, P., Borrelli, P., Meusburger, K., Yu, B., Klik, A., Lim, K.J., Yang, J.E., Ni, J., Miao, C., Chattopadhyay, N. and Sadeghi, S.H. 2017. Global rainfall erosivity assessment based on high-temporal resolution rainfall records. Nat. Sci. Rep., 7: 4175.

Peng, R.S. 2011. River training and equilibrium sediment transport of the lower Yellow River. Yellow River, 33(3): 3-7 (in Chinese).

Qiang, Xu, Xiaolong Wang, Bo Xiao and Kelin Hu 2019. Rice-crab coculture to sustain cleaner food production in Liaohe River Basin, China: An economic and environmental assessment. Journal of Cleaner Production, 208: 188-198.

Rodríguez-Blanco, M., Arias, R., Taboada-Castro, M., Nunes, J. and Keizer, J. 2016. Potential Impact of climate change on suspended sediment yield in NW Spain: A case study on the Corbeira catchment. Water, 8(10): 444.

Toffolon, Marco and Vignoli, Gianluca 2007. Suspended sediment concentration profiles in nonuniform flows: Is the classical perturbative approach suitable for depth-averaged closures? Water Resour. Res., 43(4): W04432.

Tu, T., Carr, K.J., Ercan, A., Trinh, T., Kavvas, M.L. and Nosacka, J. 2017. Assessment of the effects of multiple extreme floods on flow and transport processes under competing flood protection and environmental management strategies. Science of the Total Environment. Eng., 607-608: 613-622.

Wu, Baosheng, Liu Kejing, Shen Hongbin and Zhou Liyan 2015. Calculation method of sediment transport and sedimentation in the Inner Mongolia reach of the Yellow River. Advances in Water Science 26(03): 311-321 (in Chinese).

Wu, Kai, Tang Dengyin and Xie Xianqun 2000. Changing tendency of river runoff at lower reaches of the Huanghe River and countermeasures for reducing its effects. Geographical Research, 19(4): 377-382.

Xiong, Jingdong 2005. Analysis of Scouring and Silting of Rivers in the Middle and Lower Reaches of Liaohe River and Planning for Remediation. Master's, Hohai University, Nanjing, Jan.1 (in Chinese).

Yan, Jun and Hu Chunhong 2004. Calculation method and application of sediment transport volume in the lower reaches of the Yellow River. Sediment Research, 4: 25-32. (in Chinese).

Yan, Jun, Liu Wei and Liang Biao 2013. Effect of flow fluctuation on sediment transport efficiency in the lower Yellow River. Hydroelectric Power Report, 32(05): 103-108 (in Chinese).

Yang, S. Q. 2005. Sediment transport capacity in rivers. J. Hydraul. Res., 43(2): 131-138.

Yang, Shu-Qing, Sung-Cheol Koh, In-Soo Kim and Young-Chae Song 2007. Sediment transport capacity-An improved Bagnold formula. Int J. Sed Res., 22(1): 27-38.

Yaseen, Z.M., El-Shafie, A., Jaafar, O., Afan, H.A. and Sayl, K.N. 2015. Artificial intelligence based models for stream-flow forecasting: 2000-2015. J. Hydrol., 530: 829-844.

Yesuf, H.M., Assen, M., Alamirew, T. and Melesse, A.M. 2015. Modelling of sediment yield in Maybar gauged watershed using SWAT, northeast Ethiopia. Catena, 191-205.

Zhao, Haibin, Yang Chunjing and Wang Jun. 2017. Analysis of sediment transport volume and sediment transport efficiency in the lower reaches of the Yellow River. Journal of Yellow River Conservancy Technical College, 29(01): 1-6 (in Chinese).

Zhao, Q.H., Zhu, G.W. and Qiu, H. 2011. Analysis of conveying mechanism of wind-driven current forming the sediment distribution in Taihu Lake. J. Hydraul Eng., 42(*2*): 173-179 (in Chinese).

Nature Environment and Pollution Technology
An International Quarterly Scientific Journal

p-ISSN: 0972-6268
e-ISSN: 2395-3454

Vol. 18 | No. 4 | pp. 1157-1167 | 2019

Original Research Paper | Open Access

Control of Air Pollutants Emission and Improvement of Incineration Rate During Incineration of Oily Sludge-Based Briquette

Mingming Du*(**), Fengchao Wang, Jinling Li*(**), Tao Yu** and Chengtun Qu*(**)†**

*State Key Laboratory of Petroleum Pollution Control, CNPC Research Institute of Safety and Environmental Technology, Beijing, 102206, China

**Shaanxi Oil and Gas Pollution Control and Reservoir Protection Key Laboratory, Xi'an Shiyou University, 710065, Xi'an, China

†Corresponding author: Chengtun Qu

Nat. Env. & Poll. Tech.
Website: www.neptjournal.com

Received: 07-04-2019
Accepted: 01-06-2019

Key Words:
Oily sludge
Briquette
Additives
Air pollutants
Emission control

ABSTRACT

The incineration technology of oily sludge-based briquette makes great contributions to oily sludge treatment. In order to resolve these problems, air pollutants (SO_2 and organic gas) emission and low incinerating rate during the briquette incineration, the effects of additives ($CaCO_3$, CaO; K_2CO_3, Na_2CO_3, NaCl; $KMnO_4$, KNO_3, $NaNO_3$; Fe_2O_3, $KClO_3$) on the generating gas and incinerating rate during incineration were studied. The results show that $CaCO_3$ is more effective than CaO for fixing sulphur into residue, and K_2CO_3 improved the sulphation efficiency of calcium-based additives, which is more useful than NaCl and Na_2CO_3 did. As for the incinerating rate of briquette, $KMnO_4$ is more effective than KNO_3 and $NaNO_3$. The maximum of incinerating rate of briquette is improved from 0.38 to 0.6 g/min and Fe_2O_3 and $KClO_3$ can apparently reduce the release of organic gas during the incineration of briquette. But $KClO_3$ can greatly reduce the release of sulphur. When the adding amount of $CaCO_3$, K_2CO_3, $KMnO_4$ and $KClO_3$ is 16‰, 12‰, 18‰, 6‰ respectively in the process of briquette preparation, the sulphation efficiency reached the maximum of 95.3%, and there is still an extremely small amount of organic gas in flue gas. $CaCO_3$, K_2CO_3, $KMnO_4$ and $KClO_3$ used in emission control of air pollutants and full combustion of briquette during incineration of oily sludge based-briquette, demonstrates high efficiency and low emission compared to other additives tested in this study.

INTRODUCTION

Oily sludge, composed of petroleum, minerals and water, generating from oil industry, has been listed in the Chinese national hazardous waste lists (Hu et al. 2013), and there is almost more than three million tons of oily sludge in China (Zhang et al. 2012), which leads to serious impacts on the ecological environment. For example, hydrocarbons, heavy metals and a large amount of petroleum hydrocarbon in oily sludge seriously affect the water, soil and air (Souza et al. 2018).

By now, there have been many effective methods to treat and dispose oily sludge, such as chemical cleanliness (Sahebnazar et al. 2017, Liang et al. 2017), centrifugation (Lin et al. 2017), low-temperature pyrolysis (Zhao et al. 2017), ultrasound treatment (Hu et al. 2017), biological treatment (Casarini et al. 1988), chemical oxidation (Jing et al. 2012, Matsodoum Nguemté et al. 2018) and incineration treatment (Karamalidis et al. 2008). Among these oily sludge treatments, the incineration treatment can not only minimize the volume and reuse thermal energy of oily sludge, but can also transform most of the toxic and harmful substances into steady and nontoxic substances during the process. And thus, the incineration has been considered as the mainstream technology to treat oily sludge (Hu et al. 2017, Polc et al. 2016).

As the share of non-combustible components in oily sludge is high and the calorific value is not uniform, which cause the cost of direct incineration to be huge (Xu et al. 2014). Thus, the oily sludge-based briquette has been considered to overcome the problems. Oily sludge-based briquette is a mixture of oily sludge, coal and biomass, and can be widely used in industrial boilers (Lopes et al. 2001). What is more, the technology of oily sludge-based briquette may not only resolve the problem of insufficient energy and huge cost during the direct incineration of oily sludge, but can also save the raw materials of industrial briquette. At present, there have been some studies about the preparation of oily sludge-based briquette (Magdziarz et al. 2013, Kijo-Kleczkowska et al. 2016). However, SO_2 and organic gas generated during the incineration of briquette and the low incinerating rate limit the application of briquette in industry. Fortunately, the addition of additives to briquette offers a chance to resolve the problems above. As we know different

kinds of additives play different roles, mainly reducing the release of air pollutants and promote the incineration of coal or other solid fuel (Rulkens et al. 2008, Wu et al. 2002). In addition, the kinds of calcium compounds, such as calcium magnesium acetate and calcium carbonate, can effectively reduce the produce of SO_2 in flue gas (Nimmo et al. 2004). Meanwhile, calcium magnesium acetate can simultaneously reduce NO_x and SO_x when the coal was incinerated (Guan et al. 2003). Alkaline metal compounds have also been used as the additive to coal-firing, which can enhance carbon combustion, reduce air pollutant emissions and promote the sulfation efficiency of calcium compounds (Liu et al. 2004, Li et al. 2007, Zhou et al. 1997). For example, Manquais et al. (2012) systematically performed the influence of alkali metals and alkaline earth metals on combustion performance of coal, and demonstrated that alkali metal carbonate compounds and chloride can effectively promote the burnout of coal, the more coal combustion, and lesser emissions of organic gases during combustion. However, chloride, especially sodium chloride, can distinctly shorten the burnout time of coal compared with other alkali metals and alkaline earth metals.

The above studies can provide precious experience about the coal-fired additives, but these studies concentrated on the effect of single additive on the combustion of coal. At present, there are few studies about the influence of mixed additives on the air pollutants emission of coal. Therefore, the target of this study is to select the appropriate mixed additives to control the emission of air pollutants (SO_2 and organic gas) and ensure the incinerating rate of briquettes simultaneously. In addition, the effect of adding an amount of mixed additives on the emission of air pollutants and the improvement of incinerating rate was also studied. The additives can be divided into four species: calcium-based additive (being beneficial to reducing sulphur dioxide emissions), sulphation-supporting additives (being good to improving sulphation efficiency of calcium-based additive), oxidizers (Gong et al. 2009) (being beneficial to improving the incinerating rate) and catalysts (being beneficial to control the emission of organic gas), and the four additives will be added into the briquette. All incineration experiments were carried out under the temperature of 900°C.

MATERIALS AND METHODS

Oily Sludge, Coal and Apricot Shell Samples Collection and Pretreatment

The oily sludge was obtained from ZhangGuanmiao joint station of Wuqi County, Yan'an City, China. The physical and chemical properties are presented in Table 1, and the share of non-combustible components of oily sludge is high according to the Table 1. The coal and apricot shell were obtained from Yulin, China. The elemental analysis and ash constituent results of the experimental material are given in Table 1 and Table 2.

Screening of Added Pharmaceuticals

Pharmaceuticals were added into the briquette according to a certain amount. All chemicals and reagents used were of analytical grade. Different species of calcium-based additives (CaO, $CaCO_3$) were added during the preparation of the oily sludge-based briquette, and the amount of calcium-based additive was changed, and then the oily sludge-based briquette was incinerated directly. The schematic picture of the experiment flow is illustrated in Fig. 1. The sulphur contents in residues were determined by elemental analysis with EDS (Energy Dispersive X-Ray Spectroscopy). The total sulphur in briquette was calculated by equation (1). The sulphation efficiency was calculated by equation (2). According to the equation (2).

Table 1: Ultimate analysis results of experimental materials (wt%).

Sample	Ultimate analysis (wt %)					trace element analysis (mg/kg)								
	C	H	O	S	N	Hg	Cu	Cr	Zn	As	Pb	Ba	Ni	Cd
Coal	74.68	11.13	13.23	0.8	0.16	0.02	5.11	12.42	6.85	0.9	11.8	110	15.31	0.11
Oily sludge	55.45	16.63	21.24	6.46	0.22	0.03	9.62	30.11	100	3.86	13.5	0.02	18.92	0.01
Apricot	52.36	12.92	33.92	0.06	0.81	-	0.01	-	0.21	-	-	-	0.01	-

Table 2: Analysis of ash constituents (wt %).

Sample	SiO_2	CaO	Al_2O_3	MgO	TiO_2	SO_3	K_2O	Na_2O	P_2O_5	BaO	Cr_2O_3
Coal	67.68	2.41	22.8	2.69	0.81	0.4	1.6	0.5	0.1	0.1	0.01
Oily sludge	68.55	5.47	17.3	2.46	4.73	0.09	0.03	0.02	0.01	0.01	0.01
Apricot	17.16	-	2.43	14.68	-	2.46	31.06	2.48	8.18	0	0.04

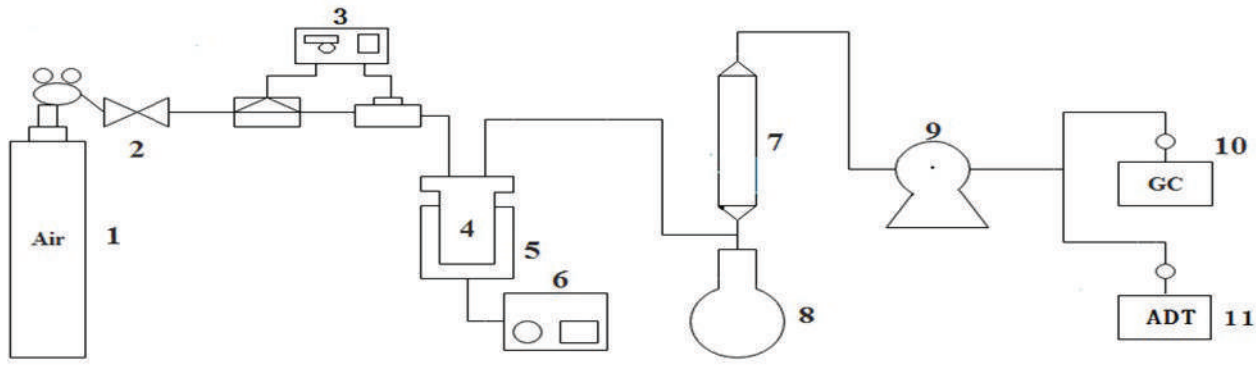

1 air cylinder 2 valve 3 volume flow controller 4 reactor 5 heating furnace 6 temperature controller 7 condenser 8 flask with round bottom 9 gas flowmeter 10 gas chromatograph 11 automatic dust (gas) tester

Fig. 1: Schematic picture of experiment flow.

$$S_T = \omega_S \times 6.64\% + \omega_C \times 0.8\% + \omega_A \times 0.06\% \quad \ldots(1)$$

(ω_S: the weight of oily sludge in briquette; ω_C: the weight of coal in briquette; ω_A: the weight of apricot shell in briquette; S_T: total sulphur in briquette)

$$\text{sulfation efficiency}(\%) = \frac{S_0}{S_T} \times 100 \quad \ldots(2)$$

Where, S_0: the weight of sulphur in residues.

The selection of sulphation-supporting additives (NaCl, Na_2CO_3, K_2CO_3) was performed after the screening of calcium-based additives. The three sulphation-supporting additives were mixed with materials (coal, oily sludge and binder) of briquette and calcium-based additive. One of the three sulphation-supporting additives that can enhance the sulaftion efficiency of calcium-based additive will be selected to add into the briquette. The screening of oxidizers ($KMnO_4$, $NaNO_3$, KNO_3), catalysts ($KClO_3$, Fe_2O_3) is similar to sulphation-supporting additives. Whereas, the selection of oxidizers is based on average incinerating rate of briquette and the sulphation efficiency of calcium-based additive. The selection of catalysts is based on the share of organic gas in flue gas and the sulphation efficiency of calcium-based additive.

Measuring the Flue Gas of Incineration

The flue gas was measured every 15 minutes with SP-3420A gas chromatograph and Laoying 3022H automatic dust (gas) tester (ADT). The sulphur released into atmosphere can be obtained by difference of the total sulphur in briquette and the sulphur contents in residue.

Measuring the Incinerating Rate of Briquette

The average incinerating rate of different incineration stages was computed by the ratio of incinerating weight loss to time. The oxidizers were screened according to the average incinerating rate, the higher the incinerating rate, the better the incineration-supporting effect of the oxidizers.

RESULTS AND DISCUSSION

Effect of the Species and Adding Amount of Calcium-Based Additive on the Sulphation Efficiency

From Fig. 2, we can see that when the amount of calcium-based additives was 10‰, the sulphation efficiency of CaO and $CaCO_3$ was 52% and 64% respectively. With the adding amount of $CaCO_3$ increased from 10‰ to 16‰, the sulphation efficiency of $CaCO_3$ increased from 64% to 83%. When the amount of $CaCO_3$ was 16‰, the sulphation efficiency of $CaCO_3$ reached the maximum value as 83%, which indicates that much sulphur transfers to residue and less sulphur transfers to atmosphere during the process of incineration. However, the added CaO slightly affects the sulphur content in incinerating residue. The maximum sulphation efficiency was 60% when CaO was used as the calcium-based additive. According to the analysis above, we can see that the addition of CaO and $CaCO_3$ can transfer part of sulphur from the flue gas to the residue in the process of incineration. When the amount of calcium-based additives was uniform, the efficiency of sulphation of $CaCO_3$ was higher than CaO. Therefore, $CaCO_3$ is more suitable for the calcium-based additives of briquette.

Effect of the Species and Adding Amount of Sulfation-Supporting Additives on the Efficiency of Sulphation

Although the sulphation efficiency of calcium-based

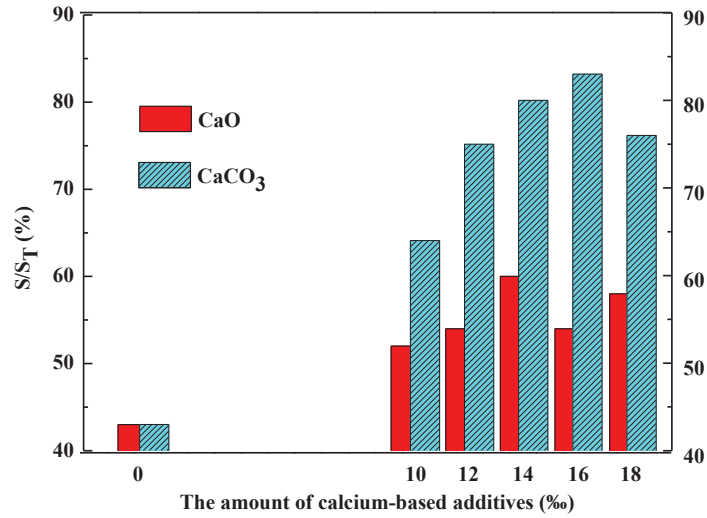

Fig. 2: Impact of the species and amount of calcium-based additives on the sulphation efficiency.

($CaCO_3$) can reach to 83%, a certain amount of sulphur was still emitted into the atmosphere in the form of sulphur dioxide. Therefore, it is necessary to add different kinds of sulphation-supporting additives (K_2CO_3, Na_2CO_3, NaCl) during the preparation of briquette to improve the sulphation efficiency of $CaCO_3$.

Fig. 3 indicates that the addition of sulphation-supporting additives has a certain effect on the efficiency of sulphation. When the amount of Na_2CO_3 was 9‰, the sulphation efficiency of $CaCO_3$ reached to a maximum value of 88%. When the amount of NaCl was 10‰, the sulphation efficiency of $CaCO_3$ reached a maximum value of 85%. In addition, the efficiency of sulphation improved with the increase of K_2CO_3, when the adding amount of K_2CO_3 was 12‰, the sulphation efficiency of $CaCO_3$ reached the maximum value of 94%. Thus, three kinds of sulphation-supporting additives increased the efficiency of sulphation of $CaCO_3$ to some extent. In addition, under the same conditions, the effect of K_2CO_3 on the sulphation efficiency of $CaCO_3$ was extremely obvious. K_2CO_3 can greatly improve the sulphation efficiency of $CaCO_3$. However, Na_2CO_3 and NaCl only slightly promote the sulphation efficiency of $CaCO_3$. Thus, K_2CO_3 is more suitable for the sulphation-supporting additives.

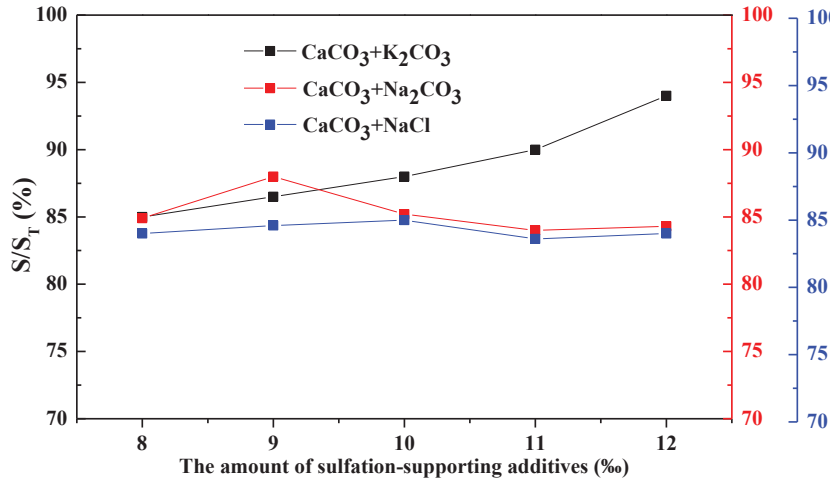

Fig. 3: Impact of species and adding amount of sulphation-supporting additives on the sulfation efficiency of $CaCO_3$.

There are two reasons why K_2CO_3 can improve sulphation efficiency of $CaCO_3$. Firstly, the added K_2CO_3 can react with SO_2, the possible reaction can be as below:

$$2K_2CO_3+2SO_2+O_2 \rightarrow 2K_2SO_4+2CO_2 \quad \ldots(3)$$

Secondly, K_2CO_3 presents a melting state at high temperature as 891°C, which can change the surface area and microstructure of CaO that is produced through decomposition of $CaCO_3$. The results of X-ray diffraction (XRD) and Scanning Electron Microscope (SEM) can also prove the above conclusions.

The (XRD) results given in Fig. 4 illustrate that the fixed sulphur by calcium-based additives turned into $CaSO_4$ when no sulphation-supporting additive was added. At the same time, barium and magnesium compounds in briquette can also act as sulphur fixation during the incineration process of briquette. Sulphur is converted to $Mg_3S_2O_8(OH)_2$ and $BaSO_4$ in the residue. In addition, $CaCO_3$ is still contained in the residue, which indicates that $CaCO_3$ is not fully utilized. When the sulphation-supporting additive K_2CO_3 was added, the fixed sulphur remained in residue in the form of $CaSO_4$, K_2SO_4 and $BaSO_4$. Calcium in the residue exists in the form of $CaSO_4$, which indicates that the added $CaCO_3$ is fully utilized. Therefore, the sulphation-supporting additive K_2CO_3 not only can react with sulphur to fix sulphur, but can also improve the utilization of $CaCO_3$.

The picture located in the upper of Fig. 5 is a sample calcined solely from $CaCO_3$ at 900°C for an hour, the bottom is the sample calcined from the mixture of $CaCO_3$ and K_2CO_3 at the same condition, and the surface characteristic of the samples above is distinctive. The surface of the upper of Fig. 5 is smooth and the bottom is coarse, which indicates that the added K_2CO_3 can promote surface area and enrich surface pore of CaO that was produced through decomposition of $CaCO_3$. The sulphation of $CaCO_3$ at high temperature contains three stages: the decomposition reaction of $CaCO_3$, the diffusion and transfer process of gaseous phase in solid phase, and the combined between CaO and SO_x. And thus, the pore and large surface area are beneficial to the release of CO_2 and the fast combination of SO_2 with CaO (Li 2012).

Effect of Oxidizers on the Incinerating Rate of Briquette

In order to increase the incinerating rate of briquette, different species of oxidizers were also added during the preparation of the briquette and average incinerating rate of the briquette was measured at 900°C. With the same amount of addition (12‰), different oxidizers were added into the briquette, the average incinerating rate of the briquette is shown in Fig. 6.

It can be seen from Fig. 6 that the oxidizers promote the incineration of the briquette and increase the incinerating rate of the briquette. Especially in the early stage, the incinerating rate has been greatly improved. Because the three kinds of oxidizers can produce oxygen under the condition of certain temperature, oxygen can promote the incineration of the briquette. However, the decomposition

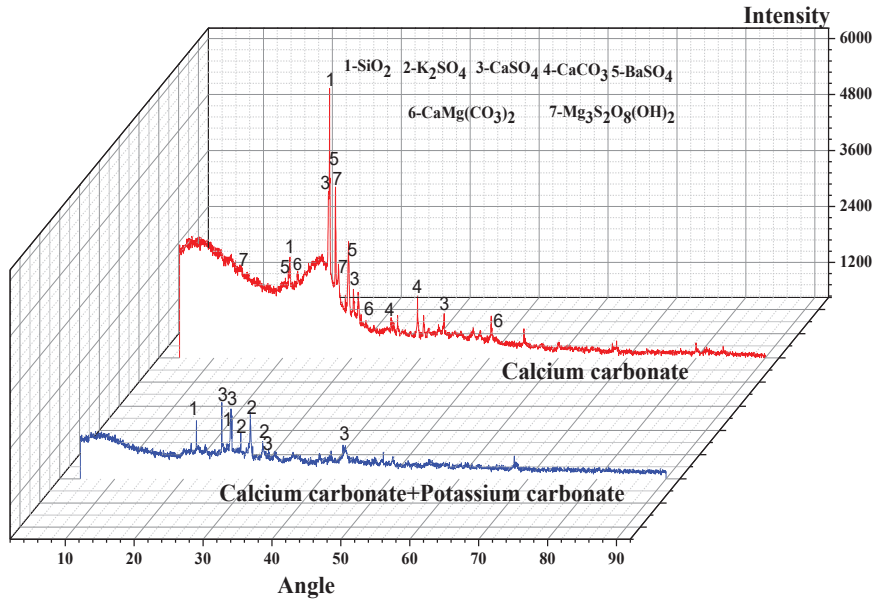

Fig. 4: The XRD spectrum of the incinerating residue.

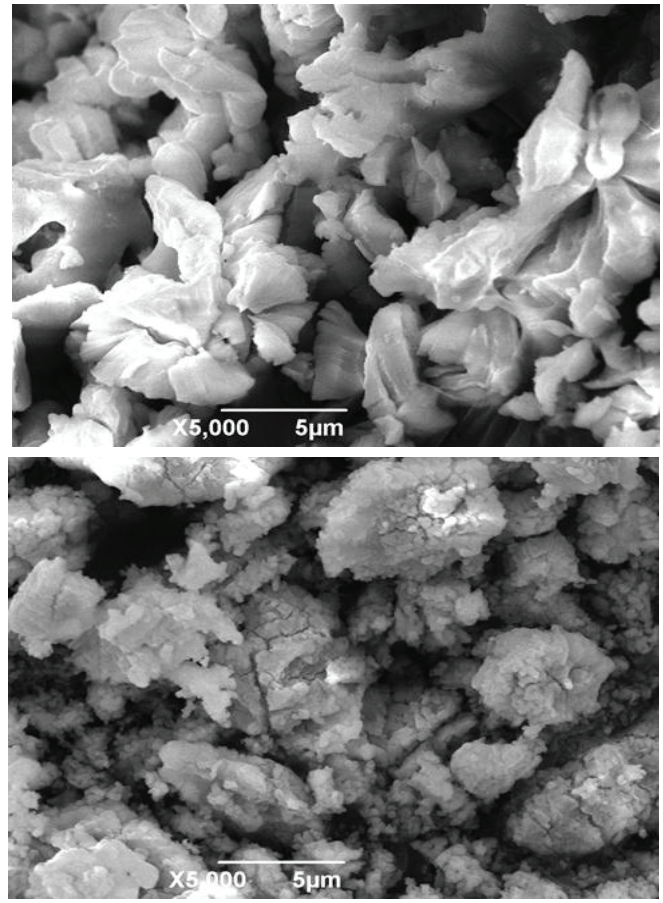

Fig. 5: SEM images of CaO produced through decomposition of $CaCO_3$.

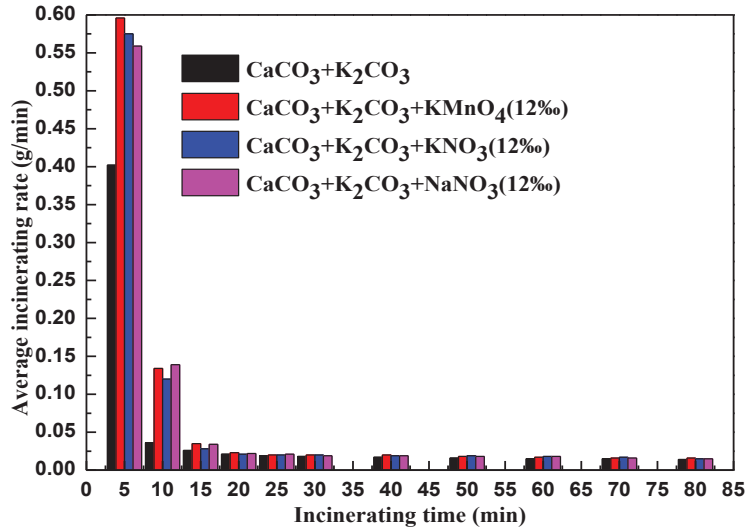

Fig. 6: Effect of oxidizers on average incinerating rate of briquette.

temperature of $KMnO_4$, KNO_3 and $NaNO_3$ to produce oxygen is respectively 240°C, 334°C and 380°C. In the incineration process, the order of the oxygen released by the three kinds of oxidizers is $KMnO_4$, KNO_3 and $NaNO_3$. Therefore, in the early stage of incineration, the incinerating rate of the briquette containing $KMnO_4$ is the highest, and the incinerating rate of the briquette containing $NaNO_3$ is the minimum. Meanwhile, $NaNO_3$ can produce oxygen continuously under the condition of heating. In other words, a certain amount of oxygen is produced in different temperature ranges. However, KNO_2 formed by thermal decomposition of KNO_3 is relatively stable (Ravanbod et al. 2016). Maybe the reason is that the incinerating rate of the briquette containing $NaNO_3$ is greater than containing KNO_3 at 10 minutes. In addition, all the three kinds of oxidizers increased the incinerating rate at the early stage of incineration. The increase of incinerating rate is mostly obvious when $KMnO_4$ was added into the briquette. Moreover, from Fig. 7, we can see that the content of NO_x in flue gas will increase when the three kinds of oxidizers were added into the briquette in the early stage of incineration. When $KMnO_4$ was used as oxidizer, the content of NOx in flue gas is not only less than that of KNO_3 and $NaNO_3$, but the content of NOx in flue gas is close to that without oxidizer. Therefore, we can think that the increase of NOx content in flue gas is due to the addition of potassium nitrate and sodium nitrate in the briquette. As the content of nitrogen in briquette is less, the addition of nitrate causes the increase of NOx concentration in the flue gas. Therefore, $KMnO_4$ was selected as the oxidizer. The possible reaction can be as below:

$$KMnO_4 \xrightarrow{\text{Under } 600^\circ C} K_xMnO_y$$
$$+O_2 \xrightarrow{\text{More than } 600^\circ C} K_2O + MnO_2 + O_2 \quad \ldots(4)$$

$$2KNO_3 \xrightarrow{\Delta} 2KNO_3 + O_2 \quad \ldots(5)$$

$$NaNO_3 \xrightarrow{\text{More than } 380^\circ C} NaNO_2$$
$$+O_2 \xrightarrow{400\sim600^\circ C} NaNO_2 + O_2 \quad \ldots(6)$$
$$+N_2 \xrightarrow{\text{more than } 700^\circ C} Na_2O + N_xO$$

It can be seen from Fig. 8 that with the increase of amount of $KMnO_4$, the incinerating rate of briquette is gradually increasing. When the content of $KMnO_4$ in briquette increased from 10‰ to 12‰, the incinerating rate of the briquette increased from 0.47 g/min to 0.58 g/min. When the content of $KMnO_4$ in briquette exceeded 12‰, the incinerating rate of briquette increased slowly, from 0.58 g/min to 0.63 g/min. The effect of $KMnO_4$ content in the briquette on the sulphation efficiency of $CaCO_3$ is shown in Fig. 9. With the content of $KMnO_4$ in the briquette increased from 10‰ to 18‰, the sulphation efficiency of $CaCO_3$ increased from 52.5% to 80.7%. However, the efficiency of sulphation decreased to 72.3% as the $KMnO_4$

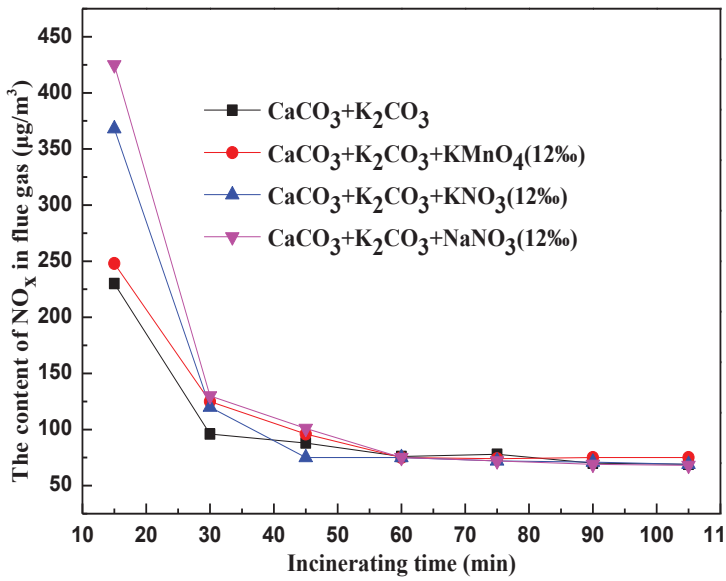

Fig. 7: Effects of oxidizer on NOx concentration in flue gas.

content of briquette was 16‰. Taking the incinerating rate and the sulphation efficiency into account, the amount of $KMnO_4$ in the briquette was determined as 18‰.

Effect of the Type and Amount of Catalysts in Briquette on the Share of Organic Gas in Flue Gas and the Sulphation Efficiency

The results in Table 4 show that Fe_2O_3 and $KClO_3$ can apparently reduce the release of organic gas during the incineration of briquette. The addition of Fe_2O_3 effectively reduces the share of CO, C_3H_8 and C_4H_{10} in flue gas. However, $KClO_3$ strongly affects the proportion of CH_4, C_2H_4, C_3H_8 and C_4H_{10} in flue gas. In addition, the addition of Fe_2O_3 and $KClO_3$ can also reduce the content of C_2H_6 and C_3H_6. It is difficult to define the type of catalysts from the share of organic gas in flue gas.

It can be seen from Fig. 10 that the catalysts Fe_2O_3 and $KClO_3$ have a certain influence on the sulphation efficiency of $CaCO_3$. With the improvement of the amount of catalyst, the sulphation efficiency of $CaCO_3$ increases gradually, and then the sulphation efficiency decreases when Fe_2O_3 was added. However, when $KClO_3$ was used to be catalyst, the trend of sulphation efficiency of $CaCO_3$ is adverse. When the amount of catalyst is identical, the effect of $KClO_3$ on sulphation of $CaCO_3$ is more obvious than that of Fe_2O_3. When the amount of $KClO_3$ is 6‰, the sulphation efficiency of $CaCO_3$ can reach 95.8%. In addition, according to the results of Table 5, organic component in flue gas distinctly decreases with the improvement of $KClO_3$. Although there is still a small amount of CO in the

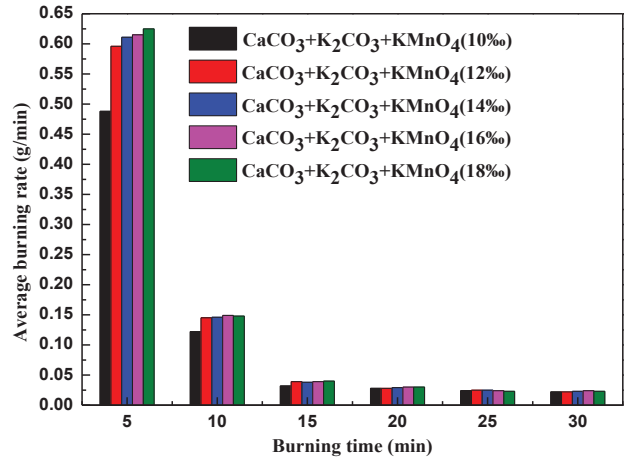

Fig. 8: Effect of the adding amount of $KMnO_4$ on average incinerating rate of briquette.

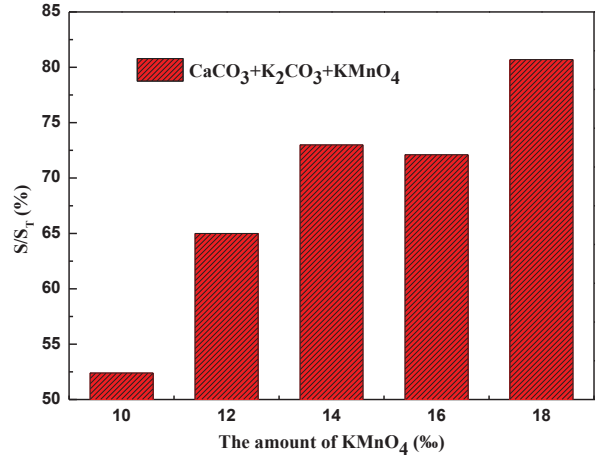

Fig. 9: Effect of the adding amount of $KMnO_4$ on the sulphation efficiency of $CaCO_3$.

Table 3: The composition of incineration gases (%).

	The composition of combustible component of incineration gases (%)						
	CO	CH_4	C_2H_4	C_2H_6	C_3H_6	C_3H_8	C_4H_{10}
No catalyst	1.2827	0.8125	0.1151	0.0986	0.1724	0.0889	0.1026
Fe_2O_3 (6‰)	0.0899	0.0020	0.0021	0.0027	0.0030	-	-
$KClO_3$ (6‰)	0.1012	0.0008	0.0014	0.0026	0.0032	0.0006	-

Table 4: Effect of catalysts in briquette on the share of combustible gas in flue gas.

	The composition of combustible component of incineration gases (%)						
	CO	CH_4	C_2H_4	C_2H_6	C_3H_6	C_3H_8	C_4H_{10}
No catalyst	1.2827	0.8125	0.1151	0.0986	0.1724	0.0889	0.1026
$KClO_3$ (6‰)	0.1012	0.0008	0.0014	0.0026	0.0032	0.0006	-
$KClO_3$ (8‰)	0.0413	0.0002	0.0012	0.0011	0.0004	-	-
$KClO_3$ (10‰)	0.0120	-	0.0006	-	-	-	-
$KClO_3$ (12‰)	0.0182	-	-	-	-	-	-
$KClO_3$ (14‰)	0.0174	-	-	-	-	-	-

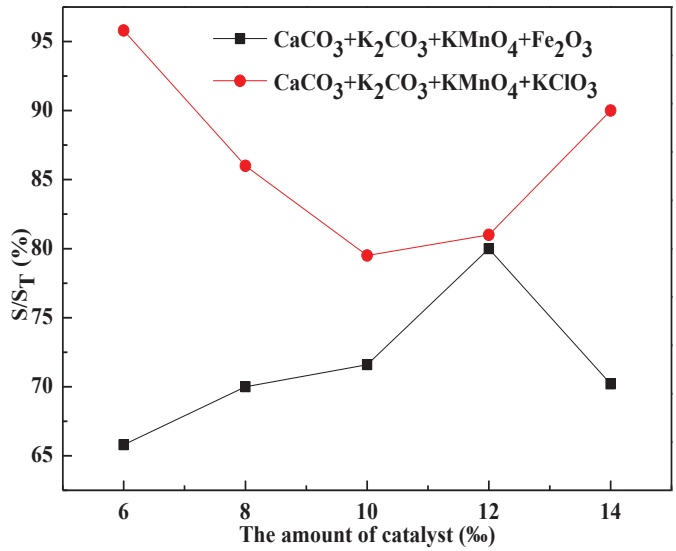

Fig. 10: Effect of varieties of catalysts and adding amount on the sulphation efficiency.

flue gas, the share of organic component in flue gas is little when the adding amount of $KClO_3$ is 6‰. Taking the share of organic component and sulphation efficiency of $CaCO_3$ into account, $KClO_3$ is more suitable for the catalyst of the briquette.

The XRD results given in Fig. 11 illustrate that the fixed sulphur was turned into $CaSO_4$ and K_2SO_4. Calcium in the residue exists in the form of $CaSO_4$, which indicates that the added $CaCO_3$ is fully utilized. The Fig. 12 is the SEM of sample calcined from the mixture of $CaCO_3$ and $KClO_3$ at 900°C. The surface of sample is coarse compared with the surface of the upper of Fig. 5, which indicates that the added $KClO_3$ can promote surface area and enrich surface pore of CaO that was produced through decomposition of $CaCO_3$. During the process of calcining, $KClO_3$ was decomposed into KCl and oxygen by thermal decomposition. The alkali metal compound KCl not only presents the molten state at high temperature, but can form the liquid phase eutectic with the low melting point with CaO produced through decomposition of $CaCO_3$, which increases the migration and

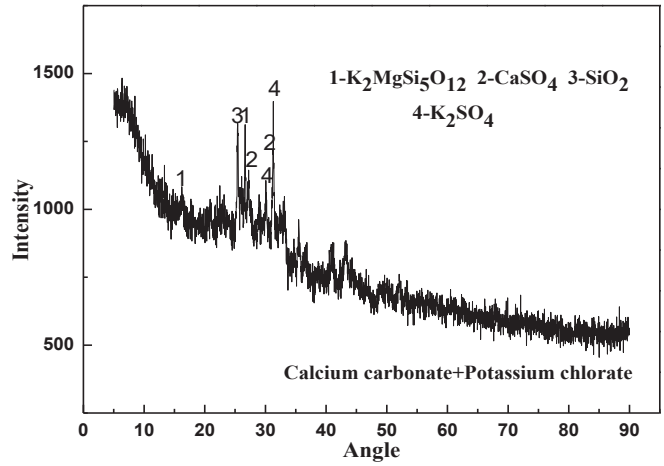

Fig. 11: The XRD spectrum of the incinerating residue (The additive of coal sample are $CaCO_3$ and $KClO_3$).

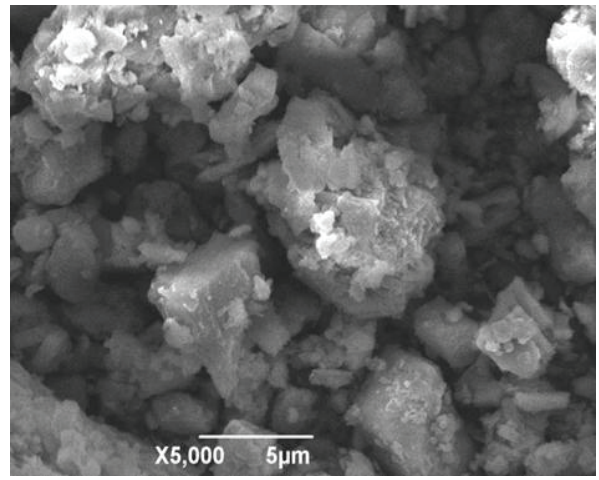

Fig. 12: SEM images of CaO produced through decomposition of $CaCO_3$ and $KClO_3$.

diffusion capacity of the alkali metal ions. The migration and diffusion of the alkali metal ions make the pore size of CaO larger, and the larger pore size is beneficial to the reaction of SO_2 and CaO (Zhou et al. 1997).

CONCLUSIONS

During the incineration of briquette, the addition of $CaCO_3$ is more effective than CaO for fixing sulphur into residue, K_2CO_3 is more useful than NaCl and Na_2CO_3 to improve the sulphation efficiency of $CaCO_3$, the order of improving sulphation efficiency of $CaCO_3$ by sulphation-supporting additives is K_2CO_3, Na_2CO_3, NaCl. The sulphur in briquette is fixed in the form of $CaSO_4$, K_2SO_4 and $BaSO_4$. The SEM and XRD results indicate that the sulphation-supporting additive K_2CO_3 not only can promote surface area and enrich surface pore of CaO produced through decomposition of $CaCO_3$, but can improve the utilization of $CaCO_3$. The addition of $KMnO_4$ is more effective than KNO_3 and $NaNO_3$ for improving the incinerating rate of briquette. However, $KMnO_4$ slightly promotes the release of sulphur.

Fe_2O_3 and $KClO_3$ can apparently promote the burning of briquette and reduce the release of organic gas during the incineration of briquette, but the effect of $KClO_3$ on sulphation of $CaCO_3$ is more obvious than that of Fe_2O_3.

The adding amount of $CaCO_3$, K_2CO_3, $KMnO_4$ and $KClO_3$ is 16‰, 12‰, 18‰, 6‰ respectively in the process of briquette preparation. The sulphation efficiency reaches

the maximum of 95.3%, the maximum of incinerating rate of briquette is improved from 0.38 to 0.6 g/min, the rate of improvement is more than 50%. And there is still an extremely small amount of organic gas in flue gas.

ACKNOWLEDGEMENTS

This work was supported by the Open Project Program of State Key Laboratory of Petroleum Pollution Control; and Shaanxi Youth Science and technology new star project (2017KJXX-49); and Scientific Research Program Funded by Shaanxi Provincial Education Department (Program No.18JS087); and Natural Science Basic Research Plan in Shaanxi Province of China (Program 2019JM-506).

REFERENCES

Casarini, D.C.P., de Macedo, R.M., Cunha, R.D.A. and Mauger, J.C.O. 1988. The development of assessment techniques to evaluate the biodegradation of oily sludge in a landfarming system. Water Science and Technology, 20(10): 231-236.

Duan, M., Wang, X., Fang, S., Zhao, B., Li, C. and Xiong, Y. 2018. Treatment of Daqing oily sludge by thermochemical cleaning method. Colloids and Surfaces A: Physicochemical and Engineering Aspects, 554: 272-278.

Gong, X. Z., Guo, Z. C. and Wang, Z. 2009. Effect of K_2CO_3 and Fe_2O_3 on combustion reactivity of pulverized coal by thermogravimetry analysis. Journal of Fuel Chemistry & Technology, 37(1): 42-48.

Guan, R., Li, W. and Li, B. 2003. Effects of Ca-based additives on desulfurization during coal pyrolysis. Fuel, 82(15): 1961-1966.

Hu, G., Li, J. and Zeng, G. 2013. Recent development in the treatment of oily sludge from petroleum industry: A review. Journal of Hazardous Materials, 261: 470-490.

Hu, G., Li, J., Zhang, X. and Li, Y. 2017. Investigation of waste biomass co-pyrolysis with petroleum sludge using a response surface methodology. Journal of Environmental Management, 192: 234-242.

Jing, G., Luan, M., Du, W. and Han, C. 2012. Treatment of oily sludge by advanced oxidation process. Environmental Earth Sciences, 67(8): 2217-2221.

Junhu Zhou, Haojie Fan and Qiang Yao, et al. 1997. Study on additives for calcium oxide combustion sulphur fixation. Journal of Environmental Science, 17: 284-288.

Karamalidis, A. K. and Voudrias, E. A. 2008. Anion leaching from refinery oily sludge and ash from incineration of oily sludge stabilized/solidified with cement. Part II. Modeling. Environmental Science & Technology, 42(16): 6124.

Kijo-Kleczkowska, A., Sroda, K., Kosowska-Golachowska, M., Musiał, T. and Wolski, K. 2016. Experimental research of sewage sludge with coal and biomass co-combustion, in pellet form. Waste Management, 53: 165-181.

Li, X.G., Ma, B.G., Xu, L., Luo, Z.T. and Wang, K. 2007. Catalytic effect of metallic oxides on combustion behavior of high ash coal. Energy & Fuels, 21(5): 2669-2672.

Liang, J., Zhao, L. and Hou, W. 2017. Solid effect in chemical cleaning treatment of oily sludge. Colloids & Surfaces, A. Physicochemical & Engineering Aspects, 522: 38-42.

Lin, Z., Wang, W. and Huang, R. 2017. Study of oily sludge treatment by centrifugation. Desalination & Water Treatment, 68: 99-106.

Liu, Q., Hu, H., Zhou, Q., Zhu, S. and Chen, G. 2004. Effect of inorganic matter on reactivity and kinetics of coal pyrolysis. Fuel, 83(6): 713-718.

Lopes, H., Trindade, T., Gulyurtlu, I. and Cabrita, I. 2001. Characterization of FBC ashes from co-combustion of coal with oily residues. Fuel, 80(6): 785-793.

Magdziarz, A. and Wilk, M. 2013. Thermogravimetric study of biomass, sewage sludge and coal combustion. Energy Conversion & Management, 75(5): 425-430.

Manquais, K. L., Snape, C., Barker, J. and McRobbie, I. 2012. TGA and drop tube furnace investigation of alkali and alkaline earth metal compounds as coal combustion additives. Energy & Fuels, 26(3): 1531-1539.

Matsodoum Nguemté, P., Djumyom Wafo, G. V., Djocgoue, P. F., Noumsi, I.K. and Ngnien, A.W. 2018. Potentialities of six plant species on phytoremediation attempts of fuel oil-contaminated soils. Water, Air, & Soil Pollution, 229: 88-106.

Nimmo, W., Patsias, A. A. and Hampartsoumian, E. 2004. Calcium magnesium acetate and urea advanced reburning for NO control with simultaneous SO reduction. Fuel, 83(9): 1143-1150.

Polc, R., Petková, K., Lalinská-Voleková, B., Jurkovic, L. and Milicka, J. 2016. Ashes from oily sewage sludge combustion: Chemistry, mineralogy and leaching properties. Acta Geologica Slovaca, 08(1): 119-130.

Ravanbod, M. and Pouretedal, H. R. 2016. Catalytic effect of Fe_2O_3, Mn_2O_3 and TiO_2 nanoparticles on thermal decomposition of potassium nitrate. Journal of Thermal Analysis & Calorimetry, 124: 1091-1098.

Rulkens, W. 2008. Sewage sludge as a biomass resource for the production of energy: Overview and assessment of the various options. Energy & Fuels, 22(1): 9-15.

Sahebnazar, Z., Mowla, D. and Karimi, G. 2017. Zero-valent iron nanoparticles assisted purification of rhamnolipid for oil recovery improvement from oily sludge. Journal of Environmental Chemical Engineering, 6(1): 917-922.

Souza, D.T.D., Benetti, C.N., Sauer, E., Paula, V.C., Freitas, A.M. and Tiburtius, E.R. 2018. Decontamination of pure and ethanol/ gasoline-contaminated soil by Fenton-like process. Water Air & Soil Pollution, 229(4): 105-114.

Wu, Z., And, Y. S. and Kawashima, H. 2002. The influence of mineral matter and catalyst on nitrogen release during slow pyrolysis of coal and related material: a comparative study. Energy & Fuels, 16(2): 451-456.

Xu, M., Liu, H., Zhao, H. and Li, W. 2014. Effect of oily sludge on the rheological characteristics of coke-water slurry. Fuel, 116(1): 261-266.

Yumei, Li. 2012. Study on desulfurization mechanism in pulverized coal combustion and composition control of sulphur solid slag. Wuhan University of Technology.

Zhang, J., Li, J., Thring, R.W., Hu, X. and Song, X. 2012. Oil recovery from refinery oily sludge via ultrasound and freeze/thaw. Journal of Hazardous Materials, 203(4): 195-203.

Zhao, S., Zhou, X., Wang, C. and Jia, H. 2017. Dewatering and low-temperature pyrolysis of oily sludge in the presence of various agricultural biomasses. Environmental Technology, 02: 1-9.

Nature Environment and Pollution Technology
An International Quarterly Scientific Journal

p-ISSN: 0972-6268
e-ISSN: 2395-3454

Vol. 18 | No. 4 | pp. 1169-1176 | 2019

Original Research Paper | Open Access

Vertical Distribution of Microplastics in Coastal Sediments of Bama Resort, Baluran National Park, Indonesia

Muhammad A. Asadi*†, Yody A.P. Ritonga*, Defri Yona* and Asus M.S. Hertika**

*Department of Marine Science, Faculty of Fisheries and Marine Science, University of Brawijaya, Malang 65145, Indonesia

**Department of Water Resources Management, Faculty of Fisheries and Marine Science, University of Brawijaya, Malang 65145, Indonesia

†Corresponding author: Muhammad A. Asadi

Nat. Env. & Poll. Tech.
Website: www.neptjournal.com

Received: 16-03-2019
Accepted: 30-05-2019

Key Words:
Microplastics
Microplastic pollution
Baluran National Park
Coastal sediments
Marine environment

ABSTRACT

Microplastic pollution is widely reported in different marine environments from shorelines to seabed of deep seas which pose an emerging threat to entire marine ecosystems. As the world's second-largest microplastics polluter, an understanding of the distribution of this type of pollution is important for the measurement of the magnitude of environmental risk. In the present study, the abundance and distribution of microplastics in coastal sediments of Bama Resort, Baluran National Park were measured at depths of 0-10 cm, 10-20 cm, and 20-30 cm. Microplastics characterization was performed using a modified flotation method while a sieve analysis was used to assess the particle size of the sediments. Results showed that there were 484 particles with a total average abundance of 116.41 ± 80.78 particles kg^{-1} DW. Fibres shared 37.8% of the total microplastics found with overall average of 43.71 ± 36.52 particles kg^{-1} DW. Overall, Tukey's multiple comparisons test showed significant differences ($P< 0.01$) in vertical distribution of microplastics in which 55.46% of particles were found at the depths of 0-10 cm, whereas at the depths of 20-30 cm, the proportion was only 15.95%. There were two types of sediments, sandy gravel and gravelly sand in which the former type of sediments holds higher microplastic particles due to its grain dominance in upper sediments. These results imply that microplastics pollute coastal sediments of Bama Resorts, BNP, and their deposition increase over time as greater microplastics frequencies were observed in upper and more recent sediment.

INTRODUCTION

In the modern era, plastic material is used in an array of products of different forms, including toys, furniture, and spacecraft as it has many incredible properties such as high strength and durability, versatile, and lightweight (Ling et al. 2017, Martin et al. 2017, Tanaka & Takada 2016). Although the benefits of using plastic products are undeniable, there are adverse effects of plastic pollution in the environment (Van Cauwenberghe et al. 2015). Millions of tons of plastic debris are currently in the marine environment from coastlines to the deep-sea, and by 2025, plastic items in the ocean are expected to accumulate by an order of magnitude (Jambeck et al. 2015, Martin et al. 2017).

In marine environment, larger plastics debris degrade into smaller pieces known as fragmentation. Over time, these plastics begin to weather due to wave action, heat, and photodegradation by ultraviolet radiation wherein those factors can breakdown the structural integrity of plastic debris and reduce to a much smaller size known as secondary microplastics. Meanwhile, plastic particles that are originally manufactured to the size of microplastics (defined as plastics <5mm) are known as primary microplastics (Andrady 2011, Laglbauer et al. 2014, Tanaka & Takada 2016).

A recent study suggests that Indonesia is second only to China as the world's largest contributor to plastic pollution in the ocean. Microplastics are even presented in the pristine area of deep-sea sediment of Western Sumatera at depth of more than 2000 meter (Cordova & Wahyudi 2016). In Bintan Island, Riau Islands Province, Indonesia, 0.45 pieces per m^3 float in 11 beach stations around the island (Syakti et al. 2018). However, as the world's second-largest plastics polluter as well as the world's largest archipelago state with about 3.3 million km^2 of territorial seas (Cordova & Wahyudi 2016, Göltenboth & Erdelen 2006), there still little is known on the microplastics distribution and abundance in most areas of Indonesia.

In Java Island, fishing activities, population growth, and industrializations of coastal areas make its intertidal areas particularly susceptible to microplastics accumulation (Manalu et al. 2017). Therefore, the measurement of microplastics abundance and distribution in Indonesian coastal areas is essential. In this study, microplastics pollution in coastal sediments of Bama Resort, Baluran Nation-

al Park (BNP) was examined. The park is a nature reserve area which may have a low anthropogenic stressor and microplastics input from its terrestrial area. Therefore, this research is expected to reveal to what extent microplastics distribute in coastal sediments of Java Island. The types of microplastic (fibre/line, foam, pellet, film and fragment) are determined to reveal the dominant types of microplastics in the research station. Particle size analysis of the sediment was also conducted to determine the link between sediment types and microplastics distribution and abundance in coastal sediments of Bama Resort, BNP.

MATERIALS AND METHODS

Description of the study area: The present study was conducted at the intertidal area of Bama resort, BNP. The park is a nature reserve located at the north-eastern extremity of Java with latitude between 7°15'S and 7°45'S and longitude between 114°18'E and 114°27'E (Sabarno 2001). It has a total area of 25,000 ha in which tropical Savannas cover about 40% of the total area. BNP has a long dry period of monsoon (8 months) with precipitation ranges from 900 to 1,600 mm per year (Hernowo et al. 2011, Macdonald & Frame 1988, Wianti 2014). BNP has gained National Park status since 1980 (Van Balen et al. 1995, Wianti 2014), and in 2016, BNP was declared as one of the UNESCO's world network of biosphere reserves (UNESCO 2016). In 26th December 2012, the Directorate General of Nature Protection and Conservation of Indonesia has divided BNP into several zones where the intertidal area of Bama resort is included in marine protected area zone with the size of 1,174.96 ha (ADB, 2018). The intertidal area of Bama resort has a mixed tide type with predominantly semi-diurnal form (unpublished data). Geographic coordinates of the research stations were between -7.842211° and -7.847140° (latitude), and between 114.459845° and 114.463213° (longitude). The map of the study area is presented in Fig. 1.

Sampling: The present study was conducted during the period of low tides in the intertidal area of Bama resort, BNP in October 2018. In each sampling station, 3 sampling plots with the size of 50×50 transect were set up parallel to the coastline with a distance of 25 m. In each transect, a total of 1.5 kg of soil, 1 kg for soil analysis and 0.5 kg for microplastics determination, was collected using a soil auger with a diameter of 7.6 cm and length of 30 cm. In each transect, soil samples were separated based on depth (0-10 cm, 10-20 cm, and 20-30 cm) and placed in plastic bags. The sediment samples were immediately transported for further laboratory analysis in Marine Science laboratory, University of Brawijaya.

Sediments analysis: Sieve shaker procedure was used to separate sediments based on their grain size. This method was chosen as the visual analysis showed that the sediment type of the research area was sand (Asadi et al. 2018). In the

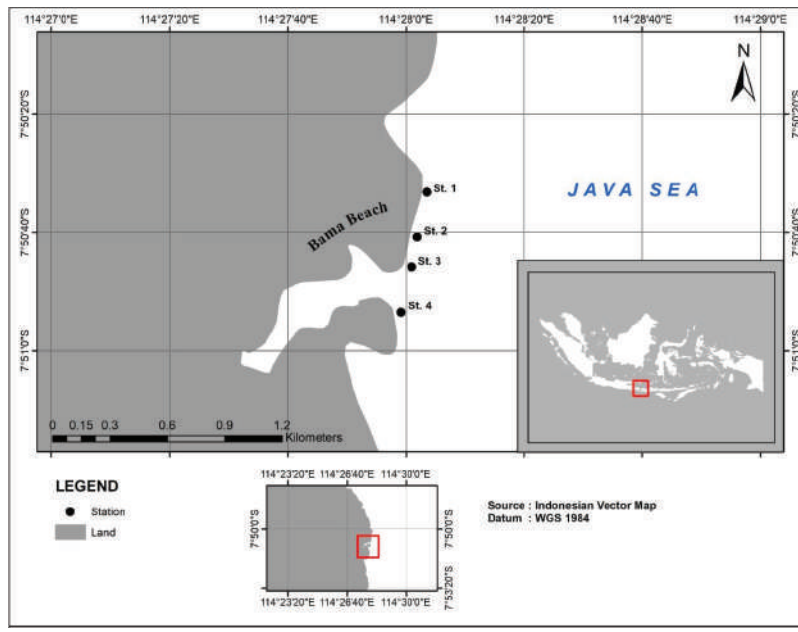

Fig. 1: Map of the sampling stations along the intertidal area of Bama Resort, BNP.

first step of this procedure, all samples were dried using an oven at approximately 90°C for 3 days in order to prepare the sieving processes. In the second step, the samples were passed through some test sieves with different mesh sieves from the size of 5 mm to 45 µm. In order to define the size ranges of the sediments, the samples were then weighted and classed using Wentworth's particle size scale. Shepard's diagram was then used to classify sediments based on the proportions of particles (Asadi et al. 2017, Di Stefano et al. 2010).

Microplastics analysis: In order to perform microplastics analysis of the sediment, a total amount of 150g of soil sample from each depth (0-10 cm, 10-20 cm and 20-30 cm) of each plot and each station was dried using a Memmert drying oven at temperature of 60°C for 48 hour to obtain dry soil samples. The selected temperature was also meant to prevent microplastics from degradation. As a microplastic has particle < 5 mm, the soil samples were then passed through a sieve test with the size of 5-mm to separate sediment with the size higher than 5 mm. Microplastic particles were extracted from the separated soil samples using the flotation method described by Kazmiruk et al. (2018) and Thompson et al. (2004) with minor modifications. In the method, the mixture of 360 g sodium chloride and filtered seawater was used to prepare a saturated saline solution with a density of 1.35 g cm^{-3}. The solution was then stirred for 2 minutes using a magnetic stirrer. After stirring, the solution was closed with aluminium foil to prevent contamination from the air and allowed to settle for 24 h. Furthermore, the supernatant of the solution was filtered through a 0.3-mm sieve test to separate and obtain identifiable microplastics (Laglbauer et al. 2014, Masura et al. 2015). Microplastic particles were visually observed using a microscope and classified based on their types as fibres, films, foams, nurdles, and fragments (Di & Wang 2018).

RESULTS AND DISCUSSION

Microplastic characterization: Among all 484 particles found, there were 183 fibers (37.8%), 159 films (32.9%), 141 fragments (29.1%), and 1 foam (0.2%). There was no plastic pellet identified within this study which confirmed that all microplastic particles found in the research areas were identified as secondary microplastics. pellets, beads, or nurdles are primary microplastics which were originally manufactured to be < 5 mm in size. They serve as raw materials in the manufacture of plastic products (Martin et al. 2017, Smith et al. 2018, Syakti et al. 2017). The dominance of fibres in sediment in this study was much lower than that of in other studies (Di & Wang 2018, Martin et al. 2017, Willis et al. 2017). Fibres constituted 85% of total microplastics in the bottom waters and sediment of the Irish continental shelf (Martin et al. 2017). In sediment of urban estuaries of Australia, fibres even contributed 87% of total items observed (Willis et al. 2017). Synthetic fibres make up a large proportion of microplastic pollution in urban areas (Hernandez et al. 2017), while intertidal area of Bama Resort is part of marine protected zone of BNP which is relatively remote area, strictly protected and managed for conservation (Wianti 2014), therefore, in the study area, there might a lack of fibres pollution from nearby households. These fibres might settle in the sediment of intertidal area of Bama resort prior to the ubiquitous of plastics throughout the marine environment.

Furthermore, microplastic particles were found in a variety of colours. Clear or transparent, white, blue, and red were most common with 44, 38, 32, and 20 particles respectively which shared 24%, 21%, 18%, and 11% respectively. Meanwhile black, brown, green, orange, and yellow were least common with 16, 12, 8, 6, and 4 particles respectively which constituted 9%, 7%, 5%, 3%, and 2% respectively. In sediments of the Three Gorges Reservoir, China, the most dominant colour was also transparent (Di & Wang 2018), while it was the second most dominant colour in many coastal waters of Indonesia (Syakti et al. 2017). Transparent colour of microplastics is partly a result of bleaching and discolouring of microplastics due to prolonged exposure of ultraviolet light (Kalogerakis et al. 2017). Photographs of microplastics found in the research stations are presented in Fig. 2.

Microplastics abundance: The number of total microplastics varied from 35.80 ± 20.07 particles kg^{-1}dry weight (DW) at station 3 to 178.45 ± 144.30 particles kg^{-1}DW at station 4 with a total average of 116.41 ± 80.78 particles kg^{-1}DW (Table 1). The results of this study reveal that microplastics pollution has become pervasive in intertidal area of Bama Resort, BNP. The abundance of microplastics in this study area was slightly higher than that found in coastal sediments of Muara Badak, Kutai Kertanegara, Indonesia which had averages of 105 particles kg^{-1}DW (Dewi et al. 2015). Although, there might be no or little direct input of microplastics from terrestrial areas of BNP, microplastics might settle in its coastal sediments from surrounding water column as buoyant microplastics can be transported by winds and surface currents, recaptured by coastal sediments. In Great Pacific Garbage Patch, a remote subtropical waters between California and Hawaii, microplastic particles even increase and accumulate exponentially (Lebreton et al. 2018). Meanwhile, in coastal sediments of Jakarta Bay, Indonesia, microplastic particles are two hundred times higher than in coastal sediments of Bama Resort in which as many as 18,405 to 38,790 particles kg^{-1} DW were

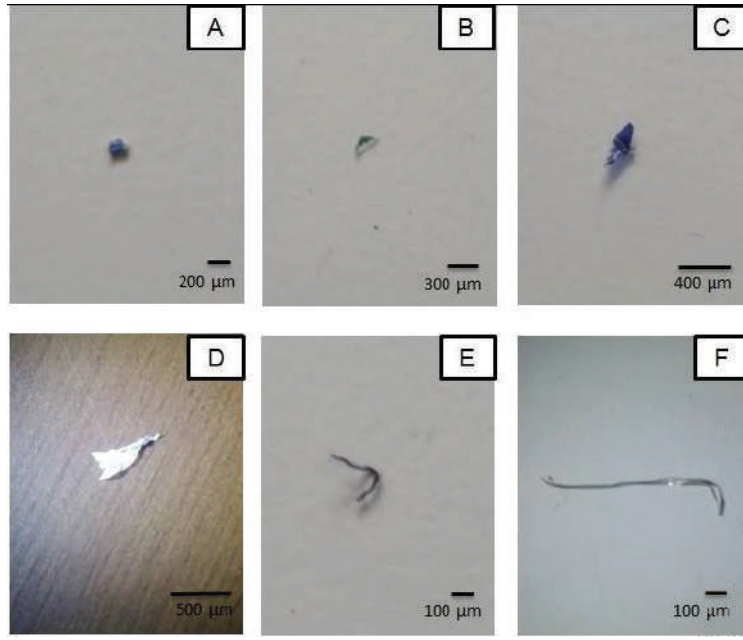

Fig. 2: The photographs of some microplastic particles found in coastal sediments of Bama Resort, BNP. Fragments (A, B), Films (C, D), Fibres (E, F).

Table 1: Microplastics abundance in the sediment of intertidal area of Bama Resort, BNP at each station at depths of 0-10 cm, 10-20 cm, 20-30 cm.

Station	Depth (cm)	Microplastics abundance (particles kg^{-1} dry weight)				Total
		Fragments	Fibers	Films	Foams	
1	0-10	88.50 ± 1.73	97.35 ± 2.65	76.70 ± 0.58	0	
	10-20	60.87 ± 2.00	34.78 ± 3.00	31.88 ± 1.53	0	153.13 ± 102.12
	20-30	20.11 ± 2.08	28.74 ± 0.58	20.47 ± 1.15	0	
2	0-10	24.02 ± 1.53	69.07 ± 3.79	54.05 ± 2.65	0	
	10-20	18.18 ± 1.73	30.30 ± 2.31	42.42 ± 1.53	0	98.27 ± 56.63
	20-30	17.86 ± 0	14.88 ± 1.15	15.02 ± 0.58	9.09 ± 0.58	
3	0-10	8.93 ± 0	5.95 ± 1.15	8.77 ± 0	0	
	10-20	21.21 ± 1.15	21.02 ± 0.58	15.02 ± 0.58	0	35.80 ± 20.07
	20-30	2.90 ± 0.58	11.59 ± 1.15	12.01 ± 1.53	0	
4	0-10	101.09 ± 2.52	153.01 ± 8.50	87.43 ± 2.52	0	
	10-20	26.88 ± 1.53	40.32 ± 1.00	56.45 ± 4.00	0	178.45 ± 144.30
	20-30	14.62 ± 0.58	17.54 ± 2.00	38.01 ± 2.31	0	
Average		33.76 ± 23.50	43.71 ± 36.52	38.19 ± 19.47	0.75 ± 1.30	116.41 ± 80.78

found in coastal sediments of the Bay.

Tukey's multiple comparisons test of Two-way ANOVA showed significant differences ($P < 0.01$) in the abundance of microplastics among fibres, fragments, films, and foams (Table 2). Fibres were the highest microplastics concentration with overall average of 43.71 ± 36.52 particles kg^{-1} DW, while foams had the least microplastics abundance with overall average of 0.75 ± 1.30 particles kg^{-1} DW (Table 1). In sediments of European waters, the overall average of microfibres concentration range from 52.60 to 157.92 items per kg DW (Gago et al. 2018). In Baynes Sound and Lambert Channel, British Columbia, Canada, microfibres

Table 2: Tukey's multiple comparison test of the overall average of microplastic types abundance (N=12).

Tukey's multiple comparisons test	Mean Diff,	95.00% CI of diff,	Significant?	Summary	Adjusted P Value
Fragments vs. Fibers	-9.948	-10.99 to -8.907	Yes	****	<0.0001
Fragments vs. Films	-4.171	-5.212 to -3.13	Yes	****	<0.0001
Fragments vs. Foams	33.01	31.97 to 34.05	Yes	****	<0.0001
Fibers vs. Films	5.778	4.736 to 6.819	Yes	****	<0.0001
Fibers vs. Foams	42.96	41.91 to 44	Yes	****	<0.0001
Films vs. Foams	37.18	36.14 to 38,22	Yes	****	<0.0001

concentration range from 100 to 300 items per kg DW (Kazmiruk et al. 2018). Microfibres are the most dominant microplastics pollution along coastal areas and have been documented to permeate the ocean's deepest points (Barrows et al. 2018). Microfibres enter marine environment via wastewater effluent and diverse non-point sources in which more than 60% of microfibres are from synthetic textiles (Almroth et al. 2018, Barrows et al. 2018). Synthetic fibres are not biodegradable in which polypropylene is the most common polymer type of microfibres found in water and sediments (Xu et al. 2018). Each 6-kilo of laundry could release more than 700,000 synthetic fibres (Napper & Thompson 2016), therefore, microfibres will continue to pollute marine environment as over 9 million tons of textile are manufactured annually (Barrows et al. 2018).

Meanwhile, fragments had an overall average of 33.76 ± 23.50 particles kg^{-1} DW in which station 4 had the highest concentration with an average of 70.29 ± 72.53 particles kg^{-1} DW (Table 1). These values were much lower than that found in the coastal sediments of Muara Badak, East Kalimantan, Indonesia, in which fragments ranged from 100.2 to 236 particles kg^{-1} DW (Dewi et al. 2015). Mussels and planktivorous fish have been reported to ingest microfibres up to 15 particles per individual of fish (Digka et al. 2018, Tanaka & Takada 2016). Fragments are among secondary microplastics derived from the degradation of larger plastic debris through natural weathering processes (Tanaka & Takada 2016). A vast majority of fragments observed during this study exhibited bleach and discolouration patterns as results of photodegradation and other weathering processes.

Microplastics distribution: Tukey's multiple comparisons test of Two-way ANOVA showed that there were significant differences ($P< 0.01$) in vertical and horizontal distribution of fragments, fibres, and films. Foams were not significant differences ($P >0.99$) in vertical distribution between depths of 0-10 cm and 10-20 cm. Horizontal distribution of foams showed significant differences ($P< 0.01$) between station 1 and 2, 2 and 3, and 2 and 4. Meanwhile, deeper sediments resulted in fewer microplastic particles in which overall 55.46% of them were found at depths of 0-10 cm, while 28.58% and 15.95% were observed at depths 10-20 cm and 20-30 cm respectively.

There were 81.34 ± 4.02 particles kg^{-1} DW of fibres at depths of 0-10 cm while they were only 18.18 ± 1.22 particles kg^{-1} DW at depths of 20-30 cm. Fragments at depths of 0-10 cm were 55.63 ± 1.44 particles kg^{-1} DW, while they were only 31.78 ± 1.60 particles kg^{-1} DW and 13.87 ± 0.81 particles kg^{-1} DW at depths of 10-20 cm and 20-30 cm respectively (Fig. 3). The results demonstrated that microplastics have been polluted the coastal areas of BNP since the past couple of decades as microplastics settled in coastal sediments prior to the presence of plastics in the marine environment. Moreover, these microplastics settle in the sediments at faster rate in the current period of time as greater plastic frequencies were found in more recent sediments. However, a study of the age of sediment and the rate of sedimentation is needed to reveal the deposition time of microplastics in the research area (Willis et al. 2017).

Sediment characteristics and microplastics abundance: Based on Wentworth scale, there were only two classes of sediments found in the sampling stations which were sand and gravel while silt and clay were not observed during laboratory analysis. Shepard's diagram classified the sediments based on the proportion of grain classes in each depth of each station in which sandy gravel types were found at the upper sediments while gravelly sand types were mostly found in the deeper sediments. Microplastic particles commonly have positive correlations with finer sediments (Ling et al. 2017). However, microplastics in this study were more ubiquitous in the coarser sediment (sandy gravel) than in the finer sediment (gravelly sand) which hold microplastics with a total average of 161.63 ± 117.64 particles kg^{-1} DW and 71.02 ± 40.44 particles kg^{-1} DW respectively. Therefore, in this study, sediment depths were much more correlated with the abundance of microplastics than that of

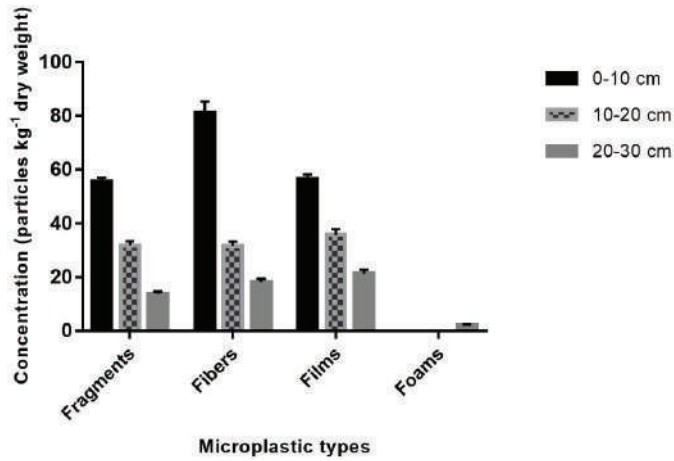

Fig. 3: Vertical distribution of microplastics at depths of 0-10 cm, 10-20 cm, and 20-30 cm.

Table 3: Total abundance of microplastics based on depths and sediment types.

Sediment types	Station	Depths (cm)	Total abundance (particles kg^{-1}DW)
Sandy gravel	1	0-10 cm	262.54 ± 4.96
	1	10-20 cm	127.54 ± 6.53
	2	10-20 cm	90.91 ± 5.57
	3	0 -10 cm	23.65 ± 1.15
	4	0-10 cm	341.53 ± 13.54
	4	10-20 cm	123.66 ± 6.53
	Average		161.63 ± 117.64
Gravelly sand	1	20-30 cm	68.32 ± 3.81
	2	0-10 cm	147.15 ± 7.96
	2	20-30 cm	56.76 ± 2.31
	3	10-20 cm	57.25 ± 2.31
	3	20-30 cm	26.5 ± 3.26
	4	20-30 cm	70.18 ± 4.89
	Average		71.02 ± 40.44

the types of sediments as more microplastics were found in the upper or younger sediments (Table 3).

CONCLUSION

Microplastics pollution was widespread in the coastal sediments of Bama Resort, BNP. There were 484 microplastics found in which fibres and films shared 37.8% and 32.9% of the total particles respectively. Transparent, white, and blue were most common colour of microplastics found with occurrences of 24%, 21%, and 18% respectively. Microplastics abundance varied from 35 to 178 particles kg^{-1} DW with a total average of 116 particles kg^{-1} DW in which fibres had an overall average of 43 particles kg^{-1} DW.

Vertical distribution of microplastics within the sediments column showed significant differences among depths in which more microplastics found in the more recent (upper) sediment. A total 55.46% of microplastics found at depths 0-10 cm whereas only 15.95% of total particles were found at depths of 20-30 cm. Sandy gravel sediments hold higher microplastics than that of gravely sand; therefore, the higher concentration of microplastics in the former sediments was due to their dominance in the upper layer of sediment. Moreover, it is concluded that microplastics

might pollute the coastal sediments of Bama Resort, BNP since some decades ago and the rate of contamination increases in more recent years.

ACKNOWLEDGEMENT

The publication of the research was supported by the Rector of Brawijaya University and the Dean of Faculty of Fisheries and Marine Science at Brawijaya University. The authors wish to thank the Baluran National Park Authorities for the access and support during the field samplings.

REFERENCES

ADB. 2018. Recommendation Report Baluran National Park. Institutional Strengthening Baluran and Bali Barat National Parks, Indonesia. Technical Assistance TA-8745 INO: Environment Conservation and Planning Specialist. Asian Development Bank, Jakarta.

Almroth, B.M.C., Åström, L., Roslund, S., Petersson, H., Johansson, M. and Persson, N.K. 2018. Quantifying shedding of synthetic fibres from textiles; a source of microplastics released into the environment. Environ. Sci. Pollut. Res. Int., 25: 1191-1199.

Andrady, A.L. 2011. Microplastics in the marine environment. Mar. Pollut. Bull., 62: 1596-1605.

Asadi, M., Yona, D. and Fikri, M.Z. 2018. Comparing carbon in sediment of primary and artificially generated mangrove forests. Disaster Adv., 11(11): 18-26.

Asadi, M.A., Guntur, G., Ricky, A.B., Novianti, P. and Andik, I. 2017. Mangrove ecosystem C-stocks of Lamongan, Indonesia and its correlation with forest age. Res. J. Chem. Environ., 21: 1-9.

Barrows, A.P.W., Cathey, S.E. and Petersen, C.W. 2018. Marine environment microfiber contamination: Global patterns and the diversity of microparticle origins. Environ. Pollut., 237: 275-284.

Cordova, M., Wahyudi, A. 2016. Microplastic in the deep-sea sediment of southwestern Sumatran waters. Mar. Res. Indones., 41(1): 27-35

Dewi, I., Budiarsa, A. and Ritonga, I. 2015. Distribution of microplastic at sediment in the Muara Badak Subdistrict, Kutai Kartanegara Regency. Depik, 4(3): 121-131.

Di, M. and Wang, J. 2018. Microplastics in surface waters and sediments of the Three Gorges Reservoir, China. Sci. Total Environ., 616: 1620-1627.

Di Stefano, C., Ferro, V. and Mirabile, S. 2010. Comparison between grain-size analyses using laser diffraction and sedimentation methods. Biosyst. Eng., 106: 205-215.

Digka, N., Tsangaris, C., Torre, M., Anastasopoulou, A. and Zeri, C. 2018. Microplastics in mussels and fish from the Northern Ionian Sea. Mar. Pollut. Bull., 135: 30-40.

Gago, J., Carretero, O., Filgueiras, A.V. and Viñas, L. 2018. Synthetic microfibres in the marine environment: A review on their occurrence in seawater and sediments. Mar. Pollut. Bull., 127: 365-376.

Göltenboth, F. and Erdelen, W. 2006. 1-Geography and geology. In: Göltenboth, F., Timotius, K.H., Milan, P.P., Margraf, J. (Eds.) Ecology of Insular Southeast Asia. Elsevier, Amsterdam, pp. 3-16.

Hernandez, E., Nowack, B. and Mitrano, D.M. 2017. Polyester textiles as a source of microplastics from households: A mechanistic study to understand microfiber release during washing. Environ. Sci. Technol., 51: 7036-7046.

Hernowo, J.B., Mardiastuti, A., Alikodra, H.S. and Kusmana, C. 2011. Behavior ecology of the Javan Green Peafowl (*Pavo muticus muticus* Linnaeus 1758) in Baluran and Alas Purwo National Park, East Java. Hayati J. Biosci., 18: 164-176.

Jambeck, J.R., Geyer, R., Wilcox, C., Siegler, T.R., Perryman, M., Andrady, A., Narayan, R. and Law, K.L. 2015. Plastic waste inputs from land into the ocean. Science, 347: 768-771.

Kalogerakis, N., Karkanorachaki, K., Kalogerakis, G.C., Triantafyllidi, E.I., Gotsis, A.D., Partsinevelos, P. and Fava, F. 2017. Microplastics generation: Onset of fragmentation of polyethylene films in marine environment mesocosms. Front. Mar. Sci., 4: 84.

Kazmiruk, T.N., Kazmiruk, V.D. and Bendell, L.I. 2018. Abundance and distribution of microplastics within surface sediments of a key shellfish growing region of Canada. Plos One, 13: e0196005.

Laglbauer, B.J.L., Franco-Santos, R.M., Andreu-Cazenave, M., Brunelli, L., Papadatou, M., Palatinus, A., Grego, M. and Deprez, T. 2014. Macrodebris and microplastics from beaches in Slovenia. Mar. Pollut. Bull., 89: 356-366.

Lebreton, L., Slat, B., Ferrari, F., Sainte-Rose, B., Aitken, J., Marthouse, R., Hajbane, S., Cunsolo, S., Schwarz, A., Levivier, A., Noble, K., Debeljak, P., Maral, H., Schoeneich-Argent, R., Brambini, R. and Reisser, J. 2018. Evidence that the Great Pacific garbage patch is rapidly accumulating plastic. Sci. Rep., 8: 4666.

Ling, S.D., Sinclair, M., Levi, C.J., Reeves, S.E. and Edgar, G.J. 2017. Ubiquity of microplastics in coastal seafloor sediments. Mar. Pollut. Bull., 121: 104-110.

Macdonald, I.A.W. and Frame, G.W. 1988. The invasion of introduced species into nature reserves in tropical savannas and dry woodlands. Biol. Invasions Nat. Reserv., 44: 67-93.

Manalu, A.A., Hariyadi, S. and Wardiatno, Y. 2017. Microplastics abundance in coastal sediments of Jakarta Bay, Indonesia. AACL Bioflux, 10: 1164-1173.

Martin, J., Lusher, A., Thompson, R.C. and Morley, A. 2017. The deposition and accumulation of microplastics in marine sediments and bottom water from the Irish continental shelf. Sci. Rep., 7: 10772.

Masura, J., Baker, J., Foster, G. and Arthur, C. 2015. Laboratory methods for the analysis of microplastics in the marine environment: Recommendations for quantifying synthetic particles in waters and sediments (NOAA Technical Memorandum NOS-OR & R-48).

Napper, I.E. and Thompson, R.C. 2016. Release of synthetic microplastic plastic fibres from domestic washing machines: Effects of fabric type and washing conditions. Mar. Pollut. Bull., 112: 39-45.

Sabarno, Y.M. 2001. Baluran Nasional Park, Savanna. Biodiversitas, 3: 207-2012.

Smith, M., Love, D.C., Rochman, C.M. and Neff, R.A. 2018. Microplastics in seafood and the implications for human health. Curr. Environ. Health Rep., 5: 375-386.

Syakti, A.D., Bouhroum, R., Hidayati, N.V., Koenawan, C.J., Boulkamh, A., Sulistyo, I., Lebarillier, S., Akhlus, S., Doumenq, P. and Wong-Wah-Chung, P. 2017. Beach macro-litter monitoring and floating microplastic in a coastal area of Indonesia. Mar. Pollut. Bull., 122: 217-225.

Syakti, A.D., Hidayati, N.V., Jaya, Y.V., Siregar, S.H., Yude, R., Suhendy, Asia, L., Wong-Wah-Chung, P. and Doumenq, P. 2018. Simultaneous grading of microplastic size sampling in the small islands of Bintan water, Indonesia. Mar. Pollut. Bull., 137: 593-600.

Tanaka, K. and Takada, H. 2016. Microplastic fragments and microbeads in digestive tracts of planktivorous fish from urban coastal waters. Sci. Rep., 6: 34351-34351.

Thompson, R.C., Olsen, Y., Mitchell, R.P., Davis, A., Rowland, S.J., John, A.W.G., McGonigle, D. and Russell, A.E. 2004. Lost at sea: Where is all the plastic? Science, 304: 838.

UNESCO 2016. Biosphere Reserves. Belambangan. URL http://www.unesco.org/new/en/natural-sciences/environment/ecological-sciences/biosphere-reserves/asia-and-the-pacific/indonesia/belambangan/ (accessed 2.13.18).

Van Balen, S., Prawiradilaga, D.M. and Indrawan, M. 1995. The distribution and status of green peafowl *Pavo muticus* in Java. Biol. Conserv., 71: 289-297.

Van Cauwenberghe, L., Claessens, M., Vandegehuchte, M.B. and Janssen, C.R. 2015. Microplastics are taken up by mussels (*Mytilus edulis*) and lugworms (*Arenicola marina*) living in natural habitats. Environ. Pollut., 199: 10-17.

Wianti, K.F. 2014. Land Tenure Conflict in the Middle of Africa van Java (Baluran National Park). 4th Int. Conf. Sustain. Future Hum. Secur. Sustain, 2013, 20: 459-467.

Willis, K.A., Eriksen, R., Wilcox, C. and Hardesty, B.D. 2017. Microplastic distribution at different sediment depths in an urban estuary. Front. Mar. Sci., 4: 419.

Xu, X., Hou, Q., Xue, Y., Jian, Y. and Wang, L. 2018. Pollution characteristics and fate of microfibres in the wastewater from textile dyeing wastewater treatment plant. Water Sci. Technol., 78: 2046-2054.

Nature Environment and Pollution Technology
An International Quarterly Scientific Journal

p-ISSN: 0972-6268
e-ISSN: 2395-3454

Vol. 18 | No. 4 | pp. 1177-1184 | 2019

Original Research Paper | Open Access

Diversity and Seasonal Variations of Plankton Communities After Major Flash Flood in the River Mandakini of Garhwal Himalaya

Deepak Singh† and Gunjan Goswami
Department of Zoology and Biotechnology, H.N.B. Garhwal University, Srinagar-Garhwal, 246174, Uttarakhand, India
†Corresponding author: Deepak Singh

Nat. Env. & Poll. Tech.
Website: www.neptjournal.com

Received: 09-03-2019
Accepted: 21-04-2019

Key Words:
CCA
Diversity
Flood
PCA
Phytoplankton
Zooplankton

ABSTRACT

Plankton diversity acts as an ecological indicator of aquatic ecosystems due to their rapid response to environmental changes. Plankton samples were collected monthly for a period of 24 months. A total of 35 genera of phytoplankton belonging to three classes, Bacillariophyceae (21 genera), Chlorophyceae (9 genera) and Cyanophyceae (5 genera) were found. The abundance of phytoplankton was in the order, Bacillariophyceae (83%) followed by Chlorophyceae (9%) and Cyanophyceae (8%). Maximum phytoplankton density in winter season was attributed to the low water temperature, gentle water velocity, high transparency, availability of sufficient nutrients and most stable substratum. Eight genera of zooplankton belonging to three major groups, Protozoa (2 genera), Rotifera (5 genera) and Copepoda (1 genus) was recorded. Shannon-Wiener diversity index of phytoplankton and zooplankton was computed maximum to be 2.61 and 1.56 respectively in the winter season. PCA indicates *Cymbella, Navicula, Synedra, Cocconeis, Achnanthidium, Amphora, Nitzschia, Tabellaria, Fragilaria, Ulothrix, Spirogyra* and *Phormidium* to be most dominant genera in the Mandakini river. Total alkalinity, water temperature, transparency, velocity, dissolved oxygen, free carbon dioxide, turbidity, phosphate and nitrate were found to be the most important factors affecting plankton diversity in the Mandakini river.

INTRODUCTION

Plankton are free-swimming or floating organisms in aquatic ecosystems divided into two major groups such as phytoplankton and zooplankton. Plankton communities occupy the base of aquatic ecosystems functioning. They show seasonal fluctuation, multi annual trends and shifts in an aquatic ecosystem. An in-depth study of plankton communities is necessary to manage aquatic resources and to predict future ecological changes (Morabito et al. 2018). They are the excellent indicators of healthy aquatic ecosystems.

Phytoplankton are chlorophyll bearing microscopic organisms consisting mainly algae and belong mainly to Bacillariophyceae, Chlorophyceae and Cyanophyceae groups. Phytoplankton, are primary producers and source of food for various animal groups like zooplankton, macroinvertebrates, fishes, etc. Zooplankton are microscopic free-swimming animals represented by taxonomic groups like protozoans, rotifers, cladocerans, crustaceans and copepods. Zooplankton consume phytoplankton and thus connect primary producers and higher trophic levels in the aquatic ecosystems.

Flood events directly affect the freshwater organisms (plankton, periphyton, macrophytes, macroinvertebrates, fish, etc.) inhabiting a river by displacing or killing them. They change the geomorphology of the river thus influencing freshwater ecosystems. The structure of river ecosystems determines the quality and quantity of habitat that is available to freshwater organisms (Death et al. 2015). The discharge and velocity of the water increase during flash flood which dilutes the water and modifies the concentration of nutrients, therefore changing the processes at biological level (Muntean & Alexoaie 2013). River flooding in Himalaya is commonly caused by heavy rainfall in a short period, river blockade failure and sometimes snow melting. The Mandakini river hit by major flash flood during 16-17 June, 2013 resulted into big loss to aquatic flora and fauna and changed the geomorphology of the Mandakini river. Therefore, the present study was conducted to observe the status of plankton density, diversity and recovery of ecosystem after this major flash flood.

MATERIALS AND METHODS

Mandakini river, a perennial glacier-fed tributary of the river Alaknanda, flows in the Rudraprayag district of Uttarakhnd Himalaya. It originates from the Chaurabari Glacier and passes through Kedarnath (3684m a.s.l.), Rambara (2722m a.s.l.), Gaurikund (1838m a.s.l.), Kund (998m a.s.l.), Chandrapuri (827m a.s.l.), Agustyamuni (760m a.s.l.), Tilwara (724m a.s.l.) and ultimately merges with the river Alaknanda at Rudraprayag (620m a.s.l.) after covering its course

of 72 km. Three sampling sites; S_1, S_2 and S_3 were selected along the Mandakini River at Kund, Agustyamuni and Rudraprayag (Fig. 1).

Monthly samples were collected from January 2014 to December, 2015 for the analysis of plankton density and diversity of the Mandakini river. The plankton collection was done by filtering 10 litres of river water through plankton net (0.1 mm mesh size) at each sampling site and samples were collected in the sample jars. While collecting water samples, minimum disturbance of water to prevent avoidance reaction by plankton was taken care of. The samples were preserved in 4% formalin in the plastic jars. The plankton taxa were identified under the light microscope and Sedgwick-Rafter cell of 1 mL capacity was used for counting the individuals. One mL of sample was transferred in Sedgwick-Rafter count cell and covered by cover slip, avoiding any kind of air bubble. Sedgwick rafter counting cell was placed under microscope after settling down of plankton for 10-15 minutes. The plankton were counted by moving the cell horizontally and the identification was done to the lowest recognizable level with the help of keys by APHA (2005), Ward & Whipple (1992), Wetzel (1979), Needham & Needham (1980) and Bellinger & Sigee 2010.

STATISTICAL ANALYSIS

The statistical analysis of the data was done using data analysis tool pack available in the MS Excel in PC. Shannon-Wiener Diversity Index, Principal Component Analysis (PCA) and Canonical Component Analysis (CCA) was done with the help of PAST version (2.1) software.

RESULTS & DISCUSSION

Phytoplankton

Phytoplankton community directly provides food for zooplankton, macroinvertebrartes and fishes of aquatic ecosystem. A total of 35 phytoplankton genera belonging to three major classes, Bacillariophyceae (21 genera), Chlorophyceae (9 genera) and Cyanophyceae (5 genera) were recorded from the Mandakini river after major flash flood (Table 1). Flash flood can deplete phytoplankton population, however it recovers soon after some months due to their short life cycle. Flood events result into increased water velocity, decreased food supply, increased sediment load and physical damage to aquatic organisms consequently affecting abundance and composition of aquatic organisms (Sagar 1986).

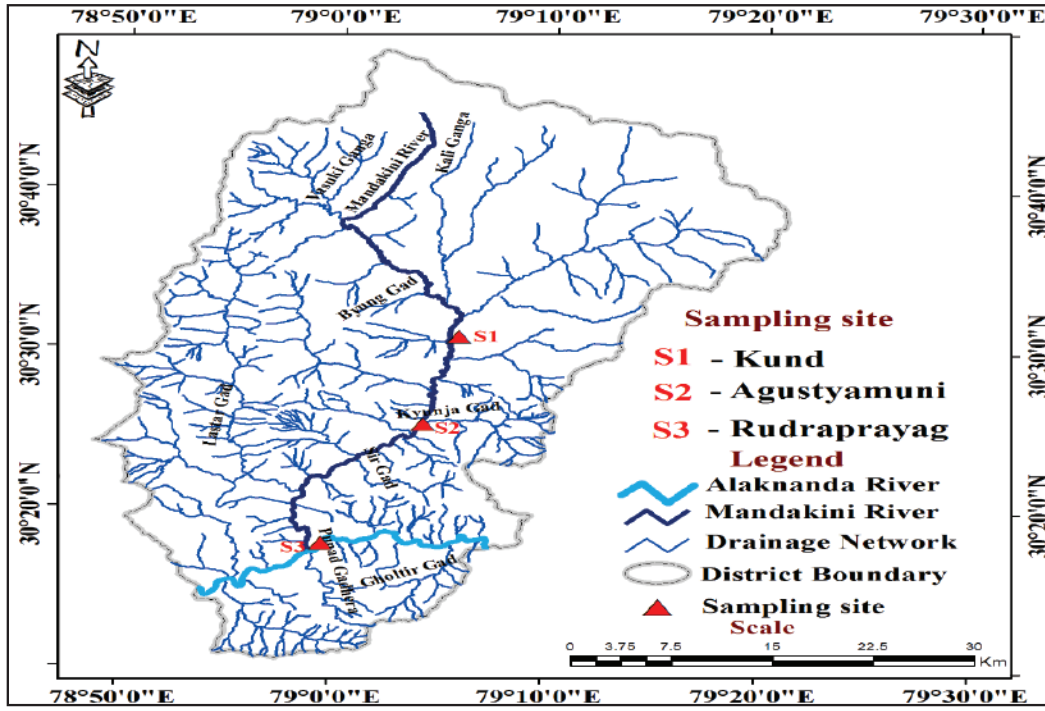

Fig. 1: Location of sampling sites in the drainage map of Mandakini river.

The average density of phytoplankton of the study area was calculated maximum (317.12±7.75 cells L^{-1}) in winter, moderate (271.02±5.54 cells L^{-1}) in summer and minimum (144.03±2.75 cells L^{-1}) in monsoon season (Fig. 2). Similar trend of seasonal fluctuation in plankton density was also observed in Ganga river and its tributaries in Garhwal Himalaya (Negi et al. 2012); river Mahanadi, Odisha (Panigrahi & Patra 2013) and Baldi river (Sharma et al. 2016). High plankton diversity and abundance in winter season was also reported by Kumar (2014) from glacial fed Goriganga river of Kumaun Himalaya, Uttarakhand. Highest plankton density during winter was attributed to the favourable environmental conditions like low water temperature, low water velocity, high transparency, availability of sufficient nutrients and most stable substratum. In monsoon season, the phytoplankton density and diversity were lowest due to high water velocity, high turbidity and most unstable substrate conditions during the period. These factors affect the growth of phytoplankton adversely in the monsoon season which was also reported from river Mahanadi by Panigrahi & Patra (2013).

The density of phytoplankton was in the order of Bacillariophyceae (diatoms) > Chlorophyceae (green algae) > Cyanophyceae (blue-green algae). A total of 21 genera of Class Bacillariophyceae were reported from the study area which included *Nitzschia, Navicula, Cymbella, Amphora, Fragilaria, Diatoma, Pinnularia, Gomphonema, Rhopalodia, Tabellaria, Cocconeis, Synedra, Encyonema, Fragilariforma, Achnanthidium, Surrirella, Gyrosigma, Cyclotella, Caloneis, Rhoicosphenia* and *Denticula.* Bacillariophyceae (83%) was a dominant class of phytoplankton and constituted a major component of producers in the study area and most resistant to water velocity. This class was also found dominant in the river Yeúilirmak, Turkey (Soylu & Gönülol 2003); Imo river, Nigeria (Ogbuagu & Ayoade 2012); Kenti River Republic of Karelia (Chekryzheva 2014) and Baldi stream, Doon valley (Sharma et al. 2016).

Chlorophyceae and Cyanophyceae were found very less in number in the Mandakini river. Their contribution was 9% and 8% respectively in the total phytoplankton population. Nine genera of Chlorophyceae (green algae) including *Ulothtrix, Hydrodictyon, Spirogyra, Chlorococcus, Cosmarium, Closterium, Desmidium, Stigeoclonium* and *Micrasterias* were recorded from the Mandakini river (Table 1). Seasonal density of Chlorophyceae was calculated to be highest (18.50±8.75 cells L^{-1}) at S_2 in summer and lowest (5.63±7.70 cells L^{-1}) at S_3 in the month of monsoon (Fig. 2). Maximum density of green algae (Chlorophyceae) in summer may be due to favourable water temperature and light intensity subsequently increasing photosynthetic activity. A total of 5 genera of Cyanophyceae (*Phormidium, Oscillatoria, Anabaena, Sprilium* and *Merismopedia*) were recorded from the study area. The average density of blue-green algae was computed maximum (25.34±8.92 cells L^{-1}) at S_3 in winter season and minimum (9.92±10.81 cells L^{-1}) at S_1 in monsoon season (Fig. 2). Hassan et al. (2004) also found a clear seasonal variation in phytoplankton communities in the ecosystem of Shatt Al-Hilla, Iraq. Maximum density of Cyanophyceae depends upon the concentration of phosphates and nitrates (Smith 1983). Phosphates and

Table 1: Plankton diversity of Mandakini river of Garhwal Himalaya (Uttarakhand).

S. No.	Types of Planktons	Name of Groups	Name of Genera	% Composition
		Bacillariophyceae	*Nitzschia, Navicula, Cymbella, Amphora, Fragilaria, Diatoma, Pinnularia, Gomphonema, Rhopalodia, Tabilaria, Cocconeis, Synedra, Encyonema, Fragilariforma, Achnanthidium, Surrirella, Gyrosigma, Cyclotella, Caloneis, Rhoicosphenia, Denticulla*	83%
1	Phytoplankton			
		Chlorophyceae	*Ulothtrix, Hydrodictyon, Spirogyra, Chlorococcus, Cosmarium, Closterium, Desmidium, Stigeoclonium Micrasterias*	9%
		Cyanophyceae	*Phormidium, Oscillatoria, Anabaena, Spirulina, Merismopedia*	8%
2	Zooplankton	Protozoa	*Tetrahymina, Loxodes*	22%
		Rotifera	*Notholca, Asplanchna, Branchionus, Dipleuchlanis propatula, Lepidella*	74%
		Copepoda	*Cyclops*	4%

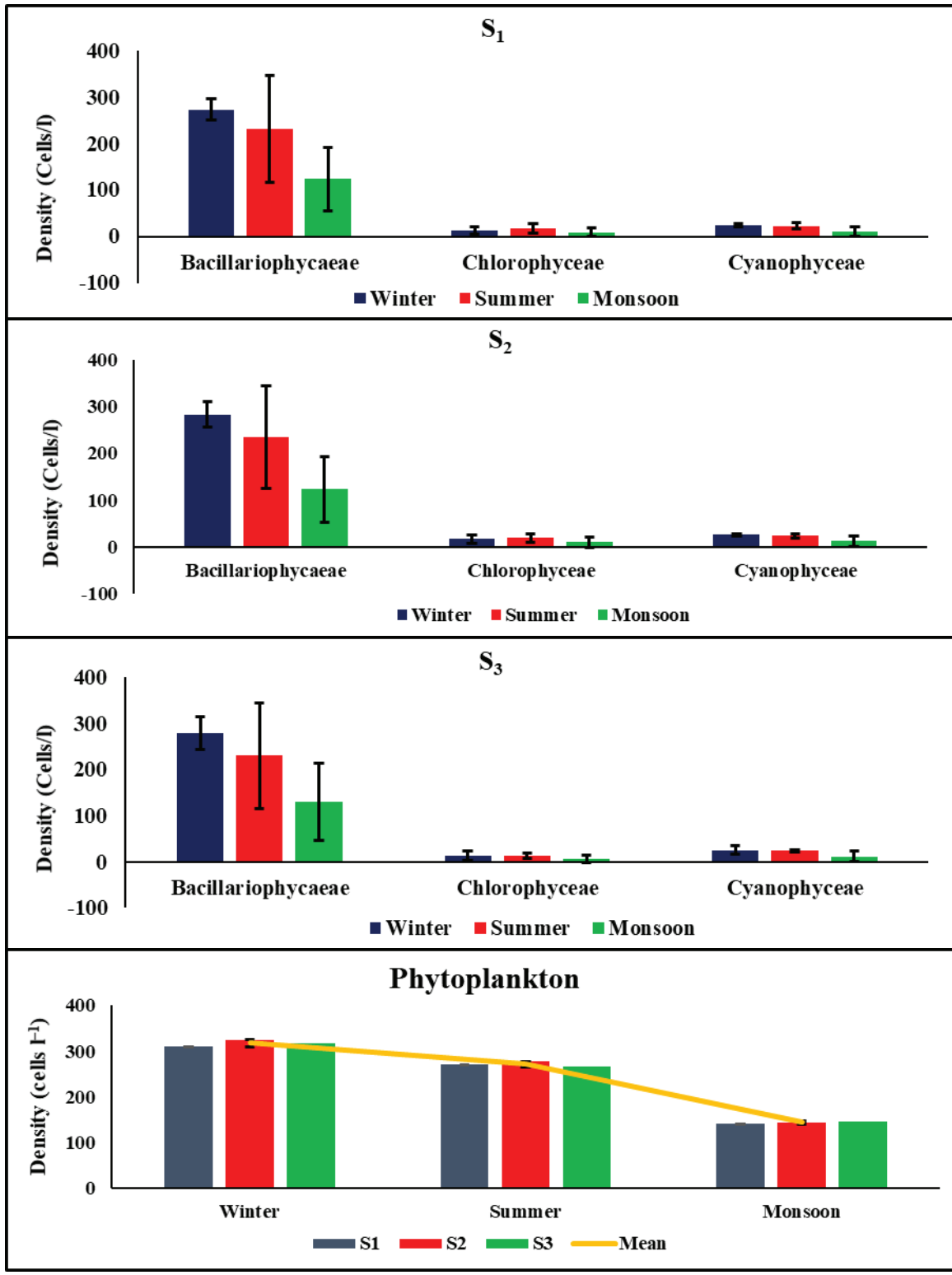

Fig. 2: Seasonal variations in the composition of phytoplankton (cells.L^{-1}) at three sampling sites (S_1, S_2 and S_3) in the Mandakini river of Garhwal Himalaya.

Table 2: Monthly variations in Shannon-Wiener Diversity Index ($\overline{H}$) computed for phytoplankton and zooplankton of the Mandakini river.

Months	Shannon-Weiner Diversity Index					
	Phytoplankton			Zooplankton		
	S_1	S_2	S_3	S_1	S_2	S_3
January	2.57	2.56	2.54	-	-	0.69
February	2.47	2.61	2.49	0.66	0.69	1.56
March	2.35	2.45	2.38	-	-	-
April	2.26	2.44	2.27	-	1.09	-
May	2.49	2.34	2.34	0.64	0.61	0.66
June	2.42	2.39	2.49	-	-	-
July	1.79	1.87	1.78	-	-	-
August	2.14	2.29	2.15	-	-	-
September	2.37	2.19	2.41	-	-	-
October	2.37	2.30	2.26	-	0.66	-
November	2.41	2.47	2.23	1.08	0.50	-
December	2.34	2.34	2.30	-	-	-

nitrates were also found to influence the phytoplankton density and diversity in the present study as shown by CCA.

Shannon-Wiener diversity index of phytoplankton ranged from 1.79 at S_3 in July to 2.61 at S_2 in the month of February in the Mandakini river (Table 2). Water velocity was the most important factor affecting the phytoplankton density and diversity mainly filamentous green and blue-green algae. The water velocity of the lotic body affecting filamentous phytoplankton was also observed in the river Alaknanda by Gusain (1994). Number of phytoplankton decrease due to turbulence and unstable substrata caused by water current was also reported by Chandler (1937) and Wetzel (1975).

Principal Component Analysis (PCA) was done for site-wise representation of various phytoplankton taxa of the Mandakini river. A total of 35 genera of phytoplankton among 3 sampling sites were selected for PCA. PC1 explained 72.004% of the variation in the parameters with eigenvalue of 2946.7. PC1 was mainly represented by phytoplankton genera like *Cocconeis*, *Navicula, Amphora*, *Nitzschia*, *Spirogyra, Ulothrix* and *Tabellaria*. PC2 explained 27.996% of the variation in the parameters with eigenvalue of 1145.7. PC2 mainly represented by genera like *Cymbella*, *Achnanthidium, Phormidium, Synedra* and *Fragilaria* (Fig. 3). Most of the phytoplankton taxa clustered in the centre of the plot indicating their common occurrence at all the three sampling sites. However, some of the taxa like *Amphora* and *Achnanthidium* prevailed at S_1, *Nistzschia*, *Tabellaria*, *Cocconeis*, *Spirogyra* and *Ulothrix* were abundant at S_2 while *Cymbella*, *Navicula*, *Synedra*, *Fragilaria* and *Phormidium* were prevalent at S_3. Statistically, there was no significant difference in the abundance of various taxa among all the sampling sites, hence the sampling site fall apart in the plot.

Canonical Correspondence Analysis (CCA) was applied to examine the effect of physico-chemical parameters on phytoplankton density among sampling sites. A total of 13 physico-chemical parameters and 12 dominant genera of phytoplankton were selected for CCA. Axis 1 explained 75.17% of the variation in the periphyton abundance with eigenvalue of 0.0047183 and Axis 2 explained 24.83% of the variation in the periphyton abundance with eigenvalue of 0.0015583. Total alkalinity, water temperature, water velocity, nitrate, turbidity, dissolved oxygen, free carbon dioxide and phosphate act as the most important parameters affecting plankton density and diversity. However, conductivity, total hardness, transparency and pH were of secondary importance. Nowrouzi & Valavi (2011) also found environmental factors affecting phytoplankton abundance and diversity in Kaftar Lake. Total alkalinity and water temperature were important parameters and favoured the growth of *Synedra* and *Fragilaria* in the present study. Water velocity favoured the taxa like *Amphora, Achnanthidium* and *Navicula*. *Cymbella, Synedra* and *Phormidium* showed positive correlation with air temperature, turbidity and free carbon dioxide. Conductivity, pH, phosphate and nitrate favoured the growth of *Ulothrix, Cocconeis* and *Nitzschia. Spirogyra* and *Tabellaria* were well supported by the pa-

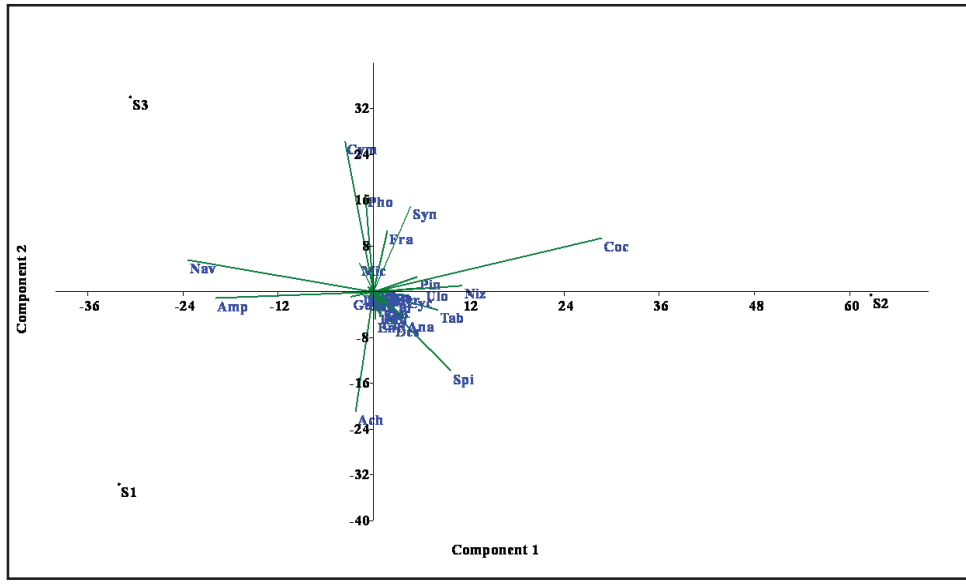

Fig. 3: PCA biplot depicting phytoplankton diversity among sampling sites (S_1, S_2 and S_3) in the Mandakin river of Uttarakhand. **Acronyms:** Niz-*Nitzschia*, Nav-*Navicula,* Cym-*Cymbella,* Amp-*Amphora*, Syn-*Synedra*, Ach-*Achnanthidium*, Tab-*Tabellaria*, Coc-*Cocconeis*, Pin-*Pinnularia*, Den-*Denticula*, Rho-*Rhopalodia,* Fra-*Fragilaria*, Cal-*Caloneis*, Dia-*Diatoma,* Gom-*Gomphonema,* Gyr-*Gyrosigma*, Enc-*Encyonema*, Frg-*Fragilariforma,* Sur-*Surirella*, Rho-*Rhoicosphenia*, Cyc-*Cyclotella,* Clo-*Closterium*, Ulo-*Ulothrix*, Sti-*Stigeoclonium*, Hyd-*Hydrodictyon*, Chl-*Chlorococcus*, Spi-*Spirogyra*, Mic-*Micrasterias*, Des-*Desmidium*, Cos-*Cosmarium*, Pho-*Phormidium*, Osc-*Oscilatoria*, Ana-*Anabaena*, Mer-*Merismapodia*, Spr-*Sprilium.*

rameters transparency and dissolved oxygen (Fig. 4).

Zooplankton

Zooplankton diversity was observed very low after major flash flood and none of the species could be collected in the first year of the study. However, 8 genera belonging to three major groups Protozoa (2 genera), Rotifera (5 genera) and Copepoda (1 genus) were found during the second year of observations. The group Protozoa was represented by two genera, *Tetrahymina* and *Loxodes.* The group Rotifera was represented by *Notholca*, *Asplanchna*, *Brachionus*, *Dipleuchlanis* and *Lepidella.* However, group Copepoda was represented by only one genus *Cyclops*. Rotifera (74%) dominated among zooplankton communities followed by Protozoa (22%) and Copepoda (4%) (Table 1). The composition and diversity of zooplankton provides information about the characteristics and quality of a water body. The nature of flood changes the aquatic biodiversity. Torrential flood destroys lotic habitats and leads to the decrease in biodiversity which was also reported in Vistula River by Napiórkowski & Naspiórkowska (2014).

Rotifera showed the maximum abundance followed by Protozoa and Copepoda in the Mandakini river during the present study. Rotifera to be abundant group of zooplankton in the river ecosystem was also noticed by many researchers in Parnapanema river, Brazil (Sampaio et al. 2002); Prairie river (Thorp & Mantovani 2005); Hinval freshwater stream at Shivpuri (Negi & Negi 2010); Haraz river, Iran (Jafari et al. 2011); Alcantara river, Italy (Rodrigues et al. 2013); Sakarya River Basin, Turkey (Dorak 2013); Cauvery river and Kapila river, Mysore (Sebastian & Yamakanamardi 2014). Rotifers can adapt themselves to adverse environmental conditions as they have a wide range of tolerance to many environmental changes. They are also used as good indicators of water quality. It was also observed by Marneffe et al. (1996), Napiorkowski (2009), Napiorkowski & Napiorkowska (2014).

Shannon-Wiener diversity index calculated for zooplankton ranged from 0.50 to 1.56 being highest in February at S_3 and lowest in November at S_2 (Table 2). The index increases slowly and reached its maximum in winter month indicating the readmission of zooplankton population after the monsoon flood. Changes in zooplankton abundance, diversity and community composition indicate the change or disturbance of environment. High diversity index indicates greater species richness and well-balanced community, while low diversity index indicates stress and impact.

13 physico-chemical parameters and 8 genera of zooplankton were selected for CCA. Axis 1 explained 82.99% of the variation in the zooplankton abundance with eigenvalue of 0.42316 and Axis 2 explained 17.01% of the variation in the zooplankton abundance with eigenvalue of 0.08673 (Fig. 5). Factors like transparency, dissolved oxygen, free carbon dioxide and turbidity were of primary importance

in affecting zoolankton abundance and diversity. However, pH, phosphate, total hardness, conductivity, velocity and nitrate were of secondary importance. Transparency and dissolved oxygen act as the most important parameters affecting the abundance of *Tetrahymina* and *Notholca. Dipleuchlanis propatula*, *Brachionus* and *Loxodes* showed a positive correlation with free carbon dioxide, turbidity, temperature and total alkalinity.

CONCLUSION

Present study concluded that plankton communities recovers soon due to the cleansing mechanism of flash flood and its density and diversity reaches maximum in winter season. The highest diversity of plankton in winter is attributed to most stable substrate conditions and favourable water quality indicating the good recovery of the ecosystem. Among phytoplankton, class Bacillariophyceae showed the maxi-

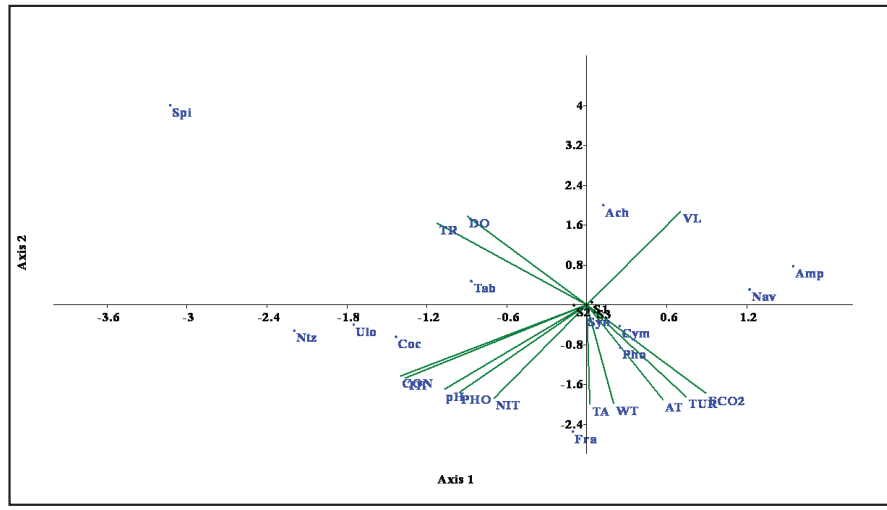

Fig. 4: CCA plot showing the effect of physico-chemical parameters on the dominant phytoplankton genera in the Mandakini river of Uttarakhand. Acronyms: AT- Air Temperature, WT-Water Temperature, TR-Transparency, VL-Velocity, TA-Total Alkalinity, TH-Total Hardness, DO- Dissolved Oxygen, FCO_2-Free Carbon Dioxide, pH-pH, PHO-Phosphates, NIT-Nitrates, CON-Conductivity, TUR-Turbidity, Niz-*Nitzschia*, Nav-*Navicula,* Cym-*Cymbella,* Amp-*Amphora*, Syn-*Synedra*, Ach-*Achnanthidium*, Tab-*Tabellaria*, Coc-*Cocconeis*, Fra-*Fragilaria*, Ulo-*Ulothrix*, Spi-*Spirogyra*, Pho-*Phormidium*.

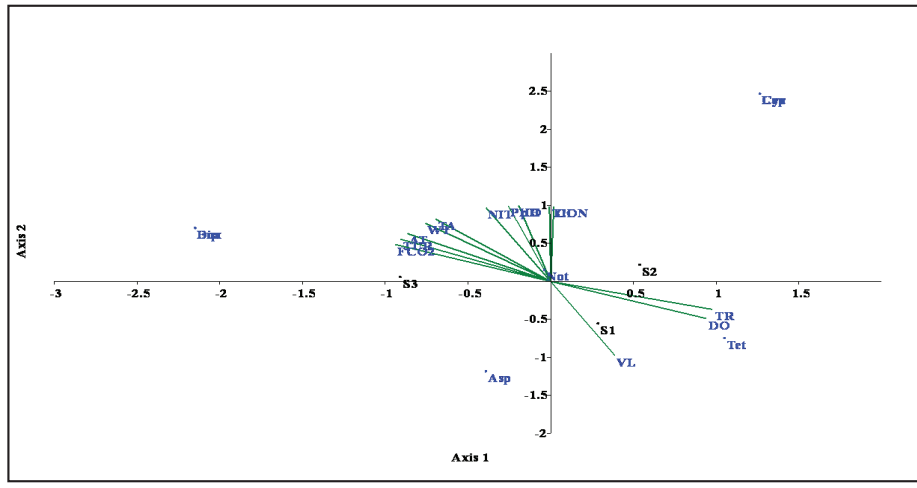

Fig. 5: CCA plot showing the effect of physico-chemical parameters on zooplankton diversity of the Mandakini river of Uttarakhand. Acronyms: AT-Air Temperature, WT-Water Temperature, TR-Transparency, VL-Velocity, TA-Total Alkalinity, TH-Total Hardness, DO-Dissolved Oxygen, FCO_2-Free Carbon Dioxide, pH-pH, PHO-Phosphate, NIT-Nitrate, CON-Conductivity, TUR-Turbidity, Tet-*Tetrahymina*, Lox-*Loxodes*, Not-*Notholca*, Asp-*Asplanchna*, Bra-*Brachionus*, Dip-*Dipleuchlanis*, Lep-*Lepidella*, Cyc-*Cyclops*.

mum abundance (83%) followed by Chlorophyceae (9%) and Cyanophyceae (8%) while Group Rotifera showed the maximum abundance (74%) followed by Protozoa (22%) and Copepoda (4%) among zooplankton in the Mandakini river. Total alkalinity, water temperature, transparency, velocity, dissolved oxygen, free carbon dioxide, turbidity, phosphate and nitrate were important physico-chemical factors regulating plankton diversity in the Mandakini river.

ACKNOWLEDGEMENT

The author (Gunjan Goswami) is thankful to University Grants Commission, New Delhi for financial support in the form of BSR fellowship during the study.

REFERENCES

APHA 2005. Standard Methods for Examination of Water and Wastewater (21st ed.). American Public Health Association, Washington, D.C., pp. 1134.

Bellinger, E.G. and Sigee, D.C. (eds.) 2010. Freshwater Algae Identification and Use as Bioindicator. John Wiley & Sons, Ltd, Publication, pp. 1-271.

Chandler, D.C. 1937. Fate of typical lake plankton in streams. Ecological Monograph 7: 445-479.

Chekryzheva, T.A. 2014. Anthropogenic changes in phytoplankton in lakes of the Kenti river system (Republic of Karelia). Water Resource, 41: 431-438.

Death, R., Fuller, I. and Macklin, M. 2015. Resetting the river template: The potential for climate-related extreme floods to transform river geomorphology and ecology. Freshwater Biology, 60(12): 2477-2496.

Dorak, Z. 2013. Zooplankton abundance in the lower Sakarya river basin (Turkey): Impact of environmental variables. Journal of Black Sea/ Mediterranean Environment, 19(1): 1-22.

Gusain, M. 1994. River Alaknanda. In: Nautiyal, P. (ed.) Mahseer the Game Fish: Natural History, Status and Conservation Practices in India and Nepal. Akashdeep Printers, New Delhi, pp. 123-135.

Hassan, F.M., Kathim, F.N. and Hussein, H.F. 2004. Effect of chemical and physical properties of river water in Shatt Al-Hilla on phytoplankton communities. E. Journal of Chemistry, 5: 323-330.

Jafari, N., Nabavi, S.M. and Akhavan, M. 2011. Ecological investigation of zooplankton abundance in the river Haraz, northeast Iran: Impact of environmental variable. Archives of Biological Science, 63(3): 785-798.

Kumar, A. 2014. Studies on diversity and abundance of phytoplankton in Glacial fed mountainous Goriganga river of Kumaun Himalaya, Uttarakhand. International Research Journal of Biological Sciences, 3(9): 65-78.

Marneffe, Y., Descv, J.P. and Thome, J.P. 1996. The zooplankton of the lower river Meuse, Belgium: seasonal changes and impacts of industrial and municipal discharges. Hydrobiologia, 319: 1-13.

Morabito, G., Mazzocchi, M.G., Salmaso, N., Zingone, A., Bergami, C., Flaim,G., Accoroni, S., Basset, A., Bastianine, M., Belmonte, G., Aubry, F.B., Bertani, I., Bresciani, M., Buzzi, F., Cabrini, M., Camatti, E., Caroppo, C., Cataletto, B., Castellano, M., Negro, P.D., Olazabal, A.D., Capua, I.D., Elia, A. C., Fornasaro, D., Giallain, M., Grilli, F., Leoni, B., Lipizer, M., Longobardi, L., Ludovisi, A., Luglie, A., Manca, M., Margirtta, F., Mariani, M.A., Marini, M., Marzocchi, M., Obertegger, U., Oggioni, A., Padedda, B. M., Pansera, M., Piscia, R., Povero, P., Pulina, S., Romagnoli, T., Rosati, I., Rossetti, G., Rubino, F., Sarno, D., Satta, C.T., Sechi, N., Stanca, E., Tirelli, V., Totti, C., Pugnetti, A. 2018. Plankton dynamics across the freshwater, transitional and marine research sites of the LTER-Italy Network. Patterns, fluctuations, drivers. Science of the Total Environment, 627: 373-387.

Muntean, H. and Alexoaie, L. 2013. Flood effects on the phytoplankton diversity of Bega river (Banat, Romania). Transylvanian Review of Systematical and Ecological Research, 15: 207-220.

Napiórkowski, P. and Napiórkowska T. 2014. The impact of catastrophic flooding on zooplankton. Polish Journal of Environmental Studies, 23(2): 409-417.

Napiórkowski, P. 2009. Influence of hydrological condition on zooplankton of oxbow lakes (old river beds) of the lower Vistula river in the city of Toruó Limnology, 4: 55-67.

Needham, J.G. and Needham, P.R. (eds.) 1980. A Guide to the Study of Freshwater Biology (5th Edition). Holden-day Inc., San Francisco.

Negi, R.K. and Negi, T. 2010. Diversity of zooplankton in the Hinval freshwater stream at Shivpuri (Garhwal region) Uttrakhand. Journal of Environment and Biosciences, 24 (2): 167-169.

Negi, R.K., Joshi P.C. and Negi, T. 2012. Seasonal variation and species composition of phytoplankton in Ganga river and its tributary at Garhwal region, Uttarakhand, India. International Journal of Environment and Ecology, 2(2): 24-30.

Nowrouzi, S. and Valavi, H. 2011. Effects of environmental factors on phytoplankton abundance and diversity in Kaftar Lake. Journal of Fisheries and Aquatic Science, 6(2): 130-140.

Ogbuagu, D.H. and Ayoade, A.A. 2012. Seasonal dynamics in plankton abundance and diversity of a freshwater body in Etche, Nigeria. Environment and Natural Resource Research, 2: 48-59.

Panigrahi, S. and Patra, A.K. 2013. Studies of Seasonal variation in phytoplankton diversity of river Mahanadi, Cuttack, Odisha. Indian Journal of Science Research, 4(2): 211-217.

Rodrígues, L.P., Granata, A., Guglielmo, L., Minutoli, R., Zagami, G. and Brugnano, C. 2013. Rotifer community structure in the Alcantara river (Sicily, Italy), using different mesh size nets: relation to environmental factors. Annales de Limnologie - International Journal of Limnology, 49: 287-300.

Sagar, P.M. 1986. The effects of floods on the invertebrate fauna of a large, unstable braided river. New Zealand Journal of Marine and Freshwater Research, 20: 37-46.

Sampaio, E.V., Rocha, O., Matsumura-Tundisi, T. and Tundisi, J.G. 2002. Composition and abundance of zooplankton in the limnetic zone of seven reservoirs of the Paranapanema river Brazil. Brazilian Journal of Biology, 62(3): 525-545.

Sebastian, K.J. and Yamakanamardi, S.M. 2014. Seasonal variations in the abundance of zooplankton groups in relation with physico-chemical parameters in three lotic ecosystems of Mysore. Acta Biologica Indica, 3(1): 499-509.

Sharma, R.C., Singh, N. and Chauhan, A. 2016. The influence of physico-chemical parameters on phytoplankton distribution in a head water stream of Garhwal Himalayas: A case study. Egyptian Journal of Aquatic Research, 42: 11-21.

Smith, V.H. 1983. Low nitrogen to phosphorus ratio favor dominance by blue-green algae in lake phytoplankton. Science, 221: 669-670.

Soylu, E.N. and Gönülol, A. 2003. Phytoplankton and seasonal variations of the River Yeúilırmak, Amasya, Turkey. Turkish Journal of Fisheries and Aquatic Sciences, 3: 17-24.

Thorp, J.H and Mantovani, S. 2005. Zooplankton of turbid and hydrologically dynamic prairie rivers. Freshwater Biology, 50: 1474-1491.

Ward, H.B. and Whipple, G.C. 1992. Freshwater Biology (W.T. Edmondson, 2nd ed.). John Willey and Sons, Inc., New York.

Wetzel, R.G. 1975. Primary production. In: Whitton, B.A. (ed.) River Ecology. Cambridge, Cambridge University Press, pp 230-247.

Wetzel, R.L. (ed.) 1979. Methods and Measurements of Periphyton Communities: A Review. ASTM Special Technical Publication, pp 1-183.

Nature Environment and Pollution Technology
An International Quarterly Scientific Journal

p-ISSN: 0972-6268
e-ISSN: 2395-3454

Vol. 18 | No. 4 | pp. 1185-1192 | 2019

Review Research Paper | Open Access

Performance Studies on Non-Edible Oil as IC Engine Fuels: A Review

Keerthan Krishna*, Krishna Murthy and G.T. Mahesha*†**

*Department of Aeronautical and Automobile Engineering, Manipal Institute of Technology, MAHE, Manipal-576104, Karnataka, India

**Department of Mechanical and Manufacturing Engineering, Manipal Institute of Technology, MAHE, Manipal-576104, Karnataka, India

†Corresponding author: G.T. Mahesha

Nat. Env. & Poll. Tech.
Website: www.neptjournal.com

Received: 13-03-2019
Accepted: 25-04-2019

Key Words:
Biodeisel
Non-edible oils
Brake specific fuel
Brake thermal efficiency
Carbon monoxide
Hydrocarbons
Oxides of nitrogen

ABSTRACT

Petroleum fuels have served mankind successfully for more than a century mainly for mobility in the form of vehicles, power generation and industrial activities. As crude oil is a fossil fuel, we cannot rely upon it forever. Transportation is the backbone for the mobility for which fuel is the basic necessity. As the petroleum products are at the verge of their extinction, finding alternative fuels is the need of the time. Alternative fuels are obtained from seeds of many edible and non-edible oil plants. Edible oils due to their consumption for cooking purposes, may not be advisable to use for commercial activity, however, non-edible oils can be attempted as a source to serve the purpose as engine fuels. Non-edible oils can be blended with the petroleum products and can be used mainly in the diesel engine with slight or no modifications. The performance studies are being carried out by various researchers all over the world using many such refined oils as engine fuels. This review paper attempts to collate the published research literature. The focus in this review paper is on analysis of availability, engine performance and pollution characteristics when oils such as *Jatropha curcas*, *Calophyllum inophyllum*, Mahua and *Pongamia pinnata* are used.

INTRODUCTION

As the world population is growing at a fast rate, the need for mobility is increasing exponentially. In today's generation even though there are many ways of transportation, the basic need for all these remains the same which happens to be the fuel. The basic fuels considered are mainly the petroleum products like gasoline, diesel, etc. serve the purpose satisfactorily. It has been predicted that the availability of these fuels is limited, and hence we cannot depend on these fuels longer. These fuels are non-renewable in nature, hence cannot be reused (Kalghatgi 2018).

Hence, there is need to find alternative fuels mainly for the purpose of transportation and power generation. At this increasing rate of fuel utilization, it is proposed that biodiesel will make an impressive commitment to the future vitality requests of the human population. Biodiesel can be acquired from edible and from non-edible oil sources (Balat 2011, Jain et al. 2018). Considering the growth in population and the expected nourishment necessity, the biodiesels from non-edible oil sources are being viewed as a substantially more secure and alternative energy source. The feedstock used for non-edible oil sources is less expensive than that of consumable oil sources, thus helping to reduce the cost per unit quantity.

Many alternative modes of transportation like electric vehicles (Novoa & Brouwer 2018, Zhou et al. 2018, Safari 2018) hybrid vehicles (Novoa & Brouwer, 2018, Claude et al. 2017, Sharaf 2018, Iwata & Matsumoto 2016, Strehler et al. 2017) solar powered cells (Novoa & Brouwer 2018, Strehler 2017, Maruthi Prasad & Krishnamoorthy 2018) and many more (Verhelst et al. 2019) are also emerging as a solution to depleting fossil fuels. However, these due to certain limitations like huge size, initial investment, maintenance cost etc. have to be still more researched and innovated. Hence, the most feasible fuel category would be the alternate fuels to serve the purpose (Kumar et al. 2018). Many alternative fuels like vegetable oils and non-edible oils have been studied by researchers and out of which the non-edible oils like *Calophyllum inophyllum*, *Jatropha curcas*, Mahua, *Pongamia pinnata,* etc. (Aniya et al. 2015, Rizwanul Fattah 2014) were found to be best in the group. Therefore, most eligible candidate for compression ignition engine application to blend with the normal diesel is the biodiesel. Biodiesel is produced by accessible assets like vegetable oils, animal fat and waste cooking oils through a synthetic procedure known as transesterification. Biodiesel has several advantages over conventional fossil fuels like smoother engine operation by enhancing better lubricity and better combustion characteristics. Biodiesel can decrease ozone-depleting greenhouse gas emission discharge to the atmosphere by bringing down CO, HC and partic-

ulate matters (Mofijur et al. 2015). According to many researchers, biodiesel obtained from animal fat is less expensive than obtained from edible/non-edible oils because animal squander is significantly produced in large quantities in slaughter houses and other meat preparing ventures. Moreover, recuperation of oils or fats from waste animal fat is less expensive than the cultivation and production of oils from edible/nonedible base. Biodiesel from animal fat has higher calorific value (Vinukumar et al. 2018) and Cetane number because of higher fatty acids. It is also possible to use biodiesel from animal fat in boilers for heating or it can be blended with other low grade fuels, to enhance some fuel attributes (Fadhil et al. 2017).

The biodiesel from non-edible oil sources have greater advantages (Hosseinzadeh-bandbafha et al. 2018) when used in IC engines. These biodiesels as studied by many researchers (Suresh et al. 2018) are either used directly or blended with conventional diesel and then used in the engine with minor or no modifications. Biodiesel oils obtained from non-edible oils are environment-friendly and non-toxic (Fazal et al. 2018) compared to conventional diesel fuel. The blend improves the mechanical efficiency of engines and emissions of sulphur dioxide.

Alternate Non-edible Oil Resources

The alternate fuels like non-edible oil resources are available around the globe in various regions. In order to overcome the present energy crisis, the available alternative fuel resources must be used effectively. Researchers around the globe are working on different alternative fuel resources and studies are going on to explore their adaptability. In this paper, the attention has been given to summarise the alternative oil resources like *Jatropha curcas*, *Calophyllum inophyllum*, Mahua and *Pongamia pinnata* and their performance studies when used as engine fuels.

Table 1 presents the basic properties of the non-edible alternative fuels considered for the present analysis.

As studied by many researchers it was found that *Jatropha curcas* contains about 20-60% of oil (Balat & Balat 2010, Negm et al. 2018, Christopher et al. 2014, Kumar et al. 2017), *Calophyllum inophyllum* about 65-75% of oil (Nanthagopal et al. 2017, Kartika 2018) Mahua about 35-50% of oil (Ashraful 201, Dhanavath et al. 2017), and *Pongamia pinnata* about 25-40% of oil by weight (Atabani 2013, Kashyap et al. 2018). Since the yield for *Calophyllum* is high, it is obvious to have at low cost which becomes an added advantage. The density of oil when observed at an average temperature of 40°C for different oils it is observed that *Jatropha* is in the range of 880-940 kg/m^3, *Calophyllum* was in the range of 888-910 kg/m^3, Mahua in the range of 816-960 kg/m^3 and *Pongamia* about 876-928 kg/m^3. From the results published, it is observed that *Jatropha* has the highest density range. The viscosity which influences the injection characteristics is minimum for *Jatropha*. The viscosity of *Calophyllum* is in the range of 4-5.3 mm^2/s, for Mahua about 2.4-5.8 mm^2/s and highest for *Pongamia* in the range of 2.7-9.6 mm^2/s. The Cetane number found from the *Jatropha curcas* oil was around 33.7-57.1, for *Calophyllum* around 57.3, for Mahua around 43.5-52 and for that of *Pongamia* oil around 42-67, whereas the diesel engines operate well with a Cetane number from 48-50 (Hosseinzadeh-bandbafha 2018). The Cetane number represents the combustion characteristics of compression ignition engine fuels. As the Cetane number increases the fuel burns faster and completely thus producing lesser harmful emissions and knocking tendency. Hence, it is preferred to have a higher Cetane number for the future alternative fuels for IC engines. When Cetane number is considered *Calophyllum* having 57.3 is highest as compared to other fuels. Thus, *Calophyllum* is a better fuel when Cetane number is compared to diesel as far as the ignition and burning characteristics are considered.

Performance Studies of Different Non-edible Oils

The results of performance studies and experimental observations by different researchers on different types of non-edible oil blend with diesel and in different proportions has been presented in Table 2.

***Jatropha curcas*:** The study (Layek 2016), using *Jatropha* as a blended fuel with diesel at different proportion of *Jatropha*, it was found that the heating value of the blend went up from 37.83 to 42.05 MJ/kg. The Brake thermal efficiency (BTE) was reduced, specific fuel consumption and the exhaust gas temperature was increased. Researchers

Table 1: Alternate non-edible oil resources.

Alternative fuel	Oil content (wt.%)	Blend density at 40°C (kg/m^3)	Blend viscosity at 40°C (mm^2/s)	Cetane number	Reference
Jatropha curcas	20-60	880-940	2.45-5.8	33.7-57.1	(Balat & Balat 2010)(Negm 2018) (Christopher 2014)(P. Kumar 2017)(Kartika 2018)(Ashraful 2014)(Dhanavath 2017) (Atabani 2013)(Kashyap 2018)
Calophyllum inophyllum	65-75	888.6-910	4-5.3	57.3	
Mahua	35-50	816-960	2.46-5.8	43.5-52	
Pongamia pinnata	25-40	876-928	2.78-9.60	42-67	

Table 2: Performance studies of different non-edible oils.

Alternative fuel	Blends studied	Observations	Operating conditions	Reference
Jatropha curcas	2.6% Jatropha and 97.4% diesel by volume.	Heating value: 37.83- 42.05 MJ/kg lower BTE, higher SFC and exhaust gas temperature.	Higher injection pressures, and preheating	(Layek 2016) (Patil & Arakerimath 2012) (Chauhan et al. 2013) (Foidl 1996) (Ramesh et al. 2006) (Mofijur et al. 2013) (Berchmans & Hirata 2008) (Chauhan 2013) (Chauhan 2013) (EL- Seesy et al. 2018) (Yunus et al. 2013)
	JBD20 (20% Jatropha oil+ 80% diesel), JBD40 (30% Jatropha oil + 70% diesel), JBD60 (40% Karanja oil + 60% diesel) (Patil & Arakerimath 2012) at 2000 rpm.	25-30% mechanical efficiency at 20% load, 40-45% mechanical efficiency at 40% load, 50-55% mechanical efficiency at 60% load, SFC varied from 0.0001-0.001kg/s for varying load from 20 to 60%, 4.2kW power.	Preheating of blend using exhaust gas.	
	JB10 (10% Jatropha + 90% diesel).	BP increased with engine speed, Higher BSFC than Diesel.	Better engine cooling	
Calophyllum inophyllum	B10, B20, B30, and B50 of biodiesel blends (How 2018)	Reduced calorific value and increased viscosity, reduction in BSEC, the increase in BTE. Decreased combustion pressure.	Increasing biodiesel concentration	(How 2018) (Ong 2014) (Rizwanul Fattah 2014) (Dwivedi et al. 2011) (Praveen et al. 2018) (Nanthagopal 2017) (Ashok 2019) (Nanthagopal et al. 2018) (Ashok 2017)
	B10, B20, B30, and B50 (Ong 2014)	Relatively low BSFC (302g/kWh) for blends compared to diesel fuel (313.8g/kWh. The BTE values for blend (10-50) varied from 23.32-20.63%.	The high thermal efficiency of B10 due to lower viscosity as compared to B20, B30, and B50.	
	B20	20% Calophyllum resulted in 1.36% lower BP and 4.9% higher BSFC compared to diesel. Reduced particulate matter.	Higher injection pressures and preheating.	
Madhuca indica	M100, M90 and M80 (Mahalingam 2017)	Higher flash point with Mahua oil was observed compared to diesel. The calorific value of Mahua for various blends was almost near to diesel.	Increasing the octanol content improved the performance.	(Mahalinga 2017) (Sonar 2015) (Kumar 2017) (Pradhan et al. 2017) (Anandkumar et al. 2015) (Pradhan et al. 2016) (Senthil & Mohan 2015)
	B09, B18 and, B27 (Sonar 2015)	Decreasing relative proportion of biodiesel, increase BTE. The maximum BTE obtained was 21.45%, 22.91%, 23.01% and 22.31% for B27, B18, B09 and B100whereas that observed for diesel was 20.06%.	Improved atomisation by preheating; higher injection pressures.	
	Mahua oil-diesel blends 10 to 100% (Kumar 2017)	The flashpoint, density and viscosity increased with increase in blend percentage. For a given blend BTE increased with increase in load and BSFC more than the neat diesel fuel.	Preheating the blend for improving the atomisation; higher injection pressures adapted.	
Pongamia pinnata	Biodiesel 100% (Nabi 2009) (Sureshkumar 2008)	The viscosity was 1.9-6Cst, the flashpoint was greater than130° C. NO_x emission was maximum with BTE almost close when compared to neat diesel fuel.	EGR used to control NOx emissions (Mahla 2018) (Shi et al. 2017).	(Nabi 2009) (Sureshkumar 2008) (Anwar & Garforth 2016) (Baiju 2009) (Shivashimpi et al. 2018) (Singh et al. 2018) (Srinivasa Rao & Anand 2015) (Dwivedi & Sharma 2014) (Karmee & Chadha 2005)
	Pongamia blend (Anwar & Garforth 2016)	The flash point increased with increase in blend. BSFC of the blend decreased with increase in load for a given concentration of the blend.	Reduction in viscosity of the fuel blend improves the combustion process.	
	LFFAK blend (Baiju 2009)	The BTE increased with increase in load, whereas the BSFC decreased with increase in load. With increase in biodiesel concentration Calorific value decreased hence power loss was observed.	Preheating the fuel blend and higher injection pressure.	

suggested that by reducing the injection pressures and preheating of the blend improves the efficiency of the engine.

When the performance of the diesel engine was studied (Patil & Arakerimath 2012), with JBD20, JBD40 and JBD60 at 2000rpm, it was observed that at 20% load, mechanical efficiency was about 25-30%, at 40% load 40-45% and at 60% load 50-55%. It was suggested that by preheating the blend using the exhaust gas the performance of the engine can be improved.

It was observed that , JB10 (10% Jatropha +90% diesel) blend in diesel engine resulted in increased BSFC as well as brake power compared to conventional diesel engine (Layek 2016).

***Calophyllum inophyllum*:** When *Calophyllum inophyllum* was blended with diesel with different proportions it was observed that calorific value decreased and viscosity increased (How et al. 2018). It was also observed that the combustion pressure and brake specific energy consumption were reduced whereas the brake thermal efficiency increased. Increasing the biodiesel in the blend could reduce the fuel consumption.

Researchers (Ong 2014) observation on diesel engine using blends B10, B20, B30, and B50 where BSFC about 302g/kWh, which was a satisfactory value compared to the conventional diesel engine (313.8g/kWh) at 1900rpm. The BTE for the above blends were from 23.3-20.6%. The maximum efficiency with B10 compared to other blends was due to increased volatility and reduced viscosity of the blend. It was suggested that reducing the NO_x emissions by some methods could lead to better performance.

In order to improve the properties Researchers (Rizwanul Fattah 2014) stated that addition of antioxidant to biodiesel blend increases the kinematic viscosity, density, flash point and reduces the calorific value, hence safe to store the blends.

***Madhuca indica* (Mahua):** The study of different blends of Mahua in diesel engine (Mahalingam et al. 2017), M100, M90, and M80 showed that flash point and calorific value for Mahua was greater than diesel. It was suggested that by increasing the octanol content better performance may be expected.

Experimental results on Mahua (Sonar et al. 2015) with different blends such as B09, B18 and B27, showed that decreasing the ratio of biodiesel increases the brake thermal efficiency. The maximum BTE noted was 21.45-22.31% for B100 to B09, whereas the BTE obtained was 20.66% for diesel. Thus, it is established that by reducing the biodiesel in the blend reduces the viscosity of the blend and hence enhances the atomization of fuel and lead to better performance.

When Mahua oil-diesel blends 10 to 100% were studied (Kumar et al. 2017), the flash point of Mahua was found to be increased. Increasing concentration of Mahua oil in the blends increases the density and viscosity of the blend. Hence, BSFC also increases with increase in the load. It was suggested that by increasing injection opening pressure and preheating the oil, the performance can be improved.

***Pongamia pinnata*:** The oil of *Pongamia pinnata* (100% biodiesel) (Nabi et al. 2009) was found to have viscosity of 1.96-9 Cst and more than 130°C flashpoint. The main problem with pure biodiesel was that the NO_x emission was very high, and thus it was suggested that reducing the NO_x emissions by some means the performance can be improved.

Study on the *Pongamia* oil blend with diesel (Sureshkumar et al. 2008) revealed that, by increasing the concentration of biodiesel the flash point and the BSFC increases. However, the BSFC decreased with increase in load. By reducing the negative effects of viscosity by some means, it is possible to improve the performance of the engine using 100% *Pongamia pinnata* biodiesel (Anwar & Garforth 2016).

Researchers observed (Baiju et al. 2009) that when LFFAK blend was used, the BTE increased with load and BSFC decreased. Due to the lower calorific value of the fuel a power loss was observed.

Emission Studies of Different Non-edible Oils

The blends of different non-edible oils at different ratios were tested in diesel engine and their performance was published by different researchers. Regulated pollutants such as carbon monoxide, hydrocarbons, particulate matters and oxides of nitrogen were analysed. The researchers' observation was that some emissions decreased for different blends of biodiesel whereas some other blends showed high emissions. When NOx emissions of biodiesel blends were compared with diesel, it was observed that the blends of biodiesel contained higher amount of emissions. The increase in NO_x with biodiesel blends could be due to inherent oxygen available in the blend. This necessitate an alternate way to decrease the NO_x emission like EGR, water injection, ammonia injection, etc. (Layek 2016, Patil & Arakerimath 2012, Chauhan 2013, Foidl 1996, Ramesh 2006, Mofijur 2013, Berchmans & Hirata 2008, Chauhan 2013, Chauhan 2013, EL-Seesy 2018, Yunus 2013, Dueso 2018). Some of the oil blends tested in CI engine by different researchers are compared in Table 3.

***Jatropha curcas*:** Researchers observed that diesel-Jatropha oil blend resulted in lower carbon monoxide and hydrocarbons when compared to neat diesel. However, NO and NO_2 emissions were on the higher side with Jatropha

blend. The formation of NO_x is mainly dependent on the temperature, local concentration of oxygen and combustion duration. It was observed that NO_x formation takes place mainly in diffusion-controlled combustion phase on the weak side of the reaction zone. NOx formation can be controlled by reducing flame temperature and minimising the combustion duration.

***Calophyllum inophyllum*:** Researchers claimed that Calophyllum-diesel blend resulted in lower CO and smoke emissions when compared to the diesel fuel. However, the NO_x emissions were higher and particulate emissions reduced from the baseline fuel. By increasing the biodiesel concentration, it is proposed that this emission performance may be improved.

***Madhuca indica* (Mahua):** Researchers (Mahalingam 2017) observed that CO and HC emission of Mahua oil were more than baseline diesel fuel. A similar trend of emissions was observed with biodiesel blends of Mahua with octanol. The general observation was that NO_x varied linearly with load.

***Pongamia pinnata*:** Researchers' findings (Nabi 2009, Sureshkumar 2008, Anwar & Garforth 2016, Baiju 2009, Shivashimpi 2018, Singh 2018, Srinivasa Rao & Anand 2015, Dwivedi & Sharma 2014, Karmee & Chadha 2005) with *Pongamia pinnata* and diesel blend shows the reduction in CO and smoke when compared with the baseline fuel. However, NO_x emissions as observed for other blends increased linearly with load.

Table 3: Emission studies of different non-edible oils.

Alternative fuel	Exhaust emissions	Reference
Jatropha curcas	Lower HC and CO whereas NO_x emissions increased (Layek 2016). HC, CO and CO_2 emissions decreased whereas NO_x increased when compared with the diesel engine (Patil & Arakerimath 2012). Reduced CO emissions by 14%, HC by 16%. However, increased NO by 7%, and CO_2 emissions by 7% relative to diesel fuel (Chauhan 2013).	(Layek 2016) (Patil & Arakerimath 2012) (Chauhan 2013) (Foidl 1996) (Ramesh 2006) (Mofijur 2013) (Berchmans & Hirata 2008) (Chauhan 2013) (EL-Seesy 2018) (Yunus 2013)
Calophyllum inophyllum	CO decreased with the increasing blend ratio, whereas NO_x emissions increased. The smoke and Particulate matters were comparatively lesser than diesel (How 2018). CO and smoke emissions were least whereas NO_x emission was higher compared to that of pure diesel, slight reduction in NO_x at 1900 rpm. However, the lowest NO_x emission for diesel fuel was 119.7 ppm at 1500 rpm (Ong 2014). Using B20 the NO_x increased whereas CO decreased. Use of Antioxidants reduced NO_x by 1.6–3.6%.CO and HC emission increased (Rizwanul Fattah 2014).	(How 2018) (Ong 2014) (Rizwanul Fattah 2014) (Dwivedi 2011) (Praveen 2018) (Nanthagopal 2017) (Ashok 2019) (Nanthagopal 2018) (Ashok 2017)
Mahua	Lower CO and HC emissions with Mahua blend compared to diesel fuel due to the presence of oxygen in Mahua. NO_x was higher for Mahua oil blend compared to diesel (Mahalingam 2017). HC emission for butanol blended Mahua biodiesel was slightly higher than diesel (Sonar 2015). Researcher's (Kumar 2017) found CO and HC emissions in Mahua blend slightly lower than diesel blend. NO_x emissions increased with increased load for Mahua blend.	(Mahalingam 2017) (Sonar 2015) (Kumar 2017) (Pradhan 2017) (Anandkumar 2015) (Pradhan 2016) (Senthil & Mohan 2015)
Pongamia pinnata	Compared to Diesel Fuel, Pongamia blend resulted in reduced CO by 50%, smoke by 43% and engine noises lightly reduced. As load increases NO_x emissions increased substantially (Nabi 2009). HC and CO emissions were decreased and Researchers (Sureshkumar 2008) found slight decrease in NO_x emissions for B40 and B60. At part load condition NO_x emission increased by 10-25% when fuelled with blends as compared to the neat diesel fuel. Under full load conditions neat diesel resulted in higher NO_x than blends (Anwar & Garforth 2016).	(Nabi 2009) (Sureshkumar 2008) (Anwar & Garforth 2016) (Baiju 2009) (Shivashimpi 2018) (Singh 2018) (Srinivasa Rao & Anand 2015) (Dwivedi & Sharma 2014) (Karmee & Chadha 2005)

CONCLUSION

The following are the observations, which can be based on the experimental results of different researchers while using non-edible biodiesel blends in CI engines:

1. Jatropha as biodiesel blend resulted in lower BTE, higher SFC and exhaust gas temperature. Pongamia gave the best brake thermal efficiencies compared to neat diesel operation.
2. Jatropha blend helps in reducing HC and CO emissions. However, NO_x emission increases.
3. For Calophyllum blend, a slightly lower BSFC as well as BTE was observed compared to diesel fuel.
4. Use of *Calophyllum inophyllum* blend resulted in decreased CO, smoke and particulate matters with increasing blend ratio, whereas NO_x emission increased compared to diesel engine operation.
5. For Mahua blend, a slightly lower BSFC as well as BTE was observed compared to diesel fuel.
6. Mahua blend helps in reducing HC and CO emissions. However, NO_x emission increases.
7. The BTE and BSFC trends for *Pongamia pinnata* was in-line with Mahua blend and Jatropha blend.
8. Pongamia biodiesel blend resulted in substantial reduction in CO and smoke emissions. However, at higher loads NO_x emissions increased significantly.

ABBREVIATIONS

CO-Carbon Monoxide
NOx-Oxides of nitrogen
BTE-Brake thermal efficiency
SFC-Specific fuel consumption
LFFAK-Low free fatty acid Karanja oil
HC-Hydrocarbons
BSEC-Brake specific energy consumption
BSFC-Brake specific fuel consumption
BP-Brake power
EGR-Exhaust gas recirculation

REFERENCES

Anandkumar, G., Balaji, S., Backiyaraj, A. and Devaradjane, G. 2015. Experimental investigation on performance and emission characteristics of Mahua biodiesel using electronic fuel injection system. Journal of Chemical and Pharmaceutical Sciences, 7: 396-399. https://doi.org/10.1016/j.egypro.2014.07.298

Aniya, V. K., Muktham, R. K., Alka, K. and Satyavathi, B. 2015. Modeling and simulation of batch kinetics of non-edible karanja oil for biodiesel production: A mass transfer study. Fuel, 161: 137-145. https://doi.org/10.1016/j.fuel.2015.08.042

Anwar, A. and Garforth, A. 2016. Challenges and opportunities of enhancing cold flow properties of biodiesel via heterogeneous catalysis. Fuel, 173: 189-208. https://doi.org/10.1016/j.fuel.2016.01.050

Ashok, B., Nanthagopal, K., Saravanan, B., Azad, K., Patel, D., Sudarshan, B. and Aaditya Ramasamy, R. 2019. Study on isobutanol and *Calophyllum inophyllum* biodiesel as a partial replacement in CI engine applications. Fuel, 235(x): 984-994. https://doi.org/10.1016/j.fuel.2018.08.087

Ashok, B., Nanthagopal, K., Subbarao, R., Johny, A., Mohan, A. and Tamilarasu, A. 2017. Experimental studies on the effect of metal oxide and antioxidant additives with *Calophyllum inophyllum* methyl ester in compression ignition engine. Journal of Cleaner Production, 166: 474-484. https://doi.org/10.1016/j.jclepro.2017.08.050

Ashraful, A. M., Masjuki, H. H., Kalam, M. A., Rizwanul Fattah, I. M., Imtenan, S., Shahir, S. A. and Mobarak, H. M. 2014. Production and comparison of fuel properties, engine performance, and emission characteristics of biodiesel from various non-edible vegetable oils: A review. Energy Conversion and Management, 80: 202-228. https://doi.org/10.1016/j.enconman.2014.01.037

Atabani, A. E., Silitonga, A. S., Ong, H. C., Mahlia, T. M. I., Masjuki, H. H., Badruddin, I. A. and Fayaz, H. 2013. Non-edible vegetable oils: A critical evaluation of oil extraction, fatty acid compositions, biodiesel production, characteristics, engine performance and emissions production. Renewable and Sustainable Energy Reviews, 18: 211-245. https://doi.org/10.1016/j.rser.2012.10.013

Baiju, B., Naik, M. K. and Das, L. M. 2009. A comparative evaluation of compression ignition engine characteristics using methyl and ethyl esters of Karanja oil. Renewable Energy, 34(6): 1616-1621. https://doi.org/10.1016/j.renene.2008.11.020

Balat, M. 2011. Potential alternatives to edible oils for biodiesel production - A review of current work. Energy Conversion and Management, 52(2): 1479-1492. https://doi.org/10.1016/j.enconman.2010.10.011

Balat, M. and Balat, H. 2010. Progress in biodiesel processing. Applied Energy, 87(6): 1815-1835. https://doi.org/10.1016/j.apenergy.2010.01.012

Berchmans, H. J. and Hirata, S. 2008. Biodiesel production from crude Jatropha curcas L. seed oil with a high content of free fatty acids. Bioresource Technology, 99(6): 1716-1721. https://doi.org/10.1016/j.biortech.2007.03.051

Chauhan, B. S., Kumar, N., Cho, H. M. and Lim, H. C. 2013. A study on the performance and emission of a diesel engine fueled with Karanja biodiesel and its blends. Energy, 56(1): 1-7. https://doi.org/10.1016/j.energy.2013.03.083

Christopher, L. P., Kumar, H. and Zambare, V. P. 2014. Enzymatic biodiesel : Challenges and opportunities. Applied Energy, 119: 497-520. https://doi.org/10.1016/j.apenergy.2014.01.017

Claude, F., Ramadan, H. S., Becherif, M. and Boulon, L. 2017. Author's Accepted Manuscript Heat Management Methodology for Enhanced Global Efficiency in Hybrid Electric Vehicles. Case Studies in Thermal Engineering. https://doi.org/10.1016/j.csite.2017.06.006

Dhanavath, K. N., Shah, K., Bankupalli, S., Bhargava, S. K. and Parthasarathy, R. 2017. Derivation of optimum operating conditions for the slow pyrolysis of Mahua press seed cake in a fixed bed batch reactor for bio-oil production. Journal of Environmental Chemical Engineering, 5(4): 4051-4063. https://doi.org/10.1016/j.jece.2017.07.034

Dueso, C., Muñoz, M., Moreno, F., Arroyo, J., Gil-lalaguna, N., Bautista, A. and Luis, J. 2018. Performance and emissions of a diesel engine using sunflower biodiesel with a renewable antioxidant additive from bio-oil. Fuel, 234(July): 276-285. https://doi.org/10.1016/j.fuel.2018.07.013

Dwivedi, G., Jain, S. and Sharma, M. P. 2011. Pongamia as a source of biodiesel in India. Smart Grid and Renewable Energy, 02(03): 184-189. https://doi.org/10.4236/sgre.2011.23022

Dwivedi, G. and Sharma, M. P. 2014. Prospects of biodiesel from Pongamia in India. Renewable and Sustainable Energy Reviews, 32: 114-122. https://doi.org/10.1016/j.rser.2014.01.009.

EL-Seesy, A. I., Hassan, H. and Ookawara, S. 2018. Performance, combustion, and emission characteristics of a diesel engine fueled with Jatropha methyl ester and graphene oxide additives. Energy Conversion and Management, 166(April): 674-686. https://doi.org/10.1016/j.enconman.2018.04.049

Fadhil, A. B., Al-Tikrity, E. T. B. and Albadree, M. A. 2017. Biodiesel production from mixed non-edible oils, castor seed oil and waste fish oil. Fuel, 210(June): 721-728. https://doi.org/10.1016/j.fuel.2017.09.009

Fazal, M. A., Suhaila, N. R., Haseeb, A. S. M. A. and Rubaiee, S. 2018. Sustainability of additive-doped biodiesel: Analysis of its aggressiveness toward metal corrosion. Journal of Cleaner Production. https://doi.org/10.1016/j.jclepro.2018.01.248

Foidl, N., Foidl, G., Sanchez, M., Mittelbach, M. and Hackel, S. 1996. *Jatropha curcas* L. as a source for the production of biofuel in Nicaragua. Bioresource Technology, 58(1): 77-82.

Hosseinzadeh-bandbafha, H., Tabatabaei, M., Aghbashlo, M. and Khanali, M. 2018. A comprehensive review on the environmental impacts of diesel / biodiesel additives. Energy Conversion and Management, 174(June): 579-614. https://doi.org/10.1016/j.enconman.2018.08.050

How, H. G., Masjuki, H. H., Kalam, M. A., Teoh, Y. H. and Chuah, H. G. 2018. Effect of *Calophyllum inophyllum* biodiesel-diesel blends on combustion, performance, exhaust particulate matter and gaseous emissions in a multi- cylinder diesel engine. Fuel, 227(April): 154-164. https://doi.org/10.1016/j.fuel.2018.04.075

Iwata, K. and Matsumoto, S. 2016. Use of hybrid vehicles in Japan: An analysis of used car market data. Transportation Research Part D: Transport and Environment, 46: 200-206. https://doi.org/10.1016/j.trd.2016.03.010

Jain, T., Singh, G., Dwivedi, G. and Nandan, G. 2018. Study of emission parameter of biodiesel from non edible oil sources. Materials Today: Proceedings, 5(2): 3581-3586. https://doi.org/10.1016/j.matpr.2017.11.607

Kalghatgi, G. 2018. Is it really the end of internal combustion engines and petroleum in transport? Applied Energy, 225(April): 965-974. https://doi.org/10.1016/j.apenergy.2018.05.076

Karmee, S. K. and Chadha, A. 2005. Preparation of biodiesel from crude oil of Pongamia pinnata. Bioresource Technology, 96(13): 1425-1429. https://doi.org/10.1016/j.biortech.2004.12.011

Kartika, I. A., Cerny, M., Vandenbossche, V., Rigal, L., Sablayrolles, C., Vialle, C. and Evon, P. 2018. Direct Calophyllum oil extraction and resin separation with a binary solvent of n-hexane and methanol mixture. Fuel, 221: 159-164. https://doi.org/10.1016/j.fuel.2018.02.080

Kashyap, S. S., Gogate, P. R. and Joshi, S. M. 2018. Ultrasound assisted synthesis of biodiesel from karanja oil by interesterification: Intensification studies and optimization using RSM. Ultrasonics Sonochemistry. https://doi.org/10.1016/j.ultsonch.2018.08.019

Kumar, D., Singh, B., Banerjee, A. and Chatterjee, S. 2018. Cement wastes as transesterification catalysts for the production of biodiesel from Karanja oil. Journal of Cleaner Production, 183: 26-34. https://doi.org/10.1016/j.jclepro.2018.02.122

Kumar, M. V., Babu, A. V. and Kumar, P. R. 2017. Experimental investigation on the effects of diesel and mahua biodiesel blended fuel in direct injection diesel engine modified by nozzle orifice diameters. Renewable Energy. https://doi.org/10.1016/j.renene.2017.12.007

Kumar, P., Srivastava, V. C. and Jha, M. K. 2017. Synthesis of biodiesel from transesterification of Jatropha oil with methanol using double metal cyanide as catalyst. Journal of Clean Energy Technologies, 5(1): 23-26. https://doi.org/10.18178/JOCET.2017.5.1.337

Layek, A. 2016. Engine performance and emission having jatropha diesel blend. International Journal of Renewable Energy Research (IJRER), 6(2): 607-613. https://doi.org/10.1234/ijrer.v6i2.3915

Mahalingam, A., Devarajan, Y., Radhakrishnan, S., Vellaiyan, S. and Nagappan, B. 2017. Emissions analysis on mahua oil biodiesel and higher alcohol blends in diesel engine. Alexandria Engineering Journal, pp. 3-7. https://doi.org/10.1016/j.aej.2017.07.009

Mahla, S. K., Dhir, A., Gill, K. J. S., Cho, H. M., Lim, H. C. and Chauhan, B. S. 2018. Influence of EGR on the simultaneous reduction of NOx-smoke emissions trade-off under CNG-biodiesel dual fuel engine. Energy, 152(x), 303–312. https://doi.org/10.1016/j.energy.2018.03.072

Maruthi Prasad, R. and Krishnamoorthy, A. 2018. Design, construction, testing and performance of split power solar source using mirror photovoltaic glass for electric vehicles. Energy, 145: 374-387. https://doi.org/10.1016/j.energy.2017.12.131

Mofijur, M., Hazrat, M. A., Rasul, M. G., & Mahmudul, H. M. 2015. Comparative evaluation of edible and non-edible oil methyl ester performance in a vehicular engine. Energy Procedia, 75: 37-43. https://doi.org/10.1016/j.egypro.2015.07.134

Mofijur, M., Masjuki, H. H., Kalam, M. A. and Atabani, A. E. 2013. Evaluation of biodiesel blending, engine performance and emissions characteristics of *Jatropha curcas* methyl ester: Malaysian perspective. Energy, 55: 879-887. https://doi.org/10.1016/j.energy.2013.02.059

Nabi, M. N., Hoque, S. M. N. and Akhter, M. S. 2009. Karanja (*Pongamia pinnata*) biodiesel production in Bangladesh, characterization of karanja biodiesel and its effect on diesel emissions. Fuel Processing Technology, 90(9): 1080-1086. https://doi.org/10.1016/j.fuproc.2009.04.014

Nanthagopal, K., Ashok, B., Saravanan, B., Korah, S. M. and Chandra, S. 2018. Effect of next generation higher alcohols and *Calophyllum inophyllum* methyl ester blends in diesel engine. Journal of Cleaner Production, 180: 50-63. https://doi.org/10.1016/j.jclepro.2018.01.167

Nanthagopal, K., Ashok, B., Tamilarasu, A., Johny, A. and Mohan, A. 2017. Influence on the effect of zinc oxide and titanium dioxide nanoparticles as an additive with *Calophyllum inophyllum* methyl ester in a CI engine. Energy Conversion and Management, 146: 8-19. https://doi.org/10.1016/j.enconman.2017.05.021

Negm, N. A., Zahran, M. K., Abd Elshafy, M. R. and Aiad, I. A. 2018. Transformation of Jatropha oil to biofuel using transition metal salts as heterogeneous catalysts. Journal of Molecular Liquids, 256: 16-21. https://doi.org/10.1016/j.molliq.2018.02.022

Novoa, L. and Brouwer, J. 2018. Dynamics of an integrated solar photovoltaic and battery storage nanogrid for electric vehicle charging. Journal of Power Sources, 399(July): 166-178. https://doi.org/10.1016/j.jpowsour.2018.07.092

Ong, H. C., Masjuki, H. H., Mahlia, T. M. I., Silitonga, A. S., Chong, W. T. and Leong, K. Y. 2014. Optimization of biodiesel production and engine performance from high free fatty acid Calophyllum inophyllum oil in CI diesel engine. Energy Conversion and Management, 81: 30-40. https://doi.org/10.1016/j.enconman.2014.01.065

Patil, D. and Arakerimath, R. 2012. Performance characteristics and analysis of jatropha oil in multi-cylinder turbocharge compression ignition engine. International Journal of Renewable Energy Research, 1(10): 50-55.

Pradhan, D., Bendu, H., Singh, R. K. and Murugan, S. 2017. Mahua seed pyrolysis oil blends as an alternative fuel for light-duty diesel engines. Energy, 118: 600-612. https://doi.org/10.1016/j.energy.2016.10.091

Pradhan, D., Singh, R. K., Bendu, H. and Mund, R. 2016. Pyrolysis of Mahua seed (*Madhuca indica*) - Production of biofuel and its characterization. Energy Conversion and Management, 108: 529-538. https://doi.org/10.1016/j.enconman.2015.11.042

Praveen, A., Lakshmi Narayana Rao, G. and Balakrishna, B. 2018. Performance and emission characteristics of a diesel engine using Calophyllum Inophyllum biodiesel blends with TiO_2 nanoadditives and EGR. Egyptian Journal of Petroleum. https://doi.org/10.1016/j.ejpe.2017.10.008

Ramesh, D., Samapathrajan, A. and Venkatachalam, P. 2006. Production of biodiesel from Jatropha curcas oil by using pilot biodiesel plant. The Jatropha Journal, 18: 1-6.

Rizwanul Fattah, I. M., Masjuki, H. H., Kalam, M. A., Wakil, M. A., Ashraful, A. M. and Shahir, S. A. 2014. Experimental investigation of performance and regulated emissions of a diesel engine with *Calophyllum inophyllum* biodiesel blends accompanied by oxidation inhibitors. Energy Conversion and Management, 83: 232-240. https://doi.org/10.1016/j.enconman.2014.03.069

Safari, M. 2018. Battery electric vehicles : Looking behind to move forward. Energy Policy, 115: 54-65. https://doi.org/10.1016/j.enpol.2017.12.053

Senthil, R. and Mohan, K. 2015. Comparison of yield and fuel properties of thermal and catalytic calophyllum inophyllum seed shell pyrolytic oil. Journal of Chemical and Pharmaceutical Sciences, pp. 119-126. https://doi.org/10.1016/j.fuel.2013.09.001

Sharaf, A. M., Omar, N., Gandoman, F. H., Zobaa, A. F., Hossam, S. and Abdel, E. 2018. Chapter 12 - Electric and hybrid vehicle drives and smart grid interfacing. In: Advances in Renewable Energies and Power Technologies. Elsevier Inc. https://doi.org/10.1016/B978-0-12-813185-5.00008-5

Shi, X., Liu, B., Chao, Z., Jingchao, H. and Zeng, Q. 2017. A study on combined effect of high EGR rate and biodiesel on combustion and emission performance of a diesel engine. Applied Thermal Engineering. https://doi.org/10.1016/j.applthermaleng.2017.07.083

Shivashimpi, M. M., Alur, S. A., Topannavar, S. N. and Dodamani, B. M. 2018. Combined effect of combustion chamber shapes and nozzle geometry on the performance and emission characteristics of C.I. engine operated on Pongamia. Energy, 154: 17-26. https://doi.org/10.1016/j.energy.2018.04.097

Singh, Y., Sharma, A., Kumar Singh, G., Singla, A. and Kumar Singh, N. 2018. Optimization of performance and emission parameters of direct injection diesel engine fuelled with pongamia methyl esters-response surface methodology approach. Industrial Crops and Products, 126(August): 218-226. https://doi.org/10.1016/j.indcrop.2018.10.035

Sonar, D., Soni, S. L., Sharma, D., Srivastava, A. and Goyal, R. 2015. Performance and emission characteristics of a diesel engine with varying injection pressure and fuelled with raw mahua oil (preheated and blends) and mahua oil methyl ester. Clean Technologies and Environmental Policy, 17(6): 1499-1511. https://doi.org/10.1007/s10098-014-0874-9.

Srinivasa Rao, M. and Anand, R. B. 2015. Production characterization and working characteristics in DICI engine of Pongamia biodiesel. Ecotoxicology and Environmental Safety, 121(2010): 16-21. https://doi.org/10.1016/j.ecoenv.2015.07.031

Strehler, M., Merting, S. and Schwan, C. 2017. Energy-efficient shortest routes for electric and hybrid vehicles. Transportation Research Part B: Methodological, 103: 111-135. https://doi.org/10.1016/j.trb.2017.03.007

Suresh, M., Jawahar, C. P. and Richard, A. 2018. A review on biodiesel production, combustion, performance, and emission characteristics of non-edible oils in variable compression ratio diesel engine using biodiesel and its blends. Renewable and Sustainable Energy Reviews, 92(March): 38-49. https://doi.org/10.1016/j.rser.2018.04.048

Sureshkumar, K., Velraj, R. and Ganesan, R. 2008. Performance and exhaust emission characteristics of a CI engine fueled with *Pongamia pinnata* methyl ester (PPME) and its blends with diesel. Renewable Energy, 33(10): 2294-2302. https://doi.org/10.1016/j.renene.2008.01.011

Verhelst, S., Wg, J., Sileghem, L. and Vancoillie, J. 2019. Methanol as a fuel for internal combustion engines. Progress in Energy and Combustion Science, 70: 43-88. https://doi.org/10.1016/j.pecs.2018.10.001

Vinukumar, K., Azhagurajan, A., Vettivel, S. C., Vedaraman, N. and Haiter Lenin, A. 2018. Biodiesel with nano additives from coconut shell for decreasing emissions in diesel engines. Fuel, 222: 180-184. https://doi.org/10.1016/j.fuel.2018.02.129

With, P., Fuels, P., Developments, R., Prices, F. B., Charging, F., Concerns, A. Q. and Coalitions, G. 2019. Powering motor vehicles: From IC engines to electric Batteries, 123-138. https://doi.org/10.1016/B978-0-12-811434-6.00006-8

Yunus, S., Rashid, A. A., Abdullah, N. R., Mamat, R. and Latip, S. A. 2013. Emissions of transesterification jatropha-palm blended biodiesel. Procedia Engineering, 68: 265-270. https://doi.org/10.1016/j.proeng. 2013.12.178

Zhou, W., Yang, L., Cai, Y. and Ying, T. 2018. Dynamic programming for new energy vehicles based on their work modes part I : Electric vehicles and hybrid electric vehicles state of charge. Journal of Power Sources, 406(July): 151-166. https://doi.org/10.1016/j.jpowsour.2018.10.047

Nature Environment and Pollution Technology
An International Quarterly Scientific Journal

p-ISSN: 0972-6268
e-ISSN: 2395-3454

Vol. 18 | No. 4 | pp. 1193-1200 | 2019

Original Research Paper | Open Access

Antibiotic Resistance of *Pseudomonas aeruginosa* in Well Waters in Irrigated Zone (Middle Atlas-Morocco)

Fatima Zahra Hafiane*, Latifa Tahri*, Najia Ameur, Rajaa Rochdi**, Karim Arifi* and Mohammed Fekhaui***

*University Mohamed V, Faculty of Sciences-Scientific Institute, Avenue. Ibn Batouta, B.P 703, 10106 Rabat, Morocco

**National Institute of Hygiene, Department of Toxicology and Hydrology, 27, Av. Ibn Batouta - BP 769 Rabat, Morocco

Nat. Env. & Poll. Tech.
Website: www.neptjournal.com

Received: 19-01-2019
Accepted: 08-04-2019

Key Words:
Pseudomonas aeruginosa
Antibiotics resistance
Water contamination
Multidrug resistance
Phenotypes
Wells

ABSTRACT

Pseudomonas aeruginosa is a bacteria which can live in freshwater, soil and plants. It is a commensal of the digestive tube, slightly abundant in human body. Its presence in wells water is a result of current anthropogenic activity and pollution loads. It is an important nosocomial pathogenic agent characterized by an intrinsic resistance to multiple antimicrobial agents which can develop high-level multidrug resistance. To assess the contamination of these well waters by this pathogenic germ, two hundred samples were collected for four seasonal campaigns between March 2017 and May 2018 with a rate of forty three (43) samples per season in an irrigated zone. The samples were analysed to identify *P. aeruginosa*, then the isolated serotypes were determined by slid agglutination test using four pools and 20 monovalent Antisera. The detected *P. aeruginosa* were tested for susceptibility to 18 antibiotics. A total of (n=85/139) isolated strains were identified as *P. aeruginosa* representing 61.15 % of prevalence among *Pseudomonas* spp. Antimicrobial resistance revealed that 68% of them are multidrug resistant, while15.09 % of strains resist at least to 7 antibiotics, 30.19% resist at least to 11 antibiotics, 13.21% resist at least to 12 antibiotics, 5.66% resist at least to 13 antibiotics, and 3.77% resist at least to 14 antibiotics. The high level resistance of *P. aeruginosa* is observed with piperacillin tazobactam (100/10µg) (84.91%), ciprofloxacin (5µg) (79.25%), imipenem (10µg) and ceftazidime (30µg) (37.58%). The resistance of phenotypes of *P. aeruginosa* strains allowed to identify (n=20/85) ESBL, (n=31/85) oxacillinase broad spectrum ES-OXA, (n=5/85) phenotype of impermeability to imipenem, (n=12/85) cephalosporinase AMPC, and (n=17/85) wild type. The results showed the high antibiotic resistance levels of *P. aeruginosa* strains from well water samples against antibiotics. Furthermore, based on the results, these well waters can be a source of *P. aeruginosa* and human and animal susceptibility to other opportunistic pathogens.

INTRODUCTION

The well waters are solicited for several uses in households, irrigation, alimentation, and considered as a vehicle for diffusion and dissemination of human associated bacteria (Pitondo-Silva et al. 2014). The World Health Organization (WHO) estimates that 80% of diseases that affect the world population are directly associated to the poor water quality, and poor sanitation system which has defective hygiene (WHO 2010). However, the presence of *Pseudomonas* spp. is the main concern in setting health-based targets for microbial safety of water. *Pseudomonas* spp. are opportunistic pathogens bacteria often found in the environment. Strains of this species generally have a very wide nutritional variance and they can live in various ecological niches (Monteil et al. 2002). These bacteria are a non-fermenting Gram negative aerobic bacilli involved in opportunistic nosocomial infections and in opportunistic infections of immunocompromised hosts (Ender et al. 2017). *Pseudomonas* is a genus of the Gamma proteobacteria class of bacteria, which belongs to the Pseudomonadacea family. This genus regroups more than 140 species including *P. aeruginosa*. The *P. aeruginosa* is highly ubiquitous in water systems and capable to acquire antibiotic resistance due to its low membrane permeability and extensive efflux pump system (Nasreen et al. 2015). The *P. aeruginosa* is a considerable pathogenic agent characterized by an intrinsic resistance to multiple antimicrobial agents and the ability to develop high level multidrug resistance through some mechanisms (El Ouardi et al. 2013). In fact, The *P. aeruginosa* forms biofilms that award a high power of colonization, resistance to antiseptics, and antibiotics (Ckd et al. 2016). Recent studies showed a rapid and worrying evolution of antibiotic resistant strains both in their number and spectrum, more and more extensive with cephalosporin resistant strains of third generation (C3G), and / or resistant to high-level fluo-

roquinolones and / or resistant to alternative therapies such as carbapenems (El Ouardi et al. 2013a). A wide range of antibiotics are used against bacterial infections. Beta-lactamases, Carbapenems, Fluoroquinolons and Aminosids are the most classes of antibiotics used clinically. However, *P. aeruginosa*, as other (extended spectrum β-lactamase: ESBL) bacteria can have a high level of activities against many antibiotics (Nedeljković et al. 2015). Carbapenems are often used as a drug of choice against the *P. aeruginosa* multidrug-resistant (MDR), but their activity is increasingly compromised by the emergence and the worldwide dissemination of resistant strains, which are implicated in numerous nosocomial infections (Maroui et al. 2015). Previous studies showed the great potential of clinical isolates of *P. aeruginosa* to acquire antimicrobial resistance. However, few studies report the resistance profile and its acquisition mechanisms in isolated environments, especially those obtained from water wells. This study aims to determine prevalence, serotype and antibiotic resistance profile of isolated *P. aeruginosa* from well waters in Middle Atlas region in Morocco.

MATERIALS AND METHODS

Site Selection and Sampling Campaign

The study area is located in Beni Mellal-Khenifra region (Fig.1), stretched out on two water tables (Beni Aamir and Beni Moussa). It covers a surface of 3600 km² in the middle basin of Oum Errbiaa. The water samples were collected directly from 43 wells in irrigated zone, during four campaigns (Table 1).

Isolation and Identification of *P. aeruginosa* Strains

From each water sample, *P. aeruginosa* was isolated and characterized according to the official Moroccan method (NM 2012). The enumeration of *Pseudomonas* spp. was carried out after the filtration of 100 mL of water sample. It was performed on Pseudomonas Cetrimide Agar (USP-EP, Oxoid CM0579) with 10 mL glycerol/L incubated at 42°C for 24-48 h. The typical colonies, that clearly showed pyocyanin production (blue green colonies and fluorescence at 360 nm), are considered as positive for *P. aeruginosa*. All colonies were confirmed using King A Agar and King

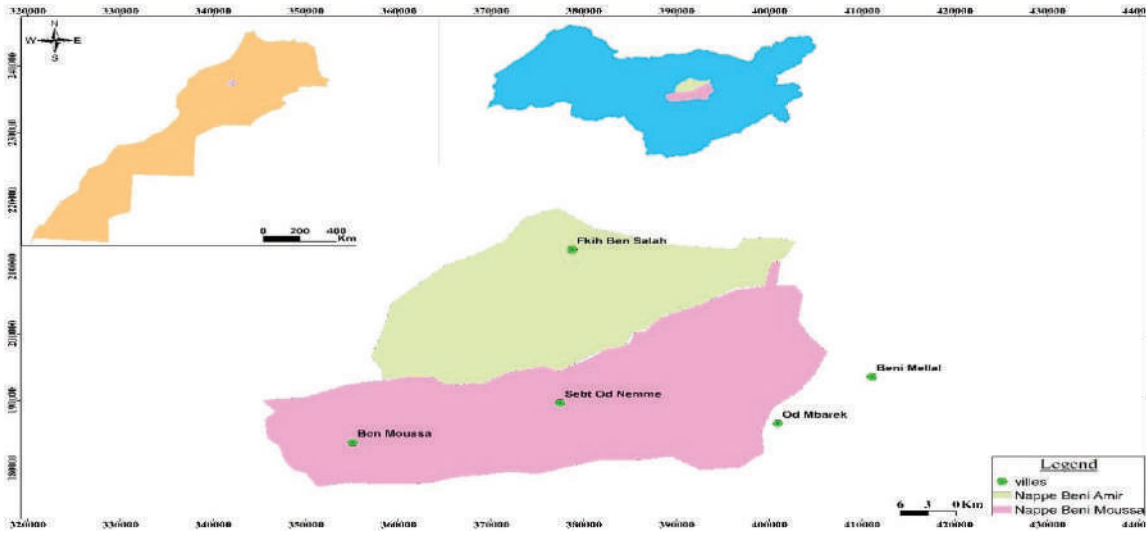

Fig.1: Location of the study area.

Table 1: Distribution of samples by zone and period of sampling.

	Campaign 1		Campaign 2		Campaign 3		Campaign 4		Campaign 5	
Zone	BM	BA	BM	BA	BM	BA	BM	BA	BM	BA
Date	13/03/2017	03/04/2017	08/05/2017	29/05/2017	10/07/2017	24/07/2017	Terrain inaccessible	Terrain inaccessible	23/04/2018	07/05/2018
Samples	20	23	21	22	23	20	0	0	23	18

B Agar (Bio-life) incubated at 42°C for 24 h. The production of specific pigments allowed the differentiation of *P. aeruginosa* and other *Pseudomonas* spp. The preliminary biochemical characterization of the strains was confirmed by using API 20 NE (Bio Mérieux).

Serotyping and Agglutination of *P. aeruginosa*

P. aeruginosa serotype isolate was determined by slide agglutination test using polyvalent and monovalent antisera (BIO-RAD). The positive agglutination is described as positive when strains cause a positive slide agglutination reaction. The monovalent is used when the corresponding polyvalent produce agglutinations.

Antibiotic Susceptibility of *P. aeruginosa* Isolates

The isolated *P. aeruginosa* was tested for susceptibility to 18 antibiotics. The susceptibility was tested by the disk diffusion method according to the recommendations of the French Society of Microbiology Antibiogram Committee CASFM/EUCAST (EUCAST/CASFM 2017). From each colony of each test strain, a suspension of 0.5 McFarland density was prepared and poured dried into the Müller-Hinton agar (OXOID, CM0337). Eighteen antibiotics were tested, including Ticarcillin (75 mg), Piperacillin (100 mg), Ticarcillin/Clavulanic acid (85 mg), Piperacillin/Tazobactam (10 mg), Ceftazidim (30 mg), Cefepim (30 mg), cefotaxime (30 mg), Imipenem (10 mg), Meropenem (10 mg), Aztreonam (30 mg), Fosfomycin (30 mg), Amikacin (30 mg), Tobramycin (10 mg), Gentamicin (10 mg), Nétilmycin (10 mg), Ciprofloxacin (5 mg), Lévofloxacin (5 mg), and Colistin (10 mg). The *P. aeruginosa* ATCC 27853 was used as a control reference strain. The isolated *P. aeruginosa* were classified as susceptible, intermediate or resistant according to the clinical interpretative criteria recommended by the CASFM/EUCAST (EUCAST/CASFM 2017). The resistance to antibiotics was determined after 24 hours, based on the inhibition zone diameter. Briefly, the detection of ESBL phenotype was performed by antagonism effect between the three different antibiotic disks (aztreonam, ticarcillin/clavulanic acid and ceftazidime) separated by 2 mm (EUCAST/CASFM,2017). Finally, to detect an ESBL phenotype in presence of cephalosporinase, combination disk test with cefepime was used and inhibition diameters were compared (EUCAST/CASFM,2017).

Statistical Analysis

The data were treated with the data processing software R Statistics 3.4.2, and XLSTAT.

RESULTS

Prevalence of *Pseudomonas* in Well Waters

Out of 200 water samples examined, the *Pseudomonas* spp. was isolated in 139 samples. Among the isolated bacterial strains, a total of n=58/139 was identified as *P. aeruginosa*. The antimicrobial activity of *P. aeruginosa* strains revealed a high level of resistance among all anti pseudomonal drugs tested. The generated results are shown in (Fig. 2).

The analysis of isolated bacterial strains showed a high resistance degree (Fig. 2) to Pepiracillin Tazobactam with (84.21%), Ciprofloxacin with (79.25%), Ceftazidim and Imipenem with (73.58%), a middle resistance degree to by Tobramycin, Levofloxacin, Amikacin with (67.92%), Gentamycin with (66.04%) and Netilemycin with (62.26%); and a low resistance degree to Aztreonam with (56.60%), Fosfoycin with (47.17%), and Meropenem with (35.85%).

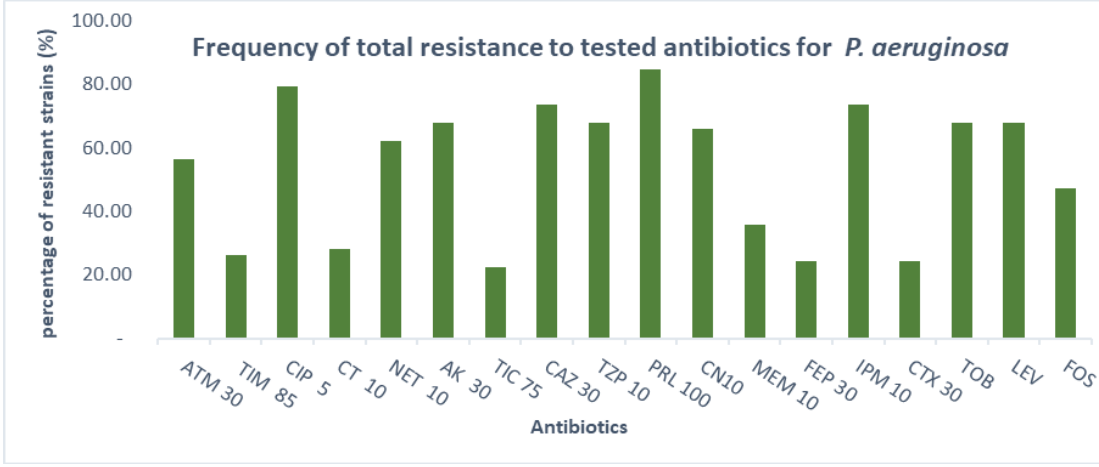

Fig. 2: Antimicrobial resistance pattern of *P. aeruginosa* isolated from wells.

The largest manifested sensitivity (Fig. 2) concerns the carboxypenicillins classes: Ticarcillin (77.36%), ticarcillin acid clavulanic (73.58%), followed by cephalosporins the 3rd and 4th generation with cefepim and cefotaxim (75.47%, 71.70%) respectively. At the end, the sensitivity was noted to Polymyxin classes: Colistin (71.70%).

A multidrug resistant strain of *P. aeruginosa* is defined as a strain which resists to more than three antimicrobial drug classes. The results revealed that 68% of strains were multidrug resistant, whereas 30.19% of strains resist at least to 11 antibiotics, 15.09 % of strains resist at least to 7 and 10 antibiotics, 13.21% of strains resist at least to 12 antibiotics, 5.66% of strains resist at least to (4, 8 and 13) antibiotics, 3.77 % of strains resist at least to 5 and 14 antibiotics, and finally 1.89% of strains resist to 9 antibiotics (Table 2).

Phenotype Antibiotics Resistance

With the disc diffusion test, the phenotypic detection marker antibiotics was sufficient to identify the wild-type phenotype and the common β-lactam resistance phenotypes of *P. aeruginosa* previously described.

Wild type phenotype: The 20% of *P. aeruginosa* strains detected wild type have natural resistance mechanism, with an absence of synergy among the aztreonam, ceftazidim and the ticarcillin acid clavulanic. Also, these isolated bacteria are susceptible to the phenotypic detection markers as the ticarcillin, imipenem, cefepim, ceftazidim, ticarcillin acid clavulanic, and the aztreonam with a diameter zone of 30mm±3. However, a smaller zone diameter given by cefotaxime is less active on these strains.

Penicillinase phenotype: The 36.5% of strains have a phenotype of the Oxacillinase broad spectrum ES-OXA class D, according to the classification of Bush Jacoby, which is resistant to the ticarcillin or intermediate/resistant to the cefepime. The activities of the cefotaxim, ceftazidim, aztreonam and the imipenem against these strains are susceptible. Consequently, when OXA-type enzymes are produced the clavulanic acid does not generally restore a susceptibility to the ticarcillin. Non-synergic effect is observed between clavulanic acid and other β-lactams, only the imipenem antagonized of cefepim/or ceftazidim activity. Finally, the activity of the cefepim was reduced.

Phenotype due to ESBL production: The 23.5% isolates of *P aeruginosa* strains contain ESBL (extended spectrum β-lactamase) phenotype class A according to the classification of Bush Jacoby which is resistant to the aztreonam, ceftazidim and all β-lactamase tested, but sensitive to the imipenem. However, a synergy effect was detected between ceftazidim, aztreonam, and the ticarcillin acid clavulanic. Consequently, the clavulanic acid can not restore susceptibility to the ticarcillin. Finally, the activity and diameter zone of the ceftazidime (≤22mm) and aztreonam (diameter ≤ 27 mm was reduced.

Phenotype cephalosporinase AMPC: The 14.1% strains of *P. aeruginosa* were detected as phenotype cephalosporinase AMPC due to constitutive depressed mutants "high-level cephalosporinase". Only the imipenem is active against these strains of *Pseudomonas aeruginosa*. However, an absence of synergy among the aztreonam, ceftazidime and the ticarcillin acid clavulanic was noted with a presence of antagonistic effect between the imipenem and cefepime. In addition, the presence of zone edges, consisting of scatter colonies was observed. Consequently, the clavulanic acid did not restore susceptibility to ticarcillin.

Phenotype impermeability to imipenem: 6% strains of *P.*

Table 2: Classification of Multi drug Resistant strains of *P. aeruginosa* isolated from wells.

	Multi Drug Resistant strains (MDR)	Percentage of Multi Drug Resistant (MDR) %
StrainsResistant to 4 Antibiotics	3	5,66
StrainsResistant to 5 Antibiotics	2	3,77
Strains Resistant to 7 Antibiotics	8	15,09
Strains Resistant to 8 Antibiotics	3	5,66
Strains Resistant to 9 Antibiotics	1	1,89
Strains Resistant to 10 Antibiotics	8	15,09
Strains Resistant to 11 Antibiotics	16	30,19
Strains Resistant to 12 Antibiotics	7	13,21
Strains Resistant to 13 Antibiotics	3	5,66
Strains Resistant to 14 Antibiotics	2	3,77

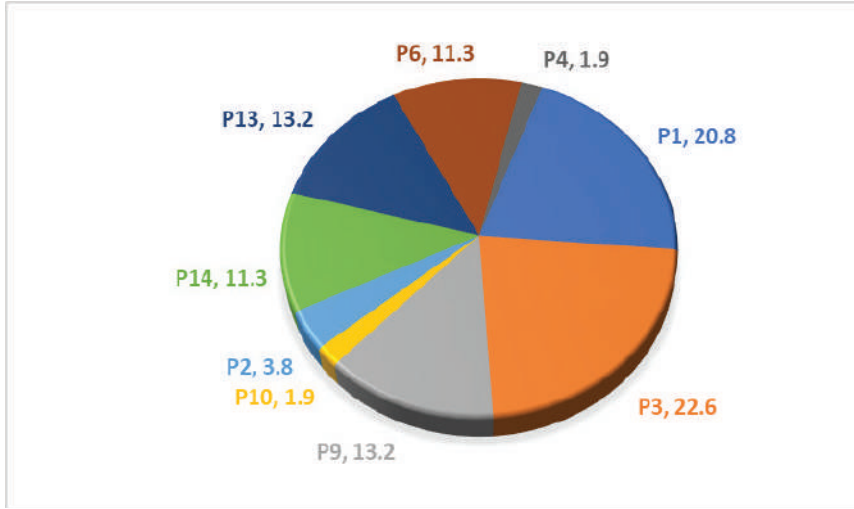

Fig. 3: Serotype distribution of *P. aeruginosa* strains isolated from wells according to the prevalence.

aeruginosa were detected using phenotype, the impermeability to the imipenem, that is showed by resistance strains to imipenem. However, this phenotype was characterized by an absence of image of synergy between the ticarcillin clavulanic acid and those of C3G and/or aztreonam. In addition, the presence of antagonistic effect between imipenem and cefepime, the diameter zone of both IPM and FEP is substantially equal.

Serogroups prevalence of *Pseudomonas aeruginosa*: In this study area, some isolates are poly-agglutinative, while others agglutinated only by polyvalent, but not monovalent antisera. Some isolates are not agglutinated with any serum, such isolates are described as non-typical. So, the following serotypes of *P. aeruginosa* are serologically identified: P1, P2, P4, P10, P3, P6, P9, P13 and P14. The most frequent serotypes are P3 with 22.6% of prevalence, followed by the serotype P1 with 20.8%. However, the serotypes P13 and P9 have (13.2%) of prevalence. While, the serotypes P6 and P14 have prevalence 11.3%, 3.8% for P2 serogroups, and finally P10 and P4 have a low percentage of prevalence with 1.9% (Fig. 3).

Cluster Analysis of *P. aeruginosa* Isolates

All *P. aeruginosa* isolates are generated to a dendrogram using Ward's method (Euclidean distances) and subjected to cluster analysis based on their inhibition zone diameter (IZD). This approach was used as a tool to resolve the difference between the MDR phenotypes of different isolates (Fig. 4). From all isolated sites, the *P. aeruginosa* strains were subjected to cluster analysis and two main clusters were observed (Fig. 4) with the number of isolates from different wells. Both clusters have sub clusters. The phenotype of oxacillinase was found only in cluster 1. The second cluster is a large cluster isolates, mixed cluster with phenotypes oxacillinase, ESBL β-lactamase and cephalosporinases, while the first small cluster detected only the ESBL isolates. However, the second cluster is a very mixed one and contains a large variance between sample areas.

DISCUSSION

P. aeruginosa has a great ability of survival strategies as the production of biofilm and pigments. It is a distributed bacterium in nature and known as a ubiquitous bacterium. However, few authors reported the presence of resistance profile and its acquisition mechanisms in the environmental isolates (Nola et al. 2017, Kawecki et al. 2017, Moussé et al. 2016).

Pathogenic species such as *Pseudomonas aeruginosa*, found in water (piped water systems, hot water systems and spa pools), may contribute to constitution of biofilm-forming microbial communities (Ugo et al. 2018), the same result were found by Ouardi et al. (2013), Marti et al. (2014), which proved that 95% of the overall biomass appear as a biofilm of *P. aeruginosa* in water of the pipe wells (El Ouardi et al. 2013, Marti et al. 2014).

Our study shows the great potential of *P. aeruginosa* isolated from well water to acquire antimicrobial resistance. The same finding was reported by Koro et al. (2016), and Marti et al. (2014) in several studies in which they highlighted the role of the environment for the dissemination of MDR organisms within human and animal, that can establish the need for great risk assessment to be fulfilled in

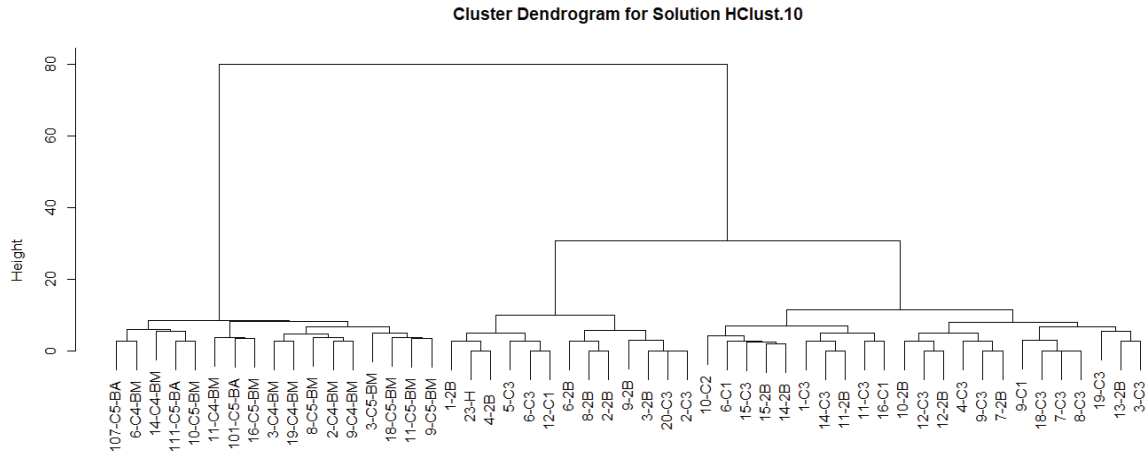

Fig. 4: Cluster analysis of *P. aeruginosa* isolated from wells water.

order to identify the presence of the *P. aeruginosa* in water, thus act as reservoir for MDR strains reported by Kümmerer (Moore et al. 2010, Kümmerer et al. 2009, Penna et al. 2009).

This study aims to evaluate the diversity of MDR phenotypes of *P. aeruginosa* found in well waters in irrigated zone of TADLA plane in Béni-Mellal region. In this study, 68% of *P. aeruginosa* strains were multidrug resistant, with 30.19% of strains resistant to at least 11 antibiotics, and 15.09 % of strains resistant to at least (7 and 10) antibiotics. Also, 61.15 % of prevalence among *P. aeruginosa* strains are resistant to all antibiotics tested. The same study was done in surface waters by Moore et al. (2010) and Kawecki et al. (2017).

The *P. aeruginosa* is widely distributed in well waters in this study area; out of 200 water samples examined, *Pseudomonas* spp. was successfully isolated from 139 samples, whose 85 strains were identified as *P. aeruginosa*. The same results were demonstrated by Alaoui et al. (2008) in Morocco, Rigas et al. (1998) in Greece, and Moore et al. (2002) in Ireland. The *P. aeruginosa* was isolated from 30.8% of the hydrotherapy pools, 72.5% of the Jacuzzis/spas, and 38.2% of the swimming pools (Alaoui et al. 2008, Moore et al. 2002).

The *P. aeruginosa* is naturally resistant to penicillin, to 1st and 2nd generation of cephalosporins, and most of the cephalosporins in 3rd generation. It has always been viewed as a microorganism which is difficult to treat because of its resistance to antibiotics. Then the treatment of the infection of the *P. aeruginosa* is based on the association of the beta-lactam and the aminoglycoside, or the fluoroquinolone and the aminoglycoside, or the beta-lactam and the fluoroquinolone. We have, therefore, chosen the antibiotics that are most frequently prescribed to course of treatment of the infection to *P. aeruginosa*.

The present study is also extended to classify *P. aeruginosa* strains according to the beta-lactamases production, 36.5% of strains present a phenotype of oxacillinase broad spectrum ES- OXA, 23.5% isolates of *P. aeruginosa* strains showed ESBL, 20 % of strains detected wild type, 14.1% strains detected as phenotype cephalosporinase AMPC and 6% strains detected with phenotype the impermeability to the imipenem. This variety of resistant phenotype strains may explain the larger number and diversity of isolates from this water; the same results were found by El Ouardi et al. (2013), Mulamattathil et al. (2014), Nasreen et al. (2015) and Nedeljković et al. (2015). The results from our study and those found in previous studies show that water acquire a great potential of resistant phenotype those are widely distributed in all water wells, thus, should be further taken with seriousness to provide an ideal treatment against the *P. aeruginosa*.

Regardless of all the results of resistant phenotypes from wells that were examined, two classes of Uréidopenicillins (84.11%) and fluoquinolons (73.6%) have the greatest antimicrobial potency of resistance. The same results showed high potency of susceptibility to the carboxypenicillins classes (75.47%), followed by the 3rd and 4th generation of cephalosporins with (73.6%). In fact, 75% of resistance to cefepim was reported by Akhabue et al. (2012). Also, a largest sensitivity is noted to polymyxin with colistin (71.70%). At the end, a low sensitivity was manifested to carbapenems (30.19%). Similar results are obtained by Moore et al. (2010) from surface water and El Ouardi et al. (2013) from groundwater, and Mulamattathil et al. (2014) and Nasreen et al. (2015) from surface and drinking water.

These results about antibiotics classes activity corroborate with the results of Ben Abdallah et al. (2008) indicated that the most active antibiotic is the colistin. It is proved by the results of studies by Maroui et al. (2015), Minchella et al. (2010) in Nimes in France on patients in the CHU.

The study highlights a variety of serogroups of *P. aeruginosa* isolated from water wells. The predominant serogroups isolated in this study are P1, P3, P6, P9, P13 and P14. These results are original and unique in the area and there are no similar results obtained from water wells. The serotype P3 is the most resistant to almost all tested antibiotics, except the colistin. The P3 serotype is widely spread due to highest resistance to antibiotics.

The fact that strains isolated in this study should be in contact with environmental, aquatic and animal strains. These results are in agreement with those from surface water and swimming pool (Stirling et al. 2008, Nola et al. 2017, Mérens et al. 2012, Ckd et al. 2016).

In addition, the importance of emergence of MDR strains could be justified by the phenotype resistant to action of carbapenems drug and polymyxins, which are the greatest choice treatment of infections by the *P. aeruginosa* resistant to multiple beta-lactam antibiotics.

CONCLUSION

This study shows a high prevalence, with a great diversity of the isolated *P. aeruginosa* from water wells and gives an idea about their antibiotic resistance profile. The presence of *P. aeruginosa* would provide information about the health risks associated with the consumption of contaminated water.

Moreover, after some investigations and various analyses, we found that different well waters used for drinking and housework and livestock beverage are not suitable. These results, which are out of standards in the analysed well waters can cause minor or severe infections to consumers. The importance of assessment and urgent actions to treat well water is clear, and the authorities need to take action against the risks related to the contamination of water in order to prevent or decrease the spread of *P. aeruginosa* in environment and well waters.

ACKNOWLEDGEMENTS

Authors gratefully to acknowledge the Department of Agricultural Development (DDA) of Tadla and Department of Irrigation and Drainage Network Management (DGRID) of Tadla for their assistance in this study. Authors also would like to acknowledge the staff for their kind help in sample collection.

REFERENCES

Alaoui, H. L., Oufdou, K. and Mezrioui, N. 2008. Environmental pollutions impacts on the bacteriological and physicochemical quality of suburban and rural groundwater supplies in Marrakesh area (Morocco). Environmental Monitoring and Assessment, 145: 195-207.

Akhabue, E., Synnestvedt, M., Weiner, M.G., Bilker, W.B. and Lautenbach, E. 2012. Cefepime-Resistant *Pseudomonas aeruginosa*. Emerging Infectious Diseases, 17(6): 1037-1043.

Ben Abdallah, H., Noomen, S., Khélifa, A. B. E., Sahnoun, O., Elargoubi, A. and Mastouri M. 2008. Susceptibility patterns of *P. aeruginosa* strains isolated in the Monastir region, Tunisia. Médecine Et Maladies Infectieuses, 38: 554-556.

Benie, C.K.D., Dadie, A., Guessennd, N.K., Kouame, N.D., Yobouet, B.A., Aka, S., Koffi, M.D. and Dosso, M. 2016. Prevalence and diversity of *Pseudomonas* spp. isolated from beef, fresh and smoked fish in Abidjan, Côte d'Ivoire. Journal of Food and Dairy Technology, 4(4): 52-61.

D'Ugo, E., Marcheggiani, S., D'Angelo, A.M., Caciolli, S., Puccinelli, C., Giuseppetti, R., Marcoaldi, R., Romanelli, C. and Mancini, L. 2018. Microbiological water quality in the medical device industry in Italy. Microchemical Journal, 136: 293-299.

El Ouardi, A., Senouci, S., El Habib, F. and Ennaji, M. M. 2013. *P. aeruginosa* in water of Hamam or Turkish bath: Serotyping and antibiotic susceptibility. Middle East Journal of Scientific Research, 15(4): 487-492.

Ender, A., Goeppert, N., Grimmeisen, F. and Goldscheider, N. 2017. Evaluation of β-D-glucuronidase and particle-size distribution for microbiological water quality monitoring in Northern Vietnam. Science of the Total Environment, (580): 996-1006.

EUCAST/CASFM (European Committee on Antimicrobial Susceptibility Testing). 2017. Societé Francaise de Microbiologie, pp. 128.

Kawecki, S., Kuleck, G., Dorsey, J.H., Leary, C. and Lum, M. 2017. The prevalence of antibiotic-resistant bacteria (ARB) in waters of the Lower Ballona Creek Watershed, Los Angeles County, California. Environment Monitoring Assessment, 89: 261.

Kümmerer K. 2009. Antibiotics in the aquatic environment. Chemosphere, 75(4): 417-434.

Maroui, I., Barguigua, A., Aboulkacem, A. and Ouarrak, K. 2015. First report of VIM-2 metallo-b-lactamases producing *P. aeruginosa* isolates in Morocco. Journal of Infection and Chemotherapy, 6-11.

Marti, E., Variatza, E. and Balcazar, J. L. 2014. The role of aquatic ecosystems as reservoirs of antibiotic resistance. Tendances Microbiologique, 22(1): 36-41.

Mérens, A., Janvier, F., Vu-thien, H., Cavallo, J. and Jeannot, K. 2012. Phénotypes de résistance aux antibiotiques de *P. aeruginosa*, Stenotrophomonas maltophilia, Burkholderia cepacia. Revue. Francophone des Laboratoires, 445: 59-74.

Minchella, A., Molinari, L., Alonso, S., Bouziges, N., Sotto, A. and Lavigne, J. 2010. Evolution of antimicrobials resistance against *P. aeruginosa* in a French University hospital between 2002 and 2006. Pathologie Biologie, 58(1): 1-6.

Monteil, H. 2002. *Pseudomonas* et apparentés. Revue Française des Laboratoires, 343: 31-40.

Moore, J.E., Moore, P.J.A., Millar, C.B., Orfèvre, C.E., Loughrey, A., Rooney P.J. and Rao J.R. 2010. The presence of antibiotic resistant bacteria along the River Lagan. Agricultural Water Management, 19(8): 217-22.

Moussé, W., Noumavo, P.A., Chabi, N. W., Sina H., Tohoyessou, M. G., Ahoy, T.A. and Baba-Moussa L. 2016. Phenotypic and genotypic characterization of extended spectrum β -lactamase *Klebsiella pneumoniae* and fluorescent *Pseudomonas* spp. Food and Nutrition Sciences, 7: 192-204.

Mulamattathil, S.G., Bezuidenhout, C., Mbewe, M. and Ateba, C.N. 2014. Isolation of environmental bacteria from surface and drinking water in Mafikeng, South Africa, and characterization using their antibiotic resistance profiles. Journal of Pathogens, Article ID 371208, pp. 1-11.

Nasreen, M., Sarker, A. and Malek, M.A. 2015. Prevalence and resistance pattern of *Pseudomonas aeruginosa* isolated from surface water. Scientific Research Publishing, 15(5): 74-81.

Nedeljković, N.S., Tiodorović, B., Kocić, B., Ćirić, V., Milojković, M. and Waisi, H. 2015 Serotipovi i rezistencija na antibiotike *P. aeruginosa* iz briseva rana Vojnosanit. Vojnosanitetski Pregled, 72(11): 996-1003.

NM (Moroccan standard ISO 16266) 2012. Producing *Pseudomonas aeruginosa*. International Water Quality: Detection and enumeration of Pseudomonas aeruginosa. Journal of Microbiological Research, 2(3): 208-212.

Nola, M., Njine, T., Sikati, V. F. and Djuikom, E. 2001. Distribution de *P. aeruginosa* et *Aeromonas hydrophila* dans les eaux de la nappe phréatique superficielle en zone équatoriale au Cameroun et relations avec quelques paramètres chimiques du milieu. Revue des Sciences de l'Eau, 14(1) :35-53.

Penna, V.T.C., Martins, S.A.M. and Mazzola, P.G. 2002. Identification of bacteria in drinking and purified water during the monitoring of a typical water purification system. BMC Public Health, 2: 1-11.

Pitondo, S.A., Martins, V. V., Fernandes, A. F. T. and Stehling, E. G. 2014. High level of resistance to Aztreonam and Ticarcillin in *P. aeruginosa* isolated from soil of different crops in Brazil. Science of the Total Environment, 473: 155-158.

Stirling, J., Griffith, M., Blair, I., Cormican, M., Dooley, J.S.G., Goldsmith, C.E., Glover, S.G., Loughrey, A., Lowery, C.J., Matsuda, M. and McClurg, R. 2008. Prevalence of gastrointestinal bacterial pathogens in a population of zoo animals. Zoonoses Public Health, 55(3): 166-172.

WHO (World Health Organization) 2010. Guidelines for Drinking Water Quality. WHO report 4th ed., Available at: http://apps.who.int/iris/bitstream/10665/44584/1/9789241548151_eng.pdf.

Nature Environment and Pollution Technology
An International Quarterly Scientific Journal

p-ISSN: 0972-6268
e-ISSN: 2395-3454

Vol. 18 | No. 4 | pp. 1201-1209 | 2019

Original Research Paper | Open Access

Adsorption of Copper Ions in Aqueous Solution by Montmorillonite-Biochar Composite

Yuanyuan Cai, Yaowei Du, Yue Wang, Jun Song, Bing Liu, Chenhu Zhang and Muqing Qiu†
College of Life Science, Shaoxing University, Shaoxing, 312000, P. R. China
†Corresponding author: Muqing Qiu

Nat. Env. & Poll. Tech.
Website: www.neptjournal.com

Received: 18-12-2018
Accepted: 27-02-2019

Key Words:
Adsorption
Copper ions
Montmorillonite-biochar composite
Peanut shell

ABSTRACT

A composite adsorbent was prepared by montmorillonite and biochar from peanut shell. The adsorption experiment of the Cu^{2+} ions from aqueous solution by the montmorillonite-biochar composite was carried out in detail. The effects of initial concentration of Cu^{2+} ions in aqueous solution and contact time on adsorption efficiency were studied. FTIR spectroscopy, SEM and TEM analyses, standard N_2 adsorption-desorption techniques, EDS and XPS were used to evaluate the physico-chemical, textural and crystalline properties of the montmorillonite-biochar composite. Results showed that the montmorillonite-biochar composite was mesoporous material. The surface of montmorillonite-biochar composite was rough with irregular layer structure. According to the experimental data, pseudo first order kinetics model and pseudo second order kinetics model were applied. The adsorption process fits well with the pseudo second order kinetics model. The predominant process is chemisorption, which involves a sharing of electrons between the adsorbate and the surface of the adsorbent. Adsorption data were correlated well by Freundlich isotherm models and adsorption process was chemical. It is concluded that the montmorillonite-biochar composite can be used as an effective adsorbent for the removal of Cu^{2+} ions from aqueous solutions.

INTRODUCTION

Economic imperatives of productivity and profitability subjected to mining companies and mineral processing industries into products of higher added value significantly reflect the level of pollution by heavy metals. The heavy metals, apart from being hazardous for living organisms when exceeding the specific limits, have accumulating characteristics in nature as they cannot be biodegraded. Removal of heavy metal ions from industrial effluents, drinking water and municipal wastewaters is a matter of serious concern due to their toxicity to various forms of life (Moî se et al. 2017).

Among the variety of heavy metal pollutants of water, copper ions appear and, as other heavy metals, are not degradable and accumulate in the living beings. Moreover, copper is one of the essential elements to human body in trace quantities, but elevated levels of copper may cause various health problems in liver, kidney and the central nervous system (Dalida et al. 2011, Cho et al. 2012). It is necessary to refine wastewaters containing copper ions before their release in the environment.

The heavy metals, having hazardous effects on health, can be treated from wastewater by using various physico-chemical methods (Sevil & Alyüz 2007). Adsorption, ion exchange, chemical settling and reverse osmosis are the most frequently preferred methods. Among them, adsorption receives considerable interest with the high efficiency in heavy metal removal. Although there are many adsorbents used in adsorption methods, activated carbon is the most common one used in wastewater treatment all over the world (Veli & Òztürk 2005). However, its high cost causes restrictions in use (Babel & Kurniawan 2003). For this reason, many studies have been carried out in order to find out effective and low-cost adsorbents. Different adsorbents are used in copper removal such as chitosan (McKay et al. 1989), eutrophic and oligotrophic marsh peat and agricultural wastes like wheat straw and cacao shell (Chen et al. 1990, Saeed et al. 2005, Qiu & Huang 2017).

The major limitation of these common methods is the production of large amount of sludge, which leads to the disposal problem, requires large capital for electricity, less number of metal ions can be removed and in some methods chemicals used are expensive. Adsorption is more advantageous in terms of its simplicity, fastness, high efficiency, regeneration, low concentrations removal, economic and environmental friendliness. These make it a better option than the common methods and create a research interest in developing low-cost adsorbents.

Copper has been removed by various adsorbents such as agricultural and industrial waste, chitosan, natural zeolite,

natural material, modified biopolymers and marine algae (Meunier et al. 2003, Sarma et al. 2015, Hannatu et al. 2017).

Natural clay is evaluated as an appropriate adsorbent due to its low cost and high removal efficiency. Its sorption capabilities come from high surface area and exchange capacities. The negative charge on the structure of clay minerals gives the capability to attract metal ions. In recent years, special attention has been focused on the use of natural resources as alternatives to conventional adsorbents. Among the alternative adsorbents, clay stands out because of its abundance and low cost compared to other adsorbents such as activated charcoal, zeolites and synthetic ion exchange resins. Moreover, clays are materials that can act as Lewis acids and offer a large ion exchange capacity in a layered structure that presents chemical and physical stability and a high specific surface area (Kumar et al. 2015, Zacaroni et al. 2015).

Based on the above considerations, the main objective of this work was to evaluate copper ions in aqueous solution adsorption onto montmorillonite-biochar composite through kinetic and equilibrium studies. In addition, the characterization of the montmorillonite-biochar composite was discussed in detail. The effects of initial concentration of Cu^{2+} ions in aqueous solution and contact time on adsorption efficiency were studied along with the adsorption equilibrium and adsorption kinetics.

MATERIALS AND METHODS

Materials

The montmorillonite was purchased from Shanghai Chemical Co. Ltd. in China and crushed to obtain clay with a diameter less than 50 μm.

The peanut shell was obtained from a local farm in Zhejiang province. It was dried for 24 h at 383 K in a heating oven and milled to obtain powders between 1 mm and 2 mm prior to use. The dried peanut shell was put into a muffle furnace at 873 K for 3 h. They were added into the 250 mL of flask containing 7 mL of distilled water and put into a thermostat water bath and agitated for 2 h. Then, they were dried for 9 h at 383 K in a heating oven and later washed with distilled water into pH value ranging from 7 to 9. They were dried for 5 h at 383 K in a heating oven again, ground and sifted into 100 meshes to finally obtain the experimental biochar.

The 10 wt % montmorillonite suspension was prepared by dispersing its powder in distilled water and stirring for 24 h. Then, the biochar from peanut shell was slowly added to the montmorillonite suspension. During the mixing process, the weight ratio of montmorillonite to biochar was kept 1:1. The reaction mixture was stirred for 2 h, separated by centrifugation and washed three times with distilled water. Then, they were dried at 383 K for 12 h to obtain the montmorillonite-biochar composite for the adsorption experiment.

All the chemicals in the study were of analytical grade and used without further purification. The wastewater of Cu^{2+} ions in aqueous solution was prepared from $CuSO_4 \cdot 5H_2O$.

Experimental Methods

Adsorption experiments were conducted in a set of 250 mL Erlenmeyer flasks containing the montmorillonite-biochar composite and 100 mL of Cu^{2+} ion solutions with various initial concentrations. The initial pH was adjusted with 1 mol/L HCl or 1 mol/L NaOH. The flasks were placed in a shaker at a constant temperature and 200 rpm. The samples were filtered and analysed.

Analytical Methods

The textural characteristics of the montmorillonite-biochar composite including surface area, pore volume and pore size distribution were determined using standard N_2 adsorption-desorption techniques. Surface morphology of the samples was determined by scanning electron microscopy (SEM) equipped with an energy dispersive X-ray fluorescence spectroscopy (EDS, Oxford Instruments Link ISIS) for analysing surface elements and transmission electron microscopy (TEM). The montmorillonite-biochar composite was also characterized by FTIR spectroscopy to identify the type of chemical bonds in the molecules present. The samples were also characterized by XPS (Thermo ESCALAB 250 electron spectrometer) using a multidetection analyser with Mg K_a radiation (1253.6 eV) under 10^{-9} Torr pressure. All the peaks were referenced with the C 1s line at 284.4 eV and fitted in terms of the XPSPEAK41 mode. The concentration of Cu^{2+} ions was obtained by atomic absorption spectrophotometry (AAS).

The amount of adsorbed Cu^{2+} ion q_t (mg/g) at different times, was calculated as follows:

$$q_t = \frac{(C_0 - C_t) \times V}{m} \quad \ldots(1)$$

Where, C_0 and C_t (mg/L) are the initial and equilibrium liquid-phase concentrations of Cu^{2+} ions respectively. V (L) is the solution volume and m (g) is the mass of adsorbent used.

Statistical Analyses of Data

All experiments were repeated in duplicate and the results were represented as the mean with standard deviation (SD). The value of the SD was calculated by Excel Software. All

error estimates given in the text and error bars in figures are standard deviation of means (mean ± SD). All statistical significances were noted at $\alpha = 0.05$ unless otherwise noted.

RESULTS AND DISCUSSION

Characterization of Montmorillonite-Biochar Composites

The textural characteristics of the montmorillonite-biochar composite including surface area, pore volume, and pore size distribution were determined using standard N_2 adsorption-desorption techniques. The surface area, pore volume and average pore size of montmorillonite-biochar composites are 6.1784 m^2/g, 0.01971 cm^3/g and 12.76 nm respectively. The International Union of Pure and Applied Chemistry-IUPAC (1985) classified the diameter of pores with width greater than 50 nm as macropores, pores from 2 to 50 nm width as mesopores, and those with diameter of less than 2 nm as micropores. Therefore, it tends to be more suitable for mesoporous materials. The characterization of montmorillonite-biochar composites can contribute to metal adsorption (Chen et al. 2008).

The micrographs are shown in Fig.1. A heterogeneous grain size was observed in the montmorillonite-biochar composite. The surface of montmorillonite-biochar composite is rough with irregular layer structure.

The montmorillonite-biochar composite was also characterized by EDS. Results of EDS analyses are shown in Fig. 2 and Table 1. It shows that C, O and Si are the major constituents in montmorillonite-biochar composite while Al, Mg, Ca, K and Fe are the minor substitute element in this layer silicate mineral. So, the montmorillonite-biochar composite possesses a negatively charged surface which

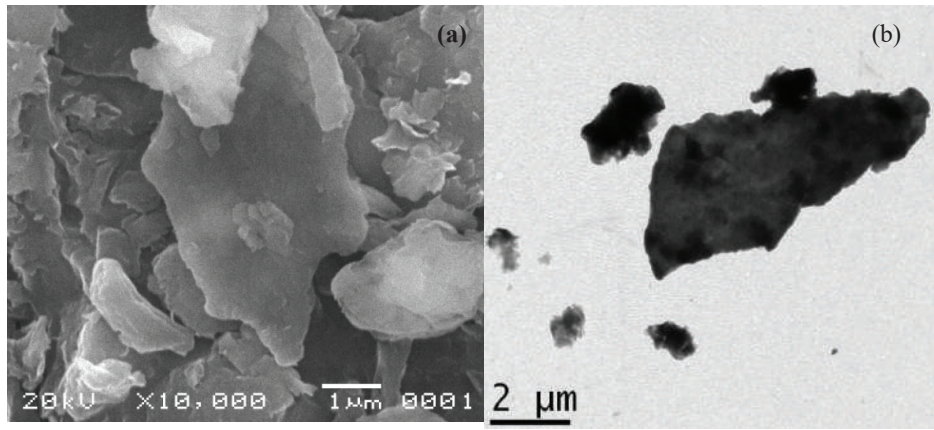

Fig. 1: SEM (a) and TEM (b) of the montmorillonite-biochar composite.

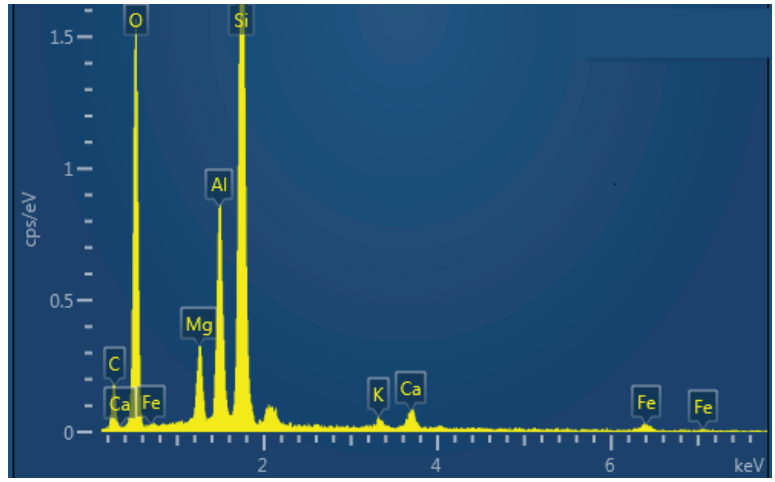

Fig. 2: EDS spectra of the montmorillonite-biochar composite.

Table 1: Chemical composition from EDS analysis.

Element	C	O	Mg	Al	Si	K	Ca	Fe
Components (%, wt)	21.40	54.96	2.34	5.51	14.04	0.29	0.79	0.67

is favourable for cationic ion adsorption (Bertagnolli et al. 2011).

Fig. 3 presents the FTIR adsorption bands of the montmorillonite-biochar composite. As shown in Fig. 3, the bands at 3417 cm^{-1}, 1837 cm^{-1} and 1511 cm^{-1} could be attributed to the stretching vibration of *–OH*, *–C=O* and *– C= C–* groups, respectively. The peaks at 1400 cm^{-1} and 1034 cm^{-1} were ascribed to *–OH* and *–C–O* groups. The bands at 839 cm^{-1}, 796 cm^{-1}, 520 cm^{-1} and 488 cm^{-1} are due to *C–O* and *–O–* vibrations (Lin & Juang 2002, Weng et al. 2007).

The montmorillonite-biochar composite was also characterized by XPS (Thermo ESCALAB 250 electron spectrometer) using a multidetection analyser with Mg K_a radiation (1253.6 eV) under 10^{-9} Torr pressure. The results are shown in Fig. 4.

As shown in Fig. 4, the C 1s XPS spectra of montmorillonite-biochar composites can be deconvoluted into three bands at 295.2, 292.3 and 284.4 eV, which were assigned to *C / N–O*, *C–O* and *C–*, respectively.

Adsorption Studies

Effect of contact time: In order to study the effect of contact time on the adsorption of Cu^{2+} ions by the montmorillonite-biochar composite, the samples were determined at 5, 10, 15, 20, 30, 40, 50, 60, 120, 180 and 240 min. The experimental results are shown in Fig. 5. At first stage, the adsorption capacity of Cu^{2+} ions increased with contact time quickly. After 30 min, there is no considerable change in Cu^{2+} ions removal. The optimum time for copper removal was 40 min. As a result of the experimental studies, it is seen that high efficiency for copper adsorption can be obtained at short time periods.

Effect of initial concentration: As presented in Fig. 6, the adsorption capacity for Cu^{2+} ions in aqueous solution increases with increase in the initial concentration of Cu^{2+} ions.

It is clear that the removal of heavy metal depends on the initial concentration. This is due to the fact that the initial Cu^{2+} ions concentration provided the necessary driving force to overcome the resistance to the mass transfer of Cu^{2+} ions between the solution and adsorbent (Langmuir 1918).

Adsorption Kinetics

In order to investigate the adsorption kinetics and mechanism, two kinetic models were used. They are the pseudo

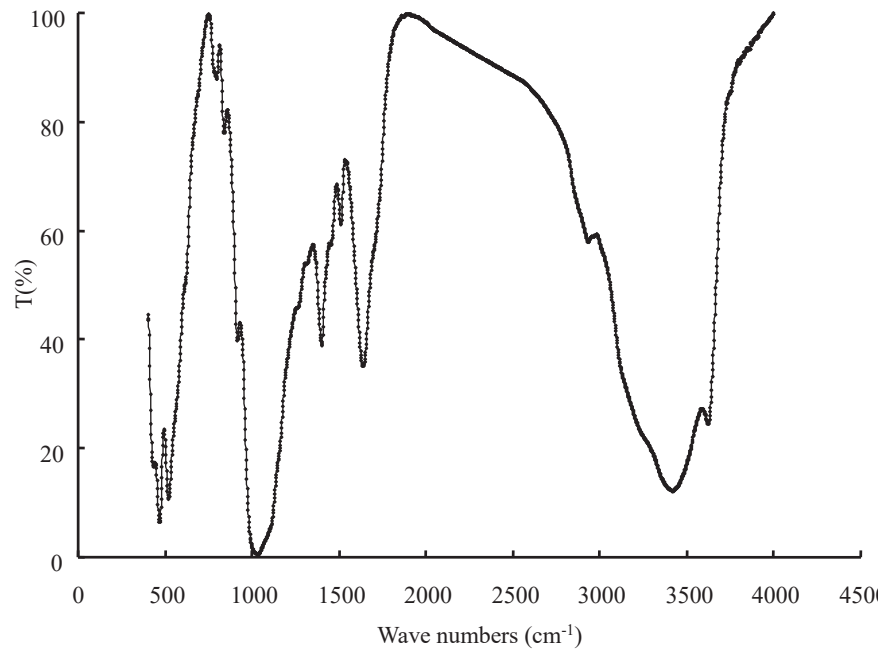

Fig. 3: FTIR spectra of the montmorillonite-biochar composite.

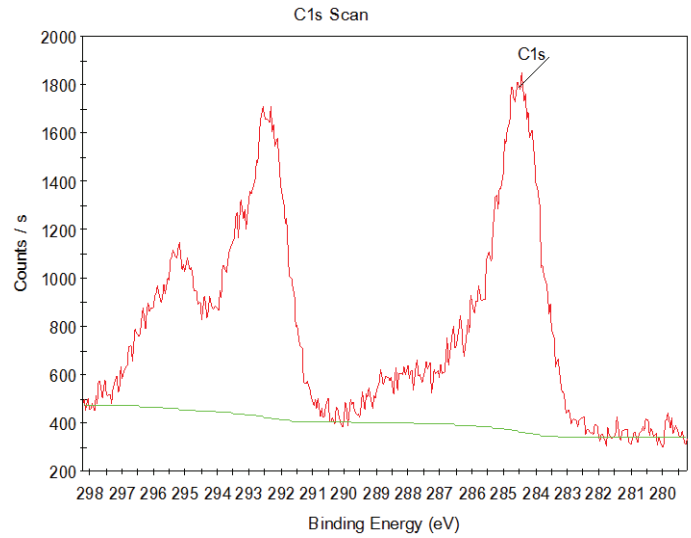

Fig. 4: XPS spectra of the montmorillonite-biochar composite.

first order kinetic model and pseudo second order kinetic model.

Pseudo first order kinetics model is generally expressed as follows (Ho 2004):

$$\frac{dq_t}{dt} = k_1\left(q_e - q_t\right) \qquad \ldots(2)$$

Where k_1 (min^{-1}) is the adsorption rate constant for the first order adsorption, q_t is the amount of copper ion adsorbed at time t (mg/g) and q_e is the amount of copper ion adsorbed at saturation (mg/g).

The integration of the Eq. (2) gives the following expression:

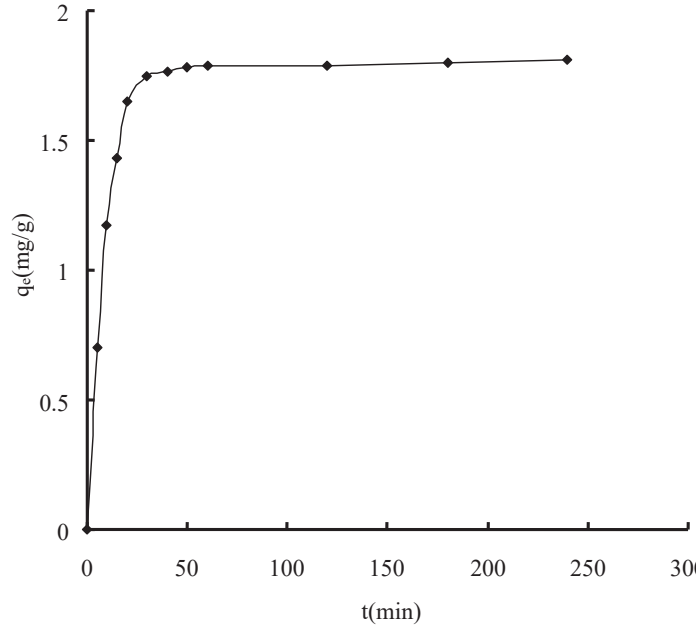

Fig. 5: Effect of contact time on the removal of copper ions by the montmorillonite-biochar composite. Initial concentration of Cu2+ ions 40 mg/L, dosage of the montmorillonite-biochar composite 4 g/L, pH 4 and temperature 303 K.

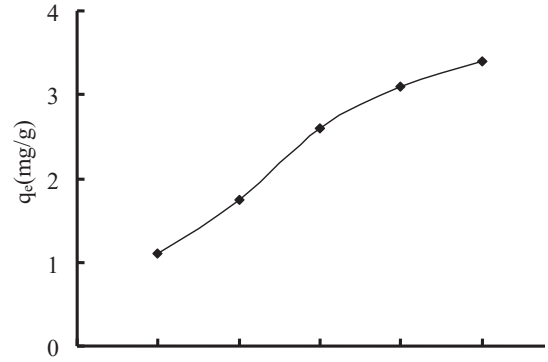

Fig. 6: Effect of initial concentration of Cu^{2+} ions on the removal of Cu^{2+} ions by the montmorillonite-biochar composite. Dosage of the montmorillonite-biochar composite 4 g/L, pH 4, contact time 180 min and temperature 303 K.

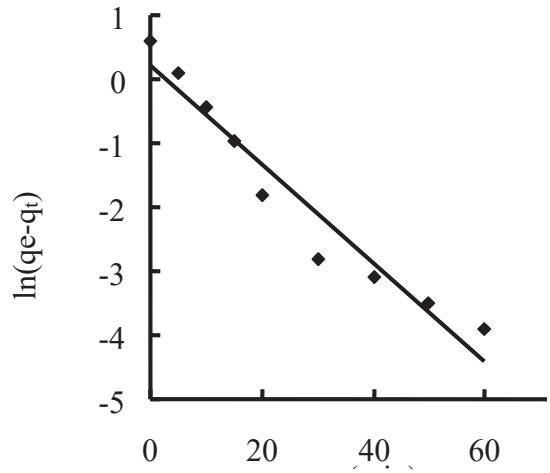

Fig. 7: Pseudo first order kinetics of Cu^{2+} ions in aqueous solution adsorption by the montmorillonite-biochar composite.

$$\ln\left(q_e - q_t\right) = -k_1 t + C_1 \quad \ldots(3)$$

Where, C_1 is the integration constant for first order reaction kinetic.

If it is supposed that $q = 0$ at $t = 0$, then:

$$\ln\left(q_e - q_t\right) = \ln q_e - k_1 t \quad \ldots(4)$$

Pseudo second order kinetics model is generally expressed as follows (Ho & McKay 1998):

$$\frac{dq_t}{dt} = k_2\left(q_e - q_t\right)^2 \quad \ldots(5)$$

Where k_2 ($g \cdot mg^{-1} \cdot min^{-1}$) is the second order reaction constant. The integration of the Eq. (5) gives the following expression:

$$\frac{t}{q_t} = \frac{1}{k_2 q_e^2} + \frac{t}{q_e} \quad \ldots(6)$$

According to experimental data, the rate constants k_1, k_2 and q_e were calculated from the slopes and intercepts of the linear plot of $\ln(q_e - q_t)$ or $\frac{t}{q_t}$ respectively (Fig.7 and Fig. 8). The values of k_1, k_2 and q_e are listed in Table 2.

Table 2: Parameter values and correlation coefficients of pseudo first order kinetics model and pseudo second order kinetics model for the adsorption of Cu^{2+} ion onto the montmorillonite-biochar composite.

Pseudo first order kinetic model			Pseudo second order kinetic model		
k_1(min)	q_e(mg/g)	R^2	k_2(mg/g·min)	q_e(mg/g)	R^2
0.077	1.23	0.94	0.071	2.04	0.99

From Table 2, it can be shown that the adsorption process fits well with the pseudo second order kinetics model according to the value of R^2. It implies that the predominant

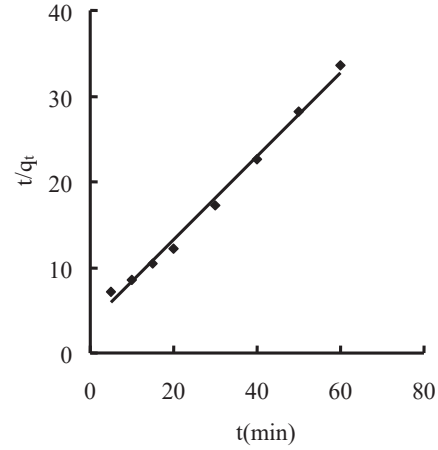

Fig. 8: Pseudo second order kinetics of Cu^{2+} ions in aqueous solution adsorption by the montmorillonite-biochar composite.

process is chemisorption, which involves a sharing of electrons between the adsorbate and the surface of the adsorbent (Vanessa et al. 2015).

Adsorption Isotherms

For solid-liquid system, adsorption isotherm is important in description of adsorption behaviour. To research on the mechanistic parameters associated with Cd^{2+} ion adsorption, the results obtained by the adsorption experiments were analysed by Freundlich model (Freundlich 1918) and Langmuir model (Langmuir 1918).

The Langmuir isotherm equation is represented by the following Eq. (7):

$$q_e = \frac{q_m K_L C_e}{1 + K_L C_e} \quad \ldots(7)$$

The integration of the Eq.(7) gives the following expression:

$$\frac{C_e}{q_e} = \frac{1}{K_L} q_m + \frac{C_e}{q_m} \quad \ldots(8)$$

Where, C_e is the equilibrium concentration of Cu^{2+} ions (mg/L), q_e is the amount of Cu^{2+} ion adsorbed (mg/g), q_m is the maximum adsorption capacity of Cu^{2+} ion (mg/g), and K_L is the Langmuir adsorption equilibrium constant (L/mg) related to the affinity of the binding sites.

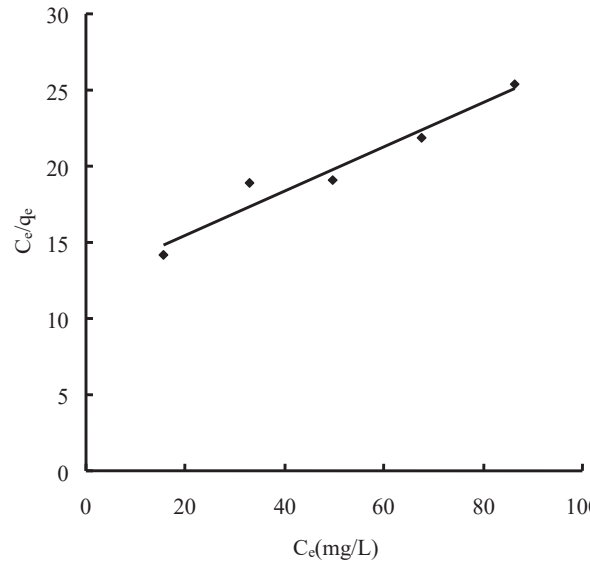

Fig. 9: Langmuir plot for the adsorption of Cu^{2+} ions onto the montmorillonite-biochar composite.

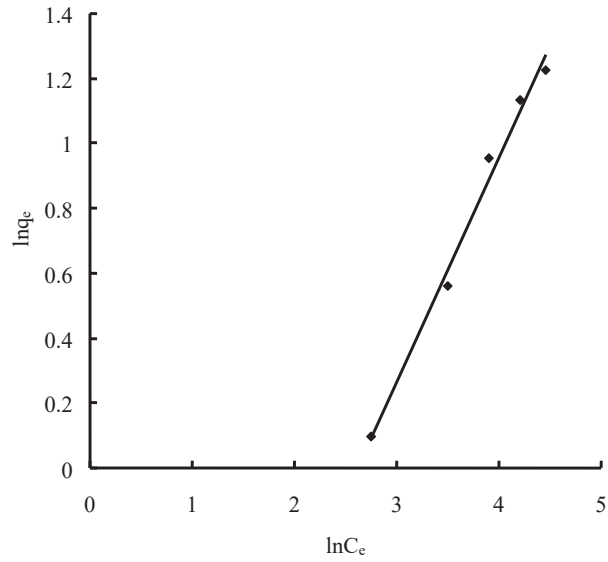

Fig. 10: Freundlich plot for the adsorption of Cu^{2+} ions onto the montmorillonite-biochar composite.

The Freundlich isotherm equation is described by the following Eq. (9):

$$q_e = K_F C_e^{\frac{1}{n}} \quad \ldots(9)$$

The integration of the Eq.(9) gives the following expression:

$$\ln q_e = \ln K_F + \frac{1}{n} \ln C_e \quad \ldots(10)$$

Where, K_F and n are the Freundlich adsorption isotherm constants, which are indicators of adsorption capacity and adsorption intensity respectively.

Two isotherm models were applied to experimental data, and results are shown in Fig. 9, Fig. 10 and Table 3.

Table 3 Parameters of Langmuir isotherm model and Freundlich isotherm model for the adsorption of Cu^{2+} ion onto the montmorillonite-biochar composite

Langmuir isotherm model			Freundlich isotherm model		
q_m(mg/g)	K_L	R^2	K_F	n	R^2
6.92	0.55	0.948	0.17	1.45	0.989

The Freundlich constant (n) for Cu^{2+} ions is within the range of 1 and 10, suggesting the adsorption of Cu^{2+} ions on the adsorbents is favourable (Das et al. 2011). The correlation coefficient (R^2) of Freundlich model for Cu^{2+} ions is higher than that of Langmuir, indicating that it has high degrees of heterogeneous distribution of active sites on the surface, presumably due to the uneven surface distribution. The adsorption process is chemical.

CONCLUSIONS

A composite adsorbent was prepared by montmorillonite and biochar from peanut shell. The adsorption experiment of the Cu^{2+} ions from aqueous solution by the montmorillonite-biochar composite was carried out in detail. Results showed that the montmorillonite-biochar composite was mesoporous material. The surface of montmorillonite-biochar composite has roughness and irregular layer structure. It is also determined that the adsorption is completed in relatively short time periods. The Cu^{2+} ions in aqueous solution adsorption onto the montmorillonite-biochar composite are well described with the pseudo second order reaction kinetics and Freundlich isotherm models respectively.

ACKNOWLEDGEMENTS

This study was financially supported by the Project of Science and Technology Plan in Shaoxing City (2017B70058).

REFERENCES

Babel, S. and Kurniawan, T.A. 2003. Low-cost adsorbents for heavy metal uptake from contaminated water. J. Hazard. Mater., 9: 219-243.

Bertagnolli, C., Kleinübin, S.J. and Silva, M.G.C. 2011. Preparation and characterization of a Brazilian bentonite clay for removal of copper in porous beds. Appl. Clay Sci., 53: 73-79.

Chen, W.J., Hsiao, L.C. and Chen, K.K.Y. 2008. Metal desorption from copper(II)/nickel(II)-spiked kaolin as a soil component using plant-derived saponin biosurfactant. Process Biochem., 43: 488-498.

Chen, X.H., Gosset, T. and Thevenot, D.R. 1990. Batch copper ion binding and exchange properties of peat. Water Res., 24: 1463-1471.

Cho, D.W., Jeon, B.H., Chon, C.M., Kim, Y.J., Franklin, W.S., Lee, E.S. and Song, H. 2012. A novel chitosan/clay/magnetite composite for

adsorption of Cu(II) and As(V). Chem. Eng. J., 200-202: 654-662.
Dalida, M.L.P., Mariano, A.F.V., Futalan, C.M., Kan, C.C., Tsai, W.C. and Wan, M.W. 2011. Adsorptive removal of Cu(II) from aqueous solutions using non-crosslinked and crosslinked chitosan-coated bentonite beads. Desalination, 275: 154-159.
Das, D., Sureshkumar, M.K., Radhakrishnan, K., Nuwar, J. and Pillai, C.G.S. 2011. Adsorptive removal of Cr(III) from aqueous solution using tripolyphosphate cross-linked chitosan beads. J. Radioanal. Nucl. Ch., 289: 275-285.
Freundlich, H.M.F. 1918. Over the adsorption in solution. J. Phys. Chem., 57: 385-470.
Hameed, B.H. and Ahmad, A.A. 2009. Batch adsorption of methylene blue from aqueous solution by garlic peel, an agricultural waste biomass. J. Hazard. Mater., 164: 870-875.
Hannatu, A. S., Mansor, B.A., Mohd, Z.H., Ibrahim, N.A., Musaa, A. and Tawfik, A.S. 2017. Nanocomposite of ZnO with montmorillonite for removal of lead and copper ions from aqueous solutions. Process Saf. Environ., 109: 97-105.
Ho, Y.S. 2004. Citation review of Lagergreen kinetic rate equation on adsorption reaction. Scientometrics, 59: 171-177.
Ho, Y.S. and McKay, G. 1998. Sorption of dye from aqueous solution by peat. J. Chem. Eng., 70: 115-124.
Kaya, A. and Őren, A.H. 2005. Adsorption of zinc from aqueous solutions to bentonite. J. Hazard. Mater. B, 125: 183-189.
Kumar, J.P., Ramacharyulu, P.V.R.K., Prasad, G.K. and Singh, B. 2015. Montmorillonites supported with metal oxide nanoparticles for decontamination of sulfur mustard. Appl. Clay Sci., 117: 263-272.
Langmuir, I. 1918. The adsorption of gases on plane surfaces of glass, mica and platinum. J. Am. Chem. Soc., 40: 1361-1403.
Lin, S.H. and Juang, R.S. 2002. Heavy metal removal from water by sorption using surfactant-modified montmorillonite. J. Hazard. Mater. B, 92: 315-326.
McKay, G., Blair, H.S. and Findon, A. 1989. Equilibrium studies for the sorption of metal-ions onto chitosan. Ind. J. Chem., 28A: 356-360.
Meunier, N., Laroulandie, J., Blais, J.F. and Tyagi, R.D. 2003. Cacao shells for heavy metal removal from acidic solutions. J. Biores. Technol., 90: 255-263.
Moĵse, F., Hervé, F.N., Samuel, L., Felipe, A.C., Luís, O.B.B. and Nito, A.D. 2017. Adsorption of copper (II) onto cameroonian clay modified by non-thermal plasma: Characterization, chemical equilibrium and thermodynamic studies. Appl. Clay Sci., 142: 136-144.
Qiu, M.Q. and Huang, P. 2017. Kinetic and thermodynamic studies on the adsorption of zinc ions from aqueous solution by the blast furnace slag. Nature Environ. Poll. Technol., 16: 639-642.
Saeed, A., Iqbal, M. and Akhtar, W. 2005. Removal and recovery of lead (II) from single and multimetal (Cd, Cu, Ni, Zn) solutions by crop milling waste (black gram husk). J. Hazard. Mater. B, 117: 65-73.
Sarma, P.J., Kumar, R. and Pakshirajan, K. 2015. Batch and continuous removal of copper and lead from aqueous solution using cheaply available agricultural waste materials. Int. J. Environ. Res., 9: 635-648.
Sevil, V. and Alyüz, B. 2007. Adsorption of copper and zinc from aqueous solutions by using natural clay. J. Hazard. Mater., 149: 226-233.
Vanessa, E.D.A., Jarbas, R.R., Solange, C., Giberto, A. and Marco, T.G. 2015. Montmorillonite and vermiculite as solid phases for the preconcentration of trace elements in natural waters: Adsorption and desorption studies of As, Ba, Cu, Cd, Co, Cr, Mn, Ni, Pb, Sr, V, and Zn. Appl. Clay Sci., 99: 289-296.
Veli, S. and Őztürk, T. 2005. Kinetic modeling of adsorption of reactive azo dye on powdered activated carbon and pumice. Fresenius Environ. Bull., 14: 212-218.
Weng, C.H., Tsai, C.Z., Chu, S.H. and Sharma, Y.C. 2007. Adsorption characteristics of copper (II) onto spent activated clay. Sep. Purif. Technol., 54: 187-197.
Zacaroni, L.M., Magriotis, Z.M., Cardoso, M.G., Santiagoa, W.D., Mendonça, J.G., Vieira, S.S. and Nelson, D.L. 2015. Natural clay and commercial activated charcoal: Properties and application for the removal of copper from cachaça. Food Control, 47: 536-544.

Nature Environment and Pollution Technology
An International Quarterly Scientific Journal

p-ISSN: 0972-6268
e-ISSN: 2395-3454

Vol. 18 | No. 4 | pp. 1211-1218 | 2019

Original Research Paper | Open Access

Retrieval of the Canopy Chlorophyll Density of Winter Wheat from Canopy Spectra Using Continuous Wavelet Analysis

Qingkong Cai*, Erjun Li†, Jiechen Pan* and Chao Chen***

*College of Civil Engineering, Henan University of Engineering, Zhengzhou, Henan 451191, China
**College of Human and Social Sciences, Henan University of Engineering, Zhengzhou, Henan 451191, China
†Corresponding author: Erjun LI

Nat. Env. & Poll. Tech.
Website: www.neptjournal.com

Received: 15-09-2019
Accepted: 18-10-2019

Key Words:
Canopy chlorophyll density
Continuous wavelet analysis
Winter wheat
Spectral indices
Hyperspectral remote sensing

ABSTRACT

Continuous wavelet analysis (CWA) has been applied to leaf-scale spectral data for quantifying leaf chlorophyll content, but its application to canopy-scale spectral data for estimating the canopy chlorophyll density (CCD) of winter wheat at different growth stages requires further analysis. This study aims to estimate CCD by applying CWA to the canopy spectra of 185 samples from Guanzhong Plain, China. The five most informative wavelet features related to CCD were identified using the CWA method. Meanwhile, 10 commonly used spectral indices were selected to compare with the CWA method. Two partial least square regression (PLSR) models based on wavelet features and spectral indices were developed and compared. Results showed that the PLSR model using wavelet features (R^2 = 0.64, RMSE = 0.43 g/m^2) was better than that using spectral indices (R^2 = 0.57, RMSE = 0.48 g/m^2) and wavelet features were less sensitive to the growth stage variation than spectral indices. This result suggested that the CWA approach can derive robust wavelet features and was more effective than spectral indices for predicting CCD from canopy-scale spectral data for an agricultural ecosystem.

INTRODUCTION

Accurate quantitative estimates of key biophysical variables are crucial for land surface models that quantify the exchange of energy and matter between the land surface and lower atmosphere (Houborg et al. 2008). Key biophysical variables include the canopy chlorophyll density (CCD), which is defined as the total amount of foliage pigment per unit ground area, that assists in determining photosynthetic capacity and predicting productivity (Nijs et al.1995). Therefore, an accurate monitor of CCD is significant for precise agriculture fertilization, which can effectively avoid the gradual decline of ecological environment caused by the excessive inputs of chemical fertilizer.

Remote sensing techniques for estimating vegetation biophysical variables have been based on either the empirical statistical approach that relates canopy variables to single spectral reflectance or vegetation indices (VIs) or the inversion of a physically based model (Boegh et al. 2002, Houborg et al. 2008). The VI approach is highly preferred for large-scale remote sensing applications due to its simplicity. Previous studies have shown that reflectance in the green, red, red edge, and near-infrared spectral regions is sensitive to a wide range of chlorophyll content in leaves and canopies (Colombo et al. 2003). VIs based on these spectral regions have been used successfully (Gitelson et al. 2005). However, the spectral index approach has apparent limitations. On the one hand, spectral indices use only two or three wavebands, not the entire spectral information provided from a reflectance curve. On the other hand, spectral reflectance relationships are site-, time-, and crop-specific, making the use of a single relationship for an entire region unfeasible (Houborg et al. 2008, Buschmann et al. 1993). The physically based model describes the transfer and interaction of radiation inside the canopy on the basis of physical laws and thus provides an explicit connection between the biophysical variables and canopy reflectance. However, this method is computationally intensive and complex and has an ill-posed nature of model inversion (Gitelson et al. 1996), thereby limiting its widespread practical use.

Continuous wavelet analysis (CWA) can decompose reflectance spectra into a number of scale components and permits the extraction of wavelet features that capture useful spectral information pertinent to quantifying forest biophysical parameters, leaf water content, and leaf chlorophyll content (Gitelson et al. 1996, Daughtry et al. 2000, Dash et al. 2004). However, previous research is limited by applying CWA to leaf reflectance spectra measured in laboratories and simulated with radiative transfer models (Daughtry et al. 2000, Atzberger 2004). Meanwhile, the efficiency of the CWA approach in estimating the CCD of winter wheat at

different growth stages from the canopy spectra still requires further study. The canopy spectra are more complex than the leaf spectra due to a number of complicating factors, such as soil background and canopy structural variation (Broge et al. 2002), which make CCD retrieval challenging. In addition, although several studies have established models for estimating CCD, most of them have focused on using single growth stage data and have not validated the sensitivity of their methods to the growth stage variation in canopy spectra, thereby limiting the widespread application of their methods.

The present study aims to investigate the spectroscopic estimation of CCD by applying the CWA method to the canopy spectra of 185 winter wheat samples from two growth stages. We apply two partial least square regression (PLSR) models based on the most informative wavelet features and optimal spectral indices to validate the sensitivity to the growth stage variation of winter wheat in CCD compared with field measurements. Specifically, the objectives of this study are as follows: (1) to select the spectral region that is sensitive to chlorophyll content and (2) to propose a strategy for improving the estimation accuracy of chlorophyll content.

DATA COLLECTION

Study Area

The three core experiment sites, namely, Juliang, Xinglin, and Rougu, are located in the Guanzhong Plain of Shanxi Province, China. They cover areas of 2.33, 6.67, and 2.00 km^2, respectively. The altitude ranges from 325 m to 800 m. The area has a monsoon climate with a hot summer and cool winter. The mean annual temperature is 12.9°C, and the mean annual precipitation is 635.1 mm with marked seasonal variations. Winter wheat is the main crop type in the area, and the main soil types are loam, clay loam, and medium. The entire growth period of winter wheat is 225 days.

Two field measurements were conducted at the growth cycle of winter wheat in 2013: one in the jointing stage (from March 31 to April 1 of 2013) and the other in the grain filling stage (from May 27 to May 28 of 2013). Sample sites were selected where soil and canopy conditions were fairly homogeneous in surrounding areas on scales of tens of meters and where the vegetation appeared healthy and capable of surviving through the experiment. The coordinate of each site was recorded with a differential GPS (Trimble 332, USA).

Canopy Hyperspectral Measurements

Canopy spectra were measured using an ASD FieldSpec FR spectroradiometer (ASD, Boulder, USA) ranging 350-2500 nm between 10:00 a.m. and 14:00 p.m. in local time (GMT+8), when the sky was slightly cloudy or had no cloud. Care was taken to avoid measuring the canopy spectra while the clouds were passing overhead. The detector was positioned vertically downward from a height of 50 cm upon the canopy. Before the canopy spectra were collected, the instrument was optimized and calibrated with a white panel (99% reflectance). To reduce instrument noise effect on the spectrum measurement, canopy spectra were measured 10 times at each point, and the average values were used as the last results. To eliminate noise effects in the data, the reflectance data were smoothed using a weighted mean moving average over a 5 nm sample. This method provided sufficient smoothing to the reflectance data without loss of fine spectral detail information (Liao et al. 2013). Due to the strong absorption effect of vapor and carbon dioxide, 350-950 nm was selected as effective data for the subsequent analysis.

Measurement of Pigments and Leaf Area Index (LAI)

A portable SPAD-502 chlorophyll meter (Minolta, Spain) was used for the nondestructive measurements of leaf chlorophyll content. At each plot, the first and second leaves from the top of the wheat were measured 10 times each, and the average values were calculated as the final SPAD. However, to use the unit-less SPAD values for validating field-based leaf chlorophyll estimates, the SPAD value must be converted to leaf chlorophyll content. Previous research has shown that the determination of leaf chlorophyll content from the same SPAD-502 meter appears to be independent of species, which was theoretically justified by Markwell (Baret et al. 1991). Thus, we used the exponential equation developed by Markwell to convert SPAD-502 field measurements into leaf chlorophyll content ($\mu g/cm^2$):

$$C_{ab} = 6.34299 \cdot \exp\left(SPAD \cdot 0.04379\right) - 6.10629 \left(RMSD = 5.4\,\mu g/cm^2\right) \quad \ldots(1)$$

Here C_{ab} is the leaf chlorophyll content. *LAI*, which scales the leaf chlorophyll content from leaf to canopy levels, was measured using LAI-2000 Plant Canopy Analyzer (LI-COR, USA). The analyzer compares the light levels above and below the canopy, which were detected in five conical rings, to infer the LAI and characteristics of the canopy architecture (Jacquemoud et al. 2000). LAI-2000 was programmed to average four observations into a single value by using one measurement obtained above the canopy and four beneath the canopy: in the row, 1/4, 1/2, and 3/4 of the way across the row. This approach provided a good spatial average for row crops of partial cover. Then, the CCD was determined as

$$CCD = C_{ab} \cdot LAI \quad \ldots(2)$$

Here, the unit of CCD is g/m^2. We eventually acquired the CCD data of two complete growth stages for 77 samples in the jointing stage and 108 samples in the grain filling stage.

RESEARCH METHODOLOGY

Continuous Wavelet Transform (CWT)

Wavelet transform is a powerful signal processing tool that has been successfully used in remote sensing image processing to extract information from various scales (Simhadri et al. 1998); it includes two variations: discrete wavelet transform (DWT) and CWT (Dash et al. 2004). The CWT can decompose a signal at a continuum of positions, and CWT outputs can be easily interpreted. In this study, we used CWT to extract spectral information for CCD estimation.

The CWT is a linear operation that uses a mother wavelet function to convert a hyperspectral reflectance spectrum into sets of coefficients (Cheng et al.,2012). The main equation of wavelet transformation is as follows:

$$\psi_{a,b}(\lambda) = \frac{1}{\sqrt{a}}\psi\left(\frac{\lambda - b}{a}\right) \quad \ldots(3)$$

Here a and b are positive numbers. a represents the scaling factor defining the width of the wavelet and b is the shifting factor determining the position. The CWT output is given by (Cheng et al. 2014).

$$W_f(a,b) = \left\langle f, \psi_{a,b} \right\rangle = \int_{-\infty}^{+\infty} f(\lambda)\psi_{a,b}(\lambda)\, d_\lambda \quad \ldots(4)$$

Here $f(\lambda)(\lambda=1,2,\ldots, n, n$ is the number of spectral bands and herein $n = 601)$ is the reflectance spectrum. $W_f(a_i, b_j)$ $(i = 1,2,\cdots,m, j = 1,2,\cdots,n)$ represents the CWT coefficients. The CWT coefficients constitute a 2D scalogram, in which one dimension is scale and the other is wavelength. Previous research has reported that the shape of the absorption features of vegetation is similar to a Gaussian or quasi-Gaussian function (Combal et al. 2002). Therefore, the second derivative of Gaussian, also known as the Mexican hat, has been used as the mother wavelet basis (Broge et al. 2002, Combal et al. 2002). In the present study, the canopy spectra ranged from 350 nm to 950 nm, and 601 bands were available. Any scale greater than $2^9 = 512$ was discarded because decomposed components at high scales did not carry meaningful spectral information. All CWT operations were performed using Matlab 2010a (Natick, MA, USA).

Wavelet Feature Selection

A squared correlation coefficient (R^2) was calculated by the Pearson's linear correlations between elements of wavelet

Table 1: Spectral indices for predicting canopy chlorophyll density.

Spectral index	Acronym	Formula	Literature
Modified chlorophyll absorption reflectance index	*MCARI*	$\left[(R_{700} - R_{670}) - 0.2(R_{700} - R_{550})\right] / (R_{700}/R_{670})$	Daughtry et al.,2000
Simple ratio	*SR*	R_{NIR}/R_{Red}	Baret et al.,1991
Transformed chlorophyll absorption in reflectance index	*TCARI*	$3\left[(R_{700} - R_{670}) - 0.2(R_{700} - R_{550})\frac{R_{700}}{R_{670}}\right]$	Haboudane et al.,2002
Structure insensitive pigment index	*SIPI*	$(R_{800} - R_{445}) / (R_{800} - R_{680})$	Peñuelas et al.,1999
Chlorophyll index using green reflectance	CHL_{green}	$\frac{R_{760-800}}{R_{540-560}} - 1$	Gitelson et al.,2006
Chlorophyll index using red edge reflectance	$CHL_{red\ edge}$	$\frac{R_{760-800}}{R_{540-560}} - 1$	Gitelson et al.,2006
Modified normalized difference	*mND*705	$(R_{750} - R_{705}) / (R_{750} + R_{705} - 2R_{445})$	Sims et al.,2002
Normalized difference vegetation index	*NDVI*	$(R_{NIR} - R_{Red}) / (R_{NIR} + R_{Red})$	Rouse et al.,1973
Normalized pigment chlorophyll ratio index	*NPCI*	$(R_{680} - R_{430}) / (R_{680} + R_{430})$	Riedell et al.,1999
Photochemical reflectance index	*PRI*	$(R_{531} - R_{570}) / (R_{531} + R_{570})$	Gamon et al.,1997

Table 2: Descriptive statistics of CCD (g/m^2) at two growth stages of 2013.

Growth period	Number of plots	Mean ± s.d.	Min	Max	Coefficient of variation
Jointing stage	77	2.14±0.68	0.46	3.81	0.32
Grain filling stage	108	2.72±0.68	0.92	4.26	0.25
Two growth stages	185	2.48±0.74	0.46	4.26	0.30

power and CCD of all spectrum samples to identify features that are sensitive to variations in CCD. The most informative features for CCD were obtained by (1) retaining features where the correlations were statistically significant (P Value<0.0001) and (2) ranking these features in descending order on the basis of the R^2 values; a threshold was applied to delineate the top 1% features that mostly strongly correlated with CCD (Gitelson et al. 1996, Daughtry et al. 2000, Broge et al. 2002). These features formed several scattered feature regions. The feature with the maximum R^2 within each region was determined and expressed as (wavelength in nm, scale). Eventually, a small number of sparsely distributed features were selected as the optimal wavelet features related to changes in CCD.

Calculation of Spectral Indices

Several spectral indices specifically designed to quantify chlorophyll concentration were calculated (Table 1). These spectral indices were derived from previous studies that tested various species, leaf structures, developmental stages, and spectral indices (Gitelson et al. 2005, Blackburn et al. 2008, Ullah et al. 2012, Asner et al. 2008, Ollinger 2011). Broad-band spectral indices, such as *SR* and *NDVI*, were included because of their frequent use in monitoring vegetation status (Wu et al. 2014). The broad-band reflectance spectra of Landsat-5 TM were adopted as the standard for integrating original hyperspectral reflectance. In addition to the above-mentioned spectral indices, the other hyperspectral indices were calculated on the basis of the wavelengths given in the formulas.

Here, R_λ is the reflectance at wavelength λ.

RESULTS AND ANALYSIS

Growth stage variation in CCD and canopy reflectance properties

The CCD and canopy reflectance properties change as growth stages vary. Table 2 shows the descriptive statistics of CCD at two growth stages. The ranges of CCD are 0.46-3.81 g/m^2 and 0.92-4.26 g/m^2 for jointing and grain filling stages, respectively. The coefficient of variation of CCD in the jointing stage (32%) is higher than that in the grain filling stage (25%). At the two stages, the range of CCD is 0.46-4.26 g/m^2 and the coefficient of variation is 30%. This finding indicates that CCD varies widely along the two growth stages. Fig. 1 shows the average reflectance spectra from the jointing stage to the grain filling stage. Notably, the reflectance in the visible (350-713 nm) regions increases and decreases in the NIR (713-950 nm) regions.

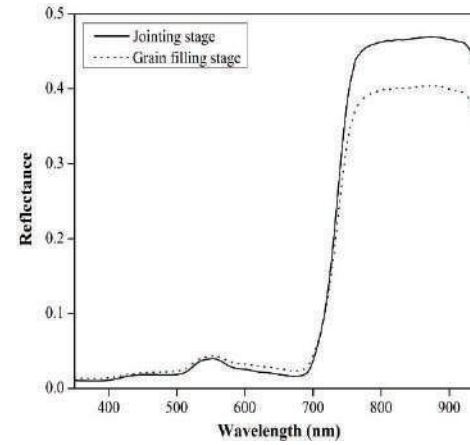

Fig. 1: Mean reflectance spectra at the jointing and grain filling stages.

Correlation of Spectral Indices with Canopy Chlorophyll Density

A correlation analysis was conducted between the 10 spectral indices from Table 1 and canopy chlorophyll density. Table

Table 3: Coefficient of determination between spectral indices and CCD (N=93).

Spectral indices	R	R^2	P Value	Spectral indices	R	R^2	P Value
SR	0.365	0.134	0.000	*mND705*	0.579	0.336	0.000
NDVI	0.533	0.284	0.000	*MCARI*	0.273	0.074	0.008
TCARI	0.053	0.003	0.612	CHL_{green}	0.059	0.003	0.574
NPCI	0.53	0.281	0.000	$CHL_{red\ edge}$	0.57	0.325	0.000
PRI	0.598	0.357	0.000	*SIPI*	0.503	0.253	0.000

Table 4: Correlations between CCD and most informative wavelet features derived from the calibration set (N=93)

Spectral metrics	Feature location		R	R^2	P Value
	Wavelength (nm)	Scale			
$WP_{513, 5}$	513	5	0.68	0.46	0.000
$WP_{730, 6}$	730	6	0.63	0.39	0.000
$WP_{800, 4}$	800	4	0.64	0.40	0.000
$WP_{835, 3}$	835	3	0.68	0.47	0.000
$WP_{897, 4}$	897	4	0.67	0.44	0.000

Table 5: Results of PLSR models based on wavelet features and spectral indices for the whole validation dataset and the dataset partitioned by growth stage.

Spectral metrics	Two stages			Jointing stage			Grain filling stage		
	R^2	RMSE	NRMSE	R^2	RMSE	NRMSE	R^2	RMSE	NRMSE
Wavelet features	0.64	0.43	23.6%	0.58	0.50	28.2%	0.61	0.39	24.6%
Spectral indices	0.57	0.48	25.8%	0.52	0.58	32.3%	0.59	0.40	25.2%

3 summarizes the results of the correlation analysis. Seven optimal spectral indices, namely, *SR*, *NDVI*, *NCPI*, *PRI*, *mND*705, $CHL_{red\ green}$ and *SIPI*, have a significant relationship with canopy chlorophyll density (P Value<0.0001). By contrast, *TCARI*, *MCARI* and CHL_{green} show low correlation with CCD.

Wavelet Features from CWA

Five most informative wavelet feature ranges, namely, 512-515 nm, 728-732 nm, 790-804 nm, 834-836 nm, and 892-902 nm, are determined in each scale after spectral data are processed by CWA. Features with the maximum R^2 within each region, namely, (513 nm, scale 5), (730 nm, scale 6), (800 nm, scale 4), (835 nm, scale 3), and (897 nm, scale 4), are determined in the visible and near infrared regions. They are highly sensitive to CCD (P Value<0.0001) with R^2 values for the linear regression ranging from 0.39 to 0.47 (Table 4). Low-scale features (835 nm, scale 3), (800 nm, scale 4), and (897 nm, scale 4) capture narrow absorption features in the near infrared region that are influenced by pigment concentration (Gitelson et al. 2005). Feature (513 nm, scale 5) occurs on the left shoulder of the green peak and captures spectral variation in the green range. High-scale feature (730 nm, scale 6) captures broad absorption features that occur in the range of red edge absorptions (Gitelson et al. 2005, Gitelson et al. 1996, Houborg et al. 2007). The R^2 and p values show that the five informative wavelet features perform better than the spectral indices in estimating CCD.

Regression model and validation of CCD using wavelet features and spectral indices

The PLSR model 1 was constructed with the five most informative wavelet features, while the PLSR model 2 was established with the seven optimal spectral indices of significant correlation with CCD. Table 5 summarizes the results of the two PLSR models for the whole validation dataset and the dataset partitioned by growth stage. In the two growth stages, the PLSR model 1 (R^2 = 0.64, RMSE=0.43 g/m^2, NRMSE=23.6%) is better than the PLSR model 2 (R^2= 0.57, RMSE=0.48 g/m^2, NRMSE=25.8%) in estimating CCD. After the validation data are partitioned by growth stage, the prediction accuracy of the two PLSR models exhibits low R^2 values and high NRMSE values. The PLSR model 1 has R^2 =0.58 and NRMSE=28.2% for the jointing stage and R^2 = 0.61 and NRMSE=24.6% for the grain filling stage. The PLSR model 2 has R^2 =0.52 and NRMSE=32.3% for the jointing stage and R^2 =0.59 and NRMSE=25.2% for the grain filling stage. The two PLSR models exhibit highly contrasting predictive capabilities in the growth stage and always have substantially better performance in the grain filling stage than in the jointing stage. This result is partly due to that winter wheat is in the rapid growth phase at the jointing stage. The signals are more easily contaminated by the background with the lower LAI in the jointing stage than in the grain filling stage, and the coefficient of variation of CCD in the jointing stage (32%) is also higher than that in the grain filling stage (25%). Therefore, the CWA method can remove the effects of background spectral variation when quantifying concentrations of components from mixtures (Mittermayr et al. 2001). This capability can be due to that the prediction accuracy of the PLSR model 1 is better than that of the PLSR model 2 in the jointing stage. Therefore, wavelet features are more robust than spectral indices. Fig. 2 plots the measured CCD against the estimated CCD for

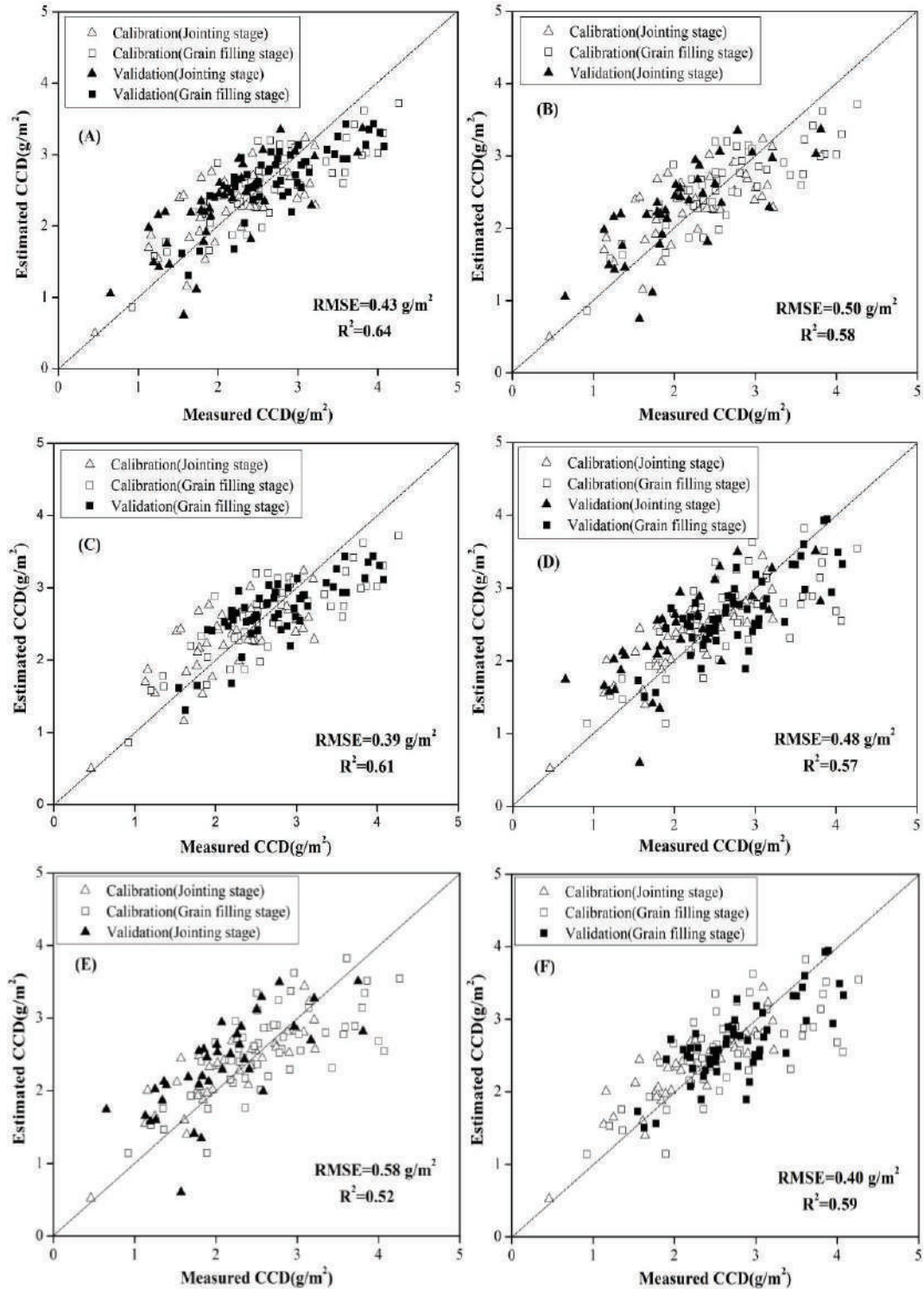

Fig.2: Plots of measured versus estimated CCD at the whole validation dataset (A and D), jointing stage (B and E), and grain filling stage (C and F) using PLSR model 1 (A, B, and C) and PLSR model 2 (D, E, and F). The predicted R^2, RMSE, and NRMSE values shown are obtained from the validation dataset.

illustrating the comparison of results and making them convincing. Ideally, the 1:1 line should be a perfect match. The figure indicates that the PLSR model 1 has points that are more convergent to the line 1:1 than the PLSR model 2 for the whole validation dataset and the dataset partitioned by growth stage. This condition indicates that the relationships between reflectance measures and CCD have been improved by the CWA method. Therefore, the CWA method can derive more robust wavelet features than the spectral indices for estimating CCD of winter wheat across different growth stages from the canopy spectra.

DISCUSSION AND CONCLUSION

This study presents the application of CWA method to canopy spectra for estimating CCD of winter wheat at two different growth stages. The CWA approach can effectively capture the meaningful spectral information that relates to CCD after the reflectance spectra are decomposed into various scales. Five most informative wavelet features, namely, (513 nm, scale 5), (730 nm, scale 6), (800 nm, scale 4), (835 nm, scale 3), and (897 nm, scale 4), are identified in the visible and near infrared regions. They are highly sensitive to CCD. Meanwhile, seven optimal spectral indices, namely, *SR*, *NDVI*, *NPCI*, *PRI*, *mND*705, $CHL_{red\ edge}$ and *SIPI* significantly correlate with CCD. They are used for further analysis. The PLSR model with the five wavelet features produces promising accuracy in estimating CCD. Specifically, the model has R^2 of 0.64, RMSE of 0.43 g / m^2, and NRMSE of 23.6%. Meanwhile, the PLSR model with seven optimal spectral indices produces less prediction accuracy of CCD. In particular, it has R^2 of 0.57, RMSE of 0.48 g / m^2, and NRMSE of 25.8%. After the validation dataset is partitioned into jointing and grain filling stages, the prediction accuracy of the two PLSR models exhibits low R^2 values and high NRMSE values. However, the PLSR model based on wavelet features still outperforms the model based on optimal spectral indices. Therefore, wavelet features are more effective than spectral indices in predicting CCD of winter wheat at different growth stages from canopy spectra for an agricultural ecosystem.

Our study extends the continuous wavelet analysis methodology to estimate chlorophyll content from leaf scale to canopy scale and exhibits promising results. However, winter wheat is the main crop in the study area. Thus, we only use winter wheat in this research. The capability of CWA in estimating CCD should be tested in the future using an extensive dataset with different crop species or at field scale with onboard hyperspectral images.

ACKNOWLEDGEMENTS

This research was supported by Doctoral Fund of Henan Institute of Engineering (D2016005). The authors are grateful to the staff of Beijing Normal University and Beijing Research Center for Information Technology in Agriculture for their support during field data collection.

REFERENCES

Asner, G.P. and Martin, R.E. 2008. Spectral and chemical analysis of tropical forests: Scaling from leaf to canopy levels. Remote Sensing of Environment, 112(10): 3958-3970.

Atzberger, C. 2004. Object-based retrieval of biophysical canopy variables using artificial neural nets and radiative transfer models. Remote Sensing of Environment, 93(1-2): 53-67.

Baret, F. and Guyot, G. 1991. Potentials and limits of vegetation indices for LAI and APAR assessment. Remote Sensing of Environment, 35(2-3): 161-173.

Blackburn, G.A. and Ferwerda, J.G. 2008. Retrieval of chlorophyll concentration from leaf reflectance spectra using wavelet analysis. Remote Sensing of Environment, 112(4): 1614-1632.

Boegh, E., Søgaard, H., Broge, N., Hasager, C.B., Jensen, N.O., Schelde, K. and Thomsen, A. 2002. Airborne multispectral data for quantifying leaf area index, nitrogen concentration, and photosynthetic efficiency in agriculture. Remote Sensing of Environment, 81(2-3): 179-193.

Broge, N.H. and Mortensen, J.V. 2002. Deriving green crop area index and canopy chlorophyll density of winter wheat from spectral reflectance data. Remote Sensing of Environment, 81(1): 45-57.

Buschmann, C. and Nagel, E. 1993. In vivo spectroscopy and internal optics of leaves as basis for remote sensing of vegetation. International Journal of Remote Sensing, 14(4): 711-722.

Cheng, T., Riaño, D. and Ustin, S.L. 2014. Detecting diurnal and seasonal variation in canopy water content of nut tree orchards from airborne imaging spectroscopy data using continuous wavelet analysis. Remote Sensing of Environment,143: 39-53.

Cheng, T., Rivard, B., Sánchez-Azofeifa, A.G., Féret, J.B., Jacquemoud, S. and Ustin, S.L. 2012. Predicting leaf gravimetric water content from foliar reflectance across a range of plant species using continuous wavelet analysis. Journal of Plant Physiology,169(12): 1134-1142.

Colombo, R., Bellingeri, D., Fasolini, D. and Marino, C.M. 2003. Retrieval of leaf area index in different vegetation types using high resolution satellite data. Remote Sensing of Environment, 86(1): 120-131.

Combal, B., Baret, F., Weiss, M., Trubuil, A., Mace, D., Pragnere, A., Myneni, R., Knyazikhin, Y. and Wang, L. 2002. Retrieval of canopy biophysical variables from bidirectional reflectance using prior information to solve the ill-posed inverse problem. Remote Sensing of Environment, 84(1): 1-15.

Dash, J. and Curran, P.J. 2004. The MERIS terrestrial chlorophyll index. International Journal of Remote Sensing, 25(23): 5403-5413.

Daughtry, C.S.T., Walthall, C.L., Kim, M.S., De Colstoun, E.B. and McMurtrey Iii, J.E. 2000. Estimating corn leaf chlorophyll concentration from leaf and canopy reflectance. Remote Sensing of Environment,74(2): 229-239.

Gamon, J.A., Serrano, L. and Surfus, J.S. 1997. The photochemical reflectance index: an optical indicator of photosynthetic radiation use efficiency across species, functional types and nutrient levels. Oecologia, 112(4): 492-501.

Gitelson, A.A., Vina, A., Ciganda, V., Rundquist, D.C. and Arkebauer, T.J. 2005. Remote estimation of canopy chlorophyll content in crops. Geophysical Research Letters, 32(8): L08403.

Gitelson, A.A., Kaufman, Y. and Merzlyak, M.N. 1996. Use of green channel in remote sensing of global vegetation from EOS-MODIS. Remote Sensing of Environment, 58(3): 289-298.

Gitelson, A.A., Keydan, G.P. and Merzlyak, M.M. 2006. Three-band model for noninvasive estimation of chlorophyll, carotenoids and anthocyanin

contents in higher plant leaves. Geophysical Research Letters, 33(11): L11402 .

Gitelson, A.A., Merzlyak, M. and Lichtenthaler, H. 1996. Detection of red edge position and chlorophyll content by reflectance measurements near 700 nm. Journal of Plant Physiology, 148(3-4): 501-508.

Haboudane, D., Miller, J.R., Tremblay, N., Zarco-Tejada, P.J. and Dextraze, L. 2002. Integrated narrow-band vegetation indices for prediction of crop chlorophyll content for application to precision agriculture. Remote Sensing of Environment, 81(2-3): 416-426.

Houborg, R. and Boegh, E. 2008. Mapping leaf chlorophyll and leaf area index using inverse and forward canopy reflectance modeling and SPOT reflectance data. *Remote Sensing of Environment*, 112(1): 186-202.

Houborg, R., Soegaard, H. and Boegh, E. 2007. Combining vegetation index and model inversion methods for the extraction of key vegetation biophysical parameters using Terra and Aqua MODIS reflectance data. Remote Sensing of Environment, 106(1): 39-58.

Jacquemoud, S., Bacour, C., Poilve, H. and Frangi, J.P. 2000. Comparison of four radiative transfer models to simulate plant canopies reflectance: Direct and inverse mode. Remote Sensing of Environment, 74(3): 471-481.

Liao, Q., Wang, J., Yang, G., Zhang, D., Lii, H., Fu, Y. and Li, Z. 2013. Comparison of spectral indices and wavelet transform for estimating chlorophyll content of maize from hyperspectral reflectance. Journal of Applied Remote Sensing, 7(1): p. 073575.

Mittermayr, C.R., Tan, H.W. and Brown, S.D. 2001. Robust calibration with respect to background variation. Applied Spectroscopy, 55(7): 827-833.

Nijs, I., Behaeghe, T. and Impens, I. 1995. Leaf nitrogen content as a predictor of photosynthetic capacity in ambient and global change conditions. Journal of Biogeography, 22(2): 177-183.

Ollinger, S.V. 2011. Sources of variability in canopy reflectance and the convergent properties of plants. New Phytologist, 189(2): 375-394.

Peñuelas, J. and Inoue, Y. 1999. Reflectance indices indicative of changes in water and pigment contents of peanut and wheat leaves. Photosynthetica, 36(3): 355-360.

Riedell, W.E. and Blackmer, T.M. 1999. Leaf reflectance spectra of cereal aphid-damaged wheat. Crop Science, 39(6): 1835-1840.

Rouse Jr, J., Haas, R.H., Schell, J.A. and Deering, D.W. 1973. Monitoring vegetation systems in the great plains with ERTS. Proceedings of the Third ERTS Symposium, Washington DC, 10-14 December, 309-317.

Simhadri, K.K., Iyengar, S.S., Holyer, R.J., Lybanon, M. and Zachary, J.M. 1998. Wavelet-based feature extraction from oceanographic images. IEEE Transactions on Geoscience and Remote Sensing, 36(3): 767-778.

Sims, D.A. and Gamon, J.A. 2002. Relationships between leaf pigment content and spectral reflectance across a wide range of species, leaf structures and developmental stages. Remote Sensing of Environment, 81(2-3): 337-354.

Ullah, S., Skidmore, A.K., Naeem, M. and Schlerf, M. 2012. An accurate retrieval of leaf water content from mid to thermal infrared spectra using continuous wavelet analysis. Science of the Total Environment, 437: 145-152.

Wu, J., Hou, L.G. and Wang, D. 2014. Estimation of chlorophyll content of corn canopy based on hyperion image. Transactions of the Chinese Society of Agricultural Engineering, 30(6): 116-123.

Nature Environment and Pollution Technology
An International Quarterly Scientific Journal

p-ISSN: 0972-6268
e-ISSN: 2395-3454

Vol. 18 | No. 4 | pp. 1219-1226 | 2019

Original Research Paper | Open Access

Simultaneous Reduction of Smoke and NO Emission Using Lower Order Alcohols in a Jatropha Methyl Ester Fuelled Compression Ignition Engine

Venkatesan Rajasekar*†, Varuvel Edwin Geo, Leenus Jesu Martin** and Beddhannan Nagalingam****

*Department of Mechanical Engineering, SRM Institute of Science and Technology, Kattankulathur-603203, India
**Department of Automobile Engineering, SRM Institute of Science and Technology, Kattankulathur-603203, India
†Corresponding author: Venkatesan Rajasekar

Nat. Env. & Poll. Tech.
Website: www.neptjournal.com

Received: 04-06-2019
Accepted: 21-06-2019

Key Words:
Jatropha oil methyl ester
Alcohol
Compression ignition engine
NO emission
Smoke emission

ABSTRACT

The objective of this work is to experimentally study the consequence of blending lower order alcohol (methanol and ethanol) with jatropha oil methyl ester (JOME) in a single cylinder, four stroke and water-cooled CI engine. 70% JOME blended with 30% methanol (J70M30) and 70% JOME blended with 30% ethanol (J70E30) are the two blends prepared to operate the engine. Experiments were conducted from 0 to 100% load at a fixed engine speed of 1500 rpm and the results were compared with base fuels. Due to the inferior physical properties of JOME, brake thermal efficiency (BTE) decreases compared to diesel at maximum load. Also, NO emissions increased by 4% and smoke opacity decreases by 10% while operating the engine with JOME compared to diesel. Simultaneous reduction of NO and smoke is achieved by blending lower order alcohol with JOME and a slight improvement in BTE is observed.

INTRODUCTION

Diesel engines operating with higher compression ratio and lean air-fuel ratio will deliver higher thermal efficiency and thus play a major role in transportation and agriculture sector. Also, diesel engines can slow down the increase in atmospheric carbon concentrations compared to gasoline engines (Sun et al. 2010). Although diesel engines produce less carbon monoxide, carbon dioxide and hydrocarbons, they emit more NO_x and smoke compared to SI engines. In addition, due to rapid depletion and increasing cost of petroleum-based fuels, biodiesel is considered to be a potential alternate fuel for the future. Prakash et al. (2018) studied the effect of operating high viscous neat castor oil (NCO) and its biodiesel (COME) in a single cylinder CI engine and observed an increase in brake thermal efficiency from 23.5% (NCO) to 29.7% (COME) and a marginal decrease in smoke opacity for COME in comparison with NCO. Thiyagarajan et al. (2016) attempted an experimental study on combustion, performance and emission behaviour of a karanja biodiesel (KO) fuelled CI engine and compared the outcome with the base fuel (diesel). They concluded that both KO and diesel have similar brake thermal efficiency under all the loads, and NO emission rises from 9.06 g/kWh (diesel) to 10.25 g/kWh (KOME) at 100% capacity.

Jatropha curcas is a large plant that belongs to the biological group of Euphorbiaceae and grows widely in most parts of India, in particular in semi-wild conditions near villages. Jatropha plant can grow rapidly almost anywhere even on gravelly, sandy and saline soils. It has hardly any special requirement with regard to soil and climate. Cetane number of Jatropha oil is high compared to diesel which makes jatropha oil as an alternative fuel for CI engine compared to other biofuels. Kumar et al. (2003) analysed the effect of using jatropha oil methyl ester in a diesel engine on performance, combustion and emission parameters. The outcome of the experiment is a small reduction in BTE due to low heating value of biodiesel and a significant reduction in CO, HC and smoke emissions. Dubey et al. (2017) operated the CI engine in dual fuel mode with jatropha oil methyl ester and turpentine oil in different ratios without any engine modification. They concluded that with BT 50, the engine parameters such as BTE, CO, HC, NO and smoke get reduced by 2.9%, 42.5%, 4.56%, 4.72% and 29.16% respectively, while CO_2 emissions increased by 10.7%, at full load. Already exhaustive research work has been carried out with jatropha oil biodiesel and reports suggest that this oil can be used directly in diesel engines without any engine modification. However, the engine performance characteristics are slightly inferior than diesel.

Alcohols have the ability to blend directly with vegetable oils and without any change in the engine setup these blends can be used directly in the existing diesel engines (Agarwal 2007). Lower order alcohol has a low viscosity,

low flash point, low boiling point and high heat of vaporization compared to neat diesel but its low cetane number makes it unsuitable as a single fuel for diesel engine operation. However, physical properties improve significantly by blending vegetable oil with alcohol in minor proportion. Primarily, a considerable reduction in density and viscosity is observed with the improvement in volatility. Yilmaz & Sanchez (2012) have tested standard diesel (D), neat biodiesel (B), biodiesel (85%)-methanol (15%) and biodiesel (85%)-ethanol (15%) in a twin cylinder CI engine and observed a reduction in NO emissions with all the tested biodiesel-alcohol blends. However, they observed a maximum reduction in NO emission with biodiesel methanol blend.

In India, ethanol is manufactured from molasses, which is a byproduct of sugar industry. It can be used in diesel engine since it is a low cost oxygenate and its use will help the rural farmers. Chelladorai et al. (2019) investigated various blends of grapeseed biodiesel and ethanol blends at full load operation to evaluate the performance and emission characteristics of a single cylinder CI engine. They concluded that blending of 10% volume of ethanol with grapeseed biodiesel increases the BTE from 26.54% to 30.04% and reduces CO, NO_x and smoke level from 0.037% to 0.03%, 945 ppm to 813 ppm and 51% to 41% opacity, respectively. Huang et al. (2009) in their work investigated the solubility of ethanol in diesel with and without the addition of n-butanol and further investigated the performance and emission parameters in a CI engine. Engine tests with diesel-ethanol blend with butanol in the following ratio Z5E10D85, Z5E20D75. Of all the combinations, Z5E25D70 blend is found to have a maximum brake thermal efficiency of 37% compared to all other blends. Subbaiah et al. (2010) have evaluated experimentally the performance and emission characteristics of rice bran oil biodiesel-ethanol blend in a CI engine with a blending ratio of 2.5 %, 5% and 7.5 %. They observed a maximum BTE with 2.5% ethanol blended with rice bran biodiesel and the BTE obtained is reported to have been 6.98% and 3.93% higher than neat diesel and biodiesel, respectively, at full load operation of the engine. Smoke emission of the biodiesel was reduced by 20% when blended with 7.5% of ethanol while a reduction in smoke of 27.47% has been recorded with 2.5% blend.

A number of research studies have shown that high isentropic bulk modulus of biodiesel causes artificial advance in injection timing, lower stoichiometric air-fuel ratio, high adiabatic flame temperature, fuel bound oxygen and radiative heat transfer as the possible reasons for the NO_x increase with biodiesel. Several techniques were proposed by numerous research studies to reduce NO_X emission in CI engine like use of oxygenates (Kasiraman et al. 2016), antioxidant additives (Varatharajan et al. 2011), emulsion (Yoshimoto et al. 1999), EGR (Mahalingam et al. 2018) and SCR (Anderson et al. 2018). Kathirvelu et al. (2017) studied the impact of operating a single cylinder CI engine with 100% JOME and blending diesel with 20% JOME. They noticed a significant increase in NO emission and lower soot emission with JOME compared to diesel. Sayin (2010) in his experiments on a single cylinder CI engine, has studied the effects of diesel-methanol and diesel-ethanol blends, respectively on the performance and exhaust emissions. Readings were observed for speeds in the range of 1000 to 1800 rpm with the engine torque at 30 Nm. They observed a decrease in brake thermal efficiency, smoke opacity, CO and HC emissions for the fuel blends in comparison to diesel.

Many research works based on biodiesel-alcohol blends have been investigated as indicated above. However, not much work has been reported on the use of jatropha oil biodiesel lower order alcohol blends as it is expected to improve the BTE with the simultaneous reduction of NO and smoke emission. Therefore, the main objective of this work is to study the effect of blending lower order alcohols (methanol and ethanol) with jatropha oil methyl ester in a CI engine on the performance, combustion and emission characteristics.

TEST FUELS

Experiments were carried out with diesel, jatropha oil methyl ester (JOME), jatropha oil methyl ester 70% + methanol 30% (J70M30), jatropha oil methyl ester 70% + ethanol 30% (J70E30). Tables 1 and 2 show the specifications of the test engine and properties of the test fuels respectively, and Fig.1 shows the schematic diagram of the experimental setup on which experiments were conducted.

Table 1: Engine specifications.

Parameter	Value
Make and Model	Kirloskar, TV1
No. of Cylinder	1
Cycle	4 Strokes
Bore	87.5 mm
Stroke	110 mm
Displacement volume	661 cm^3
Compression ratio	17.5:1
Combustion chamber	Hemispherical
Rated power	5.2 kW @ 1500 rpm
Injection timing	23° BTDC

RESULTS AND DISCUSSION

NO Emission

Fig. 2 shows the variation of nitric oxide emission with

Table 2: Properties of test fuel.

Property	Diesel	JOME	J70M30	J70E30
Density @ 15° C (g/cc)	0.840	0.880	0.843	0.852
Kinematic Viscosity @ 40°C cSt	2.95	4.57	3.37	3.53
Lower Heating value (kJ/kg)	42500	38450	32188	35615
Cetane index	45	52	38	40

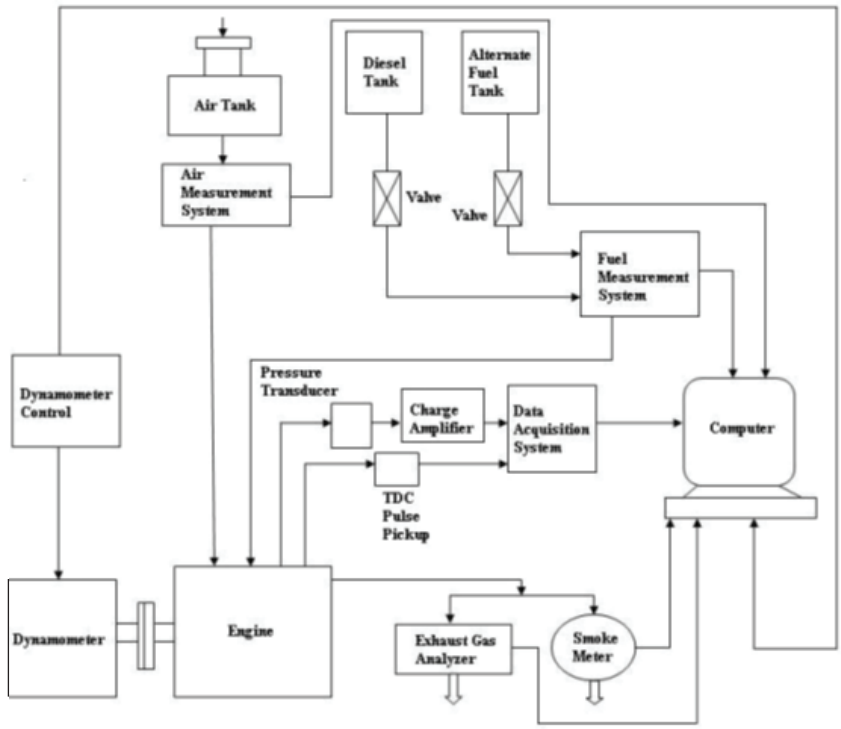

Fig. 1: Schematic diagram of the experimental setup.

respect to brake power. High in-cylinder temperature, oxygen availability, time available for reaction, presence of free radical in the hydrocarbon flame and fuel bound oxygen are the important reasons for the NO_x emission in compression ignition engines. NO emissions are slightly higher in pure biodiesel operation at all loads compared to diesel due to the oxygen content in the biodiesel. It is evident that addition of alcohol to biodiesel decreases the NO emissions significantly. At 100% load, NO emission of J70M30 and J70E30 are lower by 31.1% and 28.9%, respectively compared to JOME. High latent heat of vaporization and low heating value of methanol and ethanol reduces the in-cylinder temperature during combustion thus lowering the NO emission.

Smoke Opacity

Fig. 3 shows the variation of smoke opacity with respect to brake power. Incomplete combustion in fuel rich zone is responsible for smoke formation (Dale et al. 2007). When the engine was operated at rated load, smoke opacity of diesel and JOME are 50.7 and 45.2% respectively. JOME has lower smoke opacity due to the presence of fuel bound oxygen. Blending alcohol with JOME will further increase the oxygen concentration in the mixture. Smoke opacity of J70M30 and J70E30 are 42.8% and 43.9% respectively. Lower smoke opacity of methanol blend is due to high oxygen content of methanol (0.5% by weight) compared to ethanol (0.35% by weight).

CO Emission

Fig. 4 shows the variation of CO emission with respect to brake power. Diffusion combustion phase is responsible for more CO formation as oxidation of CO is more during pre-

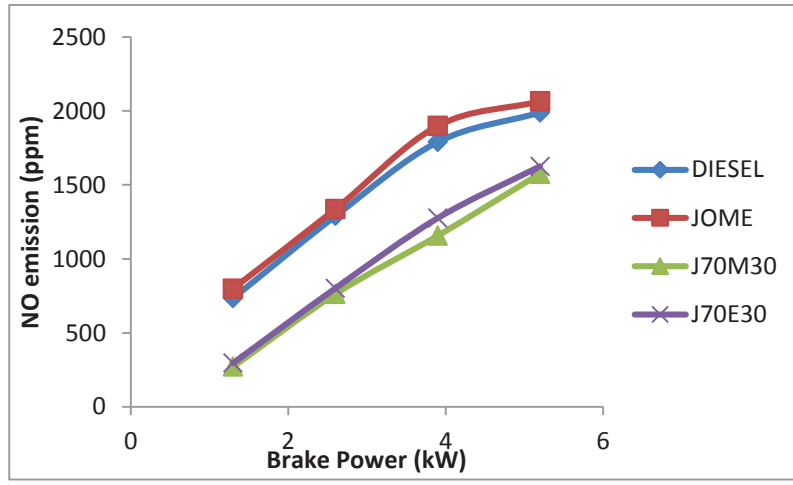

Fig. 2: Variation of NO emission at different load conditions.

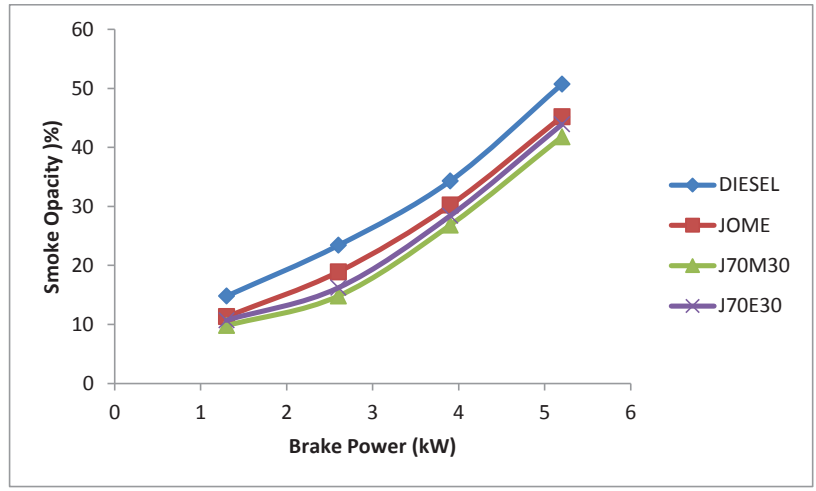

Fig. 3: Variation of smoke opacity at different load conditions.

mixed combustion phase due to high temperature. At maximum load, CO emission for diesel and JOME is 0.073 % and 0.096 % as shown in the figure. JOME emits more CO due to higher carbon content in fuel structure and poor physical properties like high viscosity and density in comparison to diesel. However, at low and part load operation, carbon monoxide emission for JOME is lower than diesel. Carbon monoxide emission is reduced to 0.072 % and 0.074 % for J70M30 and J70E30 respectively. Lower carbon monoxide emission for J70M30 and J70E30 is due to oxygen enrichment in the blend that leads to oxidation of CO.

HC Emission

Fig. 5 shows the HC emission as a function of brake power. Hydrocarbon emissions are due to incomplete combustion of hydrocarbon fuel and is a useful measure of combustion inefficiency. The figure depicts the hydrocarbon emission for J70M30 and J70E30 compared to diesel and JOME at various load operation. HC emission for diesel and JOME is 52 ppm and 61 ppm respectively at maximum load. Higher HC emission with JOME is attributed to higher C-H ratio and poor combustion leading to less combustion temperature. Hence, JOME emits higher HC emission in spite of its fuel borne oxygen atoms. J70M30 emits more HC compared to J70E30 at all loads. HC emission for J70M30 and J70E30 is 76 ppm and 71 ppm respectively at full load. Alcohol blending with biodiesel increases HC emission because of the cooling effect produced due to high latent heat of vapor-

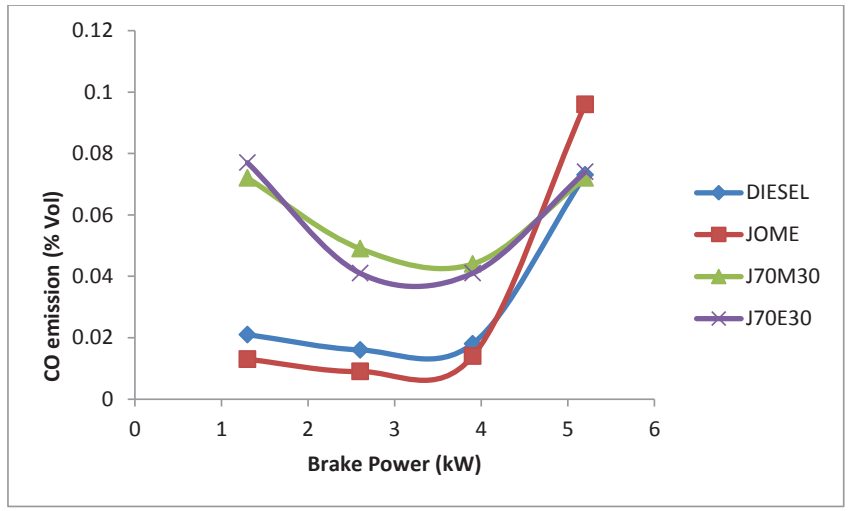

Fig. 4: Variation of CO emission at different load condition.

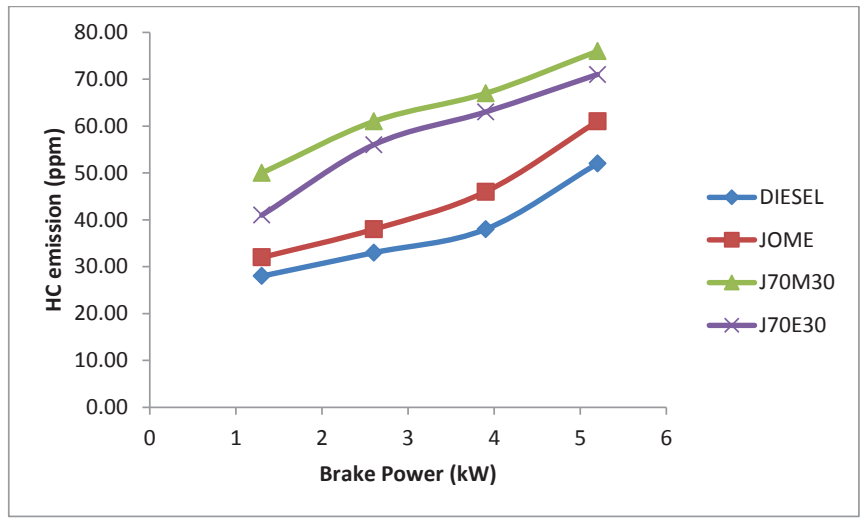

Fig. 5: Variation of HC emission at different load conditions.

ization of methanol and ethanol (Yilmaz & Sanchez 2012).

Brake Thermal Efficiency

Fig. 6 illustrates the variation of BTE with brake power. BTE indicates the quantity of power delivered for the given quantity of heat supplied. Brake thermal efficiency of diesel and JOME was found to be 34.34% and 32.24% respectively at full load. Lower brake thermal efficiency of JOME is due to high viscosity and low calorific value of the fuel compared to diesel. Methanol and ethanol addition to JOME slightly improves the brake thermal efficiency compared to diesel. The possible reason may be due to low viscosity, improved volatility and oxygen enrichment of the blend which enhances the quality of combustion.

Exhaust Gas Temperature

Fig. 7 portrays the variation of exhaust gas temperature (EGT) with brake power. It can be observed that EGT increases with increase in load since the quantity of fuel supply increases with load. At full load, exhaust gas temperature of JOME (356°C) is slightly higher than diesel (351°C). High viscosity of JOME leads to slow atomization and vaporization of air-fuel mixture and hence the exhaust gas temperature of JOME is more than diesel. Alcohol ad-

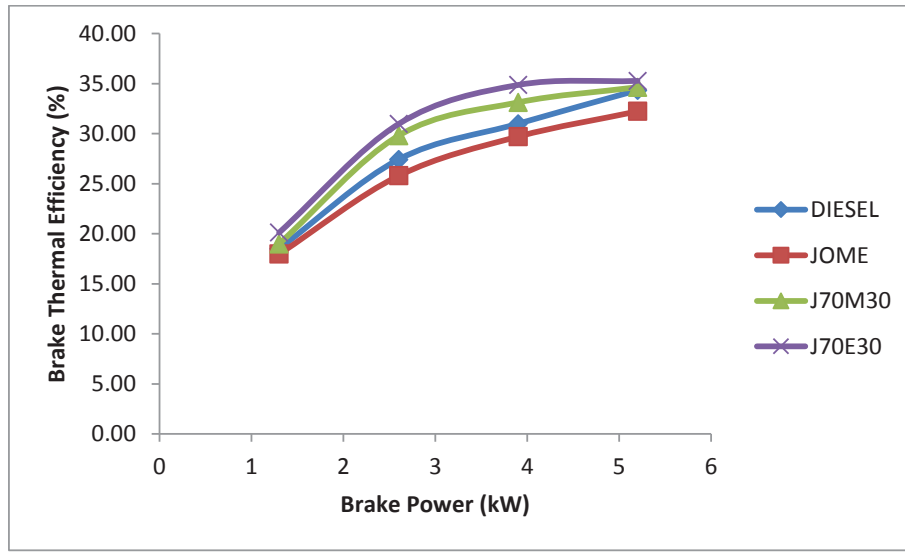

Fig. 6: Variation of BTE at different load conditions.

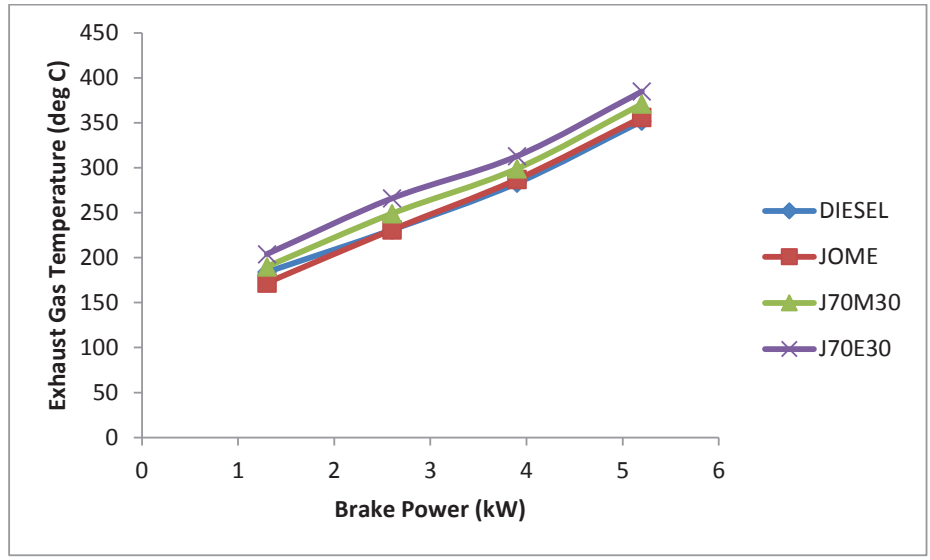

Fig. 7: Variation of exhaust gas temperature at different load conditions.

dition increases the EGT at all loads. EGT of J70M30 and J70E30 is 371°C and 385°C respectively at full load.

Net Heat Release

Fig. 8 shows the variation of heat release with crank angle for diesel, JOME, J70M30 and J70E30 at full load. Peak heat release for diesel and JOME is 47.5 J/°CA and 44.3J/°-CA, respectively. Maximum heat release is lower for JOME due to its high viscosity and low heating value. Due to high cetane number of JOME the peak heat release occurs early compared to diesel. With alcohol addition, the cetane number decreases and ignition delay period slightly increases leading to fuel accumulation in the cylinder which in turn delays the start of combustion and increases the maximum heat release. The peak heat release for J70M30 and J70E30 is 46.9 J/°CA and 51.4 J/°CA respectively.

CONCLUSION

The present work investigates the effect of lower order

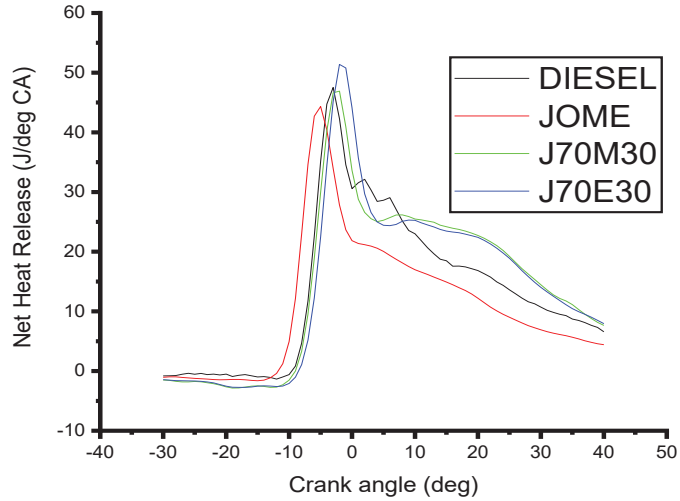

Fig. 8: Rate of heat release at 100% load.

alcohol addition with jatropha oil methyl ester to achieve simultaneous reduction of NO and smoke emission in a single cylinder CI engine. Lower order alcohols namely methanol and ethanol were blended 30% by volume with 70% JOME and tested at different load conditions.

- Blending 30% lower order alcohol with JOME reduces NO emissions significantly. NO emissions reduced by 31.1% and 28.9% for J70M30 and J70E30 respectively, compared to JOME at full load.
- JOME contains oxygen in its molecular structure and hence JOME emits less smoke compared to diesel. Smoke emission is least for J70M30 blend which is 5.3% lower than JOME and 15.6% lower than diesel, at full load.
- JOME emits slightly higher CO and HC emissions compared to diesel. Blending lower alcohols with JOME, CO and HC emissions increases further.
- BTE of JOME is slightly lower than diesel due to inferior combustion. However, addition of methanol and ethanol with JOME, enriches the blend with oxygen and improves combustion to get higher brake thermal efficiency. Maximum heat release improved with alcohol blending with JOME due to low cetane number of alcohol that delays the start of combustion.

It is concluded that J70M30 is optimum for achieving simultaneous reduction of NO and smoke without any compromise in performance of a jatropha biodiesel fuelled CI engine.

REFERENCES

Agarwal, A.K. 2007. Biofuels (alcohols and biodiesel) applications as fuels for internal combustion engines. Progress in Energy and Combustion Science, 33(3): 233-271.

Anderson, A., Devarajan, Y. and Nagappan, B. 2018. Effect of injection parameters on the reduction of NOx emission in neat bio-diesel fueled diesel engine. Energy Sources, Part A: Recovery, Utilization, and Environmental Effects, 40(2): 186-192.

Chelladorai, P., Varuvel, E.G., Martin, L.J. and Nagalingam, B. 2019. The potential impact of unsaturation degree of the biodiesels obtained from beverage and food processing biomass streams on the performance, combustion and emission characteristics in a single-cylinder CI engine. Environmental Science and Pollution Research, 26(5): 5008-5019.

Dale, R. Tree, Kenth. Svensson 2007. Soot processes in compression ignition engines, Progress in Energy and Combustion Science, 33: 272-309.

Dubey, P. and Gupta, R. 2017. Effects of dual bio-fuel (Jatropha biodiesel and turpentine oil) on a single cylinder naturally aspirated diesel engine without EGR. Applied Thermal Engineering, 115: 1137-1147.

Huang, J., Wang, Y., Li, S., Roskilly, A. P., Yu, H. and Li, H. 2009. Experimental investigation on the performance and emissions of a diesel engine fuelled with ethanol-diesel blends. Applied Thermal Engineering, 29(11-12): 2484-2490.

Kasiraman, G., Geo, V. E. and Nagalingam, B. 2016. Assessment of cashew nut shell oil as an alternate fuel for CI (Compression ignition) engines. Energy, 101: 402-410.

Kathirvelu, B., Subramanian, S., Govindan, N. and Santhanam, S. 2017. Emission characteristics of biodiesel obtained from jatropha seeds and fish wastes in a diesel engine. Sustainable Environment Research, 27(6): 283-290.

Kumar, M. S., Ramesh, A. and Nagalingam, B. 2003. An experimental comparison of methods to use methanol and Jatropha oil in a compression ignition engine. Biomass and Bioenergy, 25(3): 309-318.

Mahalingam, A., Munuswamy, D.B., Devarajan, Y. and Radhakrishnan, S. 2018. Emission and performance analysis on the effect of exhaust gas recirculation in alcohol-biodiesel aspirated research diesel engine. Environmental Science and Pollution Research, 25(13):12641-12647.

Prakash, T., Geo, V. E., Martin, L. J. and Nagalingam, B. 2018. Improved cold flow properties and combustion analysis of high viscous castor oil and its biodiesel in a CI engine. Nature Environment & Pollution Technology, 17(4): 1183-1192.

Sayin, C. 2010. Engine performance and exhaust gas emissions of methanol and ethanol-diesel blends. Fuel, 89(11): 3410-3415.

Subbaiah, G.V., Gopal, K.R., Hussain, S.A., Prasad, B.D. and Reddy, K.T. 2010. Rice bran oil biodiesel as an additive in diesel-ethanol blends

for diesel engines. International Journal of Research and Reviews in Applied Sciences, 3(3): 334-342.

Sun, J., Caton, J. A. and Jacobs, T. J. 2010. Oxides of nitrogen emissions from biodiesel-fuelled diesel engines. Progress in Energy and Combustion Science, 36(6): 677-695.

Thiyagarajan, S., Geo, V. E., Martin, L. J. and Nagalingam, B. 2016. Effects of low carbon biofuel blends with Karanja (*Pongamia pinnata*) oil methyl ester in a single cylinder CI engine on CO_2 emission and other performance and emission characteristics. Nature Environment & Pollution Technology, 15(4): 1249-1256.

Varatharajan, K., Cheralathan, M. and Velraj, R. 2011. Mitigation of NOx emissions from a jatropha biodiesel fuelled DI diesel engine using antioxidant additives. Fuel, 90(8): 2721-2725.

Yilmaz, N. and Sanchez, T.M. 2012. Analysis of operating a diesel engine on biodiesel-ethanol and biodiesel-methanol blends. Energy, 46(1): 126-129.

Yoshimoto, Y., Onodera, M. and Tamaki, H. 1999. Reduction of NOx, smoke, and BSFC in a diesel engine fueled by biodiesel emulsion with used frying oil. SAE Transactions, Journal of Fuels and Lubricants, 108: 1913-1920.

Nature Environment and Pollution Technology
An International Quarterly Scientific Journal

p-ISSN: 0972-6268
e-ISSN: 2395-3454

Vol. 18 | No. 4 | pp. 1227-1233 | 2019

Original Research Paper | Open Access

Statistical and Spatial Analyses of Zinc Concentrations in the Shallow Groundwater of Urban Area and Their Implications on Environmental Background Establishment

Feng Songbao and Sun Linhua†
School of Resources and Civil Engineering, Suzhou University, Anhui 234000, China
Key Laboratory of Mine Water Resource Utilization of Anhui Higher Education Institute, Suzhou University, Anhui 234000, China
†Corresponding author: Sun Linhua

Nat. Env. & Poll. Tech.
Website: www.neptjournal.com

Received: 27-03-2019
Accepted: 01-06-2019

Key Words:
Zinc
Groundwater
Spatial autocorrelation
Statistical analysis
Normal distribution

ABSTRACT

Based on the systematic collection of the shallow groundwater samples in the urban area of Suzhou, Anhui province, China, the concentrations of zinc have been analysed by statistical and spatial methods. The results show that the zinc concentrations in the groundwater samples are low, and all the samples can meet the national groundwater quality standard of China with Class I and II, which means that the groundwater can be used for drinking purpose. However, the zinc concentration has high coefficient of variation and low p-values of normal distribution, implying that it has been affected by anthropogenic activities, which was also demonstrated by the consistency of the distribution of the samples with high zinc concentrations and the areas with high density of human and transportation, as well as the high-high cluster of the spatial autocorrelation analysis of zinc. Based on the statistical analysis, the environmental background has been calculated to be 0-62.6 μg/L, whereas the environmental background has been calculated to be 0-69.8 μg/L with spatial analysis. They are different because of the different basis of the two methods, the former based on the hypothesis of normal distribution of the background values, whereas the latter do not need such a hypothesis.

INTRODUCTION

Groundwater is the main water supply for the industrial, agriculture and domestic use in most cities in north China. However, because of the irrational exploitation and anthropogenic pollution, the quality of the groundwater in the areas with a high density of people has been dramatically affected (Liu et al. 2005). Therefore, the scientific issues related to the groundwater have attracted a great deal of attention, and a series of scientific or engineering discoveries have been reported, such as regional hydro-geology, hydrochemistry, groundwater pollution, modelling and management (Zhang et al. 1996, Zhang et al. 2003, Kemper 2004, Zhang et al. 2012, Rodríguez-Lado et al. 2013).

The environmental background is the concentration (mostly, the range of concentrations) of the chemical elements in a relatively clean area (with low contribution of anthropogenic activities), and is the basis to determine the pollution degree of a regional environment (Reimann et al. 2005, Reimann & Garrett 2005). For the management of groundwater, environmental background is important, because it is needed for identifying the pollution of the groundwater and, it is also the destination of the environmental protection (Liu et al. 2014).

Suzhou is an important city with coal production in northern Anhui Province, China, and it is also a city with a long period of groundwater utilization. The water for industrial and domestic purposes is mainly obtained from the underground, especially from the shallow and deep pore water. In recent years, with the continuous development of the urban economy and the scale of the city, the demand for industrial and domestic water is increasing, and the problems related to the development and utilization of groundwater resources are exposed more and more, which restricts the sustainable development of the city and the health of the people in the area (Li et al. 2004, Liu & Liang 2014, Lin & Peng 2016).

Because of the importance of groundwater for the development of the Suzhou city, the shallow groundwater in the urban area has been taken as the research object. Based on systematic sampling and the measurement of the zinc concentrations, statistical and spatial autocorrelation analyses have been applied to the data, for getting the statistical information about the zinc concentration and their spatial

distribution, as well as the environment background of zinc in the groundwater, which can provide scientific information for the protection and utilization of the shallow groundwater in the area. For the shallow groundwater in the urban area, the transportation has long been identified to be one of the main sources of pollution because of the penetration of the recharge water from the surface to the underground, and zinc has long been identified to be the typomorphic element related to the wearing of tire (Sarkar et al. 2011), that is why we chose zinc as the study element therein.

MATERIALS AND METHODS

Study Area

Suzhou is the north gate of the Anhui province, China. It is located at the south of the Huang-Huai plain, adjacent to Xuzhou of Jiangsu and Heze of Shandong in the north, Yongcheng of Henan in the west, and Suqian of Jiangsu in the east. There are many rivers in the area, including the Kui, Sui, Tuo and Hui rivers, all of them flow from northwest to southeast, and ended in the Huai River or the Hongze lake. The annual precipitation is 857 mm, with an average temperature of 14.4 degrees (centigrade).

There are three aquifer systems in the study area, including the loose layer, the coal bearing sandstone and the limestone aquifer systems from shallow to deep. However, most of the water supply in the city is taken from the first one (loose layer aquifer system), which can also be subdivided into four aquifers (1^{st}- 4^{th}) from shallow to deep. All the groundwaters in the loose layer aquifer system of the urban area are recharged by the water from two ways: (1) the horizontal runoff from the mountain area located in the north of the city, and (2) the penetration from the vertical direction in the urban area, that is why the anthropogenic activities in the surface can affect the groundwater environment.

Sampling and Analysis

A total of 62 shallow groundwater samples were collected from the shallow wells of the local residents (<30m), that is why the locations of the samples look random. The sample locations are shown in Fig. 1. Before sampling, a 2.0 L polyethylene bottle that has been cleaned in the laboratory has been rinsed three times with the well water similar to the samples. The samples were acidified to be pH<2 by HNO_3 to prevent the adsorption of the elements by the bottle, and finally labelled and sent to the laboratory for processing. The GPS location and site conditions (including the flow of people, life, industry, and traffic related information) have been recorded.

In the laboratory, all the samples were filtered through 0.22 μm film before analysis, for removing debris. The concentration of zinc was analyzed by atomic absorption spectrometer, and the quality control was carried out by standard sample (the correlation coefficient between actual and measured concentrations was higher than 0.99). All the analysis was conducted in the Engineering Research Center of Coal Mine Exploration, Anhui province, China.

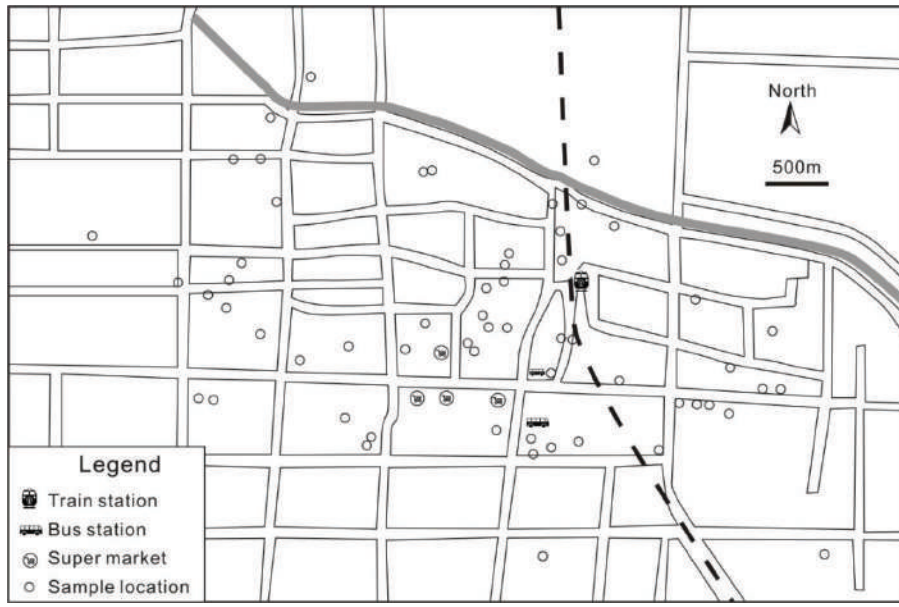

Fig. 1: Locations of the groundwater samples.

Data Treatment

Firstly, all the data were processed for statistical analysis by the Mystat 12 software, for calculating the maximum, minimum and mean values, standard deviation, coefficient of variation and the p-value of the normal distribution test, and then the contour map of the zinc concentrations was constructed by the Surfer 11 software (with natural neighbour grid method), and finally the spatial autocorrelation analysis by the Geoda 1.8.3 software. For avoiding the influence of the non normal distribution data for the spatial cluttering, all the zinc concentrations were firstly transformed by Box-cox with the Minitab 14 software. Finally, the local spatial autocorrelation (LISA) is processed to obtain the significant map and the spatial clustering map.

At present, there are two kinds of methods for determining environmental background values, including the geochemical method and statistical method. Among these two, the statistical method is the most commonly used one, because it is hard to find a place without anthropogenic influence, which was needed for the geochemical method. There are some kinds of methods related to the statistical method, e.g. the relative cumulative frequency, the normal distribution, the regression analysis, the outlier test, the iterative standard deviation and so on (Reimann et al. 2005, Reimann & Garrett 2005), and all of these methods have a same basis that the background values of the sample obey the normal distribution (or lognormal distribution).

In this study, two kinds of methods have been applied for the establishment of the environment background value:

(1) The box plot by the Mystat 12, which based on the assumption that the environmental background value in line with the normal distribution. After processing, the samples outside the lower and upper hinge of the box plot were removed (repeated until no abnormal samples), and then the mean and standard deviation of the rest of the samples were calculated. The environmental background value was then calculated to be mean ± 2*standard deviation.

(2) Based on the spatial autocorrelation analysis, the basis is that there is no significant change of the concentrations in the sample relative to its adjacent samples. Therefore, the samples for calculating the environmental background values only consider the non significant samples (without high-high, low-low, high-low and low-high clusters) after spatial autocorrelation analysis, then the environmental background values were calculated by the mean ± 2*standard deviation.

RESULTS AND DISCUSSION

Concentrations

According to the groundwater quality status, health of people and the goal of environmental protection, the quality of the groundwater has been classified into five degrees according to the National Standard of China (GB/T 14848-93): Class I and II (≤0.5 mg/L), natural background; Class III (≤1.0 mg/L), suitable for drinking, industrial and agricultural use; Class IV (≤5.0 mg/L), suitable for industrial and agricultural use (can also be used for domestic purpose after treatment); Classes V (>5.0 mg/L), not suitable for any purpose. In this study, the zinc concentrations of the groundwater are 2.54-225 μg/L (mean = 40.4 μg/L) (Table 1). In comparison with the National Standard of China, all the samples can be classified to be Class I and II. However, does it mean that the zinc in the groundwater has not been affected by human activities?

In environmental studies, coefficient of variation (CV) is always used for analyzing the degree of anthropogenic contribution of pollutants: when CV < 0.10, it means low anthropogenic contribution, whereas CV > 0.90 means high anthropogenic contribution (Peters et al. 1997, Xie et al. 2011). In this study, the groundwater samples have a relatively high CV (0.937), which probably means that the zinc in the groundwater has been influenced by anthropogenic activities. Moreover, the p-value of normal distribution test is <0.01, which means that the zinc concentrations in this study cannot pass the normal distribution test (p> 0.05), which also indicates the anthropogenic contribution (Reimann et al. 2005, Reimann & Garrett 2005). Even after log transformation, the CV is also > 0.10 and the p-value < 0.05, which also means anthropogenic influence.

Spatial Distribution of Zinc

The contour map of the zinc concentrations in this study is shown in Fig. 2. As can be seen from the figure, three areas with high zinc concentrations can be found in the central and central-east of the study area. In comparison with the sample locations in the Fig. 1, it can be found that the groundwater samples with high zinc concentrations are located near the train station, bus station and the business area. During the period of sampling, we found that the three areas are characterized by high density of people and transportation. Because, except for the geogenic origin (weathering of rocks), another important source of zinc in the environment is the transportation related tire erosion, which can release Zn, Pb and Cu simultaneously (Sarkar et al. 2011).

Table 1: Statistical description of zinc in this study (μg/L).

N	Min	Max	Mean	SD	CV	p-value
62	2.54	225	40.4	37.8	0.937	<0.01

Spatial Autocorrelation Analysis

According to the classification of Moran'I index (Anselin 1995), all the samples can be subdivided into two

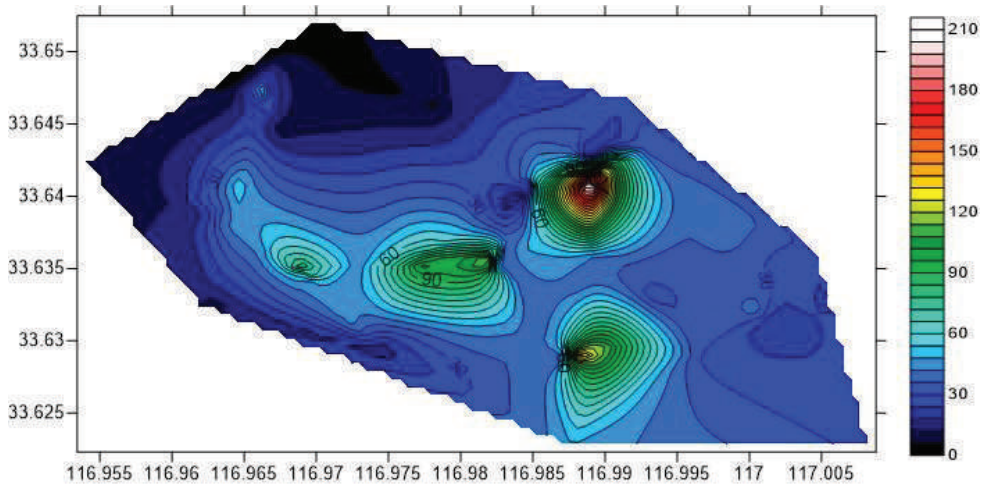

Fig. 2: Contour map of zinc concentrations (μg/L).

major categories: one is "not significant", and another is "significant". Samples classified into the former are considered as the environmental background samples in this study, and the samples classified into the latter can be divided into four sub categories: high-high, low-low, low-high and high-low, which represent the relationship between the concentration of a sample and its surrounding ones. The hot spot includes the high-high samples, and the freezing spot includes the low-low samples, whereas the low-high and high-low samples are abnormal ones, which may be related to the influence of other factors (Moran 1948, Ord & Getis 1995, Diniz-Filho et al. 2003, Zhao et al. 2009). The result of spatial autocorrelation analysis is shown in Fig. 3.

As can be seen from the figure the 31 samples are classified to be "non significant" samples, whereas the sample numbers classified to be high-high, low-low, low-high and high-low clusters are 20, 4, 3 and 4, respectively. It can also be noticed from the figure that the samples divided into the high-high cluster are mainly concentrated in the area between the train station (north), bus station (south)

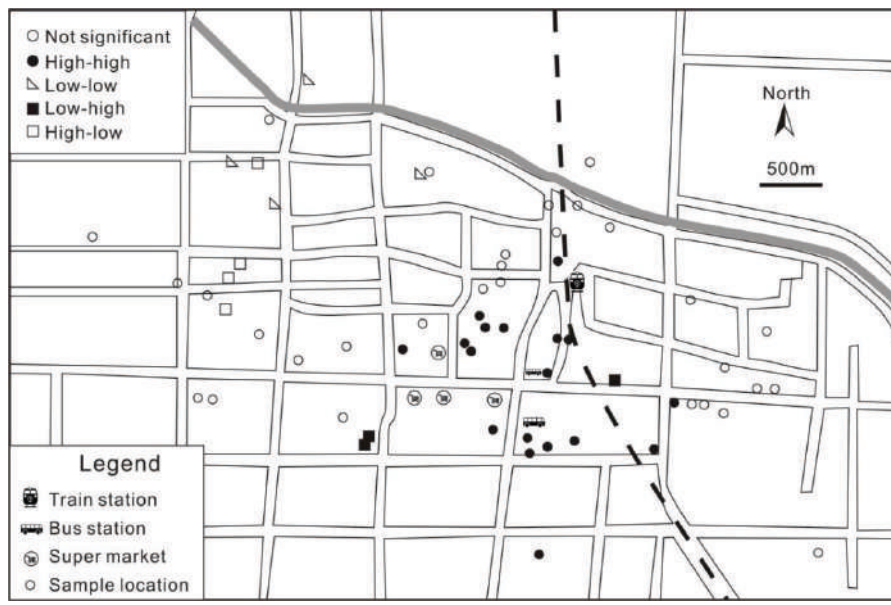

Fig. 3: Results of spatial autocorrelation analysis.

and the commercial district (west). Therefore, this area can be called as "hot spot". This area is consistent with the distribution of the samples with high zinc concentrations in Fig. 2, which implies that the high density of human and transportation is the main influencing factor. In contrast, the low-low cluster samples are located in the north of the study area, where there is the newly constructed urban area with low density of humans. Further, for the low-high and high-low abnormal samples, they reflect that the concentrations of zinc in these samples are "mutation" relative to the surrounding ones, and may be a reflection of natural or anthropogenic disturbance (Moran 1948, Ord & Getis 1995, Diniz-Filho et al. 2003, Zhao et al. 2009).

Establishment of the Environmental Background

Fig. 4 is the density plot of zinc concentrations. It can be seen from the figure that the concentrations of the zinc have three peaks, which probably indicates that the zinc in the groundwater without anthropogenic influence might follow the normal distribution (the first peak in the Fig. 4). Based on the box plot of the zinc concentrations, there are 6 samples with zinc concentrations higher than 100 μg/L can be considered as outliers (Fig. 5). After removing them, the remaining 56 samples were calculated and the average value was 30.0 μg/L with standard deviation of 16.3 μg/L (Table 2). Therefore, the background value calculated by the statistics method is 0-62.6 μg/L (less than 0 and replaced by 0).

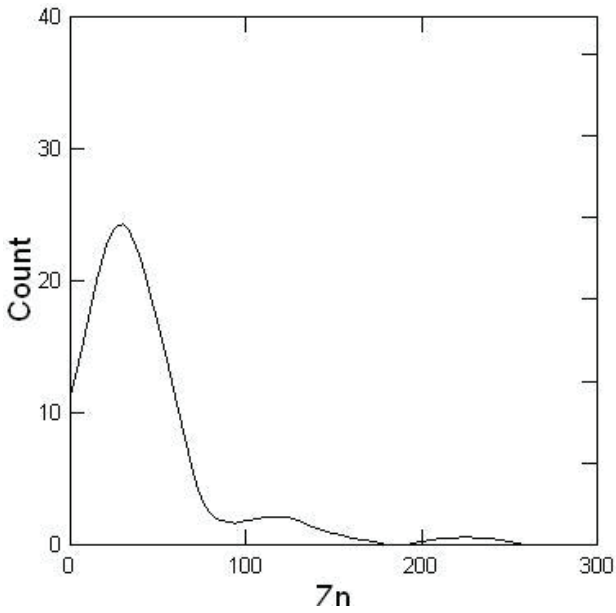

Fig. 4: Density plot of the zinc concentrations.

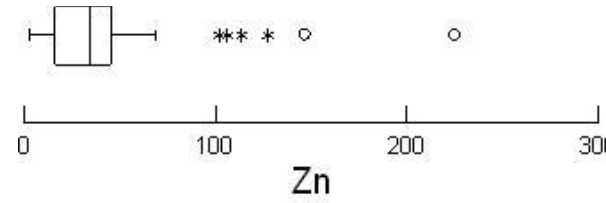

Fig. 5: Box plot of the zinc concentrations.

As to the spatial autocorrelation analysis, the above mentioned 31 samples belonging to the "non significant" category were calculated, the mean value was 29.1 μg/L with the standard deviation of 20.3 μg/L (Table 2). Therefore, the background value calculated by the spatial autocorrelation analysis method is 0-69.8 μg/L (less than 0 and replaced by 0).

Table 2: Statistical descriptive of zinc samples after outlier remover(μg/L).

	N	Min	Max	Mean	SD	CV	p-value
Zn^1	56	2.54	69.1	30.0	16.3	0.544	>0.15
Zn^2	31	2.54	102	29.1	20.3	0.699	<0.01

Note: 1 and 2 are the samples after outlier remover based on the box plot and spatial autocorrelation analysis, respectively.

COMPARISON AND DISCUSSION

For comparison, the iterative standard deviation, distribution function method (Nakić et al. 2007) and QQ plot (Panno et al. 2006) have also been applied for calculation. The results show that the environmental background values of zinc in the groundwater are 0-58.9 μg/L (iterative standard deviation) and 0-72.9 μg/L (distribution function). As can be seen from the QQ diagram (Fig. 6), there was an inflection point at the 69.1 μg/L, and therefore, it can be determined that the environmental background value was 2.54 to 69.1 μg/L.

According to the results obtained by the above methods, it can be synthesized that the calculated environmental background values are different with each other, and the main reason for this difference is their different basis: for the statistical methods (including box plot, QQ plot and iterative standard deviation, distribution function), the basis is that the background samples follow the normal distribution, whereas the spatial analysis focused on the "non mutation" feature (no significant spatial autocorrelation).

During the application, if the distribution of the element/pollutant can be determined or demonstrated, the statistics method (or the method with same principle, such as the iterative standard deviation and the probability distribution

plot (Panno et al. 2006, Nakić et al. 2007) can be considered. However, if the distribution of data is uncertain, the method of spatial analysis should be chosen.

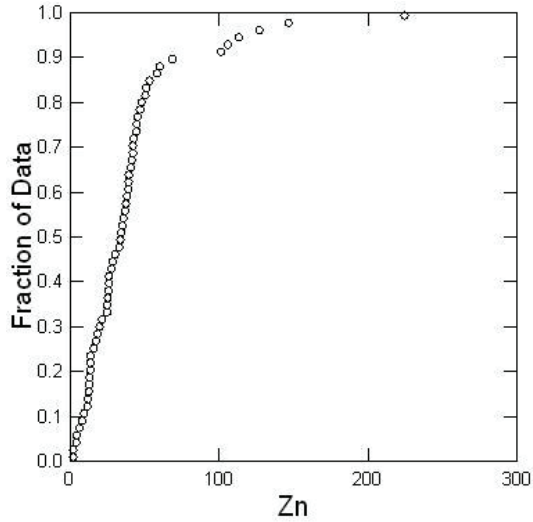

Fig. 6: QQ plot of the zinc concentrations.

CONCLUSIONS

Based on the systematic sampling and the measurement of the zinc concentrations of the shallow groundwater in Suzhou, Anhui province, China, the statistical and spatial autocorrelation analyses have been processed for the zinc concentrations, and the following conclusions have been obtained:

1. All the groundwater samples can meet the requirement of zinc concentrations of the Class I and II of the national groundwater quality standard of China, which means that they can be used for drinking purpose, however, they have medium CV and low p-value of normal distribution test, implying that the groundwater have been influenced by human activities;
2. The spatial distribution of the zinc concentration suggests that the samples with high concentrations of zinc are located near the train station, bus station and the business area, consistent with the hot spot identified by spatial autocorrelation analysis, and indicating that high density of human and transportation are the main factors influencing the zinc in groundwater;
3. The environmental background calculated by statistical and spatial analyses is 0-62.6 and 0-69.8 μg/L, respectively. They are different because of the different basis of the two methods. And during the application, they can be used with different conditions.

ACKNOWLEDGEMENTS

This work was financially supported by the program of teacher applied competence development workstation in Suzhou University (2018XJYY07), the Foundation of Scholarship Leaders (Reserve) in Suzhou University (2018XJHB08) and the Academic Funding for Top-talents in Disciplines of Universities in Anhui Province (GXB-JZD48).

REFERENCES

Anselin, L. 1995. Local indicators of spatial association-LISA. Geographical Analysis, 27(2): 93-115.

Diniz-Filho, J.A.F., Bini, L.M. and Hawkins, B.A. 2003. Spatial autocorrelation and red herrings in geographical ecology. Global Ecology and Biogeography, 12(1): 53-64.

Kemper, K.E. 2004. Groundwater-from development to management. Hydrogeology Journal, 12(1): 3-5.

Li, L., Qin, F.G. and Chen, M.H. 2004. Elementary analysis on high iron content of groundwater. Ground Water, 26(4): 260-261.

Lin, M.L. and Peng, W.H. 2016. Concentrations and health risk assessment of heavy metals in groundwater in rural areas of Suzhou City. Water Resources Protection, 32(06): 114-120.

Liu, Q. and Liang, H. 2014. The application of electrometric method and numerical simulation to evaluate groundwater resources in the Suzhou city, Anhui province. Chinese Journal of Engineering Geophysics, 11(5): 688-692.

Liu, G.D., Wu, W.L. and Zhang, J. 2005. Regional differentiation of non-point source pollution of agriculture-derived nitrate nitrogen in groundwater in northern China. Agriculture, Ecosystems & Environment, 107(2): 211-220.

Liu, W.B., Feng, C.E. and Gao, C.R. 2014. Background value of groundwater environment in Hetao Plain. Earth Science Frontiers, 21(4): 147-157.

Moran, P.A.P. 1948. The interpretation of statistical maps. Journal of the Royal Statistical Society. Series B (Methodological), 10(2): 243-251.

Nakić, Z., Posavec, K. and Bačani, A. 2007. A visual basic spreadsheet macro for geochemical background analysis. Ground Water, 45(5): 642-647.

Ord, J.K. and Getis, A. 1995. Local spatial autocorrelation statistics: Distributional issues and an application. Geographical Analysis, 27(4): 286-306.

Panno, S.V., Kelly, W.R., Martinsek, A.T. and Hackley, K.C. 2006. Estimating background and threshold nitrate concentrations using probability graphs. Ground Water, 44(5): 697-709.

Peters, A., Döring, A., Wichmann, H.E. and Koenig, W. 1997. Increased plasma viscosity during an air pollution episode: A link to mortality. The Lancet, 349(9065): 1582-1587.

Reimann, C., Filzmoser, P. and Garrett, R.G. 2005. Background and threshold: Critical comparison of methods of determination. Science of the Total Environment, 346(1): 1-16.

Reimann, C. and Garrett, R.G. 2005. Geochemical background-concept and reality. Science of the Total Environment, 350(1): 12-27.

Rodríguez-Lado, L., Sun, G., Berg, M., Zhang, Q., Xue, H., Zheng, Q. and Johnson, C.A. 2013. Groundwater arsenic contamination throughout China. Science, 341(6148): 866-868.

Sarkar, D., Datta, R. and Hannigan, R. 2011. Concepts and Applications in Environmental Geochemistry (Vol. 5). Elsevier.

Xie, Y., Chen, T.B., Lei, M., Yang, J., Guo, Q.J., Song, B. and Zhou, X.Y. 2011. Spatial distribution of soil heavy metal pollution estimated by different interpolation methods: Accuracy and uncertainty analysis.

Chemosphere, 82(3): 468-476.
Zhang, B., Song, X., Zhang, Y., Han, D., Tang, C., Yu, Y. and Ma, Y. 2012. Hydrochemical characteristics and water quality assessment of surface water and groundwater in Songnen plain, Northeast China. Water Research, 46(8): 2737-2748.
Zhang, W.L., Tian, Z.X., Zhang, N. and Li, X.Q. 1996. Nitrate pollution of groundwater in northern China. Agriculture, Ecosystems & Environment, 59(3): 223-231.
Zhang, X., Pei, D. and Hu, C. 2003. Conserving groundwater for irrigation in the North China Plain. Irrigation Science, 21(4): 159-166.
Zhao, X.F., Huang, X.J., Zhang, X.Y., Zhu, D.M., Lai, L. and Zhong, T.Y. 2009. Application of spatial autocorrelation analysis to the COD, SO_2 and TSP emission in Jiangsu Province. Environmental Science, 30(6): 1580-1587.

Nature Environment and Pollution Technology
An International Quarterly Scientific Journal

p-ISSN: 0972-6268
e-ISSN: 2395-3454

Vol. 18 | No. 4 | pp. 1235-1241 | 2019

Original Research Paper | Open Access

Construction Dust Emission Features and Management and Control Measures-A Case Study of Zhengzhou City, Henan Province

Xie Ying chuan† and Liu Chang ling
*School of Urban Construction, Henan Polytechnic Institute, Nanyang 473000, China
†Corresponding author: XieYing chuan

Nat. Env. & Poll. Tech.
Website: www.neptjournal.com

Received: 05-09-2019
Accepted: 08-10-2019

Key Words:
Building construction
Construction dust
Emission features
Control measures
Dust emission

ABSTRACT

Industrial development and urbanization progress have been rapidly increasing in China, consequently accelerating infrastructure constructions, such as real estates and public facilities. Building construction dust has become one of the main sources of atmospheric particulate matter (PM) pollution in China. In this study, a typical building in Zhengzhou City was taken as an example, wherein the total suspended particle (TSP) and PM_{10} and $PM_{2.5}$ indicators in the foundation excavation phase of the building construction were comprehensively monitored. The emission levels of both indicators were analyzed, and the periodic change laws of dust concentration and the correlations among TSP, PM_{10}, and $PM_{2.5}$ were quantitatively measured. Results indicate that the PM_{10} and $PM_{2.5}$ concentrations at the monitoring points in the downwind direction of prevailing wind were higher than those in the upwind direction. TSP, PM_{10}, and $PM_{2.5}$ concentrations reached the maximum values at 10:00-12:00 in the morning of most days, and the TSP concentration was maintained at 250-500 μg/m^3. Moreover, the coefficient of determination between TSP and PM_{10}/$PM_{2.5}$ was 0.8164/0.8376, signifying favorable correlations. The proposed management and control measures include perfecting the construction dust pollution control and management system, establishing the responsibility management mechanism of construction dust, realizing the comprehensive refined control of construction dust, promoting the innovation of building construction dust control technology, and improving the environmental consciousness for building construction dust control. These findings can serve as references for construction dust source pollutant emission control and as scientific decision-making bases for environmental researchers and managers in this field.

INTRODUCTION

Various human activities have been causing increasingly severe impacts on the environment. Resource consumption-type economic construction and extensive-type urbanization have aggravated the environmental pollution in China, and the large emission of particulate matters (PMs) is a major contributor of this phenomenon. To improve the atmospheric particulate pollution status in most cities in China, environmental protection is continuously strengthened in various regions and departments. Emissions from various sources have also been controlled. However, air pollution is not optimistic at all. Building construction dust pollution is caused by dust emissions from potential dust sources, such as construction sites, building materials, or buildings in the surrounding atmospheric environment under manual or natural activities. Building construction dust is mainly derived from the following emission processes: (1) on-site earthwork construction (e.g. earthwork excavation using an excavator), (2) dust due to vehicle running processes, and (3) dust from on-site construction machinery and transport vehicles.

The Henan Province in Central China has a large population and is now in a large-scale construction era. Housing construction areas in the building industry increase every year (Fig. 1), accompanied by the commencement and implementation of large-scale constructions. As a result, the particulate pollution problem is becoming increasingly serious. Over the years, construction activities are continuously conducted in various cities in the province. Most construction operations are implemented in an outdoor environment. The transportation, loading and unloading, stacking, and earthwork construction of engineering materials emit large quantities of PMs during the construction process. With the rapid expansion of the construction regions and areas in the Henan Province, PM emissions also rise. Consequently, air pollution in surrounding regions can become more violent than before, thereby causing a series of adverse effects.

EARLIER STUDIES

Scholars have conducted profound studies and published considerable literature regarding the emission features and

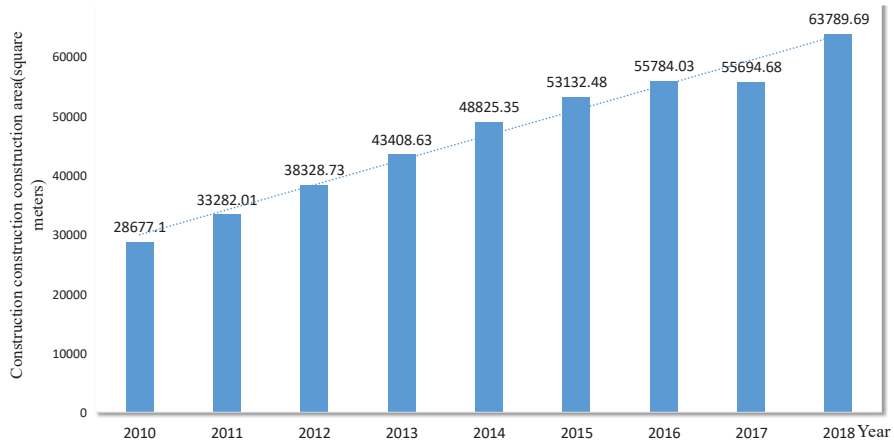

Fig. 1: Housing construction areas in the building industry in Henan Province during 2010-2018.
[Data derived from the database of National Bureau of Statistics of China (http://data.stats.gov.cn/)]

management and control measures of building construction dust. However, no universally applicable quantitative models have been established. The only extensively recognized dust emission estimation method is the Compilation of Air Pollutant Emissions Factors method, which was established by the Environmental Protection Agency of America (EPA). Lee et al. (2001) stated that due to the rapid economic development in Taiwan, large quantities of building sands and gravels are necessary to support the civil constructional engineering development. Their modelling results manifested that the actual dust emission data are associated with wind velocity, soil humidity, soil silt content, and quantity of trucks; this model can serve as a convenient tool in predicting dust emissions from building sand gravel processing plants. Kinsey et al. (2004) reported that when no construction site is available, vehicles carry the dusts and sediments to nearby roads, thereby causing re-entrainment of dusts under the action of external force. In addition, $PM_{2.5}$ is mainly derived from automobile exhausts but is not earth adhered to vehicle wheels. Muleski et al. (2005) conducted an experimental study on the PM_{10} and $PM_{2.5}$ emission factors of building construction-related operations. They discovered that building earth is the most important PM emission contributor, and that truck loading, rubble dumping, slurry, and dirt are the main sources of building dust. Zhao et al. (2006) hypothesized that PMs are the main pollutants in the urban ambient air in North China and performed a dust resuspension experiment in six northern cities in China. Their results indicated that the PM_{10}, construction waste, soil, cement, and coal combustion in the six cities are the primary causes for the increase in resuspended dusts. The rubble industry is a small-scale industry in India where most operations are manually performed. Sivacoumar et al. (2009) investigated the high-dust generation sources of 72 crushing machines and monitored the surrounding communities. Their findings revealed that the environmental dust concentration and occupational exposure level greatly exceed the standard values. Tian et al. (2009) built a mathematical model similar to the exposure profiling method recommended by the EPA to analyse the data of over 40 construction sites in the suburbs of Beijing. This model outputted a favourable scientific basis and use value. Kassomenos et al. (2010) conducted a correlation analysis of the influence factors of PM_{10} concentration and discovered that the PM_{10} in Birmingham is mainly influenced by building dust. They also reported that climatic factors can greatly affect the PM_{10} concentration. According to Guttikunda et al. (2013) PM_{10} pollution is mainly caused by the dusts induced by automobile exhaust gases and building construction, whereas $PM_{2.5}$ is the mixture of automobile exhaust gas, industrial coal combustion, and waste incineration. Peng et al. (2013) introduced a vertical scanning micro pulse laser radar system to determine the PM_{10} and $PM_{2.5}$ emission factors of heavy and light vehicles on a construction site. They also developed a new method to realize the rapid field measurement of PM emissions from urban dust sources. Pianalto et al. (2013) utilized the remote sensing data collected by special land satellite mapping units in the south of Arizona from 1994 to 2009. They found that the dust sources generated by local building construction exert a remarkable effect on air pollution. Li et al. (2014) measured the dust pollution caused by different types of construction activities during the major structural construction phase in two residential areas in Beijing. The total suspended particulate (TSP) concentration and a dust sampling instrument were set as the monitoring index and

monitoring equipment, respectively. Their comparative analysis indicated that variations are evident in the dust pollutions induced by different construction activities. Wu et al. (2005) surveyed the building dust prevention and control status in China. They also determined the main sources of construction dusts through content analysis, field investigation, questionnaire survey, and experienced professionals. They further proposed several countermeasures, including formulating pertinent laws and regulations, enacting proper charging schemes, developing feasible monitoring systems, and reinforcing trainings and propagandas on the basis of the survey results. Faber et al. (2015) reported that the emission from construction sites accounted for 17% of the total PM_{10} emission in Germany. By investigating three typical construction sites in the main city areas in Chongqing and collecting data through field investigation, Yongjie et al. determined the PM emission intensity of construction dust and annual average PM emission. They also proposed suggestions for building dust management to serve as decision-making references (Yongjie et al. 2016). Domestic and foreign studies on building construction dust are mainly concentrated on TSP and PM_{10} emission features. Only few researches involve $PM_{2.5}$ emission features. Most studies directly use emission factors but ignore the building emission factors suitable for local conditions. In addition, these studies calculate the quantity of building construction dusts according to the overall unified emission level. Few researches have conducted the analysis on different construction phases. Many studies related to construction dust focus on the estimation of overall dust emission without considering the quantitative dust analysis of internal construction activities of different projects. Thus, determining the construction activities that cause severe dust pollution is difficult. To provide a reference for environmental air quality management, the present study focuses on the analytical study of PM_{10} and $PM_{2.5}$ emission features during the concrete process-foundation excavation-in a typical construction site in Zhengzhou City, Henan Province.

SURVEY AND EXPERIMENTAL METHODS

Respondents

In recent years, large-scale construction works (e.g. buildings, roads, and bridges) are present in Zhengzhou, causing environmental particulate pollution. To objectively reflect the particulate emission levels during foundation excavation processes, a large-scale construction site in the main city area of Zhengzhou was selected as an example of a PM monitoring site. The construction site is a quasi-rectangular foundation pit with a length of 230 m, width of 160 m, and cumulative earth volume of 368,000 m^3. The carrier vehicles were operated in the evening during the construction period, and no carrier vehicle was operated during daytime when the sampling was conducted. Four monitoring points (A, B, C, and D) were set at the four corners of the monitoring site.

EXPERIMENTAL PROCESS

The foundation excavation at the monitoring site lasted for 47 days in 2018. However, the actual sampling time was only 12 days because 17 days were rainy days, and normal construction was not executed for 18 days due to road problems. The TSP and the inhalable PMs (i.e., PM_{10} and $PM_{2.5}$) were selected as dust monitoring indicators during the deep foundation excavation phase. The measuring meteorological parameters include temperature, humidity, wind direction, and wind velocity.

***Preparation of filter membrane samples*:** Quartz filter membrane was used to collect PM_{10} and $PM_{2.5}$. The membrane was preprocessed before sampling and placed in a muffle furnace for 8 h at 500°C for calcination. The membranes were allowed to cool and then dried for 24 h in a dryer. An electronic balance with a precision of ± 0.01 mg was used to weigh the membranes until a constant weight was reached. The mean value of three measured weights was taken as the mass.

***Preparation of sampling instrument*:** A flow meter was used to calibrate the flow quantity of the atmospheric particulate sampler one day before sampling. The cutter head, filter membrane groove, and other parts of the sampler were scrubbed using dust-free paper and absolute alcohol to avoid polluting the filter membrane.

***Collection of PM samples*:** The four monitoring points A, B, C, and D were respectively set at the east, south, west, and north corners of the monitoring site. The TH-150AII intelligent medium-flow sampler (Wuhan Tianhong Environmental Protection Industry Co. Ltd) was used, and the PM_{10} and $PM_{2.5}$ cutter heads were respectively utilized to obtain the PM_{10} and $PM_{2.5}$ samples at the height of 2.5 m above the ground (air flow quantity = 100 L/min). The construction peak was from 10:00 to 15:00, during which sampling was performed for 5 h. After completing the sampling, related parameters were recorded, and the filter membrane was sealed in the dryer for the follow-up analysis.

Processing of PM filter membrane samples: The mass of the filter was obtained using the method described later. The mass difference of the filter membrane before and after sampling was divided by the acquired standard volume in the current sampling process to calculate the corresponding PM_{10} and $PM_{2.5}$ concentrations by using the formula below.

$$c_{pm} = \frac{c_1 - c_2}{v}, \qquad \ldots(1)$$

Where, c_{pm} is the mean concentration of atmospheric PMs, μg/m^3; c_1 and c_2 are respectively the masses of the filter membrane before and after sampling, *mg*; *v* is the sampling volume, m^3.

Acquisition of related data: An anemorumbometer was used to conduct the simultaneous monitoring of the instantaneous and average wind speeds and directions in the construction site. The recorded PM data from the monitoring station beside the construction site served as the background values of the PM emissions. Other data, including barometric pressure, temperature, and relative humidity in this region in Zhengzhou were collected from the Henan meteorological website.

RESULT ANALYSIS

Analysis of PM_{10} and $PM_{2.5}$ Emissions

The overall PM_{10} and $PM_{2.5}$ concentrations at points B and D were relatively large, whereas those at points A and C were relatively small (Figs. 2 and 3). According to the data collected by the on-site anemorumbometer, the prevailing wind on the monitoring site during the sampling period was the northeast wind, in which points A and C were located in the upwind direction, whereas points B and D were in the downwind direction. The PM_{10} and $PM_{2.5}$ concentrations at point B (489 μg/m^3) on June 6 were higher than those in other sampling days (245 μg/m^3) because the work intensity at the construction site that day was large. The wind speed also reached the maximum value of 2.17 m/s during the sampling period, and both PM concentrations were partially high.

Periodic Change Laws of Dust Concentration

The per hour mean concentrations of TSP, PM_{10}, and PM2.5 were used to draw the time-dependent graph to observe the change laws of the three concentrations in one day. Twelve data were compared, all of which demonstrated strong similarities. The data from May 18 were selected as the representative for the detailed analysis. The wind speed and direction on this day were relatively stable, and the difference between points B and D was minor. The data of the former are displayed in Fig. 4.

The TPS, PM_{10}, and $PM_{2.5}$ concentrations reached the maximum values at 10:00-12:00 before gradually declining. During lunch break (12:00-13:00), the concentrations dropped and then increased. The TSP concentration was constant at 250-500 μg/m^3.

Correlation Analysis of TSP, PM_{10} and $PM_{2.5}$

The obtained TSP concentration was used to perform a correlation analysis of the monitored PM_{10} and $PM_{2.5}$ concentrations (Fig. 5). The variations in the TSP, PM_{10}, and $PM_{2.5}$ concentrations were kept identical, which implies that the three might have exhibited favourable correlations among each other. This inference was presented in Fig. 5. The correlation between TSP and PM_{10}/$PM_{2.5}$ matched with the coefficient of determination being 0.8164/0.8376. In addition, a linear correlation existed between TSP and PM_{10}. A correlation analysis between PM_{10} and $PM_{2.5}$ was also conducted, and the results indicated a strong high linear correlation between the two.

Management and Control Measures

Perfecting the construction dust pollution prevention and control management system: Laws and regulations and local stipulations have initially divided the power among various administrative departments concerned with construction dust pollution. However, due to the difference in

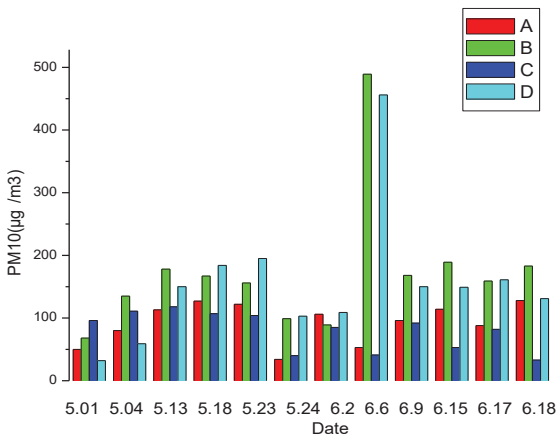

Fig. 2: PM_{10} concentration distributions at the four monitoring points during the foundation excavation phase.

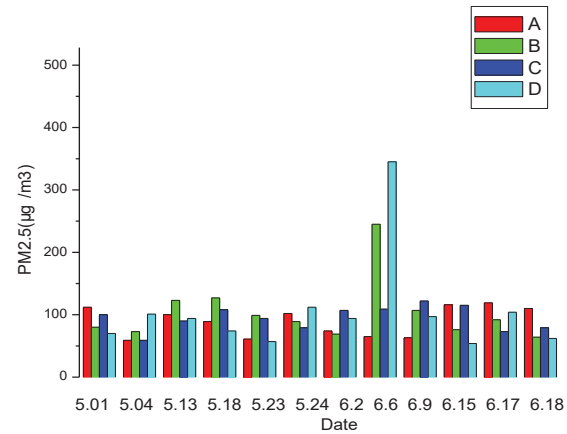

Fig. 3: $PM_{2.5}$ concentration distributions at the four monitoring points during the foundation excavation phase.

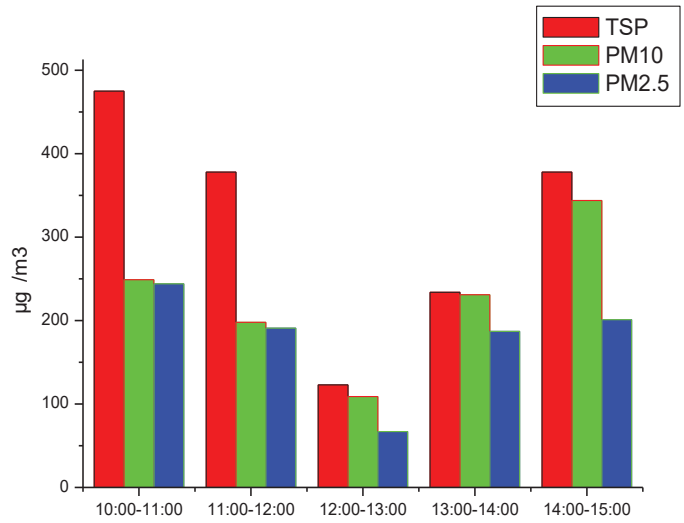

Fig. 4: Concentration change graph at point B on May 18.

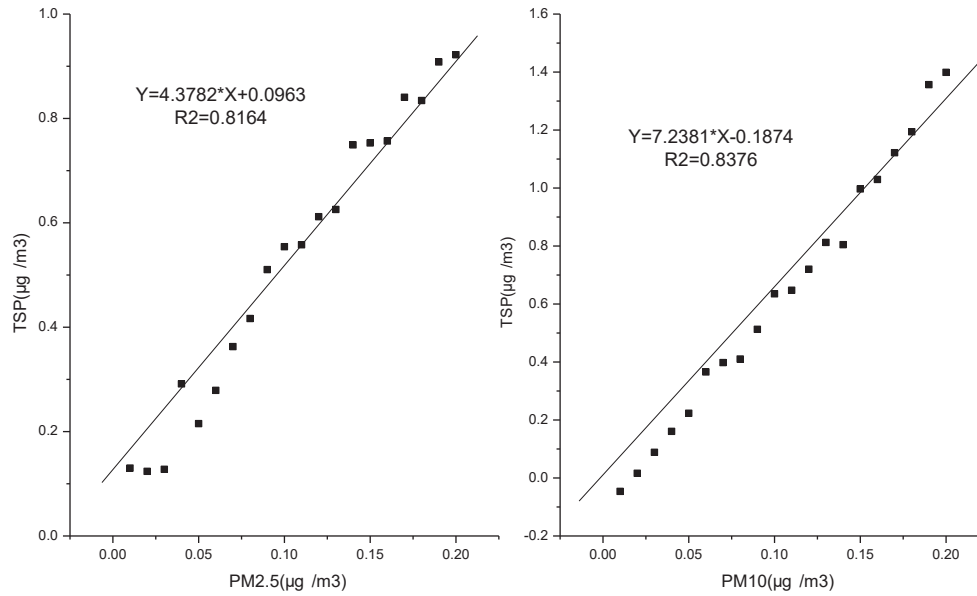

Fig. 5: Correlation analysis of TSP, PM_{10}, and $PM_{2.5}$.

time, regions, and related environment in actual operations, the power-crossing phenomenon can inevitably exist in the management process of the departments. For instance, urban management law enforcement department is usually involved in the demolition of existing buildings, and shantytown renovation management department is in charge with the demolition of buildings in shantytowns and villages in cities. Similarly, the competent administrative departments of land and resources are involved in the demolition of buildings with illegal use of land. Competent planning administrative departments handle the demolition of buildings that violate the planning process. In addition, city appearance administrative and transportation management departments are in charge of the transportation and demolition of residual building materials. To address these issues, a corresponding information sharing system and platform should be devel-

oped by assigning the environmental protection department as the leading organization and other related departments as constituent parts. Subsequently, the problems arising during the governance process and innovative opinions and suggestions must be discussed and summarized. This way, a strong coordination can be achieved among various departments, and construction dust pollution prevention and control problems can be efficiently solved.

Establishing a responsibility management mechanism for construction dust: To establish a responsibility management and assessment mechanism and form a system guided by the leader, the dust management and control systems and standards should be polished first. Related responsibilities and tasks should be executed according to these systems and standards. A management model that integrates dust control and safety construction should be developed, and full-scope supervision and assessment must be implemented to manage and control the entire process. The building construction project manager should serve as the principal of the entire project, develop the overall plans, and emphasize the importance of solving the dust pollution problem. Post managers should focus on and include dust management in the working range of the entire process management and control. They must also realize the corresponding managerial steps according to their own tasks and responsibilities. Group leaders should actively follow the command of the project department, manage dust pollution control, and construct an assessment mechanism to control dust pollution. Last, the project department head should sign a letter of responsibility with the other in-charge personnel to strengthen dust management and control.

Conducting comprehensive and refined construction dust management and control: The engineering project is divided into several areas, such as construction, living, and administrative areas. The construction area should be swept and watered by the structural unit to maintain cleanliness. Carrier vehicles must be washed to ensure a dust-free state. Other areas must also be cleaned. The keeper of the cement bunker, which is a critical control area, should take full responsibility for the area's cleaning work. Cement materials should be sealed using bags and separately stored from other materials. In addition, the cement bunker must be comprehensively sealed to ensure that the bunker is tidy. Additional attention should be paid to the transportation of construction wastes, which should be sealed before transporting using automatic flip vehicles. Any vehicle without such equipment should not be admitted to the site. Cargo deadweights must be controlled to ensure that the seal of the compartments does not have any gap. The automatic turnover process should also be gradually promoted to prevent the dust problem caused by any violent actions.

Promoting technological innovation for construction dust control: Some fences or sheds should be established before the formal architectural engineering construction. The immobility, stability, appearance and sealing state of the fence facilities must also be ensured. No fence situation or unsealed fence is allowed on the construction site. In addition, hardening treatment should be performed at the site's exits and entrances, trunk roads, material stacking area, office area, and living area with concretes. Daily cleaning work must be performed. Protective work should also be conducted at on-site material stacking areas. Moreover, some earthwork on the site should be covered or greened and solidified, depending on the building requirements and stipulations. Specific personnel should be assigned to clean and ensure the good state of construction vehicles running in and out of the site, especially those that transport sands, earthwork, and mucks, which should be shielded to guarantee air tightness and proper containment to prevent dust pollution (i.e., contents that can cause dust pollution are not exposed). Water carts, mist-spraying cannons, and other spray systems can be installed to perform dust removal work on the construction site. These systems are reliable means that can effectively reduce dust generation and realize dust pollution governance.

Improving environmental consciousness for construction dust management and control: To radically improve the environmental consciousness of construction personnel, the propaganda work of dust pollution governance should be strengthened to instill awareness on the destructive and harmful effects of dust pollution on air quality. The hazards and governance measures of dust pollution can be endorsed through related media so that people can be aware of the importance of dust governance. The guiding and supervisory roles of the media can be utilized to promote the effective implementation of urban building construction and dust pollution governance in China.

SUMMARY

With the continuous acceleration of economic development and urbanization progress in China, PM pollution has become a serious problem that influences the air quality in China. Moreover, PM concentration has become an important index that manifests atmospheric conditions. As the infrastructure construction in Zhengzhou continuously develops, dust pollution due to building construction is becoming increasingly severe, and construction dust is gradually becoming a major pollution source of atmospheric PMs. In this study, a typical building in Zhengzhou was taken as a case study to monitor the amounts of TSPs, PM_{10}, and $PM_{2.5}$ concentrations during the foundation excavation phase. The results show that the PM_{10} and $PM_{2.5}$ concentrations at the monitoring points in

the downwind direction of the prevailing wind are generally higher than those in the upwind direction. The TSP concentration is constant at 250-500 μg/m^3 in most days, and the coefficient of determination between TSP and PM_{10}/$PM_{2.5}$ is 0.8164/0.8376. The emission reduction of building construction dust can be promoted by perfecting the construction dust pollution prevention and control system, establishing the responsibility management mechanism for construction dust, performing comprehensive and refined management and control of construction dust, facilitating technological innovation for building dust control, and improving the environmental consciousness on building dust management and control. In the future, an in-depth study should be conducted by polishing the analysis on the emission factors of building construction dust and performing periodic dust monitoring of the entire construction site. Differences among emission factors in various construction phases during different seasons must also be considered.

REFERENCES

Faber, P., Drewnick, F. and Borrmann, S. 2015. Aerosol particle and trace gas emissions from earthworks, road construction, and asphalt paving in Germany: Emission factors and influence on local air quality. Atmospheric Environment, 122: 662-671.

Guttikunda, S.K., Kopakka, R.V., Dasari, P. and Gertler, A. W. 2013. Receptor model-based source apportionment of particulate pollution in Hyderabad, India. Environmental Monitoring and Assessment, 185(7): 5585-5593.

Kinsey, J. S., Linna, K. J., Squier, W. C., Muleski, G. E. and Cowherd, C. 2004. Characterization of the fugitive particulate emissions from construction mud/dirt carryout. Journal of the Air & Waste Management Association, 54(11): 1394-1404.

Kassomenos, P., Vardoulakis, S., Borge, R., Lumbreras, J., Papaloukas, C. and Karakitsios, S. 2010. Comparison of statistical clustering techniques for the classification of modelled atmospheric trajectories. Theoretical and Applied Climatology, 102(1-2): 1-12.

Lee, C.H., Tang, L.W. and Chang, C. T. 2001. Modelling of fugitive dust emission for construction sand and gravel processing plant. Environmental Science & Technology, 35(10): 2073-2077.

Li, X. D., Su, S. and Huang, T. J. 2014. Field dust monitor and distribution analysis during the main structure construction. J. Eng. Manag., 28: 1-5.

Muleski, G. E., Cowherd, Jr. C. and Kinsey, J. S. 2005. Particulate emissions from construction activities. Journal of the Air & Waste Management Association, 55(6): 772-783.

Pianalto, F.S. and Yool, S.R. 2013. Monitoring fugitive dust emission sources arising from construction: A remote-sensing approach. GlScience & Remote Sensing, 50(3): 251-270.

Peng, S., Ke, D., Chao, M., Kai, W. and Yang, W. 2013. Measuremental method of fugitive dust mass emissions from construction activities using vertical-scanning LIDAR system. Acta Optica Sinica, (3): 0301005.

Sivacoumar, R., Mohan Raj, S., Chinnadurai, S.J and Jayabalou, R. 2009. Modelling of fugitive dust emission and control measures in stone crushing industry. Journal of Environmental Monitoring, 11(5): 987-997.

Tian, G. Huang, Y. H. and Li, G. 2009. Establishment and application of four-dimensional fluxes emission factor model for construction fugitive dust Environmental Science, 30(4): 1003-1007

Wu, Z., Zhang, X. and Wu, M. 2015. Mitigating construction dust pollution: state of the art and the way forward. Journal of Cleaner Production, 112: 1658-1666.

Yongjie, D., Hong, R., Weiguang, C., Beibei, Q. and XianRui, M. 2016. Effect of construction dust on urban pm 2.5 emission characteristics: A case study of the main urban area of Chongqing, China. Nature Environment & Pollution Technology, 15(3): 833-840.

Zhao, P., Feng, Y., Zhu, T. and Wu, J. 2006. Characterizations of resuspended dust in six cities of North China. Atmospheric Environment, 40(30): 5807-5814.

Nature Environment and Pollution Technology
An International Quarterly Scientific Journal

p-ISSN: 0972-6268
e-ISSN: 2395-3454

Vol. 18 | No. 4 | pp. 1243-1248 | 2019

Original Research Paper | Open Access

Photodegradation of Congo Red Dye Via Simple and Effective Air Oxidation Using Copper(II) Chloride and Sunlight

Preeja P. Thattil and A. Leema Rose†
PG and Research Department of Chemistry, Holy Cross College (Autonomous), Affiliated to Bharathidasan University, Tiruchirappalli-620 002, Tamil Nadu, India
†Corresponding author: A. Leema Rose

Nat. Env. & Poll. Tech.
Website: www.neptjournal.com

Received: 20-03-2019
Accepted: 31-05-2019

Key Words:
Congo red dye
Photodegradation
Air oxidation
Copper(II) chloride dihydrate

ABSTRACT

This paper reports the study of photodegradation of Congo red dye which is a major pollutant in dyeing industry using copper(II) chloride dihydrate as a catalyst. The rate of degradation is improved by direct supply of air instead of using other strong oxidants. The effects of other parameters such as pH, catalyst dosage, initial dye concentration and irradiation time were studied. It was found that over 100% of the dye removal can be effectively achieved within 90 minutes of air oxidation at pH 11 and a catalyst dosage of 0.4g/L. The kinetics on the rate of degradation of the dye has also been examined by using UV-Visible spectroscopic technique. Air oxidation of Congo red dye using $CuCl_2.2H_2O$ was found to obey pseudo-first-order kinetics with respect to the substrate concentration. The study suggests the use of homogeneous $CuCl_2.2H_2O$ catalyst for the photodegradation of dyes of reactive azo dye category. Future studies on the use of catalytic activity of $CuCl_2.2H_2O$ for industrial effluents containing azo dyes as a major pollutant can be affected.

INTRODUCTION

Effluents from the textile, paper, leather, food and other industries increase the level of pollutants in our water bodies. More predominantly, the wastewater let out from the textile industries contains the chemicals associated with the dyeing process. Also, the wastewater generated by the textile industries contains an excess amount of non-fixed dyes especially the azo dyes (Riga et al. 2007, Mittal et al. 2013). Congo red dye is frequently used in the industries as an anionic dye, because of its complex structure and various diazo aromatic groups present. Congo red dyes are banned in many countries due to serious health concerns. Its structural stability makes it highly resistant to biodegradation and its bright colour and toxic nature are undesirable to the environment (Lachheb et al. 2002, Bark et al. 2010, Abo-Farha 2010). The structure of Congo red dye is shown in Fig. 1.

Due to the toxicity, mutagenic and carcinogenic characteristic of these dyes, their removal from the water bodies has become a serious concern. The advanced oxidation processes (AOPs) are the most recently employed wastewater treatment technologies, among which the catalytic air oxidation is a technique that uses a catalyst for the degradation of effluents, which require high chemical oxygen demands (Rivas et al. 2005A, Rivas et al. 2005B, Li et al. 2008). Copper(II) halides are moderate oxidizing agents (Allen et al. 2013, Bhargava et al. 2007). Air containing oxygen (21%) is highly atom-economical, environmentally benign, and abundant oxidant, which makes it ideal in many ways. The high activation energies in the reactions of oxygen require the use of catalyst. In combination with air oxidation, the chemistry of copper catalysis increases because the oxygen used here can act as a sink for electrons (Kyoung-Hum Kim et al. 2011, Cuauhtémoc et al. 2008, Guolin Jing et al. 2013). With these considerations in mind, we have developed an affordable, readily available and eco-friendly catalyst for the photocatalytic-oxidation of organic azo dyes. The main objective of the study is to evaluate the degradation efficiency of Congo red dye by using copper(II) chloride dihydrate as a catalyst. The kinetic studies were performed for the degradation process of Congo red dye.

EXPERIMENTAL

Materials and Methods

All the chemicals used in this experiment were of analytical grade. The $CuCl_2.2H_2O$ was purchased from Qualigens Fine Chemicals (purity 98%). The air pump used for the experiment was purchased from RS Electricals, the air supplied is 2.5L/min. The pH of the solution was measured using Elico Digital pH meter. The Dye used for representing organic dyes is Congo red because it is readily soluble in water. Thus, it is prepared using distilled water and used for all the experiments. The instrument UV-Visible spectropho-

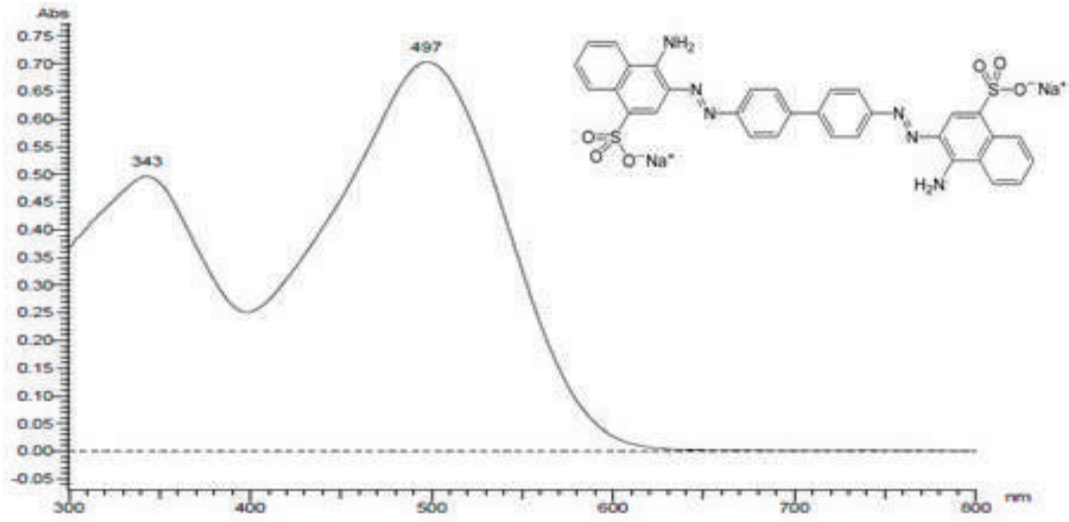

Fig. 1: UV-Visible spectrum and chemical structure of Congo red dye.

tometer (Hitachi U2910) was used to monitor the decolourization of Congo red dye for all the parameters optimized.

Photocatalytic Degradation Experiments

All the photocatalytic experiments were carried out on sunny days between 11 a.m. to 2 p.m. The sunlight intensity was measured by LT Lutron LX-10/A digital Lux meter. The intensity was nearly constant during the experiments. The average sunlight intensity was measured to be (1250 × 100) ± 100 Lx. About 0.01g/L Congo red dye was prepared as the stock solution, from which 50mL was withdrawn for each experiment. Before exposing the dye solution to sunlight irradiation, the initial absorption peak was recorded. To evaluate the effect of initial dye concentration, the concentration of the dye was varied from 0.01 to 0.05g/L and the percentage decolourization was calculated using the formula $(C_0\text{-}C_t)/C_0 \times 100$, where C_0 is the initial concentration of the dye solution and C_t is the concentration of the dye solution at time *t*. The experiment was continued for 3 hours, by withdrawing 1mL of the dye solution for every 30 minutes of irradiation. The effect of pH was studied by adjusting the solution using 0.1N NaOH and 0.1N HCl. The amount of the catalyst was varied from 10 mg to 50 mg for 0.01g/L of Congo red dye solution and the sufficient amount of catalyst for decolourization was optimized. The blank experiments were performed in the dark at room temperature following the above procedure.

RESULTS AND DISCUSSION

To determine the degradation efficiency of the copper(II) chloride catalyst, the experiments were carried out under solar light irradiation on sunny days during 11:00 a.m. to 2:00 p.m. and also in the dark conditions at room temperature. The initial absorption of the Congo red dye using UV-visible spectrophotometer showed an intense peak at 498 nm which is the characteristic peak for Congo red dye. A decrease in the intensity of absorption was observed during the course of the reaction. When 0.01g/L of the dye solution was stirred in the dark along with the copper(II) chloride salt, the calculated percentage decolourization was found to be only 31% within 90 minutes whereas the dye solution stirred under the sunlight radiation showed 85% decolourization. To improve the rate of degradation, along with copper chloride salt, air was pumped through the dye solution, which led to complete decolourization of Congo red dye as shown in Fig. 2.

Effect of Initial Dye Concentration

The effect of initial dye concentration was studied by varying the concentration of the dye from 0.01g/L to 0.05g/L keeping the amount of the catalyst 0.4g/L as fixed. When the dye concentration was 0.01g/L, complete decolourization of the dye solution is achieved, whereas it has drastically reduced to 46% at 0.05g/L as shown in Fig. 3. The degradation efficiency of the dye was found to decrease with an increase in the initial concentration of the dye solution. The intensity of the solution gets increased by increasing the concentration of the dye and thereby the path length of the photons entering into the solution gets decreased. Hence, the generation of hydroxyl and superoxide radical is limited. On further increasing the concentration of the dye solution, the length of penetration of light is further reduced and the photodegradation becomes negligible (Dafare et al.

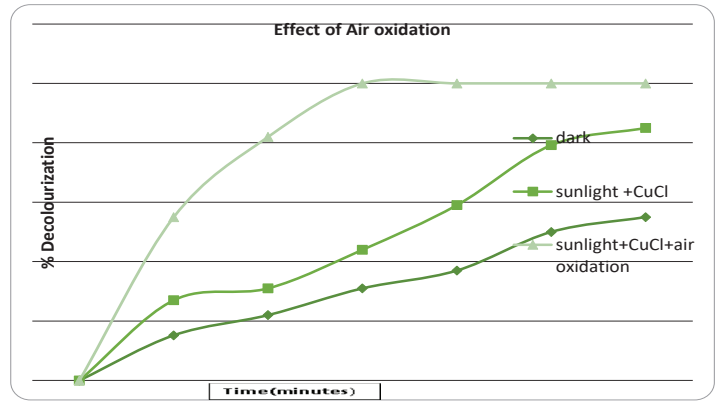

Fig. 2: Decolourization efficiency for (0.01g/L) of Congo red dye solution with 20mg of copper chloride as catalyst with pH 11 under varying conditions.

2013, Movahedi et al. 2009).

Effect of Catalyst Loading

Experiments were carried out by varying the amount of the copper(II) chloride catalyst for 0.01g/L of the dye solution shown in Fig. 4.

The maximum degradation efficiency was obtained for 20mg of the catalyst, beyond which an increase in the amount of catalyst led to the decrease in dye degradation, which may be due to the fact that, when the catalyst loading was high, there is an increase in turbidity of the suspension and shrinking of the effective photoactivated volume of suspension takes place, and thus, the photocatalytic performance of the copper catalyst gets decreased (Hatwar et al. 2016). Hence, catalyst loading was optimized to 0.4 $g.L^{-1}$ for further study.

Effect of pH

The pH of the dye solution in the present study was varied by adding solutions of NaOH and HCl. At 60 minutes, about 82% of the dye was removed at pH 11 as shown in Fig. 5. However, in the acidic pH, a change in colour from Congo red to violet took place which continued on decreasing the pH from 5 to 3 and increasing the time of sunlight irradiation. This may be due to:

i. The metachromatic property of the dye in strongly acidic solutions.
ii. Aggregation phenomenon of the dye molecules.

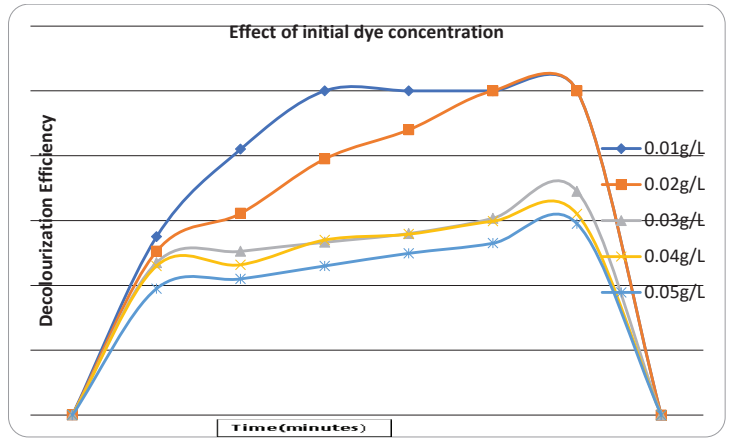

Fig. 3: Decolurization efficiency for varied concentration of congo red dye Solution (0.01g/L to 0.05g/L) with 20mg of copper chloride as catalyst with varying pH range from 3-12.

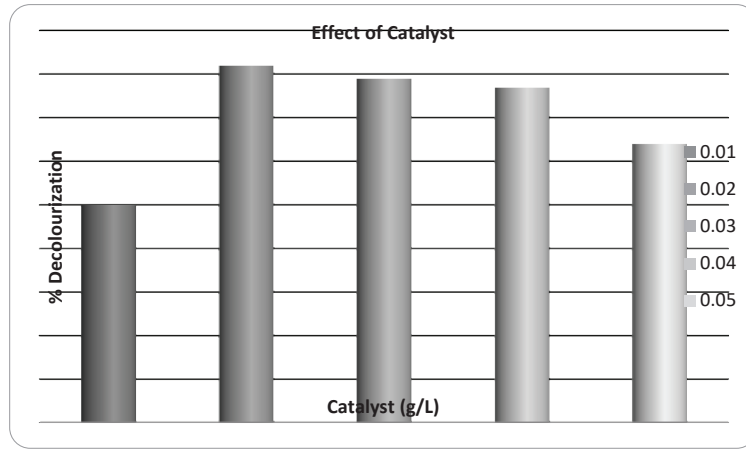

Fig. 4: Decolourization efficiency for 50mL (0.01g/L) of Congo red dye solution with varying amount (10mg to 50mg) of copper chloride as catalyst at pH range 11.

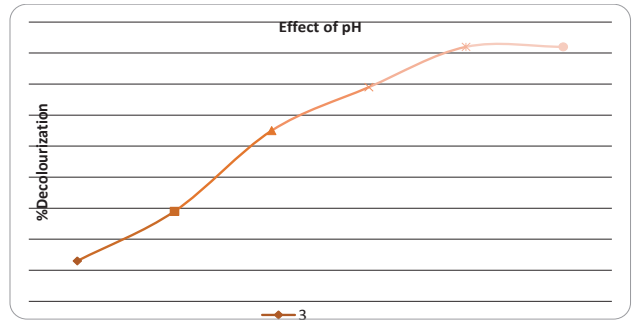

Fig. 5: Decolourization efficiency for 50mL (0.01g/L) of congo red dye solution with 20mg of copper chloride as catalyst with varying pH range from 3-12.

At alkaline pH, the more availability of hydroxyl radicals led to the dye degradation (Movahedi et al. 2009, Hatwar et al. 2016, Elaziouti et al. 2001).

Kinetic Studies

Studies from the previous research work show that most of the catalytic air oxidation (CAO) processes follow pseudo-first-order kinetics with respect to pollutant concentration (Eftaxias et al. 2001, Bhargava et al. 2016, Garg et al. 2010, Santos et al. 2004)). The first-order rate expression can be written as:

$\ln C_0/C_t = k.t$

Where, C_0 is the initial dye concentration, C_t is concentration of the dye at time t, k is the reaction rate constant. Fig. 6 shows the plot of $\ln C_0/C_t$ versus t giving a straight line for 0.01g/L of the Congo red dye solution with 20mg of the copper chloride dihydrate salt as the catalyst, the rate constant value is 0.0092 and the R^2 value is 0.9693. All the data points are positioned well on a straight line and validate the assumption.

Removal of Homogeneous Copper Ions After the Catalytic Reaction

The major drawback of using a metal ion as a catalyst in degradation of the organic pollutant is that the recovery of the metal ion from the solution is a tedious process. In the present work, the copper ions used, are considered to be toxic for microorganisms and aquatic life if present in excessive concentrations. Hence, copper needs to be eliminated from the treated water before subjecting to post bio-treatment or final disposal in a water body. Studies from the previous research work have shown that pH adjustment in a range of 6.0-8.0 gives the maximum precipitation of copper in the form of insoluble copper hydroxide (Garg et al. 2005). At higher pH values (>8.0), the formed metal hydroxide species were dissolved again in the solution. However, in the

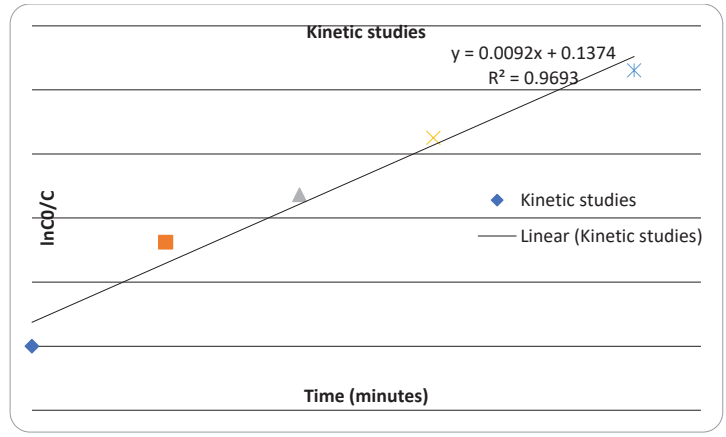

Fig. 6: The plot of lnC_0/C Vs time for 0.01g/L of Congo red dye solution.

present study, the amount of copper chloride catalyst used is well below the permissible standards (0.4g of copper salt for 0.02g/L of the dye solution) for discharge in inland surface water given by the Central Pollution Control Board, New Delhi, India (CPCB 2012).

CONCLUSIONS

The use of $CuCl_2.2H_2O$ as a homogeneous catalyst in the degradation of Congo red dye was shown to be remarkably greater and the air oxidation implemented along with the copper(II) chloride catalyst in the degradation of Congo red dye enhanced the photo-degradation process. Treatment of Congo red dye under direct sunlight showed 100% decolourization within 90 minutes of reaction time and only 31% degradation took place under dark condition. Control experiments demonstrated that both sunlight, copper chloride catalyst as well as air oxidation were needed for the effective destruction of dye. The highest percentage decolourization of Congo red dye is obtained under the alkaline pH. The observations of these investigations clearly demonstrate the importance of choosing the optimum degradation parameters to obtain high degradation rate, which is essential for any practical application of photocatalytic oxidation processes. The photocatalytic degradation of Congo red dye in the solution follows pseudo-first order reaction kinetics. As a whole, copper(II) chloride salt used as a catalyst for the decolourization of Congo red dye was nontoxic, economically viable and environmentally benign under the present reaction conditions. Future work may be extended for decolourization of the textile effluents containing dyes as major pollutants.

ACKNOWLEDGEMENTS

The authors sincerely thank Dr. S. Thennarasu, Senior Principal Scientist, Department of Organic and Bio-organic Chemistry, Central Leather Research Institute, Chennai, for his valuable suggestions given for the successful completion of the work. We also thank the PG and Research Department of chemistry, Holy Cross College, Trichy for providing the necessary laboratory facilities.

REFERENCES

Abo-Farha, S.A. 2010. Photocatalytic degradation of monoazo and diazo dyes in wastewater on nanometer-sized TiO_2. Journal of American Science, 6(11): 130-142.

Allen, S. E., Walvoord, R. R., Padilla-Salinas, R. and Kozlowski, M. C. 2013. Aerobic copper-catalyzed organic reactions. Chem. Rev., 113: 6234-6458.

Barka, N., Qourzal, S., Assabbane, A., Nounah, A. and Ait-Ichou, Y. 2010. Photocatalytic degradation of an azo reactive dye, Reactive Yellow 84, in water using an industrial titanium dioxide coated media. Arabian Journal of Chemistry, 3(4): 279-283.

Bhargava, S. K., Tardio, J., Jani, H., Akolekar, D. B., Fö1ger, K. and Hoang, M. 2007. Catalytic wet air oxidation of industrial aqueous streams. Catal. Surv. Asia, 11(1-2): 70-86.

Bhargava, S. K., Tardio, J., Prasad, J., Fö1ger, K., Akolekar, D. B. and Grocott, S. C. 2006. Wet oxidation and catalytic wet oxidation. Ind. Eng. Chem. Res., 45(4): 1221-1258.

CPCB 2012. General standards for discharge of environmental pollutants Part-A: Effluents. The Environment (Protection) Rules, 1986. Central Pollution Control Board, India.

Cuauhtémoc, I., Del Angel, G., Torres, G. and Bertin, V. 2008. Catalytic wet air oxidation of gasoline oxygenates using Rh/g-Al_2O_3 and Rh/g-Al_2O_3-CeO_2 catalysts. Catalysis Today, 133: 588-593.

Dafare, S., Deshpande, P.S. and Bhavsar, R.S. 2013. Photocatalytic degradation of Congo red dye on combustion synthesized Fe_2O_3. Ind. J. Chem. Tech., 20: 406-410.

Eftaxias, A., Font, J., Fortuny, A., Giralt, J., Fabregat, A. and Stüber, F. 2001. Kinetic modelling of catalytic wet air oxidation of phenol by simulated annealing. Appl. Catal. B., 33(2): 175-190.

Elaziouti, Laouedj, N. and Ahmed, B. 2011. ZnO-assisted photocatalytic degradation of Congo red and benzopurpurine 4B in aqueous solution. J. Chem. Eng. Process Technol., 2: 106.

Garg, A., Mishra, I. M. and Chand, S. 2005. Thermo-chemical precipitation as a pretreatment step for the COD and colour removal from

pulp and paper mill effluent. Ind. Eng. Chem. Res., 44(7): 2016-2026.

Garg, A., Mishra, I. M. and Chand, S. 2010. Oxidative phenol degradation using non-noble metal based catalysts. Clean, 38(1): 27-34.

Guolin, Jing, Minhming, Luan and Tingting, Chen 2013. Wet air oxidation of oily sludge using Ni^{+} catalyst. Environmental Progress & Sustainable Energy, 32: 99-102.

Hatwar, C.R., Deshpande, P.S., Dafare, S., Talwatkar, Bhavsar, R.S. and Hatwar, L.R. 2016. Photocatalytic degradation of Congo red dye on combustion synthesized cazro3 catalyst under solar light irradiation. Current Advanced Research, 5(8): 1170-1174.

Kyoung-Hun, Kim and Son-Ki, Ihm 2011. Heterogeneous catalytic wet air oxidation of refractory organic pollutant in industrial wastewaters: A review. Journal of Hazardous Materials, 186: 16- 34.

Lachheb, H., Puzenat, E., Houas, A., Ksibi, M., Elaloui, E., Guillard, C. and Herrmann, J.M. 2002. Photocatalytic degradation of various types of dyes (Alizarin S, Crocein Orange G, Methyl Red, Congo Red, Methylene Blue) in water by UV-irradiated titania. Appl. Catal., B, 39: 75-90.

Li, Y., Wang, J. and Liu, Y. 2008. Degradation of landfill leachate and short chain organic acids by catalytic wet air oxidation over Mn/Ce and Co/Bi catalysts. 2nd International Conference on Bioinformatics and Biomedical Engineering, iCBBE, Art. No. 4535973: pp 3047.

Mittal, A., Thakur, V. and Gajbe, V. 2013. Adsorptive removal of toxic azo dye Amido Black 10B by hen feather. Environmental Science and Pollution Research, 20(1): 260-269.

Movahedi, M., Mahjoub, A.R. and Janitabar-Darzi, S. 2009. Photodegradation of Congo red in aqueous solution on ZnO as an alternative catalyst to TiO_2, J. Iran. Chem. Soc., 6(3): 570-577.

Riga, A., Soutsas, K., Ntampegliotis, K., Karayannis, V. and Papapolymerou, G. 2007. Effect of system parameters and of inorganic salts on the decolourization and degradation of Procion H-exl dyes: Comparison of H_2O_2/UV, Fenton, UV/Fenton, TiO_2/UV and TiO_2/UV/H_2O_2 processes. Desalination, 211(1-3): 72-86.

Rivas, F. J., Beltra´n, F. J., Carvalho, F. and Alvarez, P. M. 2005A. Ozone promoted wet air oxidation of landfill leachates. Ind. Eng. Chem. Res., 44: 749.

Rivas, F. J., Beltra'n, F., Carvalho, F., Gimeno, O. and Frades, J. 2005B. Study of different integrated physical-chemical + adsorption processes for landfill leachate remediation. Ind. Eng. Chem. Res., 44: 2871.

Santos, A., Yustos, P., Quintanilla, A. and García-Ochoa, F. 2004. Lower toxicity route in catalytic wet oxidation of phenol at basic pH by using bicarbonate media. Appl. Catal. B., 53(3): 181-194.

Nature Environment and Pollution Technology
An International Quarterly Scientific Journal

p-ISSN: 0972-6268
e-ISSN: 2395-3454

Vol. 18 | No. 4 | pp. 1249-1255 | 2019

Original Research Paper | Open Access

Development of Hybrid Membrane from Clay/TiO_2-PVA for Batik Wastewater Treatment

Anwar Ma'ruf*†, M. Agus Salim Al Fathoni*, Agus Mulyadi Purnawanto and Rina Asih Kusumajati***
*Chemical Engineering Department, Universitas Muhammadiyah Purwokerto Jl. Raya Dukuh Waluh Kembaran, Purwokerto, 53182, Indonesia
**Agrotechnology Department, Universitas Muhammadiyah Purwokerto Jl. Raya Dukuh Waluh Kembaran, Purwokerto, 53182, Indonesia
†Corresponding author: Anwar Ma'ruf

Nat. Env. & Poll. Tech.
Website: www.neptjournal.com

Received: 27-02-2019
Accepted: 30-05-2019

Key Words:
Hybrid membranes
Clay/TiO_2
PVA polymer
Batik wastewater

ABSTRACT

Hybrid membranes are currently being developed to find the membrane that is having good chemical and thermal resistance. This research devotes to the development of hybrid membrane from clay/TiO_2 with PVA polymer and its application for colour wastewater filtration. The results show that the optimum concentration of PVA is 5%. At this condition, the hybrid membrane has a bulk density of 2 g/cc and porosity of 23.13%. The hybrid membrane produces the coefficient rejection of 79.48%. At the higher concentration of PVA, the filtration becomes not effective because the flux of membrane is very low.

INTRODUCTION

The growth of batik clothing in Indonesia rises very significantly. The production of batik clothing is done on a household scale. From an economic aspect, this would be good as it could improve the economy of the community, but in terms of environment is not interesting. The production of batik clothing in a household, causes problems in terms of the management of the colour liquid wastewater produced.

There are several processes to treat colour wastewater. Coagulation process can be used to treat colour wastewater using coagulant. Malakootian & Fatehizadeh (2010) treated the colour wastewater by coagulation process using caustic soda and lime. Mohamed et al. (2014) treated the dye wastewater by coagulation process using aluminium sulphate (alum), polyaluminium chloride (PAC) and magnesium chloride ($MgCl_2$).

Adsorption process can also be used to reduce the dye contaminant in the wastewater. There are kinds of adsorbent that can be used as adsorbents such as zeolite (Wang et al. 2009), activated carbon (Malik 2004) and microbial biomass (Rahman & Akter 2016, Lata et al. 2008).

Membrane separation process is extensively applied in process industries to concentrate, purify, improve the final product and wastewater treatment. Ultrafiltration, nanofiltration and reverse osmosis processes are effective for dye removal (Abid et al. 2012), Lau & Ismail 2009, Kawiecka-Skrowron & Majeska-Nowak 2011, Majeska-Nowak & Kawiecka-Skowron 2011). The characteristics of textile effluents are a very wide range of composition in terms of pH, acidity/alkalinity, type of dyes and other contaminants and may be quite hot (50-80°C). Hence, the membrane to be used for such an application should have good chemical as well as thermal resistance.

The composite membranes of ceramic/polymer are currently being developed to find the membrane that have good chemical and thermal resistance. Gongping et al. (2012) developed the ceramic/polymer composite by dip coating process for pervaporation. Biron et al. (2015) developed ceramic/polymer membrane for protein separation. The polymer used was polyamide 66 (PA66) deposited by dip coating on the inner surface of a alumina-based (Al_2O_3) microporous tube.

This research will explore the development of hybrid membrane from clay/TiO_2 ceramic and polyvinyl alcohol (PVA) by dip coating process and its characteristics. The application of the membrane for separation of batik wastewater also will be deeply studied.

MATERIALS AND METHODS

Materials

Clay was obtained from Kebumen district, Indonesia. TiO_2 was purchased from Merck. Rice starch and methylene blue

were purchased from the local market at Purwokerto, Indonesia.

Ceramic Membrane Support Preparation

Clay was crushed to the size of < 45 μm. The crushed clay was then mixed with TiO_2 (0, 5 and 10%w). The mixture was then placed at O-ring casting with the diameter of 3.2 cm and the thickness of 1 cm and pressed at 5 tons for 30 minutes. The mixture was then calcinated at the temperature of 900°C for 6 hours.

Hybrid Membrane Development

The hybrid membrane was developed by dip coating process. PVA polymer and citric acid (crosslinker) were dissolved in water and then homogenized and heated by ultrasound bath at 60°C for 30 minutes. Ceramic membrane support was dip coated at the polymer solution for 24 hours. The hybrid membrane was drying at 60°C for 6 hours then at 120°C for 2 hours. The development step of hybrid membrane production is shown in Fig.1.

RESULTS AND DISCUSSION

Characteristics of the Ceramic Support

The characterization of the prepared ceramic membrane was designed to evaluate the effect of TiO_2 content on the profile of the ceramic rheology. Fig. 2 shows the influence of TiO_2 on the bulk density of the ceramic membranes. The optimum addition of the TiO_2 is 5%w and will produce the bulk density of 1.8 gr/cm^3. At the addition of the TiO_2 of 10%w, the bulk density of the membrane will decrease. Hristov et al. (2012) reported the density of ceramic membrane developed from natural zeolite was 1.86 g/cm^3 at temperature calcination of 900°C. Bhattacharyya et al. (2005) showed that the bulk density of ceramics is influenced by sintering temperature. At the sintering temperature of 1200-1250°C, the bulk density will increase with the addition of TiO_2. But, the bulk density will decrease at the sintering temperature more than 1250°C.

The porosity of the membranes was determined by the gravimetric method using water as the wetting liquid (Singh & Bulasara 2013). To take into account the variation in the dimensions of membranes, their thickness and diameter were measured at different locations and the average values were used for calculating the membrane porosity. The porosity of ceramic membrane was determined by the equation:

$$Porosity,\ \% = \frac{(w_w - w_d)}{V_b} \text{ x } 100\% \qquad \ldots(1)$$

Where, w_w is the wet weight of the ceramic membrane; w_d is the dry weight of the ceramic membrane; and V_b is volume bulk of the ceramic membrane.

Fig. 3 shows the value of porosity of ceramic membranes. The porosity of the ceramic membranes will increase slightly due to the addition of TiO_2 powder. The optimum value of TiO_2 is 5%w. At this condition, the porosity

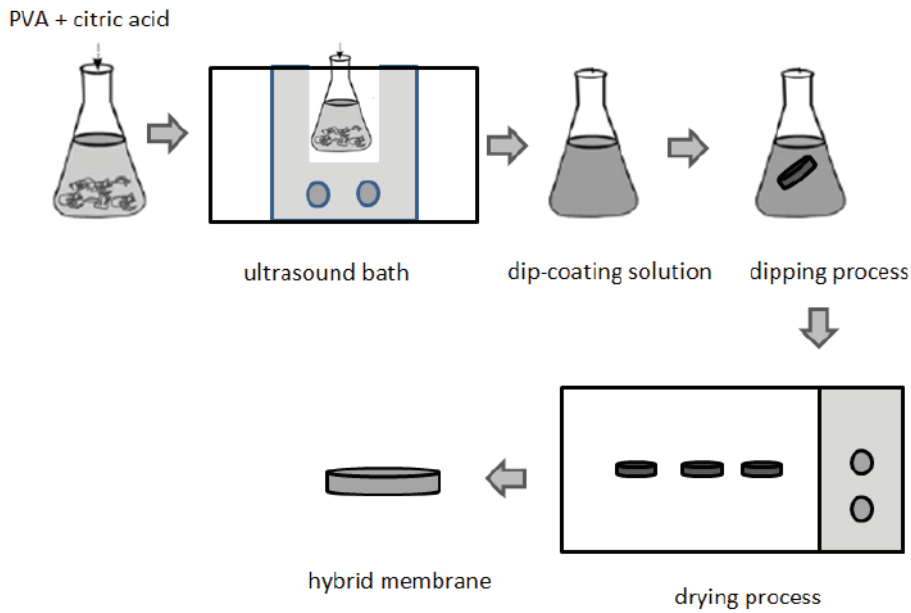

Fig. 1: The procedure of hybrid membrane production.

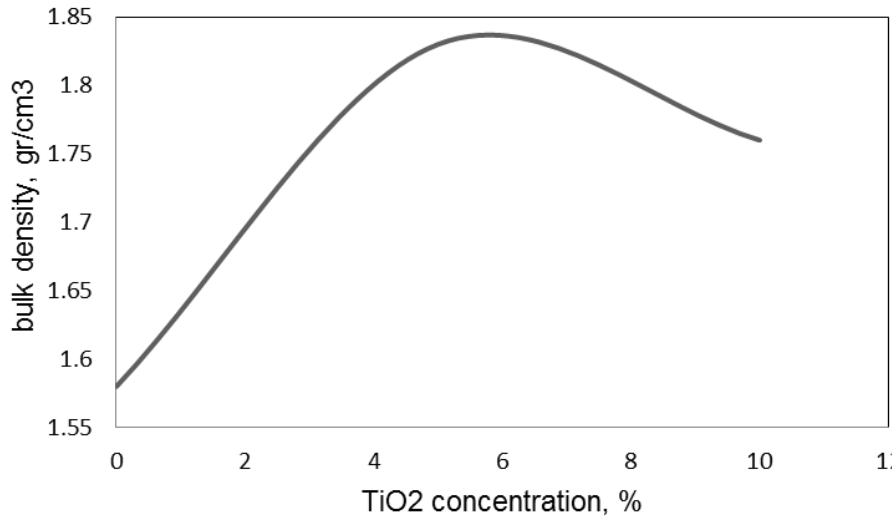

Fig. 2: The influence of TiO_2 concentration on the bulk density.

of the membrane is 28.67%. Singh & Bulasara (2013) reported the porosity of ceramic membrane from fly ash as 34.8% at the optimum sintering temperature of 900°C. Talidi et al. (2011) reported that the porosity of ceramic membranes developed from pyrophyllite clay decreased from 47% at 900°C to 31% at 1200°C.

Fig. 4 illustrates SEM pictures of ceramic membranes at the sintering temperature of 900°C in this work. Observation of the SEM pictures indicates that the membranes did not possess any cracks or surface defects. The SEM image analysis is a simple and reliable method to determine the pore size distribution of ceramic membranes in microfiltration range. Fig. 4 also shows that addition of TiO_2 influences the porosity of the membranes. The ceramic membrane becomes more porous due to the addition of TiO_2 powder.

Characteristics of Hybrid Membrane

The dip-coating process of the ceramic membrane will affect the bulk density of ceramic membrane (Fig. 5). This phenomenon can be explained that the polymers fill the

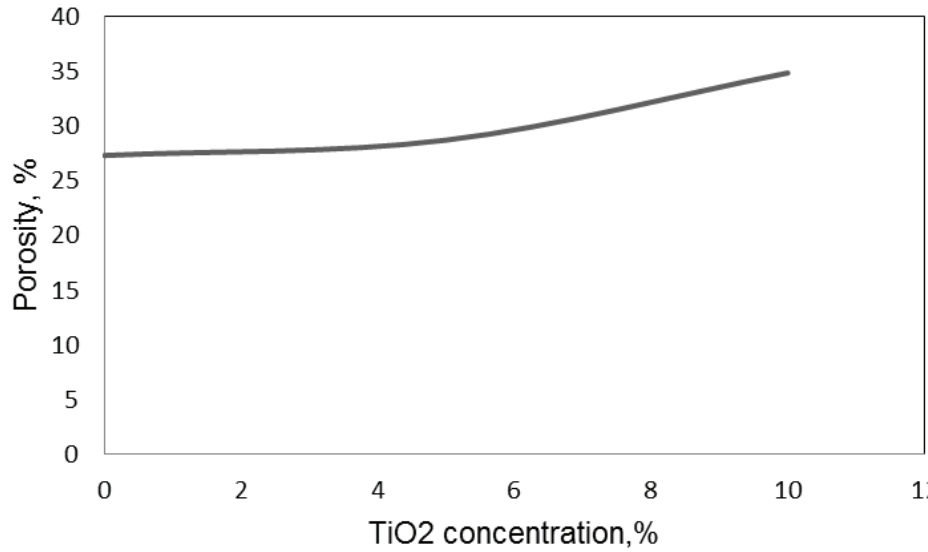

Fig. 3: The influence of TiO_2 concentration on the porosity.

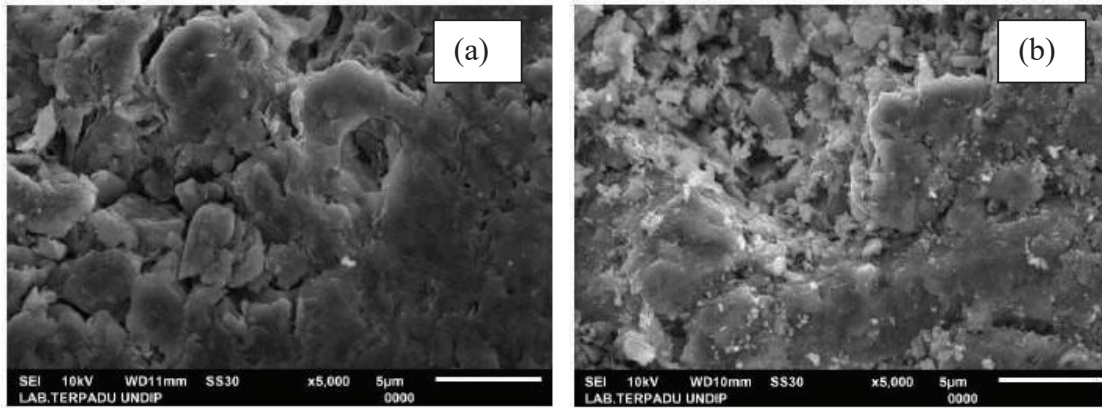

Fig. 4: SEM images of ceramic membranes. (a) 0% TiO_2; (b) 10%TiO_2.

pores of the ceramic membrane. Consequently, the porosity of the hybrid membranes will decrease (Fig. 6). It can be seen that the porosity of hybrid membrane is only 6.66% at the concentration of PVA of 10%. PVA is soluble in water, so the utilization of PVA as coating solution need crosslinker materials. In this research, citric acid was used as a crosslinker (Lusiana et al. 2016, Shi et al. 2015).

Fig. 7 shows the morphology of hybrid membrane. From the figure, the polymer coated the clay particles. The PVA polymer besides fills the pores of the ceramic membrane, and also strengthens the linkage of clay particles. The membrane becomes non fragile. The visualization of hybrid membranes at various concentrations of PVA can be seen in Fig. 8. At higher concentration of PVA polymer, the membrane becomes denser and strengthen.

Ultrafiltration of Colour Wastewater Using Hybrid Membranes

A synthetic solution of colour wastewater was prepared by dilution of 1 gram of methylene blue (wantex) into 1 L water. The concentration of dye was analysed by TDS meter. The filtration process was done at the pressure of 5 bars. Fig. 8 shows the water before and after filtration process. The hybrid membranes successfully separate the dye contaminant of the water.

Based on total dissolved solids (TDS), rejection coefficient (R) can be calculated by the equation:

$$R,\% = \left(1 - \frac{Cp}{Cf}\right) x100\% \qquad \ldots(2)$$

Where, Cp is the concentration of permeate and Cf is

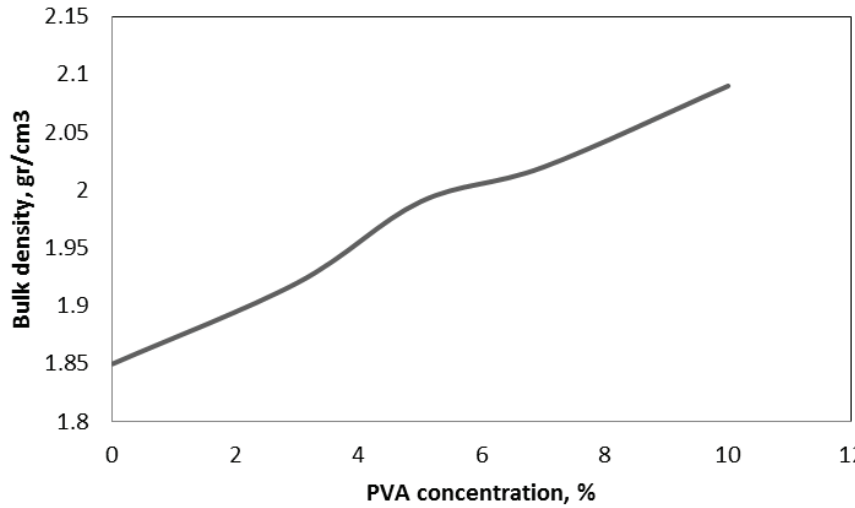

Fig. 5: The bulk density of the hybrid membranes.

the concentration of feed. The calculation shows that the maximum rejection is 79.48% (Fig. 10). It can be achieved by using a hybrid membrane with concentration of PVA as 5%. Fig. 11 shows the flux of the hybrid membranes during the filtration process. The flux of the hybrid membrane ranges from 0.0102 to 0.0037 mL/cm^2.minute (PVA 5%). At the higher concentration, the flux of membrane is very low and it can not be done.

CONCLUSION

The hybrid membrane developed from clay/TiO_2 and PVA is applicable for colour wastewater treatment. At higher concentration of PVA polymer, the membrane becomes denser and strengthen. The maximum concentration of PVA solution is 5%. The coefficient rejection that can be achieved is 79.48%.

ACKNOWLEDGMENT

The authors acknowledge the Ministry of Research Technology and Higher Education of Indonesia for funding this research.

REFERENCES

Abid, M. F., Zablouk, M. A. and Abid-Alameer, A. M. 2012. Experimental study of dye removal from industrial wastewater by membrane technologies of reverse osmosis and nanofiltration. Iran. J. Environ. Heal. Sci. Eng., 9(17).

Bhattacharyya, S., Das, S. K. and Mitra, N.K. 2005. Effect of titania on fired characteristics of triaxial porcelain. Bull. Mater. Sci., 28(5): 445-452.

Biron da, S., Poletto, P., Duarte, J., Zeni, M., Perez, C. and dos Santos, V. 2015. Preparation and characterization of pa66/alumina composite membrane. Mater. Res., 18(4): 748-755.

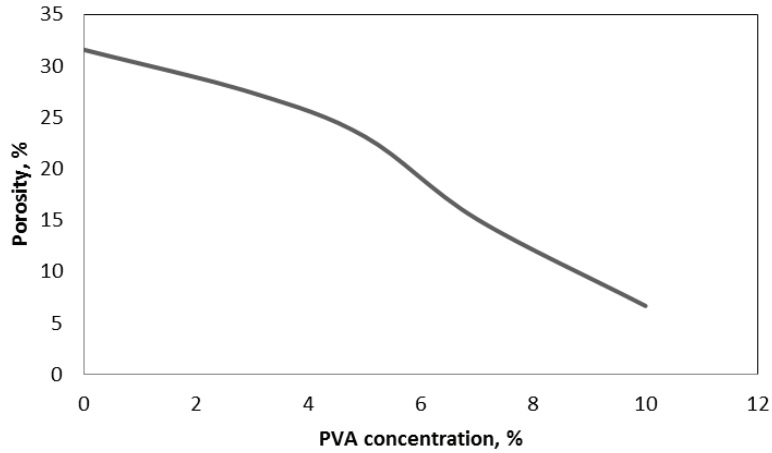

Fig. 6: The porosity of the hybrid membranes.

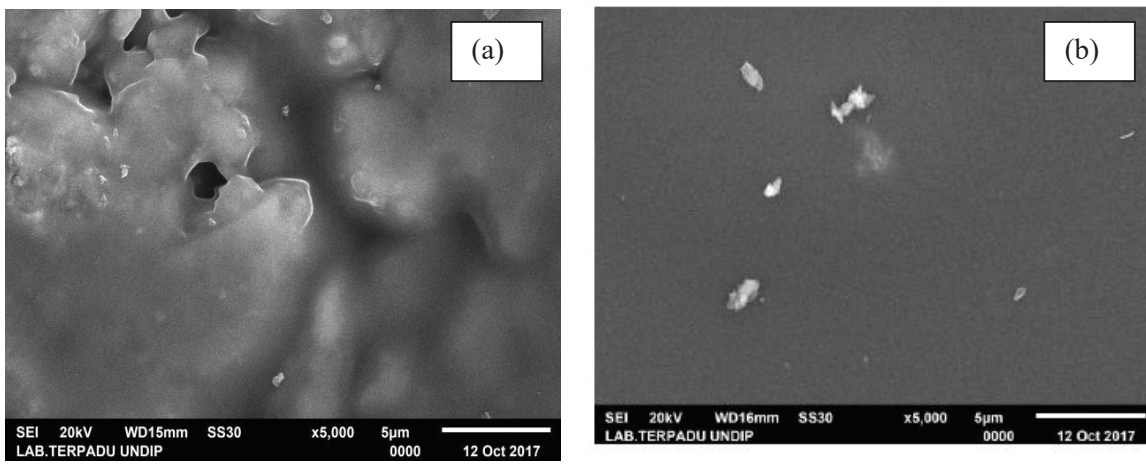

Fig. 7: The morphology of the hybrid membrane: (a) PVA 5%; (b) PVA 7%.

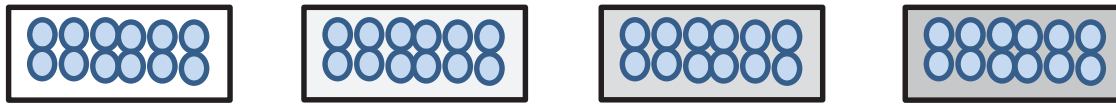

Fig. 8: The visualization of the hybrid membrane at various polymer concentrations.

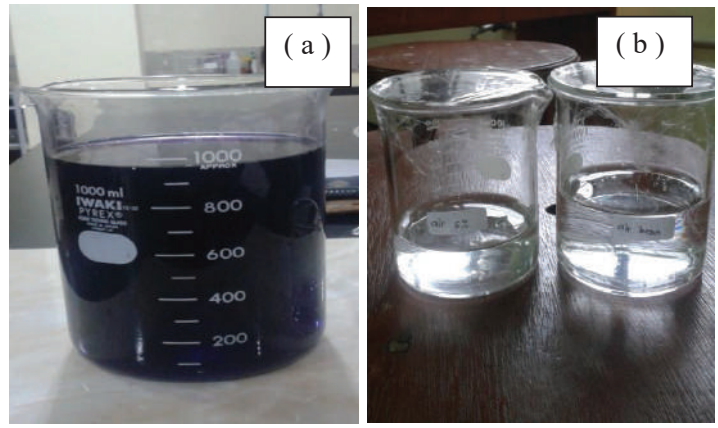

Fig. 9: Colour of batik wastewater: (a) before filtration; (b) after filtration.

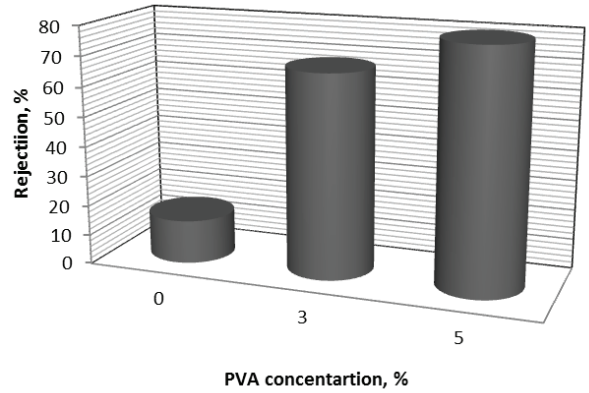

Fig. 10: Rejection coefficient of the filtration process.

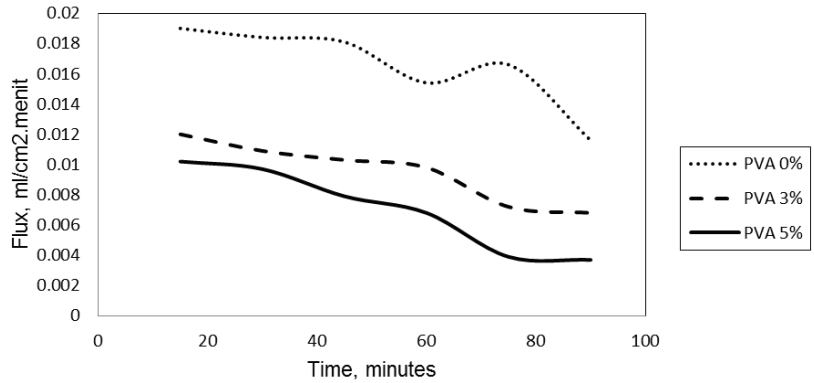

Fig. 11: Flux of hybrid membrane during the filtration process.

Gongping, L., Wang, W., Wanqin J. and Nanping, X. 2012. Polymer/ceramic composite membranes and their application in pervaporation process. Chinese J. Chem. Eng., 20(1): 62-70.

Hristov, P., Yoleva, A., Djambazov, S., Chukovska, I. and Dimitrov, D. 2012. Preparation and characterization of porous ceramic membranes for micro-filtration from natural zeolite. J. Univ. Chemical Technol. Metall., 47(4): 476-480.

Kawiecka-Skowron, J. and Majewska-Nowak, K. 2011. Effect of dye content in a treated solution on performance of the UF ceramic membrane. Environ. Prot. Eng., 37(2): 5-12.

Lata, H., Mor, S., Garg, V.K. and Gupta, R. K. 2008. Removal of a dye from simulated wastewater by adsorption using treated parthenium biomass. J. Hazard. Mater., 153(1-2): 213-220.

Lau, W.J. and Ismail, A.F. 2009. Polymeric nanofiltration membranes for textile dye wastewater treatment: Preparation, performance evaluation, transport modelling, and fouling control - A review. Desalination, 245(1-3): 321-348.

Lusiana, R.A., Siswanta, D. and Mudasir. 2016. Preparation of citric acid crosslinked chitosan/poly(Vinyl alcohol) blend membranes for creatinine transport. Indones. J. Chem., 16(2): 144-150.

Majewska-Nowak, K. and Kawiecka-Skowron, J. 2011. Ceramic membrane behaviour in anionic dye removal by ultrafiltration. Desalin. Water Treat., 34(1-3): 367-373.

Malakootian, M. and Fatehizadeh, A. 2010. Colour removal from water by coagulation/caustic soda and lime. Iran. J. Environ. Heal. Sci. Engi., 7(3): 267-272.

Malik, P.K. 2004. Dye removal from wastewater using activated carbon developed from sawdust: Adsorption equilibrium and kinetics, J. Hazard. Mater., 113(1-3): 81-88.

Mohamed, R.M.S.R., Nanyan, N.M., Rahman N.A., Kutty N.M.A.I and Kassim A. H. M. 2014. Colour removal of reactive dye from textile industrial wastewater using different types of coagulants. Asian J. Appl. Sci., 2(5): 650-657.

Rahman, F.B.A. and Akter, M. 2016. Removal of dyes form textile wastewater by adsorption using shrimp shell. Int. J. Waste Resour., 6(3).

Shi, J.J. and Yang, E.L. 2015. Green electrospinning and crosslinking of polyvinyl alcohol/citric acid. J. Nano Res., 32: 32-42.

Singh, G. and Bulasara, V. K. 2013. Desalination and water treatment preparation of low-cost microfiltration membranes from fly ash. Desalin. Water Treat., 1-9.

Talidi, A., Saffaj, N., El Kacemi, K., Younssi, S. A., Albizane, A. and Chakir, A. 2011. Processing and characterization of tubular ceramic support for microfiltration membrane prepared from pyrophyllite clay. Sci. Study Res. Chem. Chem. Eng. Biotechnol. Food Ind., 12(3): 263-268.

Wang, C., Li, J., Wang, L., Sun, X. and Huang J. 2009. Adsorption of dye from wastewater by zeolites synthesized from fly ash: Kinetic and equilibrium studies. Chinese J. Chem. Eng., 17(3): 513-521.

Nature Environment and Pollution Technology
An International Quarterly Scientific Journal

p-ISSN: 0972-6268
e-ISSN: 2395-3454

Vol. 18 | No. 4 | pp. 1257-1263 | 2019

Original Research Paper

Open Access

Health Cost of Dust Pollution of Architectural Engineering Construction in Construction Site: Evidence from China

Hu Zhaoguang*, Ma Xiaorui and Shan Wei***†**

*College of Civil Engineering and Architecture, Zhengzhou University of Aeronautics, Zhengzhou, 450046 China
**Department of Engineering Economics, Henan Finance University, Zhengzhou 451464, China
***Northeast Forestry University, Harbin, 150040, China
†Corresponding author: Shan Wei

Nat. Env. & Poll. Tech.
Website: www.neptjournal.com

Received: 08-09-2019
Accepted: 10-10-2019

Key Words:
Architectural engineering
Architectural construction
Dust pollution
Health costs
Construction site

ABSTRACT

Toxic and harmful gases, noise, industrial dust, loads, and job posture in architectural engineering construction are the different factors that influence health loss of construction workers. Among them, construction dust is a primary occupational health threat among construction workers. Accordingly, this study aims to analyze the dust pollution hazard in the architectural construction process and quantitatively estimate the health loss of construction workers. It uses a case study based on an earthwork stage in a construction site at Zhengzhou City, Henan Province, China. Environmental health risks were evaluated by using the exposure parameter method, while estimating the health losses of different objects caused by earthwork in this construction site. Results demonstrated that dust in the earthwork site was caused by the cement process and moving vehicles. Cementers and road cleaners suffered the most threats from dust with dust exposure dosages of 0.48 and 0.21 mg/kg·d, respectively. The health losses of cementers and road cleaners reached CNY 19,342.74 and CNY 14,532.36, respectively. A reduction on health costs caused by dust pollution in architectural engineering construction is possible through the following proposed measures: strengthening the monitoring of the construction workers' level of exposure to dust pollution, establishing a health management system for construction workers, focusing on the effect of environmental supervision mechanism, and standardizing the emission standards of construction dust pollution. Results could provide some references in understanding the current status and distribution law of dust pollution in construction sites, promoting the implementation of health management and protection system for construction workers, enhancing the working environment of construction workers, and quantitatively estimating the total health influences of architectural engineering.

INTRODUCTION

A considerable amount of dust is produced during architectural construction. Construction dust accounts for a large proportion of the total dust pollution in urban areas. Dust pollution threatens the physical health of workers in the architectural construction site and the people conducting activities in surrounding places. Long-term exposure to high-concentration construction dust may significantly increase the annual morbidity and death rates from cardio-cerebrovascular diseases. Atmospheric particle pollutants and health-effect endpoint, especially their relationship with death, have been proven in different countries with different types of atmospheric pollution and different pollution ranges. Architectural construction uses several machines for foundation excavation, piling, and concrete stirring while producing remarkable noise. Long-term exposure to noises may seriously influence physical health. Harmful gases (e.g., formaldehyde, benzene, and radon) produced during the decoration and use of buildings can stimulate the eyes, nose, throat, and skin and trigger the cancerization of cells in the human body. This phenomenon increases the probability of leukemia and nasopharynx and lung cancers. Dust pollution can affect the physical health of construction workers and people conducting activities in surrounding areas. Given that dust pollutants have a complicated composition, particulate matters are chosen as the symbolic pollutants in the quantitative assessment of health loss caused by atmospheric pollution. The total suspended particulate (TSP) is defined in aerodynamics as the sum of particulate matters smaller than 100 μm and closely related to the epidemiology of health-effect endpoint of a certain group.

As a provincial city of Henan Province in China, Zhengzhou has a large population and rapid development in the architectural construction industry. Fig. 1 shows that the annual growth rate of investment in real estate development and constructed floor area of real estate enterprises in Zhengzhou City increased significantly from 2007 to 2017 at 102% and 34%, respectively. Despite the rapid growth of architectural engineering in Zhengzhou City, the improvement of health

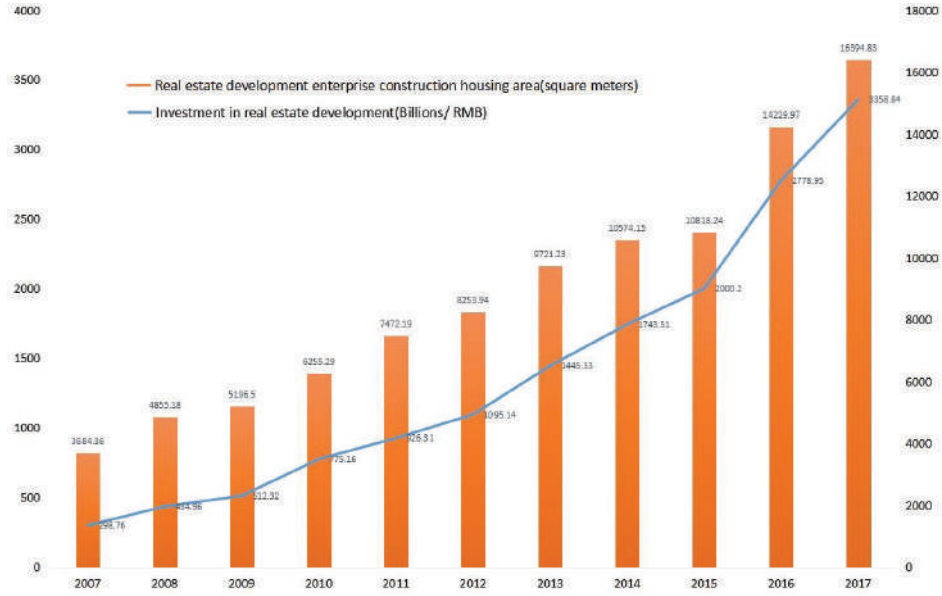

Fig. 1: Investment on real estate development and construction floor area of real estate enterprises in Zhengzhou City from 2007 to 2017. (The data are collected from the Statistical Yearbook of Henan Province.)

loss remains unclear. At present, determining whether or not dust emission and health cost caused by construction activities exceeds the requirements of national standards is difficult without an objective monitoring and assessment system of dust-induced health cost. In addition, the emission intensity of dust varies in the different construction stages, and various groups in the site suffer diverse health losses from dust. This difference further increases the difficulties in the practical implementation of relevant laws and regulations. The distribution law of practical dust-induced health cost in different construction stages and worker groups can be established by investigating the current status of dust pollution in construction sites and distribution patterns in different stages to enable the adoption of additional effective protective measures for different worker groups and subsequently formulating relevant regulations. Doing so will pave the way for the implementation of a feasible health management and security system for construction workers to improve the working environment of construction workers.

EARLIER STUDIES

Studies have reported on the health loss caused by architectural construction. These studies have focused on the health cost analysis in the different construction stages, construction workers, and construction procedures. As for environmental pollution caused by dust in construction sites, Ghandour et al. (1983) explored the dust deposit rate and composition in the Helwan industrial zone in Cairo, Egypt; they then found that construction cement industry is the main source of atmospheric pollution. Lee et al. (2001) believed that abundant building sand and gravel supported the development of civil constructional engineering in Taiwan's economy, but the processing plants of building sand and gravel were a major source of air pollution and dust emission. Chow et al. (2003) collected profile data concerning six chemical sources of geological dust in San Joaquin Valley, California by using the systematic sampling and analytical method. Accordingly, considerable amounts of dust were found to contain many heavy metal elements that might damage physical health. Svoboda et al. (2016) demonstrated that the population in urban areas was highly concentrated due to accelerated urbanization, while dust pollution produced by construction activities remarkably influenced the environment. Wu et al. (2017) offered that modern industrialized development in China led to the continuous growth of construction dust emission and thus intensified environmental pollution. Meanwhile, they investigated the status of dust control in China's construction industry and put forward an insight into relieving dust pollution in the construction industry. Zuo et al. (2017) determined that dust pollution in the process of architectural construction is an inevitable type of environmental pollution, and managers must learn how to control dust pollution in the environment and use innovative

technologies for dust pollution control. Xue et al. (2017) specified that construction areas in Beijing increased due to population growth, economic development, and continuously increasing demand for living and office spaces; consequently, such factors led to dust pollution from different construction activities. The continuously increasing dust emissions in construction sites in Beijing City have been found to cause a remarkable pressure over environmental pollution. With respect to health loss caused by dust pollution in construction sites, Bergdahl et al. (2004) conducted a follow-up survey on 317,629 male construction workers exposed to air containing inorganic dust (including asbestos, man-made mineral fiber, cement, concrete, and quartz dust) in Sweden from 1971 to 1999, their findings showed that construction workers' occupational exposure might increase the death rate caused by chronic obstructive pulmonary disease. Tak et al. (2008) assessed the occupational health conditions of workers in a highway tunnel project from the perspective of ergonomics and represented the degree of distortion of relevant body parts during construction operations. Zhang et al. (2008) pointed out that dust produced by construction projects was an important cause of atmospheric pollution and might cause harm to the physical health of humans. They then proposed a method for evaluating the environmental influences of dust and proved the scientificity of this evaluation system through a case study. House et al. (2010) investigated the morbidity of hearing loss among 169 construction workers and concluded that a statistically significant correlation exists between construction work and low hearing level. Johncy et al. (2011) carried out a tracking detection on the cardiopulmonary functions of 61 construction workers and compared them with another set of 61 ordinary people (control group) with similar physical conditions. They found that construction work caused certain influences on the cardiopulmonary function of the human body, and such influences became very significant after working in the construction industry for more than 10 years. Šukys et al. (2011) examined the economic loss in the construction industry due to failure in occupational safety and health requirements. Their research method reflected the occupational safety and economic benefits of health investment. Finally, certain policy suggestions were proposed to reduce the quantity of occupational diseases and working accidents. Abrar et al. (2017) evaluated the health conditions of workers during a highway restoration work in Lahore City by choosing six sites; they then concluded that noises, vibration, dust, asphalt smoke, poor working postures and injuries in the construction site were major threats to the physical health of workers. Nioi et al. (2018) determined that construction workers exposed to sunshine for a long time and excessive exposure to solar ultraviolet light triggered the workers' susceptibility to skin cancer. According to existing studies, developed countries abroad all believed that dust pollution caused by construction activities seriously affected the physical health of different types of workers. Tracking investigation is a popular research method that analyzes the damaging effects of different construction factors based on practical health conditions of workers and construction activities and the environment of different worker groups. Given the existence of many construction sites, acquiring the environmental data of construction sites is easy. The management level of different construction sites may also cause different health losses of construction workers. In this study, environmental parameters can correspond to health parameters of construction workers by introducing the exposure parameter method to analyze the physical health of construction workers. This study aims to provide good references for health management of architectural construction and the quantitative assessment of other health loss factors.

BRIEF INTRODUCTION TO THE MODEL AND DATA SPECIFICATION

Brief Introduction to the Model

The exposure parameter method is an important approach for assessing the environmental health risk of one or several harmful compounds. It describes the quantity and rates of exposure of the human body to foreign matters through breathing, oral intake, and skin by using the exposure parameters. Hence, this method can calculate the absorbed dosage of harmful substances by the human body from the environment. Based on accurate estimation of the human body's absorbed dosage of harmful substances, harmful compounds in the existing health risk evaluation system are divided into threshold (generally non-carcinogenic) and threshold-free (generally carcinogenic) compounds.

The accurate calculation of *ADD* in the health risk assessment is important:

$$\mathrm{ADD}=\frac{C\times IR\times EF\times ET\times ED}{BW\times AT} \quad \ldots (1)$$

Where, *C* is the environmental concentration of harmful substances and acquired directly from the original monitoring data before this study (mg/m^3). *IR* is the respiratory rate that refers to the volume of absorbed human by human in the unit time under a certain temperature (m^3/h). *EF* is the exposure frequency that refers to the frequency of the human body being exposed to the environment and expressed by the number of exposure days in a year. In this study, *EF* is the annual number of construction d/a workers' working days (d/a). *ET* is the continuous exposure time (h/d). *ED* is the continuous exposure time (a). *BW* is the body weight used as the main reference of evenly distributed exposure dosage

(kg). *AT* is the total exposure time that refers to the time a human body is exposed to the environment throughout his/her life; *AT* refers to the total years of construction work from employment to retirement (a). Finally, the unit of calculated *ADD* is mg/kd·d.

After calculating *ADD*, its health risk is represented by the damage index (*R*) in the health risk evaluation because TSP in dust belongs to the threshold compound. Health risk is calculated as follows:

$$R=\frac{ADD}{RFD}\times 10^{-6} \quad \ldots(2)$$

Where, *ADD* is the calculated exposure dosage of the human body to harmful substances in the exposure parameter method. It refers to the human body's adsorbed dosage of harmful substances when the concentration of harmful substances reaches a certain value. *ADD* is calculated by using the Eq. (1). *RFD* is the reference dosage of the substance, and the numerical value of different compounds was obtained from the exposure parameter manual issued by United States Environmental Protection Agency. *R* is a dimensionless parameter denoting the health risk of health exposure of the human body.

Risk is distributed to the relevant diseases according to proportions, and the disability-adjusted life year (*DALY*) was calculated on the basis of the damage factor of different diseases. In addition, the risk in Eq. (2) is a life-long exposure risk. Therefore, the following risk of practical damage is the product of the calculated life-long exposure risk and the ratio of continuous exposure time and lifetime:

$$DALY=n\times\sum_t R\times Q_i\times W_i\times L_i\times P_i \quad \ldots(3)$$

Where, *R* is the health risk of dust calculated from Eq. (2). Q_i is the risk factor of different diseases, that is, the distribution proportion of risks in different types of damage. W_i is the damage factor of the disease with a value between 0 and 1. L_i is the average expected residual life. P_i is the number of affected people. *n* is the number of exposure times, that is, the relevant days in the construction stage. Finally, the value of life year (WTP) of health loss caused by dust is calculated as follows:

$$WTP = DALY \times VLY \quad \ldots(4)$$

Where, *VLY* is the value of life year per unit *DALY*. Therefore, the year of disability and loss can be expressed by the currency (RMB/year). From Eqs. (1) to (4), the social payment willingness of *VLY* for dust-induced health loss can be calculated.

DATA SPECIFICATION

Dust-induced health loss analysis requires days in the construction period and number of workers in the different stages of a specific project. The construction period in the different stages somewhat varies in each project. On the basis of the analysis of a residential community in Zhengzhou City, the construction process can be divided into earthwork, main structural construction, and secondary structure and indoor decoration stages. In this study, the earthwork stage was monitored from May 1, 2018 to July 23, 2018. By analyzing data gained from in-situ monitoring of construction sites, the distribution situations and pattern of dust concentration in the earthwork stage were summarized. Finally, health loss caused by dust pollution in the earthwork construction stage was calculated.

RESULT ANALYSIS

Classification of Construction Workers

Unlike the direct monitoring of dust concentration in the construction environment, this study evaluated health loss of employees in the construction industry, including construction workers and site managers. On the basis of early preliminary analysis of dust monitoring data, dust concentrations in different regions of different stages were analyzed, and the environmental concentration in different regions of a construction site was obtained. The worker groups in these regions might suffer different health losses from exposure to dust due to the remarkable differences in dust concentration among the different regions in a construction site. Accordingly, Table 1 lists the evaluation objects in the earthwork stage in different regions.

Estimation of Dust Exposure Dosage

In this case, the residential community in Zhengzhou City is in the earthwork stage. A deep and large foundation exists,

Table 1: Health loss evaluation objects in the earthwork stage.

Objects	Number	Activity range
mManagers	28	Office building in the construction site
Road cleaners	17	Two sides of the road
Cementer	18	Cement processing region
Rebar processing staff	16	Rebar processing region
Foundation operators	49	Foundation operation region

and the total earth volume is over 450,000 m^3. The two types of dust involved in the earthwork stage are siliceous and cement dust. The former comes from soil and is diffused into the air by passing vehicles or natural wind. The latter is from the dry cement used in construction and is diffused during machinery processing and dumping. The dust data in the earthwork stage were monitored throughout the entire stage. Table 2 presents the monitoring results in the different regions.

Table 2 shows that the average dust concentration at different points is higher than the national standards in the earthwork stage. Moreover, a certain difference exists in terms of dust concentration at the different regions of the construction site. Hence, different workers in the construction site may suffer from different health costs from dust pollution. The construction worker group is the closest to the direct emission source of dust pollution in the construction site, and they suffer the most serious health loss from dust pollution. Foundation excavation is not the main source of dust in the construction site. Thus, the dust pollution it creates leads to small health losses among construction workers. In the earthwork site, dust comes from cement processing and passing vehicles. Cementers and road cleaners at both sides of the roads suffer the most serious health loss from dust pollution. Dust from cement processing falls under high-intensity emission in a short period. Although the emission peak of dust is high, it disperses rapidly. Relevant workers shall adopt relevant protective measures from dust pollution.

According to monitoring data and Eq. (1), the exposure dosage of different groups to dust in the earthwork stage is calculated. Table 3 lists the results.

Table 3 shows that cement dust emission generally occurs in the machinery processing of cement. Cementers must directly pour abundant dry cement into a machine. The vibration of the machine and wind pressure produced during operation cause a considerable amount of cement particles to fly in the air and produce high-concentration dust emission. Consequently, the dust exposure dosage of cementers is substantially higher than those of other worker groups. Road cleaners are the second major group exposed to dust pollution. Cleaners are required to clean the surface in the earthwork stage, which results in dust flying into the air. Therefore, the dust exposure dosage of road cleaners is also maintained at a relatively high level.

WTP Value of Health Cost

Based on previous calculation, the WTP values of health costs of different groups were calculated using Eqs. (2)-(4). Fig. 2 illustrates the results.

Dust-induced health risk and health cost of different worker groups are compared (Fig. 2). Foundation operators and managers suffer relatively small dust-induced health costs. In the earthwork stage, road cleaners and cementers suffer the highest health risks and costs caused by dust pollution. In this case study, the total number of construction workers was around 65. Construction workers are the principal victims of dust-induced health costs. Health costs of cementers and road cleaners reached RMB 19,342.74 and RMB 14,532.36, respectively. This finding is explained by the high-intensity emission the dust production has in a short

Table 2: Dust concentration and number of affected people at different points.

Points	Type of dust	Test time	Concentration range (mg/m^3)	Average concentration (mg/m^3)
Office building	Siliceous dust	12	0.63–0.98	0.76
Rest area of workers	Siliceous dust	16	0.38–1.84	1.35
Rebar processing region	Siliceous dust	8	0.54–1.20	0.98
Foundation operation region	Silicious dust	9	0.12–1.65	1.03
Two sides of the road	Silicious dust	15	1.39–7.83	5.39
Cement processing region	Silicious dust	23	1.98–29.49	12.56

Table 3: Exposure dosage of different groups to dust in the earthwork stage (ADD).

No.	Staff composition	C (mg/m^3)	IR (m^3/h)	EF (d/a)	ET (h/d)	ED (a)	BW (kg)	AT (a)	ADD (mg/kg.d)
1	Managers	0.76	0.48	308	8	0.15	63.83	73	0.03
2	Rebar processing staff	0.98	0.48	308	8	0.15	63.83	73	0.04
3	Foundation operators	1.03	0.48	308	8	0.15	63.83	73	0.04
4	Road cleaners	5.39	0.48	308	8	0.15	63.83	73	0.21
5	Cementer	12.56	0.48	308	8	0.15	63.83	73	0.48

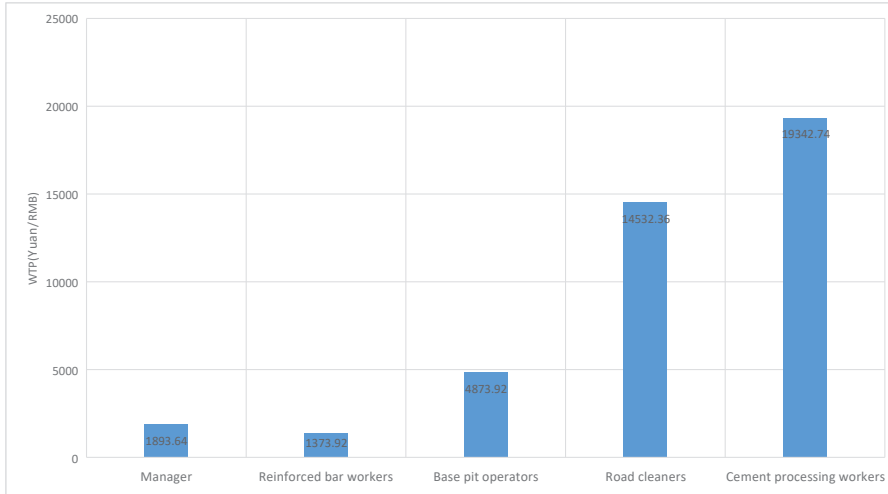

Fig. 2: WTP value of health costs of different worker groups.

period via cement processing. Although the dust emission peak is high, it disperses rapidly. Therefore, cementers need targeted protection. The hardening pavement combined with watering is an effective method of controlling dust on the road. Notably, watering can effectively decrease dust concentration and has high cost performance. However, pavement hardening can considerably reduce cumulative dust. The combination of watering and pavement hardening can control dust concentration within a standard range.

POLICY SUGGESTIONS

Strengthening the monitoring of the different construction worker groups' level of exposure to dust pollution: Following the spatial distribution of workers in the construction site and construction activity characteristics of different groups, this study formulated a set of overall construction monitoring scheme covering earthwork, the main structural construction, and indoor decoration. This scheme could realize dust monitoring in a specific region of the construction site. The research conclusions could provide a theoretical foundation for investigating the direct source of dust pollution in the construction site and analysing the distribution pattern of dust.

Apart from the earthwork stage, high-concentration dust in the two other stages is produced in a closed operation space. Therefore, the protection of involved workers and indoor ventilation conditions can be improved. Moreover, strengthening the supervision of managers in key-closed working areas is suggested to protect the occupational health of relevant workers.

Setting up a health management system for construction workers: A scientific and authoritative dust-induced health cost database was formed by recording and collecting the above health cost data to further supplement the environmental dust concentration data in practical projects. Accordingly, a series of standard regulations and management methods, such as dust concentration and health management standards of construction workers in the construction region, could be formulated further to provide practical management guarantee to the occupational health of construction workers. The research mode of monitoring, calculation, and analysis on dust supervision and assessment in construction sites can be further promoted. This research mode closely related to management can be applied to other contexts involved in the exposure parameter method, such as monitoring of a specific toxic substance and health cost assessment in the decoration stage. The results can provide references for implementing specific monitoring and management mechanisms to identify similar factors causing occupational health risks.

Focus on the environmental monitoring system: After trials and practices in China, the environmental supervision organization cooperates with the construction unit on the basis of a contract and offers construction unit technological services as the social third party. The environmental supervision organization and construction unit have a common goal to promote the environmentally friendly completion and acceptance of projects. The construction unit shall change its view regarding the environmental supervision organization from an administrative unit into a cooperative partner. Moreover, the construction unit shall make full use of the environmental supervision organization not only in the construction process but also in employee training to increase the consciousness and operation level of workers in terms

of dust pollution control. The construction unit shall focus on the role of the environmental supervision organization in dust pollution control and exploit its cooperative power rather than limit its function to supervision and management.

Standardizing the emission of dust pollution in the construction site: Dust pollution control in the construction site requires corresponding supervision and emission standards. The installation of an advanced dust tester is suggested in core areas of the construction site to test the content of particulates. Then, the test data shall be uniformly uploaded into the detection platform, and the dust supervision system will immediately send alarms upon exceeding the standards. The majority of construction sites have installed online dust supervision devices according to the requirements of relevant departments. Additional enterprises of supervision device manufacturing are increasingly participating in dust pollution control in construction sites with the development of dust online monitoring in construction and demolishing sites. On the basis of the scientific charging standard and method for dust emission, other administrative sanctions (e.g., punishment per day) shall be adopted to penalize enterprises with exceeding emission of dust pollution.

CONCLUSIONS

Dust pollution is a major atmospheric pollution in the architectural construction stage that causes serious health costs to the human body. Dust pollution will cause serious health losses to workers and managers in the construction site and to the people living and conducting activities in surrounding areas.

Accordingly, this study carried out a case study on the basis of the earthwork stage of a construction site in Zhengzhou City, Henan Province, China. Environmental health risk was assessed by using the exposure parameter method, and health costs to different construction workers in the study area were estimated. The results demonstrated that the dust exposure dosage of cementers and road cleaners reached 0.48 and 0.21 mg/kg·d, and their health costs amounted to RMB 19,342.74 and RMB 14,532.36, respectively. This study further provided some policy suggestions, including strengthening the monitoring of different construction worker groups' level of exposure to dust pollution, setting up a health management system of construction workers, focusing on the environmental monitoring system, and standardizing the emission of dust pollution in the construction site. Finally, it suggests further currency value estimation of dust-induced health costs throughout the construction period of a project, a big data analysis concerning health costs throughout the construction period, analysis on the relationship between different construction management modes and dust emissions, and implementation of the specific toxic substance monitoring and health-cost assessment in a specific construction stage.

REFERENCES

Abrar, A., Cheema, K.J., Saif, S. and Mahmood, A. 2017. Health status assessment of workers during construction phase of highway rehabilitation projects around lahore, Pakistan. Journal of Occupational Health, 59(1): 74-80.

Bergdahl, I. A., Toren, K., Eriksson, K., Hedlund, U., Nilssonz, T., Flodin, R. and Jarvholm, R. 2004. Increased mortality in COPD among construction workers exposed to inorganic dust. European Respiratory Journal, 23(3): 402-406.

Chow, J.C., Watson, J.G., Ashbaugh, L.L. and Magliano, K.L. 2003. Similarities and differences in PM10 chemical source profiles for geological dust from the San Joaquin Valley, California. Atmospheric Environment, 37(9-10): 1317-1340.

Ghandour, M. F. M. E., Salam, M. S. A., Hindy, K. T. and Kamel, M. M. 1983. Studies on air pollution from construction plants in Helwan industrial area-I. Total dust deposition over the area. Atmospheric Environment, 17(2): 305-309.

House, R. A., Sauve, J.T. and Jiang, D. 2010. Noise-induced hearing loss in construction workers being assessed for Hand-arm Vibration Syndrome. (Quantitative Research) (Report). Can J Public Health, 101(3): 226-229.

Johncy, S.S., Ajay, K.T., Dhanyakumar, G., Raj, N.P. and Samuel, T. V. 2011. Dust exposure and lung function impairment in construction workers. J. Physiol. Biomed Sci., 24(1): 9-13.

Lee, C. H., Tang, L. W. and Chang, C. T. 2001. Modeling of fugitive dust emission for construction sand and gravel processing plant. Environmental Science & Technology, 35(10): 2073-2077.

Nioi, A., Wendelboe-Nelson, C., Cowan, S., Cowie, H., Rashid, S., Ritchie, P., Cherrie, M., Lansdown, T.C. and Cherrie, J.W. 2018. A randomised control crossover trial of a theory based intervention to improve sun-safe and healthy behaviours in construction workers: study protocol. BMC Public Health, 18(1): 259.

Svoboda, P. and Kurth, H. 2016. Environment effects - Dust pollution and soil protection. Applied Mechanics and Materials, 843: 111-117.

Šukys, R., Čyras, P. and Šakėnaitė, J. 2011. Economical loss due to non-compliance with requirements personnel safety and health in lithuanian construction sector. Journal of Civil Engineering & Management, 17(2):168-176.

Tak, S.W., Paquet, V., Woskie, S., Buchholz, B. and Punnett, L. 2008. Variability in risk factors for knee injury in construction. Journal of Occupational and Environmental Hygiene, 6(2): 113-120.

Wu, Z., Zhang, X. and Wu, M. 2016. Mitigating construction dust pollution: State of the art and the way forward. Journal of Cleaner Production, 112: 1658-1666.

Xue, Y.F., Zhou, Z., Huang, Y.H., Wang, K., Nie, T., Nie, L. and Qin, J.P. 2017. Fugitive dust emission characteristics from building construction sites of Beijing. Environmental Science, 38(6): 2231-2237.

Zuo, J., Rameezdeen, R., Hagger, M., Zhou, Z. H. and Ding, Z. K. 2017. Dust pollution control on construction sites: Awareness and self-responsibility of managers. Journal of Cleaner Production, 166: 312-320.

Zhang, Z. and Fan, W. U. 2008. Health impairment due to building construction dust pollution. Journal of Tsinghua University, 48(6): 922-925.

Nature Environment and Pollution Technology
An International Quarterly Scientific Journal

p-ISSN: 0972-6268
e-ISSN: 2395-3454

Vol. 18 | No. 4 | pp. 1265-1273 | 2019

Original Research Paper | Open Access

Performance, Emission and Combustion Characteristics of Safflower, Neem and Corn Biodiesels Fuelled in a CI Engine

K. Balasubramanian*† and K. Purushothaman**

*Department of Mechanical Engineering, Sathyabama Institute of Science and Technology, Chennai-600119, India
** Department of Mechanical Engineering, St. Peter's College of Engineering and Technology, Chennai-600054, India
†Corresponding author: K. Balasubramanian

Nat. Env. & Poll. Tech.
Website: www.neptjournal.com

Received: 06-06-2019
Accepted: 21-06-2019

Key Words:
Safflower oil
Neem oil
Corn oil
Biodiesel
Smoke emissions

ABSTRACT

Renewable fuels are desirable as alternate fuels with ignition quality equivalent to diesel and its combustion parameters, but unsuitable for direct operation in diesel engines as fuel because of their higher viscosity. Hence, fuel and engine-based modifications are being developed to improve the performance, emission and combustion behaviour of the compression ignition engines. The higher viscosity of fuel oil does not let it vaporize even after it is being injected into the combustion chamber. Therefore, converting the higher viscosity of vegetable oil into biodiesel improves the atomization resulting in better combustion. Issues related to the use of biodiesel as working fuel are its oxidation stability and performance. In this study, safflower oil, neem oil and corn oil are used as fuel oils. The experimental results displayed a significant increase in the brake thermal efficiency of 28.25% for corn oil methyl ester (COME). HC and CO emissions are lower with corn oil methyl ester. At full load, the smoke emission reduces slightly with corn oil methyl ester about 58% opacity respectively, but it is still lower than diesel having 66.2% opacity.

INTRODUCTION

In recent years, vehicles have become one of the major sources of pollution in urban areas, especially from diesel engines. The use of diesel engine is increasing especially in heavy vehicles due to its higher torque and better fuel economy compared to gasoline fuelled engines. The faster depletion of fossil fuels and stringent emission norms demand an alternate source, to replace the conventional fossil fuel. Factors much needed for this search of alternative fuel is lower emission, stability and availability of the fuel, distribution of the fuel, and its effect on the engine durability which ensures smooth operation of engine. Extensive prior research in last three decades, for using non edible oil (Agarwal et al. 2007, Edwin Geo et al. 2008, Sureshkumar et al. 2008, Nabi et al. 2009, Dhananmurugan et al. 2015, Thiyagarajan et. al. 2016 and Prakash et al. 2018) paves the fundamental understandings to make scientific conclusion and decisions.

Vlada et al. (2018) analyse the biodiesel production from corn oil as a feedstock via the transesterification, the obtained biodiesel was blended with diesel and respective fuel blends were formed. The fuel properties of the biodiesel were analysed, performances and exhaust gas emissions of corn-based biodiesel and its blends with diesel fuel were tested. Finally, issues related to the environmental and socio-economic impacts of corn-based biodiesel production and its distribution were also tackled. The increased biodiesel production from corn oil has reduced CO_2 emissions.

Jayashri et al. (2017) investigated the emission and performance characteristics of CI engine fuelled with blends of Neem oil biodiesel. Biodiesel is prepared from Neem oil by transesterification technique by adding 1% v/v H_2SO_4. The tests were conducted with the respective combination of B10, B20, B30 blends. The experimental results show that lower emissions and higher performance are seen in B10 blend than the other blends and diesel. The brake thermal efficiency was higher than diesel, and CO, HC and NO_x emissions were 23%, 8.5% and 22% lower than diesel.

Ali et al. (2013), made an analysis in considering the aspects related to the production of biodiesel from Neem oil and investigated the fuel properties. The seeds of Neem contain 30-40% of oil; the obtained biodiesel from the neem oil by transesterification are mono alkyl esters. The optimum conditions to achieve maximum yield of biodiesel were investigated at different temperatures and with different molar ratio of Neem oil and methanol.

Atuldhar et al. (2012) investigated the performance, emission and combustion behaviour of biodiesel and its various blends with diesel, and compared with baseline data in a direct injection CI engine. BSFC for biodiesel and its blends was higher than diesel, and BTE of all biodiesel blends was found to be higher than diesel. CO and HC emissions for biodiesel fuelled engine were lower than die-

sel but NO emissions were higher for biodiesel blends. Heat release rate for all biodiesel blends was almost identical to diesel. Combustion duration for biodiesel blends was found to be shorter than diesel.

Ilkılıc et al. (2011) converted the neat safflower oil into biodiesel using transesterification process with the catalysts of sodium hydroxide (NaOH) and methanol. The biodiesel was blended with diesel fuel by 5% (B5), 20% (B20) and 50% (B50) by volume. The tests were conducted in a single cylinder CI engine to compare biodiesel blends with diesel. The results show that the average performance reductions were 2.2%, 6.3% and 11.2% for B5, B20 and B50 fuels. BSFC was increased by 2.8%, 3.9% and 7.8% as average for B5, B20 and B50, respectively. Considerable reductions were seen in PM and smoke emissions with the use of biodiesel. CO emissions also decreased for biodiesel blends while NOx and HC emissions increased. But the increases in HC emissions can be neglected as they have very low amounts for all test fuels.

Senthil Kumar et al. (2015) evaluated the use of kapok methyl ester in a single-cylinder direct injection CI engine. The investigation was made to analyse the performance and emission characteristics. The results show that exhaust gas temperature and specific fuel consumption are increased for rich blends of Kapok methyl ester, but dip in brake thermal efficiency. The NOx emission was higher than that of diesel at all load conditions. The lean blend of the Kapok methyl ester shows appreciable engine efficiencies, lower values of smoke, and lower CO and HC emissions.

SAFFLOWER, NEEM AND CORN OILS

Safflower Oil

Safflower is a highly branched, herbaceous, thistle-like annual plant. It is commercially cultivated for vegetable oil extracted from the seeds. The seed of safflower oil is white in colour and has a lot of proteins and fats. The extracted oil from these safflower seeds is colourless and flavourless. It is basically same as sunflower oil but safflower oil is more nutritious. It has less fatty acid than olive oil. Safflower seeds usually have 40% of oil by weight. The plant has yellow, orange or red flowers. Each branch will usually have from one to five flower heads containing 15 to 20 seeds per head. Safflower is native to arid environments having seasonal rain. It grows a deep tap-root which enables it to thrive in such environments.

Neem Oil

India is a largely agrarian society with more than a hundred million families dependent on farming for a living. The liberalized Indian economy still depends on the success of agricultural production and 35-40% of India's national income comes from agricultural sources. It is indigenous to India and found in tropical and subtropical regions like Pakistan, Bangladesh, Sri Lanka, and Myanmar. The Siwalik hills, dry forests of Andhra Pradesh, Karnataka and Tamil Nadu (India) are the main habitat of the wild population. Neem is a renewable source of various useful products, seeds and leaves being of particular interest. A fully-grown tree yields about 50 kg fruits and about 350 kg leaves annually. From about 14 million neem trees that grow in India, 0.7 million metric tonnes of fruits and about 5 million metric tonnes of leaves, besides, 83,000 tonnes of Neem oil and 3,30,000 tonnes of Neem cake are expected to be produced annually.

Corn Oil

In India, nearly 2.6 thousand quintals of corn oil is produced in corn-based factories. Average cumulative extraction capacity of these factories is 2.41 thousand tones/day. On an average these factories can extract 3.0-3.5% oil from corn, which contains 5-6% of oil. Thus, there is immense scope to increase the production of corn oil only by improving the efficiency of oil extraction from corn germs. The properties of test fuels as given in Table 1.

Table 1: Properties of test fuels.

PROPERTIES	DIESEL	SME	NOME	COME
Density@15˚C (g/cc)	0.840	0.8929	0.910	0.876
Kin. Viscosity@40˚C (cSt)	3.6	6.61	4.2	4
Lower Calorific Value (kJ/kg)	42,700	38,646	39,820	39930
Cetane Index	45-55	34	55	54

TRANSESTERIFICATION PROCESS

Fig. 1 shows the esterification test setup employed for the transesterification process. Neat safflower, neem and corn oil was converted into biodiesel through the alkaline transesterification reaction for which sodium hydroxide/potassium hydroxide (NaOH/ KOH) was used as a catalyst with methanol. One percent of sodium hydroxide catalyst was dissolved in methanol by 50% in volume and mixture was added to the safflower oil. Then the prepared mixture was stirred at 60ºC for 30 minutes. After that, the reactant material was poured into a transparent vessel and allowed for cooling at room temperature for 8 hrs. It was allowed to settle for separation of glycerol as the bottom layer. The upper layer of biodiesel was put into another transparent vessel for washing with an equal amount of water. The respective biodiesel was heated above 100ºC for 10-20 minutes to re-

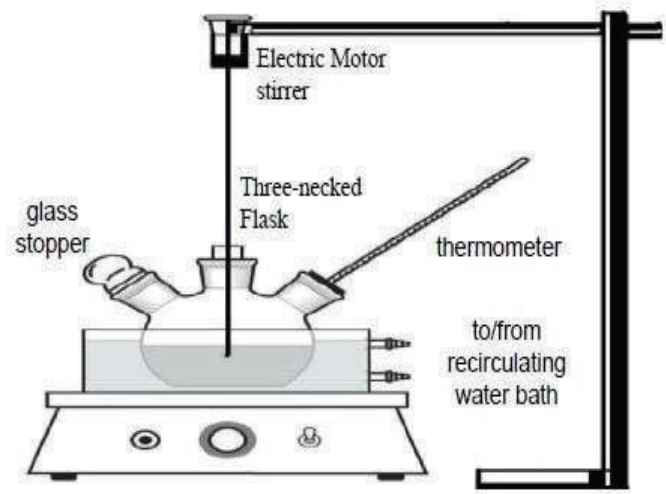

Fig. 1: Schematic diagram of the esterification test setup.

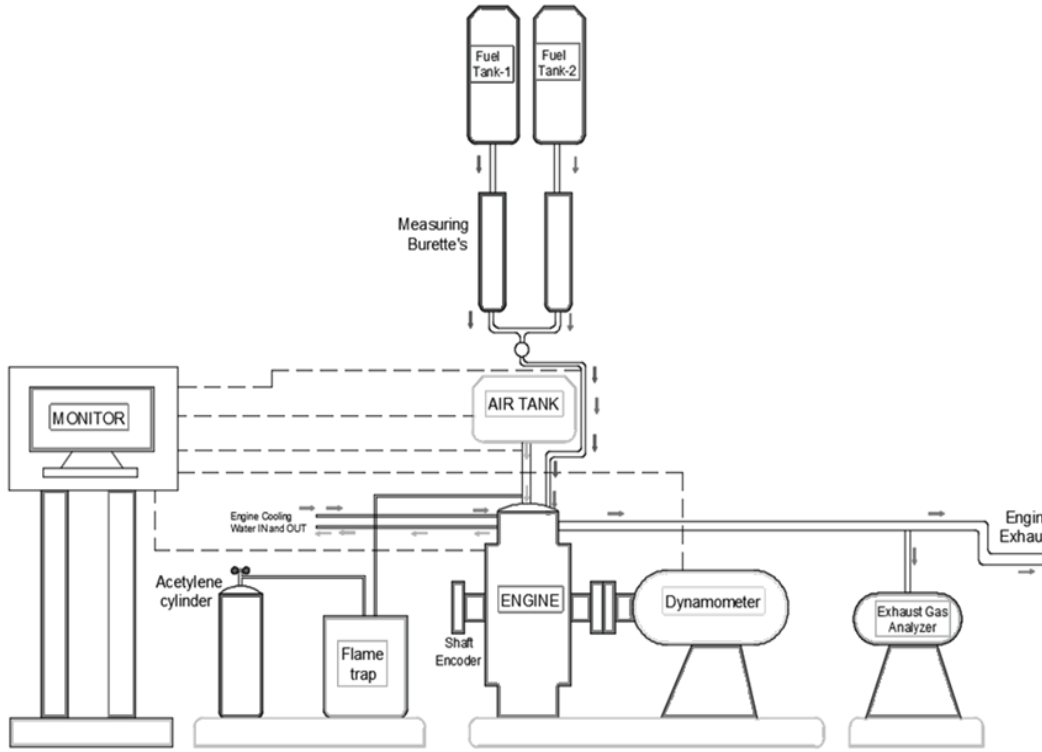

Fig. 2: Schematic diagram of experimental setup.

move excess water. Then the biodiesel was cooled down to room temperature for 10-20 minutes before use.

EXPERIMENTAL SETUP AND TEST PROCEDURE

The tests were conducted in a single cylinder 4 stroke compression ignition engine developing a rated power output of 5.2 kW at 1500 rpm. The specifications of the test engine are given in Table 2. Eddy current dynamometer was employed in loading the engine, the experimental setup was supported with the data acquisition system. In-cylinder pressure was measured using a piezoelectric transducer and charge amplifier. A schematic diagram of the experimental

setup is shown in Fig. 2. A precision optical-electronic encoder with a resolution of up to 1°CA was used. An oxide of nitrogen and unburnt hydrocarbon emission was measured using a Non-Dispersive Infrared (NDIR) based exhaust gas analyser. Smoke was measured by % opacity using AVL smoke meter. K-type thermocouple was employed to measure the exhaust gas temperature. The optimum fuel injection timing has been set to 23°CA bTDC for diesel, SME, NOME and COME at various loading conditions. The 'Engine Soft' software was interfaced with the engine with the help of suitable hardware so that the sensors and transducers provided the required input to the software for the calculation of performance parameters.

RESULTS AND DISCUSSION

Performance Characteristics

Brake thermal efficiency

Table 2: Engine specifications

Make	Kirloskar
Model	TV1
Type of Engine	4 stroke single cylinder, CI, Vertical, Water cooled
Rated power	5.2 kW @ 1500 rpm
Compression ratio	17.5:1
Engine bore	87.5mm
Stroke	110mm
Cubic capacity	661.5cm3
Loading device	Eddy current dynamometer

Fig. 3 shows the variation of brake thermal efficiency with respect to brake power for various test fuels at different load conditions. Brake thermal efficiency for diesel, safflower methyl ester (SME), neem oil methyl ester (NOME) and corn oil methyl ester (COME) is 30.74%, 26.10%, 27.27% and 28.25% respectively, at full load. The higher viscous and dense nature of SME leads to the poor combustion characteristics resulting in decrease in brake thermal efficiency, when compared to all test fuels. The poor spray characteristics with large size fuel particles, resulting in poor atomization and vaporization; mixing becomes improper leading to late and sluggish combustion. The properties of NOME and COME favour the combustion, having lower viscosity, density and higher calorific values when compared to SME. Hence, combustion and subsequent heat release are good, contributing to higher brake thermal efficiency for COME compared to SME and NOME. The brake thermal efficiency for COME at full load was 28.25% where for diesel it was 30.74%.

Brake Specific Energy Consumption (BSEC)

Fig. 4 shows the variation of brake specific energy consumption with respect to brake power for various test fuels at different load conditions. Brake specific energy consumption for diesel, SME, NOME and COME are 11.68 MJ/kWh, 13.65 MJ/kWh, 13.20 MJ/kWh and 12.75 MJ/kWh respectively, at full load. Brake specific energy consumption was lower for COME due to the better volatility, reduced viscosity and density leading to better combustion as a result of good air fuel mixture preparation. Brake spe-

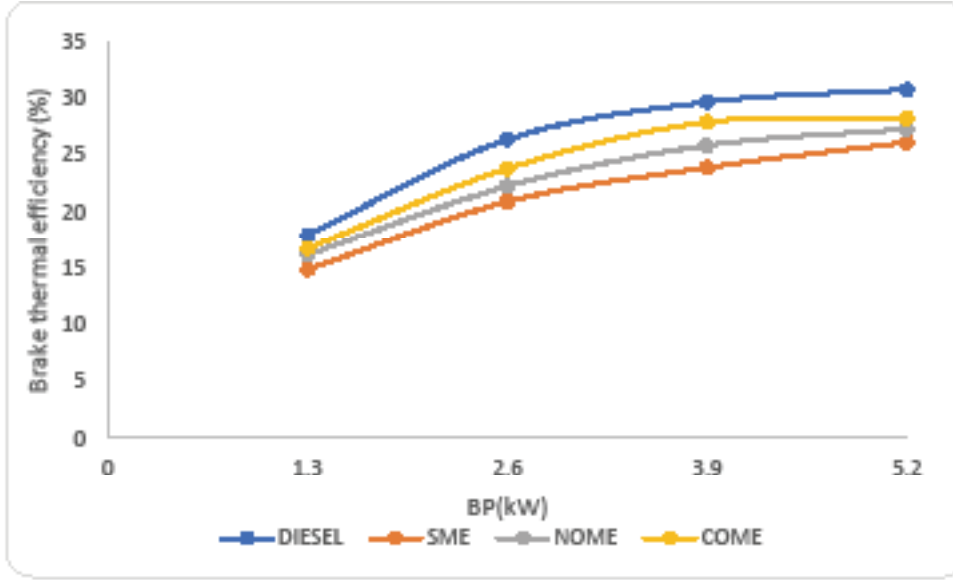

Fig. 3: Variation of brake thermal efficiency with brake power.

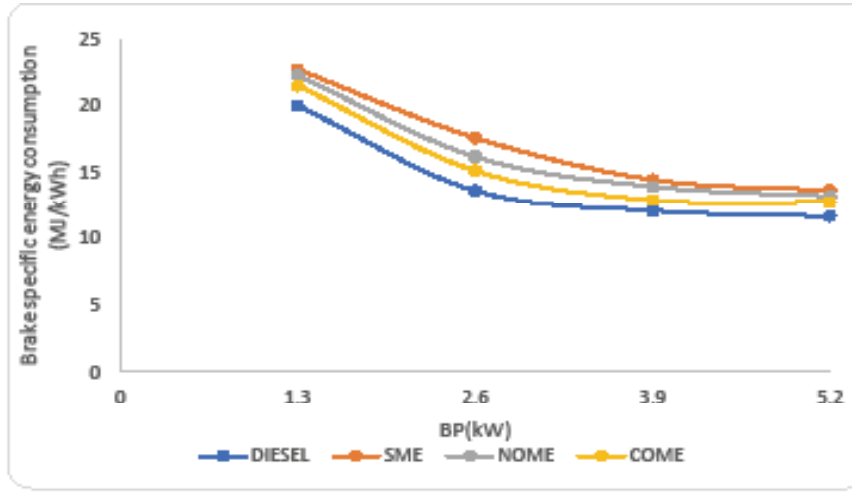

Fig. 4: Variation of brake specific energy consumption with brake power.

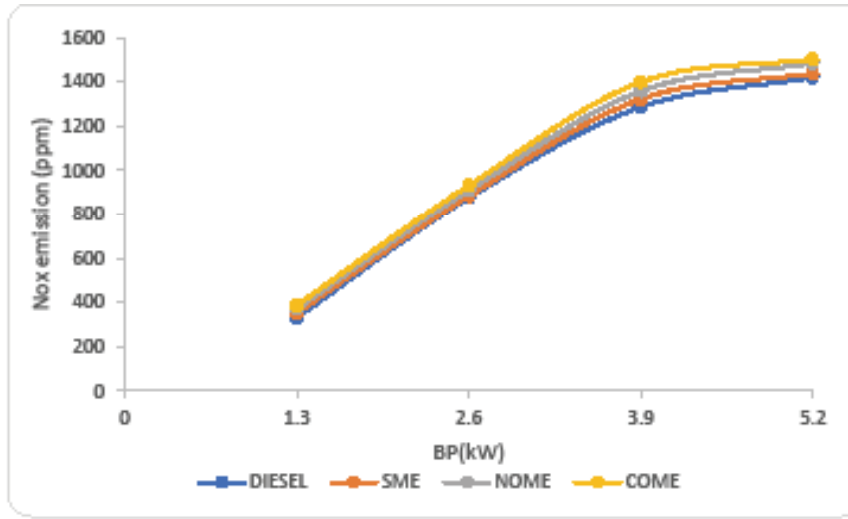

Fig. 5: Variation of nitric oxide emission with brake power.

cific energy consumption for the base diesel was 11.68 MJ/kWh. Lower heating value of SME requires larger fuel flow rates to maintain constant power output from the same engine.

Emission Characteristics

Nitric oxide emission (NO)

Fig. 5 shows the variation of NO emission with respect to brake power for various test fuels at different load conditions at a speed of 1500 rpm. NO emission for diesel, SME, NOME and COME was 1419 ppm, 1437 ppm, 1483 ppm and 1502 ppm respectively, at full load. NO emission was lower for SME in comparison with diesel, due to its increased viscosity and density, ending up in sluggish combustion. The heat released during the premixed combustion phase is less which results in lower in-cylinder temperature and hence lower NO formation. At full load, SME produces 1437 ppm NO emissions, which is lower compared to NOME and COME. The favourable conditions for NO emission are increased in-cylinder temperature and the availability of O_2 molecule, the increased trend of NO emission was visible in COME and other tested fuels. The fuel properties like viscosity and density favours along with oxygen availability in the fuel increases the heat release rate compared to SME. Producing NO emission of 1502 ppm for COME even higher when compared to diesel operation.

Smoke emission

Fig. 6 shows the variation of smoke emission with respect to brake power for various test fuels at different load condition. At full load, smoke emission for diesel, SME, NOME and COME is 66.2%, 64.5%, 60.93% and 58% opacity respectively. SME, NOME and COME emitted less smoke emission when compared to diesel due to the presence of oxygen available in the biodiesel which oxidises the soot particles at higher temperature.

Hydrocarbon Emissions (HC)

Fig. 7 indicates the variation of HC emissions with respect to brake power for various test fuels at different load condition. HC emissions for diesel, SME, NOME and COME was 52 ppm, 50 ppm, 48 ppm and 45 ppm respectively, at full load. The reduction in HC emissions with SME, NOME and COME is due to the presence of oxygen in the biodiesel molecular structure which oxidises unburnt HC emissions to CO_2 and H_2O at elevated temperatures.

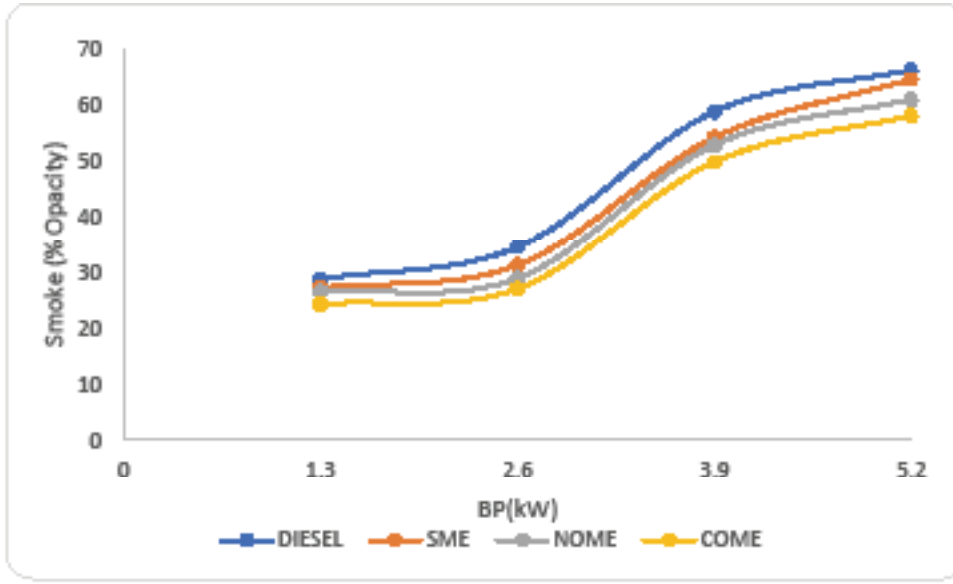

Fig. 6: Variation of smoke emission with brake power.

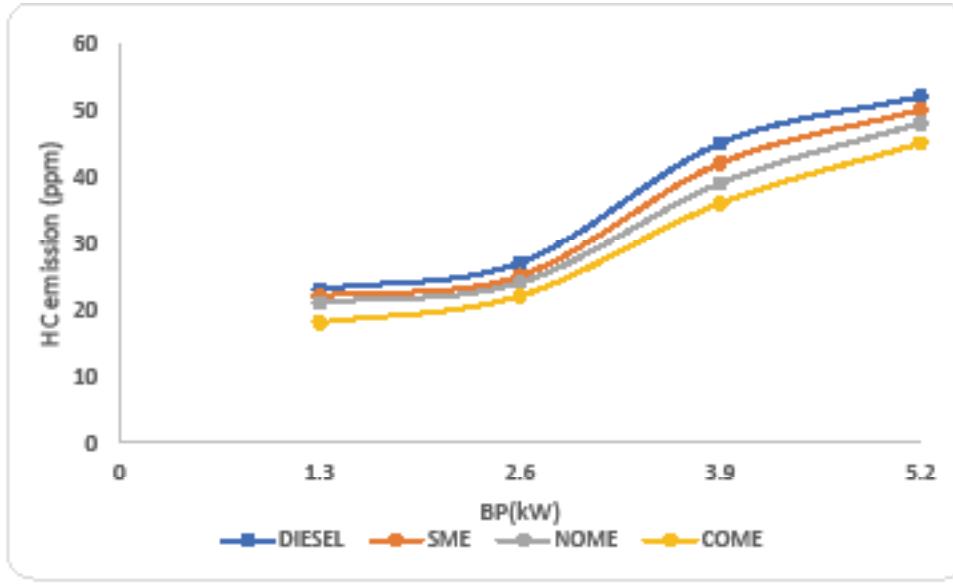

Fig. 7: Variation of hydrocarbon emission with brake power.

Carbon Monoxide Emission (CO)

Fig. 8 shows the variation of CO emission with respect to brake power for various test fuels at different load conditions. At full load, CO emission for diesel, SME, NOME and COME is 0.285%, 0.273%, 0.254% and 0.233% volume respectively. It was observed that SME, NOME and COME emitted less CO emission compared to diesel; the availability of oxygen in biodiesel causes the effect of reduced emissions. SME emitted higher CO emission compared to NOME and COME, which is mainly attributed to slow and incomplete combustion because of poor volatility and higher viscosity of SME that causes less atomization, vaporization and non-uniform air-fuel mixture preparation.

Combustion Characteristics

Heat release rate

Fig. 9 shows the heat release rate with respect to crank angle for various test fuels at full load. The heat release rate for diesel, SME, NOME and COME when fully loaded was 51.44 J/°CA, 40.92 J/°CA, 43.07 J/°CA and 44.49 J/°CA re-

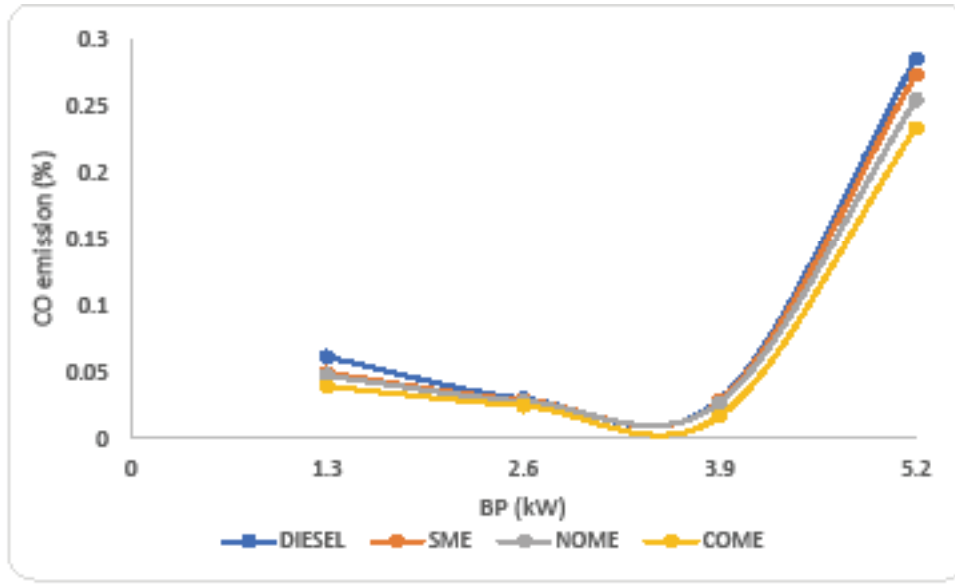

Fig. 8: Variation of carbon monoxide emission with brake power.

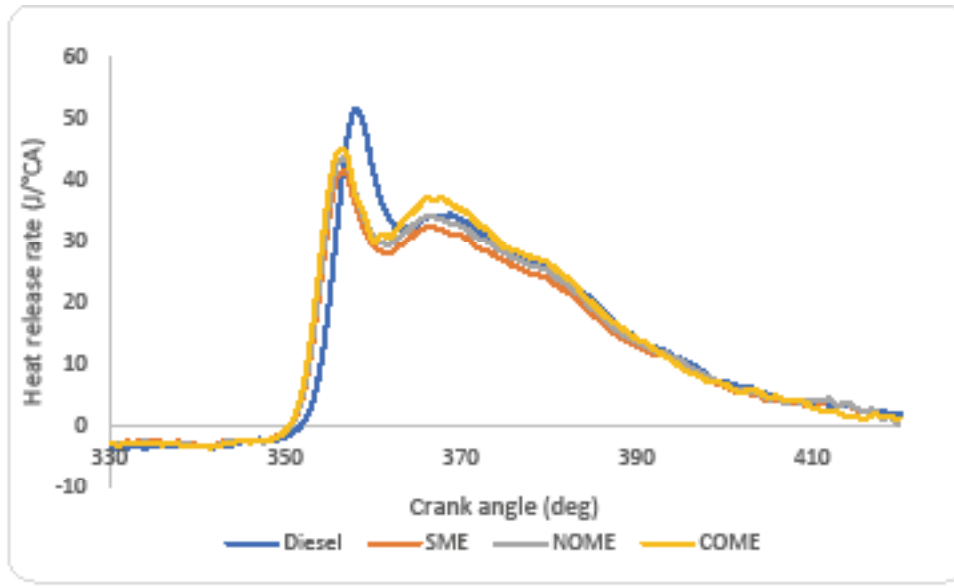

Fig. 9: Variation of heat release rate with crank angle at full load.

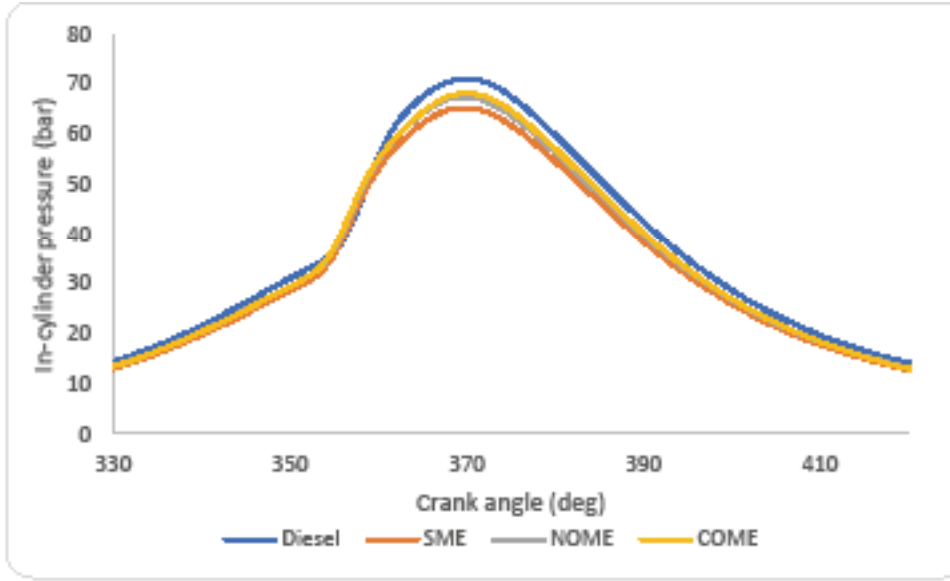

Fig. 10: Variation of in-cylinder pressure with respect to crank angle at full load.

spectively, at full load. The two segments of the heat release are the period of uncontrolled combustion and controlled combustion. Particular interest with combustion studies has been with uncontrolled combustion. It was observed that uncontrolled combustion for diesel, associated with high rate of heat release rate compared to SME, NOME and COME. Due to the high viscosity of SME and subsequently with a reduction in fuel-air mixing rates, less fuel is being prepared for premixed combustion with SME. Therefore, more burning takes place in the diffusion phase rather than in the premixed phase with SME. The rapid heat release is the indication of brake thermal efficiency and NO emission. A higher heat release rate correlating to higher NO emission, which can be realized from Fig. 5. Also, higher diffusion combustion is the indication of smoke emission which is evident from Fig. 6. The end of the rapid combustion has been defined as the dip after the premix spike leading to the diffusion combustion. Higher heat release rate in rapid combustion has been observed in COME compared to SME as a result of lower viscosity of the biodiesel. Higher heat release rate of COME in the rapid combustion phase results in higher peak pressure with lower smoke level and higher NO emission.

In-cylinder Pressure

Fig. 10 displays the variation of in-cylinder pressure with respect to the crank angle at full load. In-cylinder pressure of 71.1 bar, 65.29 bar, 67.4 bar and 68.2 bar was measured for diesel, SME, NOME and COME. It can be noted that higher heat release takes place for diesel operation in comparison with SME, NOME and COME due to better combustion, which results in higher peak pressure. In the case of SME, less fuel-air mixture is prepared during premixed combustion phase, resulting in lower heat release rate, and hence lower peak pressure. Heat release has been delayed and more heat release occurred during the diffusion phase which results in lower peak pressure, higher exhaust gas temperature and lowers useful energy conversion. With COME operation, combustion improves, and hence higher heat release takes place thereby cylinder peak pressure occurs closure to diesel operation.

CONCLUSIONS

A single cylinder four stroke CI engine run with various biodiesels such as safflower methyl ester (SME), neem oil methyl ester (NOME) and corn oil methyl ester (COME). Performance, emission and combustion parameters were examined at different loading conditions of 1.3, 2.6, 3.9 and 5.2 kW and a constant speed of 1500 rpm. The performance, emission and combustion data were examined and compared with diesel. The following conclusions are made:

- At full load, the brake thermal efficiency with SME is 26.10% whereas diesel shows 30.74%. With COME, the combustion improves with a lower viscosity of the fuel, which results in better fuel spray characteristics and air-fuel mixture formation leading to better brake

thermal efficiency of 28.25% for COME, which is closer to diesel.

- Brake specific energy consumption of 13.65 MJ/kWh is measure for SME; higher than that of diesel (11.68 MJ/kWh). The increased viscosity of SME leads to poor and incomplete combustion. COME operation reduces the brake specific energy consumption to 12.75 MJ/kWh which is closer to diesel operation, at full load.
- At full load, NO emissions are 1437 ppm, 1483 ppm and 1502 ppm for SME, NOME and COME. With SME, less heat is released during the premixed phase due to poor air-fuel preparation. However, COME operation results in higher combustion temperature with improved combustion because of oxygen availability in the fuel structure. Hence, NO emissions for COME are higher than diesel (1419 ppm) respectively.
- At full load HC emissions are 52 ppm, 50 ppm, 48 ppm and 45 ppm for diesel, SME, NOME and COME. With COME operation HC emissions are lower when compared to diesel (52 ppm) operation. The oxygen present in the fuel molecular structure gets better combustion and also reduced HC emissions.
- At full load, CO emission is 0.285%, 0.273%, 0.254% and 0.233% for diesel, SME, NOME and COME. With COME operation, CO emission is lower when compared to diesel operation. The reduced CO emission with biodiesel is attributed to the presence of oxygen which oxidises CO to CO_2.
- At 100% load, smoke emission is 66.2%, 64.5%, 60.93% and 58% opacity for diesel, SME, NOME and COME. SME, NOME and COME emit less smoke emission when comparison to diesel due to the presence of oxygen in biodiesel which oxidises the soot particles at a higher temperature.
- HRR for diesel, SME, NOME and COME is 51 J/°-CA, 40.92 J/°CA, 43.07 J/°CA and 44.49 J/°CA respectively, at full load. Heat release rate is higher for COME compared to SME and NOME due to increases the premixed combustion phase leading to higher BTE.

REFERENCES

Agarwal, D. and Agarwal, A.K. 2007. Performance and emissions characteristics of Jatropha oil (preheated and blends) in a direct injection compression ignition engine. Applied Thermal Engineering, 27(13): 2314-2323.

Ali, M. H., Mashud, M., Rubel, M. R. and Ahmad, R.H. 2013. Biodiesel from neem oil as an alternative fuel for diesel engine. Procedia Engineering, 56: 625-630.

Dhananmurugan, A. and Subramanian, R. 2015. Emission and performance characteristics of a diesel engine operating diesel-Bael (*Aegle marmelos*) biodiesel blends. Nature Environment and Pollution Technology, 14(2): 331-336.

Dhar, A., Kevin, R. and Agarwal, A.K. 2012. Production of biodiesel from high-FFA neem oil and its performance, emission and combustion characterization in a single cylinder DICI engine. Fuel Processing Technology, 97: 118-129.

Edwin Geo, V., Nagarajan, G. and Nagalingam, B. 2008. Studies on dual fuel operation of rubber seed oil and its bio-diesel with hydrogen as the inducted fuel. International Journal of Hydrogen Energy, 33(21): 6357-6367.

Ilkılıc, C., Aydın, S., Behcet, R. and Aydin, H. 2011. Biodiesel from safflower oil and its application in a diesel engine. Fuel Processing Technology, 92(3): 356-362.

Nabi, M.N., Rahman, M.M. and Akhter, M.S. 2009. Biodiesel from cottonseed oil and its effect on engine performance and exhaust emissions. Applied Thermal Engineering, 29(11-12): 2265-2270.

Nair, J.N., Kaviti, A. K. and Daram, A.K. 2017. Analysis of performance and emission on compression ignition engine fuelled with blends of Neem biodiesel. Egyptian Journal of Petroleum, 26(4): 927-931.

Prakash, T., Edwin Geo, V., Leenus Jesu Martin and Nagalingam, B. 2018. Improved cold flow properties and combustion analysis of high viscous castor oil and its biodiesel in a CI engine. Nature Environment and Pollution Technology, 17(4): 1183-1192.

Senthil Kumar, T., Senthil Kumar, P. and Annamalai, K. 2015. Experimental study on the performance and emission measures of direct injection diesel engine with Kapok methyl ester and its blends. Renewable Energy, 74: 903-909.

Sureshkumar, K., Velraj, R. and Ganesan, R. 2008. Performance and exhaust emission characteristics of a CI engine fuelled with *Pongamia pinnata* methyl ester (PPME) and its blends with diesel. Renewable Energy, 33(10): 2294-230.

Thiyagarajan, S., Edwin Geo, V., Leenus Jesu Martin and Nagalingam, B. 2016. Effects of low carbon biofuel blends with karanja (*Pongamia pinnata*) oil methyl ester in a single cylinder CI engine on CO_2 emission and other performance and emission characteristics. Nature Environment and Pollution Technology, 15(4): 1249-1256.

Veljkovic, V.B., Biberdzic, M.O., Bankovic-Ilic, I.B., Djalovic, I.G., Tasic, M.B., Njezic, Z.B. and Stamenkovic, O.S. 2018. Biodiesel production from corn oil: A review. Renewable and Sustainable Energy Reviews, 91: 531-548.

Nature Environment and Pollution Technology
An International Quarterly Scientific Journal

p-ISSN: 0972-6268
e-ISSN: 2395-3454

Vol. 18 | No. 4 | pp. 1275-1281 | 2019

Original Research Paper | Open Access

Impact of Land Use Change on Hydrological Response of Krueng Aceh Watershed in Aceh Province, Indonesia

Bos Ariadi Muis

Department of Agrotechnology, Faculty of Agriculture, Teuku Umar University, Jl. Alue Peunyareng, Aceh Barat Regency 23615, Aceh Province, Indonesia

Nat. Env. & Poll. Tech.
Website: www.neptjournal.com

Received: 28-02-2019
Accepted: 30-05-2019

Key Words:
Hydrology
Land use change
Land degradation
DAS Krueng Aceh
Watershed management

ABSTRACT

Population growth and improvement in the people's economy have caused the need for space to grow and have changed land use in the Krueng Aceh watershed. This study on the effect of changes in land use on the Krueng Aceh watershed hydrological response as a step to anticipate water shortage in the future using the geographical information analysis and the river regime coefficient (RRC) method approach. The results of this study revealed that the functional shifts from primary forests to production forests and from brushland to ricefield and settlements increased the RRC value from 14.59 to 56.74 in the last 20 years. The hydrological response showed that 18% of the water had the potential to not infiltrate and become runoff. The effect is a reduction in groundwater supply, flooding in the rainy season, drought in the dry season, and clean water scarcity in the future. The management of the future must be based on one river, one planning, and one management system principle.

INTRODUCTION

The land use changes in developing countries happen rapidly, from land covered by vegetation to developed land (Erkossa et al. 2015) and this has a global impact on the environment (Turner et al. 2007, Lambin et al. 2011). This phenomenon is caused by the rapid population growth and the increased development of the people's economy (Sherbinin et al. 2007). The need for space for agricultural land (Brandt & Philip 2006) and infrastructure development (Pereira et al. 2015) continues to increase. Uncontrolled land functional shifts which do not heed soil and water conservation principles have led to decreased water catchment areas, critical soil conditions (Tesfaye et al. 2014, Kieti et al. 2016), and a disrupted watershed hydrological cycle (Chen et al. 2012, Wang et al. 2014, Zhang et al. 2016), causing runoff to increase and affecting the fluctuations of the river discharge, reducing the groundwater supply (Niraula et al. 2015, Chithra et al. 2015) and causing water scarcity as in the Krueng Aceh watershed at present.

The Krueng Aceh watershed is located in Aceh Province, Indonesia. It covers an area of 197,903.62 ha (Muis et al. 2016). Krueng Aceh watershed has an important role in maintaining the water system as the supplier of water with a good quantity, quality, and continuity for the people living from upriver to downriver and could ensure the sustainability of the water resources (Muis et al. 2017). However, the condition of the Krueng Aceh watershed is currently believed to have undergone soil degradation due to deforestation, which has led to fluctuations in the river discharge ratio. Study results have revealed that the size of the primary forest has decreased. Nasrullah et al. (2010) stated that in 1994 there were 112,776 ha (57%) of primary forest, and according to Husnan et al. (2010) in 2002, it had become 94,178 ha (47.6%), and in 2005 only 79,141 ha (40%) of the primary forest remained. The results of the most recent study (LIF 2013) in 2010 identified a primary forest of 31,812 ha or 16.07% in the entire Krueng Aceh watershed. Land use changes in the Krueng Aceh watershed are believed to be probably continue to this day because observations of the Krueng Aceh river flow have shown that there is a large amount of runoff in the rainy season and drought in the dry season, indicating soil degradation. The purpose of this research was to study the effect of changes in land use on the Krueng Aceh watershed's hydrological response in order to anticipate water scarcity in the future.

MATERIALS AND METHODS

Time and Location

This study was conducted from July to December 2017 in the Krueng Aceh watershed, Aceh Province, Indonesia. The total area of this research site was 197,903.62 ha. It is geographically located at 5°10'38"-5°41'03"N and 95°46'49"-95°41'11"E (Fig. 1). The materials used for this study were a digital administrative map of Aceh Province at a scale of 1:100.000, a topographical map at a scale of 1:100.000, a Krueng Aceh watershed land use map at a

scale of 1:100.000, a soil type map at a scale of 1:250.000, precipitation data from 7 precipitation observation stations (Indonesian Agency for Meteorology, Climatology, and Geophysics (BMKG) Sultan Iskandar Muda Airport, BMKG Mata Ie, BMKG Indrapuri, Montasik Station, Jantho Station, Seulimum Station, Saree Station), and data of the Krueng Aceh river discharge for the period 1994-2014 from the Sumatra I Regional River Agency. The field survey equipment used was a global positioning system (GPS). For map data analysis the software ArcGIS 10.2 was used.

Spatial Analysis of Land Use

Land use changes in the Krueng Aceh watershed were analysed using a spatial analysis method by utilizing a geographical information system temporally so that it could give the most recent perspective of the land use and the changes that have occurred (Foresman 1997, Musavi 2015). The secondary data used were taken from the 1994-2014 digital land use map of the Krueng Aceh watershed from the Aceh Besar Regency, Aceh Province Regional Development Planning Agency. The land use data were analysed with the ArcGIS software. Using the overlay method through an intersect process (Tiede 2014) by overlaying the 1994 Krueng Aceh watershed land use map with the 2004 map, new spatial data were obtained. The 2004 land use map was again overlaid with the 2014 map, resulting in spatial data of the changes in land use in the Krueng Aceh watershed for the period 1994-2014.

Analysis of the River Regime Coefficient

If there is a biophysical changing activity in a watershed, it will cause a response in the river flow discharge. The river's discharge is measured using a tool called the AWLR (Automatic Water Level Recorder) at the river flow observation station in Kampung Darang, Sumatra I Regional River Agency Banda Aceh City. The discharge data are used to discover the maximum (*Qmax*) and minimum (*Qmin*) average daily discharge per year between 1994-2014, by using the month basic planning method (Limantara 2010), and the result was the river regime coefficient. The river regime coefficient (RRC) is the ratio between the maximum discharge (*Qmax*) and the minimum discharge (*Qmin*) in one period, namely the highest discharge during the rainy season and the lowest during the dry season in a certain watershed. A high discharge ratio suggests that the runoff is very high during the rainy season, and a low runoff shows drought in the dry season. The standard river regime coefficient in this study refers to the Minister of Forestry of the Republic of Indonesia's regulation Number P.61/ Menhut-II/2014 pertaining to monitoring and evaluation of watersheds which is presented in Table 1.

To understand the changes in the watershed's carrying capacity in relation to the runoff quality, quantity, and continuity, it is necessary to discover the runoff coefficient. The runoff coefficient (C) is the ratio between the runoff depth (Q) and the precipitation depth (P) in one year. The C value was obtained from the discharge volume (m^3) from the measurement using an AWLR which was converted to millimetres (mm). The value of P was obtained from the results of the measurements of 7 precipitation observation stations (BMKG) using an ARR (Automatic Rainfall Recorder) and an observatory ombrometer, which was then analysed using the Thiessen polygon method (Arsyad 2010). The standard C value used referred to Minister of Forestry of the Republic of Indonesia's regulation Number P.61/Menhut-II/2014 which is presented in Table 2.

Table 1: Standard value of river regime coefficient

Indicator	Parameter	RRC Value	Classification
Water Discharge	$RRC = \frac{Q_{max}\left(m^3/sec\right)}{Q_{min}\left(m^3/sec\right)}$	< 20	Extremely low
		20 - 50	Low
		50 - 80	Moderate
		80 - 110	High
		> 110	Extremely high

Source: MFRID 2014.

Table 2: Standard value of runoff coefficient

Indicator	Parameter	C Value	Classification
Direct runoff	$C = \frac{Volume\ of\ Discharge\left(mm\right)}{Rainfall\left(mm\right)}$	< 0.2	Extremely low
		0.2 - 0.3	Low
		0.3 - 0.4	Moderate
		04 - 0.5	High
		> 0.5	Extremely high

Source: MFRID 2014.

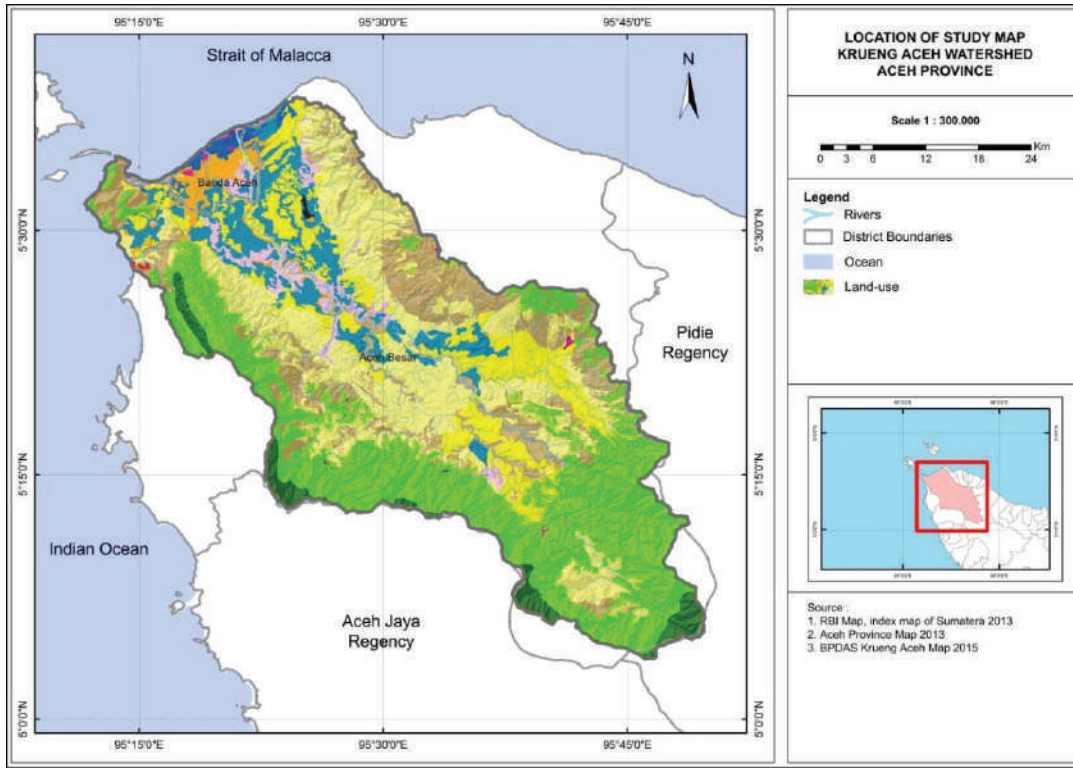

Fig. 1: Location of study in Krueng Aceh watershed, Aceh Province, Indonesia

RESULTS AND DISCUSSION

Land use Change in Krueng Aceh Watershed

There are 14 types of land use in the Krueng Aceh watershed: airport, primary forest, secondary forest, production forest, settlement, mining, dryland agriculture, mixed dryland agriculture, savannah/grassland, ricefield, brush, fish farming, bodies of water, and open land. Land use in the Krueng Aceh watershed in 1994 was dominated by secondary forests at 60,365.37 ha (30.50%), followed by savannah/grassland at 44,560.79 ha (22.52%), and rice fields at 30,421 ha (15.37%).

Land use in the Krueng Aceh watershed during the period 1994-2004 underwent a comprehensive and very dynamic change. The reduction in land size was dominated by brushland at 765.95 ha (5.18%), followed by secondary forest land at 114.21 ha (0.19%), and primary forest land 113.10 ha (1.07%). The decrease in land size was caused by functional shifts to ricefields which increased by 461.62 ha (1.49%), dryland agriculture which increased by 366.28 ha (1.54%), and production forests which increased by 73.62 ha (28.53%). The increase in the size of ricefields and dryland agriculture land was because the prices of a number of agricultural commodities rose (BPS 2005), encouraging the farmers to plant these superior commodities by utilizing the brushland and clearing secondary forest land.

Land use change in the Krueng Aceh watershed during the period 2004-2014 included growth in the size of land used for rice fields 593.38 ha (1.89%), production forests 235.75 ha (47.74%), settlements 44.94 ha (1.07%), and mixed dryland agriculture 33.04 ha (0.55%). As a result, in 2014 the remaining primary forests in the Krueng Aceh watershed only covered 9,999.50 ha (5.05%) of the total Krueng Aceh watershed area. The main cause of the reduction in the size of the primary forests was logging to fulfil the demand for timber used in the rehabilitation and reconstruction in the aftermath of the Aceh earthquake and tsunami on 26 December 2004 for the construction of temporary shelters and 75,000 units of permanent housing (BRR 2005). Land use change in the Krueng Aceh watershed in the past 20 years are presented in Table 3 and visually in Fig. 2.

The Effects of Land Use Change in the Krueng Aceh Watershed's Hydrological Response

The rainfall in the Krueng Aceh watershed area in the last

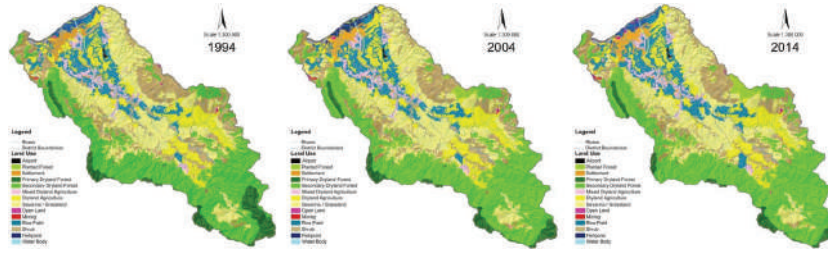

Fig. 2: Land use change in Krueng Aceh watershed during the period 1994-2014.

Table 3: Land use change of Krueng Aceh watershed during the period of 1994-2014.

No	Land use	Land use area			Land use changes			
		1994	2004	2014	1994-2004		2004-2014	
		(ha)	(ha)	(ha)	(ha)	(%)	(ha)	(%)
1	Airport	151.87	151.87	151.87	0.00	0.00	0.00	0.00
2	Primary dryland forest	10724.71	10611.61	9999.50	-113.10	-1.07	-612.11	-6.12
3	Secondary dryland forest	60365.37	60251.16	60193.55	-114.21	-0.19	-57.61	-0.10
4	Planted forest	184.46	258.08	493.83	73.62	28.53	235.75	47.74
5	Settlement	4107.79	4137.93	4182.87	30.14	0.73	44.94	1.07
6	Mining	90.66	107.60	90.91	16.94	15.74	-16.69	-18.36
7	Dryland agriculture	23386.75	23753.03	23524.19	366.28	1.54	-228.84	-0.97
8	Mixed dryland agriculture	5972.02	5982.50	6015.54	10.48	0.18	33.04	0.55
9	Savanna/Grassland	44560.79	44586.42	44600.09	25.63	0.06	13.67	0.03
10	Rice field	30421.00	30882.62	31476.00	461.62	1.49	593.38	1.89
11	Shrub	15563.22	14797.27	14761.00	-765.95	-5.18	-36.27	-0.25
12	Fishpond	1336.40	1342.56	1363.56	6.16	0.46	21.00	1.54
13	Water body	797.15	797.15	797.15	0.00	0.00	0.00	0.00
14	Open land	241.43	243.82	253.56	2.39	0.98	9.74	3.84
	Krueng Aceh watershed	197903.62	197903.62	197903.62	-	-	-	-

20 years was 2767.73 mm/year with an average of 131.80 mm/month. The highest rainfall was in December at 383.24 mm, and the lowest was 4.13 mm in July. Some of the rain that falls to the surface of the ground would infiltrate and the rest becomes runoff. The runoff produced by the Krueng Aceh watershed was monitored and measured using an AWLR, creating a graph for the correlation between the water surface height and time and produced discharge data. The river discharge data produced from the measurements were one of the very important hydrological data in observing the behavior of the effect of the changes in land use in the Krueng Aceh watershed.

The Krueng Aceh river discharge data for the period 1994-2014 (Fig. 3) revealed a maximum discharge (*Qmax*) of 76.60 m^3/second which occurred in October, and a minimum discharge (*Qmin*) of 1.35 m^3/second in July. The analysis results of the average annual *Qmax*for the past 20 years demonstrated a trend that increased exponentially from 32.25 m^3/second in 1994 to 45.60 m^3/second in 2004, and in 2014 the maximum discharge increased to 76.60 m^3/second. This differed from the *Qmin* distribution pattern which decreased linearly every year from 2.21 m^3/second in 1994 to 1.35 m^3/second in 2014.

The Krueng Aceh watershed is a paddy field development area and the leading sector for the people of Aceh Besar Regency's livelihood. The Aceh Besar Regency Government has planned to increase the area of rice fields by 2,500 ha in 2032. The increased ricefield area will have a direct contribution to the increase in runoff rate because there is a waterproof layer formed during mechanized soil

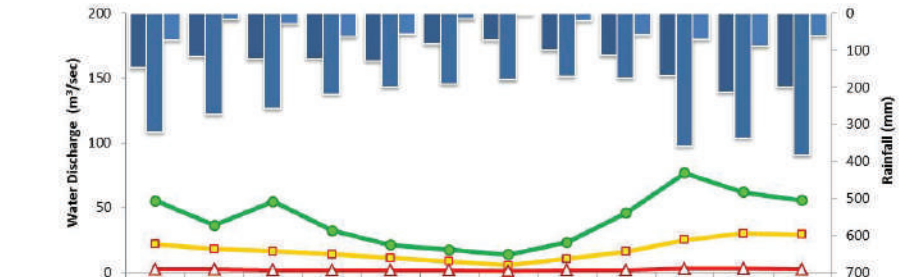

	Jan	Feb	Mar	Apr	May	Jun	Jul	Aug	Sep	Oct	Nov	Dec
Rainfall avg	147.03	116.70	123.07	121.62	127.83	83.04	71.45	99.26	112.67	168.77	212.00	198.12
Rainfall max	320.90	273.36	257.14	218.12	198.87	190.04	179.22	170.79	174.42	358.67	336.83	383.24
Rainfall min	71.79	16.96	27.27	62.66	55.96	14.63	4.13	19.67	57.64	70.19	88.22	60.51
Q avg	21.61	17.98	16.21	13.83	10.85	8.37	5.16	10.34	15.85	25.09	30.03	29.07
Q max	55.14	36.12	54.72	32.07	21.15	17.30	13.57	23.16	45.60	76.60	61.62	55.34
Q min	2.00	2.25	1.85	1.38	1.49	1.83	1.35	1.43	1.49	2.61	3.03	2.41

Fig. 3: The correlation between rainfall and water discharge of Krueng Aceh watershed in the period 1994-2014.

tilling which packs the soil. The application of a monoculture agricultural system which disregards planting according to the contour lines will also increase the runoff rate and decrease the watershed's supporting capacity, which will strongly affect the Krueng Aceh watershed's characteristics. The characteristics of a watershed can be seen from the fluctuations in its river discharge. The smaller the river regime coefficient, the better the hydrological condition of a watershed is, but if it rises from year to year, it means the condition of the watershed is compromised.

Fig. 4 shows that the Krueng Aceh river regime coefficient rose from 14.59 in 1994 to 32.79 in 2004 and rose again drastically to 56.74 in 2014. This proves that the Krueng Aceh watershed has undergone soil degradation due to a functional shift of the land from primary forest to production forests, brush to rice fields and settlements, thus causing the rain that falls to the ground to not fully infiltrate. The effect is a reduction in the availability of groundwater, water scarcity in the dry season, and unfulfilled domestic water demands.

The population growth that reached 2.12% per year and the increased growth in the people's economy have become factors that drive the increase in the need for land and have the potential to land use change in the Krueng Aceh watershed. The results of the runoff coefficient (C) analysis revealed that changes from vegetation-covered land to non-vegetation-covered land could affect the microclimate, from the evaporation process to the transpiration, condensation, and precipitation processes. Krueng Aceh watershed's hydrological response is shown by the value of C which

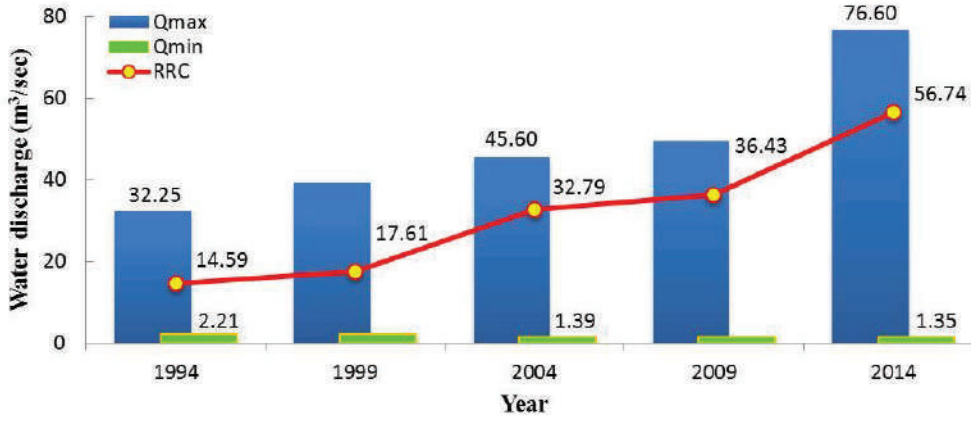

Fig. 4: Impact of land use change on hydrological response of Krueng Aceh watershed.

Table 4: Impact of land use change on runoff coefficient in Krueng Aceh watershed.

Year	Rainfall (mm/year)	Average discharge (m^3/sec)	Total discharge (m^3)	Volume of rainfall (m^3)	C
1994	1 391.45	11.51	362 962 587	2 753 737 159	0.13
2004	1 722.73	16.54	521 568 499	3 409 341 422	0.15
2014	1 957.95	22.14	698 332 423	3 874 844 319	0.18

increases linearly every year, from 0.13 in 1994 to 0.15 in 2004, and then 0.18 in 2014 (Table 4). This proves that the soil's ability to store rainwater has decreased, causing 18% of the potential water from the total precipitation in 2014 to be unable to infiltrate, becoming runoff and flowing to the river and being discarded to the sea. Field conditions revealed that there is a tendency for the Krueng Aceh watershed to become critical in the future. The effects of changes in land cover will reduce the groundwater supply, cause flooding in the rainy season, drought in the dry season, and scarcity of clean water for the people in the Krueng Aceh watershed.

CONCLUSION

Population growth and growth of the people's economy have caused changes in the land use in the Krueng Aceh watershed. Land use changes from vegetation-covered land to non-vegetation-covered land have disturbed the groundwater absorption system and affected the characteristics of the Krueng Aceh watershed. Krueng Aceh watershed's hydrological response showed that the higher the precipitation rate in the area, the higher the peak discharge is. Runoff increases in the rainy season and the groundwater supply decreases. The results of this study revealed that the Krueng Aceh watershed has undergone soil degradation and has the tendency to become critical and will lead to scarcity of clean water in the future.

ACKNOWLEDGEMENT

The author would like to thank the Ministry of Research, Technology, and Higher Education of the Republic of Indonesia which has supported and provided financial support for this research.

REFERENCES

Arsyad, S. 2010. Konservasi Tanah Dan Air. IPB Press, Bogor.

BPS 2005. Indonesia Central Agency of Statistics. 2005. Aceh Besar in figures 2005. Statistics of Aceh Besar Regency, Aceh Besar.

BRR 2005. Agency for the Rehabilitasi and Reconstruction of Aceh and Nias. 2005. Report of Aceh and Nias a year after tsunami. BRR Aceh-Nias, Banda Aceh.

Brandt, J.S. and Philip, A.T. 2006. Land use - land cover conversion, regeneration and degradation. Landscape Ecology, 21: 607-623.

Chen, H., Xu, C.Y. and Guo, S. 2012. Comparison and evaluation of multiple GCMs, statistical downscaling and hydrological models in the study of climate change impacts on runoff. J. Hydrol., 434-435: 36-45.

Chithra, S.V., Nair, M.V.H., Amarnath, A. and Anjana, N.S. 2015. Impacts of impervious surfaces on the environment. Int. J. Engineer Sci. Inven., 4(5): 27-31.

Erkossa, T., Wudneh, A., Desalen, B. and Taye, G. 2015. Linking soil erosion to on-site financial cost: Lessons from watersheds in the Blue Nile basin. Solid Earth, 6: 765-774.

Foresman, T. W. 1997. Methods for spatial and temporal land use and land cover assessment for urban ecosystems and application in the greater Baltimore-Chesapeake region. Urban Ecosystems, 1: 201-216.

Husnan, H., Pawitan, G., Irianto, K., Murtilaksono and Basri, H. 2010. Estimation Model of Basin Water Yield of Five Main Rivers in Aceh Province. Ph.D. Thesis.

Kieti, R. N., Kauti, M. K. and Kisangau, D. P. 2016. Biophysical conditions and land use methods contributing to watershed degradation in Makueni County, Kenya. J. Ecosys. Ecograph., 6: 216.

Limantara, L. M. 2010. Hidrologi Praktis. Lubuk Agung, Jakarta.

Lambin, E. F. and Meyfroidt, P. 2011. Global land use change, economic globalization, and the looming land scarcity. Proc. Natl. Acad. Sci. USA, 108(9): 3465-3472.

LIF (Leuser International Foundation) 2013. Krueng Aceh watershed. http://www.leuserfoundation.org/index.php?option=com_content&view=%20article&id=148:das-krueng-aceh&%20catid=40:-das-krueng-aceh.

MFRID (Ministry of Forestry Republic of Indonesia Decree) 2014. Monitoring and evaluation of watershed management No. P.61/Menhut-II/2014. Ministry of Forestry Republic of Indonesia.

Musavi, N. 2015. Identification of land use/cover changes mapping in an urban area using satellite imagery and support vector machine algorithm (case study: Some'esara). J. Bio. & Env. Sci. 7(1): 543-556.

Muis, B.A., Murtilaksono, K., Jaya, I. N. S. and Haridjaja, O. 2016. Analysis potency of water availability and water demand in Krueng Aceh watershed. Int. J. Sci. Basic App. Res., 29(1): 191-201.

Muis, B. A., Murtilaksono, K., Jaya, I. N. and Haridjaja, O. 2017. Analysis of water demands for freshwater aquaculture ponds in Krueng Aceh watershed, Aceh Province, Indonesia. AACL Bioflux, 10(5): 1119-1126.

Nasrullah, N. and Kartiwa, B. 2010. Analisis alih fungsi lahan dan keterkaitannya dengan karakteristik hidrologi DAS Krueng Aceh. J. Tanah dan Iklim, 31(7): 81-98.

Niraula, R., Meixner, T. and Norman, L. M. 2015. Determining the importance of model calibration for forecasting absolute/relative changes in streamflow from LULC and climate changes. J. Hydrol., 522: 439-451.

Pereira, P., Gimeìnez-Morera, A., Novara, A., Keesstra, S., Jordán, A., Masto, R.E., Brevik, E., Azorin-Molina, C. and Cerdà, A. 2015. The

impact of road and railway embankments on Runo and soil erosion in eastern Spain. Hydrol. Earth Syst. Sci. Discuss., 12: 12947-12985.

Sherbinin, A. E., Carr, D., Cassels, S. and Jiang, L. 2007. Population and environment. Annu. Rev. Environ. Resour., 32: 345-373.

Turner, II, B. L., Lambin, E. F. and Reenberg, A. 2007. The emergence of land change science for global environmental change and sustainability. Proc. Natl. Acad. Sci. USA, 104(52): 20666-20671.

Tesfaye, A., Negatu, W., Brouwer, R. and Zaag, P.V.D. 2014. Understanding soil conservation decision of farmers in the Gedeb watershed, Ethiopia. Land Degrad. Develop., 25: 71-79.

Tiede, D. 2014. A new geospatial overlay method for the analysis and visualization of spatial change patterns using object-oriented data modeling concepts. Cartography and Geographic Information Science, 41(3): 227-234.

Wang, R., Kalin, L., Kuang,W. and Tian, H. 2014. Individual and combined effects of land use/cover and climate change on Wolf Bay watershed streamflow in southern Alabama. Hydrol. Process, 28: 5530-5546.

Zhang, L., Nan, Z., Xu,Y. and Li, S. 2016. Hydrological impacts of land use change and climate variability in the headwater region of the Heihe river basin, Northwest China. PloS ONE, 11: 1-25.

Nature Environment and Pollution Technology
An International Quarterly Scientific Journal

p-ISSN: 0972-6268
e-ISSN: 2395-3454

Vol. 18 | No. 4 | pp. 1283-1291 | 2019

Original Research Paper | Open Access

Structures and Anaerobic Metabolic Activity of Attached Microbial Communities During Biofilm Formation in Aquaculture Systems

Jialei Li*(**), Zhifei Li*(***), Jun Xie*(**)†, Guangjun Wang*(***), Kai Zhang*(***), Ermeng Yu*(***), Wangbao Gong*(***) and Jingjing Tian*(***)

*Key Laboratory of Tropical and Subtropical Fishery Resource Application and Cultivation, Pearl River Fisheries Research Institute, Chinese Academy of Fishery Sciences, Guangzhou 510380, China
**Shanghai Ocean University, Shanghai 201306, China
***Guangdong Ecological Remediation of Aquaculture Pollution Research Center, Guangzhou 510380, China
†Corresponding author: Jun Xie

Nat. Env. & Poll. Tech.
Website: www.neptjournal.com

Received: 31-03-2019
Accepted: 01-06-2019

Key Words:
Biofilm
Anaerobic conditions
Breeding system
Carbon metabolism
High-throughput sequencing

ABSTRACT

In this study, the structural characteristics of the attached microbial community during biofilm formation and the metabolic requirements under anaerobic conditions were evaluated. In particular, 16S rDNA sequencing technology was used to study the structural changes of the attached microbial community during biofilm formation (day 0, 10, 20, and 30) in an aquaculture system, and Biolog microplate technology was used to study metabolic characteristics under anaerobic conditions during biofilm formation. The AWCD (average well colour development), an indicator of carbon metabolism, of attached microorganisms during biofilm formation under anaerobic conditions differed significantly among time points ($P < 0.05$), and the carbon source utilization capacity was enhanced. Under anaerobic conditions during biofilm formation, the utilization of amines in six major carbon sources was the highest, followed by polymers, carbohydrates, amino acids, and carboxylic acids, and the utilization of phenols was the lowest. Under anaerobic conditions, the utilization rate by the attached microorganisms during biofilm formation was highest for Tween 40, followed by Tween 80, D-xylose, 4-hydroxybenzoic acid, α-D-glucose-1-phosphate, L-phenylalanine, and phenylethylamine. The 16s rDNA sequencing results showed that the dominant phyla of attached microorganisms during biofilm formation were mainly Proteobacteria, Bacteroidetes, Firmicutes, and Cyanobacteria. On the 10th and 20th days of biofilm formation, attached microorganisms were enriched for *Rhodobacter* of α-Proteobacteria and *Janthinobacterium* of β-Proteobacteria, which play important roles in biofilm denitrification. However, on the 30th day, enriched bacteria included the Burkholderiales of β-Proteobacteria, the Xanthomonadaceae and *Thermomonas* of γ- Proteobacteria, which function in cyanide decomposition.

INTRODUCTION

Aquaculture organisms generally use only 20-30% of the nitrogen source in their feed, and the remainder enters the water body as residual matter and faeces (Avnimelech et al. 2006, Piedrahita et al. 2003). The resulting increase in non-ionic ammonia and nitrite nitrogen in the water will inhibit the growth of aquaculture organisms and even lead to death (Xia et al. 2010, Reddy-Lopata et al. 2006). This is a major issue in high-density intensive farming.

Denitrification by biofilms is a core step in ecological restoration. As an economical, effective, and eco-friendly biological denitrification technology (Huang et al. 2017), biofilms contain both anaerobic and aerobic zones for simultaneous aerobic nitrification and anaerobic denitrification. This will enrich both nitrifying and denitrifying bacteria and accelerate the oxidation of ammonia nitrogen and nitrite nitrogen into nitrate nitrogen, thereby improving the removal efficiency (Flemming et al. 2010). Biofilms consist mainly of microorganisms and their extracellular polymers. The spatial distribution of microorganisms in a biofilm is distinct, and denitrification is directly related to the structure of the attached microbial communities (Rittmann et al. 2018, Zhang et al. 2010). In the early stage of biofilm formation, the surface is dominated by an aerobic layer, where aerobic bacteria are dominant. Eventually, facultative anaerobic and anaerobic layers form (Nogueira et al. 2002, Kang et al. 2005). As biofilm formation progresses, denitrifying bacteria dominate (Qian et al. 2011).

The metabolic characteristics of denitrifying bacteria in the facultative anaerobic and anaerobic layers can provide a basis for the screening of carbon sources (electron donors) required for denitrification by biofilms. Biolog technology for studying carbon source metabolic characteristics is a well established method for screening biofilm carbon sources (denitrifying electron donors). Liu et al. (2015)

studied the carbon metabolism characteristics of microbial communities in different water treatment units of recirculating aquaculture systems for eels and found that microbial communities show preferences for certain carbon sources on ECO plates, which functioned as electron donors that increased the rate of denitrification. Zhu et al. (2017) and Li et al. (2014) used Biolog technology to study the carbon source metabolism of biofilm microbial communities in aquaculture systems and achieved the improved metabolic activity.

Anaerobic denitrification mainly occurs in the facultative anaerobic and anaerobic layers. Therefore, it is important to investigate the metabolic activity of carbon sources in biofilm microorganisms under anaerobic conditions to identify appropriate carbon sources for denitrification. In this study, an ecological base was used for the growth of microorganisms in an aquaculture system, and Biolog microplate technology was employed to study the characteristics of carbon metabolism in microbial communities under anaerobic conditions during biofilm formation. High-throughput sequencing was used to examine the structures of microbial communities during biofilm formation. We aimed to explore the differences in carbon metabolism under anaerobic conditions and structural changes of attached microbial communities during biofilm formation. The results improve our understanding of the process of anaerobic denitrification in biofilms and provide a theoretical basis for studies of biofilm denitrification mechanisms and for the improvement of the biofilm denitrification capacity.

MATERIALS AND METHODS

Experimental Design

The experiment was conducted at the test site of the Pearl River Fisheries Research Institute of the Chinese Academy of Fishery Sciences. A 2 × 2 m cement pond filled to a depth of 1.0 m with water was used. The cement pond was exposed to sunlight and disinfected before use. Forty grass carps were placed in the pond, weighing 75 ± 0.5 g. The daily feeding amount was 2% of their total weight which gradually increased to 3%. The ecological base was AquaMat, which was 1 × 1 m in size and 0.2 cm thick. The specific surface area was 200 m^2/m^2, and its relative density was 240 g/m^2. One end of the long side of the AquaMat was kept intact, and the other end was cut into strips of 0.05 m × 0.8 m, which were ideal dimensions for the flow of water and fish movement.

At the beginning of the experiment, one AquaMat was placed in the aquaculture water. Samples were collected from the upper, middle and lower parts of the AquaMat on day 0, 10, 20, and 30. The samples were placed in a sterilized 50 mL centrifuge tube, kept at 4°C, and brought to the laboratory for subsequent processing.

Water Quality Testing

The pH, temperature, dissolved oxygen, electrical conductivity, and total dissolved solids were tested on-site using a portable multi-parameter water quality meter (YSI Professional Plus, Yellow Springs, OH, USA). Total nitrogen (TN) was determined by the alkaline potassium persulphate digestion-UV spectrophotometric method (GB 11894-1989).

Analysis of Anaerobic Metabolism of Biofilm Microorganisms Using Biolog-ECO Microplates

Five grams of the samples were added to 150 mL of 0.9% sterile saline solution. Pure nitrogen gas was injected into the solution to ensure an anaerobic environment, and the mixture was shaken for 2 h. The fully mixed microbial suspension was sealed and placed in an anaerobic incubator and aliquots of equal size were obtained. The sample solution was poured into a sterile pipette basin in the anaerobic incubator and then pipetted into a pre-heated 25°C Biolog-ECO microplate, where 150 mL of the sample was added to each well. The loaded Biolog-ECO microplate was covered and cultured at a constant temperature of 25°C. After 48 h, the microplate was removed from the anaerobic incubator and absorbance at 590 nm was determined. The average optical density at 48 h was used for subsequent data processing.

The average well colour development (AWCD) was used as an indicator of carbon metabolism of the microbial communities. The AWCD was calculated from the measured absorbance of Biolog-ECO with the formula $AWCD = \sum(Ci - R)/n$. Here, Ci is the absorbance of the carbon source wells, R is the absorbance of the control wells, and n represents the total number of carbon sources (i.e., 31). The change in AWCD over time was plotted.

Diversity indexes were obtained, including the Pielou's index, Simpson's index (i.e., the dominance index), Shannon-Wiener index, and the McIntosh's index. The Shannon-Wiener index reflects the abundance and evenness of microorganisms, the Simpson's index indicates the dominance of the most abundant species in the microbial community, and the McIntosh's index is based on the Euclidian distance of the community in multidimensional space (Magurran et al. 1988).

The utilization rates of carbon sources by biofilm microbial communities under anaerobic conditions were calculated. The physiological and metabolic characteristics of the microorganisms in water using carbon substrates in the 96 wells were analysed. The Biolog-ECO microplate (ECO Microplate; Matrix Technologies Corporation, Maumee,

OH, USA) contained 3 sets of 31 different carbon sources (including 6 amino acids, 12 saccharides, 5 carboxylic acids, 4 polymers, 2 amines, and 2 phenols), and there were 3 replicates for each microplate. Based on the colour change of the wells, the rate of carbon utilization under anaerobic conditions was determined. The maximum value for the average AWCD of the six types of carbon sources at the four sampling time points was set to 100%, from which the relative utilization rates of the six types of carbon sources at different time points were calculated.

Analysis of Microbial Community Structures

Four grams of AquaMat was added to a conical flask filled with 150 mL of sterile deionized water and mixed for 2 h in a shaker at 25°C and 180 r/min. The mixture was then vacuum-filtered with a 0.2 μm microbial membrane filter, and the membrane filter was cut into pieces with sterile scissors and stored in a 50 mL sterile centrifuge tube. For microorganisms in the aquaculture water body, a 150 mL water sample was obtained using a measuring cylinder and vacuum-filtered with a 0.2 μm microbial membrane filter. The subsequent steps were the same as those described above. Microbial DNA was extracted using the OMEGA Water DNA Kit (Omega, Norwalk, CT, USA).

The concentration and purity of DNA were evaluated by 1% agarose gel electrophoresis. The DNA was diluted to 1 ng/μL with sterile deionized water, and the V4 hypervariable region of the 16S rDNA gene was amplified using 515F and 806R primers with sample-specific barcodes (Ni et al. 2017). PCR was performed using a 30 μL reaction volume, containing 15 μL of a high-efficiency high-fidelity enzyme mixture (Phusion® High-Fidelity PCR Master Mix; New England Biolabs, Ipswich, MA, USA). The PCR products were mixed in equal proportions, and the mixture was purified using a GeneJET Gel Extraction Kit (Thermo Scientific, Waltham, MA, USA). The sequencing library was constructed with the NEBNext Ultra DNA Library Prep Kit for Illumina (New England Biolabs) and adapter sequences were added. Finally, the library was sequenced using the Illumina MiSeq platform, and 250-bp paired-end reads were generated. Miseq sequencing was carried out by Beijing Nohe Corporation (Beijing, China).

The paired-end reads of the original DNA fragments were combined using Flash, and the combined labels were assigned to each sample based on the sample-specific barcodes. A sequence analysis was performed using UPARSE (Edgar et al. 2013), and sequences with ≥97% similarity were assigned to the same operational taxonomic unit (OTU). Representative sequences for each OTU were selected and annotated with appropriate classification information using the RDP classifier (Wang et al. 2007). Perl scripts were used to analyse α-diversity and β-diversity.

Data Analysis

A principal component analysis (PCA) and heat map analysis were performed using the vegan package in R. Other statistical analyses were implemented in SPSS18.0, and the experimental data were presented as arithmetic means ± standard deviation. One-way analysis of variance (ANOVA) with Duncan's multiple range test was used to compare means among groups and the significance level was set to $P < 0.05$.

RESULTS

Basic Water Quality in the Pond

During the experiment, the water temperature of the grass carp pond was kept at about 30°C. The dissolved oxygen was kept at above 6.0 mg/L. The pH was maintained at about 7.4. The electrical conductivity was kept between 0.31 ± 0.03 and 0.40 ± 0.01 μS/cm. The TN was maintained at 4.89 ± 1.31 to 6.97 ± 1.48 mg/L. The water quality was generally stable (Table 1).

Analysis of the AWCD and Functional Diversity of Biofilm Microbial Communities under Anaerobic Conditions

The AWCD, Shannon index, Simpson's index, Pielou's index, and McIntosh's index were calculated from the optical density (C-R) of the ECO microplates at 48 h (Table 2). The AWCD values for the attached microorganisms during biofilm formation under anaerobic conditions differed significantly among time points ($P < 0.05$). The AWCD value for the attached microorganisms during biofilm formation

Table 1: Characteristics of aquaculture water.

	Temperature (°C)	Dissolved oxygen (mg/L)	pH	SPC (μS/cm)	TN (mg/L)
0d	30.7±0.75	5.78±1.16	7.22±0.02	0.35±0.10	4.89±1.31
10d	29.8±0.95	6.2±0.46	7.64±0.24	0.40±0.01	5.74±2.07
20d	31.8±0.26	5.94±0.35	7.32±0.26	0.31±0.03	6.97±1.48
30d	31.3±0.4	6.07±0.08	7.48±0.34	0.36±0.03	5.27±0.18

Table 2: AWCD and diversity indexes for biofilm microbial communities under anaerobic conditions.

	AWCD	Shannon-Weiner index	Simpson index	Pielou index（E)	McIntosh index
day 0	0.37±0.03[a]	2.53±0.21[a]	0.99±0.01[a]	1.04±0.08[b]	3.53±0.21[a]
day 10	0.72±0.10[b]	2.86±0.10[b]	0.98±0.002[b]	0.69±0.02[a]	5.75±0.51[b]
day 20	0.79±0.07[b]	3.00±0.31[b]	0.98±0.003[b]	1.01±0.10[b]	6.04±0.48[b]
day 30	0.77±0.10[b]	2.91±0.09[b]	0.98±0.01[a]	0.99±0.03[b]	5.87±0.56[b]

Note: Different superscript letters in the same column show significant differences between treatments ($P < 0.05$), n = 6

under anaerobic conditions at day 0 was significantly lower than those at day 10, day 20 and day 30 ($P < 0.05$), but the AWCD values at day 10, day 20 and day 30 were not significantly different from each other ($P > 0.05$). During biofilm formation, the capacity of biofilm microorganisms to utilize carbon sources under anaerobic conditions improved significantly. The Shannon index and the McIntosh's index at day 0 were significantly lower than those at day 10, 20 and 30 ($P < 0.05$).

The Simpson's indices at day 10 and day 20 were significantly higher than those at day 0 and day 30 ($P < 0.05$); the Pielou's index was at lowest on day 20.

Analysis of the Efficiency of Carbon Source Utilization by Biofilm Microorganisms under Anaerobic Conditions

Utilization rates were highest for amines under anaerobic conditions, followed by polymers, carbohydrates, amino acids, and carboxylic acids, and the utilization rate of phenols was the lowest (Fig. 1). The capacity to utilize amines under anaerobic conditions was significantly different among sampling times ($P < 0.05$). Amine utilization was lower at day 0 than at other sampling times. The amine utilization rate was highest at day 10, followed by day 20 and day 30. The utilization rate of polymers increased over time and reached a maximum of 58.18% on day 30. The carboxylic acid utilization rates were significantly different among time points ($P < 0.05$), with a continuous increase until day 20 (reaching a maximum of 49.37%), followed by a decrease on day 30. The carbohydrate utilization rates were 48.05%, 49.24% and 48.57% on day 10, day 20 and day 30, respectively, and the lowest rate was observed on day 0. The phenol and amino acid utilization rates were similar; the utilization rates for the two carbon sources were lowest on day 0 and decreased on day 20. Across sampling times, the quantity of microorganisms was lowest on day 0, as was their carbon source utilization rate. Over time, biofilm microorganisms gained a greater capacity to utilize the six major carbon sources under anaerobic conditions, but the carbohydrate utilization rate did not change substantially after day 10. In general, biofilm microorganisms showed metabolic preferences for amines, polymers, carbohydrates, amino acids, and carboxylic acids under anaerobic conditions, and their metabolic capacity for the six carbon sources improved over time.

Under anaerobic conditions, there were significant differences in the ability of the microorganisms to use 31 differ-

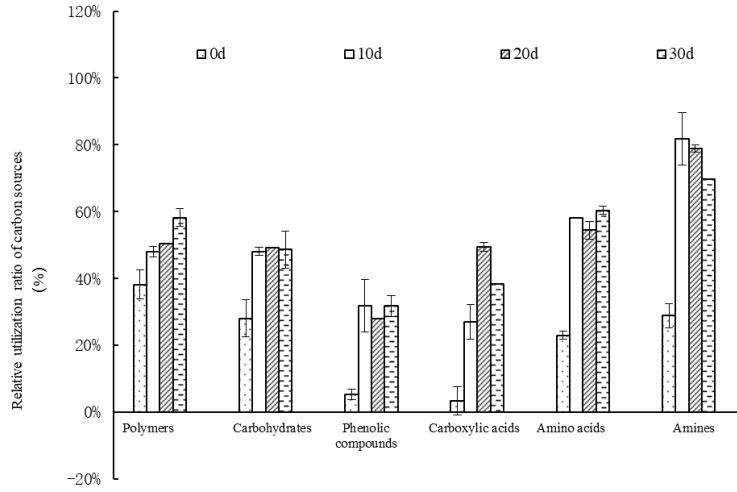

Fig.1: Relative utilization rates for six carbon sources at different sampling points under anaerobic conditions.

ent carbon sources under anaerobic conditions (Fig. 2). Only half of the 31 carbon sources were utilized by the biofilm microorganisms under anaerobic conditions, and the relative AWCD values for each carbon source were different. The carbon sources with high utilization rates exhibited greater demand by the microorganisms under anaerobic conditions, while low utilization rates indicated reduced or no demand for those carbon sources under anaerobic conditions. In this study, we set the baseline carbon source utilization rate as a total utilization rate of 4% on each microplate.

The number of high-utilization (>4%) carbon sources under anaerobic conditions was lowest on day 0, with only three carbon sources, while on day 10, day 20 and day 30, there were 11 high-utilization carbon sources (Fig. 2). During biofilm formation, the change in high-utilization (>4%) carbon sources under anaerobic conditions was similar to the change in AWCD activity. Both were lowest on day 0, with significantly higher values on day 10, day 20 and day 30 than those on day 0 ($P < 0.05$). With biofilm formation and the improvement in the carbon utilization capacity under anaerobic conditions, the utilization rates of α-D-glucose-1-phosphate, β-methyl-D-glucoside, Tween 40, D-galacturonic acid, 4-hydroxybenzoic acid, L-phenylalanine, and phenethylamine were significantly higher compared with those on day 0. The carbon sources that consistently showed high utilization rates were Tween 80 and D-xylose.

Analysis of Attached Microbial Communities during Biofilm Formation

In a cluster analysis, applying a standard threshold of 97% similarity, 24566 bacterial sequences were generated and 10154 OTUs were identified. During biofilm formation, the relative abundances of biofilm microorganisms differed significantly over time (Fig. 3). On day 0, the dominant phyla in the aquaculture water were Proteobacteria (29.1%), Bacteroidetes (20%), Planctomycetes (14.8%), Cyanobacteria (9%), Verrucomicrobia (9%) and Actinobacteria (8.6%). On day 0, the dominant phyla in biofilms were Proteobacteria (51.1%) and Bacteroides (26.9%). On day 10, the structures of the biofilm microbial communities in biofilms changed, and Firmicutes (32%) became a dominant phylum. On day 20, the dominant phyla in the

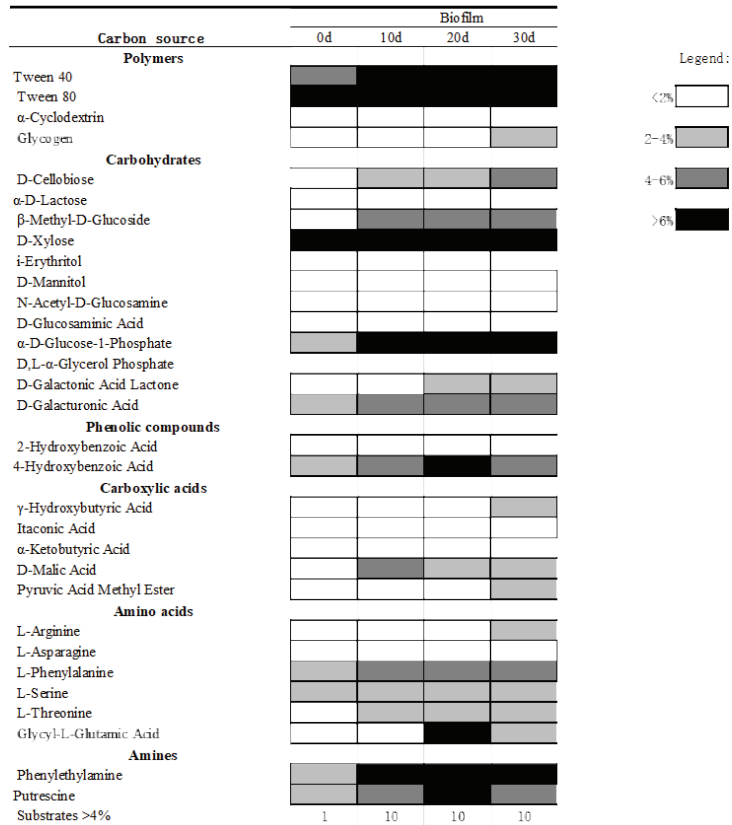

Fig. 2: Pattern of utilization (based on AWCD values) for 31 carbon substrates by adherent microbes in biofilms under anaerobic conditions.

attached microorganisms also included Planctomycetes (5.9%), while Proteobacteria (45.7%), Firmicutes (32.8%), and Bacteroides (11%) were still among the dominant phyla. On day 30, the dominant phyla in biofilms included Proteobacteria (51.1%), Bacteroidetes (21.4%), Planctomycetes (8.6%) and Cyanobacteria (6.5%).

A PCA showed that PC1 (53.65%) and PC2 (15.62%) explained up to 69.27% of the total variance. The scores for these two principal components were plotted to visually evaluate the changes in microbial community structure during biofilm formation (Fig. 4). On day 0, the microorganisms in the water body differed substantially from the biofilm microorganisms at each subsequent point; the microbial community structures were quite different. Points for day 10 and day 20 were highly clustered, and the biofilm microbial community structures were similar. The points at these two sampling times were distant from those at day 0 and day 30, and the biofilm microbial community structures were significantly different.

During biofilm formation, the microbial community structure formed by microbial succession (Fig. 5). At the beginning of the experiment, the microbial community

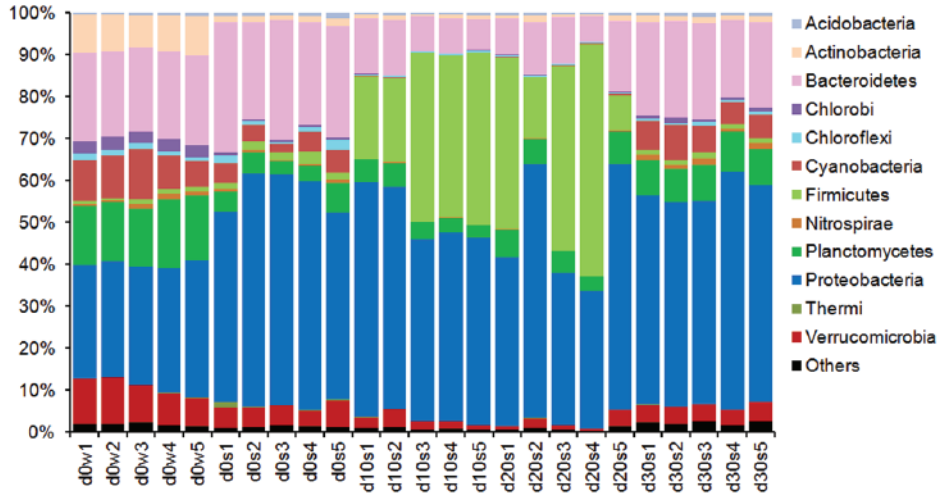

Fig. 3: Composition of dominant phyla during biofilm formation. d, sampling time; w, water body; s, biofilm.

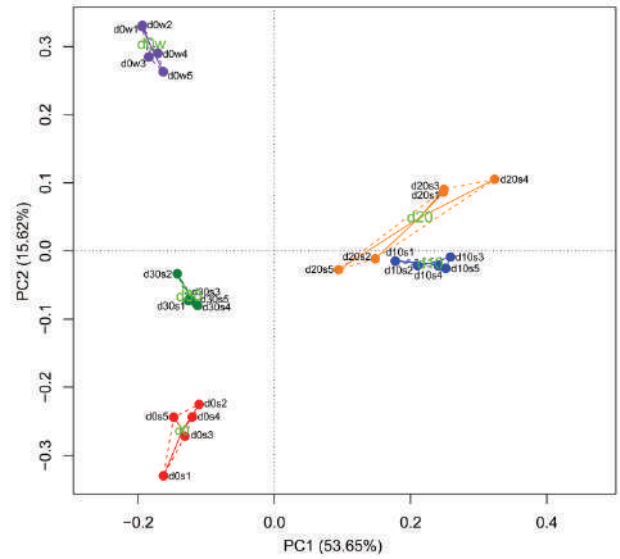

Fig. 4: Principal component analysis of community structure during biofilm formation. d, sampling time; w, water body; s, biofilm.

structure in the water body was highly similar to that of the biofilm at day 0. The clustering patterns of biofilm microorganisms on day 10 and day 20 indicated that they had similar community structures; the biofilm microorganisms on day 0 and 30 also clustered together. On day 0, Pirellulaceae, Cryomorphaceae, Stramenopiles, and Cerasicoccaceae did not attach to the biofilm substrate on day 0, and the biofilm microorganisms were dominated by Saprospiraceae and *Rubrivivax*. Over time, the abundances of *Rhodobacter*, Planococcaceae, *Flectobacillus*, *Bacillus* and *Aeromonas* increased significantly; the abundances of Saprospiraceae and *Rubrivivax* were lower on day 0 than on day 10. On day 20, there were significant increases in *Janthinobacterium* and *Alicyclobacillus* in the biofilm compared with abundances on day 10. On day 30, *Paucibacter* and *Thermomonas* showed high abundances in biofilms.

DISCUSSION

The capacity of biofilm microorganisms to utilize carbon sources under anaerobic conditions gradually improved during the process of biofilm formation in the aquaculture system. The AWCD value reflects the overall metabolic capacity on different carbon sources; a faster rate of change indicates higher metabolic activity (Xi et al. 2005). Under anaerobic conditions, the AWCD value for biofilm microorganisms was lowest on day 0 ($P < 0.05$); on day 20 and day 30, the biofilm microorganisms had the highest metabolic capacity on carbon sources under anaerobic conditions. These results are consistent with those of Li et al. (2014) for changes in the carbon source metabolism of microbial communities in grass carp aquaculture ponds. Changes in the Shannon index, Simpson's index, Pielou's index, and McIntosh's index were generally consistent with the results for carbon source metabolic activity. It is possible that during biofilm formation, increases in the quantity and variety of microorganisms directly cause changes in metabolic activity under anaerobic conditions (Liang et al. 2015).

During biofilm formation, the amine utilization rate under anaerobic conditions was highest among the six types of carbon sources, followed by polymers, carbohydrates, amino acids, and carboxylic acids, and the phenol utilization rate was lowest. According to previous studies of efficient carbon sources under aerobic conditions, biofilm microorganisms have the greatest preference for amino acids, followed by carboxylic acids and sugars (Zhu et al. 2017, Wang et al. 2013, Yang et al. 2009), indicating preferences for carbon sources under anaerobic conditions. The difference might be explained by the fact that biofilm microorganisms limit the metabolic activity of aerobic microorganisms under anaerobic conditions, while the metabolic activities of anaerobic and facultative anaerobic microorganisms are less affected, resulting in reduced demand for carboxylic acids and sugars. We speculated that amines were the main carbon sources contributing to anaerobic denitrification mediated by biofilms. In this study, Biolog technology was used to analyse the dynamic characteristics of carbon source metabolism in biofilm microbial communities under anaerobic conditions. We found that carbon sources utilized under anaerobic conditions were significantly different from those utilized under aerobic conditions. The carbon sources with the highest utilization rates included α-D-glucose-1-phosphate, Tween 40, D-xylose, Tween 80, 4-hydroxybenzoic acid, L-phenylalanine, and phenethylamine. Compared

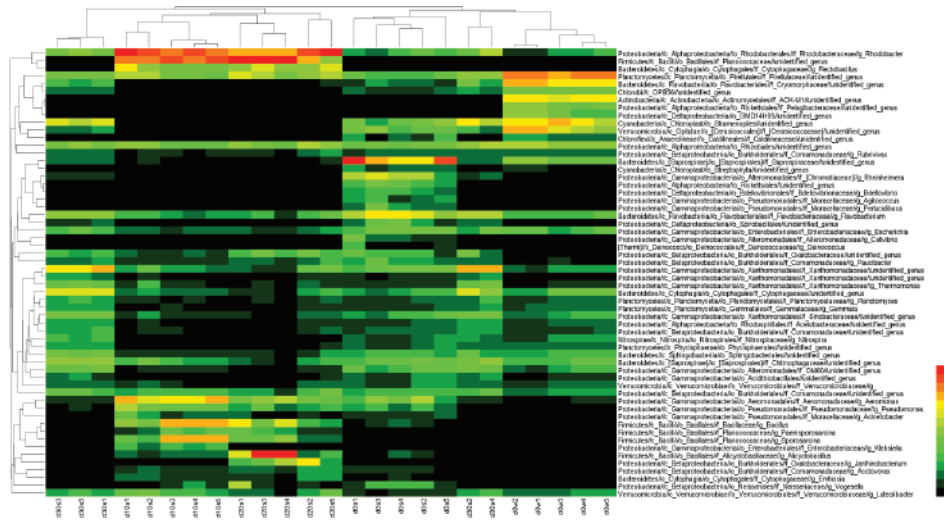

Fig. 5: Heatmap profile of the dominant OTUs of attached microorganisms during biofilm formation d, sampling time; w, water body; s, biofilm.

with the carbon sources utilized by biofilm microorganisms under aerobic conditions, the types of carbon sources used by denitrifying bacteria under anaerobic conditions were significantly reduced (Liu et al. 2015, Li et al. 2014, Cao et al. 2014), which might be explained by the reduced metabolic activity of the aerobic bacteria under anaerobic conditions and the rather intact carbon source metabolic activity of anaerobic and facultative bacteria.

In this study, we performed a PCA of the microbial community structures in the aquaculture water and during biofilm formation. The microbial community structures during biofilm formation were similar over time, but there was a significant difference between those at the initial stage (day 0) and the final stage (day 30). During biofilm formation, microorganisms became abundant, the thickness of the biofilm increased, and the diversity of the attached microbes increased. After the biofilm stabilized, the dominant phyla began to grow, which limited the colonization of other microbial species and affected the structure of the microbial communities.

The dominant phyla during biofilm formation were Proteobacteria, Firmicutes, Bacteroides, and Cyanobacteria, consistent with previous studies (Li et al. 2017, Yu et al. 2016). Highly abundant bacteria during biofilm formation included Saprospiraceae, *Rubrivivax, Rhodobacter, Janthinobacterium, Paucibacter,* and *Thermomonas*. The dominant bacteria Saprospiraceae at the beginning of biofilm formation (Day 0) might have played an important role in the degradation of carbohydrates and proteins (Fu et al. 2017). Under anaerobic conditions, the photosynthetic bacteria *Rubrivivax* can use ammonia as a hydrogen donor for photosynthesis and hydrogen production (Verméglio et al. 2012). On day 10 and 20, biofilms were enriched for the denitrifying bacteria *Rhodobacter*, belonging to the class α-Proteobacteria. Studies have shown that *Rhodobacter* can perform amination and denitrification using amines as carbon and nitrogen sources (Heylen et al. 2006, Zhang et al. 2005), the denitrifying bacteria enriched on day 20 also included *Janthinobacterium*, belonging to the class β-Proteobacteria, which play important roles in denitrification (Heylen et al. 2007, Fang et al. 2011). On day 30, *Paucibacter*, which belongs to Burkholderiales under the class β-Proteobacteria and the phylum Proteobacteria, was highly abundant in biofilms. On day 30, the dominant bacteria in the biofilms were Xanthomonadaceae and *Thermomonas* in the class γ-Proteobacteria and the phylum Proteobacteria, which can decompose environmental pollutants and compounds that are difficult to degrade (Wang et al. 2015). Proteobacteria is important in the denitrification process, and most denitrifying bacteria belong to the phylum β-proteobacteria (Takahashi et al. 2011, Chu et al. 2013, Ye et al. 2011). In this experiment, most of the highly-abundant bacteria during biofilm formation were denitrifying bacteria, which played an important role in the anaerobic denitrification process mediated by biofilms.

In conclusion, as biofilm formation progressed and as the AWCD values for biofilm microorganisms under anaerobic conditions increased significantly ($P < 0.05$), the utilization capacity of carbon sources gradually improved. During biofilm formation, the utilization of the six types of carbon sources under anaerobic conditions was significantly different from that under aerobic conditions. Under anaerobic conditions, the biofilm microorganisms exhibited the highest utilization of amines, while under aerobic conditions, demand was higher for polymers and amino acids. The utilization of single carbon sources by biofilm microorganisms under anaerobic conditions was also different from that under aerobic conditions. The demand for single carbon sources under anaerobic conditions was significantly lower than that under aerobic conditions. A high-throughput sequencing analysis indicated that the dominant phyla in the biofilm included Proteobacteria, Bacteroides, Firmicutes and Cyanobacteria. Bacteria with high abundances during biofilm formation included *Rhodobacter* of phylum α-Proteobacteria, *Janthinobacterium* and *Burkholderiales* of β-Proteobacteria, and Xanthomonadaceae and *Thermomonas* of γ-Proteobacteria. *Rhodobacter* and *Janthinobacterium* play important roles in denitrification mediated by biofilms.

ACKNOWLEDGEMENTS

This work was supported by the National Natural Science Foundation of China (31802348), the Science and Technology Planning Project of Guangdong Province, China (2016A020210023), the Natural Science Foundation of Guangdong Province, China (2015A030313699), and the Modern Agro-industry Technology Research System (grant number CARS-45-21).

REFERENCES

Avnimelech, Y. 2006. Bio-filters: The need for a new comprehensive approach. Aquacultural Engineering, 34(3): 172-178.

Cao, Y.C., Li, Z.J., Wen, G. L., Yuan, C. L., Yang, Y. Y., Hu, X. J. and Lin, X. T. 2014. Dynamics of microbial community and its metabolisms of different carbon sources in Tilapia ponds. Journal of Agro-Environment Science, 33(1): 172-177.

Chu, L. and Wang, J. 2013. Denitrification performance and biofilm characteristics using biodegradable polymers PCL as carriers and carbon source. Chemosphere, 91(9): 1310-1316.

Edgar, R. C. 2013. UPARSE: highly accurate OTU sequences from microbial amplicon reads. Nature Methods, 10(10): 996-998.

Fang, F., Wang, S.M., Feng, C.J. and Chen, S.H. 2011. Community structure of denitrifying bacteria in a hybrid AS-biofilm process under aerobic condition. Chinese Journal of Ecology, 30(3): 430-437.

Flemming, H. C. and Wingender, J. 2010. The biofilm matrix. Nature Reviews Microbiology, 8(9): 623.

Fu, C., Yue, X., Shi, X., Kok, K, N. and How, Y, N. 2017. Membrane fouling between a membrane bioreactor and a moving bed membrane bioreactor: Effects of solids retention time. Chemical Engineering Journal, 309: 397-408.

Heylen, K., Vanparys, B., Gevers, D., Wittebolle, L. and Boon, N. 2007. Nitric oxide reductase (norB) gene sequence analysis reveals discrepancies with nitrite reductase (nir) gene phylogeny in cultivated denitrifiers. Environmental Microbiology, 9(4): 1072-1077.

Heylen, K., Vanparys, B., Wittebolle, L., Verstraete, W., Boon, N. and Vos, P. D. 2006. Cultivation of denitrifying bacteria: Optimization of isolation conditions and diversity study. Applied and Environmental Microbiology, 72(4): 2637-2643.

Huang, C., Shi, Y., Xue, J., Zhang, Y., EI-Din, M, G. and Liu, Y. 2017. Comparison of biomass from integrated fixed-film activated sludge (IFAS), moving bed biofilm reactor (MBBR) and membrane bioreactor (MBR) treating recalcitrant organics: Importance of attached biomass. Journal of Hazardous Materials, 326: 120-129.

Kang, C. L., Guo, J., Guo, P., Zhao, Y. and Dong, D. 2005. Biosorption of Cd^{2+} by the organic components of surface coatings in natural waters. Ecology and Environment, 14(5): 636-639.

Li, Z. F., Wang, G. J., Xie, J., Yu, E. M., Yu, D. G. Xia, Y. and Wei, N. 2014. Microbial carbon metabolic characteristics of biofilm communities in the grass carp culture pond based on Biolog-ECO plates. Journal of Fisheries of China, 38(12): 1985-1995.

Li, Z., Che, J., Xie, J., Wang, G. Yu, E., Xia, Y., Yu, D. G. and Zhang K. 2017. Microbial succession in biofilms growing on artificial substratum in subtropical freshwater aquaculture ponds. FEMS Microbiology Letters, 364(4): 1-7.

Liang, Y. C., Hu, Z. B., Tu, W. L., Lu, H. Jiang, Z. and Liu, K. H. 2015. Effectiveness of carbon fiber based biofilm carrier remediation technology on urban black-odorous water. Chinese Journal of Environmental Engineering, 9(2): 603-608.

Liu, Y., Li, L., Sun, D. H., Zhu, Y. H. Tan, H. X. and Xu, B. 2015. Carbon metabolism of microbial communities in biofilters of recirculating aquaculture system cultured with *Anguilla marmorata*. Journal of Fisheries of China, 39(10): 1539-1548.

Magurran, A, E. 1988. Ecological Diversity and its Measurement. Princeton University Press.

Ni, J., Li, X., He, Z. and Xu, M. Y. 2017. A novel method to determine the minimum number of sequences required for reliable microbial community analysis. Journal of Microbiological Methods, 139: 196-201.

Nogueira, R., Melo, L. F., Purkhold, U., Wuertz, S. and Wagner, M. 2002. Nitrifying and heterotrophic population dynamics in biofilm reactors: Effects of hydraulic retention time and the presence of organic carbon. Water Research, 36(2): 469-481.

Piedrahita, R.H. 2003. Reducing the potential environmental impact of tank aquaculture effluents through intensification and recirculation. Aquaculture, 226(1-4): 35-44.

Qian, W., Lu, K. H., Zheng, Z. M., Lu, Z. M., Xie, L. F. and Zhang, K. X. 2011. Purifying effects of enhanced bioreactor on the wastewater in recirculating aquaculture systems. Journal of Fisheries of China, 35(1): 104-115.

Reddy-Lopata, K., Auerswald, L. and Cook, P. 2006. Ammonia toxicity and its effect on the growth of the South African abalone *Haliotis midae* Linnaeus. Aquaculture, 261(2): 678-687.

Rittmann, B. E. 2018. Biofilms, active substrata, and me. Water Research, 132: 135-145.

Takahashi, M., Yamada, T., Tanno, M., Tsuji, H. and Hiraishi, A. 2011. Nitrate removal efficiency and bacterial community dynamics in a denitrification process using poly (L-lactic acid) as the solid substrate. Microbes and Environments, 26(3): 212-219.

Verméglio, A., Nagashima, S., Alric, J., Arnoux, P. and Nagashima, K.V.P. 2012. Photo-induced electron transfer in intact cells of *Rubrivivax* gelatinosus mutants deleted in the RC-bound tetraheme cytochrome: Insight into evolution of photosynthetic electron transport. Biochimica. et Biophysica. Acta (BBA)-Bioenergetics, 1817(5): 689-696.

Wang, J. H., Wu, Y. H., Feng, Y. F., Lu, H. Y., Zhou, H. and Yang, L. Z. 2013. Effects of hyper-entrophic nitrogen and phosphorus additions on the functional and formational diversity of periphyton biofilms. Ecology and Environmental Sciences, 22(7): 1236-1243.

Wang, Q., Garrity, G. M., Tiedje, J. M. and Cole, J. M. 2007. Naive Bayesian classifier for rapid assignment of rRNA sequences into the new bacterial taxonomy. Applied Environmental Microbiology, 73(16): 5261-5267.

Wang, Z., Liu, L., Guo, F. and Zhang, T. 2015. Deciphering cyanide-degrading potential of bacterial community associated with the coking wastewater treatment plant with a novel draft genome. Microbial Ecology, 70(3): 701-709.

Xi, J. Y., Hu, H. Y., Jiang, J. and Qian, Y. 2005. Metabolic properties of the microbial community in the biofilters using biolog microplates. Environmental Science, 26(4): 165-170.

Xia, S. D., Li, Y., Wang, W. Q., Tang, S. Q. and Wang, M. Q. 2010. The characteristics of immunity and digestibility about juvenile *Litopenaeus vannamei* fed with different protein diet. Journal of Hydroecology, 3(5): 76-81.

Yang, Y. Y., Li, Z. J., Liang, X. H., Liang, R. J., Hong, M. N. and Chen, Y. Q. 2009. Influences of Bacillus on metabolic functions of microbial communities in fishponds. Journal of Microbiology, 29(3): 11-17.

Ye, L., Shao, M. F., Zhang, T., Tong, A. H, Y. and Lok, S. 2011. Analysis of the bacterial community in a laboratory-scale nitrification reactor and a wastewater treatment plant by 454-pyrosequencing. Water Research, 45(15): 4390-4398.

Yu, E., Xie, J., Wang, J., Ako, H., Wang, G. J., Chen, Z. H. and Liu, Y. F. 2016. Surface-attached and suspended bacterial community structure as affected by C/N ratios: relationship between bacteria and fish production. World Journal of Microbiology and Biotechnology, 32(7): 116-125.

Zhang, G.Y. and Chen, P. Q. 2005. Isolation, identification and characteristics of aerobic denitrifying bacteria. Journal of Microbiology, 25(6): 23-26.

Zhang, L. Y., Rao, B. Q., Xiong, Y., Liu, H., Liu, Y. D. and Shen, Y W. 2010. The micobial mechanism of horizonal constructed wetland used to treated black-odor river. Acta Hydrobiologica Sinica, 34(2): 256-261.

Zhu, Y. H., Tan, H. X., Sun, D. H., Luo, G. Z., Wang, J. and Liu, Y. 2017. Analysis of carbon metabolism diversity characters of moving bed biofilm reactor at different biodegradation process in recirculating aquaculture systems using Biolog-ECO method. Journal of Shanghai Ocean University, 26(1): 64-74.

Nature Environment and Pollution Technology
An International Quarterly Scientific Journal

p-ISSN: 0972-6268
e-ISSN: 2395-3454

Vol. 18 | No. 4 | pp. 1293-1298 | 2019

Original Research Paper | Open Access

Environmental Pollution Caused by the Transportation Industry and Influencing Factors of Carbon Emission: A Case Study of Jiangxi Province, China

Yating Huang
School of Transportation and Logistics, East China Jiao Tong University, Nanchang, 330013, China
Corresponding author: Yating Huang

Nat. Env. & Poll. Tech.
Website: www.neptjournal.com

Received: 12-09-2019
Accepted: 15-10-2019

Key Words:
Transportation industry
Environmental pollution
Carbon emission
Influencing factors

ABSTRACT

With the accelerating industrialization and urbanization in China, the energy consumption of the transportation industry in the country is increasing quickly, and its proportion to the total social energy consumption is significantly growing. The transportation industry is a main source of carbon emission in urban areas. The unreasonable structure of energy consumption, the low proportion of new-energy use, and low energy utilization influence the energy-saving and emission reduction in the transportation industry. Thus, in this work, the influencing factors of transportation-induced carbon emission were estimated to analyze the environmental pollution caused by the transportation industry further. Regression analysis was performed on the environmental pollution caused by the transportation industry and the influencing factors of carbon emission in Jiangxi Province, China. Subsequently, a random STIRPAT model was constructed, and the influencing factors of carbon emission from the transportation industry in Jiangxi Province from 2007 to 2017 were analyzed through the partial least squares (PLS) method. Regression results based on the PLS method were relatively ideal. Increases in gross domestic product per capita, population size, passenger person kilometers, rotation freight transport kilometers, and the number of car ownerships can intensify transportation-induced carbon emission. This emission is increased when transportation energy intensity declines, but can be significantly inhibited by increased energy prices. The conclusions of this study can provide references for the continuous optimization of the energy use structure in the transportation industry, saving of energy resources, reduction of greenhouse gas and pollutant emission, and acceleration of low carbonization in the transportation industry.

INTRODUCTION

Energy is an important pillar of economic and social development. Energy development and utilization promote economic development and progress. Recently, the transportation industry has become a major consumer of energy and the main source of CO_2 and pollutant emissions in the world. With the accelerating urbanization and industrialization in China, the energy consumption of the transportation industry in the country is increasing. Transportation industry has been ranked second in energy consumption for several successive years, only next to industrial energy consumption. Energy is an essential production element in national economic development, and it is the vein of national economies. As a fundamental industry that supports economic development, the transportation industry highly depends on energy. However, it can fully support national economies and drive the development of all industries in social economies only with sufficient energy supply. With the continuous large-scale energy consumption in the transportation industry, traffic pollution (including the quantity, concentration, and duration of the smoke, dust, and harmful gases emitted by vehicles) not only has exceeded the self-cleaning capacity of the atmospheric environment under natural states but also produces noises that are outside of the regulated range, thus exposing people and other creatures to pollution damages. Traffic pollution can be influenced by various factors of vehicles, such as traveling density, vehicle modes, fuel, operating state of vehicles, road conditions, and local physical geographic environments. Traffic pollution changes continuously at different moments and in various seasons.

Jiangxi is an important province with a large population in central China and has remarkable geological advantages in transportation. The transportation industry has rapidly developed. Figure 1 shows that rotation freight transport kilometers (RFTKs) were 228.549 billion tons/km in 2008 and 452.863 billion tons/km in 2018, showing an annual growth rate of 9.8%. This observation fully reflects the rapid development of the transportation industry in Jiangxi Province. The number of vehicles increased continuously during this rapid development, thereby significantly intensifying the traffic

pollution in Jiangxi Province. The secondary photochemical smog formed by nitric oxides emitted by vehicles and the secondary pollution formed by ozone, particulates, and dust has become irreversible and severe regional and seasonable environment pollution problems in Jiangxi Province.

EARLIER STUDIES

Many in-depth studies on traffic pollution and the influencing factors of carbon emission have been reported worldwide. Transportation energy consumption is becoming a major source of total energy consumption for economic and social development in different countries. Air pollutants and greenhouse gas emissions brought by the excessive primary energy consumption of the transportation industry need to be controlled. Concerning traffic pollution, Duke et al. (1995) believed that vehicle repair, vehicle refueling, vehicle cleaning, and activities on paved roads and vehicle storage areas may cause water pollution in transportation the department. Rondinelli et al. (2000) stated that the influences of the transportation industry on the natural environment (e.g., air, water, and land resources) are becoming increasingly complicated and proposed some reasonable measures to prevent environmental pollution and natural resource degradation caused by the transportation industry. Mao et al. (2012) argued that the transportation industry in China has become a primary CO_2 emission source, which induces a large number of regional atmosphere pollutants. He believed that taxing for CO_2 emission might be an effective policy tool. Shrivastava et al. (2013) believed that most cities in India are experiencing extremely high levels of air pollution and found that transportation contributes largely to environmental pollution. Finally, an evaluation model for traffic pollutant emissions and effective measures for reducing traffic pollution have been proposed. Anenberg et al. (2019) believed that emissions from the transportation sector are the main cause of air pollution, which is a major contributor to global environmental health risks. Zhou et al. (2018) concluded that the rapid growth of transportation energy consumption and CO_2 emission brings considerable challenges to the energy demands and environmental problems in China. With respect to the influencing factors of transportation-induced carbon emission, Zhang et al. (2011) studied the influencing factors of the transportation energy consumption in China during 1980-2006 by using the LMDI method and found that the continuous growth of traffic turnover is the principal influencing factor. Energy intensity reduction caused by technological progress inhibits the growth of transportation energy consumption. Krautzberger et al. (2012) applied the Malmquist-Luenberger index of productivity model and compared the development of CO_2 productivity in the commercial transportation industry in Europe during 1995-2006. He found that the transportation industry's sensitivity to carbon emissions changed significantly in most European countries, and the average productivity efficiency declined to some extent. Chung et al. (2013) studied transportation-induced carbon emissions in China from 2003 to 2009 and found that the high growth rate of diesel consumption in freight transportation was the main contributor to the overall energy consumption growth. Tiwari et al. (2013) investigated the causes of energy consumption changes in the transportation industry in India and found that

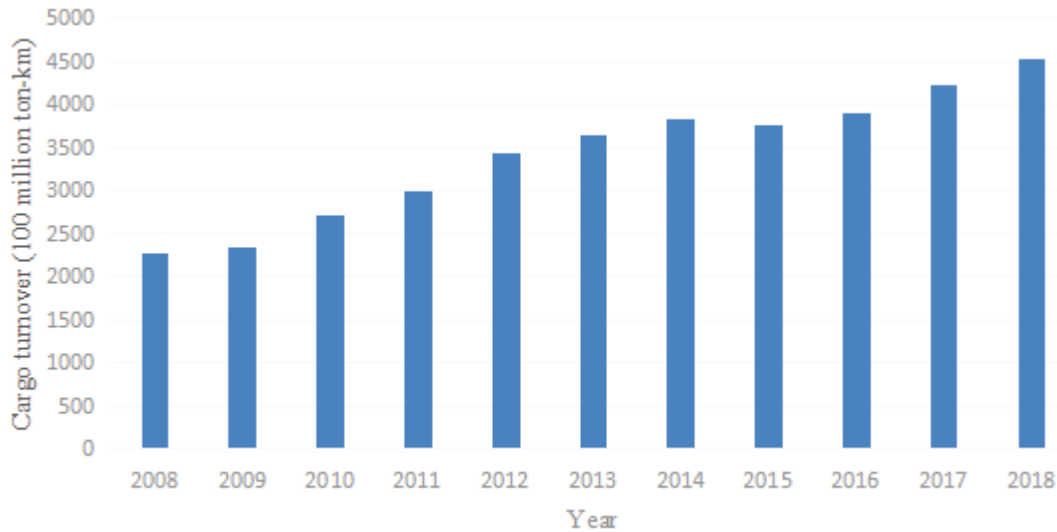

Fig. 1: RFTKs in Jiangxi Province from 2008 to 2018.
(Data source: Statistical Yearbook of Jiangxi (2009-2019))

changes in energy consumption are attributed to the growth of freight volume, structural change or mode transformation, and energy intensity. Xu et al. (2015) applied the vector autoregression model to analyze the influencing factors of transportation-induced CO_2 emission in China and found that energy efficiency plays a dominant role in CO_2 emission reduction. Moreover, the large-scale use of private cars, the continuous growth of RFTK, and accelerating urbanization can significantly influence the growth of CO_2 emission in the transportation industry. Fan et al. (2016) analyzed the influencing factors of transportation-induced carbon emission in Beijing based on the extended Kaya identical equation and concluded that economic growth, energy intensity, and population size are major positive driving factors of such emission. Lin et al. (2017) investigated the influences of gross domestic product (GDP) per capita, energy intensity, carbon intensity, and total population in China's transportation industry on CO_2 emission from 1980 to 2010 through quantile analysis and found that GDP, energy intensity, and carbon intensity affect carbon emission more than urbanization. Based on Beijing-Tianjin-Hebei panel data during 1995-2016, Guo et al. (2019) analyzed the driving factors of CO_2 emission in the transportation industry. Guo found that transportation energy intensity and economic effect are the major causes of increased CO_2 emission, whereas energy structural effect is the main reason for reduced CO_2 emission in the transportation industry. Most scholars emphasized the national level of transportation-induced carbon emission and preferred to use the factor decomposition method to analyze basic indexes, such as economy, population, energy intensity, and car ownership. A case study of Jiangxi Province centered at RPK, RFTK, and energy price was conducted to provide policy suggestions for energy saving and emission reduction and for realizing green sustainable development in the transportation industry.

MODEL CONSTRUCTION AND DATA SOURCE

STIRPAT Model

Environmental deterioration is generally the collaborative consequence of demographic factors, economic development, and technological development. In the 1970s, the IPAT equation was produced to study the action mechanism among demographic development, wealth, technological progress, and the environment. To overcome the shortcomings of the IPAT equation, Dietz et al. (1994) constructed a random STIRPAT model of the IPAT equation. This model involves a randomness variable in addition to the original variables of the IPAT model, thus enabling superior empirical analysis. Thus, an extensible random environmental effect assessment model was formed. The detailed STIRPAT model can be expressed as formula (1):

$$I_i = aP_i^b A_i^c T_i^d \varepsilon_i \quad \ldots(1)$$

Where, I_i denotes the environmental factors; P_i denotes the demographic factors; A_i is the affluence degree; I_i is the technological level; b, c, and d are the parameters that have to be estimated; and ε_i is a random error term. This model assumes that ecological environmental pressure is accompanied by the combined influences of population size, affluence degree, and technological level. The model formula is expressed as an exponential function; however, it is generally transformed into logarithmic form for convenient operation in practical studies, thereby not only potentially eliminating the possible heteroscedasticity problem but also possibly estimating parameters through linear regression. After the natural logarithms, the model is rewritten as formula (2):

$$LnI_i = a + bLnP_i + cLnA_i + dLnT_i + \varepsilon_i \quad \ldots(2)$$

On the basis of the concept of elastic coefficient, the regression coefficient of the equation reflects the elastic relationship between dependent and independent variables. It reflects changes in the dependent variables for each 1% change in an independent variable when other independent variables are fixed. The STIRPAT model still maintains the original product structure of the IPAT equation. Population, affluence, and technology are still decisive factors that influence the environment. Meanwhile, the STIRPAT model accepts unit root test and allows the decomposition of environmental and technological factors. For the flexibility of the STIRPAT model, relevant variables can be added into the original model in accordance with the research goal. The extended relevant factors are included into the STIRPAT model in this study on the basis of development changes in the transportation industry in Jiangxi Province and current traffic pressure. The influence degrees of economic level, population size, energy intensity, RPK, RFTK, energy price, and the number of car ownerships on carbon emission are analyzed thoroughly. The expanded model can be expressed as formula (3):

$$\ln C_i = a + b_1(\ln GDP_i) + b_2(\ln POP_i) + b_3(\ln ENE_i) \\ b_4(\ln PAS_i) + b_5(\ln FRE_i) + b_6(\ln PRI_i) + b_7(\ln VEC_i) + \varepsilon_i \quad (3)$$

Where, C_i denotes the environmental influences and is expressed by transportation-induced carbon emission in Jiangxi Province. *GDP* refers to the GDP per capita. *POP* is the popularization size. *ENE* is the energy intensity. *PAS* is RPK and *FRE* is RFTK. *PRI* is the energy price. *VEC* is the number of car ownerships, and ε_i is a random error.

Generally, population change, social and economic development, and technological innovation are connected, influenced, and constrained mutually. Therefore, time series data involving these three factors often have multiple collinearity problems. Multiple collinearities can not only increase the variance of parameter estimation but also exclude important explanatory variables from the model, thus ignoring the meaning of the significance test of variables. Therefore, a regression analysis based on partial least squares (PLS) is conducted. This regression analysis integrates the characteristics of multiple linear regression, principal component analysis, and typical correlation analysis. PLS can screen and extract principal components that influence dependent variables mostly in the system and recognize valid information in the regression process.

DATA SOURCE

Time series data in Jiangxi Province during 2007-2017 were selected. Data about energy use and energy intensity in the calculation were collected from the China Energy Statistical Yearbook. During carbon emission estimation, the carbon emission coefficients of different energy sources were the carbon emission coefficient adopted by the Energy Research Institute of National Development and Reform Commission. Per capita consumption level was transformed into the constant price in 2007. Data about population size, RPK, RFTK, and the number of car ownerships were selected from the *Statistical Yearbook of Jiangxi* during 2008-2018. Energy price data were obtained from the *Price Yearbook of China*.

RESULT ANALYSIS

PLS regression results were calculated using the SIMCA-P software (demo version 11.5). Table 1 lists the results.

Table 1: PLS regression results.

Variable	Nonstandardized coefficient	Standardization coefficient
C_i	−23.041	4.685
GDP	1.654	0.178
POP	3.158	0.194
ENE	−0.629	−0.287
PAS	0.541	0.125
FRE	0.875	0.116
PRI	−3.871	−0.268
VEC	0.784	0.381
$R^2X(cum)$	0.845	-
$R^2Y(cum)$	0.821	-
$Q^2(cum)$	0.904	-

Table 1 indicates that $R^2X(cum)$, $R^2Y(cum)$, and $Q^2(cum)$ are indicators of the fitting degree of the extracted principal components, and all values are higher than 0.8, indicating that PLS regression results are relatively ideal. Economic factors are the most important factors that influence transportation-induced carbon emission in Jiangxi Province. Economic growth increases transportation-induced carbon emission in Jiangxi Province, and every 1% growth of GDP per capita may increase transportation-induced carbon emission by 1.654%. Jiangxi Province has been exhibiting rapid economic growth since 2008. In particular, economic development has increased residential income after the implementation of the "central China" development, thereby promoting an increase in consumption level and changes in lifestyle and travel modes. Products consumed by residents produce abundant CO_2 emission in the transportation link. The economy of Jiangxi Province will maintain a stable and high growth rate over a long period in the future, which may increase transportation-induced carbon emission to an excessive extent. Population growth also significantly increases carbon emission. Every 1% increase in population size may result in 3.158% growth transportation-induced carbon emission in Jiangxi Province. Recently, the population size of Jiangxi Province has been increasing quickly because the province has been undertaking industries from coastal regions, and the processing and manufacturing industries have been attracting abundant employees. Population growth in Jiangxi Province may lead to increased energy demands and traffic pressure in cities and may accelerate population mobility. As a result, transportation-induced carbon emission continues to increase. Transportation-induced carbon emission increases with the reduction of energy intensity. The increase in transportation-induced carbon emission is the collaborative consequence of multiple factors. On the one hand, increased carbon emission caused by demographic changes and economic development offsets the reduced carbon emission brought by technological progress. On the other hand, energy consumption can be saved by the increased energy utilization after technological progress, accompanied by increased demands for new energy sources, due to the rebounding effect. The collaborative consequence is manifested by increased carbon emission upon technological developments. As the industrial upgrade in Jiangxi Province continues in the future, technological progress still has a large development space. The transportation-induced carbon emission increases with RPK, which is related to the economic development level in Jiangxi Province. Large-scale spatial migration of the population exists in Jiangxi Province due to accelerating urbanization. In particular, the perfecting of traffic infrastructures, such as the Shanghai–Kunming railway and highways, has brought significant growth in passenger

capacity to Jiangxi Province and facilitated economic development and energy consumption, resulting in the continuous growth of carbon emission. The increase in RFTK increases transportation-induced carbon emission. RFTK can influence transportation-induced carbon emission more than RPK. With evident geological traffic advantages, Jiangxi Province has an exerted effort to develop a modern logistics industry. Freight transportation considerably depends on railways and shipways. The favorable railway and shipping transportation conditions in Jiangxi Province establish a good foundation for the development of this modern logistics industry. Transportation-induced carbon emission in Jiangxi Province is decreased by 3.871% for every 1% increase in energy price, showing a significant inhibition effect. Energy price growth forces some transportation enterprises to reduce activities, thus decreasing carbon emission. Private cars are convenient for the travel of residents. The proportion of passengers in public transportation declines with an increased number of car ownerships, thus further increasing transportation-induced carbon emission.

POLICY SUGGESTIONS

Strengthening formulation and implementation of tax policy for traffic pollution: Tax policy for pollution is a compulsory environmental policy formulated by the government. For traffic pollution, a certain tax will be collected from vehicles with excessive emissions or under environmental standards. The collected taxes will be applied to improve environmental quality. According to the preset of the Pigou Institute, external marginal cost is internalized into the private cost to stimulate dischargers to lower emissions and pollution discharge amounts. The charging system for traffic pollutant emission will be implemented to vehicle users of households, individuals, and organizations. Traffic pollutant emission charges for each vehicle shall be calculated from the total annual pollutant emission of traffic loads in Jiangxi Province. Vehicle users shall pay for pollutant emission during the annual inspection, thus inhibiting the use frequency of vehicles. Guiding and encouraging people to use vehicles with small emission capacity and encouraging enterprises to produce vehicles with small emission capacity are important measures for saving energy and reducing emissions because vehicles with small emission capacity have small weights, small oil consumption, and relieved environmental pollution.

Accelerating development of low-energy consumption transportation mode: Considerable effort shall be exerted to promote high economic growth in Jiangxi Province. Currently, the proportions of transportation mode and energy consumption of highways in Jiangxi Province are significantly higher than those of other transportation modes. Government shall accelerate the construction of a comprehensive energy-saving traffic system and fully develop relative advantages of different transportation modes through the overall planning of the comprehensive traffic system. A reasonably balanced development of different transportation modes with considerations for the natural geological environment and economic development status will be promoted in Jiangxi Province. Moreover, the connection and information levels of infrastructure in the comprehensive traffic system shall be improved to realize the fast transshipment of passengers and freight and increase transportation service quality and efficiency. Investment and support for railway, ship, and tube transportation shall be increased. Jiangxi Province shall increase the proportion of transportation modes with low single consumption and guide bulk cargo to energy-saving environmentally friendly transportation modes. The attractions of the railway to freight transportation and the railway transportation service quality of passengers and freight shall be improved. The advantages of speed and comfort of high-speed railway relative to highways shall be developed.

Increasing technological innovation level in the transportation industry: Jiangxi Province shall accelerate the improvement of transportation tools and the development of clean energy sources. Outdated vehicles with high energy consumption will be eliminated, and the development of transportation vehicles toward large-sized and diesel consumption types will be guided. In addition, the province shall promote the development of new-energy vehicles, increase the fast charging technology of electric vehicles, and improve the cruising power of batteries. Subsidies to electric vehicles shall be increased, and the competitive edges of new-energy vehicles relative to traditional vehicles will be strengthened. Railway transportation shall promote the use of electric locomotives, gradually decrease the proportion of diesel locomotives, and reduce dependence on petroleum products. Substantive efforts shall be made to promote the update of old ships and develop ships toward large and professional types. The province shall popularize clean-energy products (new electric cars). Nowadays, the energy supply shortage is severe, and pollution is intense. The government shall formulate relevant regulations to develop and use new energy sources and the developed tail gas purification devices. The government requests car owners to install this device. On the basis of the overall transportation industry, the current situation of pollutant emission (traffic pollution shall be classified independently in general surveys of secondary pollution) shall be analyzed. Moreover, emission reduction technologies shall be developed, demonstrated, and popularized. Studies on monitoring pollutant emission reduction and verification technologies shall be conducted. Jiangxi Province must formulate and adjust national emission standards and price policies in favor of emission reduction to

increase the proportion of railway transportation. It should likewise implement relevant industrial pollution control technological standards and norms.

Increasing public consciousness in transportation-related environmental protection: The government shall increase publicity and public consciousness about environmental protection through television, broadcast, WeChat, MicroBlog, network media, newspapers, forums, and brochures, especially in rural areas. These efforts can guide the public to abandon bad habits of carelessly throwing waste and spitting in public areas. They can also advocate afforestation, energy saving, emission reduction, and recycling (e.g., focusing on the classification and recycling of household wastes, reasonable processing of waste straws, reducing the use of white waste bags, advocating vehicles with small emission capacity, using public transportation, and reducing the use of pesticides). Environmental protection education shall be offered in schools, and environmental protection curriculums should be established. Government affairs related to transportation-related environmental protection shall be open to the public to increase information transparency. The public shall be motivated to supervise traffic pollution behaviors, and attention shall be given to public reporting and relevant rewarding systems.

CONCLUSIONS

The transportation industry is a typical high-energy-consumption industry. The energy consumption by the transportation industry in China has been increasing with social economic and industrial development, which causes a considerable challenge to energy saving in the entire society and industry. In this work, a case study of Jiangxi Province is conducted. A random STIRPAT is constructed, and the influencing factors of transportation-induced carbon emission in Jiangxi Province during 2007-2017 are analyzed through PLS regression. The results demonstrate that transportation-induced carbon emission is positively related to GDP per capita, population size, RPK, RFTK, and the number of car ownership, but negatively related to traffic energy intensity. With the increase in energy price, transportation-induced carbon emission can be inhibited significantly. Energy-saving and emission reduction in the transportation industry can be realized by strengthening the formulation of tax policy for traffic pollution, accelerating the development of low-energy-consumption transportation modes, improving technological innovation of the transportation industry, and increasing public consciousness in transportation-related environmental protection. Thus, the province should conduct further studies on the systematic influencing factors of transportation-induced energy consumption, transportation-induced energy consumption in different economic development regions, and influencing mechanisms on transportation energy consumption, as well as different transportation modes in influencing factors of energy consumption.

ACKNOWLEDGEMENTS

This study is supported by Research Projects of Humanities and Social Sciences for Universities in Jiangxi Province (No. SZZX1802).

REFERENCES

Anenberg, S.C., Miller, J., Henze, D.K., Minjares, R. and Achakulwisut, P. 2019. The global burden of transportation tailpipe emissions on air pollution-related mortality in 2010 and 2015. Environmental Research Letters, 14(9): 094-012.

Chung, W., Zhou, G. and Yeung, I. M. 2013. A study of energy efficiency of transport sector in China from 2003 to 2009. Applied Energy, 112: 1066-1077.

Duke, L. D. and Chung, Y. J. 1995. Industrial storm water pollution prevention: Effectiveness and limitations of source controls in the transportation industry. Waste Management, 15(8): 543-558.

Dietz, T. and Rosa, E.A. 1994. Rethinking the environmental impacts of population, affluence and technology. Human ecology review, 1(2): 277-300.

Fan, F. and Lei, Y. 2016. Decomposition analysis of energy-related carbon emissions from the transportation sector in Beijing. Transportation Research Part D: Transport and Environment, 42: 135-145.

Guo, M. and Meng, J. 2019. Exploring the driving factors of carbon dioxide emission from transport sector in Beijing-Tianjin-Hebei region. Journal of Cleaner Production, 226: 692-705.

Krautzberger, L. and Wetzel, H. 2012. Transport and CO_2: Productivity growth and Carbon Dioxide Emissions in the European commercial transport industry. Environmental and Resource Economics, 53(3): 435-454.

Lin, B. and Benjamin, N. I. 2017. Influencing factors on carbon emissions in China transport industry. A new evidence from quantile regression analysis. Journal of cleaner production, 150: 175-187.

Mao, X., Yang, S., Liu, Q., Tu, J. and Jaccard, M. 2012. Achieving CO_2 emission reduction and the co-benefits of local air pollution abatement in the transportation sector of China. Environmental Science & Policy, 21: 1-13.

Rondinelli, D. and Berry, M. 2000. Multimodal transportation, logistics, and the environment: Managing interactions in a global economy. European Management Journal, 18(4): 398-410.

Shrivastava, R. K., Neeta, S. and Geeta, G. 2013. Air pollution due to road transportation in India: A review on assessment and reduction strategies. Journal of Environmental Research and Development, 8(1): 69.

Tiwari, P. and Gulati, M. 2013. An analysis of trends in passenger and freight transport energy consumption in India. Research in Transportation Economics, 38(1): 84-90.

Xu, B. and Lin, B. 2015. Carbon dioxide emissions reduction in China's transport sector: A dynamic VAR (vector autoregression) approach. Energy, 83: 486-495.

Zhou, Y., Fang, W., Li, M. and Liu, W. 2018. Exploring the impacts of a low-carbon policy instrument: A case of carbon tax on transportation in China. Resources, Conservation and Recycling, 139: 307-314.

Zhang, M., Li, H., Zhou, M. and Mu, H. 2011. Decomposition analysis of energy consumption in Chinese transportation sector. Applied Energy, 88(6): 2279-2285.

Nature Environment and Pollution Technology
An International Quarterly Scientific Journal

p-ISSN: 0972-6268
e-ISSN: 2395-3454

Vol. 18 | No. 4 | pp. 1299-1304 | 2019

Original Research Paper | Open Access

Some Studies on the Removal of Chromium from Aqueous Solutions by an Adsorbent Obtained from *Terminalia chebula*

Monangi Murali†, R. Srinivasa Rao and Priya Darshini Pradhan
Department of Civil Engineering, Raghu Engineering College, Visakhapatnam-531162, India
†Corresponding author: Monangi Murali

Nat. Env. & Poll. Tech.
Website: www.neptjournal.com

Received: 19-04-2019
Accepted: 31-05-2019

Key Words:
Terminalia chebula
Chromium removal
Adsorbent
Heavy metals
Drinking water

ABSTRACT

Several methods of treatment have been suggested for the removal of chromium from raw water, which include chemical precipitation, reverse osmosis, ion exchange, foam formation, etc. The main disadvantages of the above processes are that they produce a large amount of sludge and there are no possibilities of metal recovery as they are very costly. The use of plants and other plant materials for the removal of the heavy metals has already been reported in the literature as the non-conventional adsorbents. In the present work, an attempt has been made to check the suitability of *Terminalia chebula* powder for removing chromium from raw water by adsorption and for suggesting an environmental friendly as well as economically feasible solution to overcome the problems due to the presence of toxic pollutants like chromium in drinking water. Batch experiments were conducted using aqueous solution of chromium to determine the chromium removal. *Terminalia chebula* powder (commonly known as karakkaya locally) has been collected locally and used as an adsorbent for all the batch experiments. Variation of chromium removal with dosage of adsorbent and initial pollution concentration is studied.

INTRODUCTION

Chromium can exist in different oxidation states like Cr^{3+}, Cr^{5+}, Cr^{6+}. In the water environment, chromium exists primarily in the form of chromates ($Cr3^{+}$). Wastewater from industries such as chrome leather tanning, metallurgy, chrome plating, textiles, ceramics, photography and photoengraving contains moderate to excessive amounts of hexavalent chromium compounds beyond the conventional statutory limit of 0.1 mg/L. Remediation of these effluents is necessary because in humans Cr(VI) causes lung cancer, ulcers, nasal septum perforations, and damage to the kidneys (Farai et al. 2014). During the transformation of chromium in water environment, oxidation of Cr^{3+} and reduction of Cr^{6+} takes place depending upon environmental parameters. Furthermore, there is no evidence to indicate that the trivalent (Cr^{3+}) form is detrimental to human health. But, hexavalent chromium (Cr^{6+}) is a powerful oxidant which can easily penetrate the biological membranes and irritate cells. High concentration of chromium is toxic to plants, animals as well as to humans. Most of the toxic effects of the chromium to man are associated with its occupational exposure rather than its intake with diet and water. Several methods of treatments have been suggested for removal of chromium which, include precipitation, reverse osmosis, ion-exchange, foam formation, etc. The main disadvantages of the above processes are that they produce a large amount of sludge and there is no possibility of metal recovery. The use of plants and other plant materials for the removal of the heavy metal have already been reported in the literature as the non-conventional adsorbents. Ahmad et al. (2005) studied the removal and recovery of chromium from synthetic and industrial wastewater using bark of *Pinus roxburghii* as an adsorbent. They found that percent recovery of chromium from industrial wastewater by column operation and batch process are 85.8% and 65% respectively. They concluded that *Pinus roxburghii* bark can be used as a cost-effective adsorbent for removal and recovery of chromium from wastewater. Nouri Sepehr et al. (2005) studied the chromium bioremoval from tannery industries effluent by *Aspergillus oryzae*. Venkateswarlu et al. (2007) studied the removal of chromium from an aqueous solution using *Azadirachta indica* (neem) leaf powder as an adsorbent. Deng et al. (2009) studied the biosorption of Cr(VI) from aqueous solutions by non-living green algae *Cladophora albida*. They found that the abundant and economic biomass *Cladophora albida* could be used for the removal of Cr(VI) from wastewater by the reduction of toxic Cr(III). Rajor & Kunal (2013) studied the absorption of chromium and nickel from aqueous solution by bacteria isolated from

electroplating unit effluent. They concluded that the bioaccumulation is efficient and cost-effective eco-friendly process and the isolated bacterial strains, which can tolerate high concentration of heavy metals, can be used for metal recovery process. Samson et al. (2016) studied the removal of hexavalent chromium from aqueous solutions by adsorption on modified groundnut hull. They found that the uptake of hexavalent chromium, being among the major pollutants from our industries, by modified and unmodified groundnut hull can be made. Krishna & Ravindhranath (2012) studied the removal of chromium(VI) from polluted waters using powders of leaves or their ashes of some herbal plants. They made an attempt to explore the surface sorption abilities of powders of leaves and their ashes of some herbal plants. Soundari et al. (2018) studied the removal of chromium from industrial waste water by adsorption using coconut shell and palm shell. They concluded that activated charcoal powder can be used to remove chromium(Cr) from tannery effluent. Dessalew (2017) studied the removal of chromium from industrial wastewater by adsorption using coffee husk. They stated that heavy metals are discharged from different industries into freshwaters and easily absorbed by fish and other aquatic organisms. Small concentrations can be toxic because heavy metals undergo bioconcentration. Chromium is an essential element that is required in small amounts for carbohydrate metabolism but becomes toxic at higher concentrations. Bahadur & Mishra (2014) studied adsorptive removal of Cr(VI) from aqueous solution by sugarcane biomass. They investigated the influence of pH, initial concentration of metal ion and contact time on maximum adsorption capacity of Cr(VI). In the present work, a study of the efficiency of removal of chromium using *Terminalia chebula* has been made.

MATERIALS AND METHODS

Terminalia chebula fruit was taken and washed with distilled water. Then the fruit was exposed to sunlight until it was completely dried. After that *Terminalia chebula* was made into small pieces and with the help of grinder those pieces were made into fine powder. A stock solution was prepared by dissolving 0.283 g of potassium dichromate in one litre of distilled water so that in 1mL, 100 µg of chromium is present. Then the working solution of different concentrations was obtained from the stock solution by appropriate dilution with distilled water for the batch experiments. Ultraviolet-visible spectroscopy or ultraviolet-visible spectrophotometer (UV-Vis or UV/Vis) refers to absorption spectroscopy or reflectance spectroscopy in part of the ultraviolet and the full, adjacent visible spectral regions. This means that it uses light in the visible and adjacent ranges. The absorption or reflectance in the visible range directly affects the perceived color of the chemicals involved. Hence, UV-Vis spectrophotometer was used to determine chromium. Batch experiments were conducted using diluted aqueous solutions of chromium with an adsorbent dosage ranging from 0.1 g to 0.4 g.

RESULTS

In the first batch experiment, different amounts of *Terminalia chebula* powder (adsorbent) were added to the chromium solution of different concentrations to find the effect of *Terminalia chebula* on % chromium removal. The results obtained are presented in Table 1 and Fig. 1. In the second batch experiment, different amounts of *Terminalia chebula* (adsorbent) powder was added to the same concentration chromium solution to estimate the most effective dosage of the adsorbent. The results obtained are presented in Table 2 and Fig. 2. In the third batch experiment, chromium solutions of different concentrations were used for the same amount of *Terminalia chebula* powder (0.1 g) to find out the effect of initial chromium concentration on percentage removal. The results obtained are presented in Table 3 and Fig. 3. In the fourth batch experiment, chromium solutions of different concentrations were used to find out the effect of adsorbent dosage on chromium removal. The results obtained are presented in Table 4 and Fig. 4.

Table 1: Results of first batch experiment

S. No.	Amount of *Terminalia chebula* powder	Initial chromium concentration (µg/L)	Final chromium concentration (µg/L)	% chromium removed
1.	0.1 g	13 µg/L	11.0 µg/L	15.38
2.	0.2 g	26 µg/L	11.5 µg/L	55.76
3.	0.3 g	39 µg/L	12.5 µg/L	67.90
4.	0.4 g	52 µg/L	12.0 µg/L	76.92

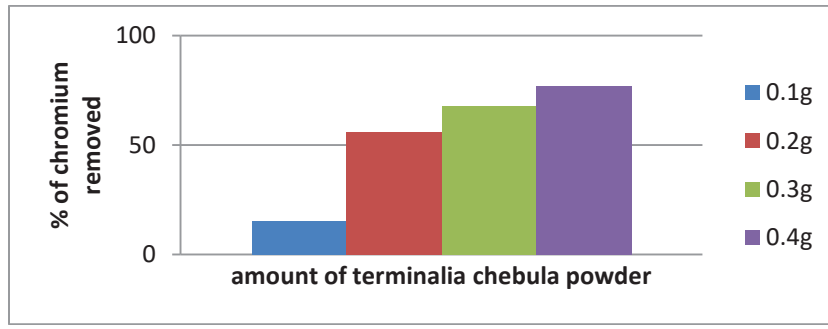

Fig. 1: Results of the first batch experiment.

Table 2: Results of the second batch experiment.

S. No.	Amount of *Terminalia chebula* powder (g)	Initial chromium concentration (µg/L)	Final chromium concentration (µg/L)	% of chromium removed
1.	0.1 g	30 µg/L	15 µg/L	50.00
2.	0.2 g	30 µg/L	11 µg/L	63.34
3.	0.3 g	30 µg/L	11 µg/L	63.34
4.	0.4 g	30 µg/L	10 µg/L	66.67

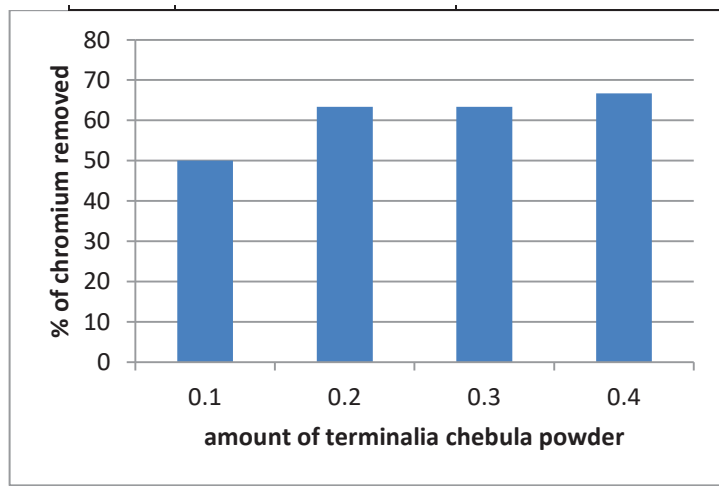

Fig. 2: Results of the second batch experiment.

Table 3: Results of the third batch experiment.

S. No.	Amount of *Terminalia chebula* powder (g)	Initial chromium concentration (µg/L)	Final chromium concentration (µg/L)	% of chromium removed
1	0.1	4	3.5	12.5
2	0.1	6	3	50
3	0.1	8	2	75.00
4	0.1	12	2.6	78

Table Cont....

S. No.	Amount of *Terminalia chebula* powder (g)	Initial chromium concentration (µg/L)	Final chromium concentration (µg/L)	% of chromium removed
5	0.1	14	3	78.57
6	0.1	16	3.34	79.125
7	0.1	18	3.03	83.12
8	0.1	22	3.64	83.43
9	0.1	24	3.04	87.33
10	0.1	28	3.02	89.21
11	0.1	32	3.36	89.5
12	0.1	34	3.5	89.7
13	0.1	36	3.001	91.66
14	0.1	38	2.74	92.78
15	0.1	42	3.08	92.85
16	0.1	44	2.81	93.62
17	0.1	46	2.89	93.7
18	0.1	48	3	93.95
19	0.1	52	3	94.23
20	0.1	56	2.8	95
21	0.1	64	2.5	96.09
22	0.1	68	2.2	96.76
23	0.1	72	2.2	96.95
24	0.1	76	2	97.36
25	0.1	84	2	97.6
26	0.1	88	1.84	97.98
27	0.1	92	1.56	98.3
28	0.1	96	1.34	98.6

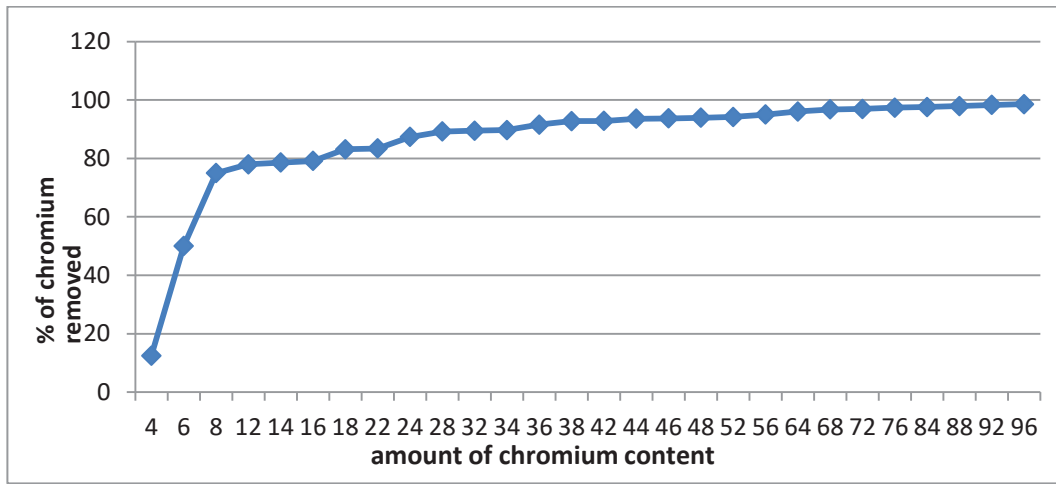

Fig. 3: Results of the third batch experiment.

Table 4: Results of the fourth batch experiment.

S. No.	Amount of *Terminalia chebula* powder (g)	Initial chromium concentration (µg/L)	Final chromium concentration (µg/L)	% chromium removed
1	0.3	8	5.5	31.25
2	0.3	12	7	41.67
3	0.3	14	8.07	42.29
4	0.3	16	8	50
5	0.3	18	8	55.56
6	0.3	22	7	68.19
7	0.3	24	7.5	68.75
8	0.3	26	7.5	71.15
9	0.3	28	6	78.57
10	0.3	32	6.75	78.9
11	0.3	34	6.97	79.5
12	0.3	36	7	80.56
13	0.3	38	7.2	81.05
14	0.3	42	7.16	82.95
15	0.3	44	7	84.09
16	0.3	46	7	84.78

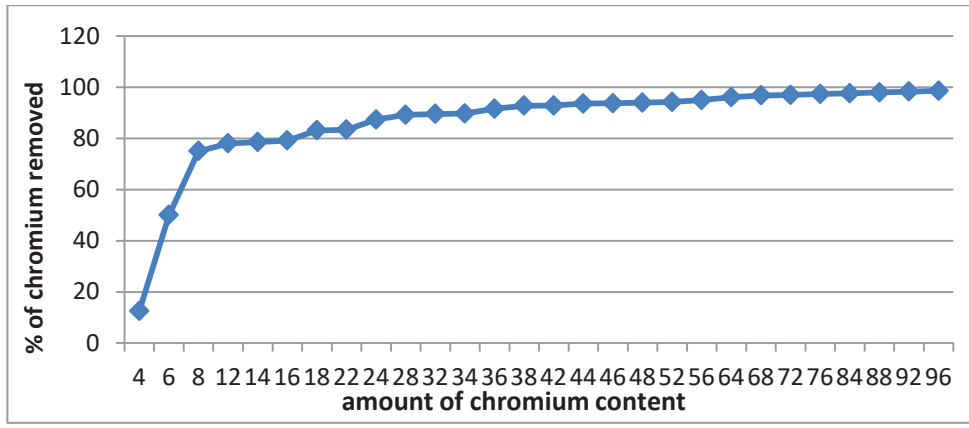

Fig. 4: Results of the fourth batch experiment.

DISCUSSION

In the first batch experiment, different amounts of *Terminalia chebula* powder were added to the chromium solution of different concentrations at the suitable dosages of the adsorbent for chromium removal from aqueous solution. It was observed that the percentage chromium removal is increased as the amount of chromium content and adsorbent dosage increase, which is evident from Fig. 1. In the second batch experiment, different amounts of *Terminalia chebula* powder were added to the same concentration chromium solution to estimate the most effective dosage of the adsorbent for chromium removal from aqueous solution. It is observed that % chromium removal is increased as the adsorbent dosage increases and effective dosage of adsorbent is 0.2 g, which is evident from Fig. 2. To find out the effect of initial chromium concentrations on percentage removal, chromium solution of different concentrations was used in the third batch experiment. It was observed that as the initial concentration is increased, the percentage of chromium removal is also increased, which is evident from

Fig. 3. To find out the effect of adsorbent dosage on percentage removal, two different dosages (0.1 g and 0.3 g) were used in the third and fourth batch experiments. It was observed that the percentage of chromium removal is increased if the adsorbent dosage is increased. But percentage removal is depended on initial concentration also.

CONCLUSIONS

Based on the results of batch experiments, following conclusions can be made.

- The percentage of chromium removal depends upon several parameters including adsorbent dosage and initial concentration of pollutant in the process of adsorption.
- Use of *Terminalia chebula* powder can be recommended as an adsorbent for safe removal of toxic pollutants like chromium. The unused *Terminalia chebula* powder in the drinking water is not harmful to public health as it is a good food supplement/medicinal plant material.
- Most of the municipalities are not able to completely purify the raw water (for drinking water) due to lack of sufficient funds. They usually follow only conventional treatment methods like sedimentation, filtration and chlorination which cannot remove most of the problematic pollutants including chromium compounds, which may be present in raw water. Lower income households can use the *Terminalia chebula* powder easily and economically for complete purification as they are not able to afford commercially available branded domestic water purifiers.

REFERENCES

Ahmad, R., Rao, R.A.K. and Masood, M.M. 2005. Removal and recovery of Cr(VI) from synthetic and industrial wastewater using bark of *Pinus roxburghii* as an adsorbent. Water Quality Research Journal, 40(4): 462-468.

Bahadur, K.D. and Mishra, P. 2014. Adsorptive removal of Cr(VI) from aqueous solution by sugarcane biomass. Research Journal of Chemical Sciences, 4(5): 32-40.

Deng, L., Zhang, Y., Qin, J., Wang, X. and Zhu, X. 2009. Biosorption of Cr(VI) from aqueous solutions by nonliving green algae *Cladophora albida*. Minerals Engineering, 22(4): 372-377.

Dessalew, Berihun 2017. Removal of chromium from industrial wastewater by adsorption using coffee husk. Journal of Material Sciences & Engineering. 119(14): 827-830.

Farai, Mutongo, Olga, Kuipa and Pardon, K. Kuipa 2014. Removal of Cr (VI) from aqueous solutions using powder of potato peelings as a low cost sorbent. Hindawi Publishing Corporation, Vol. 2014, Article ID 973153.

Krishna, V. V. and Ravindhranath, K. 2012. Removal of chromium(VI) from polluted waters using powders of leaves or their ashes of some herbal plants. Journal of Experimental Sciences, 3(4): 01-09.

Nouri Sepehr, M., Nasseri, S., Mazaheri Assadi, M. and Yaghmaian, K. 2005. Chromium bio removal from tannery industries effluent by *Aspergillus oryzae*. Iran. J. Environ. Health. Sci. Eng., 2(4): 273-279.

Rajor, A. and Kunal 2013. Absorption of chromium and nickel from aqueous solution by bacteria isolated from electroplating unit effluent. IJEP, 33(3): 213-221.

Samson, O.O. and Tella, A.C. 2016. The Removal of hexavalent chromium from aqueous solutions by adsorption on modified groundnut hull. Beni-suef University Journal of Basic and Applied Sciences, 5: 377-388.

Soundari, L., Agilan, A. and Rajarajan, K. 2018. Removal of chromium from industrial waste water by adsorption using coconut shell and palm shell. International Journal of Pure and Applied Mathematics. 119(14): 827-830.

Venkateswarlu, P., Ratnam, M.V., Rao, D.S. and Rao, M.V. 2007. Removal of chromium from an aqueous solution using Azadirachta indica (neem) leaf powder as an adsorbent. International Journal of Physical Sciences, 2(8): 188-195.

Nature Environment and Pollution Technology
An International Quarterly Scientific Journal

p-ISSN: 0972-6268
e-ISSN: 2395-3454

Vol. 18 | No. 4 | pp. 1305-1311 | 2019

Original Research Paper | Open Access

Enzymatic Analysis and Effect of Vermicompost Production from Banana Leaves Waste Using Epigeic Earthworm *Eudrillus euginea*

Jannathul Firdous*, V. Bharathi†, S. Durga Devi** and J. Jayachitra*****

*Cluster for Integrative Physiology and Molecular Medicine (CIPMM), Faculty of Medicine, Royal College of Medicine Perak, Universiti Kuala Lumpur, Jalan Greentown, 30450 Ipoh, Perak, Malaysia

**Department of Biochemistry, Shrimati Indira Gandhi College, Tiruchirappalli, India

***Post Graduate Research Department of Biochemistry, Rabiammal Ahamed Maideen College for Women, Tiruvarur, India

†Corresponding author: Bharathi V.

Nat. Env. & Poll. Tech.
Website: www.neptjournal.com

Received: 01-04-2019
Accepted: 02-07-2019

Key Words:
Organic waste
Banana leaves
Eudrillus euginea
Vermicompost
Enzymatic analysis

ABSTRACT

Recycling of organic waste with enormous nutrients gives soil fertility when added to the soil and reduce the usage of chemical fertilizers. Vermicomposting process of recycling the bio-organic waste by earthworms contains efficient nutrients with low levels of toxic contents. In the present study, banana leaves waste was mixed with cow dung in different ratios. The earthworm *Eudrillus euginea* was later added to the compost. Total organic matter (TOM), total organic carbon (TOC), pH, EC, total alkalinity and phosphorus were analysed and compared for different ratios of vermicompost at different day intervals. Microorganisms present in vermicompost were isolated and analysed for their enzymatic activities. Compost maturity was also observed by FTIR application. Results showed that the vermicompost quality was improved with positive catalase and protease enzymatic activity. FTIR analysis showed the proper maturation of vermicompost with reduced complex structures such as aromatic compounds, polysaccharides and polypeptides. It was concluded that composting of organic wastes by vermicomposting promote humification, increased microbial activity and enzyme production, which in turn increase the aggregate stability of soil particles resulting in better aeration with pollution-free technique.

INTRODUCTION

Organic wastes such as agricultural waste and household waste are useful raw materials when recycled. Even though these wastes are disposed off by landfill or incineration, the waste cannot be stabilized and could be pathogenic (Hill et al. 2013). When disposing of the waste through landfill, there may be a chance of landfill leachate often containing toxic compounds that can leach into groundwater contaminating drinking water. Incineration if done in an improper way can create air pollution and also produces a small amount of ash that should be again landfilled. Vermicomposting is the best-known process for biological stabilization of organic wastes (Domínguez et al. 2010). Vermicomposting gives a product without any waste, which in turn increase the yield of produce.

Vermicomposting is the simple biotechnological process that utilizes earthworms to give a finely divided, peat-like material with high porosity. It also has excellent structure and good moisture-holding capacity (Singh et al. 2010). Due to its numerous biological properties, vermicomposting is used to promote sustainable agriculture by enhancing the growth of plant growth promoting bacteria in the soil and controls the plant pathogen (Chauhan & Singh 2015). Vermicompost, therefore, can be effectively used as a carrier medium for *Azospirillum, Rhizobium* and phosphate solubilisers. Traditionally vermicompost is prepared with animal manure as the main substrate and when applied to the soil acts as a good soil conditioner and fertilizer. In recent years organic waste like banana leaves is found to be the good manure vermicompost (Raj et al. 2017). This highly nutritious and easily digestible fruit contains high levels of potassium and calcium content. Banana leaves were used as a primary writing surface in southeast Asia during ancient days. In countries like Malaysia, India and Vietnam, banana leaves are used to wrap food to seal its freshness. In terms of medicinal value, banana leaves contain polyphenols and polyphenol oxidase, an enzyme that produces L-DOPA, used in the treatment for Parkinson's disease (Ethiraj et al. 2018).

Earthworms processing the compost are naturally terrestrial soft bodied animals with uniform ring-like structures. During dry weather, earthworms aerate the soil and help in maintaining the moisture through supply of organic

matter. Epigeics earthworm species are phytophagous that live above the mineral soil surface. They have greater potential in decaying the organic waste (Singh et al. 2010). During vermicompost production, studying the enzymatic activities are most important to check the soil fertility and ecosystem status. They are also used to describe the fast driven process of vermicomposting. Moreover, microbes are the primary decomposers in composting. Microbial enzymes play an important role in making the compost more effective (Lakshmanan & Muthunarayanan 2016). In considering all the factors, the present study was done to check the possibility of converting natural Banana leaves wastes *(Musa paradisiaca)* into value-added vermicompost using epigeic earthworm *Eudrillus euginea,* to check the nutrient value of the vermicompost in terms of total organic matter (TOM), total organic carbon (TOC), pH, EC, total alkalinity and phosphorus, to isolate and identify the bacteria present in the vermicompost, to qualitatively check the enzyme (protease and catalase) activity of the isolated bacterial strains and to detect the structural changes of the vermicompost produced from banana leaves using FTIR.

MATERIALS AND METHODS

Collection of organic wastes and earthworm: Cow dung was collected from a dairy yard at an Agricultural field near Sooriyur, Trichy. Banana (*Musa paradisiaca*) leaves waste was collected from Trichy district near Woraiyur. The epigeic earthworms *Eudrillus euginea* were obtained from Periyar Maniyamai University, Tanjore.

Experimental set-up: Plastic tub containers suitable for aeration were taken. Banana leaves were chopped into small pieces and cow dung was then mixed with banana leaves in three different ratios (500g:500g), (400g:600g) and (600g:400g) respectively. Soil with banana leaves was taken as a control in the ratio of 500g:500g. After 15 days of decomposition, 50 non-ciliated earthworms were introduced into vermicompost plastic containers. The moisture content was maintained at 60-80% throughout the study period by periodic sprinkling of adequate quantities of water. The containers were kept in the dark under identical ambient conditions (room temperature 25 ± 3°C). The present study followed the method described by Gopal et al. (2009) with few modifications.

Physico-chemical analysis: The physico-chemical parameters such as pH, electrical conductivity (EC), total organic carbon (TOC), total organic matter (TOM) and phosphorous were analysed as per Boran et al. (2017).

Isolation of microorganisms from vermicompost samples: The isolation and identification of microorganisms from the manure sample was done by the spread plate technique. To 99mL of the sterile distilled water, 5g of the manure sample was added. From this, 1mL was transferred aseptically to 9mL of sterile distilled water to obtain 10^1-10^6 dilutions and 1mL from each dilution was transferred aseptically into sterile Petri plates. Nutrient agar medium was used to estimate the total heterotrophic bacteria. The plates were further subjected to incubation at 30°C ± 2°C for 24hrs for the isolation of bacterial colonies. After confirming the organism by the zone formation by qualitative analysis, the isolated colonies were subjected for catalase and protease enzymatic activity as it was mainly involved in the degradation of biological wastes. Proteolytic activity was identified by a clear zone around the cells as reported by Naik et al. (2008). To determine the catalase activity, the sample was inoculated with simple streaked and the plates incubated at 37ºC for 24hrs. Then hydrogen peroxide was added to each plate, which suddenly gets fumes in the plates (Iwase et al. 2013).

FTIR: The FTIR spectroscopy provides information about the chemical structure of the material analysis of the composting process. It is a reliable technique for compost maturity determination. Several indicator bands in the spectra such as functional groups represent the components or metabolic products present which indicate the degradation or stabilization process. The FTIR spectra of vermicompost obtained from banana leaves waste was compared for initial and final stage as described by (Bhat et al. 2017).

RESULTS AND DISCUSSION

The vermicompost has been prepared with cow dung and different quantities of banana leaves waste, along with the earthworm population. The compost was analysed for the parameters such as pH, EC, TOC, TOM and phosphorus.

Variation in pH: The pH is one of the most frequent parameters used to characterize the vermicompost quality. The pH range of 6.0-8.5 is found to be suitable for the soil in order to ensure compatibility with most plants (Cerozi & Fitzsimmons 2016). Slight changes in pH were noted in three different ratios with control as shown in Fig. 1. The pH shift was due to mineralization of nitrogen and phosphorus into nitrates and orthophosphate (Jalali et al. 2014).

Variation in EC: The EC values were increased significantly in final vermicompost as shown in Fig. 2. Initial decline was due to loss of organic matter and release of different mineral salts in available forms such as phosphate, ammonium, potassium, etc. (Mahaly et al. 2018).

Variation in phosphorus: Total phosphorus was greater in 60 days vermicompost than in the initial (20 days) as shown

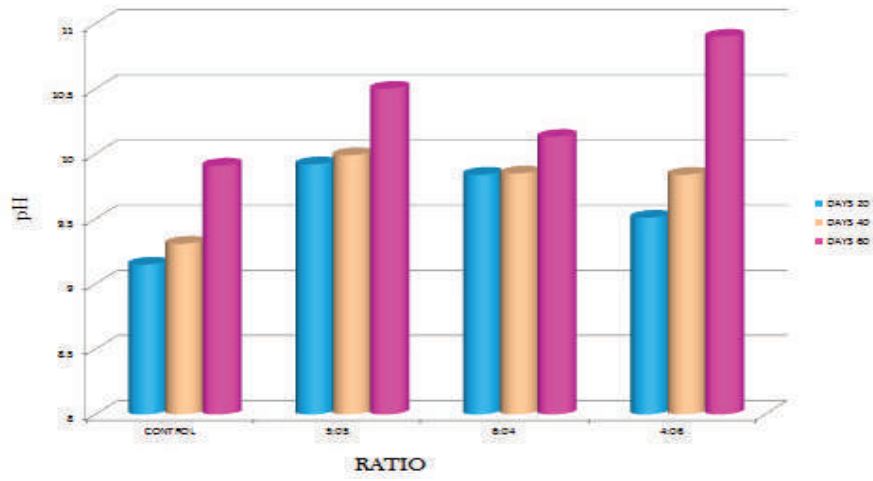

Fig. 1: Comparison of pH during different stages of vermicomposting.

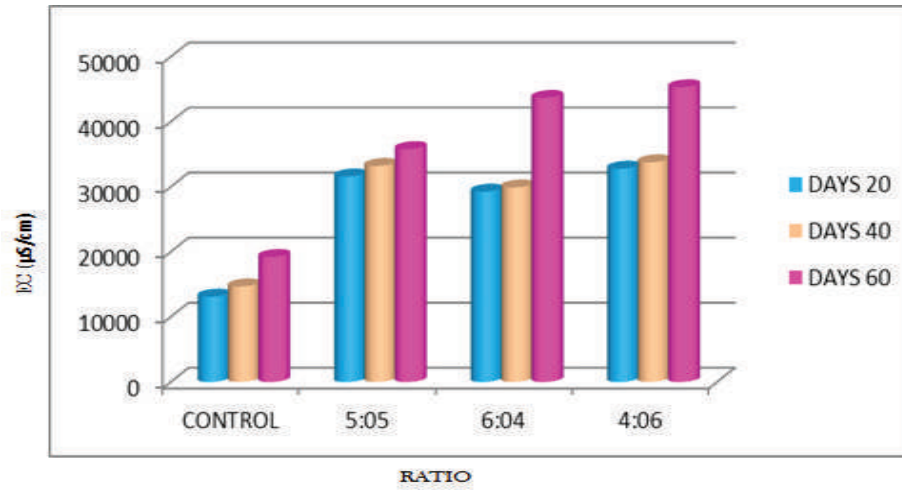

Fig. 2: Comparison of electrical conductivity during different stages of vermicomposting.

in Fig. 3. Total phosphorus content of banana leaf waste after earthworm activity was performed partly by earthworm gut phosphates and further release was attributed by the phosphate solubilizing microorganisms present in worm casts (Ramnarain et al. 2019).

Variation in TOC: The total organic carbon (TOC) in banana leaves waste reduced when compared to their initial levels as shown in Fig. 4. Loss of TOC was due to its removal in the form of CO_2 during vermicomposting. The earthworms are responsible for such modification to promote the carbon losses from the substrate through microbial respiration in the form of CO_2 (Aira et al. 2007).

Variation in TOM: The decomposition of organic matter reduces the amount of TOM as shown in Fig. 5 but leaves the compost enriched with nitrogen at 60th day where cow dung was mixed in high ratio with banana leaves waste. Many such wastes were readily decomposed by soil microbes with release of end products such as carbon dioxide and water. The results are in accordance with the study done by Kaushik & Garg et al. (2004) with the solid textile mill sludge that acts as an excellent substrate when mixed with cow dung.

Enzyme activity: The isolated microorganisms were analysed for their enzyme activity. The organisms showed pro-

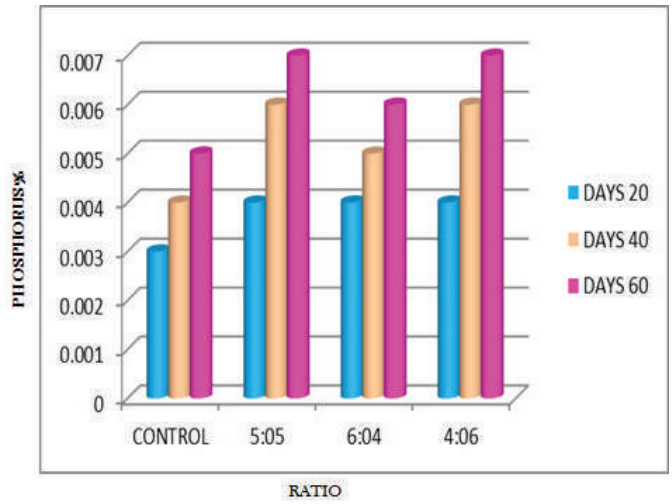

Fig. 3: Comparison of phosphorus during different stages of vermicomposting.

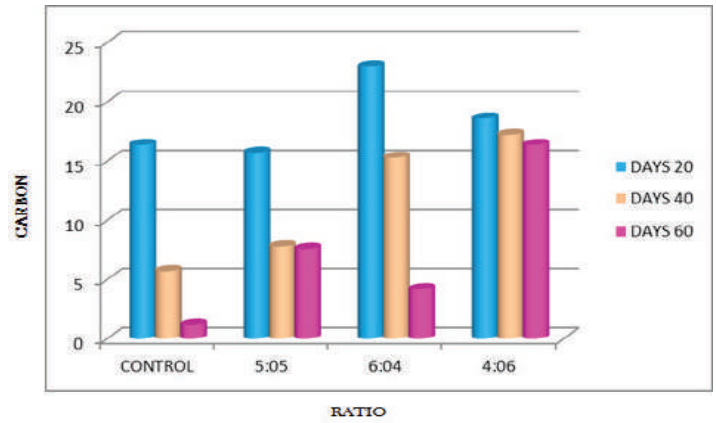

Fig. 4: Comparison of total organic carbon during different stages of vermicomposting.

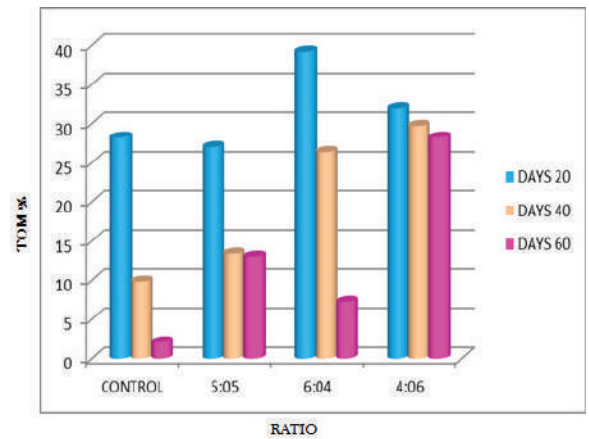

Fig. 5: Comparison of total organic matter during different stages of vermicomposting.

Fig. 6: Isolation of catalase producing bacteria from Vermicompost.

Fig. 7: Isolation of protease producing bacteria from vermicompost.

tease and catalase activity as shown in Figs. 6 and 7. Microorganisms are the primary decomposers to favouring the composting, which has increased enzymatic activity and results in the digestion of soil organic matter. Humic like substances present in the vermicompost are usually rich in microbes with high enzymatic activity (Arslan Topal et al. 2008).

FTIR: FTIR spectra for initial and final stages of banana leaves waste vermicompost samples is shown in Fig. 8. By comparing the initial and final stage there was a strong hydrogen bond due to -OH stretch was observed at 3423.70 cm^{-1} and 3417.90 cm^{-1}. There was the partial mineralization of cellulose material. The phenolic compounds were observed at 1091.90 cm^{-1} and 1093.22 cm^{-1} respectively. Several other bonds at peak range of 790.08 cm^{-1}, 791.46 cm^{-1}, 691.72 cm^{-1}, 693.02 cm^{-1}, 538.44 cm^{-1}, 539.96 cm^{-1}, 466.12 cm^{-1} and 466.26 cm^{-1} were observed. While comparing the initial and final vermicompost produced by *Eudrillus euginea,* slight increase in bands were observed when initial vermicompost was subjected to FTIR. Hence, the result

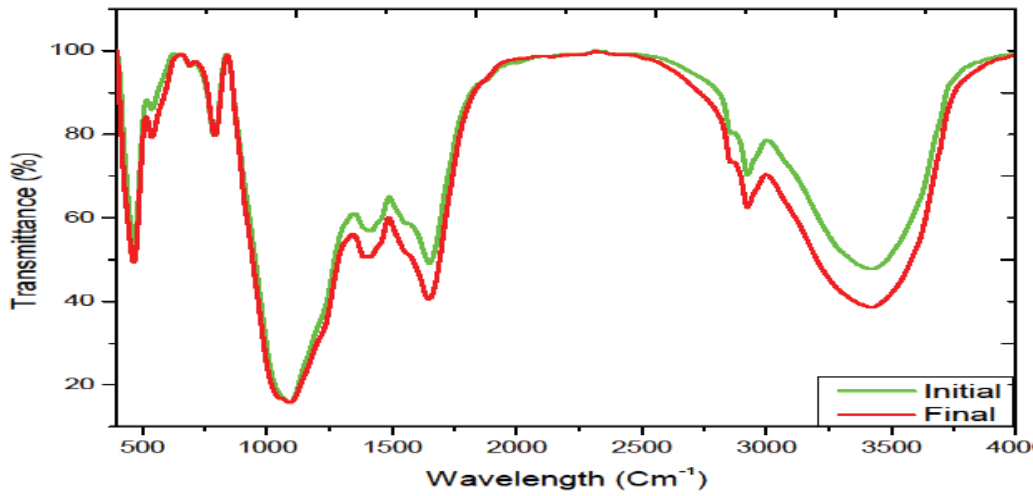

Fig. 8: FTIR Spectrum for initial and final stage of banana leaves waste vermicompost.

confirms the reduction of aromatic structure, polypeptides and polysaccharides in the vermicompost prepared from banana (*M. paradisiaca*) leaf waste and proves the maturity of compost. Results are aligning with study report by Sentil Kumar et al. (2013), where the vermicompost showed maturity with increased nitrogen and reduced mineral activities. They studied the vermicompost produced from flower waste inoculated with biofertilizers.

CONCLUSION

The present study demonstrates the role of earthworms and microorganisms during the degradation of banana leaves waste. The role of bacterial species in terms of their enzyme activity was highlighted. Cow dung mix with banana leaves waste in ratio of 6:5 yields good results when compared to control and other samples. FTIR results show the reduction of both aliphatic and aromatic structures in the vermicompost which is associated with extensive organic matter mineralization. Genomic DNA isolation for identification of bacterial species that possess enzymatic activity has to be done for future research. Hence, the present study concludes that the banana leaves waste generated could be managed by converting the waste into a good quality manure using earthworms by the process of vermicomposting.

REFERENCES

Aira, M., Monroy, F. and Domínguez, J. 2007. *Eisenia fetida* (Oligochaeta: Lumbricidae) modifies the structure and physiological capabilities of microbial communities improving carbon mineralization during vermicomposting of pig manure. Microbial Ecology, 54: 662-671.

Arslan Topal, E. I., Öbek, E., Kirbag, S., İPek, U. and Topal, M. 2008. Determination of the effect of compost on soil microorganisms. International Journal of Science and Technology, 3: 151-159.

Bhat, S. A., Singh, J. and Vig, A. P. 2017. Instrumental characterization of organic wastes for evaluation of vermicompost maturity. Journal of Analytical Science and Technology, 8: 2.

Boran, D., Namlı, A. and Akça, M. 2017. Determination of quality parameters of vermicompost under different thermal techniques. Fresenius Environmental Bulletin, 26: 5205-5212.

Cerozi, B. and Fitzsimmons, K. 2016. The effect of pH on phosphorus availability and speciation in an aquaponics nutrient solution. Bioresource Technology, 219: 778-781.

Chauhan, H. and Singh, K. 2015. Potancy of vermiwash with neem plant parts on the infestation of *Earias vittella* (Fabricius) and productivity of okra (*Abelmoschus esculentus*) (L.) Moench. Asian Journal of Research in Pharmaceutical Sciences, 5: 36-40.

Domínguez, J., Aira, M. and Gómez-Brandón, M. 2010. Vermicomposting: Earthworms enhance the work of microbes. In: Insam, H., Franke-Whittle, I. and Goberna, M. (eds.) Microbes at Work: From Wastes to Resources. Berlin, Heidelberg: Springer Berlin Heidelberg, pp. 93-114.

Ethiraj, S., R, V. and Kumar, M. 2018. Polyphenol oxidase beyond enzyme browning, a review. Microbial Bioprospecting for Sustainable Development. Joginder Singh. (eds.), Springer Nature, pp. 203-222.

Gopal, M., Gupta, A., Sunil, E. and Thomas, G. 2009. Amplification of plant beneficial microbial communities during conversion of coconut leaf substrate to vermicompost by *Eudrilus* sp. Current Microbiology, 59: 15-20.

Hill, G., Baldwin, S. and Lalander, C. 2013. The effectiveness and safety of vermi-versus conventional composting of human feces with Ascaris Suum Ova as model Helminthic Parasites. Journal of Sustainable Development. 6: 1-10.

Iwase, T., Tajima, A., Sugimoto, S., Okuda, K.I., Hironaka, I., Kamata, Y., Takada, K. and Mizunoe, Y. 2013. A simple assay for measuring catalase activity: A visual approach. Scientific Reports, 3: 3081.

Jalali, M., Mahdavi, S. and Ranjbar, F. 2014. Nitrogen, phosphorus and sulfur mineralization as affected by soil depth in rangeland ecosystems. Environmental Earth Sciences, 72: 1775-1788.

Kaushik, P. and Garg, V. K. 2004. Vermicomposting of mixed solid textile mill sludge and cow dung with the epigeic earthworm *Eisenia foetida*.

Bioresource Technology, 90: 311-316.

Kumar, D.S., Kumar, P.S., Rajendran, N.M. and Anbuganapathi, G. 2013. Compost maturity assessment using physicochemical, solid-state spectroscopy, and plant bioassay analysis. Journal of Agricultural and Food Chemistry, 61(47): 11326-11331.

Lakshmanan, R. and Muthunarayanan, V. 2016. Enzymatic analysis of natural and artificial banana leaf waste in vermicomposting and composting technique. Journal of Advanced Applied Scientific Research, 6: 2454-3225.

Mahaly, M., Senthilkumar, A. K., Arumugam, S., Kaliyaperumal, C. and Karupannan, N. 2018. Vermicomposting of distillery sludge waste with tea leaf residues. Sustainable Environment Research, 28: 223-227.

Naik, P. R., Raman, G., Narayanan, K. B. and Sakthivel, N. 2008. Assessment of genetic and functional diversity of phosphate solubilizing fluorescent pseudomonads isolated from rhizospheric soil. BMC Microbiol, 8: 230.

Raj, K., Nandhivarman, M., Thongni, P., Muthulingam, P. and Gopalsamy, P. 2017. Utilization of agrowastes for vermicomposting and its impact on growth and reproduction of selected earthworm species in Puducherry, India. Nature Environment and Pollution Technology, 16: 1125-1133.

Ramnarain, Y. I., Ansari, A. A. and Ori, L. 2019. Vermicomposting of different organic materials using the epigeic earthworm *Eisenia fetida*. International Journal of Recycling of Organic Waste in Agriculture, 8: 23-36.

Singh, J., Kaur, A., Vig, A. P. and Rup, P. J. 2010. Role of *Eisenia fetida* in rapid recycling of nutrients from bio sludge of beverage industry. Ecotoxicology and Environmental Safety, 73: 430-435.

Nature Environment and Pollution Technology
An International Quarterly Scientific Journal

p-ISSN: 0972-6268
e-ISSN: 2395-3454

Vol. 18 | No. 4 | pp. 1313-1318 | 2019

Original Research Paper | Open Access

Soil Organic Carbon and Silt-Clay Relationships in the Soil Orders of Northern Agriculture Region (NAR), Western Australia

Ahmed Hasson*, Abdulhussien Alaskary and Muhsin Jweeg*****
*Fusion Ltd., Birmingham, UK
**University of Baghdad, Baghdad, Iraq
***College of Technical Engineering, Al-Farahidi University, Baghdad, Iraq

Nat. Env. & Poll. Tech.
Website: www.neptjournal.com
Received: 15-02-2019
Accepted: 30-04-2019

Key Words:
Soil texture
Soil organic carbon
Silt-clay relationship
Soil orders

ABSTRACT

There are no recognized data about the relationships between soil organic carbon and soil texture in Northern Agriculture Region (NAR), Western Australia (WA). Such information is central in understanding the impact of silt and clay content of soil profile soil organic carbon. In order to describe mathematically this relation, twenty-one soil orders highly weathered soils (mostly sandy soils) in Northern Agricultural Region, Western Australia under similar climate, vegetation and topography were sampled at 120 cm depth and analyzed for texture and total SOC concentration. The SOC concentration was directly and linearly correlated with the combined clay + silt (but not to clay alone) content for all depths. The intercept and slope of these linear relations decreased with depth following exponential and logarithmic functions ($P < 0.001$, $R^2 = 0.81$ and 0.76, respectively). These mathematical functions permitted the adjustment of the intercept and slope parameters of a SOC = a + b (clay + silt) function for any depth in the 0-120 cm interval. This profile pedotransfer function precisely estimated SOC concentration ($P < 0.0001$, $R^2 = 0.90$) up to 120 cm of the studied soils. Using data from different soil orders, estimated vs. measured SOC relations with similarly high R^2 values were obtained, despite slopes and intercepts were different than 1 and 0. This indicates that for the NAR, WA the textural control of SOC varies predictably with depth, and the proposed model can be calibrated to estimate SOC in subsurface layers of highly weathered soils.

INTRODUCTION

The most studied abiotic factor affecting soil organic carbon (SOC) concentration is climate, more particularly temperature and precipitation (Jenny 1941, Parton et al. 1987, Burke et al. 1989 and Hasson et al. 2013). Within the same climatic zone, however, the dominant effect on SOC concentration is that of soil moisture regimes (Davidson & Lefebvre 1993) or poor drainage (Tan et al. 2004), followed by soil texture. There exists ample evidence based on local or regional data sets that point to a direct relationship of clay and SOC concentrations with similar soil moisture regimes in temperate (Kay et al. 1997, Tan et al. 2004) and tropical regions (Feller et al. 1991, Bernoux et al. 2002). However, other researchers question the validity of this relationship, because of low correlation of SOC with clay concentrations (McDaniel & Munn 1985, Lugo & Brown 1993 and Percival et al. 2000), probably due to the use of clay content as the sole measure of texture, limited textural ranges, and wide variation of environmental factors. Indeed, a proper approach to this issue must be a ceteris paribus, as used by Jenny (1941) to study how variations in a single soil-forming factor would genetically control soil properties. Likewise, Kay (1998) proposed to select soils developed from similar parent material and under similar climate, in order to better predict effects of management, drainage and topography on SOC concentration.

Pedo-transfer functions (PTFs) are mathematical functions using routinely measured soil properties as inputs to predict others not so easily determined, such as soil-moisture relations (Wösten 2002). The differential physical-chemical properties of SOC and clay and the correlation of their contents in soil allow their efficient use as parameters in PTFs to predict soil structural properties (Kay et al. 1997). However, the fundamental effect of soil depth is usually ignored in PTFs, which are mostly based on surface depths or horizons. It has been known that in many cases, but not all, SOC concentrations decrease exponentially with depth (Hasson & Jweeg 2014, Webster 1978). Bosatta & Ägren (1996) included a clay content parameter in their attempt to depth-model SOC and N concentrations, but they used a rather limited textural range data set (180-300 g clay kg^{-1}). For temperate forest soils, Arrouays & Pélissier (1994) agreed that the decrease in SOC concentration with depth is better explained by an exponential function, as also reported by Bernoux et al. (1998) for a wide textural range

of Amazonian forest soils. Nevertheless, these models approach solely the effect of soil depth on SOC concentration or stocks for individual pedons. In contrast, this work aims to describe the depth effect on the complex and poorly understood relationship between soil texture and SOC concentration. An additional and more applied goal is to create a depth-weighted or profile PTF, defined here as an equation predicting a soil property (SOC) as a function of depth, based on its relationship to other properties (texture).

To achieve this goal, samples were obtained from highly weathered, tropical soils derived from different parent material and with different textures, but developed under similar climate, vegetation, and topography (all located on interfluves with < 2% slope).

MATERIALS AND METHODS

Site Description

The study area lies within the northern wheat/sheep belt of Western Australia. The area received an average of 350-450 mm annual rainfall. Evaporation average is 2500 mm at the coast of the south to 2900 mm/annum in the north east of the study site. The total area of the study is more than 2 million ha mostly grown with crops mostly wheat, lubin and barley and pastures, annuals, perennials and tagasaste fodders with annual temperature of maximum is 30°C to minimum of 6°C. The effective rainfall to evaporation ratio of the region is P/E0.7 = 0.54

There are approximately 50 soil groups existing in western Australia, out of which 21 soil groups have been included in this study. The soil orders are defined by attributes such as texture and change in texture with depth. The common group of soils is yellow deep sand covering 30% of the survey area, followed by red-brown harden soil 13% and reed loam earth 12%. The other soil grouping individually less than 10%. The series spans eight soil orders of the Australian Soil Classification (Rogers 2002). Most common soil orders are the Tenosols (occupied 50%) followed by Kandosols 29%) and Calcarosols and Sodosols less than 1%.

Analytical Procedures

Disturbed soil samples were collected at 0-10, 10-20, 20-30, 30-40, 40-70, 70-90 and 90-120 cm depths. Using data from different soils orders, estimated vs measured SOC relations, the soil orders, texture and SOC were evaluated in air-dried samples (Bernoux 2002).

Various descriptive parameters of the soil C dynamics at the study sites were measured: litter-fall C inputs, C-CO_2 emissions from soil respiration, root C content (0-30 cm), SOC forms, and content and TN (at 0-15 and 15-30 cm).

For sampling soils, soil cores (10 cm diameter) were collected within each subplot from 0 to 15 cm and 15-30 cm depths, and mixed to create an average sample. Soil samples were sieved through a 2 mm sieve and stored at 4°C until analysis. To evaluate distinct functional pools of organic matter with different turnover times, the following fractions were analysed.

Total organic C (TOC) was determined using the Walkley and Black method (Walkley Black 1934). This method was preferred over high temperature combustion method due to the presence of significant amounts of carbonates in the soils of the sites. Saline soil samples were treated with a silver sulphate solution to eliminate interference by chlorides during the analysis (Quinn & Salomon 1964).

Humic substances C (HSC) was determined by 16 h of shaking with 0.1 M sodium pyrophosphate (Stevenson 1997) (proportion 1:100 soil:extractant), centrifugation at 15, 316 g and filtration through MN 640 d filter paper (Macherey-Nagel; Düren, Germany). HSC content was corrected by subtracting the contents of WSC and HWC from the result obtained. Total N (TN) was determined by the standard Kjeldahl method (Benton 1991).

The results obtained were expressed on the basis of the dried-weight area ($g.m^{-2}$ or $kg.m^{-2}$), computed using the values of bulk density, coarse fragments, and soil water content. Bulk density was determined by drying at 105°C and weighing the soil core samples of 250 cm^3. Coarse fragments were determined using soil wet sieving. Soil water content was analysed gravimetrically at 105°C.

RESULTS AND DISCUSSION

The twenty-one soil orders are widely common soils in Northern Agriculture Region, Western Australia. Silt content varied between 73 and 1019 g/kg in Arsinic Orthic Tenosol and Brown Sonoco respectively (Figs. 1-3). In all the soils, clay content varied between 39 and 2760 g/kg in Ferric Bleached Orthic Tenosol and Sub Red Sodosol respectively. In general, soil orders have increased in clay content with depth and significant differences ($P<0.05$) in soil organic carbon but no significant differences in silt and clay content at the soil Horizon A, 0-15 cm depth (Fig. 4).

There is no significant correlation between soil organic carbon, silt or clay but there are low to high significant correlations between soil organic carbon and both silt and clay content at all the seven depths under all soil orders of NAR, WA (Figs. 7, 8 and Table 1), this agreed with that with Lugo (1997), McDaniel & Munn (1999) and Percival et al. (1999s).

The data in Fig. 5 also show that both, the intercept and slope of the SOC vs. (clay + silt) relations, decrease with

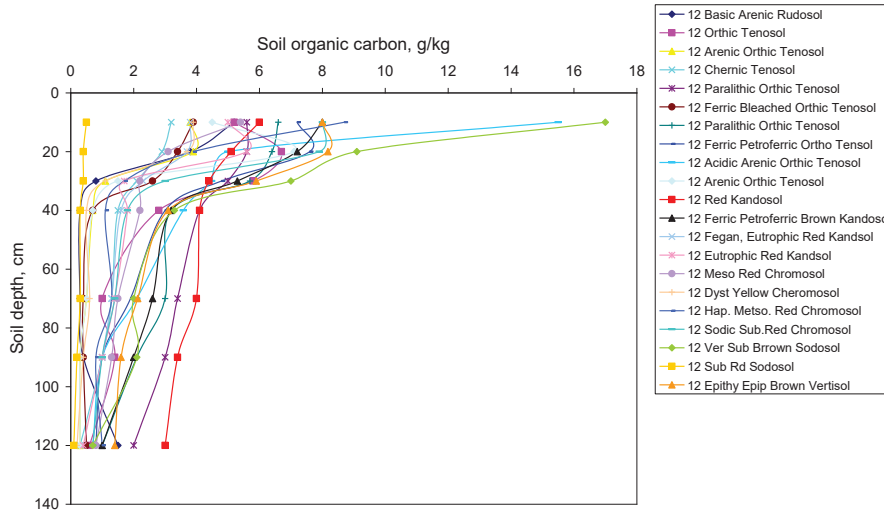

Fig. 1: Distribution of soil organic carbon with depths for the soil orders of NAR, Western Australia.

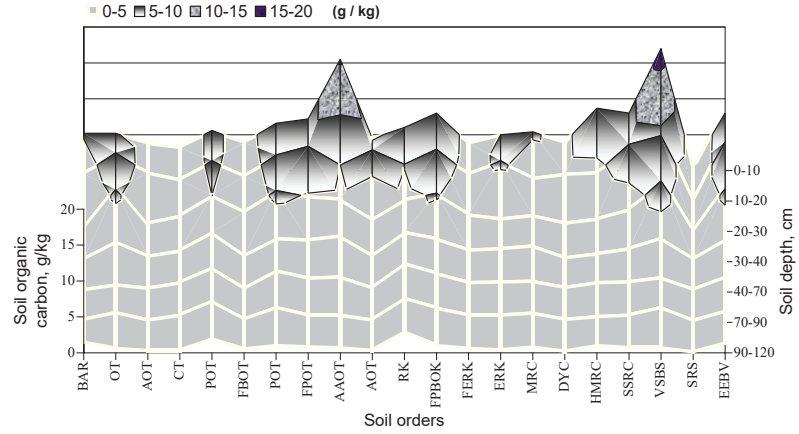

Fig. 2: The distribution of SOC with depths in soil orders.

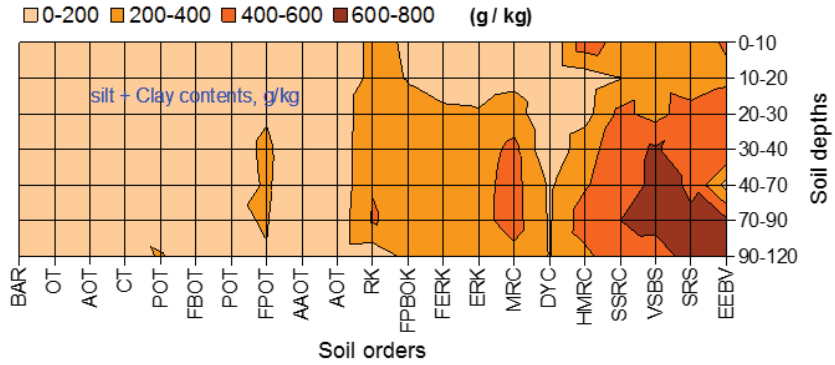

Fig. 3: The distribution of silt and clay content with depths in the soil orders.

Table 1: Relationships between SOC and clay-silt content in different soil depths.

Depth (cm)	Interception (a)	Slope (b)	R^2
0-10	0.0129	3.4541	0.8733
10-20	0.0135	2.9802	0.8009
20-30	0.0118	1.1121	0.8632
30-40	0.01	0.3391	0.7422
40-70	0.0111	0.5681	0.834
70-90	0.0076	0.3811	0.8464
90 -120	0.009	0.42640	8172

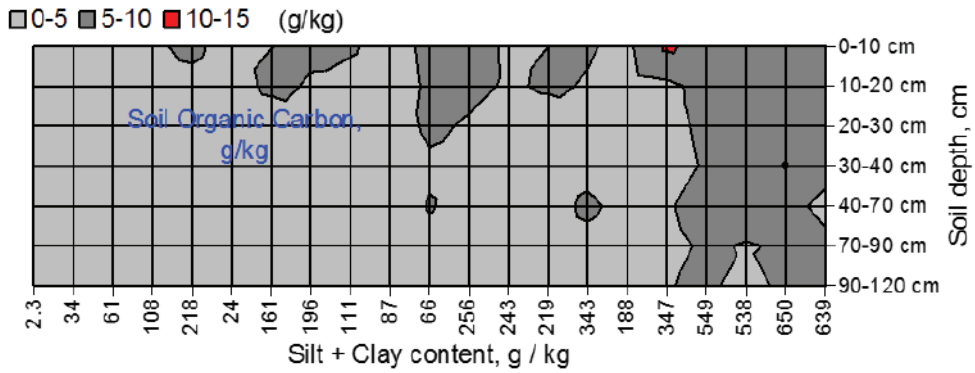

Fig. 4: The distribution of SOC with silt and clay content in depths of the soil orders.

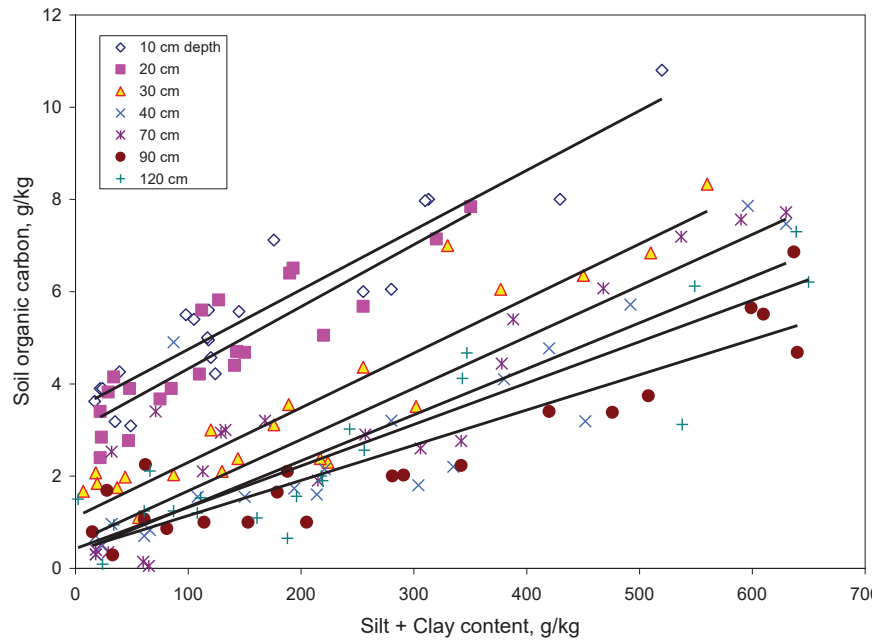

Fig. 5: The relationships between SOC and silt and clay content, g/kg of soil orders at seven depths.

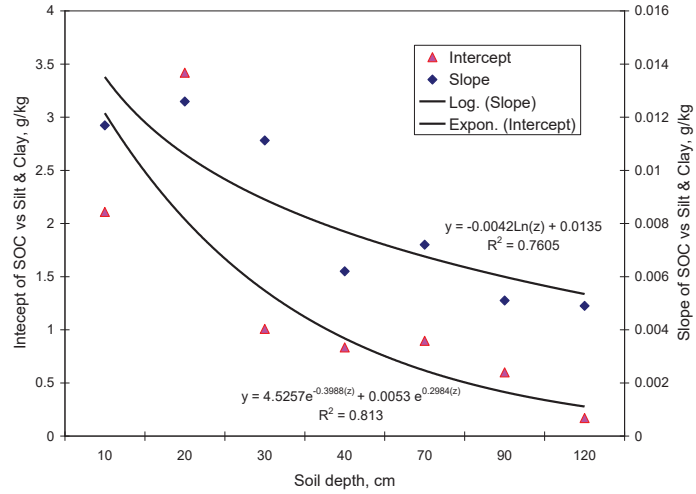

Fig. 6: The relationships between intercept A and slope b with depth z.

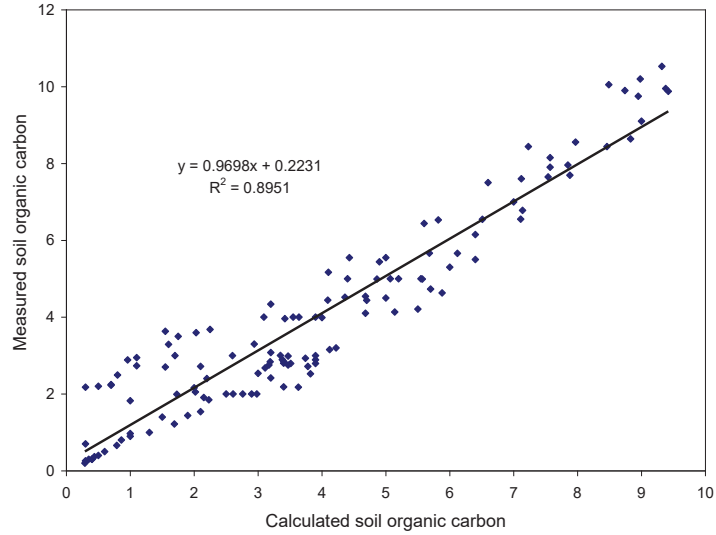

Fig. 7: The relationship between observed and calculated SOC.

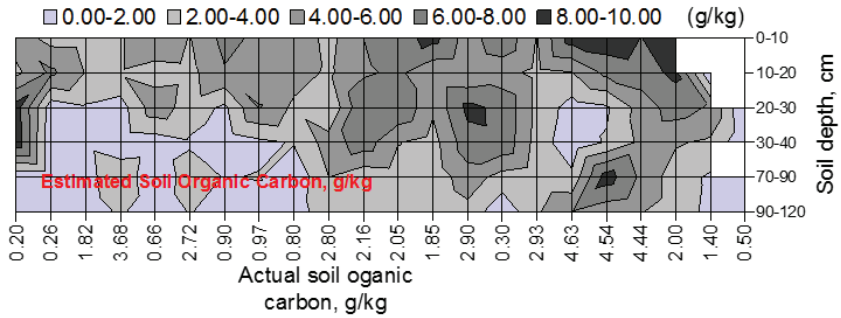

Fig. 8. The contour plots of estimated SOC at each depth of NAR. The darkest colour that show up to 8-10 g/kg and the lightest colour show up to 0-2 g/kg of SOC.

increasing soil depth, following respectively sum of exponentials and logarithmic functions (Figs. 6-7). Therefore, the intercept and slope parameters of the depth-specific relation SOC (g kg^{-1}) = a + b*(clay + silt, g kg^{-1}) can be estimated for use in a profile PTF for the 0-120 cm depth as follows:

$$SOC\ (z) = (4.5257e^{-0.3988(z)} + 0.0053e^{-0.2984(z)}) + [(-0.0042 * Ln\ (z) + 0.204 * (silt + clay)]$$

With a better fit for SOC values below 10 g.kg^{-1}, mostly associated with subsurface layers. However, the high determination coefficients indicate that the depth effect on the SOC vs. clay + silt relation was mathematically the same.

In this study, the strong relation between SOC vs. (clay + silt) concentrations implies an equal although negative SOC vs. sand (20-2000 μm) relation, as also reported by (McDaniel & Munn1999). Additionally, total N and SOC concentrations were strongly correlated as:

$$N = 0.143 + 0.063 * SOC,$$

$P<0.0001$, $R^2 = 0.956$. Thus, in non-amended, highly weathered tropical soils where N is mostly in organic form, total SOC and N concentrations can be simulated using textural data of subsoil layers (Fig. 8).

It is also important to note that linear SOC vs. (clay + silt) relations, or exponential and logarithmical functions for intercept and slopes, may not be the best descriptors for every region, and different functions must be tested for each region. In this study, intercepts were also well predicted by power (= $24.85D^{-0.5715}$, $R^2 = 0.986$, for $D>0$ cm) 0.0129(z) + 3.45 for z = 0 cm depth, $R^2 = 0.87$), which are easier to calculate than the sum of exponentials function but resulted in slightly poorer fits for the equation:

$$\text{Measured SOC} = 0.9698\ (\text{estimated SOC}) + 0.2231,\quad R^2 = 0.895$$

Additional research is currently being conducted to describe the textural and depth control on SOC partition through particle-size separates and SOC storage (mass/area).

CONCLUSIONS

Such information is central in understanding the impact of silt and clay content of soil profile on soil organic carbon. The soil organic carbon concentration was significantly and linearly correlated with the combined both elements, but not clay alone, for all depths. The intercept and slope of these linear relations decreased with depth following exponential and logarithmic functions.

REFERENCES

Arrouays, D. and Pelissier, P. 1994. Modeling carbon storage profiles in temperate forest humic loamy soils of France. Soil Science, 157(3): 185-192.

Benton, Jones J.R. 1991. Kjeldahl Method for Nitrogen Determination. Athens, GA: Micro-Macro Publishing, 79.

Bernoux, M.C.S., Carvalho, B. Volkoff and Cerri, C.C. 2002. Soil carbon stocks. Soil Sci. Soc. Am. J., 66: 888-896.

Bosatta, E. and Ågren, G.I. 1996. Theoretical analyses of carbon and nutrient dynamics in soil profiles. Soil Biology and Biochemistry, 28(10-11): 1523-1531.

Burke, C.M., Yonkers, W.J., Parton, C.V., Cole, K. Flach and Schimel D.S. 1989. Texture, climate, and cultivation effects on soil organic matter content in US grassland soils. Soil Sci. Soc. Am. J., 53: 800-805.

Davidson, E.A. and Lefebvre, P.A. 1993. Estimating regional carbon stocks and spatially covarying edaphic factors using soil maps at three scales. Biogeochemistry, 22(2): 107-131.

Feller, E., Fritsch, R. Poss and Valentin, C.1991. Effect de la texture sur le stockageet la dynamique des matièresorganiquesdansquelques sols ferrugineux et ferralitiques (Afrique de l'Ouest, en particulier), Cah. OrstomSér. Pédol., 26: 25-36.

Hasson, A., Wiley, T. and Woolston, G. 2013. Whole soil sampling to compare carbon sequestration under perennial pastures of Western Australia. Nature Environment and Pollution Technology, 12(2): 203.

Hasson, A. and Jweeg, M. 2014. Soil organic carbon sequestration under pastures in arid region. Nature, Environment and Pollution Technology, 13(4): 57-62.

Jenny, H. 1941. Factors of Soil Formation-A System of Quantitative Pedology (1994 edition), Dover Publications Inc., Mineola, NY, pp. 281.

Kay, L. 1998. Soil structure and organic carbon: A review. In: R. Lal, J. Kimble, R. Follett and Stewart, (Editors), Soil Processes and the Carboncycle, CRC Press, Boca Raton, FL :169-197.

Lugo, A.E. and Brown, S. 1993. Management of tropical soils as sinks or sources of atmospheric carbon. Plant and Soil, 149(1): 27-41.

Lugo, A.E. 1997. The apparent paradox of reestablishing species richness on degraded lands with tree monocultures. Forest Ecology and Management, 99(1-2): 9-19.

McDaniel, P.A. and Munn, L.C. 1985. Effect of temperature on organic carbon-texture relationships in mollisols and aridisols 1. Soil Science Society of America Journal, 49(6): 1486-1489.

Quinn, J.G., Salomon, M. 1964. Chloride interference in the dichromate oxidation of soil hydrolyzates. Soil Sci. Soc. Am. Proc., 28: 456.

Parton, D.S. Schimel, C.V. Cole and Ojima, D.S. 1987. Analysis of factors controlling soil organic matter levels in Great Plains Grasslands. Soil Sci. Soc. Am. J., 51: 1173-1179.

Percival, H.J., Parfitt, R.L. and Scott, N.A. 2000. Factors controlling soil carbon levels in New Zealand grasslands: Is clay content important? Soil Sci. Soc. Am. J., 64: 1623-1630.

Rogers, G.L. 1965. Geraldton region land resources survey. Land Resources Series Report No. 13.

Stevenson, F. J. 1994. Humus Chemistry: Genesis, Composition, Reactions. John Wiley and Sons, New York, Inc., pp. 496.

Tan, R., Lal, N.E. Smeck and Calhoun, F.G. 2004. Relationships between surface soil organic carbon pool and site variables. Geoderma, 121(3-4): 187-195.

Wösten, P .2002. Encyclopedia of Soil Science, M. Dekker, NYC: 967-971.

Walkley, A. and Black, A. 1934. An examination of the Degtjereff method for determining soil organic matter and proposed modification of the chromic acid titration method. Soil Sci., 37: 29-38.

Nature Environment and Pollution Technology
An International Quarterly Scientific Journal

p-ISSN: 0972-6268
e-ISSN: 2395-3454

Vol. 18 | No. 4 | pp. 1319-1323 | 2019

Original Research Paper | Open Access

A Feasible and Green Approach for Developing Hydrogen Energy

Wenting Zhang*, Yifeng Liu and Yingmei Xu*†**

*School of Statistics and Mathematics, Zhongnan University of Economics and Law, Wuhan 430000, China
**Hubei Power Exchange Center, State Grid Hubei Electric Power Company, Wuhan 430000, China
†Corresponding author: Yingmei Xu

Nat. Env. & Poll. Tech.
Website: www.neptjournal.com

Received: 16-09-2019
Accepted: 18-10-2019

Key Words:
Green approach
Hydrogen energy
Hydropower
LCOE

ABSTRACT

Hydrogen is recognized as the green energy with the greatest potential for future development, but currently, China's hydrogen production is highly dependent on raw fossil materials, which conflicts with the original intention of developing hydrogen energy. As the abandoned hydropower problem in Southwestern China is serious. The current strategy can be focused using surplus hydropower to produce hydrogen in a green way. In this study, the technical cost and advantage of hydrogen produced using surplus hydropower using the levelized cost of energy model was analyzed. The results show that cheap surplus hydropower will considerably reduce the cost of hydrogen produced using electrolyzing water, and the cost is comparable to that of coal gasification hydrogen production. The hydropower to be abandoned by Southwestern China annually can drive the hydrogen production with 1.2 million tons per year, providing a technically and economically feasible approach to developing hydrogen energy.

INTRODUCTION

Hydrogen is recognized as the most promising type of secondary energy due to its high calorific value, clean emissions, and huge prospective reserves on earth. The development and use of this clean energy is strategically important for solving the two major crises, energy shortages and environmental pollution, currently plaguing humankind.

Since 2011, China has been the world's largest producer and consumer of hydrogen energy. However, the hydrogen energy production process in China is not green; more than 80% hydrogen energy is produced using raw fossil materials, especially coal and natural gas. Using coal and natural gas to produce hydrogen not only requires a large quantity of raw fossil materials and large amounts of heat, but also produces environmental pollutants through waste residue and waste liquid. This obviously conflicts with the original intention of developing clean hydrogen energy.

Two kinds of clean raw materials for hydrogen production have not been fully used in Southwestern China: water and the electric power generated by hydro power. As the capability of installed hydro power generation is far higher than the local demand, a large amount of water and the hydro power are abandoned every year. If the to-be-abandoned water and hydro power were used to produce hydrogen using the electrolysis water method, the redundant hydro power energy could be stored in the form of hydrogen, and the hydrogen-producing process would be greener.

The major problem is that when using the industrial electricity price, the cost of hydrogen produced using the electrolysis water method is much higher than using raw fossil materials (Cao 2017). The cost of producing hydrogen with the electrolysis water method is about USD $5.2/kg, whereas the cost of using raw fossil materials to produce hydrogen is about USD $1.67/kg (Cao 2017). As the to-be-abandoned water and hydro power can be sold much cheaper than the industrial electricity price and raw fossil materials, the cost of hydrogen produced by the electrolysis water method can hopefully be reduced to a competitive level. In this study, we focused on whether it is feasible to lower the cost of hydrogen production using the to-be-abandoned water and hydro power in Southwestern China.

STATE OF ART

Developing hydrogen energy has been a common goal in most developed countries. Japan has announced a national strategy to build a hydrogen society by 2040 (Mao 2016), Germany and France planned to develop hydrogen industry for a greener traffic system (Mao 2016), the USA planned to substitute hydrogen for fossil energy by 2030. China has introduced a strategy to develop hydrogen energy and become the world's largest hydrogen producer (Mao 2016).

As the hydrogen process in China is not green, and environmental pollution continues to increase, some scholars are calling for hydrogen to be produced with renewable energy and materials (Zou et al. 2019, Yi et al. 2018). For example, Yi et al. (2018) stated that hydrogen can be produced by

water electrolysis with solar or wind power. However, this idea is not without its issues. In China, wind and solar energy resources are concentrated in the northwest, where water resources are in extremely short supply. Long-distance electric power transport will increase the hydrogen production costs. Thus, using solar or wind power in water electrolysis is not appropriate, but the sufficient hydro power and water in Southwest China can be used for hydrogen production.

Few studies have focused on the issue of whether producing hydrogen using the to-be-abandoned hydro power in Southwest China is technically and economically feasible. The levelized cost of energy (LCOE) model is a useful method for evaluating the cost of energy per unit in production (Lina et al. 2018), and it has been widely used in evaluating energy cost, such as: Ioannou et al. (2017) use it in accounting the cost of a wind farm, Vazquez & Iglesias (2015) use it in tidal resource cost accounting, Mikel et al. (2016) use it to account a solar project's cost. In this study, we built a cost accounting model and prove the feasibility of this new approach to producing hydrogen.

METHODOLOGY

Modeling for Accounting Levelized Cost of Energy

According to the definition of LCOE, a project's net present value cost is equal to the net present value of profit. The equation can be written as

$$I_0 - V_R \cdot (1+r)^{-N} + \sum_{n=1}^{N} C_n \cdot (1+r)^{-n} = \sum_{n=1}^{N} P_n \cdot E_n \cdot (1+r)^{-n} \quad \ldots(1)$$

Where, I_0 indicates the initial investment amount of the project, V_R indicates the residual value of the asset, n indicates the years of project operation, N indicates the project's operational life, C_n indicates the project's annual expenditure cost in year n, r indicates the discount rate, P_n indicates the energy price in the year n, and E_n indicates the quantity of energy produced in the year n. Then, the LCOE can be obtained from Equation (1) and written as

$$\mathrm{LCOE} = P_n = \frac{I_0 - \dfrac{V_R}{(1+r)^N} + \sum_{n=1}^{N} C_n \cdot (1+r)^{-n}}{\sum_{n=1}^{N} E_n \cdot (1+r)^{-n}} \quad \ldots(2)$$

Where, C_n includes the costs of initial fixed asset investment, taxes, asset depreciation, and project operation and maintenance. C_n can be expressed as

$$C_n = OPE_n + TAX_n - I_{dn} \quad \ldots(3)$$

Where, OPE_n indicates the project's operation and maintenance costs, TAX_n indicates the tax costs, and I_{dn} indicates the asset depreciation costs. E_n in Equation (2) can be written as

$$E_n = W_s \cdot H_n \cdot (1 - R_n) \quad \ldots(4)$$

Where, W_S indicates the project's production capability per hour, H_n is the project's production hours in year n, and R_n indicates the project's production loss rate in the year n.

The variables I_{dn}, OPE_n, and TAX_n can be specifically written as

$$\begin{cases} I_{dn} = I_0 (1-v) \cdot N^{-1} \\ T_{an} = E_n \cdot P_n \cdot \tau_a \\ T_{bn} = T_{an} \cdot \tau_b \cdot \\ T_{cn} = (E_n \cdot P_n - T_{an} - T_{bn} - I_{dn} - OPE_n) \cdot \tau_c \\ TAX_n = T_{an} + T_{bn} + T_{cn} \\ OPE_n = E_n \cdot (w_1 \cdot g + w_2 \cdot l_n) \end{cases} \quad \ldots(5)$$

Where, v is the asset's residual value rate, T_{an} is the project's value added tax paid in year n, T_{bn} is the project's surtax paid in year n, T_{cn} is the project's income tax paid in year n, τ_a is the value added tax rate, τ_b is the surtax rate, τ_c is the income tax rate, w_1 is the cost of electric power used in water electrolysis, w_2 is the project's variable cost per unit hydrogen output, g is the quantity of electricity needed per unit hydrogen output, and l_n indicates the increasing coefficient for project's operation and maintenance. Substituting Equations (3)–(5) into Equation (2), the LCOE is:

$$LCOE = \frac{I_0 - V_R \cdot (1+r)^{-N} - I_0 (1-v) \cdot N^{-1}}{\sum_{n=1}^{N} E_n \cdot (1+r)^{-n}} + \frac{E_n \cdot (w_1 \cdot g + w_2)}{\sum_{n=1}^{N} E_n \cdot (1+r)^{-n}} + \frac{T_{an} + T_{bn} + T_{cn}}{\sum_{n=1}^{N} E_n \cdot (1+r)^{-n}} \quad \ldots(6)$$

From Equation (6), the LCOE can be obtained by the rolling years' iteration calculation.

Modeling for Cost Sensitivity Analysis

The purpose of cost sensitivity analysis is to analyze the influence on hydrogen production cost when relative parameters change. The cost sensitivity of hydrogen production can tell that, which parameters should to be exogenously regulated, for the proper cost control. Consider the equation (6) as a function:

$$LCOE(x_1, x_2, \cdots x_i) \quad \ldots(7)$$

Where, $x_1, x_2, \ldots, x_i$ indicate the relative parameters in the cost calculation of hydrogen production. Then the sensitivity analysis can be written as:

$$F_j = \frac{\Delta LCOE_j}{LCOE_0} \cdot \frac{x_{j0}}{\Delta x_j} \quad \ldots(8)$$

Where, $1 \le j \le 1$. x_{j0} indicates the initial value of parameter x_j. Δx_j indicates the change value of parameter x_j. $LCOE_0$ indicates the cost of hydrogen production when all the parameters are set as the initial values. $\Delta LCOE_j$ indicates the change rate of hydrogen production cost when the parameter x_j changes with the value Δx_j. F_j indicates the sensitive value when the parameter x_j changes.

RESULTS AND DISCUSSION

Parameters Setting

According to actual tax amounts and, raw materials and hydrogen output prices in China, the parameters for LCOE calculation were set as following: I_0 = USD \$1.1 billion; N = 30 years; V_R = 5%; the depreciation rate of assets = 4.75%; W_s = 162 kg/hour; H_n = 2400 hours/year; w_1 = USD \$21.43/MWh (Lin, et al. 2016), w_1 = USD \$0.71 /kg; g = 0.05 MWh/kg (Lin et al. 2016); τ_a =17%, τ_a =8%, τ_c =25%, r=6.5%. l_n was set to 0 when $0 \le n \le 5$; l_n was set as 1.05 when $6 \le n \le 15$; l_n was set as 1.08 when $16 \le n \le 25$; and l_n was set as 1.10 when $26 \le n \le 30$. R_n was set to 0 when $0 \le n \le 5$, 3% when $6 \le n \le 15$, 6% when $16 \le n \le 25$, and 9% when $26 \le n \le 30$.

Calculation and Comparison of Hydrogen Production Costs

By bringing the parameters above into Equation (6), we obtained the following: First, if using traditional electricity to produce hydrogen by water electrolysis with the industrial electricity price, the LCOE of hydrogen would be USD \$4.87/kg. This result is close to the result reported by Cao (2017). This means the model built in this study is accurate. Second, if using the to-be-abandoned water and hydro power in Southwestern China, the LCOE of hydrogen would be reduced to USD \$1.90/kg. Compared with the costs of other hydrogen producing methods, the advantage of this result is shown in Fig. 1.

Fig. 1 shows that the LCOE of hydrogen obtained using to-be-abandoned water and hydro power is significantly lower. The accumulated after-tax cash flow can be obtained from the rolling years' iteration calculation. Compared to the same project using traditional industrial electricity, the accumulated after-tax cash flows are shown in Fig. 2.

Fig. 2 shows that during the project's life, using to-be-abandoned water and hydro power can result in project profitability, whereas the use of traditional industrial electricity results in project losses.

In summary, Figures 1 and 2 prove that using to-be-abandoned water and hydro power can water electrolysis can be competitive in the hydro market.

COST SENSITIVITY ANALYSIS

In the reality, the parameters of value-added tax rate and assets depreciation rate are relatively fixed, while the parameters of hydrogen price and project's surtax rate may fluctuate. Thus, in this study, six parameters are selected as the investigation objects, and the change rates are set as 10% and -10%. Then the sensitivity coefficients of hydrogen production' LCOE to the parameters are obtained according to the equation (8). The results are depicted in Table 1.

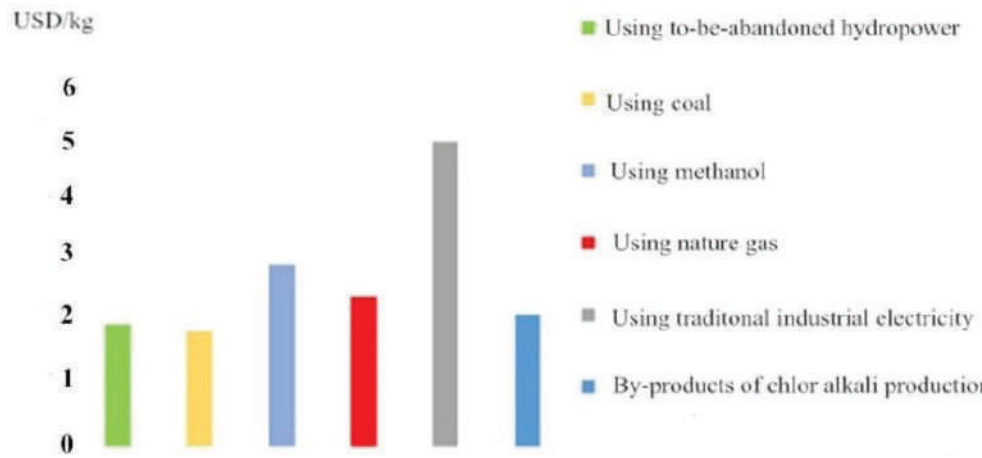

Fig. 1: Cost comparison of different hydrogen production methods.

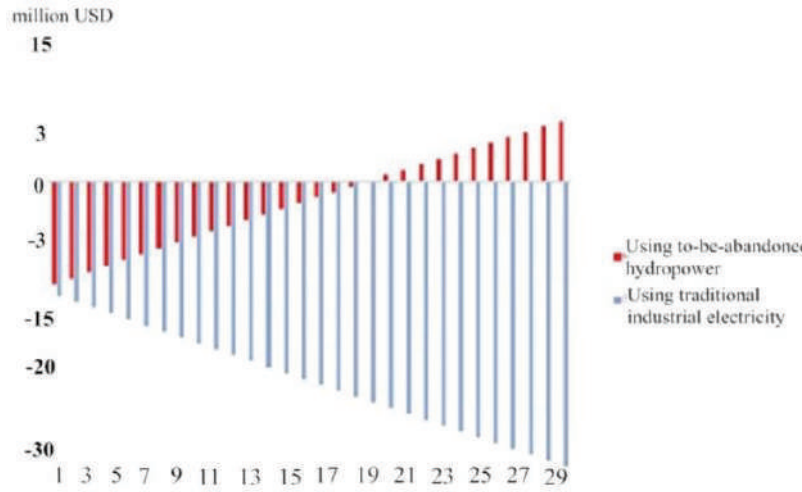

Fig. 2: Comparison of accumulated after-tax cash flows.

Table 1: Sensitivity analysis.

Parameters	LCOE (USD/kg)		Sensitivity Coefficient	
	+10%	-10%	+10%	-10%
Annual hydrogen production quantity	13.965	12.942	0.478	0.290
Discount rate	13.032	14.008	-0.222	-0.510
Project's variable cost per unit hydrogen output	13.720	12.937	0.294	0.294
Hydrogen price	14.407	12.261	0.809	0.801
Price of to-be-abandoned hydropower	13.891	12.766	0.422	0.422
Surtax rate	13.354	13.303	0.019	0.019

It can be found from Table 1 that, the LCOE of hydrogen production project is most sensitive to the hydrogen price, followed by the parameters of price of to-be-abandoned hydropower, discount rate and annual hydrogen production quantity. The LCOE is least sensitive to the parameters of surtax rate and project's variable cost per unit hydrogen output. The specific analyses are as following:

First, the hydrogen price is positively related to project's to-be-paid value-added tax, which is vital to the LCOE. If the hydrogen price rises, LCOE will be also pulled up. But the change rate of LCOE is smaller than that of hydrogen price. This phenomenon is implying that, hydrogen price rigidity will be more welcomed by the project.

Second, as the project' LCOE is sensitive to the price of to-be-abandoned hydropower, it is vital to minimize the potential cost of power transmission. Therefore, it is necessary for the project to be built adjacent to hydropower plants.

In addition, as the LCOE is not sensitive to surtax rate and project's variable cost per unit hydrogen output, the cost fluctuation in human resources and equipment maintenance will not shock the LCOE significantly.

Since 2014, the amount of annual abandoned hydro power in Southwestern China was more than 60 million MWh, and a single project could use 0.019 MWh/year. So, more than 3000 projects can be built for fully using the energy and more than 1.2 million tons of hydrogen could be produced every year. Therefore, developing this green hydrogen production method is technically and economically feasible. In this case, the wasted energy in Southwestern China can be fully used.

CONCLUSIONS

This study provides a feasible approach to solving the energy waste and green hydrogen production problems in Southwest China. Using the LCOE model, we proved that the cost of hydro production can be significantly reduced when using the to-be abandoned water and hydro power, and the cost would be competitive in the hydrogen market. The to-be-

abandoned hydro power is capable of producing more than 1.2 million tons hydrogen annually. We predicted that this feasible approach to hydrogen production will have positive environmental and social benefits.

REFERENCES

Cao, X.H. 2017. Key to development and application of hydrogen energy. Petroleum Processing and Petrochemicals, 48(9): 1-6.

Ioannou, A., Angus, A. and Brennan, F. 2017. Stochastic prediction of offshore wind farm LCOE through an integrated cost model. Energy Procedia, 107: 383-389.

Lin, J., Zhang, Y.C., Song, Y.H. and Zeng, R. 2016. Consumption model and economic feasibility analysis for using the to-be-abandoned hydro power based on the energy internet in China. Energy of China, 38(4): 5-9.

Lina, R., Fredrik, H., Mikael, O. and Filip, J. 2018. The marginal system LCOE of variable renewables: Evaluating high penetration levels of wind and solar in Europe. Energy, 152: 914-924.

Mao, Z.Q. 2016. The era for hydrogen energy is coming. Solar Energy, (7): 16-19.

Mikel, D.P., Jose, L.D., Lluís, T. and Oriol, G. 2016. Technical and economic comparison of various electrical collection grid configurations for large photovoltaic power plants. IET Renewable Power Generation, 11(3): 226-236.

Vazquez, A. and Iglesias, G. 2015. LCOE (Levelised Cost of Energy) Mapping: A new geospatial tool for tidal stream energy. Energy, 91:192-201.

Yi, W.J., Liang, Q. and Pei, Q.B. 2018. Enhance the hydrogen application in china's energy system to accelerate the energy transition: Status and progress. Environmental Protection, 46(2): 30-34.

Zou, C.N., Zhang, F.D., Zheng, D.W., Sun, F.J., Zhang, J.H., Xue, H.Q., Pan, S.Q., Zhao, Q., Zhao, Y.M. and Yang, Z. 2019. Strategic role of the synthetic hydrogen production and industry in energy independence of China. Natural Gas Industry, 39(1): 1-10.

Nature Environment and Pollution Technology
An International Quarterly Scientific Journal

p-ISSN: 0972-6268
e-ISSN: 2395-3454

Vol. 18 | No. 4 | pp. 1325-1331 | 2019

Original Research Paper | Open Access

Guar Gum Hydrogel Beads for Defluoridation from Aqueous Solution: Kinetic and Thermodynamic Study

Anushree Srivastava*, Madhu Kumari and Kumar Suranjit Prasad*†**

*Centre of Environmental Science, Institute of Interdisciplinary Studies, University of Allahabad, Prayagraj, Uttar Pradesh, India

**Department of Botany, B. R. A. Bihar University, Muzaffarpur, Bihar, India

†Corresponding author: Kumar Suranjit Prasad

Nat. Env. & Poll. Tech.
Website: www.neptjournal.com

Received: 29-11-2018
Accepted: 04-02-2019

Key Words:
Guar gum
Hydrogel beads
Defluoridation
Bio-sorbent
Fluoride

ABSTRACT

In the present research work, batch adsorption study was carried out to optimize the fluoride removal capacity of guar gum hydrogel beads from aqueous solution. The adsorption capacity was found to be 71.2 mg/g. The FTIR spectrum revealed the presence of functional groups that might be involved in fluoride adsorption. Adsorption of fluoride onto bio-sorbent was investigated as a function of pH, adsorbent dosage and time. The experimental equilibrium sorption data well fitted to the Langmuir mo del and the sorption kinetics for the bio-sorbent was found to follow second order rate expression. The negative values of ΔG° suggest that the sorption of fluoride onto the bio-sorbent was spontaneous and exothermic due to the negative value of ΔH°. The negative ΔS° value for the guar gum was found to be decreasing in randomness at the solid-liquid intersection.

INTRODUCTION

Fluoride in drinking water can be beneficial as it plays an important role in mineralization of bones and teeth but its excess uptake causes incurable dental and skeletal fluorosis. The main source of fluoride in groundwater is weathering and leaching of rocks containing minerals such as fluorite, fluorapatite, cryolite etc. (Carrillo-Rivera et al. 2002). According to World Health Organization (WHO) norms, the upper limit of fluoride concentration in drinking water is 1.5 mg/L. It is estimated that more than 200 million people worldwide depend on groundwater that contains a high concentration of fluoride. According to WHO guideline, the permissible limit for fluoride in drinking water is 1.5 mg/L. Various defluoridation technologies have been developed to reduce the fluoride concentration in water such as adsorption, ion exchange and precipitation to reduce fluoride level in the water. Among these methods, adsorption technique seems to be a promising technique for fluoride removal, because of ease of operation and selectivity of many natural adsorbents from various plant extracts and animal sources that have been tried as defluoridation agents. Seeds of the drumstick (Parlikar & Mokashi 2013), biomass of white rot fungus (Amin et al. 2015), tamarind seeds (Murugan & Subramanian 2006), leaf ash of *Syzygium cumini* (Tirkey et al. 2018) eggshell powder (Kashi et al. 2015), tea waste loaded to Al-Fe (Cai et al. 2015), porous starch loaded with common metal (Xu et al. 2017) and *Aloe vera* extract (Prasad et al. 2014) are few among them. Guar gum is obtained from the beans of the *Cyamopsis tetragonoloba* plant. Chemically, it is an exopolysaccharide composed of galactose and mannose (Khan et al. 2017). Guar gum has been used as an adsorbent for Hg (Singh et al. 2015), Cr (Maity & Ray 2016), and Pb (Pandey & Ramontja) ions removal. The present study explores the utility of guar gum for the removal of fluoride from aqueous solution.

MATERIALS AND METHODS

Guar beans were collected from the plant *Cyamopsis tetragonoloba* and left under the sun to dry for 3 to 4 days. The dried seeds were then crushed into a fine powder. The sodium salt of gum was made by mixing 10 g of powder into 100 mL, 1 M NaOH. Unreacted excess NaOH was removed by washing with 10 volume of double-distilled water. Ionotropic gelation method was carried out for beads preparation. Hydrogel beads were prepared by dropwise addition of 1% sodium salt of gum into 200 mL of 0.2 M $CaCl_2$ solution. The FTIR analysis was performed with attenuated total reflectance Fourier transform spectrometer at wave number ranging from 400-4000 cm^{-1} with a resolution of 4 cm^{-1} to determine the chemical constituent of guar gum powder that might be helpful for fluoride removal from aqueous solution. Adsorption experiments were car-

ried out with 50 mL of 100 mg/L fluoride solution on a magnetic stirrer at 28°C for 60 min. The adsorbent of 2 g was added to the fluoride solution. Adsorption experiments were carried out with 50 mL of 100 mg/L fluoride solution on a magnetic stirrer at 28°C for 60 min. The adsorbent of 2 g was added to the fluoride solution. The adsorption of fluoride onto adsorbent was studied under different conditions including pH, temperature, contact time and biomass doses. In kinetic studies, the initial fluoride concentration was set to 100 mg/L, and the samples were analysed at certain time intervals. Also, the effect of the temperature was observed by conducting the experiments at five different temperatures (28, 36, 42, 48 and 52°C) in order to obtain thermodynamic parameters. The concentration of fluoride in the solutions was determined by ion exchange chromatography (Metrohm Eco IC). A calibration curve was obtained using NaF standard solutions with different fluoride concentrations ranging from 2.5 to 10 mg/L.

The percentage sorption of F ions was calculated by the following equation:

$$\text{Sorption } \% = \frac{C_i - C_f}{C_i} \times 100 \quad \ldots(1)$$

The amount of fluoride adsorbed was calculated from the following equation:

$$q_e = \frac{(C_i - C_f)\ V}{M} \quad \ldots(2)$$

Where C_i and C_f are the initial and final concentrations of F ions in the aqueous solution (mg/L), respectively. V is the volume (L) of test solution and M is the mass nano-adsorbent (g) used.

RESULTS AND DISCUSSION

The FT-IR spectrum revealed the presence of carboxylic, hydroxyl and methyl groups. Fig. 1 shows the spectrum of guar gum powder. The peak located around wave number 3400 can be assigned as the involvement of the OH group. The adsorption peaks located in a wave range of 1800-1500 can be assigned as peaks due to the presence and involvement of C=C. The peak at 1,601 cm^{-1} is due to the asymmetrical -COO- stretching vibration (Helm & Naumann 1995) (Kishor et al. 2007).

Effect of pH on Adsorption

The adsorption data obtained for the effect of different pH values from 4 to 9 on defluoridation are shown in Fig. 2(a). The maximum adsorption capacity of 97.2% was observed at a pH value of 7, however, the adsorption capacity declined with the increase of pH value. The favourable neutral pH range observed for this study was found to be similar and reported by Hamamoto & Kishimoto (2017), Sujana et al. (1998) and Das et al. (2003). Many researchers have also found that the acidic pH also has good removal capacity for fluoride as reported by Wu et al. (2007) and He et al. (2018).

Effect of Contact Time

The effect of contact time on adsorption of F ion was investigated by performing an experiment by varying contact

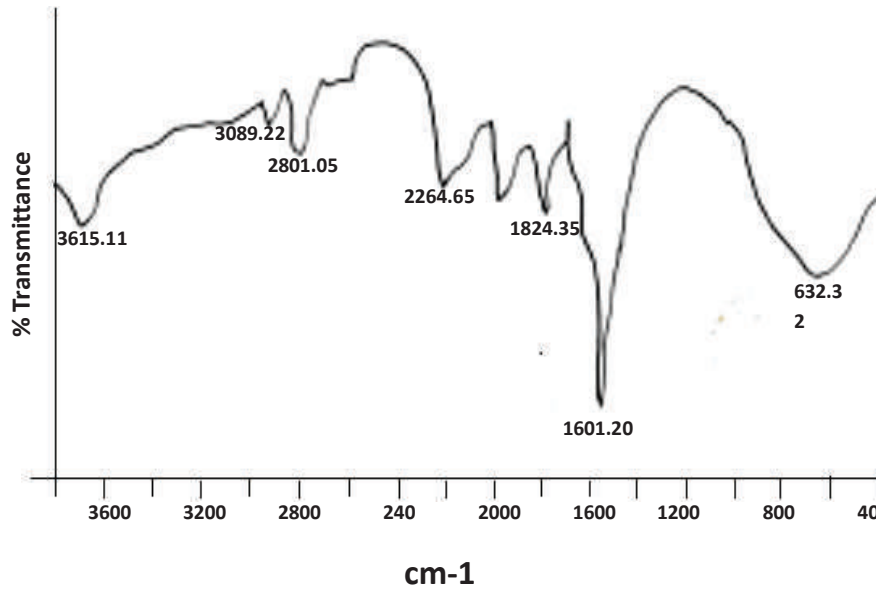

Fig. 1: FT-IR spectra of fluoride adsorbed Guar gum hydrogel beads.

time from 5 to 60 min using the adsorbent dose 2 g/L with an initial concentration of fluoride solution of 100 mg/L at 28°C. The effect of contact time on fluoride removal efficiency is shown in Fig. (2b). The maximum adsorption capacity for fluoride on equilibrium time was found to be 98%. It was also found that further increase in contact time showed very less change in the result, which concluded that 60 min was equilibrium contact time for fluoride removal.

Effect of Biomass Dosage and Fluoride

The pattern for adsorption of F ion at different doses of adsorbent indicated a little change in sorption of fluoride upon an increase in the amount of biomass beyond 2 g (Fig. 3a). Maximum sorption occurred when 2 g of the adsorbate was subjected to sorption studies. Similarly, an increase in F ion concentration to more than 200 mg/L, when biomass doses were 2 g, did not enhance overall sorption in batch sorption model (Fig. 3b).

Adsorption Isotherms

The adsorption isotherm for fluoride removal by guar gum was determined by Langmuir and Freundlich model. The Langmuir model works on the hypothetical assumptions of monolayer surface interaction whereas the Freundlich model applicable to both monolayer as well as multilayer adsorption. A linear form of Langmuir isotherm can be defined according to the following formula:

$$\frac{1}{Q_e} = \frac{1}{K_{LQ_mCe}} = \frac{1}{Q_m} \quad \ldots(3)$$

Where, Q_e is the adsorbate concentration on the adsorbent (mg/g), C_e is the equilibrium concentration of adsorbate in the solution (mg/L), Q_m is the monolayer sorption capacity of the adsorbent (mg/g) and K_L is the Langmuir sorption constant (L/mg), relating the free energy of sorption. Langmuir isotherm was obtained by plotting 1/Qe Vs. $1/C_e$ values, which showed a linear relationship between the two (Fig. 4a). The coefficients of determination (R^2) were found to be 0.998 for F ion sorption. The maximum sorption capacity (Q_m) was found to be 71.2 mg/g, while K_L value was calculated as 0.017 L/mg for F ion sorption.

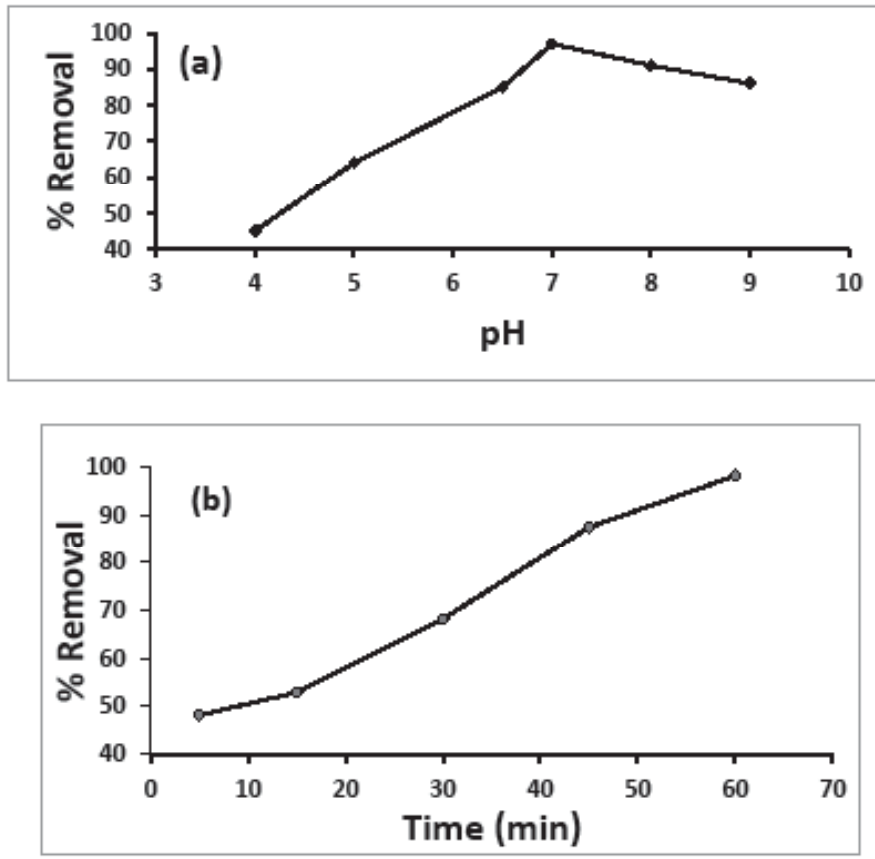

Fig. 2: Effect of pH (a), effect of contact time (b) on adsorption of fluoride onto Guar gum hydrogel.

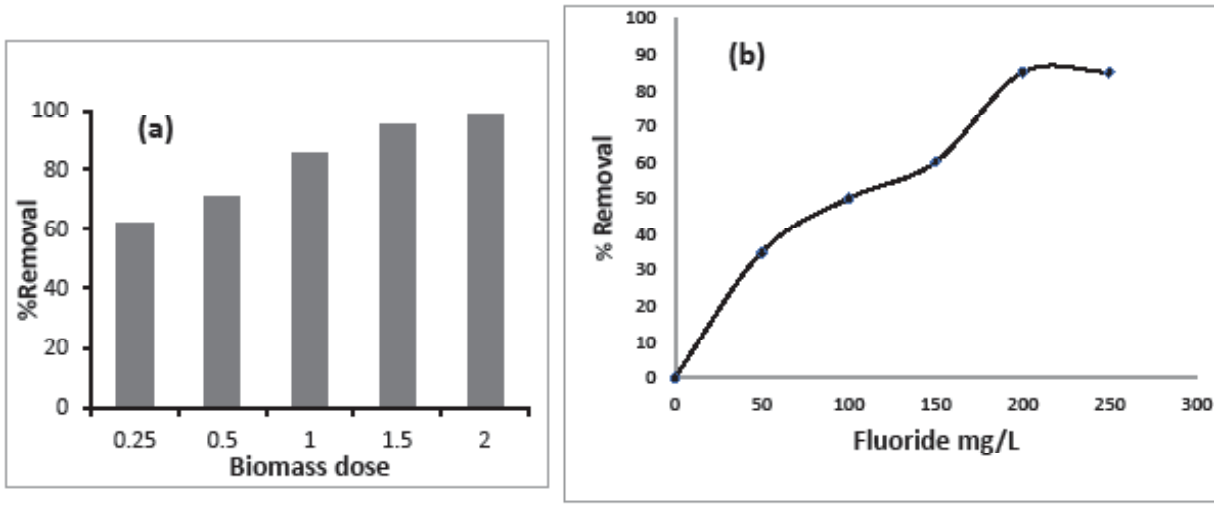

Fig. 3: Effect of biomass doses (a) (2g/L at 30°C) for removal efficiency & effect of adsorbate concentration (F^-, 200 mg/L).

Another study by Ghosh et al. (2014) reported a maximum adsorption capacity of 19.5 mg/g.

The Freundlich model assumes a heterogeneous adsorption surface and active sites with a different energy. This isotherm can be explained by the following formula:

$$\text{Log } q_e = \text{Log } K_f + \frac{1}{n}\text{Log } C_e \quad \ldots (4)$$

Where, K_f is a constant relating the sorption capacity and 1/n is an empirical parameter relating to sorption intensity, which varies with the heterogeneity of the material. The Freundlich isotherm was obtained by plotting Log q_e Vs. Log C_e values, which showed a linear relationship between the two (Fig. 4b). Values of K_f and n were found to be 1.28 and 2.51 for F ion sorption respectively. The R^2 value was found to be 0.803. These results suggested that the Langmuir isotherm model best fitted the equilibrium data since it presented a higher R^2 value than the Freundlich model.

Adsorption Kinetic Models

Pseudo-first order and Pseudo-second order kinetic models were used to analyse the sorption rate of F ions on guar gum. The linear form of the equation is given as:

$$\log(q_e - q_t) = \frac{\log q_e - k_t t}{2.303} \quad \ldots(5)$$

Where, q_e (mg/g) are the amount of fluoride adsorbed at equilibrium, q_t (mg/g) is the amount of fluoride adsorbed at any time and k_1 is the rate constant of the equation (min^{-1}). The linear graph obtained by plotting log (q_e-q_t) versus t and the values for rate constant can be calculated by the slope of the plot (Fig. 5a). The sorption kinetics was also

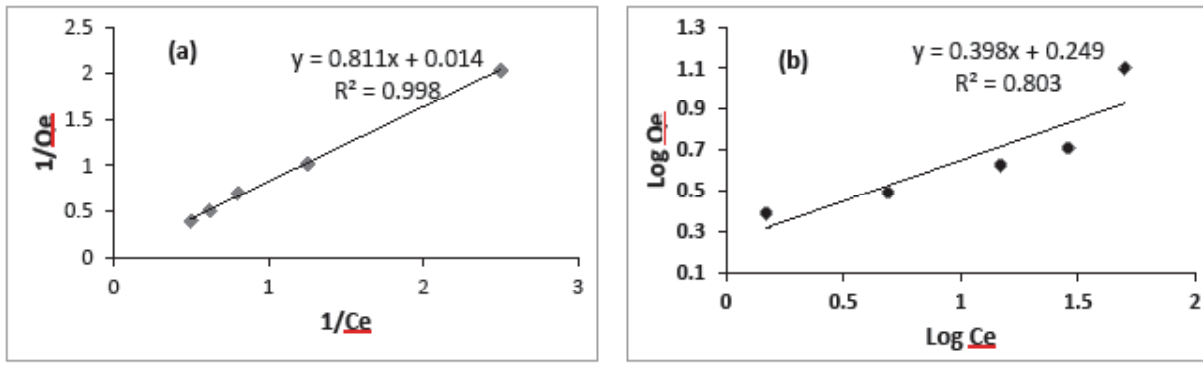

Fig. 4: Langmuir (a) and Freundlich (b) isotherm for adsorption of fluoride on prepared beads.

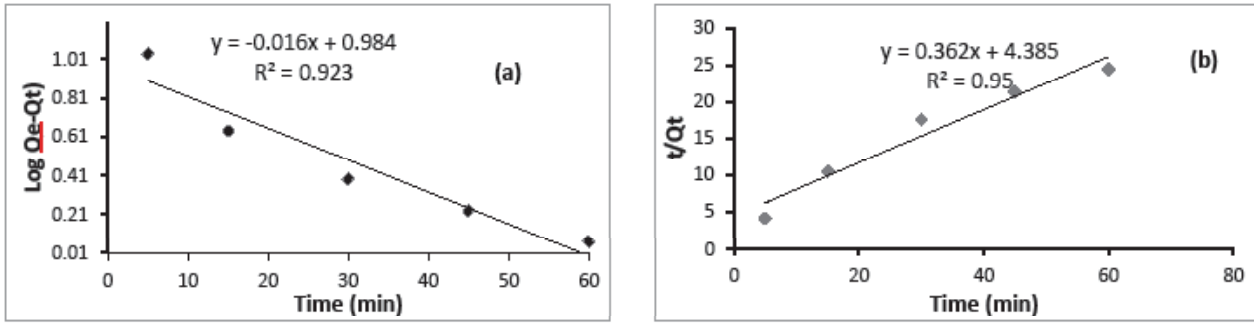

Fig. 5: Adsorption kinetic models for F^- ion uptake pseudo-first-order model for F^-(a) and pseudo-second-order model for F^- ions (9b).

studied by pseudo-second-order model. The linear form of pseudo-second-order equation is given as:

$$\frac{t}{q_t} = \frac{1}{k_2 q_e^2} + \left(\frac{1}{q_e}\right) t \qquad \ldots(6)$$

Where, k_2 is the equilibrium rate constant (g/mg/min). If the pseudo-second-order kinetic equation is applicable, the plot of t/qt against t should give a linear relationship, from which q_e and k_2 can be determined from the slope and intercept of the plot (Fig. 5b). The values of the correlation coefficient of the pseudo-second-order model were found to be 0.95 which is higher than the pseudo-first-order model, i.e. 0.92. Compared to the pseudo-first-order equation, the pseudo-second-order model can explain the sorption kinetic behavior of F ion with a good correlation coefficient. In the study by Teutli-Sequeira et al. (2014) adsorption kinetic data were best fitted on pseudo-second-order kinetic.

Thermodynamic Studies

Thermodynamic parameters of an adsorption process are important to determine the nature of adsorption. Gibb's free energy change, ΔG°, is the fundamental criterion of spontaneity. Reactions occur spontaneously at a given temperature if ΔG° is a negative value. The thermodynamic parameters of Gibb's free energy change, Δ*G* for the adsorption processes are calculated using the equation (7).

$$\Delta G^\circ = -RT \ln K_D \qquad \ldots(7)$$

Where R is the universal gas constant (8.314 J/mol K), T is temperature (K) and K_D (q_e/C_e) is the distribution coefficient (Alagumuthu & Rajan 2010). The enthalpy (ΔH°) and entropy (ΔS°) parameters were estimated from the following equation:

$$\ln K_D = \left(\frac{\Delta S^o}{T}\right) - \left(\frac{\Delta H^o}{RT}\right) \qquad \ldots(8)$$

The negative ΔG° values indicated the thermodynamically feasible and spontaneous nature of the sorption. The increase in the negative value of ΔG° with an increase in temperature suggested lesser feasibility of sorption at high temperatures. In most of the cases, adsorption of fluoride is

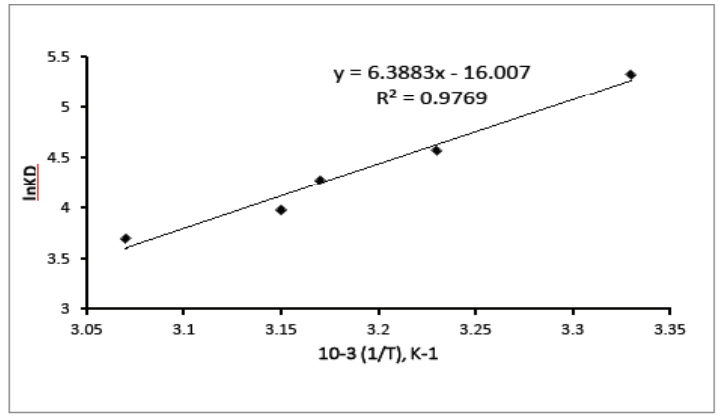

Fig. 6: Plot of ln KD Vs. 1/T for the estimation of thermodynamic parameters for sorption of F^- ions on to guar gum hydrogel beads.

found to have a negative value of ΔG^o which confirmed the spontaneous nature of adsorption (Gopal & Elango 2007, Gao et al. 2009, Boparai et al. 2011, Swain et al. 2011, Jin et al. 2015). The ΔH and ΔS were calculated from the slope and intercept of the plot of ln K_D versus 1/T (Fig. 6) and found to be -52.29 and -133.09 respectively. The negative H° indicates the exothermic nature of sorption (Chaudhry et al. 2017). The enthalpy or the heat of sorption ranging from 2.1 to 20.9 kJ/mol corresponds to physical sorption whereas ranging from 20.9 to 418 kJ/mol is regarded as chemical sorption (Prasad et al. 2014). Therefore, the ΔH° value suggests that the sorption process of F ion occurred due to chemisorption. The negative ΔS° value suggested a decrease in the randomness at the solid-liquid interface during the sorption process.

CONCLUSIONS

The removal capacity of guar gum powder fluoride was found to be 98% with 71.2 mg/g at optimal experimental condition. The negative values of ΔG° and ΔH° indicate the spontaneous and exothermic nature of adsorption respectively. ΔH° value suggests that the adsorption process occurred due to chemisorption. The negative value of ΔS° suggests the decrease in randomness at the solid-liquid interface. Guar gum is eco-friendly low-cost biosorbent that has been used for removal of other metals as well as dye from solution but to the best of our knowledge this is for the first time that guar gum based hydrogel beads is used for removal of fluoride.

ACKNOWLEDGEMENT

KSP would like to acknowledge the grant, SR/FTP-120/ES/2014 given by SERB, New Delhi for conducting this research work.

REFERENCES

Alagumuthu, G. and Rajan, M. 2010. Equilibrium and kinetics of adsorption of fluoride onto zirconium impregnated cashew nut shell carbon. Chem. Eng. J., 158: 451-457.

Amin, F., Talpur, F.N., Balouch, A., Surhio, M.A. and Bhutto, M.A. 2015. Environmental nanotechnology, monitoring and management biosorption of fluoride from aqueous solution by white-rot fungus *Pleurotus eryngii* ATCC 90888. Environ Nanotechnology, Monit Manag., 3: 30-37.

Boparai, H.K., Joseph, M. and O'Carroll, D.M. 2011. Kinetics and thermodynamics of cadmium ion removal by adsorption onto nano zerovalent iron particles. J. Hazard. Mater., 186: 458-465.

Cai, H.M., Chen, G.J., Peng, C.Y., Zhang, Z.Z., Dong, Y.Y., Shang, G.Z., Zhu, X.H., Gao, H.J. and Wan, X.C. 2015. Removal of fluoride from drinking water using tea waste loaded with Al/Fe oxides: A novel, safe and efficient biosorbent. Appl. Surf. Sci., 328: 34-44.

Carrillo-Rivera, J.J., Cardona, A. and Edmunds, W.M. 2002. Use of abstraction regime and knowledge of hydrogeological conditions to control high-fluoride concentration in abstracted groundwater: San Luis Potosí Basin, Mexico. J. Hydrol., 261: 24-47.

Chaudhry, S.A., Khan, T.A. and Ali, I. 2017. Zirconium oxide-coated sand based batch and column adsorptive removal of arsenic from water: Isotherm, kinetic and thermodynamic studies. Egypt. J. Pet., 26: 553-563.

Das, D.P., Das, J. and Parida, K. 2003. Physicochemical characterization and adsorption behavior of calcined Zn/Al hydrotalcite-like compound (HTlc) towards removal of fluoride from aqueous solution. J. Colloid Interface Sci., 261: 213-220.

Gao, S., Cui, J. and Wei, Z. 2009. Study on the fluoride adsorption of various apatite materials in aqueous solution. J. Fluor. Chem., 130: 1035-1041.

Ghosh, A., Chakrabarti, S., Biswas, K. and Ghosh, U.C. 2014. Agglomerated nanoparticles of hydrous Ce(IV)+Zr(IV) mixed oxide: Preparation, characterization and physicochemical aspects on fluoride adsorption. Appl. Surf. Sci., 307: 665-676.

Gopal, V. and Elango, K.P. 2007. Equilibrium, kinetic and thermodynamic studies of adsorption of fluoride onto plaster of Paris. J. Hazard. Mater., 141: 98-105.

Hamamoto, S. and Kishimoto, N. 2017. Characteristics of fluoride adsorption onto aluminium(III) and iron(III) hydroxide flocs. Sep. Sci. Technol., 52: 42-50.

He, J., Cui, A., Ni, F., Deng, S., Shen, F. and Yang, G. 2018. A novel 3D yttrium based-graphene oxide-sodium alginate hydrogel for remarkable adsorption of fluoride from water. J. Colloid. Interface Sci., 531: 37-46.

Helm, D. and Naumann, D. 1995. Identification of some bacterial cell components by FT-IR spectroscopy. FEMS Microbiol. Lett., 126: 75-79.

Jin, H., Ji, Z., Yuan, J., Li, J., Liu, M., Xu, C., Dong, J., Hou, P. and Hou, S. 2015. Research on removal of fluoride in aqueous solution by alumina-modified expanded graphite composite. J. Alloys Compd., 620: 361-367.

Kashi, G., Mehree, A., Zaeimdar, M., Khoshab, F. and Madaree, A.M. 2015. Removal of fluoride from urban drinking water by eggshell powder. Bulg. Chem. Commun., 47: 187-192.

Khan, T.A., Nazir, M., Ali, I. and Kumar, A. 2017. Removal of chromium (VI) from aqueous solution using guar gum–nano zinc oxide biocomposite adsorbent. Arab. J. Chem., 10: S2388-S2398.

Kishor, P.B.K., Ramadevi, R. and Kumar, R. 2007. Isolation and characterization of mucous exopolysaccharide (eps) produced by *Vibrio furnissii* strain VB0S3. J. Microbiol. Biotechnol., 17: 44-51.

Maity, J. and Ray, S.K. 2016. Enhanced adsorption of Cr(VI) from water by guar gum based composite hydrogels. Int. J. Biol. Macromol., 89: 246-255.

Murugan, M. and Subramanian, E. 2006. Studies on defluoridation of water by tamarind seed, an unconventional biosorbent. J. Water Health, 4: 453-461.

Pandey, S. and Ramontja, J. 2016. Guar gum-grafted poly(acrylonitrile)-templated silica xerogel: Nanoengineered material for lead ion removal. J. Anal. Sci. Technol., 7(1): 24

Parlikar, A. S. and Mokashi, S.S. 2013. Defluoridation of water by *Moringa oleifera*- A natural adsorbent. Int. J. Eng. Sci. Innov. Technol., 2: 245-252.

Prasad, K.S., Amin, Y. and Selvaraj, K. 2014. Defluoridation using biomimetically synthesized nano zirconium chitosan composite: Kinetic and equilibrium studies. J. Hazard Mater., 276: 232-240.

Singh, V., Singh, P. and Singh, A. et al. 2015. Hg(II) adsorption by alginate-guar gum templated titania spheres: Kinetic and isotherm studies. Adv. Mater. Lett., 6: 664-669.

Sujana, M.G., Thakur, R.S. and Rao, S.B. 1998. Removal of fluoride from aqueous solution by using alum sludge. J. Colloid. Interface Sci., 206: 94-101.

Swain, S.K., Patnaik, T., Singh, V.K., Jha, U., Patel, R.K. and Dey, R.K. 2011. Kinetics, equilibrium and thermodynamic aspects of removal of fluoride from drinking water using meso-structured zirconium phosphate. Chem. Eng. J., 171: 1218-1226.

Teutli-Sequeira, A., Solache-Ríos, M., Martínez-Miranda, V. and Linares-Hernández, I. 2014. Comparison of aluminum modified natural materials in the removal of fluoride ions. J. Colloid Interface Sci., 418: 254-260.

Tirkey, P., Bhattacharya, T. and Chakraborty, S. 2018. Optimization of fluoride removal from aqueous solution using Jamun (*Syzygium cumini*) leaf ash. Process Saf. Environ. Prot., 115: 125-138.

Wu, X., Zhang, Y., Dou, X. and Yang, M. 2007. Fluoride removal performance of a novel Fe-Al-Ce trimetal oxide adsorbent. Chemosphere, 69: 1758-1764.

Xu, L., Chen, G. and Peng, C. et al. 2017. Adsorptive removal of fluoride from drinking water using porous starch loaded with common metal ions. Carbohydr. Polym., 160: 82-89.

Nature Environment and Pollution Technology
An International Quarterly Scientific Journal

p-ISSN: 0972-6268
e-ISSN: 2395-3454

Vol. 18 | No. 4 | pp. 1333-1338 | 2019

Original Research Paper | Open Access

Natural Background Gamma Radiation Levels in the Environs of Proposed Petro-chemical Industry Near Jadcherla, Telangana State, India

G. Srinivas Reddy*, K. Vinay Kumar Reddy, B. Linga Reddy** and B. Sreenivasa Reddy**†**
*Mahatma Gandhi Institute of Technology, Gandipet, Hyderabad-500075, India
**Chaitanya Bharathi Institute of Technology, Gandipet, Hyderabad-500075, India
†Corresponding author: B. Sreenivasa Reddy

Nat. Env. & Poll. Tech.
Website: www.neptjournal.com

Received: 31-05-2019
Accepted: 21-06-2019

Key Words:
Background radiation
Gamma radiation levels
Petrochemical industry
Radioactive dust

ABSTRACT

A survey of environmental gamma radiation levels is attempted in the geographical site under construction to establish a petrochemical industry. The knowledge of natural background radiation is one of the significant steps in establishing the chemical industry. Some chemical operations such as chemical refinement may sometimes influence the natural radiation levels. The attempt of measurement of natural background gamma levels in the present paper is to establish the baseline data, which on further measurements will be useful to analyse the changes in natural background radiation levels at the time of operation of a chemical plant. The present investigation shows the activity levels of gamma radiation in the site under construction at 65 locations. The gamma levels are found to vary from 1459 μGyy^{-1} to 2765 μGyy^{-1} with the average of 2141±304 μGyy^{-1}. It is to be noted from the study that the average gamma radiation levels at two sample locations, cement mixing point (2307 μGyy^{-1}) and stone crushing point (2529 μGyy-1) have been elevated. The elevated radiation levels at the two sample locations can be attributed to the radioactive dust emitted in the process of crushing stones and cement mixing.

INTRODUCTION

Natural background gamma radiation from natural sources and the exposure of human beings is a continuous and unavoidable feature. Earth cannot be without the presence of natural radionuclides, as they naturally exist in rocks and soil. The environmental gamma radiation dose from natural sources is the most significant and immediate concern to lead the situation of the radioactive pollutant environment (Spycher et al. 2015). The environmental gamma radiation levels vary in different regions and depend on factors like the radiation properties of soil and rock, natural properties of building construction materials, and the lifestyle of the dwellers (Nambi et al. 1986, UNSCEAR 1993, Dade 1996, Sreenivasa Reddy et al. 2005, Sreenath Reddy et al. 2010, Srinivas Reddy et al. 2015). Environmental gamma radiation is caused by radioactive elements with a long half-life, which exists in primary rocks of the earth's crust. This is caused by the decay of uranium and thorium as natural radioactive resources that pollute environmental resources of their surroundings (Kardan et al. 2013, Soltani et al. 2014).

There have been significant studies in the investigation of gamma radiation around the petrochemical industry for the analysis of the impact on the radioactive pollution due to the different operations of producing the petrochemical products (Mansour et al. 2012, Emelue et al. 2014). The process of production in petrochemical industry may cause the generation of naturally occurring radioactive materials. The contamination of radionuclide with petroleum and natural gases will be the source for gamma radiation (UNSCEAR 2000). In addition, gamma radiation is used as a nuclear diagnostic technique to investigate the distillation columns in petrochemical industry (Vernal et al. 2003). A very few studies were carried out on the dose received by the workers in petrochemical industries unlike ordinary dwellings and mining environs (Smith et al. 2003, Avwiri & Agbalagba 2012, Samad et al. 2017). In the present study, the environmental gamma radiation levels at various sample locations that are under construction for chemical industry have been worked out. The interest in the present investigation is to establish the baseline data of natural background gamma radiation levels at different zones of the proposed area under construction for petro-chemical industry. There may be fluctuations in natural gamma radiation levels due to the influence of chemical operations carried out in the industry in the future. The baseline data established in the present investigation will be useful for the analysis of radioactive pollution levels, if any, at the time of plant operation.

MATERIALS AND METHODS

Study Area: The present study was carried out in the

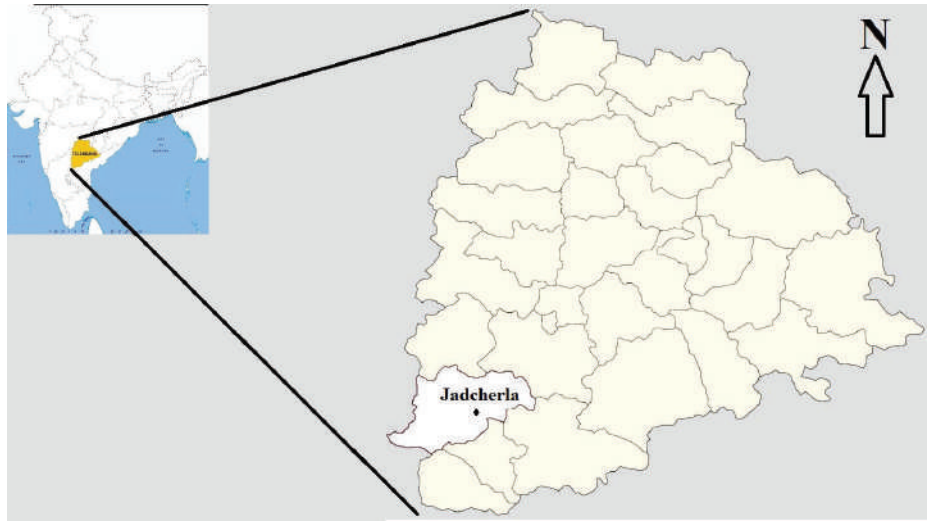

Fig. 1: Location map in Jadcherla of Mahabubnagar district, Telangana state, India.

Table 1: Estimated natural background gamma radiation levels at different locations.

Location	Natural background gamma radiation levels (μGyy^{-1})	Location	Natural background gamma radiation levels (μGyy^{-1})	Location	Natural background gamma radiation levels (μGyy^{-1})
S1	2419	S24	2227	S47	2035
S2	2342	S25	2227	S48	2035
S3	2496	S26	2112	S49	1728
S4	2304	S27	2150	S50	1766
S5	2381	S28	2150	S51	1651
S6	2342	S29	2189	S52	1690
S7	2304	S30	2381	S53	1728
S8	1882	S31	2573	S54	1958
S9	2266	S32	2688	S55	1459
S10	2342	S33	2688	S56	1574
S11	2304	S34	2304	S57	1574
S12	2074	S35	2227	S58	1958
S13	2074	S36	2419	S59	1958
S14	1997	S37	2611	S60	1997
S15	2035	S38	2458	S61	1805
S16	2150	S39	2496	S62	1843
S17	2150	S40	2419	S63	1882
S18	2074	S41	2650	S64	1920
S19	2150	S42	2726	S65	1920
S20	2189	S43	2765	Min	1459
S21	2112	S44	1766	Max	2765
S22	2150	S45	1766	Average	2141
S23	2112	S46	2035	S.D.	304

area located at 2 km distance from Jadcherla town in Mahabubnagar district of Telangana state, India and 90 km south-west from Hyderabad, the capital of the State. In 2011, Jadcherla was upgraded from village to town. It is a historical town known for its cultural heritage. Fig. 1 shows the study area of natural background radiation levels in a proposed petrochemical industry, which is in the initial stage of construction.

Measurement of radiations: Measurements of radiation were made at 65 number of sample locations selected randomly by covering most of the places in geographical site under construction for this study. A portable NaI crystal based μR-survey meter (Ms. Nucleonix Systems Limited, Hyderabad make) type UR705 and measures gamma dose-rate in the range of 1 μR/h to 9999 μR/h was employed in the present investigation. This portable survey meter, designed around integrally coupled 1″ × 1″ NaI (Tl) scintillator to a 1 1/2″ PMT, will offer an optimum performance in counting low-level gamma radiation dose rate. This unit can measure and display dose rates in the range of 0-10000 μR/hr on a dot matrix LCD Display. Dose rates close to natural background levels can be measured accurately. This unit is ideally suitable for radiometric and environmental radiation monitoring that involves low-level radiation dose rates.

The natural background gamma radiation levels were measured in two modes, (i) at the ground level and (ii) at a height of one metre from ground level at each sampling location. The data depicted in figures and tables is mean value of the both the readings. The data were acquired during day time in the outdoor environment. The diurnal variations in the gamma radiation levels were not considered. The exposure rates were converted into equivalent doses using the appropriate conversion factors (UNSCEAR 2000). The calibration of the survey meter is carried out at Ms. Nucleonix Systems Limited, Cherlapally, Hyderabad. It is also established earlier by our research group that the results of

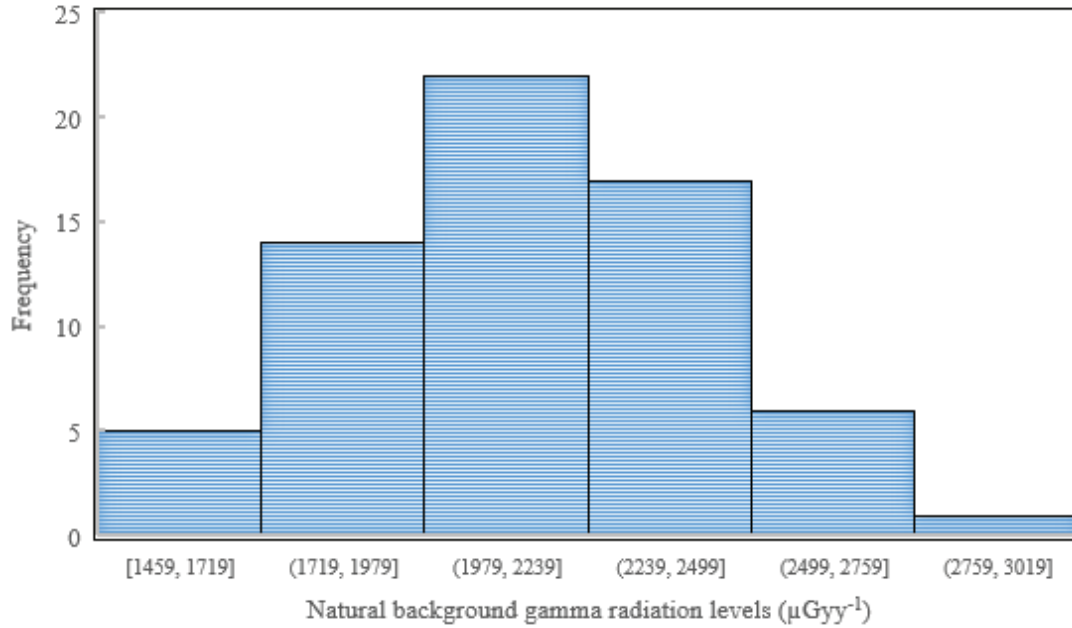

Fig. 2: Frequency distribution of natural background gamma radiation levels.

Table 2: The natural background gamma levels at different zones.

	Cement mixing point (μGyy^{-1})	Sand storage point (μGyy^{-1})	Granite storage point (μGyy^{-1})	Stone Crushing point (μGyy^{-1})	Other location points (μGyy^{-1})
Number of measurements	11	7	11	14	22
Min	1882	1997	2112	2227	1459
Max	2496	2150	2227	2765	2035
STD	155	56	42	167	165

natural background gamma radiation levels estimated by using μR-survey meter are in good agreement with data obtained by thermoluminescence dosimeters TLDs (Sreenivasa Reddy et al. 2002, 2005).

RESULTS AND DISCUSSION

The estimation of natural background gamma radiation levels was carried out at 65 locations of geographical site under construction for a petrochemical industry. The estimated average levels of environmental gamma radiation are given in Table 1. The natural background radiation levels were found to vary from 1459 μGyy^{-1} to 2765 μGyy^{-1} with the average of 2141 μGyy^{-1}. Fig. 2 depicts the frequency of occurrence of the range of the values obtained in the series of measurements of natural background gamma radiation at various locations in the study area. Frequency of occurrence of recorded values under the interval of 260 μGyy^{-1} almost obeys normal distribution. The range of recorded values of gamma data is quantified from 1719 μGyy^{-1} to 2499 μGyy^{-1} is about 82% of the total number of measurements in the study area.

The locations are categorized into 5 different zones based on the present utilization; i. Cement mixing point (S01 to S11), ii. Sand storage point (S12 to S18) where the sand for construction is stored, iii. Granite storage point (S19 to S28) where granite is stored, iv. Stone crushing point (S29 to S42) where heavy stones are being crushed into small granite pieces for construction, v. other points (S43 to S65) where buildings of various sections of chemical plantation are being built. The parameters of estimation for gamma radiation levels like number of measurements, range of measurements and standard deviation made at each sample zone under study area are given in Table 2.

The average natural background gamma levels at different zones in proposed study area are shown in the Fig. 3. The elevated mean environmental radiation levels were found to be 2529 μGyy^{-1} at the sample location zone of stone crushing point. The elevated levels of gamma radiation, recorded in this zone, can be due to environmental gamma dose rate significantly contributed by the contamination of the dust particles produced in the process of crushing the granite stones with radionuclides. The decrease in the density of dust particles spreading away in the air flow may attribute to the significant variation of environmental gamma dose rate from the point of crushing. This result is in consistence with the one observed elsewhere (Tejado et al. 2016, Silvana et al. 2018). The elevated natural background radiation

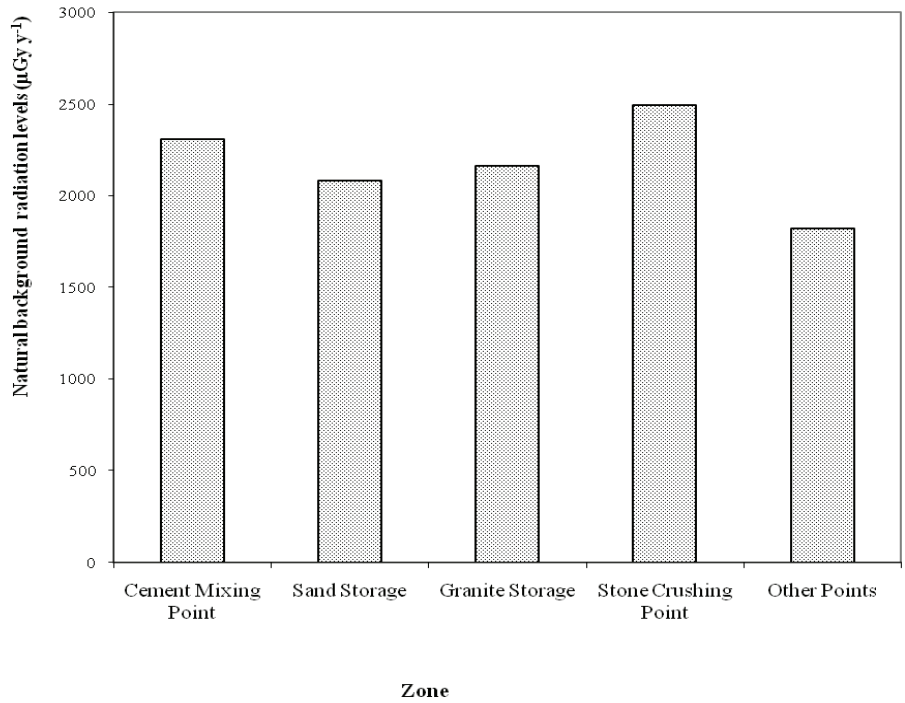

Fig. 3: Variation of natural background radiation levels at different zones.

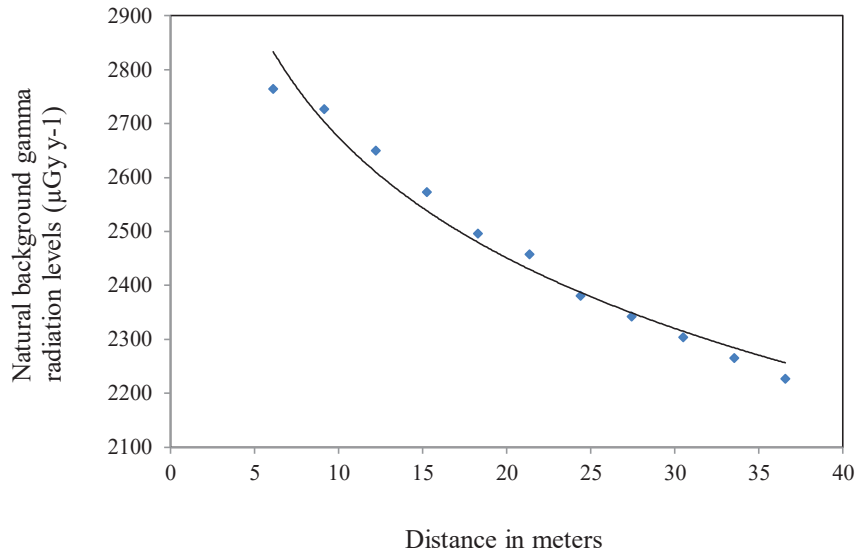

Fig. 4: Variation of natural background gamma radiation levels with distance from stone crushing point.

levels at cement mixing point can be attributed to the fly ash, which is the hoist for the elevated concentrations of natural radioactive elements.

A modest attempt has been made to see the variation of natural background radiation levels at different distances from the stone crushing point. Fig. 4 represents the variation of natural background radiation levels at different distances from stone crushing point. It depicts that the natural background radiation levels decrease as the distance increases. This indicates that the radiation levels were observed to be elevated at stone crushing point.

CONCLUSIONS

The variations of environmental gamma activity at a considerable level can be expected to be influenced by the various plant operations that involve in producing the petrochemical products. The gamma activity levels quantified in the present investigation can be a baseline data, which is of most significance to be considered in the process of establishment and construction of a plant of producing petrochemical products. The analysis of data established in the investigation is significantly useful information that can be considered in executing the further steps for the mitigation of environmental gamma dose at the time of the actual product activities being carried out in plant. In fact, the impact of meteorological conditions in the study area are not completely interpreted and quantified. It is necessary to explore the consideration of building characteristics and meteorological parameters through further investigation.

ACKNOWLEDGEMENTS

Authors thank Prof. K. Rama Reddy, Prof. P. Yadagiri Reddy and Prof. Ch. Gopal Reddy for their constant help and encouragement during the present study. Support rendered by Smt. D. Sandhyasree, Member, BoM, Chaitanya Bharathi Institute of Technology, Hyderabad during the field work is thankfully acknowledged. Authors also thank the Principal and Management of CBIT for their support at various stages of the present work.

REFERENCES

Avwiri, G.O. and Agbalagba, E.O. 2012. Studies on the radiological impact of oil and gas activities in Oil Mineral Lease 30 (Oml30) oil fields in Delta state, Nigeria. J. Pet. & Env. Biotech., 3: 115.

Dade, W. 1996. Radiation Sources: Natural Background Effects of Exposure to Low-Level Ionizing Radiation. LOP Publishing Ltd. UK, pp. 15-35

Emelue, H.U., Jibiri, N.N. and Eke, B.C. 2014. Excess lifetime cancer risk due to gamma radiation in and around Warri refining and petrochemical company in Niger Delta, Nigeria. British J. Med. & Med. Res., 4: 2590-2598.

Kardan, M.R., Amiri, M., Shabestani Monfared, A., Ashrafian Amiri, H., Tahamtan, R., Samani, F., Asadi, N. and Fahimi, Sh. 2013. Has Fukushima nuclear accident changed the local gamma rays level in Babol, Iran? J. Babol Univ. Med. Sci., 15: 108-111.

Mansour, A., Ahmed, T.S., Fayez-Hassan, M., Nabil, M. Hassan, Gomaa, M.A. and Ali, A. 2012. Measurements of radiation level around the location of NORM in solid wastes at petroleum companies in Egypt. J. Am. Sci., 8: 252-260.

Nambi, K.S.V., Bapat, V.N., David, M., Sundaram, V.K., Sunta, C.M. and Soman, S.D. 1986. Natural background radiation and population dose distribution in India. Health Physics Division, BARC Report.

Samad, A.I., Ahmed, A.H. and Ezzulddin, S.K. 2017. Assessment of nat-

ural radioactive concentration levels in the oil drilling wells in Erbil Governorate blocks. Jordan J. of Phys., 10: 23-32.

Silvana, Beltrán Torres, AttilaPetrik, Katalin ZsuzsannaSzabó, Gyozo Jordan, Jun Yao and Csaba Szabó 2018. Spatial relationship between the field-measured ambient gamma dose equivalent rate and geological conditions in a granitic area, Velence Hills, Hungary: An application of digital spatial analysis methods. J. Env. Radio., 192: 267-278

Smith, K.P., Arnish, J.J., Williams, G.P. and Blunt, D.L. 2003. Assessment of the disposal of radioactive petroleum industry waste in nonhazardous landfills using risk-based modeling. Environ. Sci. Technol., 37: 2060-2066.

Soltani, A., Safarzadeh, A., Shabestani, M.A. and Amiri, M. 2014. The estimation of annual per capita effective dose from nuclear medicine procedures in Iran. J. Babol Univ. of Med. Sci., 16: 20-24.

Spycher, B.D., Lupatsch, J.E., Zwahlen, M., Röösli, M., Niggli, F., Grotzer, M.A., Rischewski, J., Egger, M. and Kuehni, C.E. 2015. Background ionizing radiation and the risk of childhood cancer: a census-based nationwide cohort study. Environ. Health Perspect., 123: 622-628.

Sreenath Reddy, M., Gopal Reddy, Ch., Yadagiri Reddy, P. and Rama Reddy, K. 2010. Study of natural background gamma radiation levels in Hyderabad and its surroundings, Andhra Pradesh, India. Ind. J. Pure & App. Phys., 48: 778-781.

Sreenivasa Reddy, B., Gopal Reddy, Ch., Yadagiri Reddy, P. and Rama Reddy, K. 2005. Estimation of natural background gamma radiation levels in dwellings of Khammam District, Andhra Pradesh, India. Rad. Prot. Environ., 28: 301-303.

Sreenivasa Reddy, B., Yadagiri Reddy, P. and Rama Reddy, K. 2002. Natural back ground radiation levels in the environment: Urban Khammam environs-A case study. Environ. Geochem., 5: 13-16.

Srinivas Reddy, G., Vinay Kumar Reddy, K., Sreenivasa Reddy, B., Gopal Reddy , Ch., Yadagiri Reddy, P. and Rama Reddy, K. 2015. Preliminary investigation on natural background radiation levels in and around Karimnagar, Telangana State, India. Science & Tech., 1: 80-83.

Tejado, J. J., Guillén, J. and Baeza, A. 2016. Assessment of occupational exposure in a granite quarry and processing factory. J. Radiol. Prot., 36: 641-652.

UNSCEAR 1993. United Nations Scientific Committee on the Effects of Atomic Radiation, Ionizing Radiation: Source and Effects of Ionizing Radiation. United Nations, New York.

UNSCEAR 2000. United Nations Scientific Committee on the Effects of Atomic Radiation, Ionizing Radiation: Source and Effects of Ionizing Radiation. United Nations, New York.

Vernal, L., Mauricio, Diaz, V. F. and Duran, P. 2003. Oscar. III Scientific meeting of Chilean Nuclear Energy Commission.

Nature Environment and Pollution Technology
An International Quarterly Scientific Journal

p-ISSN: 0972-6268 e-ISSN: 2395-3454	Vol. 18	No. 4	pp. 1339-1347	2019

Original Research Paper | Open Access

Study on Site Quality Assessment of Afforestation Land Based on GA-RBF Neural Network

Chen Yuling, Wang Chengde, Wu Baoguo† and Liu Jiancheng
School of Information Science and Technology, Beijing Forestry University, Beijing 100083, China
†Corresponding author: Wu Baoguo

Nat. Env. & Poll. Tech.
Website: www.neptjournal.com

Received: 19-01-2019
Accepted: 08-04-2019

Key Words:
Site quality assessment
Chinese fir plantation
Afforestation land
GA-RBF neural network
Forest management

ABSTRACT

The assessment of forest site quality at early stages of stand development is very essential for scientific afforestation and forest management. In order to enhance the accuracy of the existing models, a new site quality assessment model based on Genetic Algorithm-Radial Basis Function (GA-RBF) was proposed to predict site index (stand dominant height). Data used in this study came from 980 permanent sample plots for Chinese fir (*Cunninghamia lanceolata*) plantations in Fujian Province, China, which were randomly divided into the training dataset (786 plots) and the testing dataset (194 plots) with a ratio of 8:2. In this paper, the GA-RBF was compared with the radial basis function (RBF) and the traditional Quantitative Theory I (QT-I) method. The results indicated that the predicted accuracy was significantly increased by using the GA-RBF model. Furthermore, we used the existing site-specific site index table of Chinese fir to test the results of the GA-RBF and the agreement was 73.2%. Therefore, we recommend the GA-RBF for assessing site quality of afforestation land.

INTRODUCTION

Site quality assessment of afforestation land at early stages of stand development is very essential for scientific afforestation and forest management (Guo 2014, Bueis et al. 2016, Dau 2018). Site index (stand dominant height at a reference age, SI) is an important indicator to evaluate site quality and widely used because it strongly correlates to forest growth and yield (Mamo & Sterba 2006, McDill & Amateis 1992, Sharma 2017, Gonzalez-Benecke et al. 2017). Many researchers developed the dominant height model for forested land based on forest stand factors such as tree dominant height and tree age (Carmean 1975, Green 1989, Nothdurft et al. 2012, Yue et al. 2014, João 2017). However, forest site quality is usually estimated using site and stand factors, many studies examined the relationships between SI and site factors such as climate (Carlos 2017, Héctor 2018, Jiang et al. 2015, Mark 2017, Gonzalez-Benecke 2015), soil (Amuakwa-Mensah 2016, Rafael 2016) and topography (Stage & Salas 2007, Mitsuda & Ito 2015, Rafael 2016). Earlier attempts adopted a Quantitative Theory I (QT-I) method for both forested land and afforestation land (Chi 1995, Yang 2004). Due to the nonlinear and complex relationship between site factors, the estimation of QT-I may have biased estimation and low prediction accuracy. The artificial neural network (ANN) machine learning algorithm is easy to estimate the nonlinear relationship, and has the characteristics of fault tolerance, self-learning and self-adaptability. In forestry research, some studies have been performed and many different machine learning algorithms proposed. Huang (2006) and Gong (2013) used back propagation (BP) neural network model to evaluate the afforestation land. But the weaknesses of slow convergence speed, unstable fitting results and over-fitting of potential data, BP neural network have been rarely applied to site quality assessment of afforestation practice, making the traditional method always occupy a dominant position (Guo 2014). To solve the above problems, this paper introduced the Radial basis neural network (RBF) to improve. RBF, which takes the radial basis function as the basis of hidden layer neurons, has the advantages of strong generalization ability, fast learning convergence, and less computation. However, RBF is prone to fall into the local optimal solution (Yingwei 1998, Xiong 2015), while genetic algorithm as an optimization method imitating the biological evolution process has the ability to search for the global optimal solution (Maillard 1999, Cook 2000, Wu 2015). Genetic Algorithm-Radial Basis Function (GA-RBF) can combine the advantages of RBF and GA. The GA-RBF has not been used to derive the site quality assessment model.

The objective of this study was to develop a site quality assessment model to estimate SI for Chinese fir in Fujian Province using the GA-RBF.

MATERIALS AND METHODS

Data

Data for this study were collected from 980 National Forest

Inventory (NFI) permanent sample plots for Chinese fir plantations in the central and western Fujian Province. The data were randomly divided into the training dataset (786 plots) and the testing dataset (194 plots) with a ratio of 8:2. For each plot, the site measurement factors (Table 1) included landform (DM), elevation (HB), aspect (PX), slope (PD), slope position (PW), soil type (TRMC) and soil thickness (TCHD). The stand measurement factors included dominant species, stand age, stand height (HT) and stand diameter at breast height (DBH).

Due to the measurement of stand dominant height (HTT) was not included in the NFI plots. For site quality assessment, the HTT can more accurately reflect the production potential of sample plots. Therefore, we established 132 temporary sample plots to derive the HTT and the equation developed was: HTT = 3.048+0.932*HT (R^2 = 0.967).

Table1: The site overview of NFI permanent sample plots.

Site Factors	Description
DM	Middle Mountain; Low Mountain; Hills
PX	South, Southeast, Southwest, North, Northwest, Northeast, East, West
PW	Ridge; Uphill; Middle Slope; Downhill; Valley
PD (°)	4 (minimum), 49 (maximum),27 (mean), 7 (standard deviation)
HB (m)	41(minimum), 1114 (maximum), 443(mean), 90(standard deviation)
TRMC	Yellow Soil; Red Soil; Yellow-Red Soil
TCHD (cm)	10 (minimum), 250 (maximum), 98(mean), 20(standard deviation)

Note: DM is the landform; PX is the aspect; PW is the slope position; PD is the slope; HB is the elevation; TRMC is the soil type; TCHD is the soil thickness.

Methods

Quantitative Theory I (QT-I) Model

The site quality evaluation of afforestation land can be speculated by the forestland with the same characteristics of site factors. Quantitative Theory I (QT-I) Model is multiple regression analysis scheme for deducing the relationship between a quantitative variable and qualitative variables. In this study, the site factors were quantified by dummy variable method. Taking the dominant average height as dependent variables and the site factors and the corresponding age as independent variables, the quantitative theory I model was established (Li 2009) as follows:

$$y_t = \sum_{i=1}^{m} \sum_{j=1}^{k} X_t(i,j) b_{ij} + b_0 \mathrm{A} + \varepsilon_i \quad \ldots(1)$$

Where, y_t denotes the stand dominant height from the plot t; $X_t(i,j)$ denotes the j^{th} categorical observation of the i^{th} site factor from the plot t; A is the stand age; b_{ij} is the coefficient of the $Xt(i,j)$; b_0 is the coefficient of the A; m is the number of site factors; k is the categorical index; and ε_i is an error term.

The entire manipulation procedure, including four steps, is described as follows:

Step 1: Initially, dummy variables were generated according to the categories of site factors. Data were divided into the training dataset (786 plots) and the testing dataset (194 plots) with a ratio of 8:2.

Step 2: The prediction equation of dominant height was developed based on the Equation 1 using the training dataset. Furthermore, the quantitative scoring table of site factors was derived.

Step 3: In order to scientifically and objectively evaluate the reliability of the prediction result based on the QT-I model, a *t*-test was conducted for the complex correlation coefficient and partial correlation coefficient of the equation.

Step 4: The standard age (20-year) of Chinese fir was substituted into the estimated Equation 1 to obtain the prediction of dominant height. Furthermore, the testing dataset was used to verify the accuracy.

Radial Basis Function (RBF) Neural Network Model

Radial Basis Function (RBF) used as the transformation function of the hidden layer of the neural network is a forward-looking neural network, which generally has three layers of network structure. RBF is not a global response function but a local response function, and is a non-negative linear function with radial symmetry and attenuation at the centre point (Fu 2017). The structure of RBF neural network is shown in Fig. 1.

Generally, the activation function of RBF can be expressed as Equation 2. In this study, self-organizing centre selection learning method was used to evaluate the quality of afforestation land. Gauss function (equation 3) was used as the RBF model.

$$R(dist) = e^{-\gamma dist^2} \quad \ldots(2)$$

Where *dist* is the distance between the input vector x and the classification node c_i, i.e. $dist = x\text{-}c_i$.

$$R(x_p - c_i) = exp\left(-\frac{1}{2\sigma^2}\|x_p - c_i\|^2\right) \quad \ldots(3)$$

Where $\|x_p - c_i\|$ is the Euclidean norm; c_i is the centre of Gaussian function; σ is the variance of Gaussian function.

Firstly, the RBF neural network which organizes the relationship between site factor and tree height is an unsupervised learning. By learning, the network can solve the

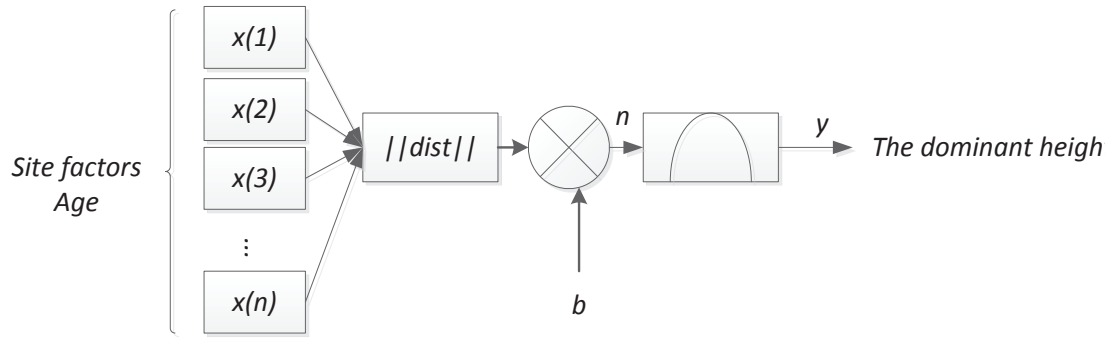

Fig. 1: The structure of RBF neural network.

centre and variance of the underlying layer basis function and determine the learning quantity. Secondly, the network was put into the process of supervised learning. The weight between the hidden layer and the output layer was obtained according to the centre and variance of the hidden layer basis function. The output expression of corresponding network can be expressed as Equation 4.

$$y_j = \sum_{i=1}^{h} \omega_{ij} exp\left(-\frac{1}{2\sigma^2} \| x_p - c_i \|^2 \right) \qquad j = 1,2,3,\ldots,n \quad \ldots(4)$$

$$\sigma = \frac{1}{P} \sum_{j}^{m} \| d_j - y_j c_i \|^2 \qquad \ldots(5)$$

Where, y_j is the jth output node of the network. The vector $x_p = \left(x_1^p, x_2^p, x_3^p, \ldots, x_m^p \right)^T$ is the pth (p=1,2,3...,N) input sample, and it represents the vector of the site factor from each plot. N is the total number of samples. c_i is the centre of network hidden layer node. w_{ij} (i=1,2,3,...,h) is the connection weight from the hidden layer to the output layer. i represents the node sequence of the hidden layer and h is the number of nodes in the hidden layer. If d is the expected output of the sample, the variance of the basis function can be expressed as Equation 5.

The entire manipulation procedure of RBF neural network, including seven steps, is described as follows:

Step 1: The site and stand factors were input for unsupervised learning, and the base function centre c was obtained based on the K-means clustering method.

Step 2: Initially, the h nodes were randomly selected from the input data as clustering centres c_i (i=1, 2, 3,..., h).

Step 3: The training dataset was grouped according to the nearest rule. The site factor vector x_p was distributed to each cluster set $\vartheta_p \left(p = 1,2,3,\ldots,P \right)$ of the input sample according to the Euclidean distance between the site factor vector x_p and the K-means clustering centre c_i.

Step 4: The clustering centre was simultaneously readjusted based on the learning situation to calculate the new clustering centre ci of training samples in all clustering sets ϑ_p. If the new clustering centre was not changed, the c_i obtained was the ultimate basis function centre of RBF. Otherwise, the Step 2 was carried out to select the clustering centre c_i again.

Step 5: The equation 5 was used to solve the variance σ_i of Gauss function (basis function). The expression of σ_i can be expressed as Equation 6.

$$\sigma_i = \frac{c_{\max}}{\sqrt{2h}} \qquad i = 1,2,3,\ldots,h \qquad \ldots(6)$$

Where $\boldsymbol{c_{max}}$ is the maximum distance of the selected centres.

Step 6: The neuron connection weight (Equation 7) between the hidden layer and the output layer was calculated by the least squares framework.

$$\omega = \exp\left(\frac{h}{c_{\max}^2} \| x_p - c_i \|^2 \right) \quad i = 1,2,3,\ldots,h; p = 1,2,3,\ldots,P \quad \ldots(7)$$

Step 7. After learning, the results of SI were obtained based on the input of site factors and the stand age.

Genetic Algorithm-Radial Basis Function (GA-RBF) Model

Genetic algorithm is a parallel and stochastic search optimization method used to simulate biological evolution process by computer technology (Liu 2013). After the initial population was set, the GA optimizes through the population search strategy and covers many individual situations in the process of inheritance, crossover and mutation (Xie 2014). In this paper, GA was applied to optimize the learning parameters of RBF model such as centre value, width of base function and connection weight between the hidden layer and the output layer. A modified Genetic Algo-

rithm-Radial Basis Function (GA-RBF) model was applied to the study of the site quality assessment of afforestation land. The optimization process of GA-RBF includes population initialization, fitness function, selection operation, cross operation and mutation operation. The entire algorithm procedure is shown in Fig. 2.

Model Evaluation

In this paper, three different strategies (the QT-I, the RBF and the GA-RBF) were compared to select the optimal one. Furthermore, the existing SI tables of Chinese fir in Fujian were used to test the accuracy of prediction. The tables were divided into three grades: Low level (SI is between 8 and 12), Medium level (SI is between 14 and 18), and High level (SI is between 20 and 22). Mean deviation (MEP), mean squared error (MSEP) and mean absolute deviation (MAEP) were used to evaluate the performance. The model that had the smallest MEP, MSEP and MAEP performed best. The functions are shown as Equations (8)-(10).

$$MEP = \sum_{i=1}^{n} \frac{y_i - \hat{y}_i}{n} \quad \ldots(8)$$

$$MSEP = \sum_{i=1}^{n} \frac{(y_i - \hat{y}_i)^2}{n} \quad \ldots(9)$$

$$MSEP = \sum_{i=1}^{n} \frac{|y_i - \hat{y}_i|}{n} \quad \ldots(10)$$

Where, y_i is the observation of the i^{th} plot; $\hat{y}_i$ is the predicted value of i^{th} observation; n is the number of plots; $\bar{y}_i$ is the mean value of the observation.

RESULTS

Analysis of QT-I Model

The items of site factors were quantified and expressed by matrix expression $X*b=Y$. Where, X was the data matrix of site factors and age, also the criterion variable independent variables; Y was the dominant height matrix; b was the score value. The score values of various items estimated by the MATLAB are given in Table 2.

The maximum score value was 2.221534 when the dummy variable of HB was higher than 500. For category X2 the score value of DM increased with terrain declining. For category X3 the dummy variable Sunny-Slope had the maximum score value. For category X4, score values were higher when the slope is smaller. For category X5, the result demonstrated a negative correlation between the slope position and the score value. For the soil thickness factor, the score value increased with the increase of the soil thickness. And the score value of red soil in category X7 was the maximum. Among the seven site factors, the higher score factor was elevation, soil thickness and landform, which indicated that the site factors correlated to forest tree could be determined by the score values of various categories. We concluded that the site conditions such as elevation higher than 500 m, hilly landform, sunny slope, steep slope 15-25, valley of slope, soil thickness > =80, and red soil were more conducive to the Chinese fir. The conclusions were consistent with the actual afforestation experiences.

The standard age (20-year) of Chinese fir in Fujian Province was introduced into the prediction equation of the dominant height, and the SI model was obtained:

SI = 2.148271 * X11 + 2.016107 * X12 + 2.221534 * X 13 + 0.367009 * X22 + 0.437051 * X23 - 0.06996 * X31 + 0.24483 * X32 + 0.75086 * X42 + 0.692169 * X43 - 0.57385 * X51 - 1.71536 * X52 - 0.8834 * X53 - 0.72789 * X54 + 0.759626 * X62 + 2.162782 * X63 + 1.53225 * X71 - 0.10188 * X73 + 6.73746 …(11)

The model was further evaluated by correlation matrix, complex correlation coefficient, partial correlation coeffi-

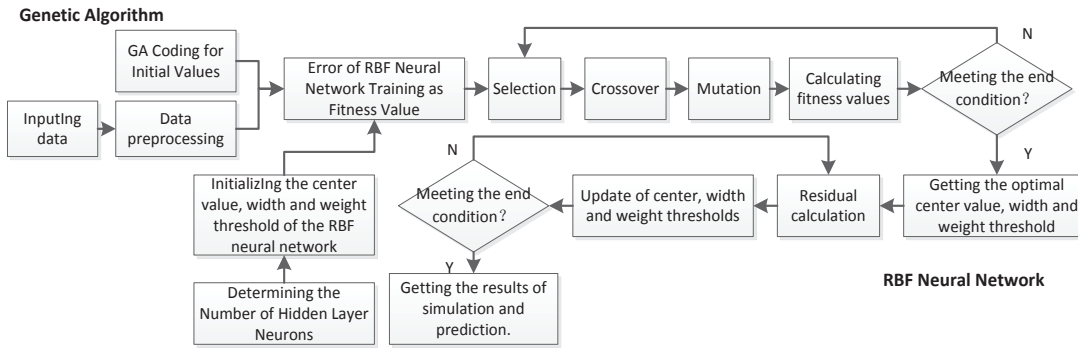

Fig. 2: Entire algorithm procedure of GA-RBF.

Table 2: The quantified scores of site factors.

Item variables	Dummy Variables	Categories	Parameters	Score Values
HB(X1)	<=300	X11	b11	2.148271
	300-500	X12	b12	2.016107
	>=500	X13	b13	2.221534
DM(X2)	Middle-Mountain	X21	b21	0
	Low-Mountain	X22	b22	0.367009
	Hills	X23	b23	0.437051
PX(X3)	Shady-Slope (north, northwest, northeast)	X31	b31	-0.06996
	Sunny-Slope (south, southeast, southwest)	X32	b32	0.24483
	Half-Sunny-Slope (east, west)	X33	b33	0
PD(X4)	Gentle-Slope <=15	X41	b41	0
	Steep-Slope 15-25	X42	b42	0.75086
	Incline >=25	X43	b43	0.692169
PW(X5)	Ridge	X51	b51	-0.57385
	Uphill	X52	b52	-1.71536
	Middle-Slope	X53	b53	-0.8834
	Downhill	X54	b54	-0.72789
	Valley	X55	b55	0
TRHD(X6)	Thin<=40	X61	b61	0
	Middle 40-80	X62	b62	0.759626
	Thick >=80	X63	b63	2.162782
TRMC(X7)	Red-Soil	X71	b71	1.53225
	Yellow-Red-Soil	X73	b73	-0.10188
	Yellow-Soil	X76	b76	0
A	-	A	b0	0.336873

Table 3: Correlation matrix of 7 site factors.

	HTT	HB	PD	PW	TRHD	TRMC	DM	PX
HTT	1	-0.06436	-0.12558	0.230546	0.090517	-0.14277	0.147322	-0.0393
HB	-0.06436	1	0.202681	-0.15513	-0.35159	0.514141	-0.78383	0.070276
PD	-0.12558	0.202681	1	-0.02356	-0.14961	0.215486	-0.17755	0.021609
PW	0.230546	-0.15513	-0.02356	1	0.051953	-0.07262	0.085855	-0.10104
TRHD	0.090517	-0.35159	-0.14961	0.051953	1	-0.3302	0.322621	0.077797
TRMC	-0.14277	0.514141	0.215486	-0.07262	-0.3302	1	-0.38228	0.045046
DM	0.147322	-0.78383	-0.17755	0.085855	0.322621	-0.38228	1	-0.13762
PX	-0.0393	0.070276	0.021609	-0.10104	0.077797	0.045046	-0.13762	1

cient and *t*-test. From the correlation matrix (Table 3), the higher correlations between the dominant height and the site factors were the slope position, topography and soil thickness. And the correlation between the elevation and soil type of was the highest value of 0.514141.

The complex correlation coefficient was calculated, indicating that the dominant height of Chinese fir had a correlation degree of 0.6354 with 7 site factors and stand age. The complex correlation coefficient demonstrated that the site factor and stand age had effects on the dominant height growth. The partial correlation coefficients between each site factor and the dominant height and their significance test results at a 95% confidence interval are given in Table 4. According to the partial correlation coefficient, the importance of influencing the site quality was as follows: HB (elevation), DM (landform) and PW (slope position).

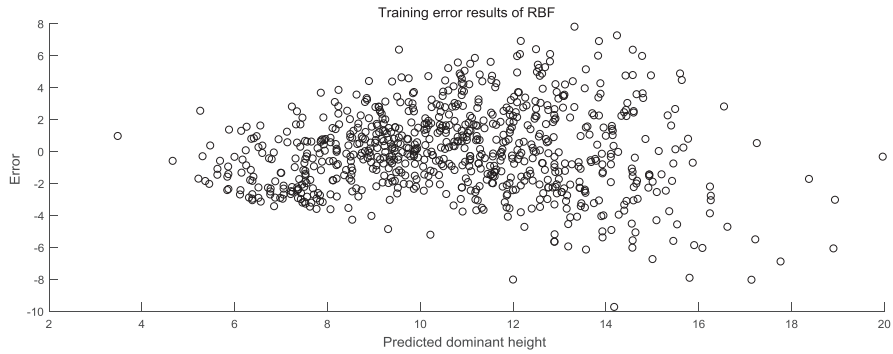

Fig. 3: Training error results of RBF neural network.

Table 4: The results of partial correlations.

Site factor	Correlation coefficient	P value
HB	0.171	0.019
DM	0.175	0.017
PX	0.009	0.908
PD	-0.098	0.183
PW	0.241	0.001
TRHD	0.029	0.691
TRMC	-0.122	0.096

Analysis of RBF Neural Network Model

The training dataset (786 plots) were used to establish the RBF model and the testing dataset (194 plots) were used to evaluate the accuracy. Twenty four notes in the input layer and 1 node in the output layer were obtained after processing of the 7 site factors through dummy variable method. The function established by the RBF neural network model was:

rbfnet=newrb (Input,Output,Goal,Spread,MN,DF) …(12)

Where the goal of network learning *goal=0.03*, the spread speed of radial basis function *spread*=1.1, the maximum number of neurons in RBF network *MN*=600, and the output interval of network *DF*=50. The target error MSE of 0.03 was achieved after 485 training sessions and the training error results are shown in Fig. 3. Results indicated that the RBF neural had better performed.

The RBF network was optimized by genetic algorithm. The parameters were set as population size of 10, evolution times of 50, crossover probability of 0.4, and mutation probability of 0.2. The GARBF neural network training results is shown in Fig. 4.

Model Evaluation

In this study, three models of QT-I model, RBF neural network and GA-RBF neural network were used to predict the dominant height according to the testing dataset. The predicted results are shown in Fig. 5. We concluded that the predicted output of RBF and GARBF were more precise than that of QT-I. The evaluation indexes of three models are given in Table 5. The GA-RBF neural network model

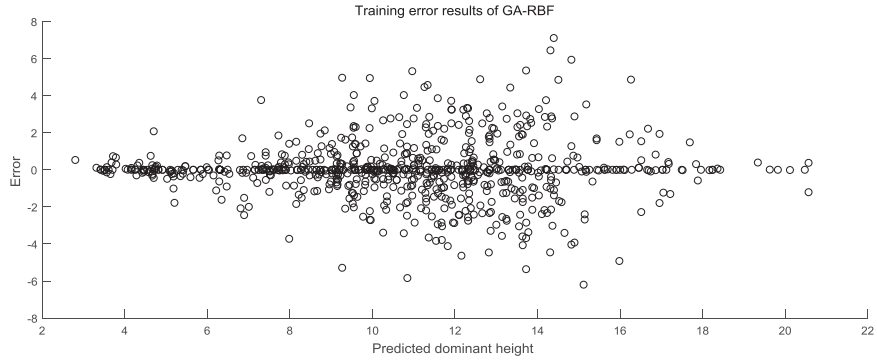

Fig. 4: Training error results of GA-RBF neural network.

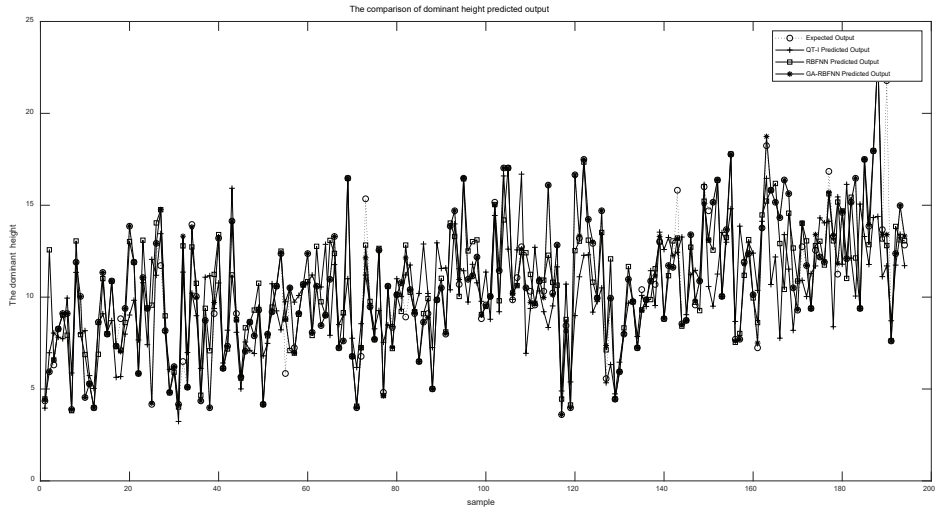

Fig. 5: The predicted results of different models.

Table 5: The evaluation indexes of three models.

Statistical indicator	QT-I Model	RBFNN Model	GA-RBFNN Model
MEP	0.3623	-3.6083E-11	2.57732E-11
MAEP	2.15783	1.50993	0.26643
MSEP	8.13933	4.69731	0.93643

Table 6: The SI evaluation results of different models.

Model	Total plot	Consistency	Inconsistency	Consistency rate
QT-I	194	89	105	45.88%
RBFNN	194	100	94	51.55%
GA-RBFNN	194	142	52	73.20%

had the smallest MEP, MSEP and MAEP and performed best.

Site Quality Assessment Result of Afforestation Land

The site quality of 194 sample plots in the testing dataset was evaluated. Firstly, the site evaluation results obtained by the standard index table of Chinese fir were used to compare the QT-I model and the RBF neural network model. The results shown in Table 6 indicated that the GA-RBF neural network model had the highest consistency of 73.20%. The GA-RBF model provided a feasible site quality evaluation strategy for afforestation land when tree species was without SI table.

DISCUSSION AND CONCLUSIONS

In this study, the dominant model of afforestation land for Chinese fir plantations was developed by three strategies such as QT-I, RBF neural network and GA-RBF model. It was shown that the GA-RBF had a high consistency with SI table and proposed to predict stand dominant height. Because of the nonlinear and complex relationships between site factors, machine learning of nonlinear branches was used to simulate the non-linear relationship with strong adaptability and flexibility. BP neural network algorithm was used to achieve site quality evaluation (Huang 2006, Gong 2013). However, because of the instability of SI prediction model based on BP neural network, traditional QT-I method has been used in afforestation practice, and the RBF neural network model developed in this paper overcame the defect of the BP neural network. Furthermore, aiming at the problem that RBF was prone to fall into the local optimal solution, the model of RBF neural network was improved by genetic algorithm with better global search ability. The

study showed that GA-RBF neural network model was better to evaluate the site quality of forestland.

It should be pointed out that the optimization of GA-RBF in this paper only showed the centre value of the hidden layer, the width of the base function and the connection weight of the hidden layer to the output layer. The optimization of the number of neurons in the hidden layer will be studied for further study. And other intelligent optimization algorithms such as simulated annealing algorithm (SA), particle swarm optimization (PSO) could also prevent falling into the local optimal solution. Whether these algorithms can further improve the prediction accuracy of the model to improve the applicability of machine learning methods in the evaluation of site quality of afforestation land will be explored.

ACKNOWLEDGMENT

This study was funded by the National Key Research and Development Program of China (Project No. 2017YFD0600906). The authors would also like to thank the reviewers for their comments, which were helpful in improving the manuscript.

REFERENCES

Amuakwa-Mensah, F. and Gren, I. M. 2016. Fungi diversity in Swedish forests: Impact of site quality on standing volume and variability in forest growth. Scandinavian Society of Forest Economics Drøbak, Norway, May, 2016, pp.76.

Bahamonde, H.A., Lencinas, M.V., Pastur, G.M., Monelos, L., Soler, R. and Peri, P.L. 2018. Ten years of seed production and establishment of regeneration measurements in Nothofagus antarctica forests under different crown cover and quality sites, in Southern Patagonia. Agroforestry Systems, 92(3): 623-635.

Bueis, T., Bravo, F., Pando, V. and Turrión, M.B. 2016. Relationship between environmental parameters and *Pinus sylvestris* L. site index in forest plantations in northern Spain acidic plateau. iForest-Biogeosciences and Forestry, 9(3): 394.

Carmean, W. H. 1975. Forest Site Quality Evaluation in the United States. Advances in Agronomy. Academic Press, 27: 209-269.

Carrijo, J.V.N., Miguel, E.P., Rezende, A.V., de Oliveira Gaspar, R., Martins, I.S. and de Meira, M.S. 2017. Morphometric indexes and dendrometric measures for classification of forest sites of '*Eucalyptus urophylla*' stands. Australian Journal of Crop Science, 11(9): 1146.

Castle, M., Weiskittel, A., Wagner, R., Ducey, M., Frank, J. and Pelletier, G. 2017. Variation in stem form and risk of four commercially important hardwood species in the Acadian Forest: Implications for potential saw log volume and tree classification systems. Canadian Journal of Forest Research, 47(11): 1457-1467.

Chen, S., Wu, Y. and Luk, B. L. 1999. Combined genetic algorithm optimization and regularized orthogonal least squares learning for radial basis function networks. IEEE Transactions on Neural Networks, 10(5): 1239-1243.

Chi, J., Li, G., Chen, J., Zeng, W., Gao, Z. and Chen, Y. 1995. Quantitative study on site quality of Pinus massoniana Plantation in Zhejiang Province. Forest Research, 8(3): 303-308.

Cook, D. F., Ragsdale, C. T. and Major, R. L. 2000. Combining a neural network with a genetic algorithm for process parameter optimization. Engineering Applications of Artificial Intelligence, 13(4): 391-396.

Dau, J. H. and Chukwu, O. 2018. Forest inventory: A basic conservation tool for sustainable forest management of Nigerian ecozones. Proceedings of 6th NSCB Biodiversity Conference, Uniuyo. 212: 218.

Fu, W., Nong, B., Zhou, X., Liu, J. and Li, C. 2017. Source recovery in underdetermined blind source separation based on RBF Network. Journal of Beijing University of Posts and Telecommunications, 40 (1): 94-98.

Gong, Yinxi. 2013. Study of Site Knowledge Discovery Based on Multivariate Forestry Information. Beijing Forestry University.

Gonzalez-Benecke, C.A., Samuelson, L.J., Martin, T.A., Cropper Jr, W.P., Johnsen, K.H., Stokes, T.A., Butnor, J.R. and Anderson, P.H. 2015. Modeling the effects of forest management on in situ and ex situ longleaf pine forest carbon stocks. Forest Ecology and Management, 355: 24-36.

Gonzalez-Benecke, C.A., Teskey, R.O., Dinon-Aldridge, H. and Martin, T.A. 2017. *Pinus taeda* forest growth predictions in the 21st century vary with site mean annual temperature and site quality. Global Change Biology, 23(11): 4689-4705.

Green, R. N., Marshall, P. L. and Klinka, K. 1989. Estimating site index of Douglas-fir (*Pseudotsuga menziesii* [Mirb.] Franco) from ecological variables in southwestern British Columbia. Forest Science, 35(1): 50-63.

Guo, Yanrong, Liu Yang and Wu Baoguo. 2014. Evaluating dividing rank and quantification of site quality of suitable land for forest in Fujian province. Journal of Northeast Forestry University, 42(10): 54-59.

Huang Jiarong, Ma Tianxiao, Wang Yanmei, Shang Tiejun, Zhao Xinzhen and Gao Guangqin. 2006. Forest site evaluation model studies on the basis of BP Neural Network. Journal of Mountain Agriculture and Biology, 25(6): 479-483.

Jiang, H., Radtke, P.J., Weiskittel, A.R., Coulston, J.W. and Guertin, P.J. 2015. Climate-and soil-based models of site productivity in eastern US tree species. Canadian Journal of Forest Research, 45(3): 325-342.

Li, Zhen Zhen and Wang Hong bin 2009. Application of quantification theory in site quality evaluation of larch-tree (*Larix kaempferi*). Heilongjiang Agricultural Sciences, 4: 119-120.

Liu, J., Wang, Q.J., Wang, X.H. and Zhang, H. 2013. Application of RBF neural network to GPS elevation fitting based on genetic algorithm. Science of Surveying and Mapping, 38(2): 143-145.

Maillard, E. P. and Gueriot, D. 1997. RBF neural network, basic functions and genetic algorithm. Neural Networks, International Conference on. IEEE, 4: 2187-2192.

Mamo, N. and Sterba, H. 2006. Site index functions for *Cupressus lusitanica* at Munesa Shashemene, Ethiopia. Forest Ecology and Management, 237(1-3): 429-435.

McDill, M. E. and Amateis, R. L. 1992. Measuring forest site quality using the parameters of a dimensionally compatible height growth function. Forest Science, 38(2): 409-429.

Mitsuda, Y. and Ito, S. 2015. Modifying the site index model of sugi planted forests in Miyazaki Prefecture considering the effects of DEM quality and scale of digital terrain analysis. Journal of Forest Planning, 20(2): 45-51.

Nothdurft, A., Wolf, T., Ringeler, A., Böhner, J. and Saborowski, J. 2012. Spatio-temporal prediction of site index based on forest inventories and climate change scenarios. Forest Ecology & Management, 279: 97-111.

Ponce, R.A., Roig, S., Bravo, A., del Río, M., Montero, G. and Pardos, M. 2017. Dynamics of ecosystem services in *Pinus sylvestris* stands under different managements and site quality classes. European Journal of Forest Research, 136(5-6): 983-996.

Sharma, M. and Reid, D.E.B. 2017. Stand height/site index equations for jack pine and black spruce trees grown in natural stands. Forest Science, 64(1): 33-40.

Stage, A. R. and Salas, C. 2007. Interactions of elevation, aspect, and slope

in models of forest species composition and productivity. Forest Science, 53(4): 486-492.

Wu, J., Long, J. and Liu, M. 2015. Evolving RBF neural networks for rainfall prediction using hybrid particle swarm optimization and genetic algorithm. Neurocomputing, 148: 136-142.

Xie, Lixia and Wang Yachao 2014. New method of network security situation awareness. Journal of Beijing University of Posts and Telecommunications, 37(5): 31-35.

Xiong, T., Bao, Y., Hu, Z. and Chiong, R. 2015. Forecasting interval time series using a fully complex-valued RBF neural network with DPSO and PSO algorithms. Information Sciences, 305: 77-92.

Yang, Wenji and Wang Xiuru. 2004. Analysis on the study of site quality evaluation in China. Research of Soil and Water Conservation, 11(3): 289-292.

Yingwei, L, Sundararajan, N. and Saratchandran, P. 1998. Performance evaluation of a sequential minimal radial basis function (RBF) neural network learning algorithm. IEEE Transactions on neural networks, 9(2): 308-318.

Yue, C., Mäkinen, H., Klädtke, J. and Kohnle, U. 2014. An approach to assessing site index changes of Norway spruce based on spatially and temporally disjunct measurement series. Forest Ecology & Management, 323(7): 10-19.

Nature Environment and Pollution Technology
An International Quarterly Scientific Journal

p-ISSN: 0972-6268
e-ISSN: 2395-3454

Vol. 18 | No. 4 | pp. 1349-1361 | 2019

Original Research Paper | Open Access

Development of Crown Profile Models for Chinese Fir Using Non-linear Mixed-Effects Modelling

Chengde Wang*(**), Baoguo Wu*(**), Yuling Chen*(**) and Yan Qi***

*School of Information Science and Technology, Beijing Forestry University, Beijing, PR China
**Institute of Forestry Informationization of Beijing Forestry University, Beijing, PR China
***China Agricultural University, International College Beijing, Beijing, PR China

Nat. Env. & Poll. Tech.
Website: www.neptjournal.com

Received: 01-02-2019
Accepted: 08-04-2019

Key Words:
Chinese fir
Crown profile model
Non-linear mixed-effects modelling

ABSTRACT

Crown profile models are key components of growth and yield models and are crucial for estimating the crown volume and constructing 3D visualization of trees. We used a total of 431 trees collected from 98 pure even-aged temporary sample plots established in Fujian Province to develop crown profile models of Chinese fir (*Cunninghamia lanceolata*).To describe the shape of tree crowns more accurately, significance tests of the effects of different stand conditions (stand age, site index, and stand density) on crown shape were conducted with one-way analysis of variance (ANOVA). Multiple comparisons based on the ANOVA results were used to classify the crown data into three groups according to stand age: Group I (young forest), Group II (medium forest), and Group III (nearly mature and mature forest). We analysed the relationships between the crown variables and stand variables and used the reparameterization approach to develop three optimal crown profile models for different age groups. Stand variables (such as stand density) further improved the prediction efficacy of the models. Considering the correlation between repeated measurement data for the same tree crown, the non-linear mixed-effects modelling (NLME) method was used to account for autocorrelation. The determination coefficients (R^2) of the above three optimal models fitted by the non-linear mixed-effects approach were 0.9214, 0.9398 and 0.9129, and their Root Mean Squared Errors (RMSEs) were 0.1246, 0.1409 and 0.1786, respectively. The determinant coefficients (R^2) of the three models fitted by the non-linear least squares (NLS) approach were 0.9015, 0.8794 and 0.8930, and their RMSEs were 0.1395, 0.2102 and 0.1878, respectively. The results indicated that the predicted accuracy was significantly increased by using non-linear mixed effects modelling compared with the NLS method.

INTRODUCTION

Tree crowns play an essential role in the photosynthesis and transpiration processes, and crown structure can not only intuitively reflect the vigour of trees (Biging 1995), but is also an indicator of inter-tree competition level (Purves 2007). The size and shape of a tree's crown are used in ecological research to simulate the above-ground biomass of trees (Carvalho 2003) and the interception of solar radiant energy (Pretzsch 2014). In addition to these applications, crown modelling is also crucial for estimating crown volume and constructing 3D visualization of trees in forest management (Dong 2016).

Crown profile models depict the shape and size of trees by predicting the radius of the crown at any height along the entire crown length (Gao 2017). These models generally fall into simple geometric models, segmented models and variable exponential models according to the equation forms. Earlier attempts that adopted simple regular geometrical shapes described the change in crown radius from the top to the base of the crown. Mohren (1987) and Marshall (2003) suggested the following model to estimate crown shape: $CR_i = (1 - di)^k$ (1-1), where d_i represents the relative crown length, and k is the model coefficient. The value of k characterized the shape of crowns for a range of geometric solids (i.e., cylinder, parabola, cone, neiloid). Nepal (1993) proposed that the location of the largest crown radius was not at the base of the tree crown and extended Equation 1-1 for the Loblolly pine (*Pinus taeda* L.). To describe the crown structure more flexibly, a variety of equations have been used such as polynomials (Baldwin 1997, Dong 2016), power functions (Rautiainen 2005), peak functions (Guo 2015) and modified Beta functions (Ferrarese 2015). Simple geometric models were thought to be excessively rigid, and researchers (Raulier 1996, Pretzsch 2002, Crecente-Campo 2013, Sadono 2015a, 2015b) adopted a segmented approach by directly dividing the entire crown into upper (i.e., mostly sun needles) and lower (i.e., mostly shade needles) crowns at the location of the largest crown radius. Gao et al. (2015) concluded that the artificially selected point in a segmented model is not differentiable, and continuous segmented models were proposed to solve this

problem. However, the model fitting of segmented equations is complex. Ferrarese (2015) and Gao (2018) used variable exponent models to represent crown shapes by changing the parameters. Compared with segmented models, variable exponent models are simpler in form, although the equation is not integral when estimating the crown volume.

Researchers have developed crown profile models for many tree species. Chinese fir is an important timber tree species in southeast China. With few exceptions, these models for Chinese fir have been estimated by ordinary least squares (OLS) or non-linear least squares (NLS). Guo (2015) and Dong (2016) used the NLS framework to develop crown profile models for Chinese fir. The relationship between crown radius and independent variables (stand variables and tree variables) is usually determined by measurements from the same tree crown. The homologous structure (i.e., measurements within a tree crown) destroys the independence between observations and invalidates the basic hypothesis of the least squares methods (West et al. 1984). Therefore, OLS and NLS tend to inflate the standard errors in the estimated parameters (Calama & Montero 2004). Non-linear mixed-effects (NLME) modelling was proposed to solve this problem (Lindstrom & Bates 1990). NLME modelling contains both fixed and random effects and provides an efficient approach to analyse repeated measurements from the same statistical unit. However, to our knowledge, few studies have applied NLME modelling to develop a crown profile model for Chinese fir.

The objective of this study was to develop a crown profile model for even-aged Chinese fir in Fujian Province (southeast China) and use NLME modelling to enhance the existing crown profile models. To describe the shape of tree crowns more accurately, we used ANOVA and multiple comparison methods to classify the crown data. Many candidate equations were compared, and the equations that performed best were selected for further analysis. The reparameterization approach was used to develop the basic crown profile models of the NLME modelling based on the models selected. We further analysed the 2D and 3D crown shapes under different forest stand growth conditions.

MATERIALS AND METHODS

Study Area and Data Collection

The study area is located in the Dali forest farm and Lanxia forest farm (115°50'~120°40'E, 23°33'~28°20'N) in Fujian province, Southeast China. The main terrain consists of hills and fewer plains with elevations between 300m and 500m. With a subtropical maritime monsoon climate, the annual average temperature of this area is 20°C and the annual average precipitation is 1756 mm. Soil types mainly include red soil, yellow soil and mountain meadow soil. The main wood species are Chinese fir, Masson's pine and *Eucalyptus grandis*.

Data for the current study were collected from 98 temporary sample plots that were established according to different age groups, stand densities and site condition types in 2015. The size of each plot was 20m×30m. Then, 4~5 trees without deflection crowns were selected from each plot for crown modelling, and a total of 413 trees were collected. For each tree, the following measurements were obtained: (1) diameter at breast height (*DBH*, cm), defined as 1.3m; (2) total tree height (*HT*, m); (3) largest crown radius (*LCR*, m) which was half of the crown width (*CW*, m); (4) height above ground to the crown base (*HCB*, m); (5) crown length (*CL*, m); (6) vertical height from the crown base to the crown position at p*CL (*CH*, m), where p is equal to 1/10, 1/4, 2/4, 3/4 and 9/10; and (7) crown radius, corresponding to *CH* (*CR*, m). *DBH* was measured to the nearest 0.1 cm and other variables were measured to the nearest 0.1m. The data were randomly divided into the model development dataset and the testing dataset with a ratio of 8:2. The crown variables are shown in Fig. 1 and stand attributes of the 98 sample plots are described in Table 1.

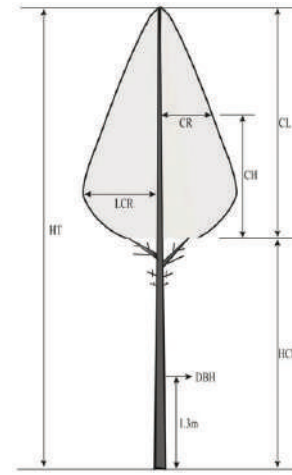

Fig. 1: Variables used to characterize an individual tree crown.

Table 1: Summary statistics of measurements of tree variables.

Tree variables	Mean	Min	Max	STD
t (years)	16	5	29	7.25
N(treesha^{-1})	1850	900	4000	60.39
DBH (cm)	16.4	5.9	33.2	5.52
HT(m)	12.6	3.0	25.5	3.91

Table cont....

CW(m)	3.6	1.6	7.6	1.05
LCR(m)	1.8	0.8	3.8	0.53
CL(m)	6.0	1.1	14.3	2.65
HCB(m)	6.4	0.3	16.3	3.17
CR(m)	1.1	0.1	3.8	0.56

Note: t = tree age, N = stand density, DBH = diameter at breast height, HT = total tree height, CW = crown width, LCR = largest crown radius ($1/2CW$), CL = crown length, HCB = height above ground to crown base, CR = crown radius, Min = minimum, Max = maximum, Mean = average value, and STD = standard deviation.

METHODS

ANOVA and Multiple Comparisons

Tree crown shape and size vary with forest stand density, management measures and tree ages. To accurately simulate the crown profile, significant tests of different stand conditions on crown profiles were conducted with one-way ANOVA at a significance level of 0.05, and LSD multiple comparisons were used to further group the crown data.

The stand site index (*SI*), the initial stand density (*SD*) and the tree age were selected as factors for ANOVA. The *LCR* and *CL* from sample data were taken as the observation variables. The *SI* was divided into 7 levels: 10(9<*SI*<=11), 12(11<*SI*<=13), 14(13<*SI*<=15), 16(15<*SI*<=17), 18(17<*SI*<=19), 20(19<*SI*<=21) and 22(21<*SI*<=22). According to the criteria for classification of forest age groups, the tree ages of Chinese fir were divided into 4 levels: young forest (<=10), medium forest (11-20), nearly mature forest (21-25) and mature forest (26-35) years. The *SD* included 6 levels: I (<1000), II (1001-1500), III (1501-2000), IV (2001-2500), V (2501-3000) and VI (>3000).

In this paper, single factor ANOVA was used to study whether there were significant differences in crown radii under different growth conditions, taking crown radius analysis under different age groups as an example. The statistical equations of ANOVA and LSD multiple comparisons are shown in Equation 1 and 2:

$$F = \frac{MSA}{MSE} \sim F\left(k-1, n-k\right) \quad \ldots(1)$$

Where, MSA is the mean square between groups, MSE is the intra-group mean square, n is the number of observed values, and k is the number of groups.

$$LSD = t_{\alpha/2}\sqrt{MSE\left(\frac{1}{n_i}+\frac{1}{n_j}\right)} \quad \ldots(2)$$

Where, $t_{a/2}$ is the critical value of the t distribution, MSE is the mean square residual in the group, and n_i and n_j represent the sizes of the ith and jth samples, respectively.

Development of the Optimal Crown Profile Models

In this study, 24 candidate model equations (Table 2) were collected, and the basic crown profile models of three modelling forms were analysed: (i) simple single equations (models 1-12), (ii) segmented equations (models 13-19), and (iii) variable-exponent equations (models 20-24). To choose the optimal models that performed best for different age groups, we compared the candidate models from Table 2 using the different age group data according to the principle of R^2 maximization and RMSE minimization. In addition, stand variables were assessed with respect to their influence on crown profiles. Therefore, we used the reparameterization method to analyse the relationships between the optimal model parameters

Table 2: Crown profile candidate models.

No.	Model equations	References
1	$CR = LCR\left(1-RCH\right)^{a_0}$	Mohren (1987)
2	$CR = LCR\left(1-RCH^2\right)^{a_0}$	McPherson (1988)
3	$CR = a_0 RCH^{a_1}\left(1-RCH\right)^{a_2}$	Nepal (1993)
4	$CR = a_0\left(RCH-1\right)/\left(RCH+1\right)+a_1\left(RCH-1\right)$	Baldwin (1997)
5	$CR = LCR(a_0\left(RCH-1\right)/\left(RCH+1\right)+a_1\left(RCH-1\right))$	Crecente-Campo (2009)
6	$CR = LCR\left(a_0\left(RCH-1\right)/\left(RCH+1\right)+a_1\left(1-RCH\right)^{a_2}\right)$	Chmura (2014)
7-1	$CR = LCR\left(a_0+a_1RCH+a_2RCH^2\right)$	Crecente-Campo (2009)

Table cont....

No.	Model equations	References
7-2	$CR = LCR\left(a_0 + a_1 RCH + a_2 RCH^2 + a_3 RCH^3\right)$	Crecente-Campo (2009)
7-3	$CR = LCR\left(a_0 + a_1 RCH + a_2 RCH^2 + a_3 RCH^3 + a_4 RCH^4\right)$	Crecente-Campo (2009)
8	$CR = LCR\left(a_0\left(RCH-1\right) + a_1\left(RCH^2-1\right) + a_2\left(RCH^3-1\right) + a_3\left(RCH^4-1\right)\right)$	Crecente-Campo (2009)
9	$CR = LCR\left(a_0 - a_1 \ln\left(RCH + a_2\right)\right)$	Guo (2015)
10	$CR = LCR\left(a_0 + a_1 RCH^{a_2}\right)$	Guo (2015)
11	$CR = a_0 - \frac{a_1}{\left(1 + a_2 RCH\right)^{1/a_3}}$	Rautiainen (2005) Guo (2015)
12	$CR = a_0 \frac{\left(1-RCH\right)^{p-1} RCH^{q-1}}{\beta\left(p,q\right)}$	Ferrarese et al. (2015)
13	$CR_U = \mathrm{LCR}\left(1 - \left(\frac{CH - L_L}{L_U}\right)^{b_0}\right)^{1/b}$	Rautiainen (2005)
14	$CR_U = LCR\left(\frac{\left(LCL - CH\right)}{L_U}\right)^{b_0}$	Crecente-Campo (2013)
15	$CR_L = LCR\left(b_0 + \left(1-b_0\right)\left(\frac{CH}{L_L}\right)^{b_1}\right)$	Crecente-Campo (2009)
16	$CR_L = LCR\left(CH^{b_0} + b_1\right)$	Dong (2016)
17	$CR = b_0\left(1-RCH\right) + b_1\left(1-RCH\right)^2 + b_2\left(1-k-RCH\right)^2 I_+$	Gao (2015)
18	$CR = b_0\left(1 - e^{-b_1\left(1-RCH\right)}\right) - b_2\left(1 - e^{-b_3\left(1-k-RCH\right)}\right) I_+$	Gao (2015)
19	$CR = b_0\left(1-RCH\right)^{b_1} - b_2\left(1-k-RCH\right)^{b_3} I_+$	Gao (2015)
20	$CR = LCR\left(e^{c_0 + c_1 RCH + c_2 RCH^2}\right)$	Hann (1998)
21	$CR = LCR\left(c_0 + c_1 e^{c_2 RCH}\right)$	Guo (2015)
22	$CR = c_0 / \left(1 + e^{-c_1\left(RCH - c_2\right)}\right)$	Guo (2015)
23	$CR = c_0\left(\frac{1 - RCH^{0.5}}{1 - c2^{0.5}}\right)^{\left(c_1 RCH\right)}$	Gao (2015)
24	$CR = c_0\left(\frac{c_2}{c_1}\right)\left(\frac{1-RCH}{c_1}\right)^{c_2-1} e^{-\left(\frac{1-RCH}{c_1}\right)^{c2}}$	Ferrarese et al. (2015)

Note: CR_U and CR_L are the crown radii of the upper and lower parts, m; *Lu* is the crown length of the upper half of the tree, m; L_L is the crown length of the lower half, m; *RCH* is relative crown length (*RCH=CH/LCL*, 0 at the base of crown and 1 at the top of crown), m;a_0, a_1, a_2, a_3, a_4, b_0, b_1, b_2, b_3, b_4, c_0, c_1, c_2, c_3 are the model coefficients; in models 17,18,19, $I_+ = \begin{cases} 0 & RCH < k \\ 1 & RCH \geq k \end{cases}$, k is the inflection point parameter of the segmented model, i.e., the maximum crown position point; in the model 12 (p, q) is a standardized function of beta distribution with parameters $p > 0$ and $q > 0$; e is the natural logarithm, 2.718.

and stand variables.

The entire analysis procedure was done in three steps. First, to obtain the estimated values of model parameters corresponding to each tree, the interpolation method was used to obtain the data between the measurement points at different positions of the crown (Gill & Biging 2002). After comparison with the commonly used interpolation algorithms, such as linear interpolation, Hermite interpolation and cubic spline interpolation, the Lagrange interpolation was selected. The optimal model was fitted with the interpolated data, and the corresponding model parameters of each tree were obtained. Assuming that a given k+1 measuring points at different crown positions, (x_0, y_0), …, (x_k, y_k), are known. The Lagrange interpolation function is shown in Equations 3 and 4:

$$L(x) = \sum_{j=0}^{k} y_j l_j(x) \quad \ldots(3)$$

Where, $l_j(x)$ is an interpolation basis function and

$$l_j(x) = \prod_{i=0, i\neq j}^{k} \frac{x - x_i}{x_j - x_i} = \frac{(x - x_0)}{(x_j - x_0)} \cdots \frac{(x - x_{j-1})}{x_j - x_{j-1}} \frac{(x - x_{j+1})}{x_j - x_{j+1}} \cdots \frac{(x - x_k)}{x_j - x_k} \quad \ldots(4)$$

Where, x_j is the jth observation of crown length measurement for each tree and y_j is the jth observation of crown radius measurement for each tree.

After the parameters were predicted, the parameter values were graphed against stand variables, and correlation analysis and stepwise regression were performed. Tree factors tested for correlation included *DBH*, *HT*, stand age, *SD* and *SI*. Those factors and the combinations of power functions that were significantly related to the parameters were selected to establish Equation 5:

$$\zeta_j = f(HT_j, DBH_j, \ldots, A, SI, SD) \quad \ldots(5)$$

Where, HT_j is total height of the jth tree, DBH_j is the diameter at the breast of the jth tree, A is the stand age, SI is stand site index, and SD is initial stand density.

Third, according to the established function ζ_j, the related stand factors were introduced into the optimal model selected to construct the new model by the reparameterization method. With the best predictor variables determined, the different grouped data were refit to the three new constructed models. The best models with selected stand variables were then used as the NLME base models. All of these calculations were performed in S-Plus software (Insightful Corporation 2007).

Non-linear Mixed-Effect Modelling

In this study, a single-level non-linear mixed effect model was used to develop the crown profile models of Chinese fir. The specific forms are as follows:

$$\begin{cases} y_{ij} = f(\varphi_{ij}, v_{ij}) + e_{ij} & i=1,\ldots,M;\ j=1,\ldots,ni \\ \varphi_{ij} = A_{ij}\beta + B_{ij}b_{ij} \\ b_i \sim N(0, D) \\ e_{ij} \sim N(0, \sigma^2 R_i) \end{cases} \quad \ldots(6)$$

Where, y_{ij} is the jth observation value of the ith group, M is the number of groups, n_i is the number of observations of the group, f is a function of parameter φ_{ij} and covariate vector $v_{ij;}$ β is the (p×1) dimensional fixed effect vector, b_i is the (q×1) dimensional random effect vector with variance-covariance matrix D, A_{ij} and B_{ij} are corresponding design matrices, e_{ij} is the error term of the normal distribution, σ^2 is the variance, R_i is the variance-covariance matrix of block i, and D is the variance-covariance matrix of random effects.

This paper introduces the application of the non-linear mixed-effects model into crown profile modelling. The model was constructed as follows:

Step 1: The key step in the NLME is to construct the parameter effects. The model with different random parameter combinations was fitted, and the mixed model with the best fitting effect was selected by comparing the mixed model fitting statistics, specifically the Akaike Information Criterion (AIC), Bayes Information Criterion (BIC) and the -2 Logarithmic Likelihood value (-2LL). A better fitting effect should have a smaller AIC, a smaller BIC, and a larger logarithmic likelihood. To avoid too many parameterization problems, the likelihood ratio test (LRT) was used to select the optimal model with different numbers of parameters, and the model with fewer parameters and the more significant model was chosen as the optimal model. The calculation formulas of AIC and BIC are as follows:

$$AIC = 2LL + 2d \quad \ldots(7)$$

$$BIC = -2LL + dln(n) \quad \ldots(8)$$

Where, LL is log likelihood, d is the number of estimated parameters of the model, and n is the number of valid observations.

Step 2: The variance-covariance structure D of random effects was determined. The variance-covariance structure depends on the number of random parameters, and the variance covariance structure of the two random parameters (u, v) is as follows:

$$D = \begin{bmatrix} \sigma_u^2 & \sigma_{uv} \\ \sigma_{uv} & \sigma_v^2 \end{bmatrix} \quad \ldots(9)$$

Where, σ_u^2 is the variance of the random parameter u, σ_v^2 is the variance of the random parameter v, and σ_{uv} is the covariance of the random parameters u and v.

In this study, the random effect variance-covariance structure D was determined by comparing the fitting effects of three variance-covariance measures: the compound symmetry structure (CS), the diagonal matrix (DM) and the positive-definite matrix (PDM). Matrix forms with small AIC and BIC and large logarithmic likelihoods were selected.

Step 3: The intra-group variance-covariance structures R_i were determined to solve the problem of intra-group error correlation and heteroscedasticity. In forestry research, R_i are calculated by Equation 10 (Davidian & Giltinan 1995). The heteroscedasticity of a mixed model is often described by an exponential function (Equation 11) or power function (Equation 12). The application of correlation structure in mixed models is mainly used to simulate the correlation between intra-group errors. The commonly used correlation structures in forestry are autoregressive (AR), moving average (MA) and autoregressive-moving-average (ARMA). AIC, BIC and logarithmic likelihood were used to compare the effects of the correlation structures, and residual distribution was used to test the elimination of heteroscedasticity.

$$R_i = \sigma^2 G_i^{0.5} \Gamma_i G_i^{0.5} \quad \ldots(10)$$

Where, σ^2 is the error variance value of the model, Γ_i is the intra-group error correlation structure, and G_i is the diagonal matrix describing the heterogeneity of variance.

$$g(u_{ij}, \alpha) = |u_{ij}|^{\alpha} \quad \ldots(11)$$

$$g(u_{ij}, \beta) = \exp(\beta u_{ij}) \quad \ldots(12)$$

Where, u_{ij} is a predicted value based on fixed effect parameters and α and β are the function parameters.

Model Validation

To evaluate the accuracy of the models, Fitting-effect statistical indicators selected were the determination coefficient (R^2, Equation 13) and the mean squared error (MSE, Equation 14). Statistical indicators used to evaluate the models were the Mean Deviation (MD, Equation 15), Root Mean Squared Error (RMSE, Equation16), the Mean Absolute Deviation (MAE, Equation 17), the AIC (Equation 18) and the BIC (Equation 19).

$$R^2 = 1 - \frac{\sum_{i=1}^{m} (y_i - \hat{y}_i)^2}{\sum_{i=1}^{m} (y_i - \overline{y_i})^2} \quad \ldots(13)$$

$$MSE = \frac{1}{n} \sum_{i=1}^{n} (y_i - \hat{y}_i)^2 \quad \ldots(14)$$

$$MD = \frac{\sum_{i=1}^{n} (y_i - \hat{y}_i)}{n} \quad \ldots(15)$$

$$RMSE = \sqrt{\frac{\sum_{i=1}^{n} (y_i - \hat{y}_i)^2}{n-1}} \quad \ldots(16)$$

$$MAE = \frac{1}{n} \sum_{i=1}^{n} |y_i - \hat{y}_i| \quad \ldots(17)$$

$$AIC = n * \ln(MSE) + 2k \quad \ldots(18)$$

$$BIC = n * \ln(MSE) + k \ln(n) \quad \ldots(19)$$

where y_i represents the observed value for the i^{th} analytic tree, $\hat{y}_i$ is the predicted value of the i^{th} observed value, m is the number of observations, n is the number of observations for testing the equation, $\bar{y}_i$ is the mean value of the observations, and k is the number of parameters.

The test of the fixed effect part in the mixed effect model is the same as that of the traditional method but the test of the random effect part is to calculate the random parameter value through the second sampling; the random parameter value(b_k) is calculated according to the Vonesh & Chinchillas (1997) method:

$$\hat{b}_k \approx \hat{D} \hat{Z}_k^T \left(\hat{Z}_k \hat{D} \hat{Z}_k^T + \hat{R}_k \right)^{-1} \hat{e}_k \quad \ldots(20)$$

Where, $\hat{D}$ is the variance-covariance matrix of random effect parameters, $\hat{R}_k$ is the intra-group variance-covariance structure, $\hat{Z}_k$ is the design matrix, and $\hat{e}_k$ is calculated by the actual value minus the predicted value calculated by the fixed effect parameter.

RESULTS

ANOVA and Multiple Comparisons

The results of LCR and LCL variance analysis (Table 3) indicated that there were significant differences in LCR and LCL under different stand ages, stand densities and site indexes at the significance level of 0.05. The results of the stand age tests are extremely significant.

Multiple comparative classification results showed that the number of LCR and LCL classifications under different site indexes were 3 and 5, respectively. The numbers of LCR and LCL classifications under different stand densities were 4 and 6, respectively. The numbers of LCR and LCL classifications under different stand ages were 3 and 3, respectively. From the results of multiple comparisons, it is not satisfactory to classify the modelling data according to site and stand density. Therefore, the modelling data were grouped by stand age. Since there was no significant

difference between nearly mature forest and mature forest, they were uniformly classified as the same group. Finally, the crown data were classified into three groups according to stand age: Group I (young forest), Group II (medium forest) and Group III (nearly mature and mature forest).

Table 3: The variance analysis of LCR and LCL under different stand conditions.

Factor	Variable	Multiple Classification Number	F value	P value
Site index	LCR	3	2.313	0.036
	CL	5	17.941	<0.000
Stand density	LCR	4	2.953	0.008
	CL	6	6.341	<0.000
Stand age	LCR	3	57.343	<0.000
	CL	3	7.212	<0.000

Development of the Optimal Crown Profile Models

By comparing the fitting results of 24 basic crown profile models (Table 2), model-1(No.1, R^2=0.7582, MSE=0.0762) had the best fitting results for young forest (Group I). The optimal basic crown profile models of medium forest (Group II) and mature forest (Group III) were model-5 (No. 5, R^2=0.8013, MSE=0.0969) and model-20 (No. 20, R^2=0.9015, MSE=0.0195), respectively.

According to the correlation test between the parameters and the tree variables, the tree variables or combinations with strong correlation among the parameters were introduced into the model to reduce the collinearity between variables and ensure the accuracy of the model. The results showed that model-1 was not correlated with the stand variables and that model-5 and model-20 were most correlated with the SD.

The optimal crown profile models were selected for Groups I-III by the reparameterization method (Equations 21-23). Table 4 shows the model fitting and model validation results. These models passed the F-test and t-test. Moreover, the validation index values of MAE (0.0480~0.0950), absolute value of MD (less than 0.03) and RMSE (0.0969~0.1406) were small. This showed that the predicted values of the models did not differ from the actual values in the testing dataset.

$$CR = LCR(1 - RCH)^{a_0} \quad \ldots(21)$$

$$CR = LCR\left(b_0 \lg(N)\left(\frac{RCH-1}{RCH+1}\right) + b_1 (RCH-1)\right) \quad (22)$$

$$CR = LCR\left(e^{c_0 + c_1 RCH + (c_2 \lg(N)) RCH^2}\right) \quad \ldots(23)$$

In Equations 21-23, a_0 and a_1 are model parameters, and *lg* is the base 10 logarithm.

Non-linear Mixed-effect Modelling

Construction of the parametric effects: In previous research methods, all parameters and combinations of the models were fitted as random effects. Based on the results of the statistical indices (AIC, BIC and LL) (Table 5), the mixed effect model showed a better performance than the NLS method. For Group I, the AIC and BIC of the mixed effect model were significantly lower than those of the basic model. For Group II, when considering a random parameter, model 2-2 was better than model 2-1 and the basic model. The significance of likelihood ratio test for model 2-3 and model 2-2 showed that adding one more random parameter significantly improved the fitting accuracy of the model. Model 2-3 showed the best performance, with an *AIC* of -137.6726, a BIC of -111.7462, and an LL of 75.83631. For Group III, when considering a random parameter, the model 3-1 had the smallest AIC and BIC. When adding one random parameter, model 3-4 was better than the other models. When considering 3 random parameters, the model 3-7 fitting did not converge.

Table 4: Model fitting and validation results of the three optimal crown profile models.

Age group	Parameter Estimates				Model fitting		Validation		
	Variable	Estimate value	S.E	P-value	R^2	MSE	MAE	RMSE	MD
Group I	a_0	0.6515	0.0130	<.0001	0.9015	0.0195	0.0950	0.1406	-0.0332
Group II	b_0	0.4314	0.0287	<.0001	0.8794	0.0443	0.0703	0.1398	0.0208
	b_1	-2.2975	0.0795	<.0001					
Group III	c_0	-0.1299	0.0207	<.0001	0.8930	0.0354	0.0480	0.0969	0.0156
	c_1	0.2727	0.1284	0.0342					
	c_2	-0.5802	0.0440	<.0001					

Construction of the variance-covariance structure: The fitting results of the variance covariance matrix are as follows. Because the model of Group I has only one parameter, the variance-covariance structure was not considered. For Group II, the fitting results of mixed models based on three different variance covariance structures were compared (Table 6), and the diagonal matrix had the smallest AIC and BIC values and the largest LL for both Group II and Group III. Therefore, in this study the diagonal matrix was taken as the variance-covariance matrix hypothesis form of random effects for medium forests and mature forests.

Autocorrelation and heteroscedasticity: To account for within-profile autocorrelation, the three correlation structures (*corAR1, corARMA* and *corCAR1*) were added to each crown profile model. The results of model fitting are given in Table 7. We concluded that for Group I and Group II, the *corARMA* structure had the most obvious improvement on the fitting effect of mixed models. For Group III, the three evaluation indicators showed that the *corCAR1* model could significantly improve the accuracy of the model. Therefore, *corCAR1* was used to describe the sequence autocorrelation structure of the crown profile model.

In this paper, power functions and exponential functions were used to account for heteroscedasticity. The power function equation performed better in the mixed model for Group I, whereas the exponential function was better than the power function for Group II and Group III.

In addition, plots of weighted residuals against predicted values for crown profile models (Fig. 2 (a-c)) showed that the residual values of the three models were uniformly distributed above and below the 0-level line. This indicated that the heteroscedasticity functions used to estimate weights were effective.

Table 8 gives the comparison of the fitting results between the mixed model and the traditional model. The

Table 5: Model fitting results based on different random effect parameters.

Age group	Model	Random effect Parameter	AIC	BIC	LL	LRT	P-value
Group I	Basic model	---	-415.5835	-407.7031	209.7917	-	-
	Model1-1	a_0	-523.0991	-511.2786	264.5496		
Group II	Basic model	---	-79.5781	-68.4667	42.7891	-	-
	Model 2-1	b_0	-127.2645	-112.4494	67.6323	-	-
	Model 2-2	b_1	-129.3998	-114.5847	68.6999	51.8218	<.0001
	Model 2-3	b_0, b_1	-137.6726	-111.7462	75.8363	14.2728	0.0026
Group III	Basic model	---	-221.0012	-204.5642	114.5006	-	-
	Model 3-1	c_0	-327.2169	-306.6707	168.6084	108.2157	<.0001
	Model 3-2	c_1	-298.9860	-278.4397	154.4930	-	-
	Model 3-3	c_2	-243.5823	-223.0361	126.7912	-	-
	Model 3-4	c_0, c_1	-336.5379	-307.7731	175.2689	17.3210	<.0001
	Model 3-5	c_0, c_2	-330.0363	-301.2716	172.0181	-	-
	Model 3-6	c_1, c_2	-319.0273	-290.2625	166.5136	-	-
	Model 3-7	c_1, c_2, c_3	--	--	--		

Table 6: Comparison of fitting results of mixed models with different variance covariance structures based on the random parameter effect.

Age group	Variance-covariance structure	AIC	BIC	LL
Group II	PDM	-127.3548	-105.1321	69.6774
	DM	-127.4096	-108.8907	68.7048
	CS	-126.1750	-107.6561	68.0875
Group III	PDM	-336.5379	-307.7731	175.2689
	DM	-338.3814	-313.7259	175.1907
	CS	-333.0058	-308.3503	172.5029

fitting results indicated that the R^2 values of the 3 basic models were 0.9015, 0.8794 and 0.8930 and that the RMSEs of the 3 basic models were 0.1395, 0.2102 and 0.1878, respectively. The R^2 values of the 3 mixed models were 0.9214, 0.9129 and 0.9398, and the RMSEs of the 3 mixed models were 0.1246, 0.1786 and 0.1409, respectively. Therefore, all accuracies of the crown profile models were improved by adding autocorrelation structures and the heteroscedasticity function. Therefore, the NLME modelling was selected to construct the crown models for Chinese fir.

Model Validations

The basic model and the mixed effect model were validated with independent testing datasets. Equation 20 was used to calculate the random parameters, and the detailed calculation procedure was performed with S-Plus software. The MD, MAE and RMSE values of the 3 indexes were used to compare the prediction accuracy with the traditional NLS method. The validation results are shown in Table 9.

We can see that the MD, MAE and RMSE values of the mixed model performed better than those of the basic

Table 7: Comparison of fitting results of mixed model based on different autocorrelation error structures.

Age group	Autocorrelation Error Structure	AIC	BIC	LL	LRT	P
Group I	No	-523.0991	-511.2786	264.5496		
	corAR1	-559.3740	-539.6731	284.6870	40.2748	<.0001
	corARMA	-561.7973	-538.1563	286.8987	44.6982	<.0001
	corCAR1	-555.8533	-536.1524	282.9266	36.7542	<.0001
Group II	No	-129.3998	-114.5847	68.6999		
	corAR1	-167.7065	-141.7800	90.8532	44.3067	<.0001
	corARMA	-175.5464	-145.9161	95.7732	54.1466	<.0001
	corCAR1	-166.3127	-140.3862	90.1563	42.9128	<.0001
Group III	No	-338.3814	-313.7259	175.1907		
	corAR1	-420.5575	-387.6835	218.2788	86.1761	<.0001
	corARMA	-394.7720	-357.8489	206.3860	79.5759	<.0001
	corCAR1	-423.0464	-390.1725	219.5232	88.6651	<.0001

Table 8: Fitting results between basic model and mixed model based on different variance functions.

Items	Parameters	Group I		Group II		Group III	
		Basic Model	Mixed Model	Basic Model	Mixed Model	Basic Model	Mixed Model
Fixed parameter	$a_0(b_0, c_0)$	0.6516	0.6573	0.4314	0.5285	-0.1297	-0.1484
	$a_1(b_1, c_1)$			-2.2975	-2.5584	0.2713	0.5123
	$a_2(c_2)$					-0.5797	-0.6690
	a_3						
Variance component	δ^2	0.0195	0.0215	0.0443	0.0100	0.0354	4.3708e-003
	δ^{2a0}		0.0064		0.0009		9.2022e-011
	δ^{2a1}				0.0002		5.3092e-002
	α		0.5491				
	β				0.4987		0.6564
Fitting indices	R^2	0.9015	0.9214	0.8794	0.9129	0.8930	0.9398
	RMSE	0.1395	0.1246	0.2102	0.1786	0.1878	0.1409

Note: α, β are the parameters of power function and exponential function.

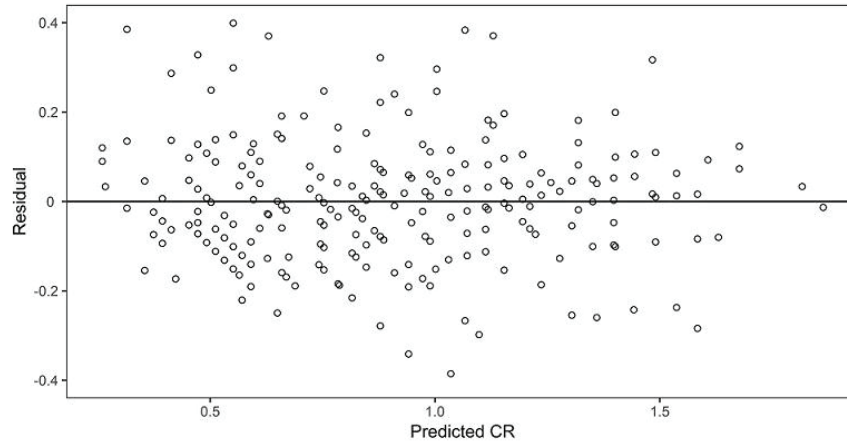

(a)

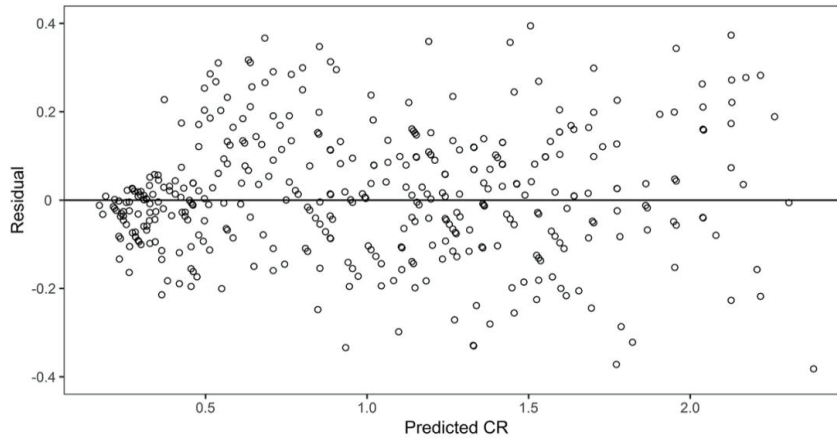

(b)

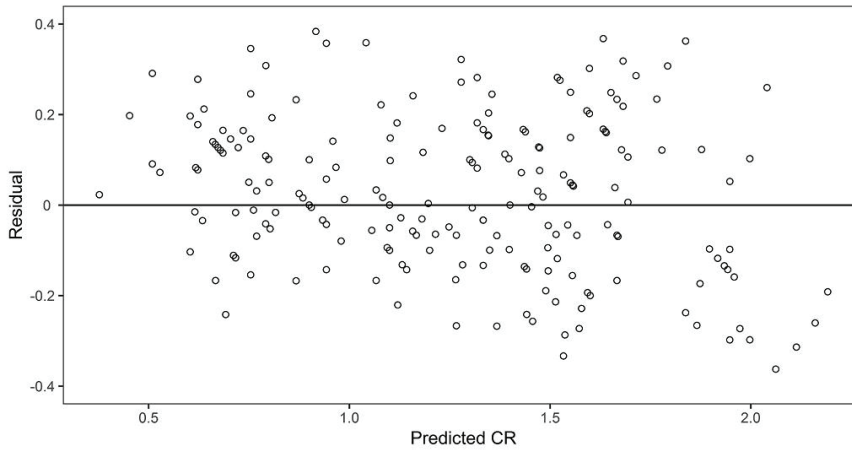

(c)

Fig. 2: Distribution of residuals for three equations predicting the crown radius of Chinese fir trees.

model. These evaluation indexes showed that incorporating random parameters significantly improved the prediction accuracy of the model.

Table 9: Validation results of crown profile models.

Age group	Model	MAE	RMSE	MD
Group I	Basic model	0.0950	0.1406	-0.0332
	mixed-effect model	0.0809	0.1008	-0.0167
Group II	Basic model	0.0703	0.1398	0.0208
	mixed-effect model	0.0514	0.1016	0.0154
Group III	Basic model	0.0480	0.0969	0.0156
	mixed-effect model	0.0214	0.0612	0.0023

DISCUSSION AND CONCLUSIONS

Tree crown shape changes regularly with changes of stand age, stand density and site index. To construct a crown profile model more accurately and improve the accuracy of the model, crown data were classified and fitted by single factor ANOVA and multiple comparison methods based on the crown survey data of Chinese fir in Fujian Province. We used age, density and site index as the objects of variance analysis to study whether these three stand factors have significant effects on LCR and CL and to classify the data by LSD difference results. The results showed that the model based on the data of different age groups was reasonable. Therefore, the modelling data were classified into three groups after the analysis of variance and multiple comparisons: I (young forest), II (medium forest), and III (nearly mature and mature forest). In our study, 24 alternative equations of crown profile models were compared.

To explore the crown shape, stand factors (density, site) and tree factor variables such as DBH and tree height, the relationships between stand factor variables were introduced in this paper into the previous optimal model by using the reparameterization method, and three new models of different age groups were developed. For Group I, the simple single equation ($CR = LCR(1-RCH)^{a_0}$) was selected, which showed that the stand variable had little effect on the model parameters. The crown profile models of Group II and Group III were $CR = LCR\left(e^{b_0+b_1RCH+(b_2\lg(N))RCH^2}\right)$ and $CR = LCR\left(c_0\lg(N)\left(\frac{RCH-1}{RCH+1}\right)+c_1(RCH-1)\right)$, respectively; and the two models were most correlated with the stand density. Therefore, the influence of stand variables on crown shape was considered in model construction, and the models constructed were more reasonable.

In this study, a single-level non-linear mixed effect model was used to develop the crown profile model of Chinese fir. To account for within-profile autocorrelation, three correlation structures (*corAR1, corARMA* and *corCAR1*) were added to each crown profile model. The structure of the power function and exponential function were used to account for heteroscedasticity. Compared with the NLS, the mixed effect model could account for the autocorrelation of crown data and performed better. The NLME model reflects the difference of crown radius at different positions in the same crown by random parameters, whereas the traditional NLS can only reflect the average change rule of crown radius. Due to data constraints, the NLME model in this study only considered the effects of repeated measurements in single-level trees. This study did not consider both sample plot and single tree level at the same time, although the accuracy of NLME may be higher if the two levels of sample plot and single trees are considered. In the future, we need to continue study on the basis of increasing sample size.

To vividly describe the crown shape of Chinese fir under different growth conditions, the crown profile models under three different age groups determined by the method of non-linear mixed effect were used to display the crowns using 2D and 3D graphics-rendering technology in Fig. 3(a-c) and Fig. 4(a-c). Fig. 3(a-c) shows 2D tree crown maps of three different groups under certain stand growth conditions. Fig. 4(a-c) shows the 3D tree crown enveloping surfaces of the corresponding groups. It can be seen that the crown shape changes with age. The height of young Chinese fir trees rapidly increases, and the lateral branches are underdeveloped. Competitive trees do not affect the crown shape. The crown shape of young Chinese fir trees is nearly conical. In the middle-aged forest stage, the growth of tree height gradually tends to be flat, the growth of lateral branches is relatively developed, and the position of maximum crown radius gradually moves up. In the mature forest stage, tree height growth is slower, and the surrounding trees impact a subject tree. The growth of lateral branches at the head of crown tips often exceeds that of the main tips, and the crown shape gradually trends to a flat top. Therefore, the crown shape can be well described by an exponential-form equation at this time.

Many forms of crown profile models have been used to simulate different tree species. However, there are few studies of crown profile models of the same tree species in different periods. The expressions of the crown profile models constructed in this study are clear and simple, and the models have substantial application value. The fitted crown profile models can be applied with only LCR, LCL and N values, which can easily be found in actual forest surveys.

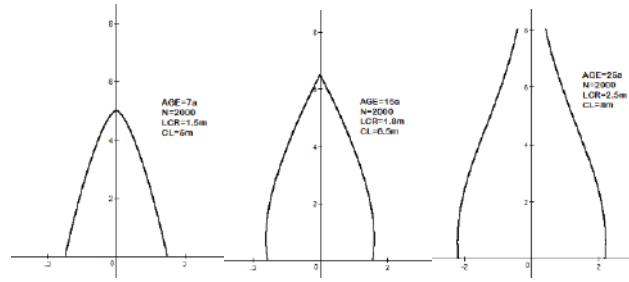

Fig. 3: 2D Crown shapes in different years. (a) Group I: AGE = 7 year, N = 2000, LCR =1.5 m, CL = 5 m; (b) Group II: AGE = 15 year, N = 2000, LC R = 1.8 m, CL = 6.5 m; (c) Group III: AG E= 25 year, N = 2000, LCR = 2.5 m, CL = 8 m.

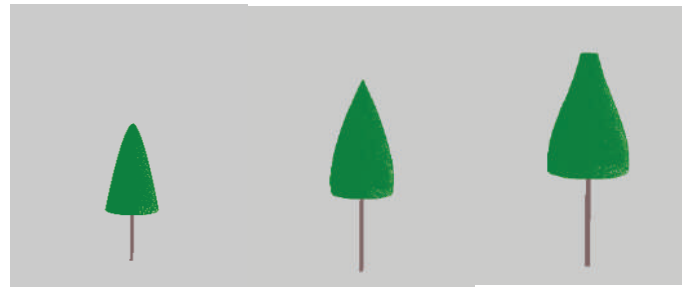

Fig. 4: 3D Crown shapes in different years. (a) Group I: AGE = 7 year, N = 2000, LCR =1.5 m, CL = 5 m; (b) Group II: AGE = 15 year, N = 2000, LCR = 1.8 m, CL = 6.5 m; (c) Group III: AGE = 25 year, N = 2000, LCR = 2.5 m, CL = 8 m.

ACKNOWLEDGEMENTS

This study was funded by the Key National Research and Development Program of China (Project No. 2017YFD0600906). The authors would also like to thank the reviewers for their comments, which were helpful in improving the manuscript.

REFERENCES

Baldwin, V.C. Jr and Peterson, K.D. 1997. Predicting the crown shape of loblolly pine trees. Canadian Journal of Forest Research, 27(1): 102-107.

Biging, G. S. and Dobbertin, M. 1995. Evaluation of competition indices in individual tree growth models. Forest Science, 41(2): 360-377.

Calama, R. and Montero, G. 2004. Interregional non-linear height diameter model with random coefficients for stone pine in Spain. Canadian Journal of Forest Research, 34(1): 150-163.

Carvalho, J.P. and Parresol, B.R. 2003. Additivity in tree biomass components of Pyrenean oak (*Qu ercuspyrenaica* Willd). Forest Ecology and Management, 179(1-3): 269-276.

Crecente-Campo, F., Álvarez-González, J.G., Castedo-Dorado, F., Gómez-García, E. and Diéguez-Aranda, U. 2013. Development of crown profile models for *Pinus pinaster* Ait. and *Pinus sylvestris* L. in northwestern Spain. Forestry, 86(4): 481-491.

Crecente-Campo, F., Marshall, P., LeMay, V. and Diéguez-Aranda, U. 2009. A crown profile model for *Pinus radiata* D. Don in north western Spain. Forest Ecology and Management, 257(12): 2370-2379.

Dong, C., Wu, B., Wang, C., Guo, Y. and Han, Y. 2016. Study on crown profile models for Chinese fir (*Cunninghamia lanceolata*) in Fujian Province and its visualization simulation. Scandinavian Journal of Forest Research, 31(3): 302-313.

Ferrarese, J., Affleck, D. and Seielstad, C. 2015. Conifer crown profile models from terrestrial laser scanning. Silva Fenn., 49: 1106.

Gao, H. and Dong, L. 2018. Modelling outer crown profile for planted *Pinus koraiensis* and *Larix olgensis* trees in Heilongjiang Province, China. Journal of Nanjing Forestry University (Natural Sciences Edition), 42(3): 10-18.

Gao, Hui-lin, Feng-ri, L.I. and Dong, Li-hu 2015. Crown-shape model of a *Pinus koraiensis* plantation in northeastern China. Journal of Beijing Forestry University. Journal of Beijing Forestry University, 37(3): 76-83.

Gao, H., Dong, L. and Li, F. 2017. Modelling variation in crown profile with tree status and cardinal directions for planted *Larix olgensis* Henry trees in Northeast China. Forests, 8(5): 139.

Gill, S.J. and Biging, G.S. 2002. Autoregressive moving average models of conifer crown profiles. Journal of Agricultural, Biological, and Environmental Statistics, 7(4): 558.

Giltinan, D. and Davidian, M. 1995. Non-linear models for repeated measurement data. In: Monographs on Statistics and Applied Probability, ISBN 772450420, Chapman and Hall.

Guo, Y.R., Wu, B.G., Zheng, X.X., Zheng, D.X., Liu, Y., Dong, C. and Zhang, M.B. 2015. Simulation model of crown profile for Chinese fir (Cunninghamia lanceolata) in different age groups. Journal of Beijing Forestry University, 37(02): 44-51.

Hann, D.W. 1998. An adjustable predictor of crown profile for stand-grown Douglas-fir trees. Forest Science, 45(2): 217-225.

Insightful Corporation 2007. S-PLUS 8. Insightful Corporation, Seattle, WA.

Lindstrom, M.J. and Bates, D.M. 1990. Non-linear mixed effects models for repeated measures data. Biometrics, pp. 673-687.

Lu, K., Zhang, H., Liu, M. and Ouyang, G. 2012. Design and implementation of individual tree growth visualization system of *Cunninghamia lanceolata*. Forest Research, 25(2): 207-211.

Marshall, D.D., Johnson, G.P. and Hann, D.W. 2003. Crown profile equations for stand-grown western hemlock trees in north. Canadian Journal of Forest Research, 33(11): 2059-2066.

Mohren, G. M. J. 1987. Simulation of forest growth, applied to Douglas fir stands in the Netherlands, Ph.D. Diss., Wageningen Agric. Univ., The Netherlands, 184 p.

Nepal, S. K. 1993. Crown Shape Modelling for Loblolly Pine: A Frontier Approach. Unpublished Ph.D. dissertation, Auburn University, Auburn, AL.

Pretzsch, H. 2014. Canopy space filling and tree crown morphology in mixed-species stands compared with monocultures. Forest Ecology & Management, 327: 251-264.

Pretzsch, H., Biber, P. and Ďurský, J. 2002. The single tree-based stand simulator SILVA: construction, application and evaluation. Forest Ecology and Management, 162(1): 3-21.

Purves, D.W., Lichstein, J.W. and Pacala, S.W. 2007. Crown plasticity and competition for canopy space: A new spatially implicit model parameterized for 250 North American tree species. PLoS One, 2(9): e870.

Raulier, F., Ung, C.H. and Ouellet, D. 1996. Influence of social status on crown geometry and volume increment in regular and irregular black spruce stands. Canadian Journal of Forest Research, 26(10): 1742-1753.

Rautiainen, M. and Stenberg, P. 2005. Simplified tree crown model using standard forest mensuration data for Scots pine. Agricultural & Forest Meteorology, 128(1-2): 0-129.

Sadono, R. 2015a. Crown model for Perhutani's teak plus from clonal seed garden aged 6 to 11 years in Madiun forest district, East Java, Indonesia. Australian Journal of Basic and Applied Sciences, 9(5): 151-160.

Sadono, R. 2015b. Crown shape development of Perhutani's teak plus from clonal seed orchards in Madiun, Saradan and Ngawi Forest District, East Java, Indonesia. Advances in Environmental Biology, 9(18): 212-221.

Wang, X., Lu, J. and Li, F. 2012. Crown profile simulation of major broadleaf species of natural secondary forest in north of China. Journal of Nanjing Forestry University (Natural Sciences Edition), 4: 004.

Nature Environment and Pollution Technology
An International Quarterly Scientific Journal

p-ISSN: 0972-6268 e-ISSN: 2395-3454	Vol. 18	No. 4	pp. 1363-1368	2019

Original Research Paper **Open Access**

Comparative Assessment of Biochemical Parameters of Plants in Industrial and Non-Industrial Areas of Western Odisha, India

Priyanka Priyadarshini and Chandan Sahu†
P.G. Department of Environmental Sciences, Sambalpur University, Jyoti Vihar-768019, Sambalpur, Odisha, India
†Corresponding author: Chandan Sahu

Nat. Env. & Poll. Tech.
Website: www.neptjournal.com

Received: 23-04-2019
Accepted: 21-06-2019

Key Words:
Ascorbic acid
Biochemical parameters
Catalase
Chlorophyll
Peroxidase

ABSTRACT

Industrialization being the main force of development has caused many changes not only in the global phenomena but also on a regional level through its ill effects on plants and animals. The present study was thus undertaken to assess the biochemical alterations in plants subjected to polluted (industrial) and non-polluted (control) environments. The results revealed that all the studied biochemical parameters (ascorbic acid, protein, carbohydrate, total chlorophyll, catalase, and peroxidase activities) showed significant variation with respect to sites ($p < 0.05$). Excepting the peroxidase activity, all other biochemical parameters showed a decline in their concentration in the polluted environment as compared to their counterparts in a non-polluted environment. The highest concentration of biochemical parameters in plants of polluted sites were: ascorbic acid (4.85 mg/g), carbohydrate (0.905 mg/g), protein (28.07 mg/g), total chlorophyll (1.13 mg/g), catalase (0.394 µmoles/H_2O_2 decomposed/min/g) and peroxidase (433.76 µmoles/GDHP/min/g) while that in the control site, the highest value of all the biochemical parameters were: ascorbic acid (8.97 mg/g), carbohydrate (1.283 mg/g), protein (48.68 mg/g), total chlorophyll (1.17 mg/g), catalase (0.434 µmoles/H_2O_2 decomposed/min/g) and peroxidase (271.25 µmoles/GDHP/min/g) respectively. Hence, it can be concluded that plants do undergo physiological stress when exposed to polluted environments and their biochemical synthesis is severely altered by pollution. However, they develop an inbuilt mechanism to counter the pollution and protect themselves in polluted or stressed environment. In the present study, peroxidase activity was primarily responsible to protect the plant in the stressed environment.

INTRODUCTION

Industries not only play an important role in the economic development of a nation but also produce both traditional pollutants (organic substances, sulphur dioxide, particulates, nitrogen oxide, etc.) and newly recognized pollutants (dioxins, furans and other toxic substances). These pollutants in various forms can cause serious damage to the biosphere.

Environmental pollution due to industries has led to a steep increase in various illnesses and it continues to affect on a daily basis. With so many small, mid and large-scale industries coming up, air pollution has taken a toll on the health of the people and the environment. With the rise in industrial pollution, global warming has been increasing at a steady pace. Melting of glaciers, extinction of polar bears, floods, tsunami, hurricanes coupled with rising in sea level, migration of species, invasion of diseases and change in oceanic currents are some of the effects of global warming.

The components of environment and living organisms nearby ecosystems are being badly affected by massive environmental pollution. It is a well-known fact that pollution creates a negative impact on human and plants. The harmful effects of pollution on vegetation have been studied by several workers (Agrawal et al. 1991, Dasgupta et al. 2002). Plants being the initial acceptor to pollutants, experience many adverse consequences like chlorosis, bleached leaves, stunted growth, necrosis, lack of pigmentation, destruction of guard cell in the stomatal region, premature defoliation etc. Besides these, ozone has been reported to decrease the photosynthetic rate and injure the intermediate-aged leaves. While SO_2 damage the plants through interveinal bleaching of leaves, fluoride creates toxicity, bleaching of the tips and margins of leaves (Caldwell 1970, Rhimi et al. 2016).

Air pollutants induce morphological, physiological and biochemical changes in plants (Seyyednejad & Koochak 2011, Areington et al. 2015). Biochemical synthesis mainly includes protein synthesis, carbohydrate synthesis, catalase activity, peroxidase activity etc. involving plant biochemistry associated with the molecular mechanism of the plant cell (Okano et al. 1985, Soda et al. 2000, Vollenweider et al. 2003, Chaudhary et al. 2008). Plants have a very important role in combating the level of air pollution in the at-

mosphere by taking up gaseous pollutants and particulates. Primarily, most of the particulate matters are deposited on the upper surface of the leaves. This deposition leads to the reduction in photosynthetic pigment like chlorophyll and carotenoids ultimately affecting the total productivity of the plant. Pollution creates a stress condition in the plant body which leads to a change in biochemical synthesis. The negative effect on the biochemical synthesis causes deterioration in the tolerance of plants.

Keeping this in view, work was undertaken to assess the biochemical parameters of plants in an industrial and non-industrial area of Western Odisha, India to analyse the impact of stress induced by the pollution due to industrial activities.

MATERIALS AND METHODS

Geographical description of the study area: The study area (experimental/polluted industrial site), selected for the present investigation, was near Hindalco aluminium smelter plant in Hirakud of Sambalpur district located at the geographical coordinates between 21.5138° N and 83.3508° E at an elevation of 161 m above MSL. The control site (non-polluted) was chosen to be the campus of Sambalpur University located at an aerial distance of 15 km from the polluted site and found within the geographical coordinates between 21.5789° N and 83.4483° E situated at an elevation of 180 m above MSL.

Sampling and selection of plant species: The study was carried out during the month of July 2018. Five evergreen plants based on their commonness to both the sites (polluted and non-polluted) were chosen for the investigation, the details of which are presented in Table 1. Leaves were carefully cut from the base of their petiole in triplicates from each plant species and wrapped in a polythene bag. The leaves present at least 6 ft above the ground were only considered for the present study. Then it was quickly transported to the laboratory for further analysis after keeping inside an ice-box. All the biochemical parameters were determined for each species taking three replicates.

Biochemical analysis of leaf: The ascorbic acid content of leaves was analysed by DCPIP (2,6-dichlorophenol indophenol) method given by Keller & Schwager (1977). Similarly, the carbohydrate and protein content of the leaves was analysed following the anthrone reagent method (Yemm & Wills 1954) and Folin's reagent method (Lowry et al. 1951) respectively. The total chlorophyll content of the leaves was analysed by the acetone method given by Arnon (1949) while the catalase and peroxidase activities in leaves were determined by the methods given by Aebi (1974) and Putter (1974) respectively.

RESULTS AND DISCUSSION

Results

The results of various biochemical parameters of plants from the control (non-industrial) and experimental (industrial) sites are presented in Table 2. It is evident from the table that ascorbic acid content ranged between 0.61 ± 0.04 (*F. religiosa*) and 8.97 ± 0.35 (*F. benghalensis*) mg/g in the control site while that in the experimental site, it ranged between 0.30 ± 0.27 (*F. religiosa*) and 4.85 ± 0.12 *(M. indica*) mg/g. The carbohydrate content ranged between 0.524 ± 0.069 *(M. indica)* and 1.283 ± 0.32 *(A. indica)* mg/g in the control site, and between 0.295 ± 0.066 *(M. indica)* and 0.905 ± 0.029 *(A. indica)* mg/g in the experimental site. The protein content of various plant species ranged between 28.48 ± 2.04 *(A. indica)* and 48.68 ± 6.3 *(F. religiosa)* mg/g in the control site, and between 10.99 ± 0.15 *(A. scholaris)* and 28.07 ± 0.7 *(F. religiosa)* mg/g in the experimental site. The chlorophyll content of various plant species, on the other hand, was observed with the highest value of 1.17 ± 0.01 and 1.17 ± 0.03 mg/g in *F. benghalensis* and *A. indica* respectively, and lowest value of 0.083 ± 0.006 mg/g in *F. religiosa* in the control site. The same in the experimental site, ranged between 0.33 ± 0.0006 *(F. religiosa)* and 0.63 ± 0.013 *(M. indica)* mg/g.

Similarly, the catalase and peroxidase activities of various plant species were found to be in the range of 0.183 ± 0.001 *(A. scholaris)* - 0.434 ± 0.004 *(F. religiosa)* μmoles/

Table 1: Description of the evergreen plant species selected for the present study.

Sl. No.	Species Name	Common Name	Family
1.	*Ficus benghalensis* (L)	Bara	Moraceae
2.	*Ficus religiosa* (L)	Peepal	Moraceae
3.	*Mangifera indica* (L)	Amba	Anacardiaceae
4.	*Alstonia scholaris* (L)	Saptaparni	Apocyanaceae
5.	*Azadirachta indica* (A. Juss)	Neem	Meliaceae

Table 2: Biochemical parameters of plants in industrial and non-industrial sites of western Odisha.

Parameters	Sites	FB	FR	MI	AS	AI
Ascorbic acid (mg/g)	Control	8.97 ± 0.35	0.61 ± 0.04	7.94 ± 0.48	4.33 ± 0.03	4.66 ± 0.04
	Experimental	2.90 ± 0.01	0.30 ± 0.27	4.85 ± 0.12	3.14 ± 0.01	4.56 ± 0.04
Carbohydrate (mg/g)	Control	0.916 ± 0.024	0.773 ± 0.029	0.524 ± 0.069	0.865 ± 0.013	1.283 ± 0.32
	Experimental	0.870 ± 0.140	0.551 ± 0.016	0.295 ± 0.066	0.457 ± 0.049	0.905 ± 0.029
Protein (mg/g)	Control	37.94 ± 5.4	48.68 ± 6.3	37.32 ± 6.3	30.36 ± 2.4	28.48 ± 2.0
	Experimental	20.82 ± 0.2	28.07 ± 0.7	12.50 ± 0.6	10.99 ± 0.8	12.07 ± 0.8
Total Chlorophyll (mg/g)	Control	1.17 ± 0.001	0.083 ± 0.006	1.12 ± 0.006	0.88 ± 0.01	1.17 ± 0.003
	Experimental	1.03 ± 0.002	0.74 ± 0.0006	1.004 ± 0.013	0.73 ± 0.009	1.13 ± 0.001
Catalase (μmoles/H_2O_2 decomp./min/g)	Control	0.214 ± 0.0008	0.434 ± 0.0016	0.237 ± 0.0021	0.183 ± 0.0014	0.189 ± 0.0021
	Experimental	0.169 ± 0.0021	0.394 ± 0.0044	0.211 ± 0.0016	0.174 ± 0.0028	0.163 ± 0.0016
Peroxidase (μmoles/ GDHP/min/g)	Control	172.55 ± 5.95	271.25 ± 37.85	268.03 ± 8.44	219.44 ± 26.79	215.93 ± 22.93
	Experimental	205.56 ± 4.81	433.76 ± 59.56	349.21 ± 13.74	283.8 ± 17.87	343.48 ± 37.11

FB = *Ficus benghalensis*, FR = *Ficus religiosa*, MI = *Mangifera indica*, AS = *Alstonia scholaris*, AI = *Azadirachta indica*

H_2O_2 decomposed/min/g protein, and 172.55 ± 5.95 *(F. benghalensis)* - 271.25 ± 37.83 *(F. religiosa)* μmoles/ GDHP/min/g respectively in the control site while that in the experimental site, it was found to be in the range of 0.163 ± 0.002 *(A. indica)* - 0.394 ± 0.001 *(F. religiosa)* μmoles/H_2O_2 decomposed/min/g protein and 205.56 ± 4.81 *(F. benghalensis)* - 433.76 ± 59.56 *(F. religiosa)* μmoles/ GDHP/min/g respectively.

The two-way ANOVA computed for various biochemical parameters between species and sites is presented in Table 3. It is evident from the table that significant variation was exhibited, both with respect to species and sites in case of the carbohydrate, protein, total chlorophyll content and catalase activity of the plants ($F_1 \geq 9.02$, $F_2 \geq 15.68$; $p < 0.05$) while, ascorbic acid content and the peroxidase activity exhibited significant variation only with respect to sites ($F_2 \geq 9.03$; $p < 0.05$).

The Pearson correlation matrix worked out between various biochemical parameters of plants in control and experimental sites is presented in Tables 4 and 5 respectively. The values marked with an asterisk (*) in the tables suggests a strong correlation at 0.05 level of significance. It is evident from the table that, in the control site, significant positive correlation was found between ascorbic acid and total chlorophyll; protein content and catalase activity; and catalase and peroxidase activity ($r \geq +0.626$; $p < 0.05$) while, significant negative correlation was observed between ascorbic acid and catalase activity; carbohydrate

Table 3: Two-way ANOVA for various biochemical parameters between various species in different sites.

Parameters	Source of Variation	SS	df	MS	$F_{tab\ at\ 0.05}$	$F_{crit\ at\ 0.05}$	S/NS
Ascorbic acid	Between Species	40.98	4	10.24	4.24	6.39	NS
	Between Sites	21.78	1	21.78	9.03	7.71	S
Carbohydrate	Between Species	0.54	4	0.13	12.87	6.39	S
	Between Sites	0.16	1	0.16	15.68	7.71	S
Protein	Between Species	448.54	4	112.13	20.10	6.39	S
	Between Sites	966.88	1	966.88	173.33	7.71	S
Total Chlorophyll	Between Species	0.14	4	0.04	9.02	6.39	S
	Between Sites	0.76	1	0.76	187.62	7.71	S
Catalase	Between Species	0.081	4	0.02	204.89	6.39	S
	Between Sites	0.002	1	0.002	21.45	7.71	S
Peroxidase	Between Species	30380.62	4	7595.15	5.69	6.39	NS
	Between Sites	21658.78	1	21658.78	16.24	7.71	S

and peroxidase activity; and total chlorophyll and catalase activity ($r \geq -0.566$; $p < 0.05$). Similarly, in the experimental site, significant positive correlation was found between ascorbic acid and total chlorophyll content; protein and catalase activity; and catalase and peroxidase activity ($r \geq +0.774$; $p < 0.05$), while significant negative correlation was observed between ascorbic acid and protein; ascorbic acid and catalase activity; protein and total chlorophyll; and total chlorophyll and catalase activity ($r \geq -0.576$; $p < 0.05$).

The percent reduction in biochemical parameters of plant leaves is given in Table 6. From the table, it was observed that only peroxidase showed increment in its activity in the plant species of the polluted site as compared to the same species in control site while all other parameters showed a reduction in concentration. In the case of ascorbic acid, *F. religiosa* showed an insignificant reduction ($p > 0.05$) while all other studied species (*F. benghalensis, M. Indica, A. scholaris, A. indica*) showed a significant reduction. Similarly, in case of carbohydrate, *F. benghalensis, M. indica* and *A. scholaris* showed an insignificant reduction ($p > 0.05$), whereas, that of protein and chlorophyll showed a significant reduction in all of the studied species ($p < 0.05$). On the other hand, catalase exhibited an insignificant reduction in *A. scholaris* only ($p > 0.05$).

Discussion

Ascorbic acid has been reported to behave as a stress reducer in plants. It is an anti-oxidant and has multiple functions

Table 4: Correlation matrix between various parameters of plants at control site.

	AA	Carbo	Prot	TC	Cat	Perox
AA	1					
Carbo	-0.151	1				
Prot	-0.367	-0.536	1			
TC	0.796*	0.292	-0.449	1		
Cat	-0.670*	-0.348	0.928*	-0.601*	1	
Perox	-0.523	-0.566*	0.481	-0.486	0.626*	1

'*' $p < 0.05$, AA- Ascorbic acid, Carbo- Carbohydrate, Prot- Protein, TC-Total Chlorophyll, Cat- Catalase, Perox- Peroxidase

Table 5: Correlation matrix between various parameters of plants at the experimental site.

	AA	Carbo	Prot	TC	Cat	Perox
AA	1					
Carbo	-0.008	1				
Prot	-0.882*	0.157	1			
TC	0.876*	-0.045	-0.576*	1		
Cat	-0.818*	-0.295	0.807*	-0.634*	1	
Perox	-0.347	-0.371	0.318	-0.354	0.774*	1

'*' $p < 0.05$, AA- Ascorbic acid, Carbo- Carbohydrate, Prot- Protein, TC-Total Chlorophyll, Cat- Catalase, Perox- Peroxidase

Table 6: Percent reduction in biochemical parameters of plant leaves.

	F. benghalensis	*F. religiosa*	*M. indica*	*A. scholaris*	*A. indica*
Ascorbic acid	67.67*	50.82	38.92*	27.48*	2.15*
Carbohydrate	5.02	28.72*	43.70	47.17*	29.46
Protein	45.12*	42.34*	66.51*	63.80*	57.62*
Chlorophyll	55.56*	60.24*	43.75*	53.41*	55.56*
Catalase	21.03*	9.22*	10.97*	4.92	13.76*
Peroxidase	-19.13*	-59.91	-30.29*	-29.33	-59.07*

'*' $p < 0.05$

through cell wall synthesis, cell division, and protection of plants against the reactive oxygen species (ROS) besides acting as an enzyme cofactor in photosynthesis (Hippeli & Elstner 1996). The present study observed a decline in the concentration of ascorbic acid in the industrial site as compared to the counterparts in the control site. This observation was against the findings reported by many workers who opined that ascorbic acid tends to increase in polluted areas since plants develop a tolerance mechanism when exposed to polluted air primarily attributed to the synthesis of ascorbic acid (Liu & Ding 2008, Rai et al. 2013). This suggests that all the selected plant species in this study have not responded well enough with respect to ascorbic acid synthesis to tolerate the air pollution and hence are likely to be affected due to the reactive oxygen species formed in the air of the polluted site.

Carbohydrate is the primary food material that helps plants to counter the stress condition. The concentration of carbohydrate reflects the carbon assimilative capacity of plants (Tripathi & Gautam 2007). Significant reduction of the carbohydrate content of plants in the polluted environment could have possibly been due to less photosynthetic activity consequent to the significant depletion of chlorophyll content of leaves. The present result suggests that the plants were severely affected due to the polluted environment thereby causing a reduction in their carbohydrate content.

Protein is the most important bio-molecule responsible for the growth and development of plants. The present study also observed a significant reduction in protein content of plants in the polluted site than the control site in all the studied species. The possible cause could have been the denaturation and breakdown of existing protein complex to amino acids assisted by enzyme activities responsible for polypeptide breakdown during the stress period (Dohmen 1990). Decrease in protein content of leaves has also been reported to cause senescence of leaves (Kar & Mishra 1976). This further suggests that the plants in polluted environment are likely to suffer from early leaf fall.

Chlorophyll content is not only associated with food production but also is closely related with ascorbic acid synthesis and therefore plays an important role in the defence mechanism of plants. Reduction in the chlorophyll content leads to yellow coloration of leaf that ultimately causes leaf senescence (Kar & Mishra 1976). The observation of a significant reduction of chlorophyll content in the studied plants could have been due to the impact of dust or particulate matter which is a common pollutant in the industrial environment. Several studies have supported the view that chlorophyll content undergoes rapid degradation under the influence of dust pollution. Our study was consistent with the findings of Prusty et al. (2005) who also reported the negative effects of dust on chlorophyll content of leaves.

Catalase and peroxidase accelerate the decomposition of hydrogen peroxide to water and oxygen. These enzymes have anti-oxidative properties mainly responsible to protect the plants from any oxidative damage caused by ROS. These enzymes have been considered as good parameters to indicate air pollution (Khan et al. 1990). Catalase activity is variable within species. Some species show an increased activity nearing senescence while others exhibit decreased activity. The present study observed an increase in the activity of peroxidase but a decrease in catalase activity. Although, both the enzymes have the same prosthetic group (iron-porphyrin), the variation in their activities has been previously reported by other workers. The increase of peroxidase enzyme activity suggests that the plant protection against the pollution stress in the industrial area was chiefly managed by this particular (peroxidase) enzyme when other protecting bio-molecule like ascorbic acid and catalase activity failed to cope up to the polluted environment. Peroxidase activity bearing a non-significant negative correlation with chlorophyll content was consistent with the findings reported by Kar & Mishra (1976) while the antagonistic relation between peroxidase activities and stress (both biotic and abiotic) is also supported by Bharwana et al. (2016).

CONCLUSION

The present investigation tried to make a comparative assessment of the biochemical parameters of plants in the industrial area of Hindalco, Hirakud against a control area located at an aerial distance of around 15 km i.e. the campus of Sambalpur University. The results clearly highlight the fact that the plants growing near the industrial area are facing serious stress condition which is reflected from the depletion in their biochemical synthesis. Their defence mechanism (primarily the peroxidase activity in this case) against the polluted environment has led to their sustenance till date. It can be inferred from the study that plants develop their own strategy to counter the pollution stress by either reducing or enhancing some of their biochemical synthesis.

REFERENCES

Aebi, H. 1974. Catalase. In: Bergmeyer, H.U., Ed., Methods of Enzymatic Analysis, Verlag Chemie, Academic Press Inc., Weinheim, NewYork, 673-680.

Agrawal, M., Singh, S.K., Singh, J. and Rao, D.N. 1991. Biomonitoring of air pollution around urban and industrial sites. Journal of Environmental Biology, 12: 211-222

Areington, C.A., Varghese, B., Ramdhani, S. and Sershen 2015. An assessment of morphological, physiological and biochemical biomarkers of industrial air pollution in the leaves of *Brachylaena* discolour. Journal of Water Air Soil Pollution, 226: 291

Arnon, D.I. 1949. Copper enzymes in isolated chloroplasts. Polyphenoloxidase in *Beta vulgaris*. Plant Physiology, 24: 1-15.

Bharwana, S.A., Ali, S., Farooq, M.A., Farid, M., Bashir, N. and Ahmad, R. 2016. Physiological and biochemical changes induced by lead stress in cotton (*Gossypium hirsutum* L.) seedlings. Academia Journal of Agricultural Research, 4(4): 160-167.

Caldwell, R.L. 1970. Effects of air pollution on vegetation. Journal of Progressive Agriculture, 22 (2): 10-12

Chaudhary, A., Chaudhary, S. and Sharma, Y.K. 2008. Study of plant in relation to ambient air quality in Lucknow city, Uttar Pradesh. Journal of Research in Environment and Life Science, 1(1): 17-20

Dasgupta, S., Laplante, B., Mamingi, N. and Wang, H. 2002. Inspection, pollution price and environmental performance: evidence from China, Journal of Ecological Economics, 32: 487-498

Dohmen, G.P., Koppers, A. and Langebartels, C. 1990. Biochemical response of Norway spruce (*Picea abies* (L.) Karst.) towards 14-month exposure to ozone and acid mist: Effects on amino acid, glutathione and polyamine titers. Environmental Pollution, 64(3-4): 375-383

Hippeli, S. and Elstner, E.F. 1996. Mechanisms of oxygen activation during plant stress: Biochemical effects of air pollutants. Journal of Plant Physiology, 148: 249-257.

Kar, M. and Mishra, D. 1976. Catalase, peroxidase and polyphenoloxidase Activities during Rice Leaf Senescence. Plant Physiology, 57: 315-319.

Keller, T. and Schwager, H. 1977. Air pollution and ascorbic acid. European Journal of Forestry Pathology, 7: 338-350.

Khan, A.M., Pandey, V., Shukla, J., Singh, N., Yunus, M., Singh, S.N. and Ahmad, K.J. 1990. Effect of thermal power plant emission on *Catharanthus roseus* L. Bulletin of Environmental Contamination and Toxicology, 44: 865-870.

Liu, Y.J. and Ding, H. 2008. Variation in air pollution tolerance index of plants near a steel factory: Implications for landscape-plant species selection for industrial areas. WSEAS Transactions on Environment and Development, 1(4): 24-32.

Lowry, O.H., Rosebrough, N.J. and Randall, R.J. 1951. Protein measurement with the folin phenol reagent. J. Biol. Chem., 193: 265-275.

Okano, K., Totsuka, T., Fukuzawa, T. and Tazaki, T. 1985. Growth responses of plants to various concentrations of nitrogen dioxide. Journal of Environmental Pollution, 38(4): 361-373

Prusty, B.A.K., Mishra, P.C. and Azeez, P.A. 2005. Dust accumulation and leaf pigment content in vegetation near the national highway at Sambalpur, Orissa, India. Ecotoxicology and Environmental Safety, 60: 228-235.

Putter, J. 1974. Peroxidase. In: Bergmeyer, H.U., Ed., Methods of Enzymatic Analysis, Verlag Chemie, Academic Press Inc., Weinheim, New York, 685-690.

Rai, P.K., Panda, L.L.S., Chutia, B.M. and Singh, M.M. 2013. Comparative assessment of air pollution tolerance index (APTI) in the industrial (Rourkela) and non industrial area (Aizawl) of India: An ecomanagement approach. African Journal of Environmental Science and Technology, 7(10): 944-948.

Rhimi, N., Ben-Ahemad, C., Elloumi, N., Athar, H.R., Noreen, S., Ashraf, M., Ben Abdallah, F. and Ben-Nasari, A.M. 2016. Morpho-anatomical and physiological changes in grapevine leaves exposed to atmospheric fluoride and sulphur dioxide pollution. Journal of Applied Ecology and Environmental Research, 14(5): 77-89

Seyyednejad, S.M. and Koochak, H. 2011. Some morphological and biochemical responses due to industrial air pollution in *Prosopis juliflora* (Swartz) DC plant. African Journal of Agricultural Research, 8 (18): 1986-1974

Soda, C., Bussotti, F., Grossoni, P., Barnes, J., Mori, B. and Tani, C. 2000. Impact of urban levels of ozone on *Pinus halepensis* foliage. Journal of Environmental and Experimental Botany, 44: 69-82

Tripathi, A.K. and Gautam, M. 2007. Biochemical parameters of plants as indicators of air pollution. J. Environ. Biol., 28: 127-132

Vollenweider, P., Ottiger, M. and Gunthardt-Goerg, M.S. 2003. Validation of leaf ozone symptoms in natural vegetation using microscopic methods. Journal of Environmental Pollution, 124: 101-118

Yemm, E.W. and Wills, A.J. 1954. The estimation of carbohydrate in plant extract by Anthrone. Biochemistry Journal, 57: 508-514.

Nature Environment and Pollution Technology
An International Quarterly Scientific Journal

p-ISSN: 0972-6268
e-ISSN: 2395-3454

Vol. 18 | No. 4 | pp. 1369-1374 | 2019

Original Research Paper | Open Access

Comparison for the Adsorption of Catechol and Hydroquinone on Activated Carbon Fibre: Kinetic Analysis

Mingzhao Shen*, Meiya Zhu, Jintao Sun*, Yunlong Zhang*, Rong Li*, Fang Niu*, Shiying Li*, Xiao Mi* and Guoting Li*†**

*Department of Environmental and Municipal Engineering, North China University of Water Resources and Electric Power, Zhengzhou 450011, China

**Library, North China University of Water Resources and Electric Power, Zhengzhou 450011, China

†Corresponding author: Guoting Li

Nat. Env. & Poll. Tech.
Website: www.neptjournal.com

Received: 22-11-2018
Accepted: 30-05-2019

Key Words:
Catechol
Hydroquinone
Adsorption
Activated carbon fibre
Toxic organic pollutants

ABSTRACT

Catechol and hydroquinone are widely applied in industrial synthesis while they are typical toxic organic pollutants. Efficient adsorptive removal of catechol and hydroquinone is highly needed. In this research, activated carbon fibre (ACF) was used for the kinetic removal of the two pollutants. As catechol and hydroquinone have different pK_a values, it was found that the highest uptake of catechol and hydroquinone was observed at pH 11.0 and 5.0, respectively. The adsorption kinetics for catechol and hydroquinone were compared. The removal of hydroquinone is higher than that of catechol at almost all the pH conditions. At pH 7.0, the uptake of catechol and hydroquinone on ACF were 125.8 and 200.4 mg/g, respectively. As both Elovich and pseudo-second-order kinetic models could better describe the adsorption process, the adsorption of catechol and hydroquinone onto ACF might be chemisorption. The rate determining step might be diffusive in nature for the uptake of catechol and hydroquinone. Linear pseudo-second-order kinetic model fitted the experimental data better than pseudo-first-order kinetic model. The presence of natural organic matter, humic acid, could inhibit the uptake of catechol and hydroquinone on ACF profoundly.

INTRODUCTION

Catechol and hydroquinone are typical organic pollutants existing in natural water environment as a consequence of anthropogenic activities. Wastewater containing catechol is usually generated by several industries including rubbers, chemical, dye, photographic, pharmaceutical, cosmetics, and oil industry. This is because catechol is used as a topical antiseptic, and in photography, fur dying, leather tanning, antifungal preservation of seed potato pieces, and in polymerization inhibitors as well as a chemical intermediate, and an antioxidant in many industries (Asfour et al. 1985, Dou 1990, Schweigert et al. 2001). Nevertheless, catechol is readily absorbed from the gastrointestinal tract, causes haemolysis, degenerates the renal tubes, diminishes liver function, and accumulates in the bone marrow (Irons 1990). Meanwhile, hydroquinone is widely used in pesticides, medicine, rubber, medicine, and the fine chemicals are considered to be hazardous and toxic to some organisms and can cause vomiting, tinnitus, nausea, and abdominal pain in humans (Xue et al. 2005). Considering the acute and chronic toxicity of catechol and hydroquinone, it is highly necessary to remove them from contaminated water.

On the other hand, as undesirable and toxic intermediates, the accumulation of catechol and hydroquinone has been reported during wet catalytic oxidation and electrochemical oxidation of phenol (Santos et al. 2002, Li et al. 2014). The accumulation of cyclic intermediate organics such as catechol and hydroquinone usually occurred because the ring-opening reaction is the most difficult step during the oxidation of aromatic pollutants. Our previous study proved that activated carbon fibres (ACF) were capable of removing these cyclic intermediate organics and effectively lower the toxicity of the effluent treated by electrochemical oxidation (Li et al. 2015).

Accordingly, the adsorption process is considered to be particularly suitable for the removal of catechol and hydroquinone because of its high efficiency, low energy consumption and environment-friendliness. Thus, there is a strong desire to find a high-performance, low-cost, and easily regenerated adsorbent to remove catechol and hydroquinone from wastewater.

Some researchers consider that the excellent absorbent materials must have high specific surface area, chemical stability, and a lot of adsorption sites (Zhao et al. 2012). Meanwhile, fibrous adsorbents have advantages such as

fast adsorption rate and ease of handling in comparison with granular adsorbents and powdered adsorbents. ACF have attracted wide attention due to their especially high removal efficiency and adsorption capacity. Due to its high chemical stability, ACF has been widely studied as a catalyst support for catalyst preparation or directly used as a catalyst (Adapa et al. 2006, Qu et al. 2007). As a result, it demonstrates that ACF is an ideal adsorbent to achieve high-efficiency adsorptive removal of organic contaminants. In this research, ACF was intentionally used for adsorptive removal of catechol and hydroquinone. Adsorption kinetics and solution pH effect were emphatically explored and discussed. The adsorption capability for catechol and hydroquinone was compared quantitatively.

MATERIALS AND METHODS

Chemicals: Catechol and hydroquinone (analytical grade) were purchased from Tianjin Kermal Chemical Reagents Co., Ltd (Tianjin, China) and used without further purification. The activated carbon fibre (ACF) was provided by Liaoning Anshan Senxin Activated Carbon Environmental Materials Co., Ltd (China). Its thickness is 2 mm and the average surface area is 1500 m^2/g. Deionized (DI) water was used throughout this study.

Batch adsorption studies: Stock solutions of catechol and hydroquinone (500 mg/L) were diluted to get desired concentration with DI water. Kinetic experiments were carried out in a 500 mL beaker. A desired amount of ACF (200 mg) was added to a conical flask containing 500 mL of catechol or hydroquinone solution with a concentration of 100 mg/L. The solution pH was maintained by adding 0.1 mol L^{-1} of HCl or NaOH unless otherwise stated. For the pH effect study, the solution pH was kept at neutral pH 7.0. The suspension was mixed with a magnetic stirrer at 160 rpm. Samples were collected at desired time intervals and filtered through a 0.45 μm pore-size membrane before measurement.

Analysis of catechol and hydroquinone: The concentration of catechol and hydroquinone was measured by an UVmini-1240 spectrophotometer (Shimadzu, Japan) to monitor emissions at the wavelength of 275 and 288 nm, respectively (McBrlde & Wessellnkt 1988, Yildiz et al. 2005). The adsorption capacity was calculated using the following equation:

$$q_e = (C_0\text{-}C_e)V/W \quad \ldots(1)$$

$$q_t = (C_0\text{-}C_t)V/W \quad \ldots(2)$$

Where, q_e and q_t (mg/g) are the adsorption capacity at equilibrium and time t (min); C_0 is the initial TC concentration, while C_e and C_t (mg/L) are the concentrations of TC at equilibrium and t (min), respectively; V (L) is the volume of solution, and W (g) is the mass of ACF.

RESULTS AND DISCUSSION

Effect of Solution pH on Catechol and Hydroquinone Adsorption

Solution pH can not only influence the species distribution of catechol and hydroquinone but also the surface properties of ACF. Effect of solution pH was investigated at pH 3.0, 5.0, 7.0, 9.0 and 11.0, respectively. As illustrated in Fig.1, the highest uptake of catechol and hydroquinone was observed at pH 11.0 and 5.0, respectively. It indicates that the removal of hydroquinone is higher than that of catechol at almost all the pH conditions. At pH 7.0, the uptake of catechol and hydroquinone on ACF was 125.8 and 200.4 mg/g, respectively. As there is lack of functional groups

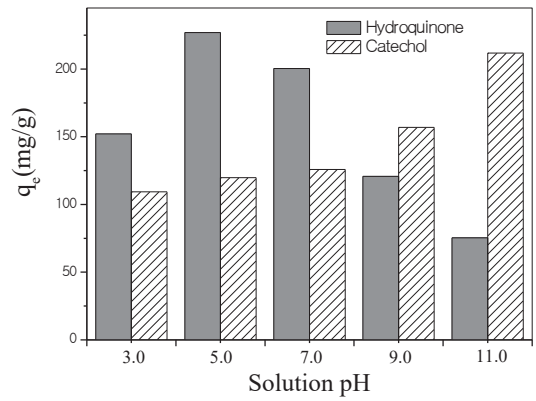

Fig.1: Effect of solution pH on the adsorption of catechol and hydroquinone onto ACF.

on ACF surface, it is deduced that the charge properties of ACF surface is quite stable. Concerning catechol (pK_a = 9.48), the catecholate anion predominates at pH ≥ 9.9, the especially higher negatively charged properties of catecholate anions might increase the electrostatic interaction and help improve the adsorption of catechol on ACF (Shakir et al. 2008). As to hydroquinone (pK_a = 10.35), the lower adsorption at higher pH may be due to the abundance of OH^- ions. The increased sorption at low pH suggests that the adsorption of the less ionic species of hydroquinone was higher than the more ionic species (Yildiz et al. 2005).

Adsorption Kinetics

As both, catechol and hydroquinone, are not stable enough for colorimetric determination in alkaline solutions, only the kinetic experiments in acidic and neutral solution were conducted for this test. The adsorption kinetics of catechol and hydroquinone onto ACF was investigated at solution pH 3.0 and 7.0, respectively. Typical kinetic models, including pseudo-first-order, pseudo-second-order and Elovich models, were used to fit the experimental data. The mathematical representations of the non-linear and linear models of pseudo-first-order and pseudo-second-order kinetics are presented below (Lagergren 1898, Ho & McKay 1999):

$$q_t = q_e(1 - e^{-k_1 t}) \quad \ldots(3)$$

$$\ln(q_e - q_t) = \ln q_e - k_1 t \quad \ldots(4)$$

$$q_t = \frac{k_2 q_e^{\,2} t}{(1 + k_2 q_e t)} \quad \ldots(5)$$

$$\frac{t}{q_t} = \frac{1}{k_2 q_e^{\,2}} + \frac{t}{q_e} \quad \ldots(6)$$

Where, q_e and q_t are the adsorption capacities (mg/g) at equilibrium and at time t (min), respectively; and k_1 (min^{-1}) and k_2 (g mg/min) are the related adsorption rate constants for pseudo-first-order and pseudo-second-order model, respectively.

The Elovich model, used to describe chemisorption occurring on the solid-liquid interface, can be written as (Kithome 1988):

$$q_t = k \ln(t) + a \quad \ldots(7)$$

Where, a (g·mg/min) and b (mg/g) are constants.

Non-linear Adsorption Kinetics

The experimental kinetic data at pH 3.0 and 7.0 were fitted by three kinetic models, and the simulated curves are presented in Fig. 2. From the non-linear kinetic fitting curves presented in Fig. 2, the experimental points are much closer to the simulated curves by Elovich and pseudo-second-order kinetic models under both the pH conditions, although Elovich kinetic model seems to be the best in this case. It is deduced that Elovich and pseudo-second-order kinetic models better described the experimental points than pseudo-first-order model. At the same time, the calculated non-linear kinetic parameters are given in Table 1. The correlation coefficients (R^2) of Elovich and pseudo-second-order models are much lower than those of pseudo-second-order model. Totally, Elovich and pseudo-second-order kinetic models are more suitable to describe the kinetic adsorption process and Elovich model is the best kinetic model for the adsorption kinetics. As both Elovich and pseudo-second-order kinetic models are used to describe the chemisorption process, the adsorption of catechol and hydroquinone onto ACF might be chemisorption. Accordingly, the rate determining step might be diffusive in nature for the uptake of catechol and hydroquinone in this case (Aharoni et al. 1991).

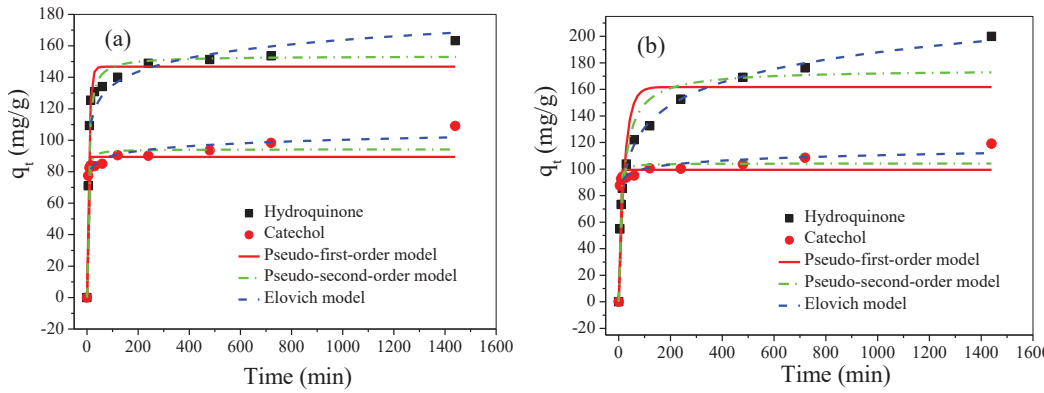

Fig. 2: Simulation of non-linear adsorption kinetics for pseudo-first-order, pseudo-second-order and Elovich models under pH 3.0 (a) and pH 7.0 (b).

Table 1: Non-linear kinetic parameters for the adsorption of catechol (CA) and hydroquinone (HQ) onto ACF.

Model	pH=3.0		pH=7.0	
	CA	HQ	CA	HQ
Pseudo-first-order model				
k_1 (min^{-1})	7.175	0.130	8.560	0.0438
q_e (mg/g)	89.38	146.8	99.49	161.8
R^2	0.895 0.902	0.964	0.914	0.860
Pseudo-second-order model				
k_2 (g/mg·min)	0.00757	0.00136	0.0078	0.00033
q_e (mg/g)	94.25	153.5	104.3	175.0
R^2	0.948 0.971	0.980	0.957	0.941
Elovich model				
a	69.75	77.01	79.86	17.28
k	4.420	12.56	4.421	24.71
R^2	0.986 0.984	0.943	0.988	0.988

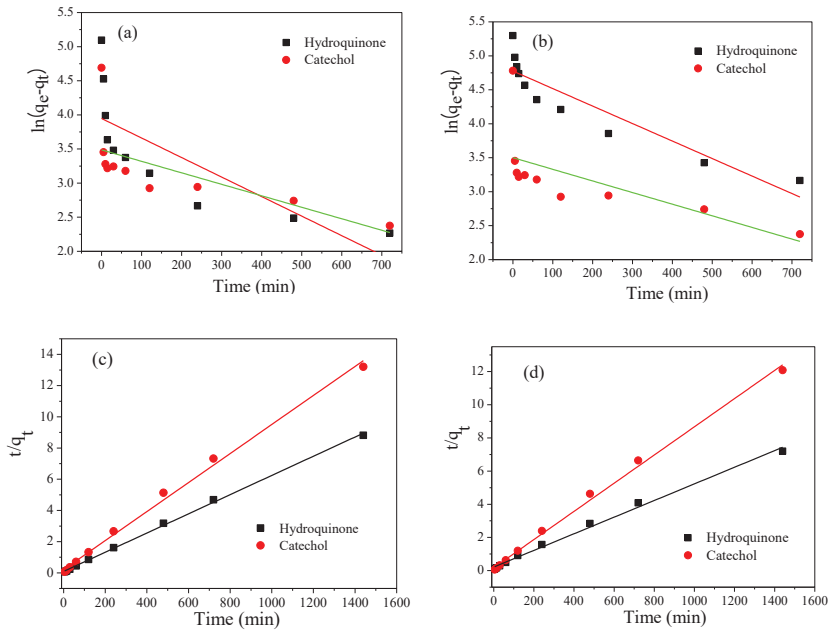

Fig. 3: Simulation of linear adsorption kinetics for pseudo-first-order (a,b) and pseudo-second-order (c,d) models under pH 3.0 (a,c) and pH 7.0 (b,d).

Linear Adsorption Kinetics

Meanwhile, both pseudo-first-order and pseudo-second-order kinetic models were employed for the linear kinetic fitting during adsorption of catechol and hydroquinone onto ACF, as illustrated in Fig. 3. By linear kinetic fitting presented in Fig. 3, pseudo-second-order kinetic model described the adsorption performance better than pseudo-first-order kinetic model. Meanwhile, the linear kinetic parameters for both models are calculated. At pH 3.0, the correlation coefficients (R^2) of pseudo-first-order models for catechol and hydroquinone are 0.569 and 0.395, respectively. As a comparison, at pH 3.0, the R^2

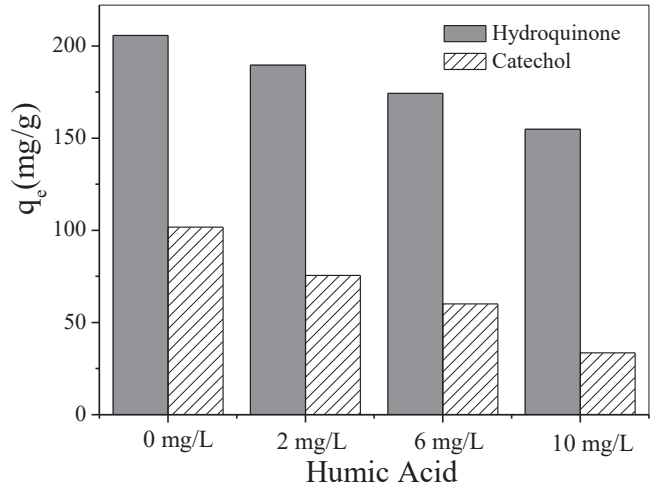

Fig.4: Effect of natural organic matter on the adsorption of catechol and hydroquinone on ACF.

values of pseudo-second-order models for catechol and hydroquinone are 0.995 and 0.995, respectively. Evidently, pseudo-second-order kinetic model better described the adsorption kinetic process. Overall, pseudo-second-order kinetic model fitted the experimental data better than pseudo-first-order kinetic model. As such, it can be inferred that chemisorption occurred during the uptake of catechol and hydroquinone on ACF.

Effect of natural organic matter on catechol and hydroquinone adsorption

Natural organic matter such as humic acid is ubiquitous in natural environment. Humic acid is a kind of macromolecule organic compound widely existing in natural water body. The existence of humic acid usually affects the adsorption and removal of pollutants from water. The effect of natural organic matter on the adsorption of catechol and hydroquinone on ACF was investigated. As presented in Fig. 4, the increasing humic acid concentration evidently decreased the uptake of catechol and hydroquinone on ACF. For catechol, the adsorption capacity reduced from 101.8 mg/g to 33.5 mg/g with an increase of humic acid concentration from 0 to 10 mg/L. For hydroquinone, the adsorption capacity reduced from 205.7 mg/g to 154.9 mg/g with an increase of humic acid concentration from 0 to 10 mg/L. As a result, the presence of humic acid could inhibit the uptake of catechol and hydroquinone on ACF profoundly.

CONCLUSION

As typical organic pollutants, catechol and hydroquinone were tentatively removed by activated carbon fibre (ACF). The highest uptake of catechol and hydroquinone was observed at pH 11.0 and 5.0, respectively. As both Elovich and pseudo-second-order kinetic models are used to describe the chemisorption process, the adsorption of catechol and hydroquinone onto ACF might be chemisorption. Accordingly, the rate determining step might be diffusive in nature for the uptake of catechol and hydroquinone. Pseudo-second-order kinetic model fitted the experimental data better than pseudo-first-order kinetic model. As such, it can be inferred that chemisorption occurred during the uptake of catechol and hydroquinone on ACF. The presence of humic acid could inhibit the uptake of catechol and hydroquinone on ACF profoundly.

ACKNOWLEDGEMENTS

The authors thank for the financial support from the foundation for university key youth teacher by Henan Province of China (2013GGJS-088).

REFERENCES

Adapa, S., Gaur, V. and Verm, N. 2006. Catalytic oxidation of NO by activated carbon fibre (ACF). Chem. Engi. J., 116: 25-37.

Aharoni, C., Sparks, D.L. and Levinson, S. 1991. Kinetics of soil chemical reactions: Relationships between empirical equations and diffusion models. Soil. Sci. Soc. Am. J., 55: 1307-1312.

Asfour, H.M., Fadali, O.A., Nassar, M.M. and El-Geundi, M.S. 1985. Equilibrium studies on adsorption of basic dyes on hardwood. J. Chem. Technol. Biotechnol., 35A: 21-27.

Dou, J.L. 1990. Occupational Medicine, Prentice-Hall International, Inc., USA.

Ho, Y.S. and McKay, G. 1999. Pseudo-second-order model for sorption process. Process Biochemistry, 34: 451-465.

Irons, R.D. 1985. Quinones as toxic metabolise of benzene. J. Toxicol. Environ. Health, 16: 673-678.

Kithome, M., Paul, J.W., Lavkulich, L.M. and Bomke, A.A. 1988. Kinetics of ammonium adsorption and desorption by the natural zeolite clinoptilolite. Soil Science Society of America, 62: 622-629.

Lagergren, S. 1898. Zur theorie der sogenannten adsorption gelöster stoffe. Kungliga Svenska Vetenskapsakademiens. Handlinga, 24: 1-39.

Li, F.Z., Li, G.T. and Zhang, X.W. 2014. Mechanism of enhanced removal of quinonic intermediates during electrochemical oxidation of Orange II under ultraviolet irradiation. J. Environ. Sci., 26: 708-715.

Li, G.T., Feng, Y.M., Chai, X.Q., Yang, Z.Y. and Zhang, X.W. 2015. Adsorption of cyclic organics generated during electrochemical oxidation of Orange II by activated carbon fibres and toxicity test. J. Water Proc. Engi., 7: 21-26.

McBrlde, M.B. and Wessellnkt, L.G. 1988. Chemisorption of catechol on gibbsite, boehmite and nanocrystalline alumina surfaces. Environ. Sci. Technol., 22: 703-708.

Qu, X.F., Zheng, J.T. and Zhang, Y.Z. 2007. Catalytic ozonation of phenolic wastewater with activated carbon fibre in a fluid bed reactor. J Colloid Interf. Sci., 309: 429-434.

Santos, A., Yustos, P., Quintanilla, A., Rodriguez, S. and García-Ochoa, F. 2002. Route of the catalytic oxidation of phenol in aqueous phase. Appl. Catal. B, 39: 97-113.

Schweigert, N., Alexander, J., Zehnder, J. and Eggen, R. 2001. Chemical properties of catechols and their molecular modes of toxic action in cells from microorganisms to mammals. Environ. Microbiol., 3: 81-91.

Shakir, K., Ghoneimy, H.F., Elkafrawy, A.F., Beheir, S.G. and Refaat, M. 2008. Removal of catechol from aqueous solutions by adsorption onto organophilic-bentonite. J. Hazard. Mater., 150: 765-773.

Xue, Y.L., Li, L. and Nie, S.Q. 2005. Studies on DNA damage of the blood cells in *Carassius auratus* induced by phenol and hydroquinone. Acta Hydrobiologica Sinica, 30: 241-243.

Yildiz, N., Gonulsen, R., Koyuncu, H. and Calimli, A. 2005. Adsorption of benzoic acid and hydroquinone by organically modified bentonites. Colloids and Surfaces A: Physicochem. Eng. Aspects, 260: 87-94.

Zhao, J.P., Ren, W.C. and Cheng, H.M. 2012. Graphene sponge for efficient and repeatable adsorption and desorption of water contaminations. J. Mater. Chem., 22: 20197-20202.

Nature Environment and Pollution Technology
An International Quarterly Scientific Journal

p-ISSN: 0972-6268
e-ISSN: 2395-3454

Vol. 18 | No. 4 | pp. 1375-1380 | 2019

Original Research Paper | Open Access

Adsorption Kinetics and Isotherms of Cr(VI) Ions in Aqueous Solution by Biochar Derived from *Torreya grandis* Nutshell

Chengcai Huang, Rui Qin, Linli Zhang, Muqing Qiu and Linfa Bao†
College of Life Science, Shaoxing University, Shaoxing, 312000, P.R. China
†Corresponding author: Linfa Bao

Nat. Env. & Poll. Tech.
Website: www.neptjournal.com

Received: 19-03-2019
Accepted: 01-06-2019

Key Words:
Cr(VI)
Biochar
Torreya grandis nutshell
Adsorption of heavy metals
Adsorption kinetics

ABSTRACT

Biochar is thought to be a good adsorption material for the adsorption of heavy metals. In this study, biochar derived from *Torreya grandis* nutshell was prepared through to be pyrolyzed under oxygen limited conditions in a muffle furnace. The adsorption experiments of Cr(VI) were carried out. Through Elemental Analyzer, Specific Surface Area Meter, Scanning Electron Microscopy, Transmission Electron Microscopy and Fourier Transform Infrared Spectroscopy, a fundamental understanding of the physical and chemical properties of biochar was gained. The results showed that it was a smooth sheet and irregular arrangement structure. The elements of C, H, O and N of biochar are 45.21%, 5.18%, 46.16% and 3.45% respectively. BET specific surface area of biochar is 42.24 m^2/g. A lot of oxygen-containing functional groups (– OH, COO –, – C – OH and so on) appeared on the surface of biochar. It can be described by the pseudo-second order kinetic rate model and Langmuir isotherm model. The adsorption process is a monolayer chemical process. The adsorption mechanism of biochar on heavy metal Cr(VI) contains the electrostatic attraction between biochar and $Cr_2O_7^{2-}$, $HCrO_4^-$ and CrO_4^{2-} ions in aqueous solution and complexation reaction of oxygen-containing functional groups (– OH, – COOH and so on) and $Cr_2O_7^{2-}$, $HCrO_4^-$ and CrO_4^{2-} ions on the surface of biochar.

INTRODUCTION

The metal of chromium and its compounds are a kind of toxic pollutants (Barrera-Díaz et al. 2012). The Cr(III) and Cr(VI) mainly exist in the environment. Cr(III) ions are relatively stable and less toxic (Litter 2015). However, Cr(VI) ions in aqueous solution have high solubility, the strong mobility, high toxicity and harmful to organisms. The concentration of Cr(VI) ions discharged from industries range from 0.1 to 100 mg/L. It is very important and urgent to treat Cr(VI) wastewater effectively (Xu et al. 2013, Du et al. 2015). At present, the treatment of Cr(VI) wastewater mainly includes chemical precipitation, redox, ion exchange, adsorption and so on. Among these treatment methods, the adsorption is widely applied into the treatment of wastewaters because of its high selectivity, economy, efficiency, simple operation and so on (Wang et al. 2016, Hu et al. 2017a).

Biochar is a good adsorption material for the adsorption of heavy metals. Biochar has a porous structure, and a lot of oxygen functional groups, such as hydroxyl, carboxyl, phenolic functional groups and so on, appear at the surface of biochar (Regmi et al. 2012, Wang et al. 2015, Park et al. 2018, Kretschmer et al. 2019). These oxygen functional groups are important for the adsorption of heavy metals. Some earlier researches showed that the adsorption mechanism of biochar on heavy metals involved electrostatic attraction, ion exchange, physical adsorption, complexation, precipitation, and a combination of multiple forces (Tong & Xu 2013, Ding et al. 2016, Park et al. 2016, Qiu et al. 2018, Hu et al. 2019). However, the adsorption mechanism for adsorption of different heavy metals is also different (Wang et al. 2015). Raw materials and pyrolysis temperature are important factors affecting the physical and chemical properties of biochar (Dutta et al. 2018, Mu et al. 2019). The adsorption capacity and characteristics of biochar for heavy metals are related to these properties. Biochar is usually prepared from terrestrial lignocellulosic materials and contains high content of carbon (Du et al. 2019). In China, the biomass resources are rich, such as peanut shells, straw, *Torreya grandis* nutshell, orange peel and so on. Most of them are burned directly, and not utilized effectively. It not only wastes resources, but also pollutes the environment. How to utilize them effectively is an urgent problem (Shen et al. 2015, Montesinos et al. 2016).

Torreya grandis is mainly grown in the relatively humid areas of southern China and distributed in Anhui and Zhejiang Provinces. Every year, a number of *Torreya grandis* nutshells are produced. In this work, *Torreya grandis* nutshell was chosen as the adsorbent. The foremost

objective of this research was to test the ability of biochar derived from *Torreya grandis* nutshell to remove Cr(VI) from aqueous solutions. Additionally, the other objectives are: (1) to gain a fundamental understanding of the physical and chemical properties of biochar derived from *Torreya grandis* nutshell; (2) to study the adsorption characteristics of Cr(VI) ions by biochar; and (3) to explore the adsorption mechanism of biochar on Cr(VI) ion in aqueous solutions.

MATERIALS AND METHODS

Preparation of Biochar

Torreya grandis nutshell was collected from croplands in a suburb of Shaoxing, China. The *Torreya grandis* nutshell samples were dried at room temperature and ground to pass through a 0.83 mm sieve. These *Torreya grandis* nutshell samples were used as feedstock for producing biochar. The ground *Torreya grandis* nutshell samples were placed in ceramic crucibles, covered with a tightly fitting lid and pyrolyzed under oxygen limited conditions in a muffle furnace. The pyrolysis temperature was 300°C and time was 4 h. Then, cooling at room temperature, biochars were ground to pass through a 0.25 mm sieve before adsorption experiments.

Characterization of Biochar

The elements of C, H, O and N were determined by Elemental Analyzer (Vario ELIII, Elementar, Germany). BET specific surface area was measured by specific surface area meter (Autosorb-iQ3). The particle microstructure of biochar was determined by Scanning Electron Microscopy (JEOL 6500F, Japan) and Transmission Electron Microscopy (JEM-F200, Japan). The functional groups on the surface of biochar were determined by Fourier Transform Infrared Spectroscopy (Bruker Tensor 27).

Adsorption Experiments

Adsorption experiments were carried out at room temperature. 0.2 g of biochar was added to the 250 mL of Erlenmeyer flask containing 50mL of 50mg/L Cr(VI) ions. pH of the solution was adjusted by 0.1 mol/L HCl or 0.1 mol/L NaOH. After the adsorption process reached the equilibrium, samples were taken out. The samples were centrifuged at 3000 r/min for 10 min, filtered through 0.45 μm filter and analyzed by atomic absorption method.

In the experiment of adsorption kinetics, the reaction time was 10, 20, 40, 60, 80, 120, 160, 200, 240, 280 and 360 min respectively. pH in solution was 2.0.

In the experiment of isothermal adsorption, the initial concentration of Cr(VI) ranged from 10 to 100 mg/L. pH in solution was 2.0, and the samples were determined at adsorption equilibrium.

Analytical Methods

The concentration of Cr(VI) was determined by atomic absorption method. The removal rate of Cr(VI) was calculated as following:

$$Q = \frac{C_0 - C_t}{C_0} \times 100\% \quad \ldots(1)$$

Where C_0 and C_t (mg/L) are the initial and equilibrium concentrations of Cr(VI) in solution respectively. Q is the removal rate of Cr(VI).

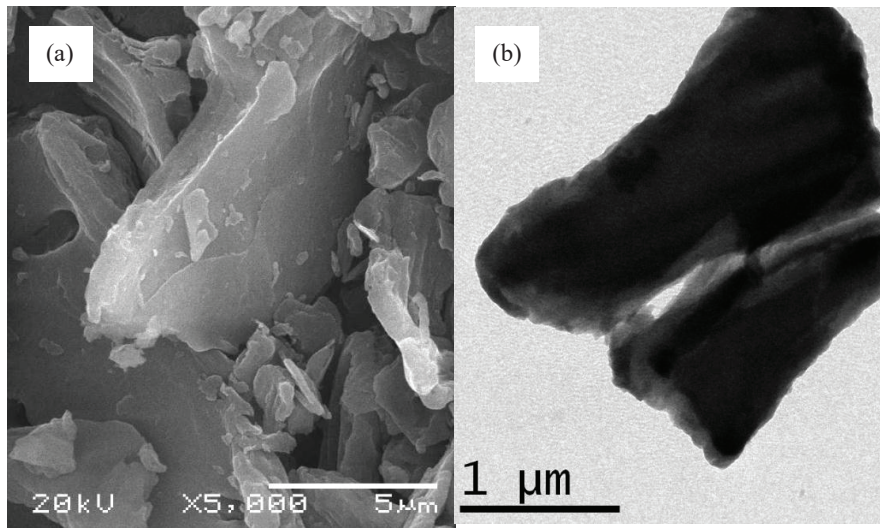

Fig. 1: SEM and TEM images of biochar, (a) SEM, (b) TEM.

Statistical Analyses of Data

All the experiments were repeated in duplicate and the result data were calculated as the mean with the standard deviation (SD). The value of the SD was calculated by Excel Software. All error estimates given in the text and error bars in figures are standard deviation of means (mean ± SD). All statistical significances were noted at α=0.05 unless otherwise stated.

RESULTS AND DISCUSSION

Characteristics of Biochar

The elements of C, H, O and N of biochar are 45.21%, 5.18%, 46.16% and 3.45%. BET specific surface area of biochar is 42.24 m^2/g. The large BET specific surface area means the high adsorption capacity. The SEM and TEM images of biochar are shown in Fig. 1.

As seen from the Fig. 1, the surface of biochar is a smooth sheet with irregular arrangement. It has a very few holes and mainly some debris particles.

The FT-IR spectra of biochar are shown in Fig. 2. From Fig. 2, it can be concluded that several bands were associated with oxygen functional groups appeared on the surface of biochar. The peaks of biochar at approximately 3903, 3422, 1512, 1401, 1060 and 612 cm^{-1} were assigned to the – *OH* stretching vibration of the – *OH* groups, the *COO*– groups, *–C–O* stretching vibration or bending vibration of *–C–OH* or *C–O* stretching and the finger print region which is related to phosphate and sulphur functional groups (Montesinos et al. 2016, Subramanian et al. 2018). In a word, there are a lot of oxygen functional groups on the surface of biochar.

Sorption Kinetics

The effect of reaction time on the removal rate of Cr(VI) by biochar is shown in Fig. 3.

As shown from Fig. 3, it can be concluded that the removal rate of Cr(VI) increases gradually as the reaction time increases. When the adsorption equilibrium is approached, the removal rate of Cr(VI) increases slowly. After the reaction time reached 120 min, the removal rate did not increase obviously. So, the adsorption equilibrium time is thought to be 120 min.

According to data from Fig. 3, the sorption kinetics was discussed in detail. In this experiment, the pseudo-first order and pseudo-second order kinetic rate models were evaluated to predict the removal rate of Cr(VI) ions by the biochar.

The pseudo-first order rate is given as (Hu et al. 2017b):

$$\ln(q_e - q_t) = \ln q_e - k_1 t \quad \ldots(2)$$

The pseudo-second order rate is given as:

$$\frac{t}{q_t} = \frac{1}{k_2 q_e^2} + \frac{1}{q_e} t \quad \ldots(3)$$

Where, q_e (mg/g) is the amount of adsorbed solute at

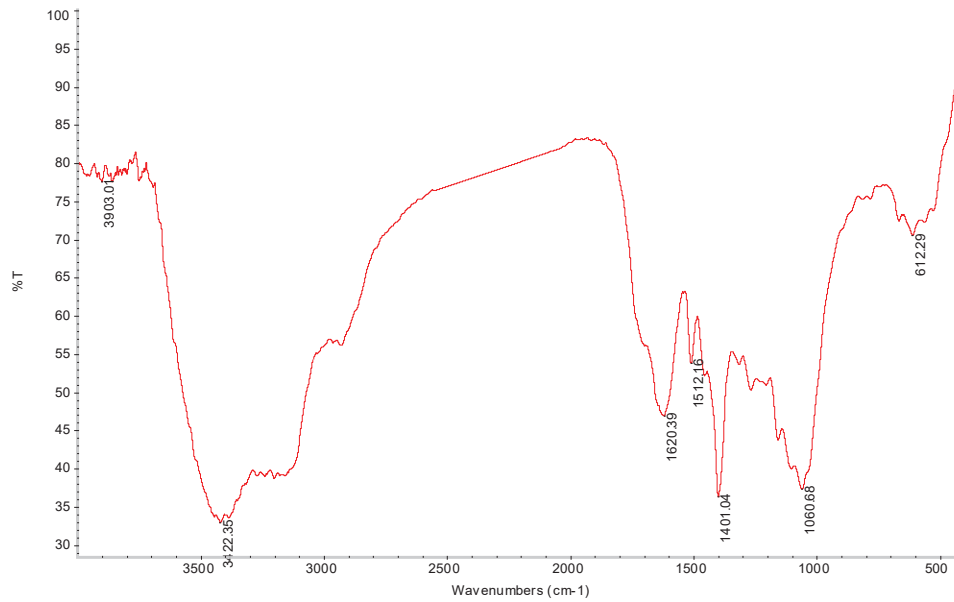

Fig. 2: FT-IR spectra of biochar.

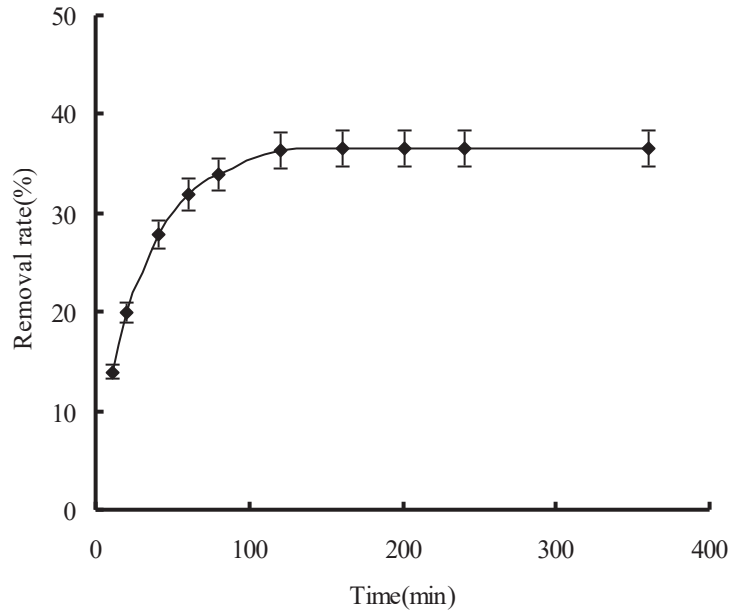

Fig. 3: The effect of reaction time on the removal rate of Cr(VI) by biochar.

equilibrium conditions, q_t (mg/g) is the amount of adsorbed solute at any time t (min), k_1 (h^{-1}) and k_2 (g/mg/h) are the model rate constant respectively.

Parameters of the pseudo-first order kinetic model and the pseudo-second order kinetic model for the description of Cr(VI) adsorption onto biochar are given in Table 1.

Table 1: Parameters of the pseudo-first order kinetic model and the pseudo-second order kinetic model for the description of Cr(VI) adsorption onto biochar.

pseudo-first order kinetic model			pseudo-second order kinetic model		
k_1 (min)	q_e (mg/g)	R^2	k_2 (mg/g·min)	q_e (mg/g)	R^2
0.49	4.62	0.892	0.21	4.95	0.998

From Table 1, it can be shown that the adsorption process fits well with the pseudo-second order kinetics model according to the value of R^2 (0.998 > 0.892). It also indicated that the adsorption of Cr(VI) by biochar is chemisorption process. The new compounds are formed on the surface of the adsorbent (Pozdnyakov et al. 2012).

Sorption Isotherm

The initial concentration of Cr(VI) was ranged from 10 to 100 mg/L. pH in solution is 2.0, and the samples were determined at 120 min. The experimental results are shown in Fig. 4.

In Fig. 4, the removal rate of Cr(VI) by biochar increases with the increase of initial concentration of Cr(VI), and adsorption reaches saturation eventually. It indicated that concentration gradient was the driving force for adsorption process. High concentration is benefitial for adsorption process. Further, the contact area and active sites on the surface of adsorbent are constant. At the first stage, Cr(VI) can be very rapidly adsorbed by biochar because of many adsorption sites. As the initial concentration of Cr(VI) increases, adsorption sites are utilized fully, and the adsorption process reaches saturation gradually.

According to data from Fig. 4, the sorption isotherms were determined. The Langmuir model and Freundlich model were used in this experiment. The Langmuir model and Freundlich model of linear forms are (Ameed & Ahmad 2009):

$$\frac{C_e}{q_e} = \frac{1}{K_L q_{max}} + \frac{C_e}{q_{max}} \quad \ldots(4)$$

$$\ln q_e = \ln K_F + \frac{1}{n} \ln C_e \quad \ldots(5)$$

Where, C_e (mg/L) is the equilibrium concentration in the solution, q_e (mg/g) is the adsorbate adsorbed at equilibrium, q_{max} (mg/g) is the maximum adsorption capacity, n is the Freundlich constant related to adsorption intensity, K_L (L/mg) and K_F ((mg/g)$^{1/n}$) are the adsorption constants for Langmuir and Freundlich models respectively.

Parameters of Langmuir isotherm model and Freundlich isotherm model for the description of Cr(VI) adsorption onto biochar are given in Table 2.

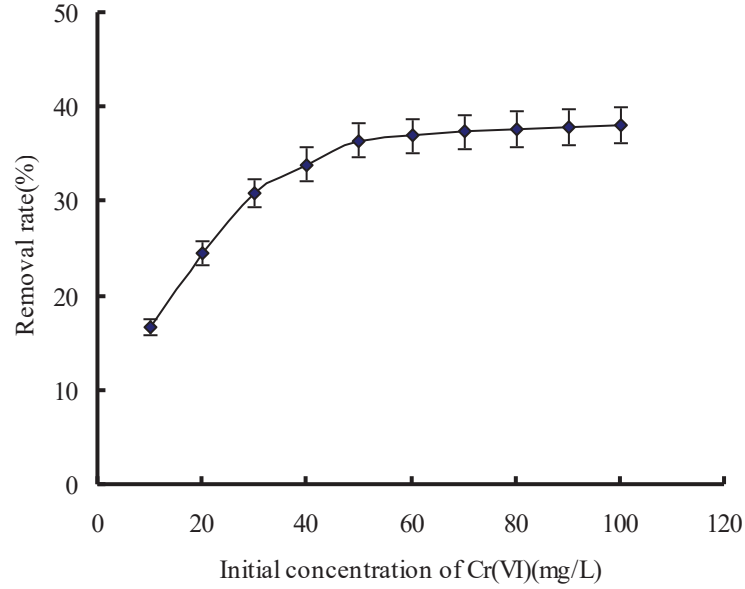

Fig. 4: The effect of the initial concentration of Cr(VI) on the removal rate of Cr(VI) by biochar.

Table 2: Parameters of Langmuir isotherm model and Freundlich isotherm model for the description of Cr(VI) adsorption onto biochar.

Langmuir			Freundlich		
q_m(mg/g)	K_L	R^2	K_F	n	R^2
5.12	0.03	0.999	1.24	0.18	0.812

From Table 2, Langmuir isotherm model can better describe the adsorption isothermal process of biochar on Cr(VI) according to the value of R^2 (0.999 > 0.812). The adsorption process is monolayer adsorption process.

Sorption Mechanism

Cr(VI) ions in aqueous solution mainly exists in the form of H_2CrO_4, $Cr_2O_7^{2-}$, $HCrO_4^-$ and CrO_4^{2-} in the environment. As the pH value in the solution is low, it mainly exists in the form of $HCrO_4^-$, a small amount of H_2CrO_4 and $Cr_2O_7^{2-}$. It is due to the presence of a large amount of H^+ ions in the solution, which leads to reaction of functional groups on the surface of the biochar with ions, such as H^+, $-OH$, $-COOH$ and so on. The positively charged of $-OH_2^+$ and $-COOH_2^+$ functional groups were appeared. These functional groups combine with $Cr_2O_7^{2-}$, $HCrO_4^-$ and CrO_4^{2-} through electrostatic interaction (Mohan et al. 2014). They were reacted with oxygen functional groups (–*OH*, –*COOH* and so on) appeared on the surface of biochar, and a lot of stable compounds were formed (Kołodyńska et al. 2012). So, it can be concluded that the adsorption mechanism of biochar on heavy metal Cr(VI) contains the electrostatic attraction and complexation reaction of oxygen functional groups.

CONCLUSIONS

1. The *Torreya grandis* nutshell can be effectively converted into the biochar, which can gain the goal of recycling waste resources. The obtained biochar derived from *Torreya grandis* nutshell is a smooth sheet and irregular arrangement structure. It has a large specific surface area and a lot of oxygen functional groups on the surface. So, it can be applied for the treatment of heavy metal.
2. The biochar can effectively remove Cr(V) in aqueous solution. It can be described by the pseudo-second order kinetic rate model and Langmuir isotherm model. The adsorption process is monolayer chemical process.
3. The adsorption mechanism of biochar on heavy metal Cr(VI) contains the electrostatic attraction and complexation reaction of oxygen functional groups.

ACKNOWLEDGEMENTS

This study was financially supported by the project of science and technology plan in Zhejiang Province (LGF19C030001) and the project of science and technology plan in Shaoxing City (2017B70058).

REFERENCES

Ameed, B.H. and Ahmad, A.A. 2009. Batch adsorption of methylene blue from aqueous solution by garlic peel, an agricultural waste biomass.

J. Hazard. Mater., 164: 870-875.

Barrera-Díaz, C.E., Lugo-Lugo, V. and Bilyeu, B. 2012. A review of chemical, electrochemical and biological methods for aqueous Cr(VI) reduction. J. Hazard. Mater., 223-224: 1-12.

Ding, Z.H., Hu, X., Wan, Y.S., Wang, S.S. and Gao, B. 2016. Removal of lead, copper, cadmium, zinc, and nickel from aqueous solutions by alkali-modified biochar: Batch and column tests. J. Indust. Eng. Chem., 33: 239-245.

Du, X.D., Yi, X.H., Wang, P., Zheng, W.W., Deng, J.G. and Wang, C.C. 2019. Robust photocatalytic reduction of Cr(VI) on UiO-66-NH_2(Zr/Hf) metalorganic framework membrane under sunlight irradiation. Chem. Eng. J., 356: 393-399.

Du, Y., Tao, Z., Guan, J., Sun, Z., Zeng, W., Wen, P., Ni, K., Ye, J., Yang, S., Du, P., and Zhu, Y. 2015. Microwave-assisted synthesis of hematite/activated graphene composites with superior performance for photocatalytic reduction of Cr(VI). RSC Adv., 5: 81438-81444.

Dutta, A.K., Ghorai, U.K., Chattopadhyay, K.K. and Banerjee, D. 2018. Removal of textile dyes by carbon nanotubes: A comparison between adsorption and UV assisted photocatalysis. Physica E Low Dimens. Syst. Nanost., 99: 6-15.

Hu, B.W., Qiu, M.Q., Hu, Q.Y., Sun, Y.B., Sheng, G.D., Hu, J. and Ma, J.Y. 2017a. Decontamination of Sr(II) on magnetic polyaniline/graphene oxide composites: Evidence from experimental, spectroscopic, and modeling investigation, ACS Sustain. Chem. & Eng., 5: 6924-6931.

Hu, B.W., Hu, Q.Y., Xu, D. and Chen, C.G. 2017b. The adsorption of U(VI) on carbonaceous nanofibers: A combined batch, EXAFS and modeling techniques. Sep. Pur. Technol., 175: 140-146.

Hu, B.W., Guo, X.J., Zheng, C., Song, G., Chen, D.Y., Zhu, Y.L., Song, X.F. and Sun, Y.B. 2019. Plasma-enhanced amidoxime/magnetic graphene oxide for efficient enrichment of U(VI) investigated by EXAFS and modeling techniques. Chem. Eng. J., 357: 66-74.

Kołodyńska, D., Wne˛ trzak, R., Leahy, J.J., Hayes, M.H.B., Kwapiński, W. and Hubicki, Z., 2012. Kinetic and adsorptive characterization of biochar in metal ions removal. Chem. Eng. J., 197: 295-305.

Kretschmer, I., Senn, A.M., Meichtry, J.M., Custo, G., Halac, E.B., Dillert R., Bahnemann D.W. and Litter, M.I. 2019. Photocatalytic reduction of Cr(VI) on hematite nanoparticles in the presence of oxalate and citrate. Appl. Catal. B: Environ., 242: 218-226.

Litter, M.I. 2015. Mechanisms of removal of heavy metals and arsenic from water by TiO_2-heterogeneous photocatalysis. Pure Appl. Chem., 87: 557-568.

Litter, M.I. 2017. Last advances on TiO_2-photocatalytic removal of chromium, uranium and arsenic. Curr. Opin. Green Sustain. Chem., 6: 150-158

Mohan, D., Kumar, H., Sarswat, A., Alexandre-Franco, M. and Pittman, C.U. 2014. Cadmium and lead remediation using magnetic oak wood and oak bark fast pyrolysis bio-chars. Chem. Eng. J., 236: 513-528.

Montesinos, V.N., Salou, C., Meichtry, J.M., Colbeau-Justin, C. and Litter, M.I. 2016. Role of Cr(III) deposition during the photocatalytic transformation of hexavalent chromium and citric acid over commercial TiO_2 samples. Photochem. Photobiol. Sci., 15: 228-234.

Mu, W.J., Du, S.Z, Li, X.L., Yu, Q.H., Wei, H.Y. and Yang, Y.C. and Peng, S.M. 2019. Removal of radioactive palladium based on novel 2D titanium carbides. Chem. Eng. J., 358: 283-290.

Park, M., Park, J., Kang, J.C., Han, Y. and Jeong, H.Y. 2018. Removal of hexavalent chromium using mackinawite (FeS)-coated sand. J. Hazard. Mater., 360: 17-23.

Park, S.H., Cho, H.J., Ryu, C. and Park, Y. 2016. Removal of copper(II) in aqueous solution using pyrolytic biochars derived from red macroalga Porphyra teners. J. Indust. Eng. Chem., 36: 314-319.

Pozdnyakov, I.P., Kolomeets, A.V., Plyusnin, V.F., Melnikov, A.A., Kompanets, V.O., Chekalin, S.V., Tkachenko, N. and Lemmetyinen, H. 2012. Photophysics of Fe(III)-tartrate and Fe(III)-citrate complexes in aqueous solutions. Chem. Phys. Lett., 530: 45-48.

Qiu, M.Q., Wang, M., Zhao, Q.Z., Hu, B.W. and Zhu, Y.L. 2018. XANES and EXAFS investigation of uranium incorporation on nZVI in the presence of phosphate. Chemosphere, 201: 764-771.

Regmi, P., Moscoso, J.L.G., Kumar, S., Cao, X.Y., Mao, J.D. and Schafran, G. 2012. Removal of copper and cadmium from aqueous solution using switchgrass biochar produced via hydrothermal carbonization process. J. Environ. Manage., 109: 61-69.

Shen, Z.T., Jin, F., Wang, F., McMilla,n O. and Al-Tabbaa, A. 2015. Sorption of lead by Salisbury biochar produced from British broadleaf hardwood. Biores. Technol., 193: 553-556.

Subramanian, G., Kumar, G.S.S., Ravi, V., Sundaresan, N.R. and Madras, G. 2018. Photochemical detoxification of Cr(VI) using iron and saccharic acid: Insights from cytotoxic and genotoxic assays. Environ. Sci. Water Res. Technol., 4: 1152-1162.

Tong, X.J. and Xu, R.K. 2013. Removal of Cu(II) from acidic electroplating effluent by biochars generated from crop straws. J. Environ. Sci., 25: 652-658.

Wang, D., He, S., Shan, C., Ye, Y., Ma, H., Zhang, X., Zhang, W. and Pan, B. 2016. Chromium speciation in tannery effluent after alkaline precipitation: Isolation and characterization. J. Hazard. Mater., 316: 169-177.

Wang, H.Y., Gao, B., Wang, S.S., Fang, J., Xue, Y.W. and Yang, K. 2015. Removal of Pb(II), Cu(II), and Cd(II) from aqueous solutions by biochar derived from $KMnO_4$ treated hickory wood. Biores. Technol., 197: 356-362.

Wang, S., Gao, B., Zimmerman, A.R., Li, Y., Ma, L., Harris, W.G. and Migliaccio, K.W. 2015. Removal of arsenic by magnetic biochar prepared from pinewood and natural hematite. Bioresour. Technol., 175: 391-395.

Xu, Z., Bai, S., Liang, J., Zhou, L. and Lan, Y. 2013. Photocatalytic reduction of Cr(VI) by citric and oxalic acids over biogenetic jarosite. Mater. Sci. Eng. C, 33: 2192-2196.

Nature Environment and Pollution Technology
An International Quarterly Scientific Journal

p-ISSN: 0972-6268 e-ISSN: 2395-3454	Vol. 18	No. 4	pp. 1381-1385	2019

Original Research Paper **Open Access**

Horizontal Distribution of Chlorophyll-α in the Gorontalo Bay

Miftahul Khair Kadim*, Nuralim Pasisingi* and Sulastri Arsad**
*Department of Aquatic Resources Management, Fisheries and Marine Science Faculty, Universitas Negeri Gorontalo, Gorontalo 96128, Indonesia
**Department of Aquatic Resources Management, Fisheries and Marine Science Faculty, Universitas Brawijaya, Malang 65145, Indonesia

Nat. Env. & Poll. Tech.
Website: www.neptjournal.com

Received: 19-02-2019
Accepted: 30-05-2019

Key Words:
Ammonia
Gorontalo Bay
Chlorophyll-α distribution
Nitrate
Phosphate

ABSTRACT

The concentration of chlorophyll-α in the Gorontalo Bay is necessary to be observed since it could describe the condition of water richness. The semi-enclosed Gorontalo Bay morphology causes the status of water fertility to be largely determined by the input of inorganic or organic materials originating from the mainland. This study aimed to figure out the concentration and horizontal distribution pattern of the chlorophyll-α then further to decide the relationship between the concentration of chlorophyll-α and the nutrients in the Gorontalo Bay. There were fifteen sub-sampling sites selected based on coastal and ecological characteristics. Results showed that the distribution pattern of chlorophyll-α in the Gorontalo Bay in June and July 2017 was dissimilar and its concentration ranged from 0.984 to 3.744 $mg.m^{-3}$. In addition, there was a positive and substantial relationship between chlorophyll-α and phosphate ($p<0.01$). Nonetheless, there was no significant correlation between chlorophyll-α and nitrate ($p>0.01$) and ammonia ($p>0.01$).

INTRODUCTION

Bay ecosystem is very dynamic because of the influence of the mainland and human impacts (Madin et al. 2016, Österblom et al. 2017). Physical, chemical, and biological conditions depend on inputs which are derived from land activities. Ecosystem balance and sustainability of aquatic biota of bay become an essential aspect that must be maintained. Water fertility is one point that contributes greatly in ensuring the balance of the marine ecosystem. The distribution of chlorophyll-ααon the water surface is an indicator which can be used to estimate water fertility.

Geographically Gorontalo Bay is a part of Tomini Bay, morphologically Gorontalo Bay is semi-enclosed waters then likely that the profile of surface chlorophyll-α distribution in these waters is local in type and different from the distribution of chlorophyll-α in Tomini Bay. The two main points that underlie the importance of studying the distribution of chlorophyll-α in the Gorontalo Bay are ecological and economic roles. Ecologically, the Gorontalo Bay is still semi-encircled waters to enable inputs from terrestrial activities that carry organic or inorganic materials which are very decisive for water fertility. Human activities in the mainland around the waters of Gorontalo Bay are relatively varied. Output and waste from human activities containing organic or inorganic materials flow into the waters through rivers and streams during rain (Cloern et al. 2016).

Gorontalo Bay has an economical purpose as this bay is a strategic zone for fishing by local fishermen. Local people whose main livelihoods are fishermen depend mainly on catches. The availability of the abundant and varied fish of the bay is meanderingly influenced by the availability of diet. Phytoplankton, the autotrophic part of the plankton community, is a key element in oceanic ecosystems and in biogeochemical cycling (Beltran-Heredia et al. 2017). The presence of it as the food of fish is determined by the water fertility aspect that can be reflected from the distribution of chlorophyll-α.

The purpose of this study was to determine the concentration and horizontal distribution pattern of chlorophyll-α and to figure out the correlation between chlorophyll-α and nutrient concentrations in the Gorontalo Bay.

MATERIALS AND METHODS

Water samples were carried out twice in June and July 2019 and collected from five different stations of land use. In the mainland near the site 1, there are rare resident settlements; near, from site 2 there are no human activities yet because of a steep cliff presence. Moreover, land use near the site 3 is Bone River estuary. In the site 4 there is an oil port and in the site 5 there are densely populated settlements. Sampling at each station was performed out on 3 sub-stations by dragging the line-transect to the offshore as presented on the sampling map on the Fig. 1.

The samples for analysis of chlorophyll-α and nutrient concentration were collected from fifteen different points then compiled into five sample bottles and taken at Hydrobiology Laboratory, Environment and Waters Biotechnology division, Universitas Brawijaya. Analysis of water samples was made referring to APHA standard procedures (APHA 1989). The water samples were collected in the column water horizontally by using plankton net (Tuney & Maroulakis 2014). The net was held by the side of the boat (while the boat was moving slowly) for approximately 1.5 minutes. A slight turn performed with the boat so that the net was towed from the inner side of the turn to avoid drifting the net under the boat.

The pigment form (chlorophyll-α) concentration was estimated by using spectrophotometer (Rice et al. 2014). The absorbance at 664 nm was used to determine the chlorophyll-α concentration in the extract through the calculation by inserting the corrected optical densities in the following equations:

$$\text{Chlorophyll-}\alpha\ (\text{mg.m}^{-3}) = 11.85\ (\text{absorbance 664 nm}) - 1.54\ (\text{absorbance 674 nm}) - 0.08\ (\text{absorbance 630 nm}) \quad \ldots(1)$$

Where, absorbance 664, 647 and 630 nm = corrected optical densities (with a 1cm light path) at the wavelength.

After determining the concentration of the pigment extract, the amount of pigment per unit volume was calculated as follows:

$$\text{Chlorophyll} - \alpha\ (\text{mg.m}^{-3}) = \frac{\text{Chlorophyll} - \alpha\ (\text{mg.L}^{-1}) \times \text{extract volume (L)}}{\text{Volume of sample (m}^3)} \quad \ldots(2)$$

DATA ANALYSIS

Data were analysed by statistical software SPSS and Microsoft Office Excel 2010. Data were subjected to correlate and bi-variety test to find significant relationship between chlorophyll-α and nutrient concentration, while *t*-test to find significant distinction between nutrients concentration during sampling ($p<0.05$) considered being significantly different. In addition, the distribution of chlorophyll-α concentrations were visualized by *ArcGIS* version 10 software with spatial interpolation technique.

RESULTS AND DISCUSSION

Concentration and Distribution of Chlorophyll-α in the Gorontalo Bay

The concentration of chlorophyll-α among the five stations was varied from 0.984 to 3.740 mg.m^{-3} during the two sampling times, June and July (Fig. 2). Averagely, the concentration of chlorophyll-α recorded during sampling was higher in July than that in June. Furthermore, the value of chlorophyll-α in the station 4 in July was the highest with the number of 3.744 mg.m^{-3}, on the other hand the lowest concentration was in the station 5 in June with the chlorophyll of 0.984 mg.m^{-3}.

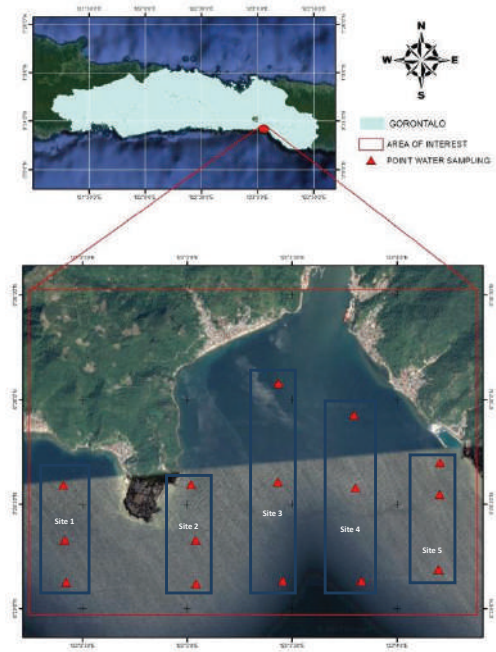

Fig.1: Sampling sites in the Gorontalo Bay.

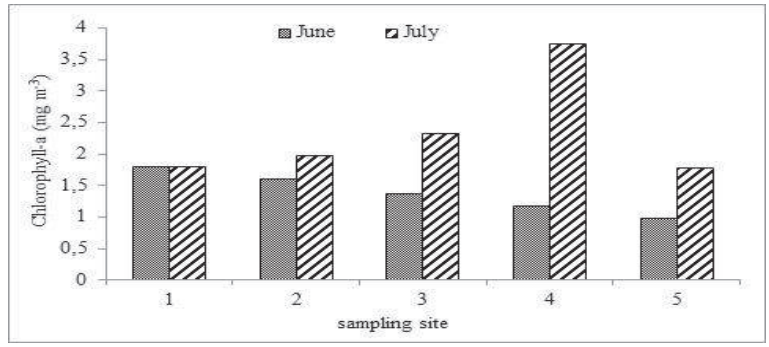

Fig. 2: Chlorophyll-α in the Gorontalo Bay at five sampling sites between June and July ($p<0.05$).

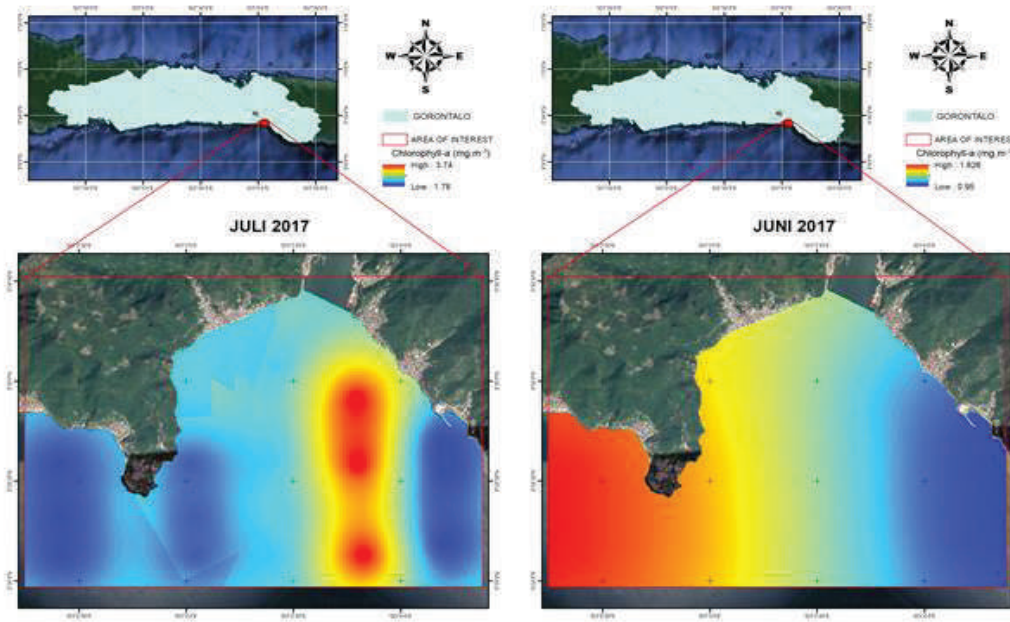

Fig. 3: Horizontal distribution of chlorophyll-α in the Gorontalo Bay in June and July 2017.

The chlorophyll-α surface concentration in the Gorontalo Bay in June was higher than that of chlorophyll-α in July. This is because a day before the sampling in July there was rain, therefore the inorganic materials that are the source of food for phytoplankton came in the bay waters through run-off. It is generally accepted that phytoplankton biomass can be reflected by concentration of chlorophyll-α (Larsson et al. 2017).

Being the predominant pigment in phytoplankton cells, chlorophyll-α has been long used as a proxy for estimating the standing stocks of phytoplankton biomass in the water column. The latter is of major importance, as phytoplankton plays a central role in the structure and functioning of aquatic ecosystems, while its abundance reflects the trophic state of a water body (Mandalakis et al. 2017). Moreover, Fig. 3 depicts that chlorophyll-α in June 2017 was different from that of July 2017.

Based on the visualization results of horizontal distribution of chlorophyll-α (Fig. 3), it showed that the chlorophyll-α distributed highly in the western area of the bay in June 2017 and in the eastward revealed low concentration. Furthermore, different trend was shown in July 2017 as there was a change in the horizontal distribution pattern of chlorophyll-α. In July the eastern part of the waters has

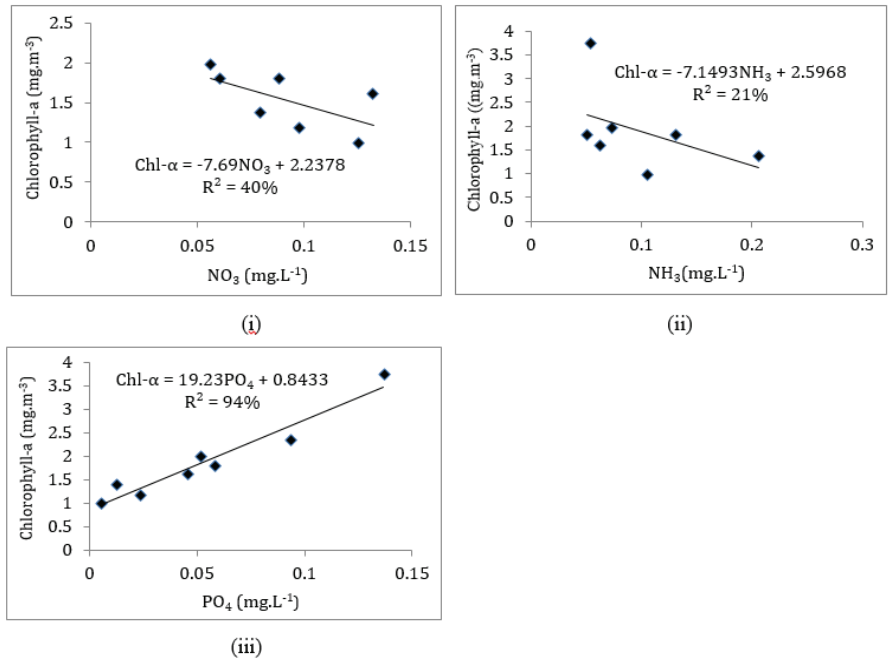

Fig. 4: Simple correlation between chlorophyll-α and (i) NO_3 (ii) NH_3 and PO_4 (iii) concentration in the Gorontalo Bay.

a high concentration of chlorophyll-α, while in the west it has low chlorophyll-α value. This fact indirectly indicates that the trophic status on the west and east parts of Gorontalo Bay in these two months is altered.

The main factor suspected to cause this spreading pattern distribution is a seasonal reversing wind season. Local fishermen informed that in June 2017, it was the end of wet season where the local wind moves from eastward to westward. Otherwise, in July it was the east wind season where the wind blows from westward to eastward. Allahdadi et al. (2017) identified that coastal current and its spatial distribution were significantly affected by open boundary conditions. Wind controls the movement of water in semi-enclosed bay of large shallow Lake Taihu, China (Li et al. 2017). The movement of wind causes a water mass transfer in the semi-enclosed Gorontalo Bay which has chlorophyll-α.

Relationship Between Chlorophyll-α and Nutrient Concentrations in the Gorontalo Bay

The concentrations of ammonia, nitrate and phosphate in the waters of Gorontao Bay in June and July of 2017 were relatively different. In the Gulf of Gorontalo in June and July, the ammonia concentration was 0.116 ± 0.213 $mg.m^{-3}$ with the least value of 0.035 $mg.m^{-3}$ and the greatest value of 0.336 $mg.m^{-3}$. Nitrate concentration was 0.091±0.074 $mg.m^{-3}$ with the lowest value of 0.042 $mg.m^{-3}$ and the highest of 0.146 $mg.m^{-3}$. The concentration of phosphate was 0.047±0.095 $mg.m^{-3}$ with the lowest concentration of 0.003 $mg.m^{-3}$ and the highest of 0.137 $mg.m^{-3}$. Phosphate concentrations in waters are lower than nitrogen (ammonia and nitrate). This is because the phosphorus has been considered a key limiting nutrient in marine systems (Redfield 1958).

The relationship between chlorophyll-α concentration with nutrients, ammonia, nitrate, and phosphate is presented in Fig. 4. It can be seen from the figure that there is a negative correlation between chlorophyll-α and ammonia and nitrate. Although based on *t*-test results the data showed no significant correlation of chlorophyll-α concentrations to ammonia and nitrate. The determination coefficient between chlorophyll-α and ammonia and nitrate was 40% and 21% respectively. Balali et al. (2013) stated that there is a significant negative correlation between chlorophyll-α and nitrate (R^2 = 26.1%) and ammonia (R^2 = 11%) as the amount of chlorophyll-α was high when the amounts of nitrate and ammonia were the lowest.

Otherwise, a positive correlation is indicated by the relationship between chlorophyll-α concentration and phosphate concentration in the waters of the Gorontalo Bay with a coefficient of determination of 94%. Furthermore, there is a positive correlation between chlorophyll-α and phosphate in the waters (Magumba et al. 2013, Hakanson & Eklund 2010, Davis & Cornwell 1991).

CONCLUSIONS

There was a positive and significant relationship between chlorophyll-α and phosphate ($p<0.01$) but no significant correlation between chlorophyll-α and nitrate ($p>0.01$) and ammonia ($p>0.01$) in the Gorontalo Bay in June and July 2017. In addition, the chlorophyll-α concentration in the Gorontalo Bay in June and July 2017 ranged from 0.984 to 3.744 $mg.m^{-3}$.

REFERENCES

Allahdadi, M.N., Jose, F., D'Sa E.J. and Ko, D.S. 2017. Effect of wind, river discharge, and outer-shelf phenomena on circulation dynamics of the Atchafalaya Bay and shelf. Ocean Engineering, 129: 567-580.

APHA 1989. Standard methods for the Examination of Water and Wastewater. American Public Health Association (APHA), American Water Works Association (AWWA) and Water Pollution Control Federation (WPCF). 17th ed., Washington, pp. 1193.

Balali, S., Hoseini, A., Ghorbnia, R., Kordi, H. and Khozani, E.A. 2013. Relationships between nutrients and chlorophyll *a* concentration in the international Alma Gol Wetland, Iran. International Journal of Aquatic Biology, 1(2): 68-75.

Beltrán-Heredia, E., Aksnes, D.L. and Cao, F.J. 2017. Phytoplankton size scaling with nutrient concentration. Marine Ecology Progress Series, 571: 59-64.

Cloer, J.E., Abreu, P.C., Carstensen, J., Chauvaud, L., Elmgren, R., Grall, J., Greening, H., Johansson, J.O.R., Kahru, M., Sherwood, E.T., Xu, J. and Yin, K. 2016. Human activities and climate variability drive fast-paced change across the world's estuarine-coastal ecosystems. Global Change Biology, 22: 513-529.

Davis, M.L. and Cornell, D.A. 1991. Introduction to Environmental Engineering. Second edition. Mc-Graw-Hill, Inc., New York, pp. 822.

Hakanson, L. and Eklund, J.M. 2010. Relationships between chlorophyll, salinity, phosphorus, and nitrogen in lakes and marine areas. Journal of Coastal Research, 263: 412-423.

Larsson, M.E., Ajani, P.A., Rubio, A.M., Guise, K., McPherson, R.G., Brett, S.J., Davies, K.P. and Doblin, M.A. 2017. Long-term perspective on the relationship between phytoplankton and nutrient concentrations in a southeastern Australian estuary. Marine Pollution Bulletin, 114(1): 227-238.

Li, Y., Jalil, A., Du, W., Gao, X., Wang, J., Luo, L., Li, H., Dai, S., Hashim, S., Yu, Z. and Acharya, K. 2017. Wind induced reverse flow and vertical profile characteristics in a semi-enclosed bay of large shallow Lake Taihu, China. Ecological Engineering, 102: 224-233.

Madin, E.M.P., Dill, L.M., Ridlon, A.D., Heithaus, M.R. and Warner, R.R. 2016. Human activities change marine ecosystems by altering predation risk. Global Change Biology, 22: 44-60.

Magumba, D., Maruyama, A., Takagaki, M., Kato, A. and Kikuchi, M. 2013. Relationships between chlorophyll-α, phosphorus and nitrogen as fundamentals for controlling phytoplankton biomass in lakes. Environmental Control in Biology, 51(4): 179-185.

Mandalakis, M., Stravinskaitė, A. and Lagaria, A. 2017. Ultrasensitive and high-throughput analysis of chlorophyll-α in marine phytoplankton extracts using a fluorescence microplate reader. Anal. Bioanal. Chem., 409: 4539-4549.

Österblom, H., Crona, B.I., Folke, C., Nystrom, M. and Troell, M. 2017. Marine ecosystem science on an intertwined planet. Ecosystems, 20: 54-61.

Redfield, A.C. 1958. The biological control of chemical factors in the environment. Am. Sci., 46: 205-221.

Rice, E.W., Baird, R.B., Eaton, A.D. and Clesceri, L.S. 2012. APHA (American Public Health Association): Standard Method for The Examination of Water and Wastewater, 22th ed. Washington DC (US): AWWA (American Water Works Association) and WEF (Water Environment Federation).

Tuney, I. and Maroulakis, M. 2014. Phytoplankton Sampling Methods: Technical Assistance for Capacity Building on Water Quality Monitoring. Ege University, Department of Biology, Turkey ENVECO S.A., Greece.

Nature Environment and Pollution Technology
An International Quarterly Scientific Journal

p-ISSN: 0972-6268 e-ISSN: 2395-3454	Vol. 18	No. 4	pp. 1387-1391	2019

Original Research Paper **Open Access**

Toxicological Study of Bifenthrin and its Metabolites on Earthworm (*Eisenia fetida*)

Gajanan Vishnu Mali
Bharati Vidyapeeth's Matoshri Bayabai Shripatrao Kadam Kanya Mahavidyalaya, Kadegaon, Dist. Sangli (MS), India

Nat. Env. & Poll. Tech.
Website: www.neptjournal.com

Received: 27-03-2019
Accepted: 31-05-2019

Key Words:
Bifenthrin
Metabolites
Earthworms
Eisenia fetida
Toxicology study

ABSTRACT

Pyrethroids are used in agricultural to control pests on a variety of crops. Bifenthrin, a synthetic pyrethroid, is a broad spectrum insecticide. It acts mainly on the nervous system of vertebrates as well as invertebrates. It is susceptible to the biodegradation by some soil bacteria. The present paper deals with the toxicological studies of bifenthrin and its metabolites benzene 1,1(methylthio) ethylidine, resorcinol and monochloro trifluromethane that were produced by a newly isolated strain of *Paracoccus siganidrum* APGM1 on earthworms, which play an important role in the improvement of the soil fertility. The toxicity was assessed by 48 hrs filter paper contact test, 14 days soil test and histopathological methods. The results of filter paper contact test revealed that the earthworms were more susceptible to bifenthrin than their metabolites. The LC_{50} value of bifenthrin and its metabolites was 6 ppm and 20 ppm respectively. The soil test showed that at 6 ppm concentration of bifenthrin, half the number of earthworms died after 14 days and with the increase in the concentration, mortality increased. At 10 ppm concentration, all the earthworms died. However, half the number of earthworms died after 14 days at the metabolite concentration of 20 ppm. The adverse effects of bifenthrin and very little effect of their metabolites on the morphological properties and structural integrity of the tissues were observed in histopathological studies. Thus, the metabolites of bifenthrin were less toxic to earthworms than the bifenthrin.

INTRODUCTION

The wide use and repeated application of synthetic pyrethroids have resulted in their constant occurrence in some environments. Usually, pyrethroids bind tightly with the soil components and therefore, they leach into the groundwater and form residues, which in turn is harmful to the ecosystems. Bifenthrin is mostly used in orchards, nurseries, homes and in agricultural crops such as corn (Ingham 2012). Because of their high toxicity to aquatic life, they have been registered as 'restricted use pesticides'. U.S. EPA has classified it as a category C pesticide as it is a possible human carcinogen (National Pesticide Information Centre 2015).

Earthworms play an important role in increasing the desirable properties of the soil. They constitute about 60 to 80% of the total animal biomass in soil (Olette et al. 2008, Jouquet et al. 2010). They are highly sensitive and susceptible to the agrochemicals as they lack hard cuticle around their body (Lanno et al. 2004, Nahmani et al. 2007). Decrease in earthworm population due to the use of pyrethroids has already been reported (Lukowicz & Krechniak 1992). Earthworms are also susceptible to the ecological changes, mostly those intrinsic to the soil. The earthworm behaviour can therefore imitate the soil contamination. Globally, earthworms are used as bioindicators for investigating chemical environmental pollution.

Many bacteria have the potential to degrade the pyrethroid pesticides including bifenthrin. There is a vital advantage of using microorganisms for degradation of pesticides. This is due to their diversity, wide dispersal and adaptation of variable metabolic pathways. In the present study, bifenthrin and its metabolites such as benzene 1, 1(methylthio) ethylidine, resorcinol and monochloro trifluromethane produced by a newly isolated strain APGM1 of bacteria *Paracoccus siganidrum* was used to determine the toxicity of bifenthrin and its metabolites to earthworm.

MATERIALS AND METHODS

Earthworms: Earthworms (*Eisenia fetida*) used in the experimental work were obtained from the earthworm culture farm in Kolhapur, India. Healthy adult worms with a well-developed clitellum (average weight, 200-250 mg) were used for the study.

48-hour contact filter paper test: Different concentrations of bifenthrin in the range of 1 to 10 ppm were prepared in distilled water. At the same time, different concentrations of metabolites in the range of 1 to 10 ppm and above obtained from the ethyl acetate extract of degradation medium were

prepared. The filter paper pieces were soaked with these different concentrations of the pesticides as well as metabolites and placed in a Petri dish. The earthworms were placed on the top of these filter papers. The experimental set was replicated three times for each of the concentration and a similar design was setup using distilled water as a control. The dishes were incubated in the dark at 20 ± 1°C for 48 hours and mortality was recorded at 12 hrs of time intervals.

14-Day soil test: The local natural soil was homogenized, air dried and sieved through 2 mm mesh. It was then mixed with different concentrations of the pesticide (1 to 10 ppm) and its metabolites. 600 g of pesticide mixed soil was taken in the plastic container of 3.5 litre capacity and 10 earthworms were placed on each container and allowed to borrow. The earthworms were fed with urine free dried and ground cattle manure (cow dung's) throughout the period of the experiment. This set up was repeated in three replicates for all the concentrations and controls were also prepared using distilled water. Mortality of earthworms was evaluated on a daily basis to determine the LC_{50} of the pesticide. To check the mortality, the test containers were emptied on a clean tray and earthworms were separated from the soil. Earthworms were judged to be dead when they fail to respond to gentle mechanical stimulations with a blunt probe.

Statistical analysis: Probit analysis was used to determine the LC_{50} value at 95% confidence level using SPSS.

Histopathological study of the earthworms: Live earthworms from each treatment including the control, metabolites and bifenthrin were taken and washed with distilled water. They were transferred into jars containing agar gel and left for another 96 hours to facilitate the removal of the sand content of the intestine, as agar is easily eaten by earthworm (Pokarzheyskii et al. 2000, Gobi et al. 2004).

The histological study of the intestine of earthworm was performed by using routine paraffin method (Humason 1979). In this, the intestine of earthworm, dissected out from the control and experimental animals were blotted free of mucus, washed thoroughly in physiological saline, cut into pieces of desired size and fixed in Bovine fluid fixative immediately after autopsy. The fixation was carried out at room temperature for 24 h, after which the tissues were transferred to 70% alcohol. Several changes of 70% alcohol were given until the yellow colour disappeared from the tissues. The tissues were then dehydrated by passing through ascending grades of alcohol, cleared in xylene, infiltrated with molten paraffin, and finally embedded in paraffin wax (58°C MP).

Tissue sections of 5 µm thick transverse sections were obtained using a rotary microtome (Leica, Germany). The sections obtained were stained in Harris hematoxylene and eosin, dehydrated using alcohol, cleared in xylene and mounted using dihydroxy phthalate xylol (DPX). The stained slides were observed in a CarlZeiss (Germany) Axio-2 Plus research microscope.

RESULTS AND DISCUSSION

48-hour filter paper contact test (LC_{50} determination): The results of filter paper contact test are presented in Table 1. It shows that the bifentrin and its degraded metabolites varied in their contact toxicities. Earthworms were more susceptible to bifenthrin than their metabolites. The LC_{50} value of bifenthrin was 6 ppm while LC_{50} value of metabolites was 20 ppm. Hence, metabolites of bifenthrin degradation are less toxic to earthworm than bifenthrin. The contact filter paper test is reported to be an excellent screening technique to assess the relative toxicity of pesticides to the earthworms. It is one of the simpler, cheaper and quick methods. It is designed in such a way that the earthworms are exposed to the toxicant both by contact and in the aquatic phase (Edwards & Bohlen 1996).

14-day soil test (LC_{50} determination): The results of the soil test are as presented in Table 2. It shows that at 6 ppm concentration of bienthrin, half the number of earthworms died after 14 days and with the increase in the concentration, mortality increased. At 10 ppm concentration, all the earthworms died. The metabolites of degraded bifenthrin were also used to check its toxicity on earthworms where it was found that at concentration of 20 ppm of metabolites (LC_{50} value of 20ppm) half the number of earthworms died after 14 days. The soil test is a better representation of natural environment of earthworms, and the pesticides are mainly absorbed by gut in this method (De Silva & Van Gestel 2009, Udovic & Lestan 2010). Therefore, the soil test is more adequate when toxicity of pesticides to earthworms is to be evaluated (Wang et al. 2011).

Histopathological Study of Earthworm

Histopathological examination of intestinal sections of control earthworms showed normal structure of wall and intact nature of circular and longitudinal muscles (Fig. 2C). In the earthworms exposed to bifenthrin, disintegration of ectodermal layer as well as circular and longitudinal muscles was found. It may be due to the necrotic effect of bifenthrin at LC_{50} (6 ppm) for 48 h. There was total damage of body wall of the *Eisenia fetida* due to the internal and ectodermal tissue erosion (Fig. 2P). However, earthworms exposed to bifenthrin metabolites at LC_{50} (20 ppm) for 48h, revealed normal structure of body wall and expansion of spaces between the longitudinal muscles with proliferation of glandular cells (Fig. 2M). These results indicate the adverse toxic effects of bifenthrin and very little effect of me-

Table 1: LC_{50} determination the pesticide and its metabolites.

Concentration of Cypermethrin (ppm)	No. of exposed earthworms	Mortality	Concentration of metabolite (ppm)	No. of exposed earthworms	Mortality
1	10	1	1	10	0
2	10	2	2	10	0
3	10	2	3	10	0
4	10	3	4	10	0
5	10	4	5	10	0
6	**10**	**5**	6	10	0
7	10	6	7	10	0
8	10	8	8	10	1
9	10	9	9	10	2
10	10	10	10	10	3
-	**-**	**-**	**20**	**10**	**5**
-	**-**	**-**	30	10	8
-	**-**	**-**	40	10	10
Control Distilled Water	10	0	Control Distilled Water	10	0

For bifenthrin		For Metabolites	
Spearman Karber Trim	: 10.00%	Spearman Karber Trim	: 10.00%
LC_{50}	: 6 pmm	LC_{50}	: 20 ppm
95% Lower confidence	: 0.02	95% Lower confidence	: 0.03
95 % Upper confidence	: 0.03	95% Upper confidence	: 0.04

tabolites of bifenthrin on the morphological properties and structural integrity of the tissues. Many earlier reports also suggest the morphological and histopathological changes in earthworms on exposure to different toxic metals and organophosphate pesticides. The disintegrations of cuticular and ectodermal membranes were recorded by Amaral et al. (2006).

Yuguda et al. (2015) also assessed the toxicity of some pesticides on earthworms (*Lumbricus terrestris*) using 48 hours contact filter paper test and 14 days soil test, and found that all the pesticides were toxic to earthworms based on LC_{50} values of 48 hours contact filter paper test while difference in toxicity profile in fourteen days soil test that was based on the pesticides classes. The toxic effects of

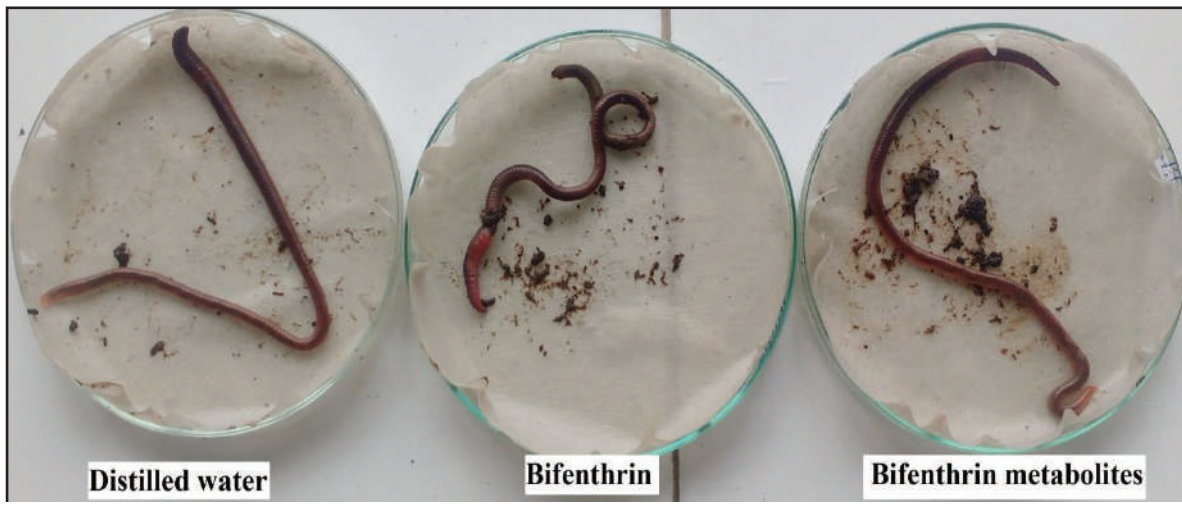

Fig. 1: Filter paper contact test with earthworms.

Table 2: LC_{50} determination.

Concentration of Cypermethrin in soil ($mg.kg^{-1}$)	No. of exposed earthworms	Mortality after 14^{th} day	Concentration of metabolites ($mg.kg^{-1}$)	No. of exposed earthworms	Mortality after 14^{th} day
1	10	1	1	10	0
2	10	2	2	10	0
3	10	2	3	10	0
4	10	3	4	10	0
5	10	4	5	10	0
6	10	5	6	10	0
7	10	6	7	10	0
8	10	7	8	10	1
9	10	8	9	10	1
10	10	10	10	10	3
			20	10	5
			30	10	7
			40	10	10
Control (Distilled water)	10	0	Control (Distilled water)	10	0

For cypermethrin		For Metabolites	
Spearman Karber Trim	: 10.00%	Spearman Karber Trim	: 10.00%
LC_{50}	: 6 $mgkg^{-1}$	LC50	: 20$mgkg^{-1}$
95% Lower confidence	: 0.02	95% Lower confidence	: 0.03
95 % Upper confidence	: 0.03	95 % Upper confidence	: 0.04

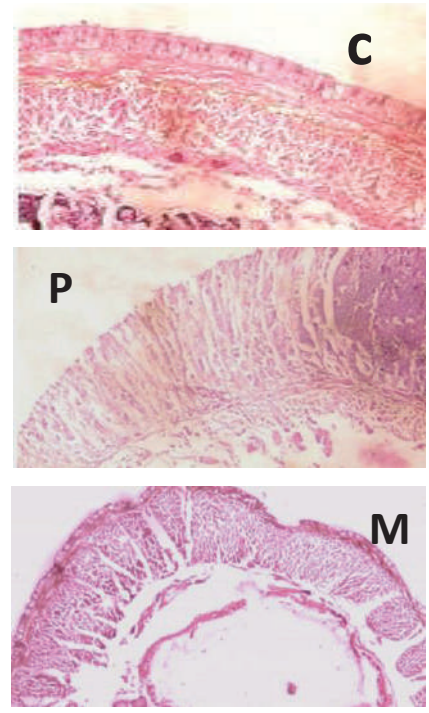

Fig. 2: C, P and M: Histology of earthworm intestine (C-control, P- Effect of bifenthrin pesticide, M-Effect of bifenthrin metabolites).

bifenthrin in soil on earthworms was also evaluated by Li et al. (2017) and reported that bifenthrin was moderately toxic in 72-h filter paper test and low toxic in 14-d soil test.

CONCLUSIONS

According to the regulation of environmental risk assessment for agricultural pesticides, the suggested standard of toxicity is LC_{50} <1 mg kg^{-1} for highly-toxic pesticides, 1-10 mg kg^{-1} for medium-toxic pesticides, and >10 mg kg^{-1} for low-toxic pesticides. With this standard, the acute toxicity of bifenthrin on earthworm was found to be medium, while acute toxicity of degraded metabolites was found to be low.

REFERENCES

Amaral, A., Soto, M., Cunha, R., Marigomez, I. and Rodrigues, A. 2006. Bioavailability and cellular effects of metals on *Lumbricus terrestris* inhabiting volcanic soils. Environ. Pollut., 142: 103-108.

Edwards, C.A. and Bohlen, P.J., 1996. Effects of agricultural practices and chemicals on earthworms. In: Biology and Ecology of Earthworms, pp. 268-299, Chapman & Hall, London.

Gobi, M., Suman, J. and Ganesan, S.V. 2004. Sublethal toxicity of the herbicide butachlor on the earthworm *Perionyx sansibaricus* and its histological changes. Journal of Soils and Sediments, 5: 62-86.

Humason, G.L. 1979. Animal Tissue Techniques. 4th ed. W. H. Freeman & Co., San Francisco.

Ingham, P.E., McNeil, S.J. and Sunderland, M.R. 2012. Functional finishes for wool-ecoconsiderations. Advanced Materials Research, 441: 33-43.

Jouquet, P., Plumere, T., Thu, T.D., Rumpel, C., Duc, T.T. and Orange, D. 2010. The rehabilitation of tropical soils using compost and vermicompost is affected by the presence of endogeic earthworms. Appl. Soil Ecol., 46: 125-133.

Kidd, H. and James, D.R. (Eds.) 1991. The Agrochemicals Handbook, Third Edition. Royal Society of Chemistry Information Services. Cambridge, UK.

Lanno, R., Wells, J., Conder, J., Bradham, K. and Basta, N. 2004. The bioavailability of chemicals in soil for earthworms. Ecotoxicol. Environ. Saf., 57: 39-47.

Li, L., Yang, D., Song, Y., Shi, Y., Huang, B., Yan, J. and Dong, X. 2017. Effects of bifenthrin exposure in soil on whole-organism endpoints and biomarkers of earthworm *Eisenia feotida*. Chemosphere, 168: 41-48.

Lukowicz-Ratajczak, J. and Krechniak, J. 1992. Effects of deltamethrin on the immune system in mice. Environmental Research, 59: 467-475.

Nahmani, J., Hodson, M.E. and Black, S. 2007. Effects of metals on life cycle parameters of the earthworm *Eisenia fetida* exposed to field-contaminated, metal-polluted soils. Environ. Pollut., 149: 44-58.

Olette, R., Couderchet, M., Biagianti, S. and Eullaffroy, P. 2008. Toxicity and removal of pesticides by selected aquatic plants. Chemosphere, 70: 1414-1421.

Pokrzheyskii, A.D., Nico, M., Straaten, V. and Semenov, V.C. 2000. Agar as a medium for removing soil from earthworm guts. Soil Biology and Biochemistry, 32: 1315-1317.

Roberts Brian, L. and Dorough Wyman, H. 1984. Relative toxicities of chemicals to the earthworm *Eisenia fetida*. Environmental Toxicology and Chemistry, 3(1): 67-78.

Takahashi, N., Mikami, N., Matsuda, T. and Miyamoto, J. 1985. Photodegradation of the pyrethroid insecticide cypermethrin in water and on soil surface. J. Pesticide Sci., 10: 629-642.

Wang, B.Z., Ma, Y., Zhou, W., Zheng, J., Zhu, J., He, J. and Li, S. 2011. Biodegradation of synthetic pyrethroids by *Ochrobacterium tritici* strain pyd-1. World J. Microbiol Biotechnol., 27: 2315-2324.

Nature Environment and Pollution Technology
An International Quarterly Scientific Journal

p-ISSN: 0972-6268
e-ISSN: 2395-3454

Vol. 18 | No. 4 | pp. 1393-1397 | 2019

Original Research Paper | Open Access

High Rate Vermicomposting of Coral Vine by Employing Three Epigeic Earthworm Species

S.G. Antony Godson*† and S. Gajalakshmi **

*Hindusthan Arts and Science College, Nava India, Coimbatore-641028, Tamil Nadu, India

**Centre for Pollution Control & Energy Technology, Pondicherry University, Puducherry, 605 014, India

†Corresponding author: S.G. Antony Godson

Nat. Env. & Poll. Tech.
Website: www.neptjournal.com

Received: 05-05-2019
Accepted: 21-06-2019

Key Words:
Earthworms
Vermicomposting
Coral vine leaves
Vermicast recovery

ABSTRACT

Use of the high-rate vermicomposting system and its relevant technology were successfully applied to accomplish direct vermicomposting of coral vine leaves - devoid of any pre-treatment/composting or amended with cow dung as earlier proclaimed protocols for the vermicomposting of various phytomass had necessitated. Three earthworm species tested were *Eisenia fetida, Eudrilus eugeniae* and *Perionyx excavatus,* and they had shown efficient vermicast recovery with few instances of mortality and good reproduction over the 150-day experiment. In this duration, all vermireactors were run in semi-continuous mode at the solid retention time of 15 days. This process enabled us to improve process efficacy of the reactor by the required pointers and systematic process monitoring. This paper substantiates the potential of the high-rate vermicomposting system in direct and potential vermicomposting of coral vine without any pre-treatment/composting or cow dung amendments. The observations have significance for enhancing process economics and therefore, process utility.

INTRODUCTION

Thermophilic composting technology has been progressively popular for large-scale disposal and utilization of different types of organic wastes, in response to the enormous amounts of organic wastes being generated every day. However, this technology does not always guarantee the high-quality products that have the potential for reclamation of soil and plants' growth, eventually, it leads to the loss of economic viability. Over the past three decades, interest towards mesophilic composting by employing earthworm to utilize degradable organic wastes into useful value-added end-product has been dramatically increased. Vermicomposting is an aerobic process in which earthworms are involved in turning waste to ensure proper stabilization, and aerobic condition thereby, lessening the need for expensive engineering to accomplish these objectives. However, the study on the efficiency of earthworms in degrading organic materials into vermicompost has been in the increasing trend, and exploration in more depth on commercial ventures is in progress (Edwards et al. 2011). The vermicompost, an end-product of the vermicomposting process, is a toxic-free material with excellent structure and stability. Thereby, it has been used as a fertilizer for plant growth hence, its economic value (Hemalatha 2013). Moreover, vermicomposts are believed to contain enzymes, hormones, and it has good porosity, bulk density, and water-holding capacity, providing an appropriate nutrient balance and improves its availability to the soil, and hence better plants' growth (Edwards & Burrows 1988, Edwards & Arancon 2004).

Conventional Versus High-rate Vermicomposting

Traditional vermicomposting, whether it is down with 'low-technology' windrow-based systems or with mechanized container-based systems (Edwards et al. 2011), is a slow process that takes 3-4 months for a given quantity of feed to be converted into vermicast. This aspect has so far governed the economics as well as the range of application of vermicomposting technology, by-and-large affecting it unfavourably. In an attempt to break free from this constraint, the hypothesis of the high-rate vermicomposting system has been employed. This led to a design process that can translate the concept into practice (Tauseef et al. 2013, Gajalakshmi et al. 2002, SankarGanesh et al. 2009). The essence of the idea is in the following attributes:

(i) The low-aspect-ratio helps earthworm feeding as well as cast deposition. Moreover, it enables harvesting of vermicompost much easier.

(ii) The low-substrate-column-height enables it to keep evenness in the moisture all over the reactor depth. Nutrient wash off is prevented because there is little scope for water collecting at the bottom and what does get collected is re-sprayed.

(iii) The sand-gravel as vermibed, which lodges in over 25% space in almost all traditional vermireactors, is replaced by wet jute cloth, which maximizes the available space of reactor, proportionately cutting down the system cost.

(iv) Earthworm numbers were increased to achieve the sustainable population growth of earthworms for a given feed. Besides, the high-density earthworm: feed ratio helps to mix causing aeration of the feed due to copious earthworm movement.

Since earthworms' metabolism relies on carbon to the maximum extent, it sequesters nearly all the carbon from the substrate as an attractive feature in one among the various merits of vermicomposting option (Banupriya et al. 2014).

The use of weed phytomass as feedstock in vermicomposting is due to the reasons like the high productivity, low input requirements, and invasive characteristics (Barney et al. 2008). However, there is no commercial facility available so far, which processes phytomass based organic wastes, such as weeds, leaf litter, or crop waste, directly into vermicompost (Tauseef et al. 2013). In this paper, we report on the attempts to generate organic fertilizer from the coral vine by employing earthworms *E. fetida*, *E. eugeniae*, and *P. excavatus*. In our earlier attempts, we have successfully achieved the sustainable, direct, and rapid vermicomposting of coral vine over the period of 150-day duration. Whereas, all the past efforts in vermicomposting different phytomass have relied on blending the plant-biomass with 30 % or more of cow dung, often with pre-composting (Rajiv et al. 2013, Vasanthi et al. 2013, Ansari & Rajpersaud 2012, Chauhan & Joshi 2010). However, we have succeeded in achieving direct and efficient vermicomposting of coral vine. Moreover, the economic and environmental obstacles to using animal manure lies on two different lines: Unlike waste biomass, cow dung is not available free of cost due to its numerous competitive applications already in existence (Abbasi et al. 2014). Collection and transport of cow dung are among the operations, which led to the emissions of CO_2, CH_4, and N_2O (Abbasi et al. 2014).

In the present study, the quantity of substrate was strengthened to the extent of four kg dry weight equivalent, to evaluate the process efficiency of vermireactors in vermicomposting of coral vine. The basic factor that controls vermireactor efficiency is the extent to which earthworms can feed upon a substrate per unit time. If vermireactors are operated such that much greater quantities of the substrates are available in the reactors than the capacity of earthworms to feed, it can be possible to know the limits of consumption. By this approach, it can also be seen whether the extent of feeding varies with the substrate or the earthworms eventually adapt to all feeds equally. With three different epigeic species of earthworm in semi-continuously operated vermireactors, the reactor operation was carried out for a 150-day duration.

MATERIALS AND METHODS

Vermireactors which are fabricated with rectangular containers made of the aluminium sheet, of length 152 cm, breadth 61.5 cm, and depth 9.7 cm, and effective volume 74.9 litres were employed. The reactors were lined with a 2 mm thick plastic sheet. The bottom of each reactor was covered with a 1 cm layer of jute cloth; as it is made of cellulose, it absorbs water quickly, facilities to breathe easily, retain moisture, and caters a favourable condition so as the earthworms can survive and function properly. The reactor was added with 15.4 kg of fresh coral vine leaves. The dry weight of the feed, achieved by oven drying to constant weight at 105 °C, was 4 kg. To each reactor, 1500 individuals of *E. fetida, E. eugeniae,* and *P. excavatus* were added. These were healthy, adult earthworms, which had been cultured in cow manure, and were picked randomly from a large population. The reactors were maintained under same favourable conditions during which daytime temperatures were 32 ± 3°C and night temperatures 29 ± 2°C. The relative humidity varied in the range 55-70%. The reactor feed was always maintained at 70 ± 10% moisture content. There was never any excess water collecting at the reactor bottom that would have needed draining. The reactors were run in semi-continuous mode, fresh weight of substrate was added with an equivalent to the dry weight of vermicast harvested. Since the reactor content was greater in an amount to handle at a single time, the grid method of harvesting was carried out throughout the experiment. A thread was used to mark the line to divide reactor into eight equal grids but was not done physically. Once every 15 days, the two grids were selected randomly to harvest vermicast. The vermicast recovered from two grids was estimated and used to calculate the whole reactor recovery in the manner of extrapolation. Moreover, this method of harvesting is easy and quick to handle, so the reactor content does not get disturbed. Equivalent quantities of fresh feed were introduced to restore the feed mass to its original level. A 3-mm mesh was used to sieve/refine castings to remove other particles. Having cocoons and juveniles not removed from the reactor the efficiency of the reactor concerning vermicast output would have been doubled and keep on increasing since those juveniles produced have started growing to become the adult to do so.

RESULTS AND DISCUSSION

The findings, encompassing five months of reactor operation in 15-day interval pulse-feed mode, are summarized in Table 1. The median/average values are given in the Table 1; the replicates agreed to within ± 10%, which may be considered adequately precise given the heterogeneity nature of the reactor feed. In the first 30 days of the reactor operation, the efficiency of vermicomposting was low. Then the rate started to increase consistently throughout the experimental period. The rate of earthworm reproduction, as reflected by the juveniles and cocoons that were generated, was also picked up after the initial lull. By the time about three months had elapsed, some of the juveniles began attaining adulthood; this was manifested in the form of appearance of a well-formed clitellum in them. As the number of adults increased from the end of the fourth month onwards, there was a dramatic rise in vermiconversion efficiency by the end of 150 days. It was sustained at that level until the completion of experiment exactly five months after the start. Overall, the vermicast output increased with respect to time in a linear fashion (Fig. 1).

The findings establish the fact that, even with the sole fresh leaves of coral vine plant, very rapid and sustained vermiconversion is achievable if the technology based on the approach of high-rate vermicomposting is employed

Table 1: Vermicast production in pre-pilot scale reactors with *E. fetida, E. eugeniae* and *P. excavatus* charged with coral vine as feed.

Days	*E. fetida*			*E. eugeniae*			*P. excavatus*		
	Vermicast production								
	(%)	Per day (g)	Per litre (g)	(%)	Per day (g)	Per litre(g)	(%)	Per day (g)	Per litre (g)
15	22.3	59.6	11.9	25.3	67.6	13.5	21.6	57.6	11.5
30	30.1	80.1	16.0	36.3	96.9	19.4	30.5	81.3	16.3
45	35.1	93.7	18.7	42.4	112.9	22.6	36.6	97.6	19.5
60	42.5	113.4	22.7	48.7	129.9	26.0	44.4	118.4	23.7
75	46.2	123.3	24.7	54.1	144.3	28.9	50.1	133.6	26.7
90	49.1	131.0	26.2	56.8	151.3	30.3	52.8	140.8	28.2
105	53.5	142.7	28.5	60.2	160.5	32.1	48.6	129.6	25.9
120	55.2	147.3	29.5	65.0	173.2	34.6	54.3	144.8	29.0
135	58.0	154.8	31.0	67.2	179.1	35.8	49.3	131.5	26.3
150	60.7	161.8	32.4	68.8	183.4	36.7	52.0	138.7	27.7
Average	50.1±8.5	133.5	26.7	57.9±9.3	154.3	30.0	48.5±5.7	129.4	25.9

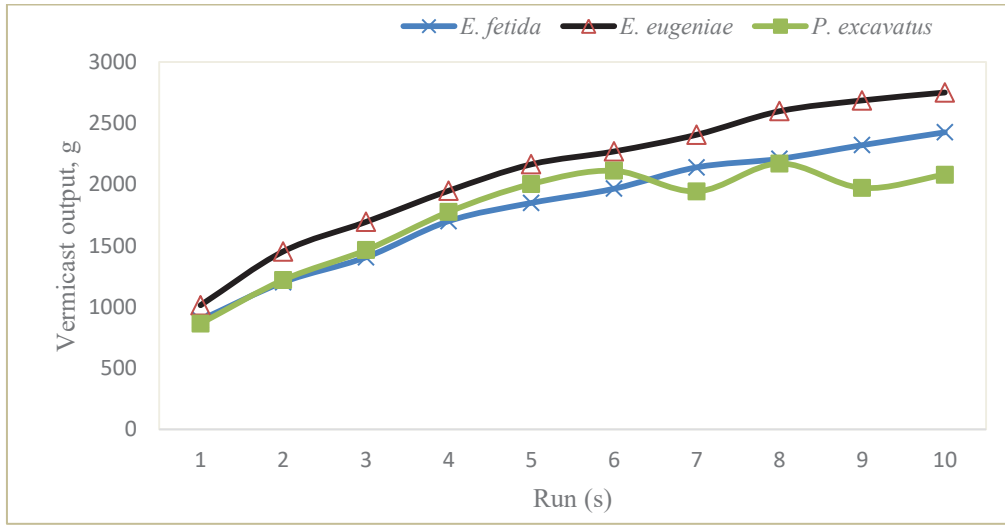

Fig. 1: Vermicast recovery (g), in pre-pilot scale reactors with *E. fetida*, *E. eugeniae*, *P. excavatus* charged with coral vine as feed.

for the purpose. The earthworms have demonstrated high reproductive rate, which has led to a linear rise in vermicast output. The pulse-fed operation eventually led to near quantitative vermiconversion of coral vine-fed vermireactors at an SRT of a mere 30, 26, 31 days from the average vermicast production of *E. fetida, E. eugeniae* and *P. excavatus* respectively, which is many times quicker than the rate achievable in conventional systems. Moreover, the latter need much higher (50% or greater) supplementation of cow dung, and other preconditioning methods. Had the juveniles produced during the experimental period—168 by *E. fetida*, 181 by *P. excavatus* and 225 by *E. eugeniae* —not been removed, the vermiconversion rate is set to be increasing consistently in every run (Table 2). It is expected that as the juveniles approach adulthood, they would begin consuming the substantial quantity of feed, thereby pushing the vermicast recovery above the plateau, which may continue until the death of the 'parent' worms that may cause a temporary lowering of production.

In fact, in view of the fast rate juvenile production, which has an average of 11, 15 and 12 earthworms per day in reactors with *E. fetida*, *E. eugeniae* and *P. excavatus*, respectively (Table 2), the feed utilization rate is probably to have been close to 100 % at the solid retention time of 28-day had the offspring been put back in the reactor. There was mortality in all the reactors, which might be due to the ageing of earthworm species. There was no significant difference, F (2, 27)=1.287, P=0.293, observed between any reactors in vermicast production. The statistical method was used to confirm this observation. One-way ANOVA was conducted to examine the significance difference between different earthworm species in vermicast production.

SUMMARY AND CONCLUSIONS

Coral vine, as a sole feed is vermicomposted by employing three epigeic species of earthworm, *E. fetida*, *E. eugeniae* and *P. excavatus*, without any pre-conditioning of feed, over a five-month span. All the three earthworm species consistently generated vermicast: *E. eugeniae* produced higher vermicast than *E. fetida* and *P. excavatus*. The average vermicast production, based on steady-state conversion from 45th day onwards, per animal per day, was 50.1 %, 57.9 % and 48.5 % with *E. fetida*, *E. eugeniae*, and *P. excavatus* respectively. All the species of earthworms reproduced successfully in the reactors. The number of juveniles produced was 168, 225 and 181; in the case of cocoons, it was 454, 500 and 591. Notwithstanding the morality in all the reactors, the vermiconversion rate was incessantly increasing in each run as the juveniles, and cocoons were not removed from the reactors. This study also describes the efficiency of vermireactors operated in the semi-continuous mode. This has enabled to demonstrate the fact that use of the high-rate vermicomposting system and relevant technology ensure the efficient and sustainable vermicomposting of coral vine leaves.

REFERENCES

Abbasi., S.A., Nayeem-Shah, M. and Abbasi, T. 2014. Vermicomposting of phytomass: Limitations of the past approaches and the promise of the clean and efficient high-rate vermicomposting technology. Journal of Cleaner Production. doi:10.1186/s40643-014-0026-4.

Ansari, A. and Rajpersaud, J. 2012. Physicochemical changes during vermicomposting of water hyacinth (*Eichhornia crassipes*) and grass clippings. International Scholarly Research Network, Article ID 984783.

Table 2: Reproduction and mortality, in pre-pilot scale reactors with *E. fetida, E. eugeniae* and *P. excavatus* charged with coral vine as feed.

Days	*E. fetida*			*E. eugeniae*			*P. excavatus*		
	Mortality	Juvenile	Cocoon	Mortality	Juvenile	Cocoon	Mortality	Juvenile	Cocoon
15	3	0	15	0	0	16	15	0	12
30	0	22	31	0	34	26	3	5	32
45	0	6	54	0	15	53	0	28	63
60	0	25	35	0	32	43	0	14	38
75	0	14	64	0	14	71	11	26	79
90	1	23	30	1	31	39	0	15	43
105	1	8	69	2	16	74	8	32	88
120	3	32	39	0	27	36	0	29	80
135	4	12	43	4	18	78	3	7	67
150	1	26	74	2	38	64	0	25	89
Total	13	168	454	9	225	500	40	181	591

Banupriya, D., Tauseef, S. M., Abbasi, T. and Abbasi S.A. 2014. Rapid conversion of paper waste into vermicast with high-rate vermicomposting technology: A proof-of-concept report. Indian J. Environ. Sci. Eng.

Barney, J.N. and DiTomaso, J.M. 2008. Non-native species and bioenergy: are we cultivating the next invader. Bioscience, 58: 64-70.

Carver R. and Nash, J. 2012. Doing Data Analysis with SPSS. Version 18.0, Fifth ed. USA.

Chauhan, A. and Joshi, P. C. 2010. Composting of some dangerous and toxic weeds using *E. fetida*. Journal of American Science, 6(3).

Edwards, C.A. and Burrows, I. 1988. The potential of earthworms composts as plant growth media. In: Edward, C.A., Neuhauser, E.F. (eds). Earthworms in Waste and Environmental Management. SPB Academic Publishing, The Hague; ISBN 90-5103-017-7, pp. 21-32

Edwards, C.A. and Arancon, N.Q. 2004. Interactions among organic matter, earthworms and microorganisms in promoting plant growth. In: C.A. Edwards, F. Magdoff, and R. Weil (ed.) Functions and Management of Soil Organic Matter in Agroecosystems, CRC Press, Boca Raton, FL, pp. 327- 376.

Edwards, C.A., Norman, Q.A. and Sherman, R. 2011. Vermiculture Technology, Earthworms, Organic Waste and Environmental Management, CRC Press. pp. 17-19.

Gajalakshmi, S., Ramasamy, E.V. and Abbasi, S.A. 2002. High-rate composting-vermicomposting of water hyacinth (*Eichhornia crassipes*, Mart. Solms). Bioresource Technology, 83: 235-239.

Hemalatha, B. 2013. Comparative evaluation of biodegradability of yard waste and fruit waste with industrial effluents by vermicomposting. Int. J. Adv. Eng. Technol., 2(2): 36-39.

Rajiv, P., Rajeshwari, S. and Venckatesh, R. 2013. Fourier transform-infrared spectroscopy and gas chromatography-mass spectroscopy: Reliable techniques for analysis of Parthenium mediated vermicompost. Spectrochim Acta A, 116: 642-645.

Sankar Ganesh, P., Gajalakshmi, S. and Abbasi, S.A. 2009. Vermicomposting of the leaf litter of acacia (*Acacia auriculiformis*): Possible roles of reactor geometry, polyphenols, and lignin. Bioresource Technology, 100: 1819-1827.

Tauseef, S.M, Abbasi, T., Banupriya, D., Vaishnavi, V. and Abbasi S.A. 2013. HEVSPAR: A novel vermireactor system for treating paper waste. Official J. Patent Off 24: 12726.

Vasanthi, K., Chairman, K. and Ranjit Singh, A.J.A. 2013. Vermicomposting of leaf litter ensuing from the trees of mango (*Mangifera indica*) and guava (*Psidium guujuvu*) leaves. International Journal of Advanced Research, 1(3): 33-38.

Nature Environment and Pollution Technology
An International Quarterly Scientific Journal

p-ISSN: 0972-6268
e-ISSN: 2395-3454

Vol. 18 | No. 4 | pp. 1399-1403 | 2019

Original Research Paper | Open Access

The Effect of Sublethal Exposure of Chlorpyrifos to Nile Tilapia (*Oreochromis niloticus*): Case Study of Twin Lakes of West Sumatra, Indonesia

Taufiq Ihsan†, Tivany Edwin and Rahma Desri Yanti
Department of Environmental Engineering, Faculty of Engineering, Andalas University Kampus Unand Limau Manis, Padang, West Sumatra, Indonesia
†Corresponding author: Taufiq Ihsan

Nat. Env. & Poll. Tech.
Website: www.neptjournal.com

Received: 07-09-2018
Accepted: 22-07-2019

Key Words:
Nile Tilapia
Chlorpyrifos
Oxygen consumption
Feed conversion
Sublethal exposure

ABSTRACT

Chlorpyrifos is one of the toxic organophosphate insecticides that is often used by farmers in West Sumatra Province. This research was conducted with the aim to analyse the level of consumption, conversion ratio, and growth rate in fish cultivated in the twin lakes of West Sumatra. The concentration variations are 1/7 and 1/14 LC_{50}-96h of chlorpyrifos. The study was conducted for 14 days. Research data analysis found the values of R = 0.75-1 for the relationship of oxygen level, conversion ratio, and growth of tilapia to the duration of exposure which means having a strong correlation. The results obtained were due to chlorpyrifos insecticide exposure on day 1 to day 14. At a concentration of 0.0054 mg/L, there was a decrease in the level of oxygen consumption of 0.0159 mgO_2 /L, an increase in feed conversion ratio of 0.8253, and the deviation flow of 2.7048%. Whereas at a concentration of 0.0108 mg/L, there was a decrease in the oxygen level of 0.0213 mgO_2 /L, increase in feed conversion ratio of 0.8201, and deviation growth by 2.7048%.

INTRODUCTION

West Sumatra is a province in Indonesia where most of the population lives from agriculture. Based on the data from the Indonesian Central Statistics Agency, as much as 64% of the area of West Sumatra is used for agricultural activities. Agricultural activities cannot be separated from the use of pesticides by farmers in supporting increased yields (Abhilash & Singh 2009, Lu & Kacew 2010, Soemirat 2009). One type of pesticide that is widely used by farmers in West Sumatra is chlorpyrifos (Food Crops and Horticulture Protection Center 2016).

Chlorpyrifos is in the form of white crystals that have a sharp odour. When chlorpyrifos enters the waters, it will kill aquatic biota such as shrimp and fish. Chlorpyrifos insecticide is non-systemic, which works when there is contact with skin or ingested and inhaled (DAS 2013, World Health Organization 2010).

Agricultural activities are also carried out in the Twin Lakes of West Sumatra because they can be used for irrigation. The Twin Lakes area is unique in that there are two lakes named Dibawah lake and Diateh lake. The area around the lakes below is used for agriculture, and the irrigation water flows to the lake Diateh area, which is a fish farming area. The results of measurement of chlorpyrifos concentration in the location of fish cultivation in lake waters are equal to 0.007 mg/L (Ihsan et al. 2018).

This agricultural activity not only triggers water pollution by pesticides but will have an impact on aquatic biota that lives in the lake (Banaee et al. 2011, Sun & Chen 2008, Zahran et al. 2018, Zhang & Zhao 2017), including fish that are cultivated by people in the twin lakes area. One fish that is usually cultivated by the community is Nile tilapia (*Oreochromis niloticus*) that will be used as a test animal in this study

Tilapia is often used as a bioindicator of water pollution because it is sensitive to physical changes and pollutants in water. In addition, tilapia is easy to cultivate and its position is at the top of the food chain in the aquatic systems (Suyanto et al. 2010).

Based on that, to see the sublethal effect of chlorpyrifos insecticide on tilapia, it is necessary to conduct sublethal toxicity tests on the parameters of oxygen consumption level, feed conversion ratio and growth of tilapia before seeing subacute potential for humans who consume (Zeljezic et al. 2017), especially cultured fish from the twin lake areas of West Sumatra.

MATERIALS AND METHODS

Tilapia acclimatization was carried out for 14 days (Halappa & David 2009). During acclimatization, test animals were fed 3 times a day, 3% of fish weight per day (Suyanto 2010). Test water was replaced by 60% when it is cloudy, and

cleaning of fish dung was done 3 times a day. The population of test animals is considered eligible for testing if death is <3% of the test animal population for 48 hours (United States Environmental Protection Agency 2002). Environmental factors measured during acclimatization were dissolved oxygen levels measured by DO meters and pH levels measured by pH meters, to monitor the right environmental conditions during the tilapia acclimatization period.

Sublethal toxicity test was carried out for 14 days which aimed to determine the effect of sublethal chlorpyrifos insecticides on tilapia (Halappa & David 2009). The experiment was carried out with three times repetition of each concentration used. Parameters observed were oxygen consumption level, feed conversion ratio and tilapia growth.

The variation of the concentration used was kept below the LC_{50}-96 h value of 0.076 mg/L (Ihsan et al. 2018) varying from 1/7 of 0.076 mg/L (0.011 mg/L) to 1/14 of 0.076 mg/L (0.005 mg/L).

The level of oxygen consumption was calculated using the volume of water in the aquarium, dissolved oxygen concentration, weight of tilapia, and duration of observation. The oxygen consumption rate was calculated using the following equation (Liao & Huang 1975).

$$OC = [(V) \times (DO_0 - DOt)] / [(W) \times (t)] \quad \ldots(1)$$

Where, OC = Oxygen Consumption Level (mgO_2/g/hour)
V = Volume of water in container (L)
DO_0 = Initial Dissolved oxygen concentration (mg/L)
DOt = Final Dissolved oxygen concentration t (mg/L)
W = Weight of testing fish (g)
t = research time (hour)

Feed conversion ratio was calculated by using the data of the amount of feed given to tilapia, the weight of tilapia at the beginning of observation, and the weight of tilapia at the end of the observation (day t).

The amount of feed conversion ratio was calculated using the following equation (Tacon 1987)].

$$FCR = \text{Feed fed (g)} / (Wt - Wo)\ g \quad \ldots(2)$$

Where, FCR= Feed Conversion Ratio
Wo = Initial weight (g)
Wt = Final weight (g)

Tilapia growth rate was calculated using the weight data of tilapia at the beginning of the observation, the weight of tilapia at the end of the observation (day t), and the time of observation. The growth rate of tilapia was calculated using the following equation (Tacon 1987).

$$SGR = [(\ln Wt - \ln Wo) / t] \times 100\% \quad \ldots(3)$$

Where, SGR = Specific Growth Rate
Wt = Final weight (g)
Wo = Initial weight (g)
t = research time (day)

The data obtained were analysed using regression-correlation statistical analysis. In the analysis of the relationship between observation time and test parameters, variable X is the time of observation and variable Y is the data of each test parameter at each concentration of chlorpyrifos used.

RESULTS

Acclimatization and observation were carried out for 14 days with the aim that the test animals can adapt to the physical state of the laboratory. Based on the observations during acclimatization, the death of test animals <3% for 48 hours was 2%, so that test animals can be used for toxicity testing. During the acclimatization period, the environmental conditions of the aquarium must be adjusted to the environmental conditions that are suitable for the maintenance of tilapia.

During the observation period, the quality of the water was monitored in order to keep the tilapia fish rearing requirements. The environmental parameters monitored were dissolved oxygen (DO), pH and temperature. Environmental conditions during acclimatization and observation can be seen in Table 1.

Table 1: Conditions during acclimatization and observation of the fish.

No.	Parameters	Acclimatization	Observation	Range based on USEPA
1	DO (mgO_2/L)	7.3-8.2	5.8-7.4	>4
2	pH	6.8-7.5	7.8-8.1	6-9
3	Temperature (^oC)	28.6-29.7	25.7-28.2	25-30

Oxygen Consumption Level

The level of oxygen consumption is an important parameter to observe the effect of a toxic substance on fish because toxic substances that enter the body of the fish will interfere with the respiratory process. The data of oxygen consumption level analysed were the relationship between oxygen consumption level on day 1, day 4, day 7, day 10 and day 14 on control, concentration 0.0054 mg/L, and concentration 0, 0108 mg/L. The graph of the relationship between the level of oxygen consumption of tilapia and the observation time can be seen in Fig. 1.

Feed Conversion Ratio

Under normal circumstances, the lower the feed conversion value, the better because the amount of feed spent to produce a certain weight will be less (Lall & Tibbetts 2009). The graph of the relationship between the ratio of tilapia

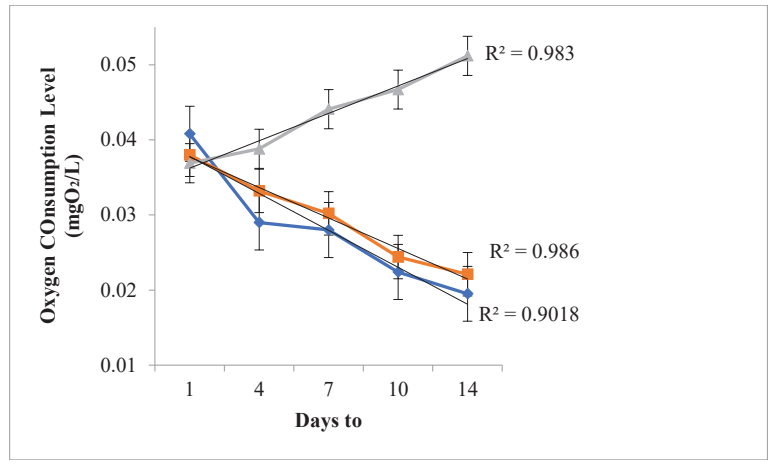

Fig. 1: The level of oxygen consumption of tilapia.

feed conversion to observation time can be seen in Fig. 2.

Growth rate

Under normal circumstances, if metabolic activity goes well, there will be an increase in the rate of growth of fish. The graph of the relationship between the growth rate of tilapia to the observation time can be seen in Fig. 3.

DISCUSSION

Oxygen Consumption Level

Based on Fig. 1, it can be seen that the level of oxygen consumption of tilapia exposed to chlorpyrifos insecticide has decreased from observations on day 1 to day 14. At a concentration of 0.0108 mg/L obtained a coefficient of determination of 0.901, and a concentration of 0.0054 mg/L of 0.986, with a correlation coefficient ranging from 0.800-1,000, which means that the relationship is very strong between observation time and oxygen consumption level of tilapia. The decrease in oxygen consumption level on day 1 to day 14 at a concentration of 0.0054 mg/L was 0.0159 mgO_2 /L and at a concentration of 0.0108 mg/L was 0.0213 mgO_2 /L.

A decrease in oxygen consumption occurs after tilapia is exposed to chlorpyrifos insecticide. This is because the chlorpyrifos insecticide is a nerve poison that will damage the respiratory nervous system of tilapia and will affect the process of oxygen diffusion resulting in a decrease in the level of oxygen consumption (Bonifacio et al. 2017, Chebbi & David 2010, Padmanabha et al. 2015). For longer the tilapia is exposed to chlorpyrifos insecticides, the level of oxygen consumption will decrease.

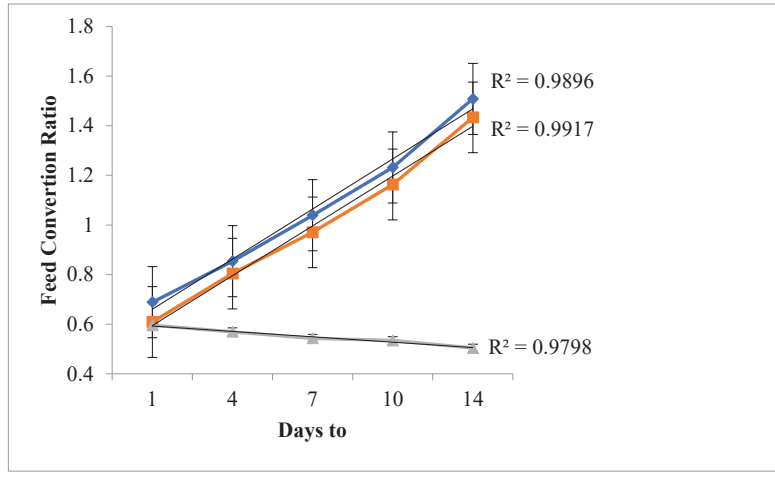

Fig. 2: The ratio of tilapia feed conversion.

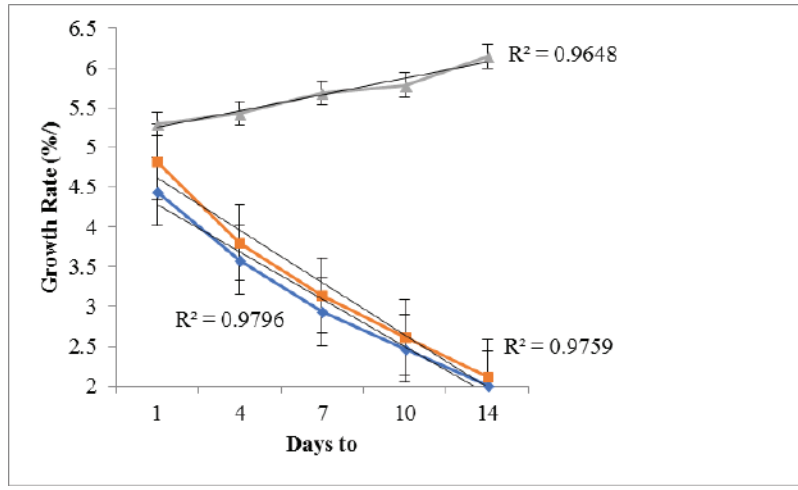

Fig. 3: The growth rate of tilapia.

Feed Conversion Ratio

Based on Fig. 2, there was an increase in the ratio of feed conversion of tilapia fish exposed to chlorpyrifos insecticide from day 1 to day 14, with a coefficient of determination of 0.989 (concentration of 0.0108 mg/L) and 0.991 (concentration of 0.0054 mg/L). Correlation coefficients ranged from 0.800 to 1.000, which means that the relationship is very strong between the test time and the tilapia feed conversion ratio. The increase in feed conversion ratio on day 1 to day 14 at a concentration of 0.0054 mg/L was 0.8253 and at a concentration of 0.0108 mg/L was 0.8201.

The lowest feed conversion ratio occurred on day 1 and the highest feed conversion ratio occurred on day 14. The increase in the value of the feed conversion ratio occurs because of the toxic effects of pesticides in the fish's body, which interfere with the function of respiration and inhibit the metabolic activity of the fish's body so that the process of digestion of food will also be disrupted (Imanpoor et al. 2011, Padmanabha et al. 2015, Saradhamani & Kumari 2011, Sunanda et al. 2016).

Growth Rate

Based on Fig. 3, it can be seen that there was a decrease in the growth rate of tilapia exposed to chlorpyrifos insecticides during the test day. At the concentration of 0.0108 mg/L, the coefficient of determination was 0.979, and at concentration of 0.0054 mg/L it was 0.975. Based on these two coefficients of determination, the correlation coefficients ranged from 0.800 to 1,000, which means that the relationship is very strong between the test time and the growth rate of tilapia. The decline in growth rate on day 1 to day 14 at the concentration of 0.0054 mg/L was 2.7048%, and at the concentration of 0.0108 mg/L was 2.4294%. Decreasing the growth rate of fish occurs due to disruption of the metabolic processes in the fish's body due to damage to the respiratory nervous system (Amiri et al. 2018, Botté et al. 2012, Floyd et al. 2008; Kim et al. 2018, Kusriani et al. 2012).

CONCLUSIONS

The longer the exposure time and the higher the concentration of chlorpyrifos insecticide exposure, the level of oxygen consumption of tilapia will decrease. The level of oxygen consumption of tilapia decreased at a concentration of 0.0054 mg/L by 0.0159 mgO_2/L, and at a concentration of 0.0108 mg/L by 0.0213 mgO_2/L.

The longer the exposure time and higher the concentration of chlorpyrifos insecticide exposure, the tilapia feed conversion ratio will increase. The increase in tilapia feed conversion ratio at a concentration of 0.0054 mg/L is 0.8253, and at a concentration of 0.0108 mg/L is 0.8201.

The longer the exposure time and higher the concentration of chlorpyrifos insecticide exposure, the growth rate of tilapia will decrease. The growth rate of tilapia decreased at the concentration of 0.0054 mg/L by 2.7048%, and at the concentration of 0.0108 mg/L by 2.4294%.

ACKNOWLEDGMENTS

This research was conducted under financial support from Faculty of Engineering, Universitas Andalas, Padang, Indonesia under contract no. 014/UN.16.09.D/PL/2019.

REFERENCES

Abhilash, P. C. and Singh, N. 2009. Pesticide use and application: An Indian scenario. Journal of Hazardous Materials, 165(1-3): 1-12.

Amiri, B. M., Xu, E. G., Kupsco, A., Giroux, M., Hoseinzadeh, M. and Schlenk, D. 2018. The effect of chlorpyrifos on salinity acclimation of juvenile rainbow trout *(Oncorhynchus mykiss*). Aquatic Toxicology, 195(November 2017): 97-102.

Banaee, M., Resource, N. and Faculty, E. 2011. Adverse effect of insecticides on various aspects of fish's biology and physiology. Insecticides-Basic and Other Applications, 6: 101-126.

Bonifacio, A. F., Ballesteros, M. L., Bonansea, R. I., Filippi, I., Amé, M. V. and Hued, A. C. 2017. Environmental relevant concentrations of a chlorpyrifos commercial formulation affect two neotropical fish species, *Cheirodon interruptus* and *Cnesterodon decemmaculatus.* Chemosphere, 188: 486-493.

Botté, E. S., Jerry, D. R., Codi King, S., Smith-Keune, C. and Negri, A. P. 2012. Effects of chlorpyrifos on cholinesterase activity and stress markers in the tropical reef fish *Acanthochromis polyacanthus*. Marine Pollution Bulletin, 65(4-9): 384-393.

Chebbi, S. G. and David, M. 2010. Respiratory responses and behavioural anomalies of the carp *Cyprinus carpio* under quinalphos intoxication in sublethal doses. Science Asia, 36: 12-17.

Das, S. 2013. A review of dichlorvos toxicity in fish. Current World Environment Journal, 8(1): 77-84.

Floyd, E. Y., Geist, J. P. and Werner, I. 2008. Acute, sublethal exposure to a pyrethroid insecticide alters behavior, growth, and predation risk in larvae of the fathead minnow (*Pimephales promelas*). Environmental Toxicology and Chemistry, 27(8): 1780-1787.

Food Crops and Horticulture Protection Center 2016. Report on Agricultural Statistics of Food Crops of West Sumatra. Padang.

Halappa, R. and David, M. 2009. Behavioural responses of the freshwater fish, *Cyprinus carpio* (Linnaeus) following sublethal exposure to chlorpyrifos. Turkish Journal of Fisheries and Aquatic Sciences, 9(2): 233-238.

Ihsan, T., Edwin, T., Husni, N. and Rukmana, W. D. 2018. Uji toksisitas akut dalam Penentuan LC50-96H insektisida klorpirifos terhadap dua jenis ikan Budidaya Danau Kembar, Sumatera Barat. Jurnal Ilmu Lingkungan, 16(1): 98.

Imanpoor, M. R., Ahmadi, A. R. and Kabir, M. 2011. Effects of sub lethal concentration of Chloramin T on growth, survival, haematocrit and some blood biochemical parameters in common carp fry (*Cyprinus carpio*). AACL Bioflux, 4(3): 280-291.

Kim, B. M., Saravanan, M., Lee, D. H., Kang, J. H., Kim, M., Jung, J. H. and Rhee, J. S. 2018. Exposure to sublethal concentrations of tributyltin reduced survival, growth, and 20-hydroxyecdysone levels in a marine mysid. Marine Environmental Research, 140: 96-103.

Kusriani, K., Widjanarko, P. and Rohmawati, N. 2012. Agreement, precision, and accuracy of epifluorescence microscopy methods for enumeration of total bacterial numbers. Jurnal Penelitian Perikanan, 1(1): 36-42.

Lall, S. P. and Tibbetts, S. M. 2009. Nutrition, feeding, and behavior of fish. Veterinary Clinics of NA: Exotic Pet, 12(2): 361-372.

Liao, I. C. and Huang, H. J. 1975. Studies on the respiration of economic prawns in Taiwan. I. Oxygen of egg up to young prawns of *Pennaeus monodon* Fabricius. Journal Fish Social, 4: 33-50.

Lu, F.C. and Kacew, S. 2010. Lu's Basic Toxicology: Fundamentals, Target Organs, and Risk Assessment. CRC Press.

Padmanabha, A., Reddy, H. R. V., Khavi, M., Prabhudeva, K. N., Rajanna, K. B. and Chethan, N. 2015. Acute effects of chlorpyrifos on oxygen consumption and food consumption of freshwater fish, *Oreochromis mossambicus* (Peters). International Journal of Recent Scientific Research, 6: 3380-3384.

Saradhamani, N. and Kumari, S. B. 2011. Impact of insecticide (chloropyrifos) on the biochemical components of the fish, *Oreochromis mossambicus* (Peters, 1852). Curr. Biotica, 5(1): 79-84.

Soemirat, J. 2009. Toksikologi Lingkungan. Yogyakarta: Gajah Mada Press.

Sun, F. and Chen, H. S. 2008. Monitoring of pesticide chlorpyrifos residue in farmed fish: Investigation of possible sources. Chemosphere, 71(10): 1866-1869.

Sunanda, M., Chandra Sekhara Rao, J., Neelima, P., Govinda Rao, K. and Simhachalam, G. 2016. Effects of chlorpyrifos (an organophosphate pesticide) in fish. International Journal of Pharmaceutical Sciences Review and Research, 39(1): 299-305.

Suyanto, R. 2010. Pembenihan dan Pembesaran Nila. Jakarta, Indonesia: Penebar Swadaya.

Tacon, A. G. J. 1987. The Nutrition and Feeding of Farmed Fish and Shrimp - A Training Manual 1. The Essential Nutrients.

United States Environmental Protection Agency 2002. Methods for Measuring the Acute Toxicity of Effluents and Receiving Waters to Freshwater and Marine Organisms, Fifth Edition October 2002. Environmental Protection Agency.

World Health Organization 2010. The WHO Recommended Classification of Pesticides By Hazard and Guidelines to Classification 2009. World Health Organization.

Zahran, E., Risha, E., Awadin, W. and Pali, D. 2018. Acute exposure to chlorpyrifos induces reversible changes in health parameters of Nile tilapia (*Oreochromis niloticus*). Aquatic Toxicology, 197: 47-59.

Zeljezic, D., Vinkovic, B., Kasuba, V., Kopjar, N., Milic, M. and Mladinic, M. 2017. The effect of insecticides chlorpyrifos, Acypermethrin and imidacloprid on primary DNA damage, TP 53 and c-Myc structural integrity by comet-FISH assay. Chemosphere, 182: 332-338.

Zhang, H. and Zhao, L. 2017. Influence of sublethal doses of acetamiprid and halosulfuron-methyl on metabolites of zebra fish (Brachydanio rerio). Aquatic Toxicology, 191(10): 85-94.

84-79 :(1)5

Nature Environment and Pollution Technology
An International Quarterly Scientific Journal

p-ISSN: 0972-6268 e-ISSN: 2395-3454	Vol. 18	No. 4	pp. 1405-1414	2019

Original Research Paper **Open Access**

A Project Design for Air Pollution Studies Over Bobodioulasso-Burkina Faso

Emetere M.E. *(****), Sanni S.E. and Okoro E.E.*****

*Department of Physics, Covenant University, P.M.B 1023, Ota, Nigeria
**Department of Chemical Engineering, Covenant University, Canaan land, Ota, Nigeria
***Department of Petroleum Engineering, Covenant University, Canaan land, Ota, Nigeria
****Department of Mechanical Engineering and Science, University of Johannesburg, APK, South Africa

Nat. Env. & Poll. Tech.
Website: www.neptjournal.com

Received: 12-02-2019
Accepted: 30-04-2019

Key Words:
Air pollution
Aerosol loading
Aerosol optical depth
Human health
MISR

ABSTRACT

This paper introduces a project design on estimating air pollution over geographical regions that have a mono-source of data acquisition. Fourteen years (2000-2013) aerosol optical depth dataset was obtained from the Multi-angle Imaging Spectro-Radiometer (MISR). The peculiar design that has been discussed in this paper focusses on human health and environmental disturbances. The secondary datasets that were generated from the primary data were aerosol loading, particles sizes, Angstrom parameter, and the statistics of the primary dataset. A computational data treatment was introduced for the determination of data reliability of the dataset. The techniques highlighted in this study are germaine to be reproduced in several geographical locations.

INTRODUCTION

Optical properties of aerosols have been found to have a significant influence on the local radiative forcing and radiation balance of the earth (Emetere et al. 2015, Emetere et al. 2016). Basic aerosols optical parameters, such as the extinction and scattering coefficients, the aerosol depth and the single-scattering phase were used to describe aerosol-solar radiation as discussed by Kokhanovsky et al. (2006). The influence of huge aerosol content in the atmosphere are found to be harmful. For example, Dunion and Velden suggested that the Saharan air layer has a significant influence on the intensity and formation of cyclones in the tropical Atlantic region (Dunion & Velden 2004). Goldenberg et al. (2001) examined the causes and implications of aerosols in the formation of Atlantic hurricanes. The information garnered from changes in long-term Saharan dust activities were monitored using information retrieved from dust measurements alongside their concentrations (Prospero & Lamb 2003, Geogdzhayev et al. 2005). Chen et al. (2002) carried out an analysis of fifty years' dataset of global-gauge observation of land precipitations/rainfall in the Sahel region. Like other scientists, it was found that high aerosol loading leads to rainfall anomalies (Emetere 2016 and 2017). Also, Evans et al. (2006) discussed the relationship between the outbreak of African dust particulates and Atlantic tropical cyclone activities. These aforementioned works help to buttress the significant effect of aerosols on environmental forces such as hurricanes and activities/performances of cyclones for filtering or separating/trapping dust particles besides their health implications, influence on agriculture and precipitation (Crippa et al. 2013). For example, in 2012, about 3 million deaths were reported to have been consequential of the aerosol-inhalation by humans, which was largely responsible for the prominence of cardiovascular and respiratory infections caused by exposures to particulate matter (PM) (Brauer et al. 2012).

Despite much understanding on atmospheric aerosols, there is a need to understand its long and short-term dangers. Drinovec et al. (2015), with the aid of an Aethalometer carried out accurate measurements of carbon-black aerosols within real time-loading. Vaselovskii et al. (2016), Bovchaliuk et al. (2016) and Rivellini et al. (2017) obtained the optical and physical properties of African dust in Senegal using a multi-wavelength Raman Lidar measurement. In this study, a project design methodology has been suggested for regions of mono-source dataset. For example, there are no or inadequate ground dataset in Bobodioulasso region of Burkina Faso. At the moment, no prior ground studies have been reported in the region. The only source of obtaining aerosol dataset is the use of satellite dataset. The main challenge of adopting mono-source dataset are progressive process error and no validation or control source. In West Africa, it has been shown that satellite and ground measurements vary significantly over some regions (Emetere 2016). Hence, it becomes extremely difficult to rely solely on a mono-source dataset. This paper is to pro-

vide a project design platform for future adoption and a good background study over Bobodioulasso-Burkina Faso. Based on the level of accuracy in the Multi-angle Imaging Spectro-Radiometer (MISR) dataset (Emetere 2017), this paper gives a valid report on the state of air pollution over Bobodioulasso-Burkina Faso.

EXPERIMENTAL DESIGN, MATERIALS AND METHODS

Bobodioulasso is located on latitude 11°10'37.74" N and longitude 4°17'52.44" W (Fig. 1). It is the second largest city in Burkina Faso. The city is known for agricultural trade and textile industry. The research location has a tropical wet and dry climate. The population is fast increasing due to recent development. The primary data were obtained from Multi-angle Imaging Spectro-Radiometer (MISR) as presented in Fig. 2. The raw dataset was initially processed using the Excel program to eliminate missing dataset and calculate the monthly average of the aerosol optical depth (AOD). The processed dataset was subjected to statistical and computational treatment. The computational data treatment was done using the C++ CERN Root codes that were developed to comparatively observe the inter-dependency of the MISR bands. To a large extent, process errors and abnormal data within the dataset can be determined.

The West African regional scale dispersion model (WASDM) for calculating aerosol loading over a region (Emetere et al. 2015):

$$\psi(\lambda) = a_1{}^2\cos\left(\frac{n_1\pi\tau(\lambda)}{2}x\right)\cos\left(\frac{n_1\pi\tau(\lambda)}{2}y\right) + \ldots\ldots a_n{}^2\cos\left(\frac{n_n\pi\tau(\lambda)}{2}x\right)\cos\left(\frac{n_n\pi\tau(\lambda)}{2}y\right) \quad \ldots(1)$$

Where, a is atmospheric constant obtained from the fifteen years aerosol optical depth (AOD) dataset from MISR, n is the tunning constant, $\tau(\lambda)$ is the AOD of the area and $\psi(\lambda)$ is the aerosol loading.

The digital voltage and Angstrom parameters of the study area can be obtained from equation (2) and (3) respectively.

$$I(555) = \frac{I_o(555)}{R^2}\exp\left(m^*\tau(555)\right) \quad \ldots(2)$$

Where, I is the solar radiance over the SPM detector at wavelength $\lambda = 555$ nm, I_o is the measure of solar radiation behind the atmosphere, R is the mean Earth-Sun distance in Astronomical Units, τ is the total optical depth (in this case, the average of each month is referred to as the total AOD, and m is the optical air mass.

$$\alpha = -\frac{d\,In(\tau)}{d\,In(\lambda)} \quad \ldots(3)$$

Where, α is the Angstrom parameter, τ is the aerosol optical depth, and λ is the wavelength.

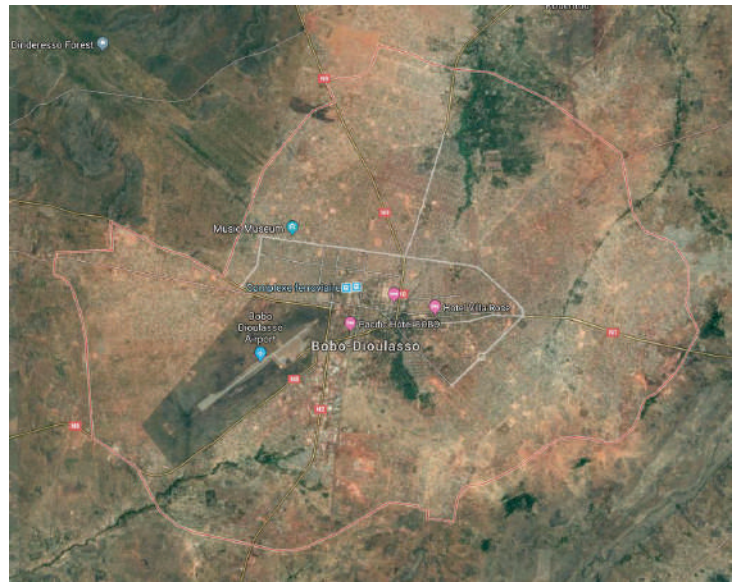

Fig. 1: Google map of Bobodioulasso.

The radius of the particles for atmospheric aerosol and back-envelope was calculated using proposals by Kokhanovsky et al. (2006).

RESULTS AND DISCUSSION

The AOD varied from January down to December as seen in Fig. 2, for all the years. Also in Fig. 2, the AOD was lowest (i.e. approximately 0.18) in November but highest (0.86) in March in the year 2010; no AODs were seen from August to September, in the year 2011, it varied between the value obtained for May (i.e. 0.4) and 0.148 (September), the highest (0.875) and lowest (0.167) AODs recorded for the year 2012 were those obtained in the months of March and December respectively whereas, no AODs were recorded in the months of July and September. For the year 2013, the highest (0.415) and lowest (0.163) AODs were obtained in the months of March, and January/October respectively with no visible presence of AODs in the months of August and December same year.

The aerosol loading dataset over Bobodioulasso is presented in Fig. 3. From the results shown in Fig. 3, the highest aerosol loading (0.9442) was obtained in the months of January, February, July and August (2000), July and

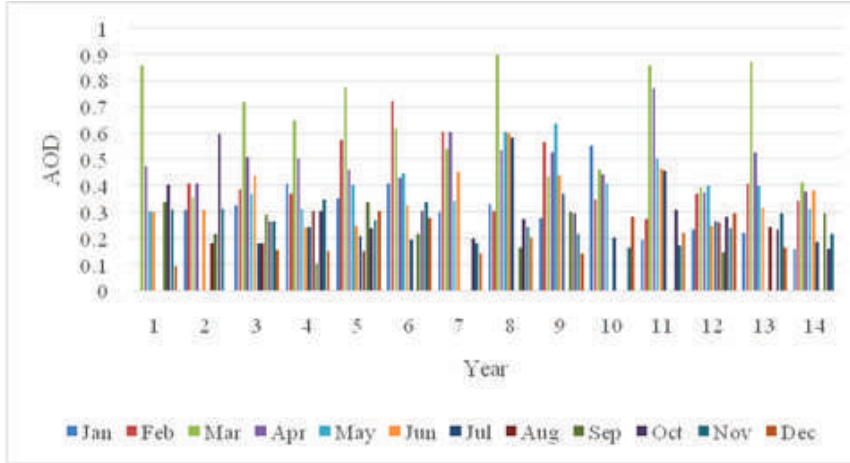

Fig. 2: AOD for Year 2000-2013.
Key: 1-14 = 2000-2013 respectively

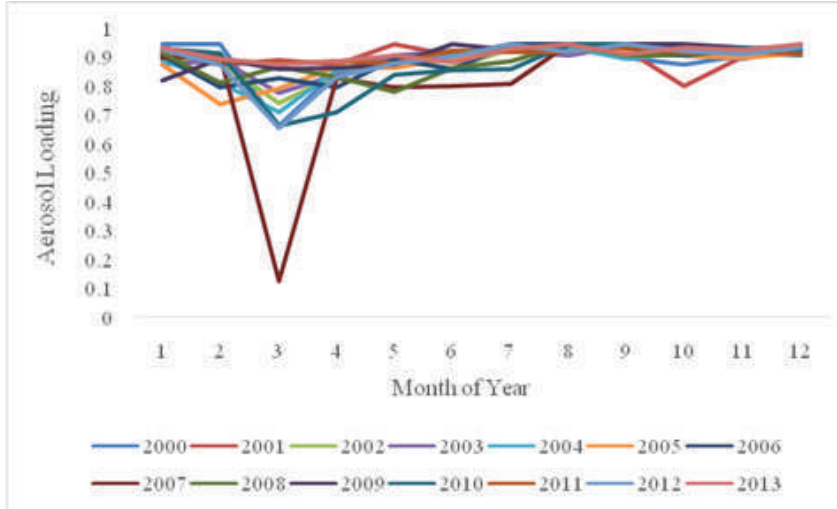

Fig. 3: Aerosol Loading for Year 2000-2013.
Key: 1-12 = Months of the year; from January-December, respectively

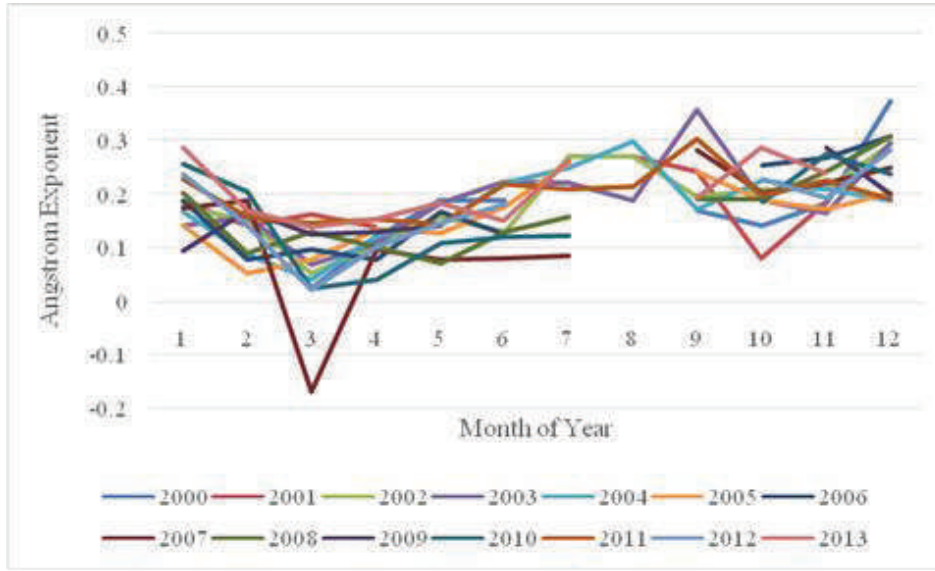

Fig. 4: Angstrom Exponent for Year 2000-2013.
Key: 1-14 = January-December, respectively

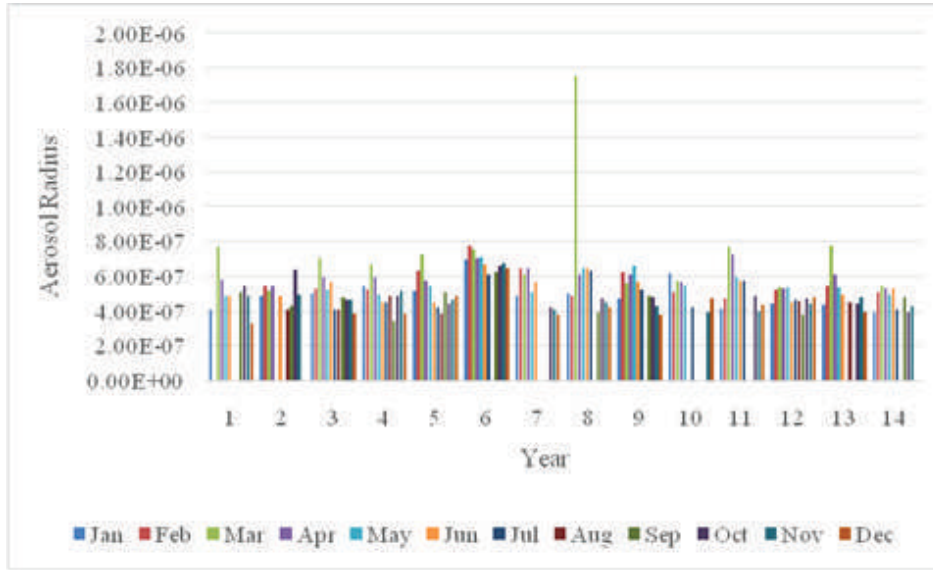

Fig. 5: Aerosol Radius for year 2000-2013.
Key: 1-14 = 2000-2013 respectively

December 2001, August 2005, July-August 2006, August 2007, August 2008 and August-October, 2009 whereas, other values were lower for other months and years.

The Angstrom parameter over Bobodioulasso is presented in Fig. 4, and the highest Amstrong value (0.374) was recorded in the month of December of the year 2000; it ranges from 0.02 (March)-0.37 (December) in 2000 with no values seen for the months of January, February, July and August of the same year. The values were in the range of 0.08 (October)-0.27 (August) approximately in 2001 with no value recorded for July and December same year, 0.05 (March)-0.293 (December) for 2002, 0.069 (March)-0.296 (December) for 2003 and 0.0399 (March)-0.297 (August) for 2004, 0.05 (February) -0.26 (July) 2005 with no values recorded August of same year, 0.08 (February)-0.31 (December) in 2006, with no values

recorded for July-September same year. It ranged between -0.17 (March) and 0.28 (September) in the year 2007 with no Amstrong value recorded for August 2007, from 0.07 (May)-0.31 (December) in 2008 with no value recorded for August 2008. The Amstrong parameter calculated for the year 2009 varies between 0.09 (January) and 0.285 (November) while no values were recorded in the months of June and August-October of same year. It was between 0.02 (March, 2010) and 0.27 (November, 2010) with no visible readings for the month of August-September. It ranged between 0.14 (May, 2011) and 0.3 (September, 2011), it was 0.02 (March)-0.282 (December) for the year 2012 whereas, the values for the months of July and September could not be determined. In 2013, calculated values of the Amstrong parameter are in the range of 0.139 (March) and 0.287 in October 2013 with the values for August and December being indeterminable same year.

The radius of the aerosols that was calculated over the research site is presented in Fig. 6. The statistical treatment of the AOD dataset is presented in Tables 2A-C.

Considering the values in Tables 1A-C, it is evident that, the radius of the particulate aerosols recorded are indicative of particles comprising of fines in the atmospheric region of Bobodioulasso in Senegal.

The mean AOD, confidence interval, variance, standard deviation, coefficient of variation, skew, kurtosis, Kolmogorov Smirnov stat. were estimated. Hence, the instrument is very reliable for taking aerosol property measurements in Bobodioulasso. The estimated AOD properties are dependent on the atmospheric conditions/activities responsible for the distribution of aerosols in the region. Furthermore, the aerosol distribution was skewed to further buttress on the accuracy of the statistical analyses. The years with the least standard deviation and coefficient of variation were indicative of high level of accuracy in the measurements whereas, the years with the highest standard deviation and coefficient of variation were indicative of how inefficiently the instrument could malfunction or give errors in the estimated values. The recorded average deviations show the influential role the particulate concentration/loading for the years

Table 1A: AOD statistics over Bobodioulasso from year 2000-2004.

Statistics	2000	2001	2002	2003	2004
Number of values	8	9	12	12	12
Number of missing values	4	3	0	0	0
Minimum	0.094	0.182	0.157	0.105	0.153
Maximum	0.861	0.599	0.722333333	0.6485	0.777333333
Mean	0.386906	0.345564815	0.342708333	0.329937	0.361416667
First quartile	0.30325	0.2865625	0.225333333	0.2455	0.244833333
Third quartile	0.441	0.40925	0.4155	0.38925	0.433333333
Standard error	0.0779726	0.040744465	0.046448295	0.0425115	0.050508824
95% confidence interval	0.184405	0.093956737	0.102232697	0.0935678	0.111169922
99% confidence interval	0.272826	0.136697681	0.144268403	0.132041	0.156880408
Variance	0.0486378	0.014941003	0.025889329	0.0216867	0.030613696
Average deviation	0.14557	0.087720165	0.120048611	0.105969	0.128944444
Standard deviation	0.22054	0.122233396	0.160901613	0.147264	0.174967699
Coefficient of variation	0.57001	0.35372	0.4695	0.44634	0.48412
Skew	1.428	0.897	1.176	0.697	1.345
Kurtosis	3.517	1.612	1.666	0.977	1.852
Kolmogorov-Smirnov stat	0.226	0.182	0.139	0.143	0.189
Critical K-S stat, alpha=.10	0.41	0.387	0.338	0.338	0.338
Critical K-S stat, alpha=.05	0.454	0.43	0.375	0.375	0.375
Critical K-S stat, alpha=.01	0.542	0.513	0.449	0.449	0.449

Table 1B: AOD statistics over Bobodioulasso from year 2005-2009.

Statistics	2005	2006	2007	2008	2009
Number of values	11	9	11	11	8
Number of missing values	1	3	1	1	4
Minimum	0.196	0.1425	0.1675	0.143666667	0.164666667
Maximum	0.724666667	0.609	2.9	0.638	0.555
Mean	0.391121212	0.375888889	0.614681818	0.384242424	0.35959375
First quartile	0.284875	0.195916667	0.253666667	0.28325	0.245375
Third quartile	0.444875	0.556875	0.596125	0.5075	0.4535
Standard error	0.048832139	0.06128345	0.233991981	0.046335619	0.047437703
95% confidence interval	0.108798006	0.141319636	0.521334134	0.103235759	0.112190168
99% confidence interval	0.154749049	0.205605975	0.741520588	0.146837576	0.165984523
Variance	0.026230356	0.033800951	0.602274719	0.023616885	0.018002685
Average deviation	0.12331405	0.157395062	0.415512397	0.126173554	0.10890625
Standard deviation	0.161957884	0.183850351	0.776063605	0.153677862	0.134174086
Coefficient of variation	0.41409	0.48911	1.26255	0.39995	0.37313
Skew	0.981	0.109	3.043	0.164	-0.17
Kurtosis	0.525	-1.772	9.678	-0.859	-1.03
Kolmogorov-Smirnov stat	0.177	0.163	0.414	0.157	0.152
Critical K-S stat, alpha=.10	0.352	0.387	0.352	0.352	0.41
Critical K-S stat, alpha=.05	0.391	0.43	0.391	0.391	0.454
Critical K-S stat, alpha=.01	0.468	0.513	0.468	0.468	0.542

Table 1C: AOD statistics over Bobodioulasso from year 2010-2013.

Statistics	2010	2011	2012	2013
Number of values	10	12	10	10
Number of missing values	2	0	2	2
Minimum	0.176666667	0.148	0.167666667	0.163
Maximum	0.860333333	0.4015	0.87475	0.415
Mean	0.425591667	0.294395833	0.370275	0.286908333
First quartile	0.22475	0.245583333	0.2355	0.188
Third quartile	0.506666667	0.3735	0.411333333	0.38125
Standard error	0.075200385	0.022389481	0.065465378	0.030550013
95% confidence interval	0.170103271	0.049279247	0.148082686	0.06910413
99% confidence interval	0.244401251	0.069541727	0.212762479	0.099287543
Variance	0.056550979	0.006015466	0.042857157	0.009333033
Average deviation	0.188008333	0.062142361	0.146396667	0.08281
Standard deviation	0.237804498	0.077559436	0.207019703	0.096607624
Coefficient of variation	0.55876	0.26345	0.5591	0.33672
Skew	0.879	-0.071	1.816	-0.151
Kurtosis	-0.293	-0.518	3.756	-1.742
Kolmogorov-Smirnov stat	0.185	0.166	0.222	0.158
Critical K-S stat, alpha=.10	0.369	0.338	0.369	0.369
Critical K-S stat, alpha=.05	0.409	0.375	0.409	0.409
Critical K-S stat, alpha=.01	0.489	0.449	0.489	0.489

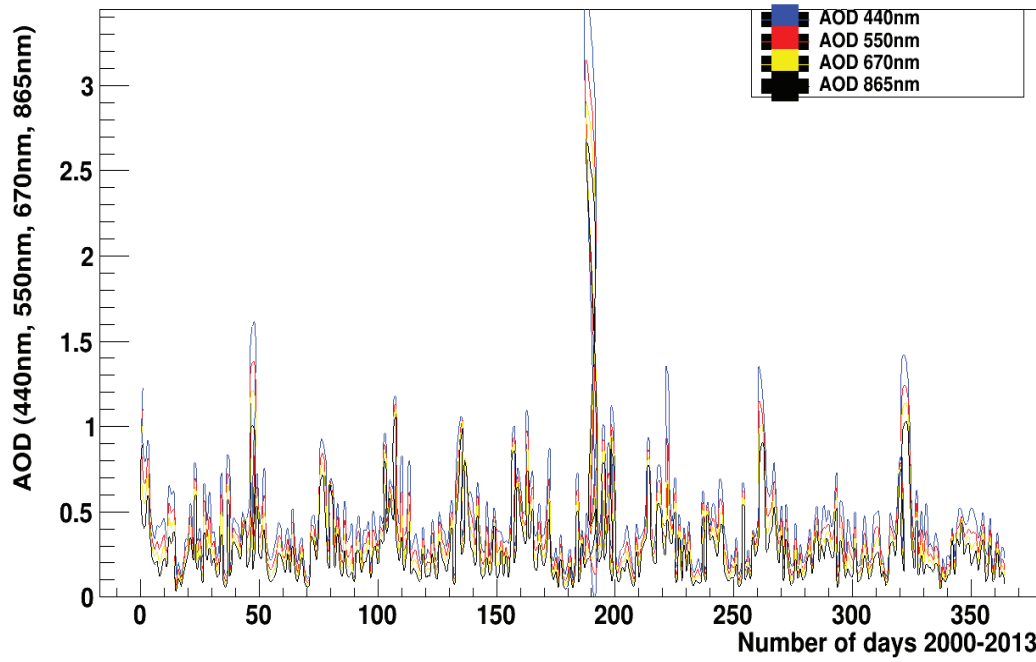

Fig. 6: Comparative analysis of the AOD wavelength of four bands.

2000-2013. Also, it can be seen that there is non-uniformity in the coefficient of variation estimated for the years thus, showing an irregularity in the atmospheric distribution of aerosols within the Bobodioulasso region. The years with the highest skews confirmed the tendency for significant effect of aerosols i.e. high tendency for pollution of the surrounding environment of Bobodioulasso.

Standard error of mean is a statement of probability that bothers on how the mean AOD deviates from the average AOD for the years; based on the estimated errors, the accuracy is in the range of 77-98%. Comparing the estimated variances, the estimated AODs for the years show that, the calculated variances are far off the actual mean of the samples by a minimum of 0.06%. The estimated average deviations are a measure of how the AODs deviate from the average AOD in the area. From the estimated standard deviations, one can see the way the measured AODs spread from the mean/median AODs for all the years. The coefficient of variation (i.e. standard deviation/mean), is a measure of the risks involved in trying to get the desired results based on the instrument/equipment used which provides evidence of inaccuracies since the risks are somewhat significant. Skewness is a measure of imbalance or asymmetry of a set of recorded AODs from the mean AODs for the different years, however, it is the degree of distortion to the left or right of a distribution as well as by how much it differs from a normal distribution. The estimated skews show that the AOD for some years were skewed to the left, hence the AODs recorded do not define a normal distribution but an asymmetric type with more of the recorded AODs positively skewed. Again, since the estimated Kurtosis for the years were more positive than negative, it then implies that the AOD distribution was characterized by thick tails compared to a normal distribution hence, it is non-platykurtic/leptokurtic. The estimated Kolmogorov values are a means of knowing if the estimated AODs belong to the same category of data i.e. not measured off the distribution, then, all the recorded values show that they are in order and can actually represent the AOD distribution for the region considered.

The computational data treatments are presented in Figs. 6-9. The computational treatment was a comparative study of the four bands of the AOD dataset obtained from MISR. Fig. 7 shows the 2D plot of the AOD of the four bands. The peak of the graph represents June-July for each of the years. It can be inferred that there are no off-data. Off-data are abnormal data noticed within the dataset. It could be inferred clearly that the highest AOD was found in 2008.

The 3D plots of each band are presented in Fig. 7. It can be observed that the AOD wavelength of 670 & 550 nm and 440 & 550 nm had the highest linearity. However, all plots show that there are relatively low deviations within each band. From the statistical treatment, the low deviation can be seen. This means that the dataset is reliable.

The individual dataset distribution was carried-out us-

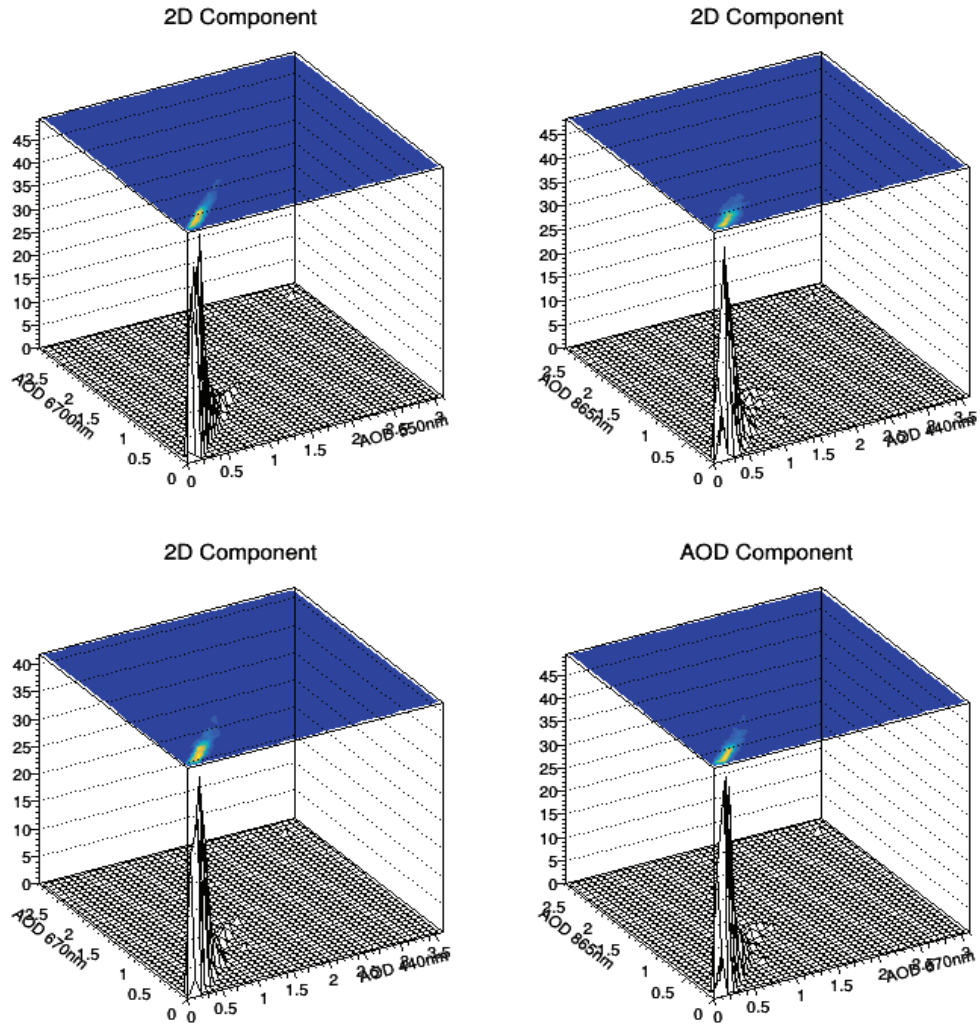

Fig. 7: Interdependency of dataset- 3D outlook.

ing the scattered plots presented in Fig. 7. The distribution of all the bands was almost the same. However, the AOD 550 nm, showed a consistent data-spread. Hence, it is computationally logical to conclude that the 550 nm dataset is the most reliable. Lastly, the individual relation of the AOD of each band to the sum of the AOD values of the remaining bands was tested in Figures 8. This type of computational treatment is christened 'linearity test'.

It was further confirmed that AOD 550 nm had the highest linearity. There was no significant deviation from the linear line from the origin. It was observed that the off-data (separate dot to the right of plot) was present in all the bands. However, it is not significant to alter the results obtained from the dataset.

CONCLUSION

In conclusion, the AOD distribution for the Bobodioulasso region is well represented within a good limit of accuracy. The distribution of aerosols in the region are a measure of the exposure levels and are indicative of potential threats or how insignificant the aerosols in a particular year may be. It was found that the statistical and computational data treatment results showed high correlation. Hence, the reliability of a mono-source can be determined. The extensive use of the AOD dataset to determine the aerosol loading angstrom parameter, radius of particulates and back-envelope of aerosol size are indication of how many variables about a geographical region can be determined from mono-source

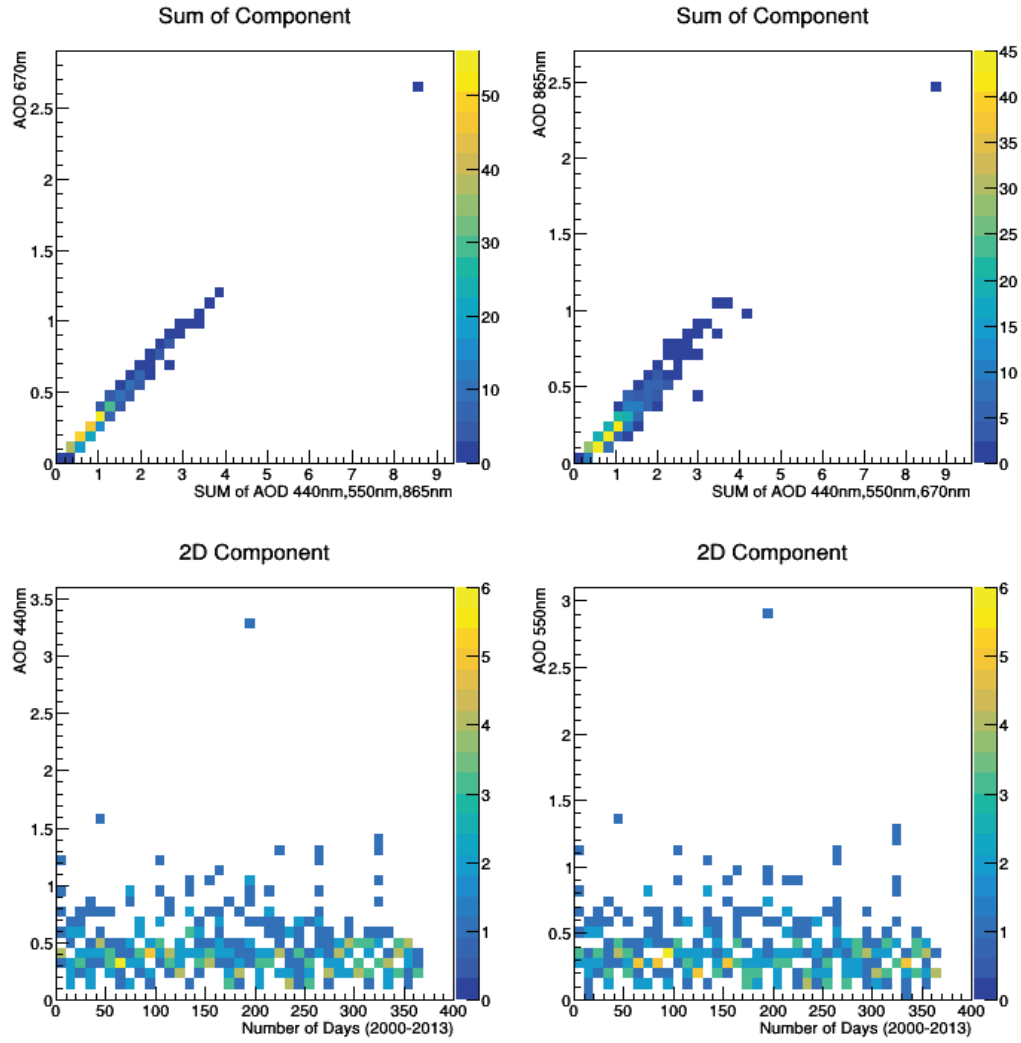

Fig. 8: Interdependency of dataset- scattered plot and linearity test.

datasets. In essence, this paper does not recommend the use of mono-source datasets over a multi-source dataset, it presents a design for carrying-out preliminary studies to guide the main studies over a geographical location.

ACKNOWLEDGEMENT

The authors appreciate Covenant University for partial sponsorship. The authors acknowledge NASA for the primary dataset.

REFERENCES

Bovchaliuk, V., Goloub, P., Podvin, T., Veselovskii, I., Tanre, D., Chaikovsky, A., Dubovik, O., Mortier, A., Lopatin, A., Korenskiy, M. and Victori, S. 2016. Comparison of aerosol properties retrieved using GARRLiC, LIRIC, and Raman algorithms applied to multi-wavelength lidar and sun/sky-photometer data. Atmospheric Measurements and Technology, 9: 3391-3405

Brauer, M., Amann, M., Burnett, R.T., Cohen, A., Dentener, F., Ezzati, M., Henderson, S.B., Krzyzanowski, M., Martin, R.V., Van-Dingenen, R., Van-Donkelaar, A. and Thurston, G.D. 2012. Exposure assessment for estimation of the global burden of disease attributable to outdoor air pollution. Environmental Science and Technology, 46: 652-660.

Chen, M., Xie, P. and Janowiak, J. 2002. Global land precipitation: A 50-yr monthly analysis based on Gauge observations. Journal of Hydrometeorology, 3: 249-266.

Crippa, M., El Haddad, I., Slowik, J.G., DeCarlo, P.F., Mohr, C., Heringa, M.F., Chirico, R., Marchand, N., Sciare, J. and Baltensperger, U. 2013. Identification of marine and continental aerosol sources in Paris using high resolution aerosol mass spectrometry. Journal of Geophysics Research, 118: 1950-1963.

Drinovec, L., Mocnik, G., Zotter, P., Prévôt, A.S.H., Ruckstuhl, C., Coz, E., Rupakheti, M., Sciare, J., Müller, T., Wiedensohler, A. and Hansen,

A.D.A. 2015. The dual-spot Aethalometer: An improved measurement of aerosol black carbon with real-time loading compensation. Atmospheric Measurements and Technology, 8: 1965-1979.

Dunion, J.P. and Velden, C.S. 2004. The impact of the Saharan air layer on Atlantic tropical cyclone activity. Bulletin of American Meteorological Society, 85: 353-365.

Emetere, M.E. 2016. Numerical modelling of west Africa regional scale aerosol dispersion. A doctoral thesis submitted to Covenant University, Nigeria, pp. 65-289.

Emetere, M.E. 2017. Impacts of recirculation event on aerosol dispersion and rainfall patterns in parts of Nigeria. Global Nest Journal, 19(2): 344-352.

Emetere, M.E., Akinyemi, M.L. and Akinojo, O. 2015. Parametric retrieval model for estimating aerosol size distribution via the AERONET, LAGOS station. Environmental Pollution, 207(C): 381-390.

Emetere, M.E., Akinyemi, M.L. and Oladimeji, T.E. 2016. Statistical examination of the aerosols loading over Kano, Nigeria: The satellite observation analysis. Scientific Review Engineering and Environmental Sciences, 72: 167-176.

Evan, A.T., Dunion, J., Foley, J.A., Heidinger, A.K. and Velden, C.S. 2006. New evidence for a relationship between Atlantic tropical cyclone activity and African dust outbreaks. Geophysics Research Letters, 33: L19813.

Geogdzhayev, I.V., Mishchenko, M.I., Terez, E.I., Terez, G.A. and Gushchin, G.K. 2005. Regional advanced very high resolution radiometer derived climatology of aerosol optical thickness and size. Journal of Geophysics Research, 110: D23205

Goldenberg, S.B., Landsea, C.W., Mestas-Nunez, W.M. and Gray, W.M. 2001. The recent increase in Atlantic hurricane activity: Causes and implications. Science, 293: 474- 478.

Kokhanovsky, A.A., Hoyningen-Huene, W.V. and Burrows, J.P. 2006. Atmospheric aerosol load as derived from space. Atmospheric Research, 81: 176-185.

Prospero, J.M. and Lamb, P.J. 2003. African droughts and dust transport to the Caribbean: climate change implications. Science, 302: 1024-1027.

Rivellini, L.H., Chiapello, I., Tison, E., Fourmentin, M., Féron, A., Diallo, A., N'Diaye, T., Goloub, P., Canonaco, F., Prévôt, A.S.H. and Riffault, V. 2017. Chemical characterization and source apportionment of submicron aerosols measured in Senegal during the 2015 SHADOW campaign. Atmospheric Chemistry and Physics, 17: 10291-10314.

Veselovskii, I., Goloub, P., Podvin, T., Bovchaliuk, V., Derimian, Y., Augustin, P., Fourmentin, M., Tanre, D., Korenskiy, M., Whiteman, D.N., Diallo, A., Ndiaye, T., Kolgotin, A. and Dubovik, O. 2016. Retrieval of optical and physical properties of African dust from multiwavelength Raman lidar measurements during the SHADOW campaign in Senegal. Atmospheric Chemistry and Physics, 16: 7013-7028

Nature Environment and Pollution Technology
An International Quarterly Scientific Journal

p-ISSN: 0972-6268
e-ISSN: 2395-3454

Vol. 18 | No. 4 | pp. 1415-1421 | 2019

Original Research Paper | Open Access

Process Optimization for the Preparation of Activated Coke from Industrial Waste Using Response Surface Methodology

Juanqin Xue*, Xiande Jing*, Shudi Hu*, Yuhong Tian*†, Yonghui Song* and Xinzhe Lan**
*Xi'an University of Architecture and Technology, Xi'an, 710055, China
**Research Centre on Metallurgical Engineering and Technology of Shaanxi Province, Shaanxi Key Laboratory of Gold and Resource, Xi'an, 710055, China
†Corresponding author: Yuhong Tian

Nat. Env. & Poll. Tech.
Website: www.neptjournal.com

Received: 13-02-2019
Accepted: 30-04-2019

Key Words:
Fine blue-coke
Coal direct liquefaction residue
Activated coke
Iodine adsorption value

ABSTRACT

Fine blue-coke and direct liquefaction residue of coal are byproducts in the process of coal chemical production. They were taken as raw materials for the preparation of activated coke by the activation of carbon dioxide. The conditions (activation temperature, activation time and carbon dioxide flow rate) for activated coke preparation were optimized by response surface methodology (RSM). Results showed that activation temperature and activation time had a significant effect on the activated coke iodine adsorption value. The synergistic effect of activation time and carbon dioxide flow had a great influence on iodine adsorption value of activated coke. RSM optimization experiment obtained the optimum activation conditions were activation temperature of 850°C, activation time of 90min and carbon dioxide flow rate of 60 mL/min. Under these conditions, the obtained activated coke iodine adsorption value can reach 401 mg/g, which could meet the needs of industrial desulphurization.

INTRODUCTION

The flue gas produced from non-ferrous metal smelting processes has become the top priority in air pollution control. Low concentration sulphur dioxide treatment methods include wet, semi-dry, dry, etc. (Bashkova et al. 2001, Siyi 2015). The traditional wet and semi-dry processing technologies have high cost, the products resulting from the treatment process are wet, and produce secondary pollution such as wastewater slag, plugging and corrosion of equipment (Gong & Yang 2018). Activated coke flue gas desulphurization technology is a resource-based dry process technology, and can also remove nitrogen oxides, dioxins, heavy metals and HCl from the flue gas, has the advantage that the product is dry and does not produce secondary pollution such as waste residue (Yan et al. 2013, Yang et al. 2017). Activated coke is desulphurizer of flue gas desulphurization technology by activated coke and is the key material to the performance and efficiency of desulphurization. The traditional preparation of activated coke is based on coal as raw material and coal tar as binder (Li 2008), so the production cost is high. Fine blue-coke and direct liquefaction residue of coal are byproducts in the process of coal chemical production (Tian et al. 2015, Zhang et al. 2012). The production cost is low using fine blue-coke and coal direct liquefaction residue as raw materials to prepare activated coke without adding adhesive. The preparation of high-quality activated coke is affected by the ratio of raw materials, carbonization temperature, carbonization time, activation temperature, activation time, activation atmosphere and other conditions, it is therefore necessary to optimize the selection of suitable preparation conditions (Gao et al. 2016, Li 2008, Zhao et al. 2016). However, the traditional test method requires a large number of experiments, and the experimental data are difficult to analyse and heavy workload.

The response surface method is often used to explore, improve, and optimize various process conditions. It can easily optimize the synergistic effects of multiple factors and facilitate the management and analysis of experimental data. Cheng et al. (2015) used Hawaiian nutshells as raw materials, using response surface methodology to optimize CO_2 physical activation of activated carbon. Di et al. (2017) used response surface methodology to optimize the enhanced coagulation process to treat micro-polluted water and optimize the optimal process conditions for coagulation treatment of micro-polluted water. Finally, it was verified by the model that the response surface method was used to optimize the feasibility and effectiveness of the enhanced coagulation process for the treatment of micro-polluted water. Theydan & Ahmed (2012) used the date kernel as the raw material and optimized the activation condition

of the activated carbon using the Box-Wilson centre composite design in response surface methodology. The results showed that the optimal conditions for $FeCl_3$ activation were activation temperature of 707°C and activation time of 76 min. The optimal conditions for $ZnCl_2$ activation are activation temperature of 717°C and activation time of 30min.

Response surface methodology is applied to the analysis of experimental data and optimization of experimental conditions. The effect of different activation conditions on the iodine adsorption value of activated coke is studied in this paper.

MATERIALS AND METHODS

Experimental raw materials: The raw materials used in the experiment were fine blue-coke and coal liquefaction residue. The fine blue-coke was from Shenmu Blue Coke Group and the direct coal liquefaction residue came from a direct liquefaction plant. Due to the fact that ash may be transferred into the activated coke during the preparation of activated coke, and high ash content is not good for activated coke. DCLR deashing is performed before the experiment. The specific method is: Take 100 g DCLR, add 25 mL HF and 175 mL H_2O in order. Stir well and put it in a fume hood for 4 hours, and then filter by suction, wash it with distilled water until it is nearly neutral, and finally dry it at 120°C. The proximate analysis and elements analysis of fine blue-coke, coal direct liquefaction residue (DCLR) and de-liquefaction residue (D-DCLR) are given in Table 1.

Preparation of activated coke: The D-DCLR was blended into a selected amount of fine blue-coke according to a certain ratio, and the mixture was evenly mixed at room temperature, some water was added to the mixture and stirred well. Under 5 MPa, it was pressed and formed into columnar strips (5 mm×10 mm), then they were dried at room temperature.

The pressed and formed columnar strips were carbonized and activated in the tube furnace under nitrogen protection. When the carbonization process was completed, the temperature was further increased to the activation final temperature, and the CO_2 gas cylinder was opened to adjust the gas flow. After the activation was completed, the entire system was cooled to room temperature under nitrogen protection.

Experimental design: Data analysis software (JMP10, Cary, NC, USA) was used for experimental design and data analysis. Three-factor and three-level response surface experiments were designed to study the synergistic effect of activation temperature, activation time, and carbon dioxide flow rate on the iodine adsorption value of activated coke. The respective ranges of the three factors are provided in Table 2, and the experimental design and experimental results are given in Table 3.

SEM characterization: The SEM analysis of activated coke was performed using a JSM-6390A scanning electron microscope to characterize the morphology of the carbonized material and the activated material. The scan voltage was 10 kV and the scan magnification was 1000x.

DATA ANALYSIS AND DISCUSSION

Analysis of variance: The variance analysis was used to evaluate the effect of each factor on the activated coke iodine adsorption value. The results are given in Table 4. The experimental design default P value of less than 0.05 has significant statistical significance (Hesas et al. 2013, Salman 2014, Sulaiman et al. 2018). Table 4 shows the activation temperature ($P = 0.0028 < 0.05$) and activation time ($P = 0.0062 < 0.05$), carbon dioxide flow ($P = 0.4308 > 0.05$), indicating that the effect of activation temperature and ac-

Table 1: Proximate analysis and elements analysis of raw material.

Sample	Proximate analysis (%)				Elements analysis (%)				
	M_t	A_{ad}	V_{ad}	FC_{ad}	C_{ad}	O_{ad}	H_{ad}	N_{ad}	$S_{t,\ ad}$
Fine blue-coke	2.15	16.77	12.07	69.01	72.88	0.3	1.06	0.88	0.6
DCLR	0.14	17.74	33.75	48.37	75.64	17.91	3.573	0.9	1.978
D-DCLR	0.26	10.62	33.19	55.93	78.24	15.4	3.733	0.96	1.667

Table 2: Parameters and their levels used for response surface design.

Factor level	Activation temperature (°C)	Activation time (min)	CO_2 flow ($mL \cdot min^{-1}$)
1	700	30	60
2	800	60	80
3	900	90	100

Table 3: The experimental conditions and results of iodine adsorption value.

Experiment sequence	Activation temperature (°C)	Activation time (min)	CO_2 flow ($mL \cdot min^{-1}$)	Iodine value ($mg \cdot g^{-1}$)
1	900	60	60	279.4
2	700	30	80	218.44
3	800	90	100	325.12
4	800	90	60	386.08
5	800	60	80	246.92
6	800	30	100	312.05
7	700	60	100	237.68
8	800	30	60	245.35
9	700	60	60	233.68
10	900	90	80	309.88
11	800	60	80	248.92
12	700	90	80	243.2
13	900	30	80	279.4
14	900	60	100	312.05
15	800	60	80	248.92

Table 4: Variance analysis of different factors

Factor	Degree of freedom	Sum of square	Mean square	F ratio	P value
Activation temperature (°C)	1	7671.2691	7671.2691	29.8813	0.0028
Error	14	21207.4029	1514.8145		
Sum	15	28878.672			
Activation time/min	1	5277.2401	5277.2401	20.5561	0.0062
Error	14	23601.4319	1685.8166		
Sum	15	28878.672			
CO_2 flow ($mL \cdot min^{-1}$)	1	188.3741	188.3741	0.7338	0.4308
Error	14	28690.2979	2049.3069		
Sum	15	28878.672			

tivation time on the iodine adsorption value are significant, while the CO_2 flow alone has no significant effect on the activated coke iodine adsorption value.

Mean value analysis: The average value of iodine adsorption values at different levels for each factor were calculated. The results are shown in Fig. 1. From the figure, it can be seen that as the activation temperature increases, the iodine adsorption value shows a trend of increasing; at the range of 700°C to 800°C the iodine adsorption value is more affected by the activation temperature. The activation process causes the activator to react with the disordered carbon in the coke and the tar and other substances present in the original pore to cause it to burn out and open the closed pore. As the activation temperature rises, the activator reacts more strongly with the coke, and an excessively high activation temperature to burn out the exposed carbon. Loss of carbon causes the pores to collapse, generating more mesopores and macropores, which reduce their adsorption capacity. The iodine adsorption value shows a tendency of decreasing first and then increasing with the prolonging of the activation time. The initial activation stage was the opening of closed pores. With the increase of activation time, the burning loss rate of carbon increases, and the decrease of micropores volume leads to the decrease of adsorption capacity of activated coke. Continue to increase activation time, so that the exposed carbon is further burned out and the new pores are formed, and the iodine adsorption value of activated coke shows an increasing trend.

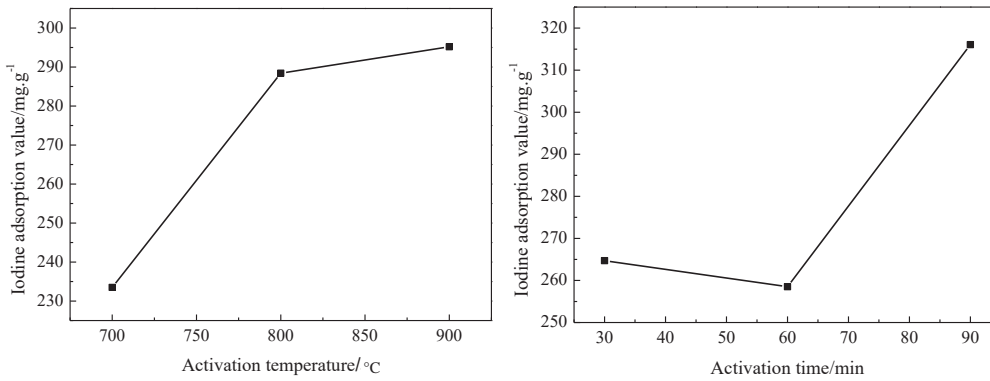

Fig. 1: The iodine adsorption value of activated coke.

Effect of activation conditions on activated coke strength and yield: Fig. 2(a) shows the effect of activation temperature on compressive strength and yield of activated coke. The results show that the compressive strength and yield of activated coke decrease with increasing activation temperature. When the activation temperature is 850°C, the compressive strength and yield of activated coke is 513.8 N and 81.03%, respectively. This is because when the activation temperature is lower, the activator reacts less with the surface of the activated coke material, the reaction is slower and the reaction depth is shallower, so the yield and the compressive strength of the activated coke are higher. When the activation temperature rises to 850°C, the reaction between the activator and the carbon material is intensified and the depth of the reaction is further deepened, resulting in serious loss of carbon material, and a large amount of hydrogen in the coal liquefaction residue is released at higher temperature, and organic components are generated more frequently. The volatiles escaped, resulting in a decrease on the yield and compressive strength. It can be seen that the higher the activation temperature, the more severe the loss of carbon material, and the lower the yield and compressive strength of activated coke.

Fig. 2(b) shows the effect of activation time on the activated coke yield and compressive strength. The results show that the compressive strength and yield of activated coke have a similar trend with the activation temperature as the activation time increases. When the activation time is 90 min, the compressive strength of the activated coke is 573.2 N and the yield is 82.26%. The activation time is continuously prolonged, and the amount of activator continuously increases, making the activator sufficiently enter the pores of the carbon material, fully reacting with the surface and interior of the carbon material, generating a large amount of volatiles to escape, and making the activated coke pores further developed. The compressive strength and yield of activated coke continue to decrease with the increased activation time.

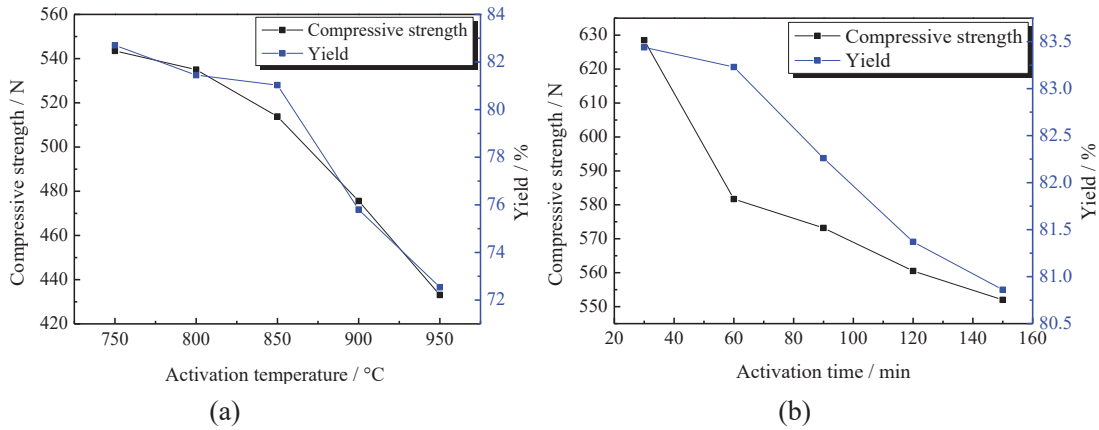

Fig. 2: The yield and strength of activated coke.

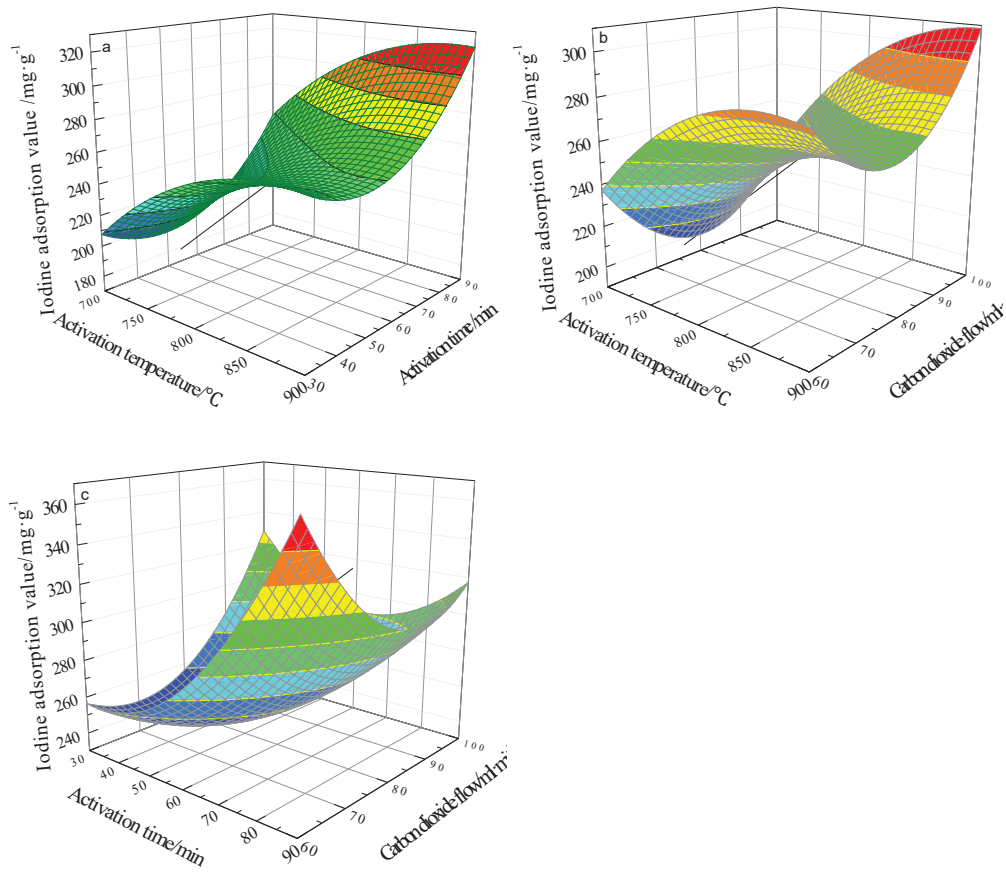

Fig. 3: Response surface map.

Parameters optimization: Response surface methodology was used to explore the optimal synergy of the three activation factors and the effect on the activated coke iodine adsorption value. The relative relationship between the dependent variable and the independent variable is calculated by the following second-order polynomial:

$$Y = 248.92 + 30.96625X_1 + 25.68375X_2 + 4.8525X_3 + 1.43X_1X_2 + 7.1625X_1X_3 - 31.0225X_2X_3 - 19.265X_1^2 + 33.075X_2^2 + 36.0745X_3^2$$

Where, X_1, X_2, X_3 are equal to

$$\frac{\text{activation temperature (°C)} - 800}{100},$$

$$\frac{\text{activation time(min)} - 60}{30} \text{ and } \frac{CO_2 \text{ flow (mL/min)} - 80}{20}$$

respectively.

The calculated values of R^2 and response surface model variance analysis are given in Table 5 and Table 6. R^2=0.96 and P=0.0069 indicate that this model is suitable for predicting the effect of various factors on the adsorption of activated coke at various levels (Ab Ghani et al. 2017, Zheng et al. 2017). The 3-D response surface plot was used to study the synergistic effect of different factors on the activated coke iodine adsorption value. The results are shown in Fig. 3.

Table 5: Summary of model data.

R^2	Adjust R^2	RMSE
0.96	0.88	16.023

Table 6: Analysis of variance of response surface quadratic model.

Source	Degree of freedom	Sum of square	Mean square	F ratio	P value
Model	9	27595.051	3066.12	11.9432	0.0069
Error	5	1283.622	256.72		
Correction sum	14	28878.672			

In Fig. 3(a), the iodine adsorption value of the activated coke as a function of activation temperature and activation time, the CO_2 flow rate is 80 mL/min. It can be seen from the figure, when the activation temperature is 900°C and the

activation time is 90 min, the iodine adsorption value of the activated coke is higher and can reach 309.88 mg/g.

In Fig. 3(b), the iodine adsorption value of the activated coke is a function of activation temperature and CO_2 flow rate, with activation time of 60 min. The figure shows that when the activation temperature is 900°C, CO_2 flow rate of 100 mL/min, the iodine adsorption value of activated coke is 312.05 mg/g.

In Fig. 3(c), the iodide adsorption value of activated coke is a function of activation time and CO_2 flow rate, with activation temperature of 800°C. The figure shows that when activation time is 90 min, CO_2 flow rate of 60 mL/min, the iodine adsorption value is 386.08 mg/g.

In summary, the synergistic effect of CO_2 flow and activation time during the activation process has a great influence on the iodine adsorption value. By optimizing the experimental conditions, the optimal experimental conditions are as follows: activation temperature 850°C, activation time 90 min, carbon dioxide flow rate 60 mL/min. The iodine adsorption value was 401 mg/g, which could meet the needs of industrial desulphurization.

SEM characterization: Fig. 4(a) is SEM photograph of sample carbonized at 600°C for 60 min. Fig. 4(b) is SEM photograph of sample activated by carbon dioxide at 900°C for 90 min. Fig. 4(a) shows that the surface of sample is dense, irregular in shape and with slits. This is due to the large amount of water and volatile matter escaping during carbonization process, which results in slit structure in the carbonized sample. Activator enters into the charcoal material in activation process and provides favourable conditions so that the activation process can be fully carried out and more pore structure can be formed. Fig. 4(b) shows that the sample after activation has rich pore structure and a relatively uniform pore distribution. This is due to the activator reacts with the carbon on the surface and inside of the carbon material under high temperature conditions, the activator continuously etched the surface and inside of the carbon material.

Desulphurization performance: At room temperature, the inlet air amount was controlled at 1300 mg/m^3, the bed height at 13 cm, and the desulphurization performance of activated coke prepared under the optimal conditions was examined. The desulphurization rate for the first 120 minutes is shown in Fig. 5.

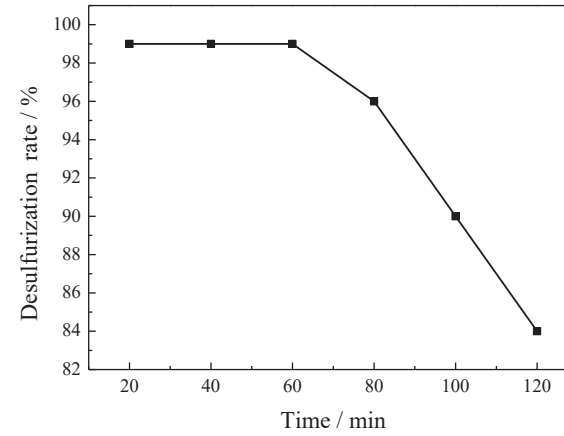

Fig. 5: The desulphurization rate of activated coke (%).

As can be seen from Fig. 5, the desulphurization rate in the first 60 minutes remains stable at 99%, and then it decreased but remained above 80%, indicating that the activated coke has a high removal rate for low concentrations of sulphur dioxide. With the extension of desulphurization time, the main reason for the decrease in desulphurization rate is that the activated sites on activated coke surface are

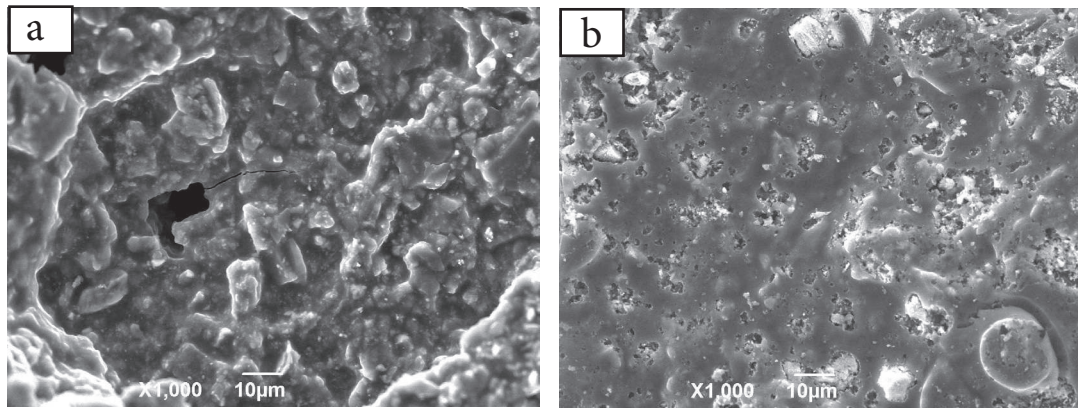

Fig. 4: The SEM analysis of activated coke.

occupied by the adsorbed gas, resulting in a reduction in the activated sites and a decrease in the desulphurization rate.

CONCLUSIONS

The activation temperature and activation time had a more significant effect on the activated coke iodine adsorption value than the carbon dioxide flow using the method of variance analysis. The synergistic effect of activation time and carbon dioxide flow had a great influence on iodine adsorption value of activated coke. RSM optimization experiment obtained better conditions: activation temperature 850°C, activation time 90 min, carbon dioxide flow rate 60 mL/min. The adsorption value of activated coke iodine prepared under these conditions was 401 mg/g. With the increase of activation temperature and activation time, the compressive strength and yield of activated coke are reduced. The carbonization process provides favourable conditions for activator to enter into the carbon material and react with it adequately. The desulphurization rate in the first 60 minutes remains stable nearly 99%.

ACKNOWLEDGEMENTS

The authors acknowledge the financial support by National Natural Science Foundation of China (Grant No. 51504180).

REFERENCES

Ab Ghani, Z., Yusoff, M.S., Zaman, N. Q., Zamri, M. F. M. A. and Andas, J. 2017. Optimization of preparation conditions for activated carbon from banana pseudo-stem using response surface methodology on removal of color and COD from landfill leachate. Waste Management, 62: 177-187.

Bashkova, S., Bagreev, A., Locke, D.C. and Bandosz, T.J. 2001. Adsorption of SO_2 on sewage sludge-derived materials. Environmental Science & Technology, 35(15): 3263-3269.

Cheng, S., Zhang, L., Xia, H., Peng, J., Zhang, S. and Zhou, C. 2015. Preparation of activated carbon from Hawaii nut shell via CO_2 activation using response surface methodology. Chinese Journal of Environmental Engineering, 9(9): 4495-4502.

Di, J., Zhao, W., Zhu, Z., An, W. and Ren, Y. 2017. Treatment of response surface methodology to optimize enhanced coagulation process for micro-polluted water. Chinese Journal of Environmental Engineering, 11(1): 27-32.

Gao, Y., Yue, Q. and Gao, B. 2016. Insights into properties of activated carbons prepared from different raw precursors by pyrophosphoric acid activation. Journal of Environmental Sciences, 41: 235-243.

Gong, Y. and Yang, Z.G. 2018. Corrosion evaluation of one wet desulphurization equipment - Flue gas desulphurization unit. Fuel Processing Technology, 181: 279-293.

Hesas, R.H., Arami-Niya, A., Daud, W.M.A.W. and Sahu, J.N. 2013. Preparation of granular activated carbon from oil palm shell by microwave-induced chemical activation: Optimisation using surface response methodology. Chemical Engineering Research & Design, 91(12): 2447-2456.

Li, J.N.K. and Hu, Y. 2008. The activated coke preparation for SO_2 adsorption by using flue gas from coal power plant. Chemical Engineering and Processing: Process Intensification, 47(01): 118-127.

Salman, J.M. 2014. Optimization of preparation conditions for activated carbon from palm oil fronds using response surface methodology on removal of pesticides from aqueous solution. Arabian Journal of Chemistry, 7(1): 101-108.

Siyi, P. 2015. Study on the removal of low concentration sulphur dioxide by ctivated carbon adsorption combined with microwave desorption. Kunming University of Science and Technology.

Sulaiman, N.S., Hashim, R., Amini, M.H.M., Danish, M. and Sulaiman, O. 2018. Optimization of activated carbon preparation from cassava stem using response surface methodology on surface area and yield. Journal of Cleaner Production, 198: 1422-1430.

Theydan, S.K. and Ahmed, M.J. 2012. Optimization of preparation conditions for activated carbons from date stones using response surface methodology. Powder Technology, 224: 101-108.

Tian, Y., Lan, X., Song, Y., Liu, C. and Zhou, J. 2015. Preparation and characterization of formed activated carbon from fine blue-coke. International Journal of Energy Research, 39(13): 1800-1806.

Yan, Z., Liu, L., Zhang, Y., Liang, J., Wang, J., Zhang, Z. and Wang, X. 2013. Activated semi-coke in SO_2 removal from flue gas: Selection of activation methodology and desulphurization mechanism study. Energy & Fuels, 27(6): 3080-3089.

Yang, L., Jiang, X., Jiang, W., Wang, P. and Jin, Y. 2017. Cyclic regeneration of pyrolusite-modified activated coke by blending method for flue gas desulphurization. Energy & Fuels, 31(4): 4556-4564.

Zhang, J., Jin, L., Liu, S., Xun, Y. and Hu, H. 2012. Mesoporous carbon prepared from direct coal liquefaction residue for methane decomposition. Carbon, 50(3): 952-959.

Zhao, B., Yi, H., Tang, X., Li, Q., Liu, D. and Gao, F. 2016. Copper modified activated coke for mercury removal from coal-fired flue gas. Chemical Engineering Journal, 286: 585-593.

Zheng, J.H., Li, H.J., Cui, H., Wang, Y., Deng, H.L., Yin, Z.Y., Yao, D.M. and Su, H. 2017. Relations between needling processing parameters and tensile strength of C/C composites. Journal of Inorganic Materials, 32(11): 1147-1153.

Nature Environment and Pollution Technology
An International Quarterly Scientific Journal

p-ISSN: 0972-6268
e-ISSN: 2395-3454

Vol. 18 | No. 4 | pp. 1423-1427 | 2019

Original Research Paper | Open Access

Plumbum (Pb) in Rainwater in West Kalimantan: Impact of Plumbum (Pb) in Community Blood

Khayan Khayan-Taufik Anwar-Slamet Wardoyo
Department of Environmental Health, Poltekkes Kemenkes Pontianak, 78124, Indonesia

Nat. Env. & Poll. Tech.
Website: www.neptjournal.com

Received: 27-03-2019
Accepted: 01-06-2019

Key Words:
Plumbum (Pb)
Rainwater
Zinc roof
Community blood
Drinking water

ABSTRACT

The low coverage of drinking water in the West Kalimantan-Indonesia region because of the limited availability of decent water as a source of drinking water is the main trigger for the community to use rainwater as a source of drinking water. The way of storing rainwater through zinc roofs and environmental pollution conditions results in rainwater being a health concern for the community because of the content of Plumbum (Pb). In this study, the characteristics of rainwater in the West Kalimantan region were investigated from rainwater collected by people from homes with zinc roofs. Rainwater samples from the collection results were analysed for the presence of Plumbum (Pb). The impact of consuming rainwater is carried out by blood Pb examination. The main problem can analyse the existence of Plumbum (Pb) in rainwater against the content of Plumbum (Pb) in the blood. The results showed that there was a correlation of Pb content in rainwater with Pb content in the blood of people who consumed rainwater as water drink ($p \leq 0.001$).

INTRODUCTION

Freshwater is abundant in the tropics, especially Indonesia, and can be used as a source of clean water and drink for the community. It is only about 20% of the 200 million people who have access to Regional Water Companies (PDAMs) (Peniwati & Brenner 2008). The rest use water sources that are not processed by Regional Water Companies, such as surface water and rainwater. Along with population growth, which is getting higher with increasingly poor environmental quality, results in high pollution of surface water and the community uses rainwater as a source of drinking water (Resosudarmo 2003, Wilopo et al. 2013).

Rainwater naturally has good quality physically, chemically and biologically except that its mineral content is low. Environmental conditions that are getting worse due to air pollution in the Industrial era can pollute rainwater (Water et al. 2017). These contaminants come from transportation, industry, and land burning activities, which often occur in the dry season (Afroz et al. 2003, Colvile et al. 2001, Harrison et al. 2009, Sastry 2002). Indonesia is a land area with peatlands with distribution in Sumatra, Kalimantan as a trigger for fires (Tacconi et al. 2007).

Characteristics of tropical communities that use roofs having zinc as roofs have their own risk of Pb content in rainwater (Meera & Ahammed 2018). Zinc roofs are made up of zinc metal using Pb coating as stainless. Due to the presence of air pollutants such as COx, SOx and NOx the rainwater becomes acidic and corrosive to metals (De la Fuente et al. 2007). In addition, contamination from burning fuel oil can result in Pb pollutants. Low pH of rainwater due to acid rain will increase the solubility of metals in water, so it will be riskier if the water is consumed (Chuan et al. 1996).

Pb content in rainwater aside from the zinc roof used to hold rainwater also occurs due to Pb exposure from the environment outside the zinc roof, for example, industrial activities, motor vehicle emissions, burning of agricultural land (peat), burning of charcoal and other materials (Sun et al. 2004, Al-Masri 2006). Furthermore, pollutants of Pb particles, especially organic Pb (tetraethyl lead and tetramethyl lead) in the air decompose rapidly due to sunlight. Tetra ethyl-Pb will decompose into triethyl-Pb, diethyl-Pb and monoethyl-Pb with the help of rainwater to become crystals and easily dissolve in water, and then enter into Rainwater Shelter (PAH) and used as a source of drinking water for the community (Zhang et al. 2015)

From several studies, the effects of long-term lead have been linked to various forms of cancer, nephrotoxicity, central nervous system effects, and cardiovascular disease in humans. Drinking water has a widely known metal exposure pathway. So that the risk as early as possible needs to be known before an acute effect occurs (Ryan et al. 2000). Detection of Pb exposure can be done through blood tests by comparing with the standards set by WHO (Edwards et al. 2009).

MATERIALS AND METHODS

Research Methods

This study uses analytical observational methods. With the aim of analysing the utilization of rainwater as a source of drinking water that passes through the roof of zinc to the content of blood Pb in the people of West Kalimantan, Indonesia. The study design used was cross-sectional. The number of research samples were from 40 houses. The research was conducted through three research objectives, namely knowing the Pb content in rainwater that passes through the zinc roof, the Pb content of the blood levels of that consume rainwater, and to analyse the risk of exposure to Pb of rainwater that is passed through a zinc roof with the content of Pb in the blood of the community of West Kalimantan, Indonesia.

Study Site

Samples come from the two targeted areas in the West Kalimantan region, Indonesia to represent urban and rural areas, namely Pontianak City and Kubu Raya Regency. Urban areas were chosen by two target locations, namely Siantan Hulu and Central Siantan Districts. Whereas Kubu Raya Regency is taken from the locations of Limbung Village and Arang Limbung Village. This research was conducted for 12 months from January to December 2016. This study was approved by the Ethics Committee for Health Research at the Ministry of Health Polytechnic Makassar (303/ KEP-PTKMKS/VII) and informed consent was given directly to the respondents to get approval and participation in this study. Rainwater samples were taken from homes with zinc roofs and rainwater storage was used as a source of random drinking water. Rainwater samples were taken with a 0-20 minute rain interval of 2.5 litres of rain. A blood sample of 5 mL was taken from the occupants of the house whose duration of residence was longest at home with the consumption of the most drinking water from rainwater. The collected samples were processed and stored for brewing to the laboratory. Decision in research participation were voluntary.

Sample Analysis

Pb analysis in water was carried out using atomic absorption spectroscopy (AAS). Standard solutions were analysed using AAS and followed by empty solutions and sample solutions (urine and blood). The measurement results of atomic absorption were recorded and calculated to obtain Pb concentration in the sample solutions (Bai et al. 2015, Islam et al. 2016). Blood lead measurement uses a voltammetric stripping technique (Ahmad et al. 2014).

Data Analysis

Data were processed by computer programs and analysed descriptively and analytically. Correlation test was used to analyse the relationship between exposure to rainwater Pb and Pb in the blood of people who consume rainwater as drinking water, to see the strength of the relationship carried out by looking at the value of *r* (Hedberg et al. 2011).

RESULTS

From the results of Pb examination in rainwater that was used by the people of West Kalimantan with four target locations, the study showed that rainwater used by the community as a source of drinking water was positive for the existence of Pb. The Pb is caused by the way the community keeps using zinc roofs and is aggravated by air pollution. The Pb level of rainwater in West Kalimantan has a mean of 137.55 µg/L with the highest distribution being in urban areas namely Upper Siantan and Central Siantan (201.34; 220.40 µg/L) compared to rural areas (56.57; 71.87) (Fig. 1a).

From testing blood samples taken from the people who consume rainwater, it shows that Pb in their blood is still at the permissible limit of ≥ 40 µg/dL. Lead levels in the blood of people who consumed rainwater as drinking water had an average of 21.79 µg/dL of drugs with the highest blood Pb in urban areas 27.48 µg/dL compared to rural areas of 16.11 µg/dL. The urban and rural areas are each represented by two target regions (Fig. 1b).

Table 1: Relationship of Pb levels in water with blood Pb.

		Pb in Blood
Pb in Water	Pearson Correlation	.674**
	Sig. (2-tailed)	.000
	N	40

** Correlation is significant at the 0.01 level (2-tailed).

From the examination, it was shown that the people who consumed drinking water came from rainwater, which was accommodated through zinc roofs which tended to have high blood lead levels. Test statistic obtained the value of p≤0,001. There is a correlation between Pb levels in rainwater consumed with blood levels of Pb blood. The relationship has a strong and positive relationship (r = 0.67) (Table 1). From the regression equation, it can be seen that the higher the Pb of rainwater, the higher the blood Pb of the community. Regression results from this study are shown in Fig. 2.

DISCUSSION

West Kalimantan region, Indonesia is a region that has a tropical climate with the intensity of rain throughout the

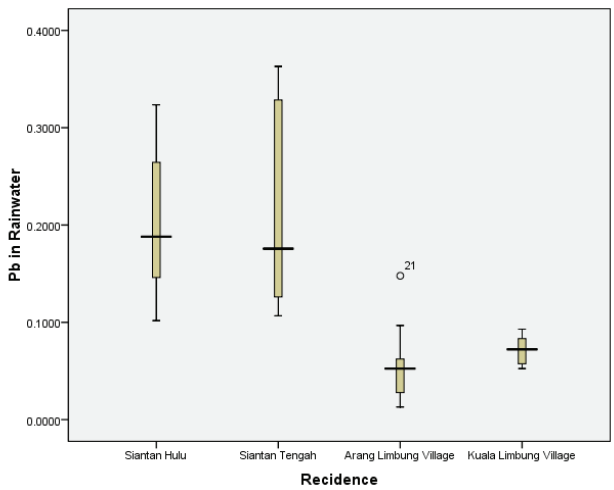

Fig. 1: a. Pb content in rainwater is utilized by the community

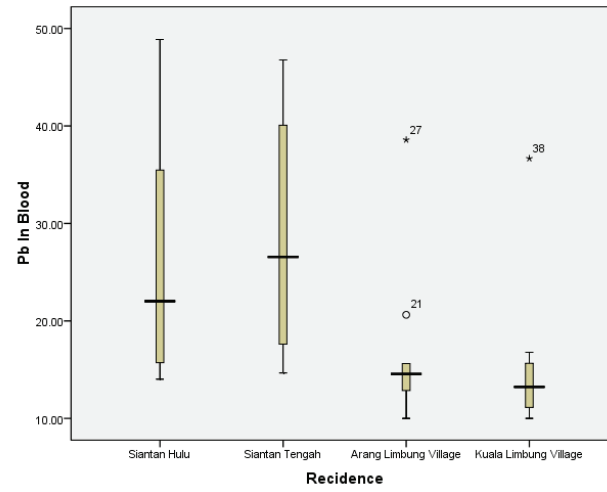

b. Pb content of the blood of people who consume rainwater

months. The abundant amount of rain in addition to the quality of surface water and poor soil triggers the community to use rainwater as drinking water (Kido et al. 2009). From the research conducted, the quality of rainwater which is considered by the community as good quality turns out to have a high lead content of 137.46 µg/L. Urban areas with higher levels of Pb in rainwater are higher than rural areas because urban areas have higher pollution levels than rural areas.

The inclusion of Pb in rainwater is caused by the presence of Pb contamination in the air from natural and human activities. Natural activities, for example are from Mount Merapi explosions and land fires. Non-natural sources or human activities are such as lead emissions from industrial and transportation activities (Zhang et al. 2015). Because of the use of leaded fuel, car and motorcycle vehicles are the main sources of lead (Pb) emissions in the air. Lead emission (Pb) released in the ambient air will be bound by

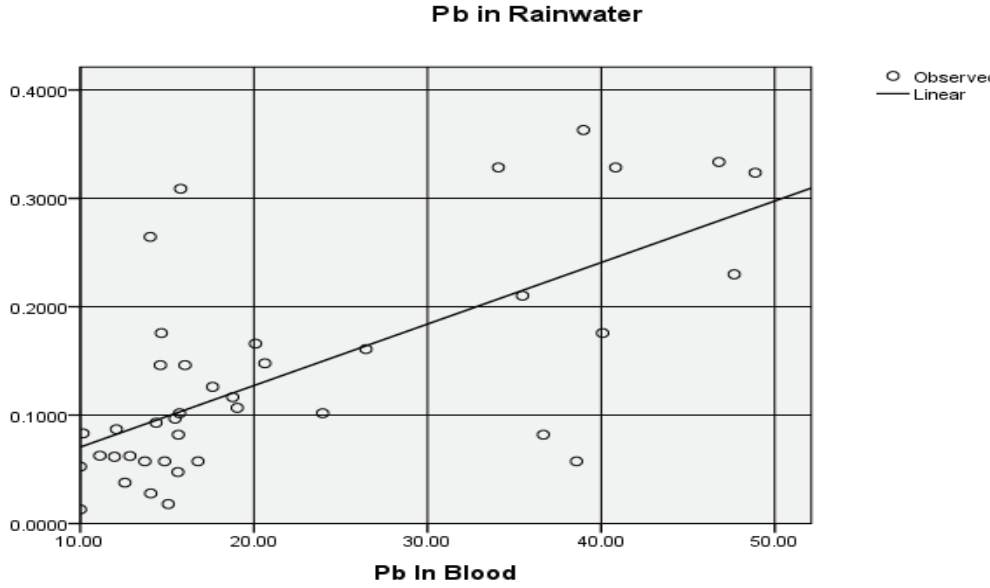

Fig. 2: Linear PB in rainwater and blood Pb.

the simultaneous decrease in rainwater. Rainwater whose natural conditions do not contain lead can be polluted by lead (Pb) (Khayan et al. 2017).

Natural activities and human activities in addition to causing lead contamination (Pb), also cause other contaminating gases such as COx, NOx, and SOx which cause acid rain and increase the solubility of lead (Pb) in rainwater (Wondyfraw et al. 2014). Acidic rainwater is corrosive to metal roofs such as zinc roofs. Zinc roof is the roof of the house in the manufacturing process using a layer of lead (Pb). Acid rain causes the zinc roof to be corrosive and release Pb in the water flowing above it (Knotkova 1992).

The impact arising from consumption of rainwater containing high Pb results in high blood Pb levels in the community. This can be seen from the measurement of blood Pb levels in people who oxidize rainwater. There is a tendency between the high exposure of Pb of rainwater and the high Pb of the blood of people who use rainwater as a source of drinking water. The statistical test results showed a significant correlation ($p \leq 0{,}001$), with a moderate strength ($r = 0.4$) between the high concentration of Pb of rainwater and the amount of Pb content in the blood of the community.

The impact of lead exposure depends on how much lead (Pb) is exposed in the body. Lead (Pb) is a metal that is toxic to humans, which can enter the body through oral (digestive), such as food or drinking water consumed. Besides having toxic properties, Pb metal has cumulative properties in the body (Wani et al. 2015). Lead (Pb), which enters the body will be distributed throughout the body through the blood and accumulates in the bones and soft tissue will cause chronic toxicity. Lead (Pb) can cause neurological, liver, kidney, haematological, circulatory, immunological, reproductive, growth, hearing, gastrointestinal and cardiovascular disorders (Zhang et al. 2015). Pb concentrations more than 50 μg/dL can interfere with the production of haemoglobin even though the blood Pb of the community is still below the standard but continued monitoring needs to be done (Khotijah et al. 2017, Liu et al. 2015). Pb exposure, in general, is more detrimental to children than adults. Children are more sensitive to low lead levels than adults. Lead poisoning (Pb) in children can cause neurological effects that contribute to lower intellectual intelligence (IQ), learning deficits, cognitive deficits, lower vocabulary abilities and grammatical reasoning, longer reaction times, worse hand-eye coordination, deficits in psychological performance, hyperactivity, and behavioural problems (Wani et al. 2015).

High levels of lead in blood (BLL) in adults will have an impact on the emergence of several diseases. Common diseases are frequent headaches, numbness in the legs, nausea, colic, tremor, nausea, and lead lines on the gums. Timabk in the blood is also related to the incidence of hypertension and anaemia (Ahmad et al. 2014).

CONCLUSION

Rainwater that is used by the people of West Kalimantan, Indonesia has the presence of Pb. The presence of Pb in the rainwater increases the blood Pb content of the people who consume it. There is a correlation between the Pb of rainwater and the blood Pb of the community with rainwater consumption ($p \leq 0{,}001$) with a positive correlation ($r = 0.67$). The relationship shows that the higher the Pb in the water consumed, the higher the blood Pb.

ACKNOWLEDGMENT

Head of the Development Agency Health Human Resources of the Republic of Indonesia, as well as the Pontianak Ministry of Health Research and Technology, which supported and facilitated this research are gratefully acknowledged. We also thank the people of West Kalimantan who participated in this research.

REFERENCES

Afroz, R., Hassan, M.N. and Ibrahim, N.A. 2003. Review of air pollution and health impacts in Malaysia. Environmental Research, 92(2): 71-77.

Ahmad, S., Khan, M.H., Khandker, S., Sarwar, A.F.M., Yasmin, N., Faruquee, M.H. and Yasmin, R. 2014. Blood lead levels and health problems of lead acid battery workers in Bangladesh. The Scientific World Journal, 7-9.

Al-Masri, M.S., Al-Kharfan, K. and Al-Shamali, K. 2006. Speciation of Pb, Cu and Zn determined by sequential extraction for identification of air pollution sources in Syria. Atmospheric Environment, 40(4): 753-761.

Bai, D., Ying, Q., Wang, N. and Lin, J. 2015. Atomic absorption spectroscopy for the determination of heavy metals in polyethylene moulding materials using Anderson-Darling statistics and top-down uncertainty estimates. In: 2015 3rd International Conference on Advances in Energy and Environmental Science, Atlantis Press.

Chuan, M.C., Shu, G.Y. and Liu, J.C. 1996. Solubility of heavy metals in a contaminated soil: Effects of redox potential and pH. Water, Air and Soil Pollution, 90(3-4): 543-556.

Colvile, R.N., Hutchinson, E.J., Mindell, J.S. and Warren, R.F. 2001. The transport sector as a source of air pollution. Atmospheric environment, 35(9): 1537-1565.

De la Fuente, D., Castano, J.G. and Morcillo, M. 2007. Long-term atmospheric corrosion of zinc. Corrosion Science, 49(3): 1420-1436.

Edwards, M., Triantafyllidou, S. and Best, D. 2009. Elevated blood lead in young children due to lead-contaminated drinking water: Washington, DC, 2001-2004. Environmental Science & Technology, 43(5): 1618-1623.

Harrison, M.E., Page, S.E. and Limin, S.H. 2009. The global impact of Indonesian forest fires. Biologist, 56(3): 156-163.

Hedberg, Y., Herting, G. and Wallinder, I.O. 2011. Risks of using membrane filtration for trace metal analysis and assessing the dissolved metal fraction of aqueous media-a study on zinc, copper and nickel. Environmental pollution, 159(5): 1144-1150.

Islam, R., Al Foisal, J., Rahman, M., Lisa, L.A. and Paul, D.K. 2016. Pollution assessment and heavy metal determination by AAS in waste water collected from Kushtia industrial zone in Bangladesh. African Journal of Environmental Science and Technology, 10(1): 9-17.

Khayan, K., Husodo, H., Sudarmadji, S. and Sugandawaty, S. 2017. Usage of filter tube to reduce Pb, turbidity and increase pH of rain water flowing through zinc rooftop house. KEMAS: Jurnal Kesehatan Masyarakat, 13(1): 41-49.

Khotijah, K., Sjarifah, I., Mahendra, P.G.O., Widyaningsih, V. and Setyawan, H. 2017. The effects of lead (Pb) exposure to blood Pb concentration and haemoglobin levels in book sellers and street vendors of Surakarta. KEMAS: Jurnal Kesehatan Masyarakat, 13(2): 286-290.

Kido, M., Syawal, M.S., Hosokawa, T., Tanaka, S., Saito, T., Iwakuma, T. and Kurasaki, M. 2009. Comparison of general water quality of rivers in Indonesia and Japan. Environmental Monitoring and Assessment, 156(1-4): 317.

Knotkova, D. and Bartoň, K. 1992. Effects of acid deposition on corrosion of metals. Atmospheric Environment. Part A. General Topics, 26(17): 3169-3177.

Liu, C., Huo, X., Lin, P., Zhang, Y., Li, W. and Xu, X. 2015. Association between blood erythrocyte lead concentrations and haemoglobin levels in preschool children. Environmental Science and Pollution Research, 22(12): 9233-9240.

Meera, V. and Ahammed, M.M. 2006. Water quality of rooftop rainwater harvesting systems: A review. Journal of Water Supply: Research and Technology-AQUA, 55(4): 257-268.

Peniwati, K. and Brenner, W. 2008. Multi-decisions rating model: Establishing rescue policies for regional drinking water companies (PDAMs) in Indonesia. European Journal of Operational Research, 186(3): 1127-1136.

Resosudarmo, B.P. 2003. River water pollution in Indonesia: An input-output analysis. International Journal of Environment and Sustainable Development, 2(1): 62-77.

Ryan, P.B., Huet, N. and MacIntosh, D.L. 2000. Longitudinal investigation of exposure to arsenic, cadmium, and lead in drinking water. Environmental health perspectives, 108(8): 731-735.

Sastry, N. 2002. Forest fires, air pollution, and mortality in Southeast Asia. Demography, 39(1): 1-23.

Sun, Y., Zhuang, G., Wang, Y., Han, L., Guo, J., Dan, M., Zhang, W., Wang, Z. and Hao, Z. 2004. The air-borne particulate pollution in Beijing-concentration, composition, distribution and sources. Atmospheric Environment, 38(35): 5991-6004.

Tacconi, L., Moore, P.F. and Kaimowitz, D. 2007. Fires in tropical forests–what is really the problem? Lessons from Indonesia. Mitigation and Adaptation Strategies for Global Change, 12(1): 55-66.

Wani, A.L., Ara, A. and Usmani, J.A. 2015. Lead toxicity: A review. Interdisciplinary Toxicology, 8(2): 55-64.

Wilopo, W., Resili, R. and Putra, D.P.E. 2013. Effect of traditional gold mining to surface water quality in Murung Raya District, Central Kalimantan Province. Journal of Degraded and Mining Lands Management, 1(1): 33.

Wondyfraw, M. 2014. Mechanisms and effects of acid rain on environment. Journal of Earth Science & Climatic Change, 5(6): 1.

Zhang, R., Wilson, V.L., Hou, A. and Meng, G. 2015. Source of lead pollution, its influence on public health and the countermeasures. International Journal of Health, Animal Science and Food Safety, 2(1): 18-31.

Nature Environment and Pollution Technology
An International Quarterly Scientific Journal

p-ISSN: 0972-6268
e-ISSN: 2395-3454

Vol. 18 | No. 4 | pp. 1429-1446 | 2019

Original Research Paper | Open Access

Assessment of Ecological Status in Seawater Around Legon Bajak Port Development Plan, Karimunjawa, Central Java, Indonesia

Slamet Isworo*† and Poerna Sri Oetari**

*Department of Environmental Health, Dian Nuswantoro University, Semarang, Indonesia

**Graduate School of Environmental Science, Diponegoro University, Semarang, Indonesia

† Corresponding author: Slamet Isworo

Nat. Env. & Poll. Tech.
Website: www.neptjournal.com

Received: 27-03-2019
Accepted: 01-06-2019

Key Words:
Ecological damage
Seaweed
Coral
Legon Bajak port
Transect method

ABSTRACT

The Legon Bajak port is a strategic port in Indonesia, because it is located in a busy and potential shipping lane. The port is adjacent to the Karimunjawa Marine National Park which is protected by the Indonesian government; therefore, this study aims to provide an overview of the ecological status of the Legon Bajak sea and the prediction of the impact of port activities on the ecological status of the Marine National Park. This research is a descriptive study by analysing seawater quality using atomic absorption spectroscopic methods, the status of biodiversity of seaweed and coral reefs with the transect method at 6 observed sample points and photos of underwater marine supporters. The results of the analysis of seawater quality indicate that it is in good condition, but when viewed from the analysis of seaweed conditions and coral cover <10%, this indicates that the ecological status is in a damaged condition and a category with a low functional value. An in-depth study is needed for the analysis of the environmental impact of the Legon Bajak port on the Karimunjawa National Marine Park Conservation Area.

INTRODUCTION

Indonesia as a maritime country and the largest archipelagic country in Southeast Asia, actively build ports to connect ports in the Republic of Indonesia in increasing the level of the national economy (Karimunjawa National Park Office 2004). Legon Bajak Port is one of the potential ports located in Kemujan-Karimunjawa Village, Jepara Regency, Central Java Province, currently functioning as a place for fishing activities for local fishermen and small-capacity cargo ship activities (pier length 149.3 meters and dock capacity up to 700 gross tons). In accordance with the National Port Master Plan Road Map, the Indonesian Government will develop the port of Legon Bajak.

The development of the Legon Bajak Port is expected to be visited by ships with a capacity of up to 6,000 GT with a dock to be extended to a total length of 293 m from the initial length of 149.3 m, in addition it is also planned to increase and improve existing dock facilities, namely by adding supporting facilities on land, so that the overall plan for developing Legon Bajak Port is around 5,516.5 m^2. This is expected to support the target of the development plan of the national port of the Republic of Indonesia. But in its development must pay attention to the ecological conditions of the Seawaters, so as not to damage the ecological system of the waters of Karimunjawa. The Indonesian government has determined the territorial waters of Legon Bajak which are included in the conservation area of seaweed ecosystems and coral reef ecosystems protected by law (Karimunjawa National Park 2015).

The plan for port development activities needs to be supplemented by an Environmental Impact Analysis document which is a document for assessing the impact on the ecological system of the Legon Bajak Seawaters (Minister of Environment of the Republic of Indonesia 2013). To evaluate the method of analysing environmental impacts, appropriate environmental parameters are needed to produce good and sustainable studies. One of the bioindicators as parameters of marine ecosystems is the ecosystem of seaweed and coral reefs. Seaweed and coral reef commodities in an area can be used as a measure of the quality of the aquatic environment. The more is variety of seaweed and coral reefs, the better is the quality of the environment. The level of water pollution can change the structure of ecosystems and reduce the number of species in seaweed, coral reefs, plankton, benthos, and nekton communities, which results in reduced diversity (Saif et al. 2012), as well as other parameters such as wave currents, wind speed, and bathymetry can affect the ecological conditions of marine waters.

The diversity of organisms in marine waters can be expressed in species diversity at the observation site, the greater the number of species in the observation location, the better the quality of the environment (Dhruba 2015). The Legok Bajak waters environment belongs to the cate-

gory of tropical coastal environment which is biologically high in biodiversity. However, the development process in the economic and industrial sectors causes a shift in biological degradation which causes a lot of environmental damage. (Skorzeny 2010).

The development and expansion of the Legon Bajak port as a commercial port must be able to minimize the development impact on the surrounding environment, the entry of pollutants causes the marine ecosystem to be degraded and damaged. Therefore, there must be an effort to preserve organisms in the sea. This study is needed to determine the initial conditions in marine ecosystems before the development of Legon Bajak port activities so that they can predict and compare the impacts that will be caused. Research on environmental impact analysis requires a baseline and an overview of the area to be studied. Research with the title of quality of seawaters around Legon Bajak port, Karimunjawa, Indonesia can be used as a general description and basic outline of research on environmental impact analysis. Of course it involves many fields of science for the analysis process.

MATERIALS AND METHODS

The study was conducted on 4 days, from 21 until 25 October 2016. It began with preparation until sampling was conducted. Natural condition at the time of sampling is wind speed 0.45 m/s-1.35 m/s with northwest direction of southeast. The most dominant speed is 0-5 knots as much as 43.03% and the average speed in the dominant direction of 4.9 knots, temperature 33.8-37.2°C with a relative humidity (RH) of 75 %-79 % at the sampling site. Methods of data collection and analysis will examine the quality of seawater and marine biota including seawater quality and coral cover data.

Seawater quality

The types of data collected by seawater quality parameters are physical and chemical parameters. Seawater sampling was taken on the planned dock, port pond and drainage area. Seawater data collection location adjusted to the estimated impact that will occur with the coordinates given in Table 1.

Analysis of seawater quality was adjusted to SNI (Indonesian National Standard) with Atomic Absorption Spectroscopy method (Agilent Technologies 2017 and National Standardization Agency 2017) and according to Water Quality Monitoring - A Practical Guide to the Design and Implementation of a Quality and Freshwater Screening

Table 1: Location of seawaters quality data collection.

No	Sampling Location	Coordinate
1	Station 1	110°28'39.925" E 5°47'14.827" S
2	Station 2	110°28'39.954" E 5°47'22.373" S
3	Station 3	110°28'46.884" E 5°47'18.103" S
4	Station 4	110°28'39.382" E 5°47'16.735" S
5	Station 5	110°28'50.092" E 5°47'20.220" S

(Primary Data 2016)

Table 2: Coordinate of sampling location aquatic biota-coral reefs.

Code	Location	Coordinate	
BK	Transects 1	S 05°47'10.5"	E 110°28'39.3"
	Transects 2	S 05°47'11.3"	E 110°28'39.3"
	Transects 3	S 05°47'12.2"	E 110°28'37.9"
	Transects 4	S 05°47'20.0"	E 110°28'34.1"
	Transects 5	S 05°47'19.0"	E 110°28'33.8"
	Transects 6	S 05°47'18.0"	E 110°28'33.9"
	Transects 7	S 05°47'17.0"	E 110°28'33.7"

Note:

BK-Transect 1: Sampling port Legon Bajak 1, BK- Transect 2: Sampling port: Legon Bajak 2, BK- Transect 3: Sampling Taka Kemujan island, BK- Transect 4: Sampling Sintok island 1, BK- Transect 5: Sampling Sintok island 2, BK- Transect 6: Sampling Cendekia island 1, BK- Transect 7: Sampling Cendekia island 2

Study Program with Atomic Absorption Spectrophotometry (Jamie & Richard 1996). The result of seawater quality analysis was analysed by comparing it with seawater quality standard, referring to Decree of State Minister of Environment Number 51 Year 2004 regarding Quality Standard of Seawater (Ministry of Environment 2004).

Aquatic Biota: Coral Reefs

The data collected is in the form of percentage of coral cover. The location of collecting marine biota data was carried out at 7 points representing the port pool, shipping lane, Kemujan island, Sintok island and Cendekia island. Data collection method is with the modification of underwater photo transports and transect methods (Kaur & Kansal 2017). In principle, this method involves two main activities of coral reef photography and transect image processing. Determination of coordinate samples with GPS research objectives by pulling 50 m transect lines parallel to the shoreline at 3-7 m depth and taking quadrant transect images every 1 m along the transect alternately on the right and left sides of the transect line. The method used to predict impacts is based on the Coral Reef Criteria, Decree of State Minister of Environment Number: 04 Year 2001 (Hill & Wilkinson 2004). Table 2 presents the coordinates of aquatic biota sampling (coral reefs).

Aquatic Biota: Seaweed

The types of data collected were seaweed abundance and cover. The location for collecting aquatic biota data are based on the coordinates given in Table 3.

Table 3: Coordinates of sampling locations of aquatic biota of seaweed.

Location	Coordinate	
Transects 1	S 05°47'10.5"	E 110°28'39.3"
Transects 2	S 05°47'11.3"	E 110°28'39.3"
Transects 3	S 05°47'12.2"	E 110°28'37.9"
Transects 4	S 05°47'20.0"	E 110°28'34.1"
Transects 5	S 05°47'19.0"	E 110°28'33.8"
Transects 6	S 05°47'18.0"	E 110°28'33.9"

Note:

BK-1: Sampling Port Legon Bajak 1, BK-2: Sampling Port Legon Bajak 2, BK-3: Sampling Around the Island of Taka Kemujan, BK-4: Sampling Around the Island Sintok 1, BK-5: Sampling Around the Island Sintok 2, BK-6: Sampling Around the Island Cendekia

The data collection method was used to determine the condition of seaweed. The method is Transect method (Buckland et al. 2007 and State Minister of Environment, 2004). Transect method sampling is a population sample method with a sample plot approach that is on a line drawn across the ecosystem area. Fig. 1 shows the map of sampling locations, for the quality of seawater, seaweed and coral reefs.

RESULTS

Based on observations of aerial photographic field data using the DJI Phantom 3 drone showing the morphological conditions of the Kemujan coast, especially in Legon Bajak, which is dominated by sandy beaches in the coastal

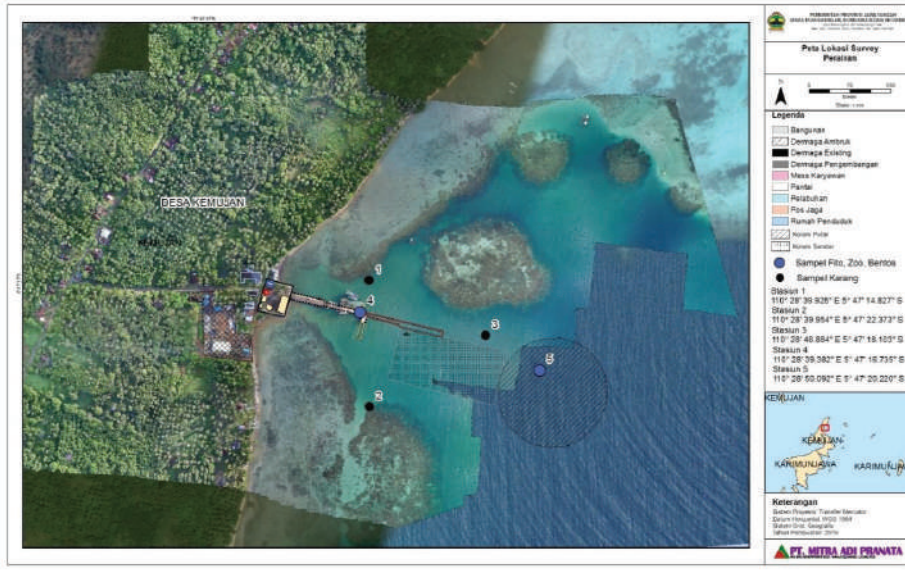

Fig. 1: Map of location of sampling of water quality, seaweed and coral (Primary Data 2017).

region. In the waters there is a coral reef ecosystem with a water base that looks sloping to the bottom of the water (Choat & Pears 2003). Coastal waters are one of the most productive ecosystems in marine waters, while based on the analysis of seawater quality, coral cover and seaweed, show the following data.

Seawater Quality

Data of seawater quality in Legon Bajak waters, based on sampling conducted on October 22, 2016 at 6 stations, at 08.00-12.00 hours with optimum temperature conditions, the sampling temperature is 28°C, with air pressure 765 mmHg, moisture 74.8-78.9%, wind speed 0.42-1.35 m/s, northwest direction of southeast wind. Table 4 gives the results of seawater quality analysis around Legon Bajak port.

Seawater Biota (Seaweed)

Observational data at the sampling site on seaweed were conducted on 23 October 2016 at 6 stations at 09.00-16.00 hours at optimum conditions. Temperature in place of sampling was 27.5°C, with air pressure of 765 mmHg, humidity of 75.5-78.5% and wind speed of 0.45-1.35 m/s with northwest direction to southeast.

Table 4: Seawater quality in Legon Bajak port.

No.	Parameter	Unit	Results analysis						Quality Standards
			AL-1	AL-2	AL-3	AL-4	AL-5	AL-6	
	Physical								
1	Brightness	m	3.3	3.5	3.4	3.2	3.3	3.1	> 3.0 (*)
2	Smell	-	No smell	No smell	No smell	No smell	No smell	No smell	Natural
3	Turbidity	NTU	0.73	0.8	1.07	0.81	0.83	1.05	< 5.0
4	Total Suspended Solid	mg/L	10	6	6	10	8	10	20.0
5	waste	-	Nil	Nil	Nil	Nil	Nil	Nil	Nil (*)
6	Temperature	OC	29.6	29.2	29.5	29.0	29.5	29.3	Natural
7	Oil Coating	-	Nil	Nil	Nil	Nil	Nil	Nil	Nil (*)
	Chemical								
1	pH	-	8.1	8.0	8.1	8.0	8.1	8.1	7.0-8.5
2	Salinity	‰	33.6	33.6	33.6	33.6	33.6	33.6	Natural
3	DO	mg/L	7.17	7.63	7.21	7.56	7.36	7.56	> 5.0
4	BOD_5	mg/L	5.225	4.995	5.226	4.767	5.676	5.145	20.0
5	Ammonia (NH_3-N)	mg/L	0.01	0.011	0.012	0.016	0.011	0.011	0.3
6	Phosphate (PO_4-P)	mg/L	0.002	0.001	0.002	0.003	0.002	0.001	0.015
7	Nitrate (NO_3-N)	mg/L	0.039	0.052	0.058	<0.005	0.056	0.052	0.008
8	Cyanide (CN)	mg/L	0.003	0.001	0.002	0.001	0.003	0.002	0.5
9	Sulphide (H_2S)	mg/L	< 0.002	< 0.002	< 0.002	< 0.002	< 0.002	< 0.002	0.01
10	Phenolic compounds	mg/L	< 0.001	< 0.001	< 0.001	< 0.001	< 0.001	< 0.001	0.002
11	Detergents (MBAS)	mg/L	0.015	0.015	0.018	< 0.010	0.014	0.018	1.0
12	Oil & Fats	mg/L	0.3	0.6	0.4	0.5	0.5	0.3	1.0
13	Mercury (Hg)	mg/L	< 0.001	< 0.001	< 0.001	< 0.001	< 0.001	< 0.001	0.001
14	Chromium (Cr (VI))	mg/L	< 0.001	< 0.001	< 0.001	< 0.001	< 0.001	< 0.001	0.005
15	Arsenic (As)	mg/L	< 0.003	< 0.003	< 0.003	< 0.003	< 0.003	< 0.003	0.012
16	Cadmium (Cd)	mg/L	< 0.001	< 0.001	< 0.001	< 0.001	< 0.001	< 0.001	0.001
17	Copper (Cu)	mg/L	< 0.001	< 0.001	< 0.001	< 0.001	< 0.001	< 0.001	0.008
18	Lead (Pb)	mg/L	< 0.003	< 0.003	< 0.003	< 0.003	< 0.003	< 0.003	0.008
19	Zinc (Zn)	mg/L	< 0.001	< 0.001	< 0.001	< 0.001	< 0.001	< 0.001	0.05
20	Nickel (Ni)	mg/L	< 0.050	< 0.050	< 0.050	< 0.050	< 0.050	< 0.050	0.05

Data Source: Primary data of measurement results in October 2016

Quality Standard *: Regulation of Environment Minister No. 51/2004, Seawater Quality Standards For Marine Biota

Table 5 gives the results of the analysis on the seaweed cover conditions at the research/sampling sites. The results of underwater observations show that there has been damage to the seaweed ecosystem as shown in Fig. 2.

Seawater Biota (Coral Reefs)

Observation data at the sampling site on coral reefs was collected on 23 October 2016 at 7 stations at 09.00-16.00 at the optimum range. Temperature at the Sampling site was 27.5°C, with air pressure of 765 mmHg, humidity 75.5-78.5%, and wind speed of 0.45-1.35 m/s with direction northwest to southeast. Indicator of coral reef damage can be analysed by calculating substrate closure conditions in research sites (Hastuty et al. 2014). Table 6 presents the condition of substrate cover of coral reefs at research sites.

DISCUSSION

Based on data measuring the quality of seawater in Lagon Bajak waters, it is seen that all parameters of research at all the points of measurement location meet the quality standard in accordance with the Regulation of the Minister of Environment No. 51 of 2004 for Marine Biota (Indonesian Government Regulation 1999) except for nitrate has exceeded the quality standard. Nitrate concentrations at all points of measurement, except at high AL-4 sites ranged from 0.039-0.058 mg/L. Nitrates are the chemical compounds needed by organisms as the primary source of nutrition. High levels of nitrates indicate that the Legon Bajak water condition is still quite good and there is no pollution yet. This shows that the Logon Bajak waters are still in good status and not polluted (Patty 2014).

The content of nitrate in Legon-Bajak seawaters comes from the process of degradation of organic materials either from anthropogenic activity or natural processes that occur in the sea. Nitrate is a chemical compound that is required in the process of metabolism of marine organisms, especially the growth of phytoplankton. However, if the nitrate content in excessive in marine waters can cause ecological disturbances by producing harmful algal blooms or eutrophication by algae. Eutrophication process causes oxygen needs to be high because the process of algae metabolism that requires a considerable amount of oxygen. The concentration of nitrate contained in seawater can cause algal bloom if it has a concentration of 200-1000 µg/L. The condition if no monitoring of nitrate in the waters around

Table 5: Types of seaweed and its cover in Legon Bajak waters of Karimunjawa National Park.

Transects	Closed Cover (%)				Total Closed (%)	Community Condition
	Enhalus acoroides	*Cymodocea rotunda*	*Halophila ovalis*	*Thallasia hemprichii*		
1	1.17			2.17	3.34	Damage
2	3.01	4.35	1.17	4.68	13.21	Damage
3	1.71	2.90		4.68	9.29	Damage
4		2.34		1,00	3.34	Damage
5		2.34		1.89	4.23	Damage
6		1.89		2.17	4.06	Damage

Source: Primary data (2016)

Fig. 2: Condition of seaweed ecosystem (*Enhalus acoroides*) in Legon Bajak waters.

Table 6: Substrate closure condition at the study site.

Location	Hard Coral	Soft Coral	Algae	Available Substrate	Mobile Substrate	Other
BK-1	54	0	10	22	12	2
BK-2	54	0	1	40	5	0
BK-3	64	0	1	29	4	2
BK-4	59	0	13	9	19	0
BK-5	57	1	0	42	0	0
BK-6	48	2	2	23	21	4
BK-7	25	1	0	32	40	2

Source Primary Data primer (2016).

Note:

BK-1: Observation Station On Legon Bajak Island 1, BK-2:: Observation Station On Legon Bajak Island 2, BK-3:: Observation station on Taka Kemujan Island BK-4: Observation station on Sintok Island 1, BK-5: Observation station on Sintok 2 Island, BK-6: Observation station on Cendekia 1 Island, BK-7 = Observation station on Cendekia Island 2

the Legon Bajak is done, possible eutrophication problem will occur (Donald Anderson et al. 2002).

The results of the analysis and observation of identified seaweed species show the presence of *Enhalus acoroides, Cymodocea rotunda, Halophila ovalis* and *Thallasia hemprichii. Halophila ovalis* is the most difficult to find, while *Cymodocea rotunda* and *Thallasia hemprichii* are the most common seaweed species found in the sampling sites. The results of the nelum to seaweed cover area showed an average percentage of 29.9%. The functional value of seaweed cover is included in the category of bad status. The higher the functional value of the seaweed cover percentage, the better, and if lower the seaweed cover, it is worse. The condition of seaweed ecosystem in the research location is seen from very low land cover condition that is <10%, indicating broken category with low functional value. No Protected Crops and Species Based on Government Regulation No. 7/1999 on plant and animal species (Indonesian Government Regulation 1999), excluding the IUCN Red Categories List of the IUCN Survival Commission, IUCN, Gland, Switzerland, 1994 (The International Union for Conservation of Nature/IUCN, 1994) and is not found in the list of Convention on Endangered Species of Endangered Species of Flora and Fauna, I, II and III. Geneva, Switzerland (The Convention on International Trade in Endangered Species of Wild Fauna and Flora/CITES, 2012). Further analysis is to look at native species of seaweed as a key species in seaweed habitat, as given in Table 7.

Coral reefs in Legon Bajak were analysed based on the percentage of coral cover conditions. The observation of coral reefs at the stations on the islands of Taka Kemojan and Sintok shows a good enough condition where coral cover is equal to or more than 50%. The observation on the island station Cendekia 1 showed moderate condition with 27% coral cover. Water quality at all the stations strongly supports coral life and coral reef recovery processes, which is demonstrated by the low algal conditions at the sampling sites. The recovery process is also supported by the availability of a substrate that is high enough above 25% (Hill & Wilkinson 2004). Table 8 explains about the genus of coral and wide coral percentage cover in the study area.

The graph in Fig. 3 shows the percentage of the coral coverage area of the observation stations on the island of on Legon Bajak 1-2, Taka Kemojan, P. Sintok 1-2 and P. Cendekia 1-2.

The coral genera found in the study area include *Acropora, Porites, Galaxea, Favia, Favites, Fungia, Isopora, Pachyseris, Montipora, Montastrea, Leptoseris, Goniastrea, Pavona, Stylloporа, Astreopora, Diploastrea* and *Millepora. Acropora* is the dominant genus of the location of the Legon Bajak 2, P.-Cendekia 1 and 2 sampling stations with a percentage of 32%, 8% and 14%. The *Porites* is the dominant genus in Taka Kemojan Station and Pulau Cendekia 1 with percentage of 43% and 8%. Other dominant genus is *Montipora* which has a closing percentage of 33% and 21% in P. Sintok 1 and 2. Other coral genera generally have a low percentage of closure, even some coral genera have very limited distribution in the study area, for example, *Galaxea, Favia, Favites* and *Pavona*. The graph in Fig. 4 shows the percentage of the coral coverage area of the observation station on the island of on Legon Bajak 1-2.

The coral genera found in the Transect Legon Bajak 1 station are *Acropora, Porites, Galaxea, Favites, Fungians, Pachyseris, Montipora, Montastrea* and *Leptoseris*. *Porites* is the most dominant coral genus in this station followed by *Pachyseris* and *Fungia*. *Porites* is coral that is very resistant

Table 7: Results of observation and analysis on the condition of seaweed ecosystem around port area and the status of ecological indigenous organisms.

Ecosystem type	The composition of the species	Status of interest in an ecological entity				Conservation status	
		Key species	Ecological value	Economical value	Scientific value	Indonesia Government Regulation No. 7 of 1999	International Union For Conservation of Nature (IUCN)
Seaweed ecosystem	*Enhalus acoroides, Cymodocea rotunda, Halophila ovalis, Thallasia hemprichii*	Not found	The seaweed cover is on average <10% so the ecological value is very low	The seaweed cover is on average <10% so the ecological value is very low	Seaweed cover is an average of <10% and existing species are the most common species so the scientific value is very low	No vegetation types included in the list of protected plants and species (appendix PP No. 7 of 1999)	*Enhalus acoroides* and *Halophila ovalis* have a low risk status (LC)

Based on the rules of protected fauna and flora, endemic flora and fauna that are key species:

1. Government Regulation No. 7/1999 on the preservation of plant and animal species
2. IUCN Red List Categories. Prepared by the IUCN Species Survival Commission. IUCN, Gland, Switzerland, 1994
3. Convention on the International Trade in Endangered Species of Wild Flora and Fauna Appendise I, II, and III. Geneva, Switzerland, 2012

Table 8: The genera of coral and wide coral percentage cover in the study area.

Genus	Location						
	BK-1	BK-2	BK-3	BK-4	BK-5	BK-6	BK-7
Acropora	2	32	0	22	15	7	12
Porites	27	16	43	3	5	8	9
Galaxea	1	0	0	0	0	0	4
Favia	0	2	0	0	0	0	0
Favites	2	0	0	0	0	0	4
Fungia	6	1	2	0	0	0	0
Isopora	0	0	0	0	12	2	8
Pachyseris	10	1	0	0	0	0	0
Montipora	1	1	0	33	21	5	10
Montastrea	1	0	2	0	0	4	0
Leptoseris	3	0	0	0	0	0	0
Goniastrea	0	0	3	0	2	0	1
Pavona	0	0	3	0	3	0	0
Styllopora	0	0	1	0	0	0	0
Astreopora	0	1	1	0	2	1	0
Diploastrea	0	0	0	0	0	0	1
Millepora	0	0	11	0	0	0	1

Source: Primary Data, 2016

Note:

BK-1: Legon Bajak 1, BK-2: Legon Bajak 2, BK-3: Taka Kemujan, BK-4: Sintok 1, BK-5: Sintok 2, BK-6: Cendekia 1, BK-7: Cendekia 2

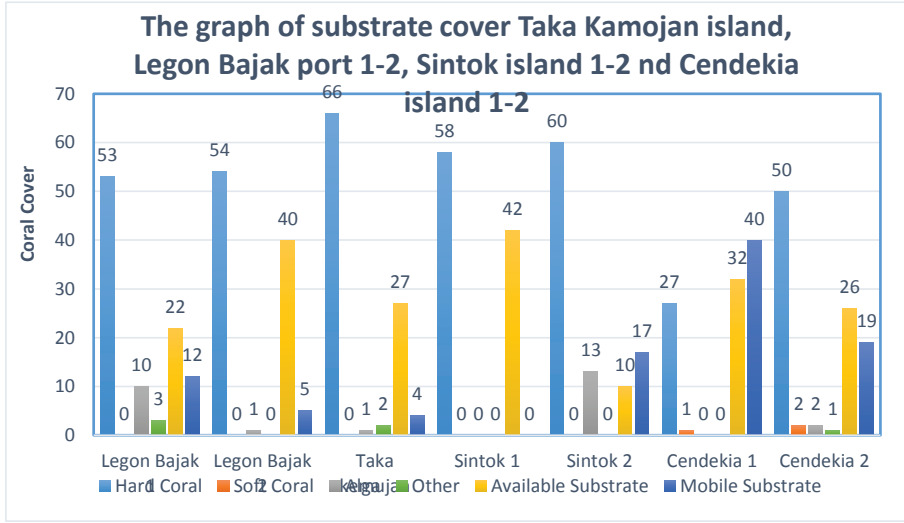

Fig. 3: Percentage of substrate cover on Legon Bajak port 1-2, Taka Kemojan island, P. Sintok island 1-2 and Cendekia island 1-2.

to environmental conditions, so it is very common in the wavy waters, whereas the *Fungia* genus is highly susceptible to strong water movement because this type of coral does not stick to the substrate. Dead coral (DC) is also common in this station with 22% cover. In the coral cover area, the Legon Bajak 2 station is dominated by the genera *Acropora* and *Porites* with a percent cover of 32% and 16%. Other types of corals in this station are *Favia, Fungia, Pachyseris, Montipora* and *Astreopora*. *Acropora* are reefs that are known to be vulnerable to poor environmental conditions but these reefs have the fastest growth rates compared to other coral species. *Porites* are the dominant coral species at the Taka Kemojan island sampling site with a cover of 43%. What is interesting is the existence of *Millepora* which reached 11% in Taka Kemojan station but not found in almost all other stations (Sweatman et al. 2005)

The graph in Fig. 5 shows the percentage of the coral coverage area of the observation station on the island of Taka Kemojan island. Stations on Sintok islands 1 and 2, although close together, have different characteristics. At Sintok island 1 station, coral species found only three species namely *Acropora, Porites* and *Montipora* with a total high cover of 58%. At Cendekia Island station 1, there is no dominant coral although the presence of coral *Acropora* and *Porites* is still higher than *Isopora* and *Montipora*. Similarly at Cendekia island station 2, no coral is very dominant. Corals *Acropora, Porites, Montipora,* and *Isopora* are the highest coral cover species on the station. *Galaxea* and *Favites* corals rarely found on other stations with 4% each cover. Based on the results of identification of coral species and the calculation of the cover, it is known that no coral species in this location, which is the key species, although because based on the average cover value >50% (good condition), the coral reef community is community key. This graph (Fig. 5) shows the percentage of substrate coral cover on observation stations Sintok 1 and 2, while at Cendekia Island 1 and 2 can be seen in the Fig. 6. The graph in Fig. 6 shows the percentage of the coral coverage area of the observation station on the island of Sintok 1 and 2.

The graph in Fig. 7 shows the percentage of the coral coverage area of the observation station on the island of Cendekia 1 and 2.

The varieties of fish and benthic organisms depend on the coral community either directly or indirectly, so that coral changes or communities will significantly bring significant changes to the coral ecosystem community. Coral communities are still a good opportunity which also have a high economic value either directly as a provider of food sources, basic ingredients of drugs, as well as indirectly such as marine tourism. Good coral conditions also have high scientific value as well as a diverse source of germplasm for exploration activities and bioprospecting of biological resources for various purposes (Sweatman et al. 2005).

Based on the conservation status analysis at locations where no species are found and coral reefs are localized as food sources, it is beneficial to the coral reef community. At coral coverage area > 50%, the country has an ecological value and a high value that supports the abundance of fish as a source of food. Coral cover > 50%, despite having high scientific value, has no protected coral reef species based on Government Regulation No. 7/1999 on plant and animal

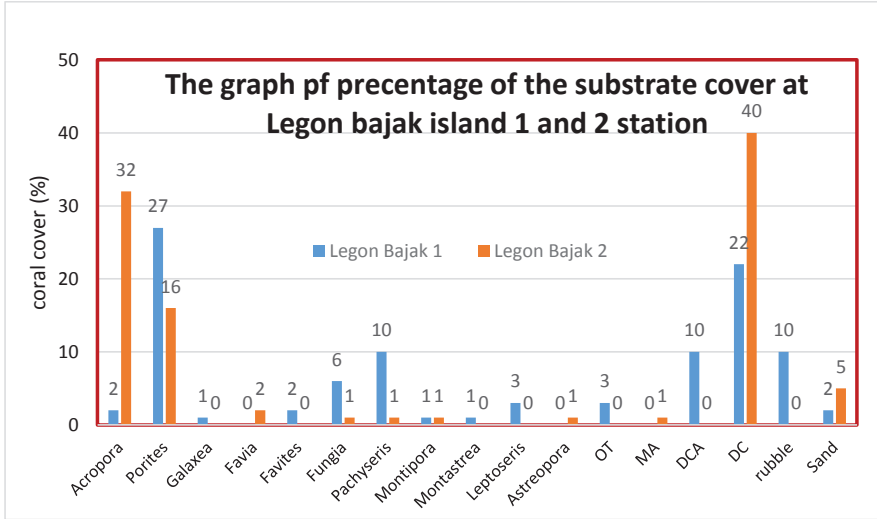

Fig. 4: Percentage of the substrate cover in the observation station Legon Bajak island 1 dan Legon Bajak island 2 (station BK-1 and BK-2).

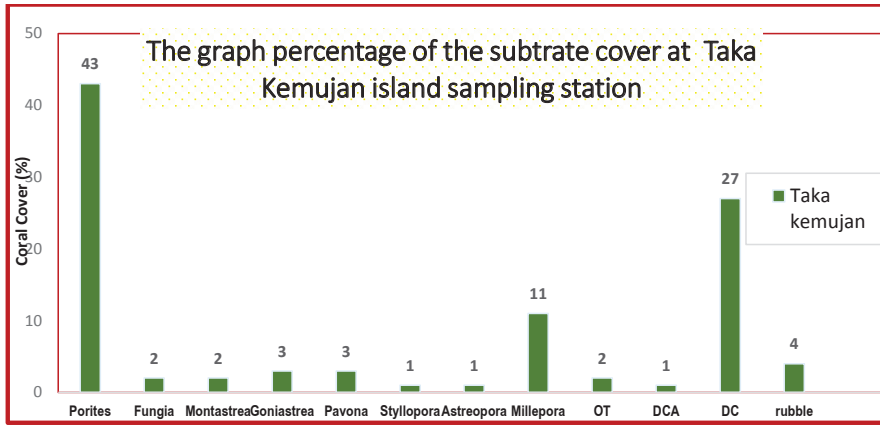

Fig. 5: The percentage of the substrate cover in the observation station Taka Kemojan island.

species (Indonesian Government Regulation 1999), excluding the Red IUCN Category List from the IUCN Survival Commission, IUCN, Gland, Switzerland, 1994 and is not found in the list of species in Endangered Species of Flora and Fauna, I, II and III. Geneva, Switzerland 2012. The status of coral interests in detail is provided in Table 9.

In this research, an analysis of the environmental parameters of the Legon Bajak port as supporting data to complement the research on the assessment of ecological status of the seawater around the Legon Bajak development plan, Karimunjawa.

Wind Speed and Wind Direction

The conditions of wind speed and direction based on secondary data from the Maritime Meteorology Station of Semarang, the Meteorology, Climatology and Geophysics Agency show that the dull waters have wind speed and wind direction in the period 2010 to 2015 as given in Table 10.

The dominant wind direction is from the east, which is as much as 31%, the second dominant direction from the northwest is 17.2%. The most dominant speed is 2-4 knots as much as 27.6% and the average speed in the dominant direction is 4 knots.

Fig. 8 shows windrose data and dominant wind direction data and average speed. Table 11 gives the data of dominant wind direction and average speed for 2005-2015 in the area around the research area.

The conditions of wind speed and wind direction are very influential on tidal patterns and surface currents. Strong wind speed and heavy rain also caused changes in

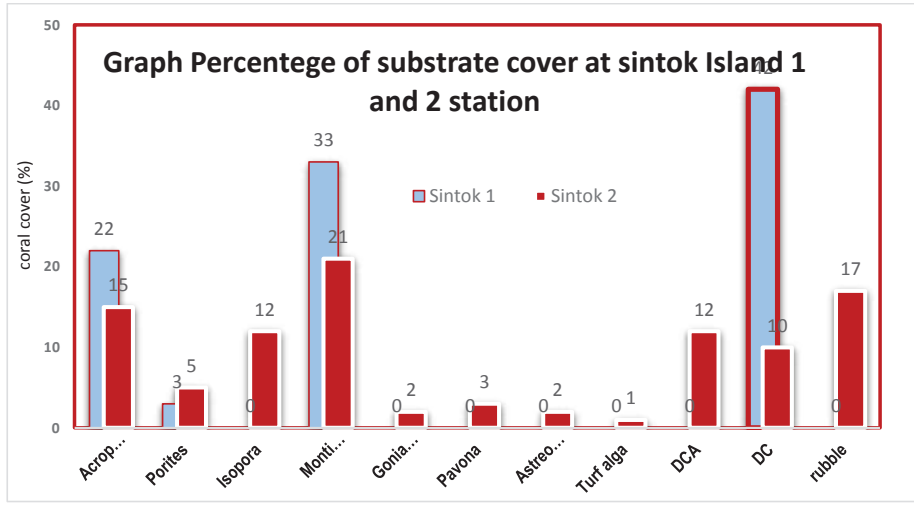

Fig. 6: The percentage of substrate cover at Sintok island 1 and 2 stations.

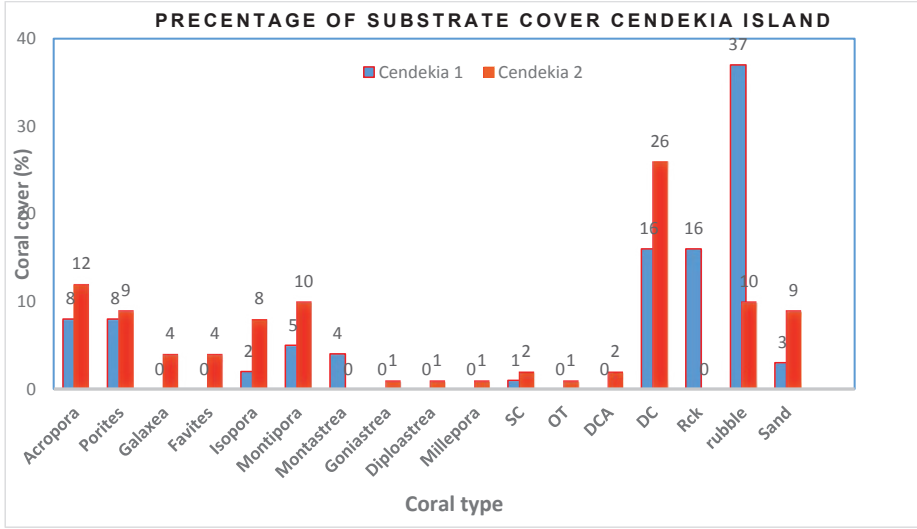

Fig. 7: Percentage of substrate cover at stations Cendekia island 1 and 2.

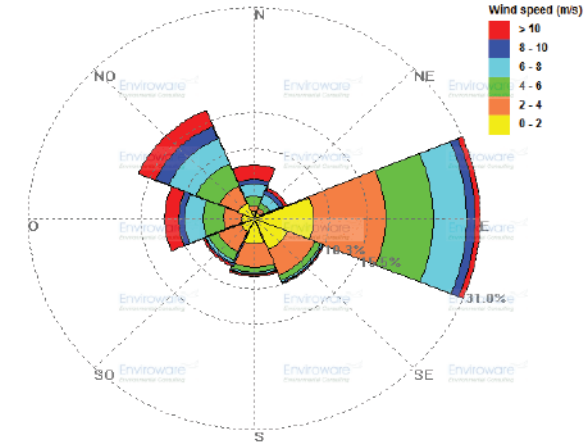

Fig. 8: Windrose data for Legon Bajak waters in 2005-2015.

Table 9: Condition of coral ecosystems in the area of the port based on the analysis of the extent of coral cover and the type of protected flora/fauna.

Ecosystem Type	Composition of Species	Status of Interest in Ecological Indigenous				Conservation Status	
		Key Species	Ecological Value	Economic Value	Scientific Value	Government Regulations N0 7, 1999	IUCN
Coral ecosystem	Reef Acropora Porites Galaxea Favia Favites Fungia Isopora Pachyseris Montipora Montastrea Leptoseris Goniastrea Pavona Styllopora Astreopora Diploastrea Millepora	It is difficult for species to determine key species but is a key community for many reef fish and other species whose lives depend on the coral community	Coral cover> 50% so it has high ecological value	Coral cover> 50% so it has a high economic value because it supports the abundance of reef fish which is partly a type of consumption	Coral cover> 50% so it has a high scientific value	No coral species were included in the list of Protected Plant and Species (appendix PP No. 7 of 1999)	The exact status can not yet be determined but many members of this coral genus encountered a red list with various statuses.

Source: Primary data, 2016

Table 10: Dominant Wind Average Speed Data for 2005-2016.

Speed (Knots)	Amount of Wind	Speed Data (%)
0 – 2	1820	25.117
2 – 4	2002	27.629
4 – 6	1307	18.038
6 – 8	1122	15.484
8 – 10	395	5.451
>10	600	8.280
Jumlah	7246	100 %

Data source: Maritime Meteorology Station, Semarang, 2016

Table 11: Dominant wind direction data and average speed for 2005-2015.

Direction	Dominant Wind Direction (%)	Average Direction Speed (Knots)
North	7.853	7.445
Northeast	4.885	6.085
East	31.024	4.425
Southeast	10.406	3.001
South	8.529	3.316
Southwest	7.673	4.067
West	12.421	6.300
Northwest	17.210	6.518

Data source: Maritime Meteorology Station, Semarang, 2016

tidal patterns and ocean currents. So changes in oceanographic parameters in these shallow waters have triggered an increase in sedimentation due to the occurrence of nearshore breaking waves and increased longshore current flows, thus further decreasing the quality of the coastal marine environment resulting in damage to coral reefs and seaweed conditions. This can make the condition of the status of coral reefs and seaweed worse (Anand Kumar Varma 2013).

Hydrooceanography

Legon Bajak waters are located in the Java seawaters which have relatively calm characteristics, can be seen from the dynamics of tides, currents, waves and morphology.

Tides

Based on the results of tidal measurements in the waters of Legon Bajak in March 2017, it shows that tides in the Legonbajak waters are diurnal tidal types where the Formzhal value is 3.03 (F > 3). Single (diurnal) daily tides have a tidal period of 24 hours 50 minutes, so that one day there is one tide and one time low tide. Tidal charts on the Legon Bajak waters, Karimunjawa are presented in Fig. 9 (Parker 2007).

***Seawaters Flow Pattern*:** Field investigations include current velocity measurements and current directions carried out from 1 to 4 April 2017 at Legon Bajak, Karimunjawa (Table 12).

Sea Wave

Based on the results of processing, the ADCP station data presented in Figs. 3-4, the following can be concluded.

The current velocity varies with the average speed in all water columns ranging from 1.71-3.1 cm/s, the minimum current speed is 0.0-0.1 cm/s, and the maximum current speed is 5.8-27.2 cm/s, with the smallest current velocity evenly at each depth (0.0-10.0 meters) and the largest current velocity in cell depth 1 (8.0-10.0 meters) (Fig. 10).

The largest current velocity at average depth is 6.8 cm/s with an average speed of 2.1 cm/s. Current speed in each cell depth can be seen in Fig. 11.

From the results of the analysis of current observation data using current rose, it can be concluded that a number of things are:

(a) The direction of the dominant current is towards the southeast to the north.
(b) The direction of the dominant current at the average depth is to the southeast and south with the frequency of occurrences of 14.75% and 13.82%. The dominant current velocity is > 0-10 cm/s with an event frequency of 100%.

The maximum speed that occurs is> 0 cm / s - 10 cm / s with an event frequency of 100%. The dominant direction at the cell-cell depth can be seen in Fig. 12. The distribution of the depth of the current average from 1 April 2017 to 4 April 2017 are given in Table 13.

Based on the results of the processing of observational flow data April 1, 2017 - April 4, 2017 at an average depth in the form of a scatter the plot addressing the direction of the current is almost in all directions with the dominant movement towards the southeast to the north, the current movement occurs at all depths. It can be concluded that the current velocity and direction are dominated by tidal factors and at the surface depth or cell 5 (0.0-2.0 meters) influenced by non tidal factors, one of which is wind. Based on current modelling data using numerical modules on the condition of moving current tide averages from north to south, while at low tide the current moves from south to north (Sofian 2010).

Wave Pattern

High Raw Data and Wave Period

Based on the results of ADCP station data processing presented in Figs. 13, following can be concluded.

(a) The maximum wave height that occurs is 13.8 cm with a period of 5.1 seconds on the second day measurement or April 2, 2017.

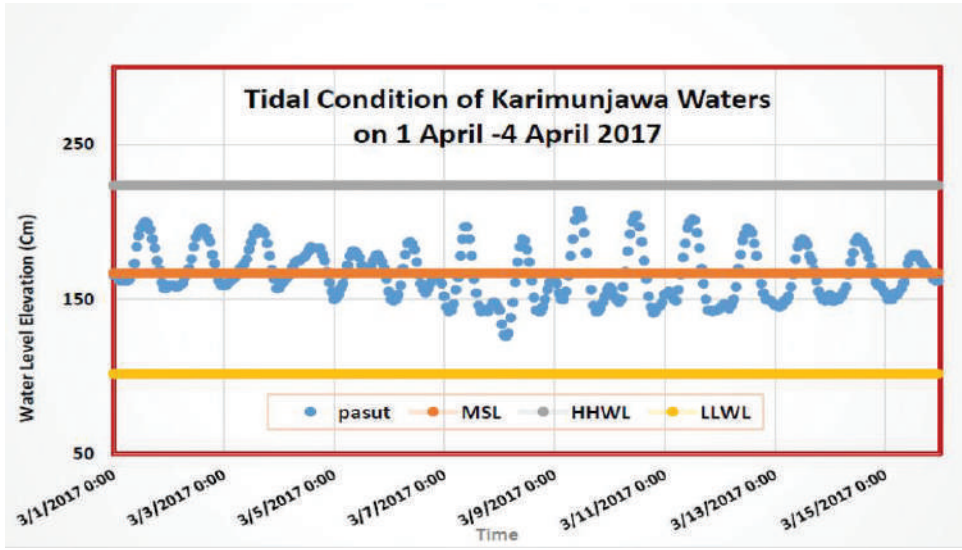

Fig. 9: Sea level elevation in Karimunjawa region (Realtime Data Geospatial Information Agency, 2017).

Table 12: Type and location of measurement: speed, current direction, wave height and wave period in Legon Bajak Waters, Karimunjawa.

Station	Coordinate	Location	Activity
Acoustic Doppler Current Profiler (ADCP)	S 05°47'15.5" E 100°28'54.3"	Marine waters	Measurement of speed, current direction, wave height and wave period with ADCP, is carried out for 3×24 hours.

(b) The wave height that occurred during the measurement was carried out in the range of 2.3-13.8 cm.
(c) The wave period that occurs during measurements is carried out in the range of 4.2 seconds to 5.5 seconds.
(d) The maximum wave period that occurs is 5.5 seconds with a wave height of 12.4 cm on the measurement of the fourth day or April 3, 2017.

The results of wave analysis based on wind data from the Meteorology and Geophysics Agency, Semarang in 2005-2014 in the Legon Bajak waters region were relatively low with a maximum of 50 annual waves around the pier reaching 1.50 m, it is estimated that ships can dock throughout the year. Whereas from waverose, waves occurring around Karimunjawa Port more than 0.50 m are estimated for 5 days in August, 4 days in May, June, September while other months are less than that. This regulation needs to be made appropriate if the development of Legonbajak port is in the construction and post-contraction stages because it can significantly affect the ecological conditions of the coast, especially the conditions of coral reefs and seaweed.

Beach Morphology

Based on the results of observations of visual field data using aerial photographs of the DJI Phantom 3 beach type Kemujan island, especially in LegonBajak, it is dominated by sandy beach in the foreshore area. Furthermore, in the

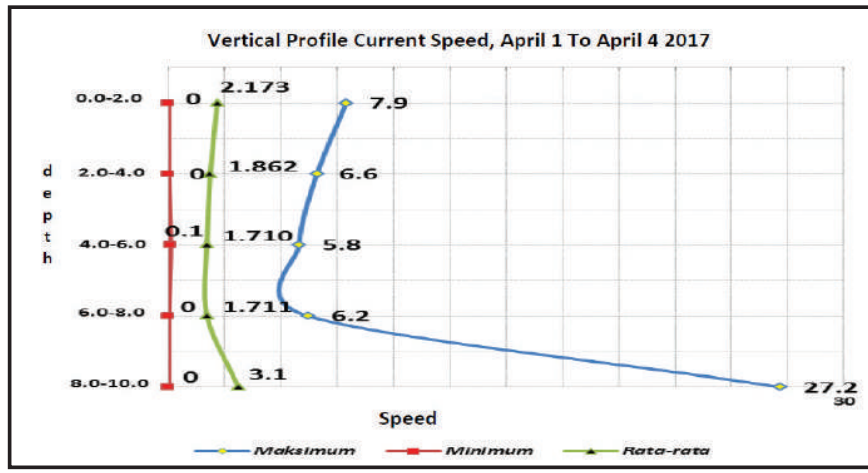

Fig. 10: Vertical profile maximum, minimum and average current speed, April 1, 2017-April 4, 2017.

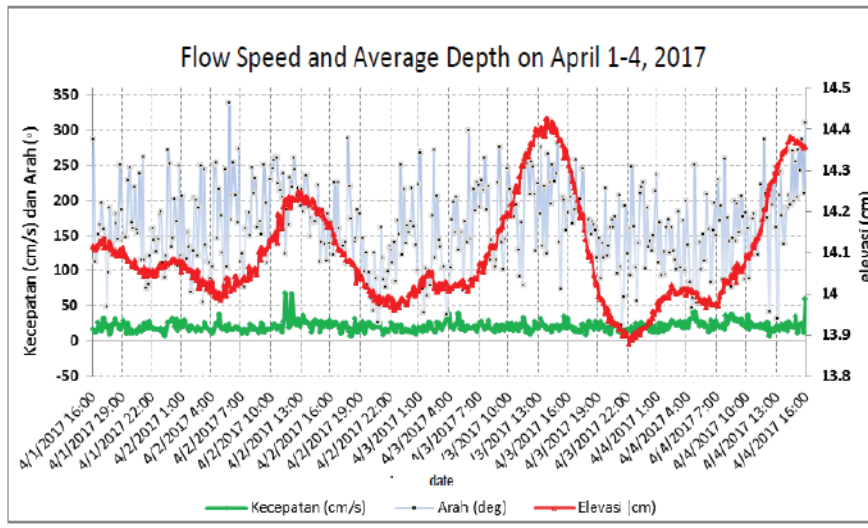

Fig. 11: Average depth current speed, April 1, 2017-April 4, 2017.

backshore area or behind the stretch of sand, the land cover is in the form of trees. In waters there is a coral reef ecosystem with a bottom of the water that looks sloping based on the depth contours resulting from bathymetry analysis (Wolanski & Elliott 2015). The coastline can change with the development of the famous Legonbajak port at the operational stage (post construction) and affect the ecological conditions of the coast. Fig. 14 shows the coastline of the waters around the port of Legonbajak (Karimunjawa waters).

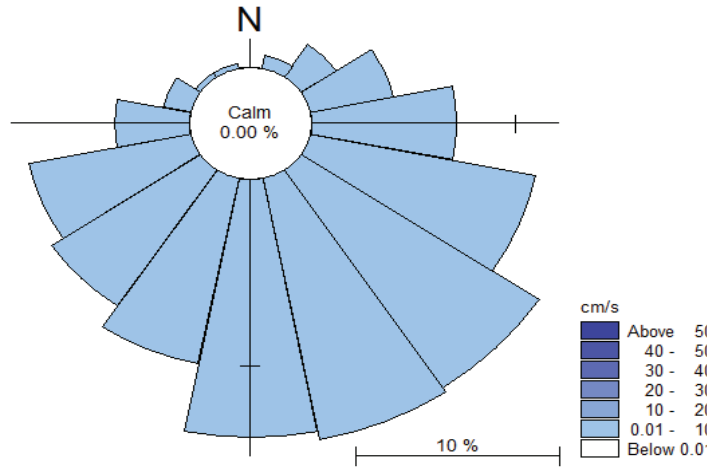

Fig. 12: Current rose depth average April 1, 2017-April 4, 2017.

Table 13: Average depth current velocity distribution April 1, 2017 - April 4, 2017.

Frequency of Current Flow in Percent (%)										
Direction		Flow Speed (cm/det)								Jumlah
		Calm	>0-10	>10-20	>20-30	>30-40	>40-50	>50-60	>60	
-		0.00	0.00	0.00	0.00	0.00	0.00	0.00	0.00	0.00
0	U	0.00	0.00	0.00	0.00	0.00	0.00	0.00	0.00	0.00
22.5	UTL	0.00	0.69	0.00	0.00	0.00	0.00	0.00	0.00	0.69
45	TL	0.00	2.07	0.00	0.00	0.00	0.00	0.00	0.00	2.07
67.5	TLT	0.00	4.15	0.00	0.00	0.00	0.00	0.00	0.00	4.15
90	T	0.00	7.14	0.00	0.00	0.00	0.00	0.00	0.00	7.14
112.5	TTg	0.00	11.06	0.00	0.00	0.00	0.00	0.00	0.00	11.06
135	Tg	0.00	14.75	0.00	0.00	0.00	0.00	0.00	0.00	14.75
157.5	TgS	0.00	13.82	0.00	0.00	0.00	0.00	0.00	0.00	13.82
180	S	0.00	13.82	0.00	0.00	0.00	0.00	0.00	0.00	13.82
202.5	SBD	0.00	10.14	0.00	0.00	0.00	0.00	0.00	0.00	10.14
225	BD	0.00	8.99	0.00	0.00	0.00	0.00	0.00	0.00	8.99
247.5	BDB	0.00	7.83	0.00	0.00	0.00	0.00	0.00	0.00	7.83
270	B	0.00	3.92	0.00	0.00	0.00	0.00	0.00	0.00	3.92
292.5	BBL	0.00	1.15	0.00	0.00	0.00	0.00	0.00	0.00	1.15
315	BL	0.00	0.23	0.00	0.00	0.00	0.00	0.00	0.00	0.23
337.5	BLU	0.00	0.23	0.00	0.00	0.00	0.00	0.00	0.00	0.23
Total		0.00	100	0.00	0.00	0.00	0.00	0.00	0.00	100
Kumulatif		0.00	100	100	100	100	100	100	100	100

Prediction of Coastline Changes in the Baseline Condition of the Initial Environment around the Port of LegonBajak

Based on the observations of visual field data using aerial photography from the DJI Phantom 3, the type of Kemujan island beach, especially in Legon Bajak, it is dominated by sandy beaches in the foreshore area. Furthermore, in the coastal area or behind a stretch of sand, land cover is in the form of trees. In the waters, there is a coral reef ecosystem with a water base that looks sloping based on the contour of the depth of the results of the sound of bathymetry. Prediction of coastline changes in the basic conditions of environmental conditions initially around the port of Legon Bajak which existed prior to development in 2016 compared to the environmental conditions in 2003, a coastline shift had occurred, predicted to be largely due to activities in the surrounding community, which would be even worse with the planned development of Legon Bajak port. Therefore, it is necessary to have a comprehensive environmental impact analysis and regulation among stakeholders who have an interest in government, society, investors and the private sector to prevent a broader coastline from causing disruption to the marine ecosystem. Fig. 15 shows that there has been a change in the coastline, as revealed by the comparison of the monitor lines in 2013 and 2016.

Based on Fig. 14, it can be said that in the northern part of the port of Legon Bajak from 2003 to 2016 the coastline accretion was 13 m (or 1 m/year). To the south of the port of Legon Bajak from 2003 to 2016, there was an 8 m (0.6 m/year) coastline abrasion.

It is estimated that the next 5 years accretion that occurs in the northern part of the port is 5 m, while to the south the port of Legon Bajak will experience an abrasion of 3 m. The creation and abrasion that occur do not cause interference to the buildings on the beach (Parker 2007).

Based on the description above, the environmental conditions without this project are categorized as poor. The construction of the pier with erection will affect the changes in the bathymetry of current and wave patterns in the waters around the port area. The changes in current and wave patterns will result in changes in sedimentation patterns that can lead to abrasion and creation (changes in shoreline), given the structure of the jetty which is protruding towards the sea, but the changes that occur are not due to the extension of the existing dock. Based on the description above, the environmental conditions with the next 5 years project remain the same as the coastline conditions for the next 5 years without projects, so that these environmental conditions are categorized as poor.

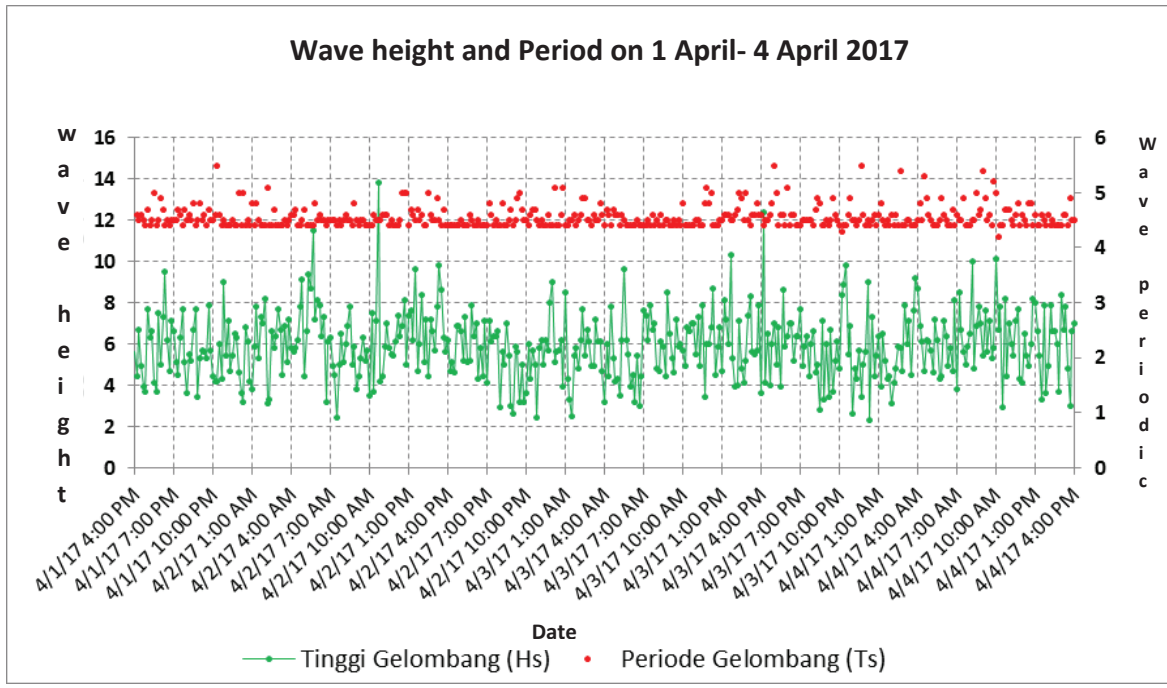

Fig. 13: Height and wave period, April 1, 2017-April 4, 2017.

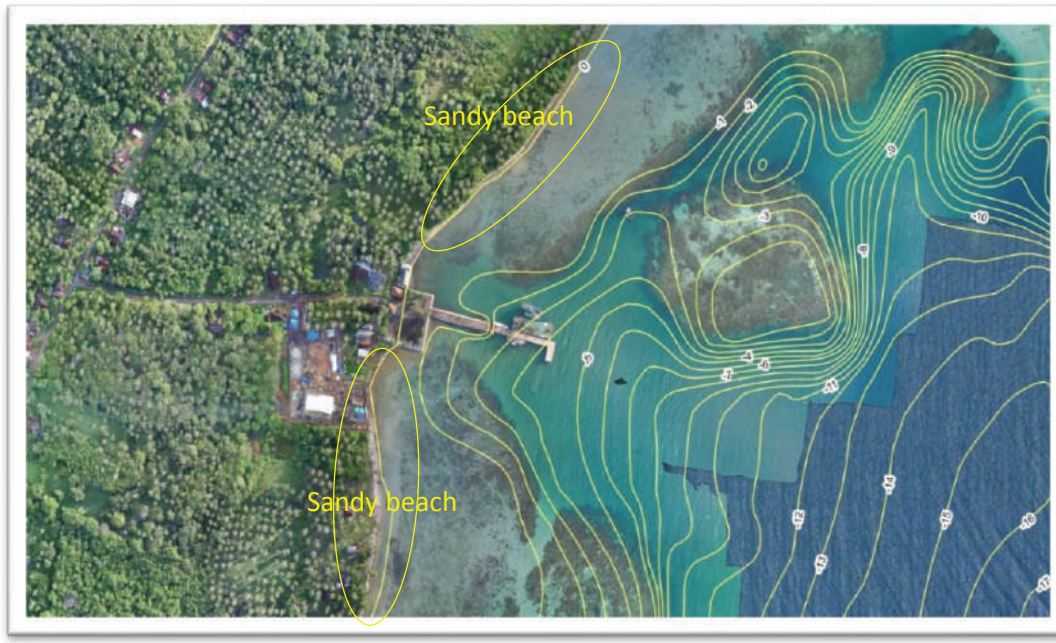

Fig. 14: Visual aerial photograph of Legon Bajak Port.

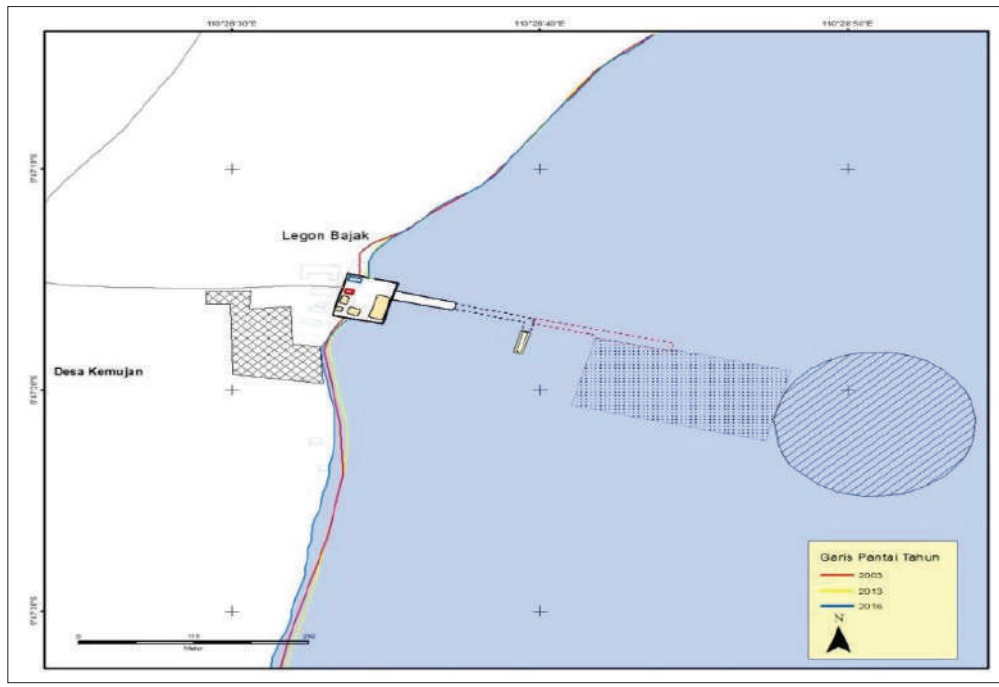

Fig. 15: Coastline conditions in 2003 and 2016.

SIGNIFICANT STATEMENTS

This study is a study of seawater quality in terms of diversity of seaweed and krang reefs. The study also examined the conditions of environmental parameters, including current, wave, climate, and bathymetry data at the study site. The purpose of this study was to find out the initial description as the basis for the ecological status of the Legon Bajak waters. The results of this study indicate that the quality of seawater is in good condition but the condition of the diversity of seaweed and coral reefs is in damaged condition, as well as environmental parameters such as currents, coastlines, bathymetry and ocean waves make it possible to increase environmental damage. Legon Bajak Port is included in the Karimunjawa water park conservation area, therefore the development and expansion of the Legon Bajak port that will be carried out by Rembang Regency must be carried out comprehensively and refer to the results of this study so that the development and expansion of port Legon Bajak will not damage sea conditions and remain sustainable.

CONCLUSION

The quality of the Legon Bajak seawater port is based on an analysis of seawater quality data that is still in good category, but if analysed based on the seaweed and coral diversity, diversity index that has been included in the damaged ecosystem category, the secondary data parameters include atus, wave and raus the sea, the coastline needs special attention from the authority of Karimunjawa National Marine Park, the local government of Rembang district, central Java Province and the Environment Ministry of the Republic of Indonesia because the Legon Bajak port includes the Karimunjawa National Marine Park Conservation Area.

ACKNOWLEDGEMENTS

This research is a study of quality and biological aspects of Environmental Impact Analysis of MAP- Environmental Consultant in cooperation with the Office of Communications and Information of Central Java Province No. 003/ MAP/BA/VIII/2016 Dated 13/08/2016 as the basis of implementation. The author is very grateful to the leaders of The Department of Transportation, Communication and Informatics, Central Java so that this research could run well. The author is also grateful to Mrs. Ir. Indah Noor Alita as the coordinator of the project, P.T. Mitra Adhi Pranata and Mr. Basyar as research assistant.

REFERENCES

Abdulrahman, E., Syaefudin, Y., Ginting, H., Mardiyanto, A., Matex, Saputra, W.B., Sukir; Abidin, Z. and Cahyadi, M.N. 2003. Survey monitoring coral reefs and installation of permanent plots. Karimunjawa National Park Hall. Semarang.

Agilent Technologies 2017. Flame atomic absorption spectrometry, Agilent Technologies Australia (M) Pty, Ltd. 679 Springvale Road Mulgrave, Victoria, Australia.

American Public Health Association 1992. Standard Methods for the Examination of Water and Wastewater, 18th edition. American Public Health Association. Washington.

Buckland, S.T., Borchers, D.L., Johnston, A., Henrys, P.A. and Marques, T.A. 2007. Line transect methods for plant surveys. Biometrics, 63(4): 989-998.

Choat, H. and Pears, R. 2003. A rapid, quantitative survey method for large, vulnerable reef fishes. In: Wilkinson, C., Green, A., Almany, J., and Dionne, S. (Eds.), Monitoring Coral Reef Marine Protected Areas. A Practical Guide on How Monitoring can Support Effective Management of MPAs. Australian Institute of Marine Science and the IUCN Marine Program Publication, pp. 68.

Convention on International Trade in Endangered Species of Wild Fauna and Flora (CITES) 2012. Convention on the International Trade in Endangered Species of Wild Flora and Fauna Appendices I, II and III. Geneva, Switzerland.

Decree of State Minister of Environment 2001. Regulation of the Minister of Environment of Indonesia number 04 2001. About criteria of raw damage of coral reef. Jakarta, Indonesia.

Decree of State Minister of Environment 2004. Regulation of the Minister of Environment of Indonesia number 200, 2004. Regarding criteria of damage raw and guidelines for seagrass status determination.

Decree of State Minister of Environment, 2004. Regulation of the Minister of the Environment Number 200 Year 2004 about regarding Criteria of Damage Raw and Guidelines for Seagrass Status Determination. Office of the Indonesian Ministry of Environment. Jakarta, Indonesia.

Donald, M. Anderson, Patricia M. Glibert and Joann M. Burkholder 2002. Harmful algal blooms and eutrophication: Nutrient sources, composition, and consequences estuaries. 25(4b): 704-726.

Hastuty, R. and Yonvitner, A.L. 2014. Coral cover and composition of reef fishes inside and outside of marine protected areas, eastern coast of Weh Island, Sabang. Depik, 3: 99-107.

Hill, J. and and Wilkinson, C. 2004. Methods for ecological monitoring of coral reefs: A resource for managers. Version 1. Australian Institute of Marine Science (AIMS), Australia.

Indonesian Government Regulation 1999. Government Regulation No. 7/1999 on the Preservation of Plant and Animal Species, Jakarta.

International Union for Conservation of Nature 1994. IUCN Red List Categories. Prepared by the IUCN Species Survival Commission, IUCN, Gland, Switzerland.

Jamie, B. and Richard, B. 1996. Water Quality Monitoring- A Practical Guide to the Design and Implementation of Freshwater Quality Studies and Monitoring Programmes. Published on behalf of United Nations Environment Programme and the World Health Organization © 1996 UNEP/WHO.

Karimunjawa National Park 2015. Statistics of Karimunjawa National Park 2015, Ministry of Environment and Forestry, Directorate General of Natural Resources Conservation and Ecosystem, Karimunjawa National Park Office, pp. 153.

Karimunjawa National Park Office 2004. Zoning of Karimunjawa National Park, Jepara Regency, Central Java Province, Ministry of Forestry, Directorate General of Forest Protection and Nature Conservation, Semarang.

Kaur, K. and Kansal, R. 2017. Review of approaches under water image enhancement. International Journal of Advance Research, Ideas and Innovations in Technology, 3(3): 493-496.

Leo, H. Holthuijsen 2007. Waves in Oceanic and Coastal Waters Delft University of Technology and Unesco-Ihe. Cambridge University Press the Edinburgh Building, Cambridge CB2 8RU, UK.

National Standardization Agency 2017. SNI 6964.8: 2015 Seawater Quality - Part 8: Seawater Sampling Method. Building I BPPT, floor 9-14. Jl. M.H Thamrin No. 8 Kebon Sirih - Central Jakarta 10340-Indonesia.

Negara, S.D. and Basu, D.S. 2017. Challenges for Indonesia to achieve its maritime connectivity plan and leverage on regional initiatives. Yusof Ishak Institute Analyse Current.

Parker, B.B. 2007. Tidal analysis and prediction. US Department of Commerce, National Oceanic and Atmospheric Administration, National Ocean Service. Center for Operational Oceanographic Products and Services.

Parmita, S. and Dhruba, D. 2015. Application of Shannon's index to study diversity with reference to census data of Assam. Asian Journal of Management Research, 5(4): 620-628.

Saif, Z.N., Madan, K. Oli and Raymond, R.C. 2012. Line transects by design: The influence of study design, spatial distribution and density of objects on estimates of abundance. The Open Ecology Journal, 5: 25-44.

Simon, I. Patty, 2014. Characteristics of phosphate, nitrate and dissolved oxygen in Gangga and Siladen Island Waters, North Sulawesi. Platax Scientific Journal, 2(2): 74-84.

Sofian, I. 2010. Scientific basis: Analysis and projection of sea level rise and extreme weather event. Indonesia Climate Change Sectorial Roadmap-ICCSR. National Planning and Development Agency (BAPPENAS), Jakarta, Indonesia.

Sweatman, H., Burgess, S., Cheal, A.J., Coleman, G., Delean, J.S.C., Emslie, M.J., Miller, I., Osborne, K., McDonald, A.J. and Thompson, A. 2005. Long-term monitoring of the Great Barrier Reef. Australian Institute of Marine Science.

The Minister of Environment of Republic of Indonesia 2012. Regulation of the Minister of Environmental State Secretary of the Republic of Indonesia Number 16-2012 regarding Regulation of the Minister of living environment on the guidelines for document preparation living environment. Jakarta.

The Minister of Environment of Republic of Indonesia 2013. Regulation of the Minister of Environment of Republic of Indonesia Number 08-2013, about Governance and Inspection of Environmental Documents and Issuance of Environmental Permit, Jakarta

The Ministry of Environment 2004. Decree of State Minister of Environment Number 51 Year 2004. Concerning water quality standard of Seawater. Jakarta, Indonesia

Varma, S. Anand Kumar, M. Srimurali, and S. Vijaya Kumar Varma 2013. Evolution of wind rose diagrams for RTPP, KADAPA, A.P., India. International Journal of Innovative Research & Development, 2(13): 150-154.

Wolanski, E. and Elliott, M. 2015. Estuarine Ecohydrology: An Introduction. Elsevier.

Nature Environment and Pollution Technology
An International Quarterly Scientific Journal

p-ISSN: 0972-6268
e-ISSN: 2395-3454

Vol. 18 | No. 4 | pp. 1447-1453 | 2019

Original Research Paper | Open Access

Policy Study on Adjustments to Electric Power Prices for China's Air Pollution Abatement

Kun Xiao*(**) and Jingdong Zhang*(**)†
*Research Center of Environment and Health, Zhongnan University of Economics and Law, Wuhan 430000, China
**School of Business Administration, Zhongnan University of Economics and Law, Wuhan 430000, China
†Corresponding author: Jingdong Zhang

Nat. Env. & Poll. Tech.
Website: www.neptjournal.com

Received: 18-09-2019
Accepted: 20-10-2019

Key Words:
CGE model
Air pollution
Electricity substitution
Electric power price
Pollution abatement

ABSTRACT

In the past decade, the deterioration in atmospheric quality caused by emissions of ambient particulate matter with an aerodynamic diameter of less than 2.5 μm (PM2.5) has become an urgent problem in China. As this problem can be mainly attributed to the large amount of coal consumption, a strategy to promote electric power substitution was initiated, and in this case, cutting the price of electricity is considered useful. However, since it was announced that the price of electric power used in the service industry will be reduced by 10%, the proper target to cut the price of electric power used in the secondary industry was under debate. By using the computable general equilibrium (CGE) model, the policy to cut the price of electric power used in the secondary industry was simulated and the effects of the policy on the economy and the environment were explored. The results show that the policy to cut electric power prices will contribute to promoting the strategy of electricity substitution, and further contribute to environmental improvement. This policy can result in positive effects on the systems of the economy and the environment at the same time, and when the target to cut the price of electric power used in the secondary industry is –3%, the maximum positive effects will be obtained: gross domestic product (GDP) growth will be accelerated by 0.015‰, while $PM_{2.5}$ emissions will be abated by 394.2 tons. Moreover, based on the unique cross-subsidy mechanism in China's electric power industry, although residents' consumption welfare can be fully compensated, less cross-subsidy will have a negative effect on the agriculture industry.

INTRODUCTION

In the past decade, China was suffering from the serious problem of air pollution. Especially, the ambient particulate matter with an aerodynamic diameter of less than 2.5 μm ($PM_{2.5}$) has led to frequent hazy weather. According to the Annual Report of Environmental Statistics in China, 2014, the amount of dust particles (including $PM_{2.5}$) emitted into the atmosphere was 17.408 million tons. According to China's Air Quality Report, in March 2018, the average $PM_{2.5}$ concentration in China's 10 main cities was approximately 5.5-7.3 times higher than the World Health Organization (WHO) safety standards (15 μg/m^3). Therefore, improving the air quality in China is an urgent issue.

It is already acknowledged that, the cause of $PM_{2.5}$ emissions in China can be mostly attributed to the high percentage taken by coal at the final consumption of energy (Zhu 2016). In this case, the Chinese government promoted a strategy of electricity substitution at the final consumption of energy. This strategy is expected to reduce $PM_{2.5}$ emission.

In order to encourage electric power consumption, the Chinese government further started to intervene and adjust the consumption prices of electricity. Experiments to cut the electricity prices for the uses in secondary industries has been attempted in a number of provinces, and in 2018, the Chinese prime minister Keqiang Li put forward a policy to cut the electricity price in the service industry by 10%.

However, the existing cross-subsidization mechanism in the electricity consumption price complicates the situation. As the secondary and service industries provide electricity consumption subsidies to residents and the agriculture, the policies to cut electricity prices may finally harm residents' consumption welfare. In addition, it is also worth discussing whether electricity substitution will lead to a positive environmental effect. In China, as more than 60% of electricity is generated by coal-fired power, and electricity substitution will increase the electricity demand, it may also result in increased coal consumption, because more coal would be needed for electricity generation.

Therefore, a comprehensive judgment is needed in making a proper policy for air pollution abatement. This study focuses on the two issues of whether the strategy of electricity substitution will promote environmental quality, and what is the proper policy for the strategy of electricity substitution.

STATE OF ART

Energy is the driving force of human civilization (Zhang

2013). The relationship between energy and economy was not confirmed until the empirical study made by Kraft et al. (1978). In later decades, this relationship was discussed in a number of other countries. Some scholars consider it bidirectional (Akkemik et al. 2012, Liddle et al. 2015), while others consider not (Dergiades et al. 2013, Hamit 2012), but the bidirectional relationship exists in China (Lu 2017).

The dualistic relationship was developed in the 1990s, when the environmental issue was taken into consideration. Nordhaus et al. (1996) were the pioneers, and the famous inverted U-shaped environmental Kuznets curve became the theoretical foundation for further studies (Wang et al. 2015). Based on these studies, the energy–economy–environment integrated (3E-integrated) system was constructed. This is an interrelated system in which energy policy will affect the three systems directly (Vera et al. 2007, Lu et al. 2017).

As the current serious problem of haze pollution in China is caused by energy consumption, some scholars have begun to analyse it and call for the strategy of electricity power substitution (Xu et al. 2017). Undoubtedly, if the policy is implemented, it will have an impact on the economy and lead to environmental effects. Meanwhile, it was found that a unique industrial mechanism, the cross-subsidy mechanism in electricity prices, may be used as an effective tool in electricity policy-making for positive economic and environmental effects (Qiao et al. 2018).

The computable general equilibrium (CGE) model is a useful tool to analyse policy shocks to the 3E-integrated system (Céline et al. 2009), and scholars have analysed how different energy policies would shock the 3E-integrated system by using the CGE model (Hélène et al. 2012, Christopher et al. 2017). But there are few studies on the following three issues: whether the current policy of cutting electricity will contribute to the strategy of electricity substitution, how the policy of electricity substitution will shock the 3E-integrated system in China, and what the proper policy details should

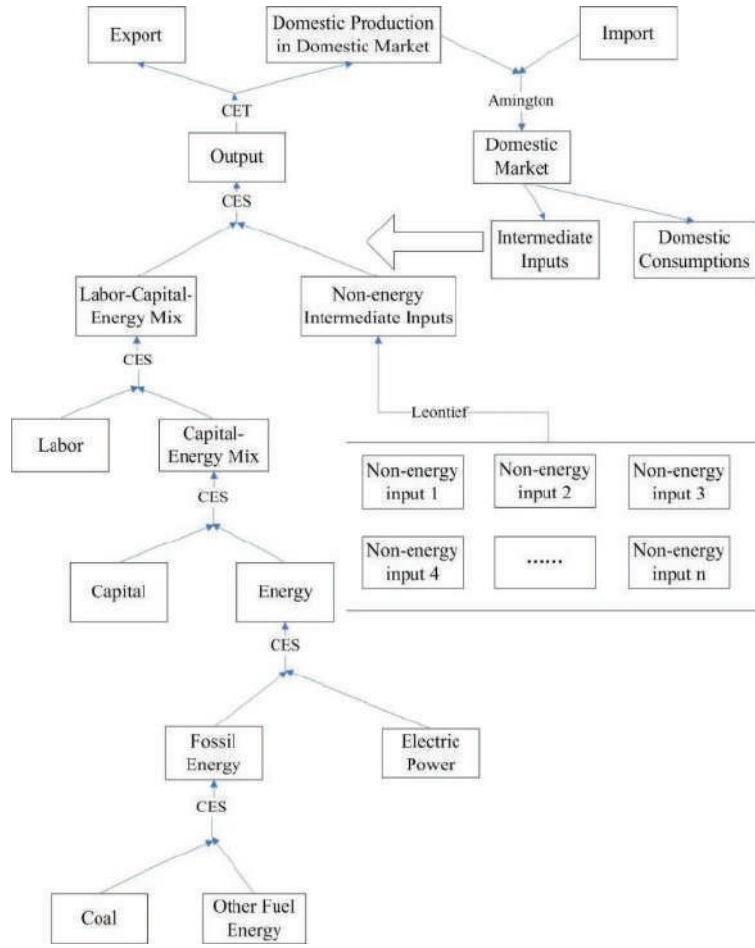

Fig. 1: Structure of computable general equilibrium (CGE) model.

be. We can use the CGE model to simulate the policy of electricity substitution, and analyse the issues above by evaluating the policy shocks.

MATERIALS AND METHODS

Cross-subsidies in electricity consumption are reflected by the distortion coefficients in electricity prices in different industries. As the electricity prices of intermediate inputs in some sectors are adjusted exogenously, while those of agriculture and residents are set as unchanged, the distortion coefficients can be the policy tools. In order to simulate the effects of this policy, we construct a corresponding static CGE model. By integrating and subdividing the relevant industrial sectors in the statistics, the model is composed of four energy sectors and seven non-energy sectors. Capital and labour are the essential production factor inputs, and the distortion coefficients of factor inputs are also introduced. Residents, enterprises, and the government are included in the domestic economic entities. The sectors are divided into non-energy and energy sectors. The non-energy sector industries are as follows: agriculture (number 1), heavy mining and processing (2), light industry (3), chemicals (4), manufacturing (5), other secondary industries (6), and service (7). The energy sector contains the following: fossil energy, including coal mining and processing (8), other fuel energy mining and processing (9), and electric power generation and supply (10).

Construction of CGE Model

The model used in this study is shown in Fig. 1, the mathematical links between different intermediate commodity and factor inputs are depicted by groups of production functions. The model is made up of two bundles: The bundle of non-energy intermediate inputs is a Leontief structure, to reflect the assumption of weak substitution between different non-energy intermediate commodities; the other bundle comprises production factors and energy intermediate inputs. Besides the Leontief production functions, the other production function in this block is the constant elasticity of substitution (CES).

The CES production function is written as:

$$QA_i = \alpha_i \cdot \left[\delta_i \cdot x_{1i}^{\frac{\varepsilon_i - 1}{\varepsilon_i}} + (1-\delta_i) \cdot x_{2i}^{\frac{\varepsilon_i - 1}{\varepsilon_i}} \right]^{\frac{\varepsilon_i}{\varepsilon_i - 1}} \quad \ldots(1)$$

Where, i indicates the serial number of the sector, QA_i indicates the output quantity of the sector's production, α_i indicates the scale factor in the production of sector I, x_{1i} and x_{2i} indicate the quantities of intermediate inputs in the production of sector I, δi indicates the share parameter between x_{1i} and x_{2i}, and εi indicates the elasticity of substitution between x_{1i} and x_{2i},.

For maximum profit and minimum cost, the optimization solution for Formula (1) will be obtained when the following condition is achieved:

$$\frac{p_{1i}}{p_{2i}} = \frac{\delta_i}{(1-\delta_i)} \cdot \left(\frac{x_{2i}}{x_{1i}}\right)^{\frac{1}{\varepsilon_i}} \quad \ldots(2)$$

Where, p_{1i} and p_{2i} indicate the prices of the two intermediate inputs. The Leontief production function can be treated as a special CES production function (when the elasticity of substitution is infinitesimal) and can be written as:

$$QINTA_{ij} = ia_{ij} \cdot QINTA_j \quad \ldots(3)$$

Where, i and j indicate the serial numbers of sector production, $QINTA_{ij}$ indicates the quantity of intermediate inputs i used in the production of sector j, $QINTA_j$ indicates the total of all intermediate inputs used in the production of sector j, and ia_{ij} indicates the input–output coefficient. For profit maximization, the solution for Formula (3) will be obtained when the following condition is achieved:

$$PINTA_j = \sum_{i=1}^{n} ia_{ij} \cdot PA_i \quad \ldots(4)$$

where $PINTA_j$ indicates the average cost of production of sector j, and PA_i indicates the cost of intermediate inputs i.

Modelling for Subsidy Mechanism in Electricity Consumption Price

The unique cross-subsidy mechanism in electricity consumption pricing has led to price distortion among industries. Although it is still unknown how the subsidy mechanism should be improved, the price distortion coefficients can be the tools to adjust the energy consumption structure.

$$PE_{\text{ave}} = \frac{\sum_{i=1}^{n} PE_i \cdot QE_i}{\sum_{i=1}^{n} QE_i} \quad \ldots(5)$$

Where, PE_{ave} indicates the average price of electricity consumption; n indicate the number of electricity consumption prices kinds; QE_i and PE_i indicate the electricity consumption quantity and price for the specific kind i. Based on Formula (5), the price distortion coefficients of electricity consumption, and the cross-subsidies can be calculated by

$$\begin{cases} e_i = \dfrac{PE_i}{PE_{ave}} \\ S_i = (1-e_i) \cdot PE_{ave} \cdot QE_i \end{cases} \quad \ldots(6)$$

Therefore, the policy of cutting the price of intermediate electricity input in the secondary and service industries is transferred to adjust the distortion coefficients of *ei*.

Calculation Method of Residents' Consumption Welfare

The policy shock on the 3E-integrated system is judged by changes in economic and environmental indicators.

Among the economic indicators, the macroeconomic indicators of GDP and CPI are chosen, and the changes of sector outputs can be used to evaluate the policy effects. Moreover, it is important to observe the changes in residents' consumption welfare: residents' expenditure function used in this model is the LES function, which is developed from the Stone–Geary utility function:

$$\begin{cases} u(Q) = \prod_{i=1}^{n} (q_i - \gamma_i)^{\beta_i} \\ \sum_{i=1}^{n} \beta_i = 1 \end{cases} \quad \ldots(7)$$

Where, $u(Q)$ is the residents' utility function, Q indicates the column vectors of commodity demands, n indicates the number of sectors, i indicates the sector's serial number, q_i indicates the commodity demand of sector i, γ_i indicates the necessity demand of sector i, and β_i indicates the marginal share of consumption. The indicators of equivalent variation (EV) and compensate variation (CV) are known as:

$$\begin{cases} EV = e(P0, u(QH1)) - E(P0, u(QH0)) \\ CV = e(P1, u(QH1)) - E(P1, u(QH0)) \end{cases} \quad \ldots(8)$$

Where, $e(P0, u(QH1))$ and $e(P0, u(QH0))$ are the expenditure functions; $P0$ and $QH0$ are the column vectors of commodity sales prices and demands, respectively, before the policy implementation; $P1$ and $QH1$ are the column vectors of commodity sales prices and demands respectively, after the policy implementation. Bringing Formula (7) into Formula (8), EV and CV can be calculated.

Calculation Method of Environmental Effects Evaluation

The policy shock will show its effects on the economy and the environment at the same time, but it is difficult to evaluate the environmental effects, because it is difficult to obtain the emission coefficients. Considering that emission coefficients are different among industries and among the types of energy, we try to evaluate the environmental effects though the economic effects.

As the two systems of environment and economy are integrated and energy consumption is positively correlated with pollution emissions, the emission coefficient can be described as

$$E_{j,k} = \sum_{i=1}^{n} (\lambda_{i,j,k} \cdot C_i) \quad \ldots(9)$$

Where, j indicates the type of energy, k indicates the type of pollution, $E_{j,k}$ indicates the pollution emissions caused by the consumption of energy j, i indicates the industry consuming energy j, C_i indicates the quantity of consumption of energy j in industry i, and $\lambda_{i,j,k}$ indicates the emission coefficient of industry i. The linear relationship between pollution emissions and energy consumption in Formula (9) can be considered valid when the change rate of C_i is slight under the policy shock.

$E_{j,k}$ can be directly obtained from the statistics and C_i can be known from the social accounting matrix (SAM), then $\lambda_{i,j,k}$ can be calculated and treated as a constant parameter. Under the policy shock, the economic system will slightly change the structure of energy demand, then the environmental effects can be evaluated.

Data and Parameters

The social accounting matrix (SAM) is the most important base data for the CGE model, because it fully describes the economic system and the equilibrium relationships. The data in the SAM are from the input–output table of 2015, the *2017 China Financial Year Book*, and the *2017 China Statistical Year Book*. We use the maximum entropy method to adjust the SAM into balance.

The substitution elasticities are collected from study by He et al. (2017), and the environmental emission coefficients (that cannot be found in the statistics) are from a study by Huo et al. (2014).

SIMULATION RESULTS

As the Chinese government has clearly announced a cut in the price of electric power used in the service industry by 10%, and debates are focused on the proper target to cut the price of electric power used in the secondary industry. In this study, the baseline scenario is that the price of electric power used in the secondary industry is not changed; we set 10 scenarios, with the target of cutting the price of electric power used in the secondary industry from 1% to 10% in each scenario and in the service industry by 10% in all scenarios. The simulation is made by using the software of GAMS.

Shocks to Economy System

In every sector's production, electric power is one of the most important raw materials, and the policy of cutting the price of electric power used in the secondary and service industries

Table 1: Changes of sector output (%).

Sector Number	Target to cut price of electricity used in secondary industry									
	–1%	–2%	–3%	–4%	–5%	–6%	–7%	–8%	–9%	–10%
1	0.3	0.3	0.3	0.2	0.1	0.00	0.05	0.1	0.1	0.1
2	0.2	0.2	0.2	0.1	0.07	0.05	0.06	0.07	0.08	0.09
3	0.4	0.4	0.4	0.2	0.1	0.00	0.05	0.1	0.2	0.2
4	0.3	0.3	0.3	0.2	0.1	0.00	0.05	0.1	0.1	0.1
5	0.3	0.3	0.3	0.2	0.1	0.00	0.05	0.1	0.1	0.1
6	0.1	0.1	0.1	0.00	0.05	0.010	0.08	0.06	0.056	0.06
7	0.4	0.4	0.4	0.2	0.1	0.00	0.1	0.2	0.2	0.2
8	–0.4	–1	–1.6	–1.2	–0.8	–0.4	–0.65	–0.9	–0.1	–0.11
9	–0.4	–0.35	–0.3	–0.2	–0.1	0.00	–0.05	–0.1	–0.1	–0.01
10	1.24	1.295	1.35	0.86	0.52	0.18	0.36	0.54	0.6	0.66

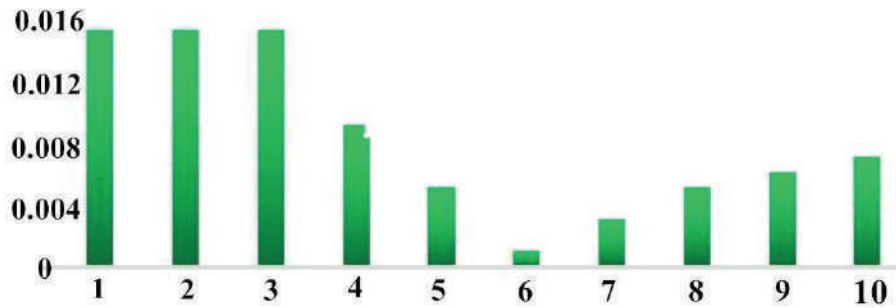

Fig. 2: Changes in GDP growth under different Scenarios.

will have an impact by changing the sectors' energy demands and outputs. Compared to the baseline scenario, the changes of sector output are shown in Table 1.

It can be seen in Table 1 that the impact on sector output is slight. Among the changes, the changes in output of coal (number 8) and electricity (10) are the most significant, and the change directions are as expected: as the price of electric power used in the secondary and service industries is reduced, an increasing demand for electric power is reasonable, and it will substitute the other energy forms (8 and 9).

Then we check the shocks on two key macroeconomic indicators, GDP growth and CPI change. Compared to the changes in GDP growth, CPI will hardly change under the policy. The changes in GDP growth are shown in Fig. 2.

It can be seen in Fig. 2 that GDP growth will be slightly increased by the policy to cut the price of electric power used in the secondary and service industries. When the target to cut the price of electric power used in the secondary industry is set from –1% to –3 % (scenarios 1, 2, and 3), the maximum effect on GDP growth is achieved (about 0.016%). The minimum effect on GDP growth is obtained when the target is set as –6% (scenario 6).

SHOCKS TO RESIDENTS' WELFARE

Besides the positive effects on sector production and the macroeconomic system, checks on economic welfare are also needed. The changes in welfare of residents' consumption (indicator: EV) and the cross-subsidy payment are shown in Fig. 3.

It can be seen in Fig. 3 that the policy to cut the price of electric power used in the secondary and service industries will increase residents' consumption welfare, while the cross-subsidy payment will decrease as an approximate linear decline. The maximum consumption welfare is obtained in scenarios 1, 2, and 3. As the cross-subsidy payment will decrease as an approximate linear decline, it may indicate that the more severe the policies are, the more resistance there will be from the agriculture.

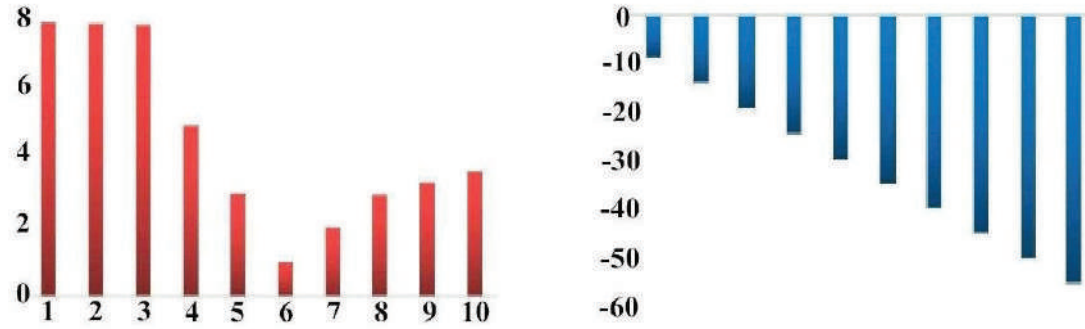

Fig. 3: Changes in EV and Cross-subsidy payment.

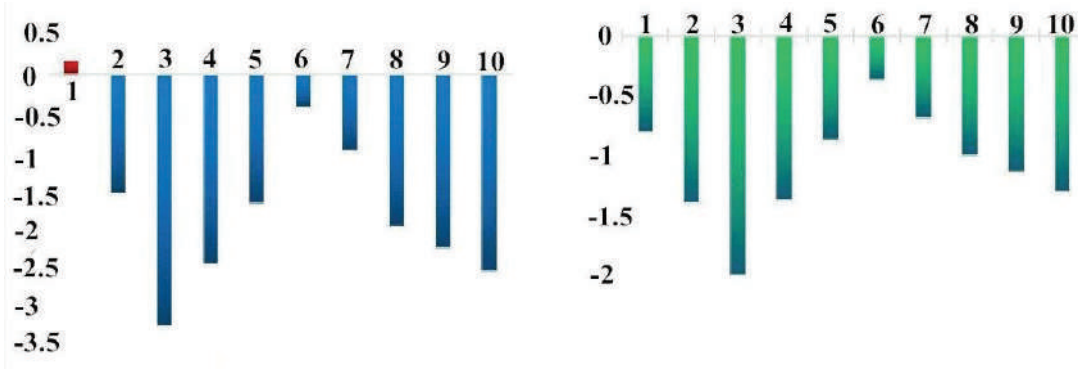

Fig. 4: Changes rates of $PM_{2.5}$ and CO_2

SHOCKS TO ENVIRONMENT

Besides the policy shock judgment from the economic view, policy shocks to the environment are equally important for comprehensive policy judgment. In Fig. 4, the policy effects on the abatement of $PM_{2.5}$ and carbon dioxide emissions are shown.

In Fig. 4, the change trends are shown as inverted U-shape curves, similar to the environmental Kuznets curve. Though the policy shocks are so slight that the maximum $PM_{2.5}$ emission abatement is only about 3.3%, while the maximum CO_2 emission abatement is only about 2%, the quantity of emission abatement is considerable, considering that CO_2 and $PM_{2.5}$ are emitted in quantities of 10 billion tons and 12 million tons, respectively, every year in China. In summary, it is obvious that the maximum positive environmental effects will be obtained when the target to cut the price of electric power used in the secondary industry is set as –3% (scenario 3).

CONCLUSIONS

This study uses the computable general equilibrium (CGE) model to study the issues of whether the policy to cut the price of electric power used in the secondary and service industries will benefit the economy and environment systems. The results show that, the electric power output will be slightly increased, the demand for coal will be reduced under the policy shocks, and the policy will contribute to the strategy of electricity substitution.

This substitution will lead to positive effects to the economic and environmental systems. The GDP growth will be slightly accelerated, and residents' welfare in consumption will be increased as well. Also, it will result in less emission of $PM_{2.5}$ and CO_2. By comparing the result curves, for the maximum positive effects, the price of electric power used in the secondary industry should be cut by –3%.

REFERENCES

Akkemik, K.A. and Göksal, K. 2012. Energy consumption-GDP nexus: Heterogeneous panel causality analysis. Energy Economics, 34(4): 865-873.

Céline, G., Stéphane, H. and Crassous, R. 2009. The resilience of the Indian economy to rising oil prices as a validation test for a global energy-environment-economy CGE model. Energy Policy, 37(11): 4259-4266.

Christopher, H., Harvey, C., Terrence, I. and David, K. 2017. Estimating the implied cost of carbon in future scenarios using a CGE model: The Case of Colorado. Energy Policy, 102: 500-511.

Dergiades, T., Martinopoulos, G. and Tsoulfidis, L. 2013. Energy consumption and economic growth: Parametric and non-parametric causality testing for the case of Greece. Energy Economics, 36: 686-697.

Hamit, H.M. 2012. Greenhouse gas emissions, energy consumption and economic growth: A panel cointegration analysis from Canadian industrial sector perspective. Energy Economics, 34(1): 358-364.

Hélène, M., Pycroft, J., Saveyn, B. and Juan, C.C. 2012. Does climate policy make the EU economy more resilient to oil price rises? A CGE analysis. Energy Policy, 47:172-179.

He, Y. and Lin, B. 2017. The impact of natural gas price control in China: A computable general equilibrium approach. Energy Policy, 107: 524-531.

Huo, H., Zhang, Q., Guan, D.B., Xin, S., Zhao, H.Y. and He, K.B. 2014. Examining air pollution in china using production- and consumption-based emissions accounting approaches. Environmental Science & Technology, 48(24): 14139-14147.

Kraft, J. and Kraft, A. 1978. On the relationship between energy and GNP. Journal of Energy and Development, 3(2): 401-403.

Liddle, B. and Lung, S. 2015. Revisiting energy consumption and GDP causality: Importance of a priori hypothesis testing, disaggregated data, and heterogeneous panels. Applied Energy, 142: 44-55.

Lu, J., Chang, H. and Wang, Y. B. 2017. Dynamic evolution of provincial energy economy and environment coupling in china's regions. China Population, Resources and Environment, 27(2): 60-68.

Lu, W.C. 2017. Greenhouse gas emissions, energy consumption and economic growth: A panel cointegration analysis for 16 Asian countries. International Journal of Environmental Research and Public Health, 14(11): 1436.

Nordhaus, W.D. and Yang, Z.A. 1996. Regional dynamic general-equilibrium model of alternative climate-change strategies. American Economic Review, 86(4): 741-765.

Qiao, X.N. and Wang, Y.B. 2018. The impact of cross-subsidization of differential power prices on industrial structure adjustment. Journal of Environmental Economics, 4: 50-54.

Xu, K., Luo, F.Z., Wei, G.Y., Wang, S.J., Liu, H. and Gao, S. 2017. Quantitative comparison and analysis of urban energy-consumption features for urban energy internet. Proceedings of the CSU-EPSA, 29(3): 50-54.

Vera, I. and Langlois, L. 2007. Energy indicators for sustainable development. Energy, 32(6): 875-882.

Wang, M. and Huang, Y.. 2015. China's environmental pollution and economic growth. China Economic Quarterly, 14(2): 557-578.

Zhang, C. 2013. Quantitative analysis of energy utilization history in human civilization. Energy Research and Management, 2: 8-11.

Zhu, C.Z. 2016. A discussion on why coal is irreplaceable in power generation in China. Sino-Global Energy, 21(2): 14-18.

Nature Environment and Pollution Technology
An International Quarterly Scientific Journal

p-ISSN: 0972-6268
e-ISSN: 2395-3454

Vol. 18 | No. 4 | pp. 1455-1458 | 2019

Original Research Paper | Open Access

Evaluation of Organophosphorus Pesticide Residue in Cotton of Tijara Tehsil, Alwar, Rajasthan

Sucheta Yadav† and Subroto Dutta
Department of Environmental Science, MDS University, Ajmer-305009, Rajasthan, India
†Corresponding author: Sucheta Yadav

Nat. Env. & Poll. Tech.
Website: www.neptjournal.com

Received: 16-03-2019
Accepted: 19-05-2019

Key Words:
Organophosphates
Pesticide residue
Monocrotophos
Cotton

ABSTRACT

Cotton is one of the most important fibres and cash crop of India, which plays a dominant role in the country's industrial and agricultural economy. About 60% of all commercialized agrochemicals, are insanely applied on cotton fields so that cotton has become one of the most polluted and chemical-intensive agricultural crops in the world. The present study was undertaken to determine the concentration of different organophosphorus pesticides residue in cotton samples collected from agriculture fields of Tijara tehsil, Alwar. A total of 150 samples were randomly collected from the cotton farm. Concentrations of all pesticides in the cotton samples were determined by GC/MS and LC-MS. About 38% of the total analysed samples were contaminated with different residues, among which 10.66% were having the concentration of pesticide residue above the MRL. The study revealed that cotton is highly contaminated with Monocrotophos (22%) followed by Acephate (10%), Chlorpyrifos (7.33%) and Profenofos (5.33%). The possible reasons for high levels of pesticides in cotton are the massive use of pesticides and farmers were not having sufficient scientific knowledge about the chemical nature of pesticides that have been used or the effects of pesticides on the environment and the effects of pesticides exposure on public health, when using them indiscriminately. The presence of pesticides in cotton samples is a serious threat to humans because they further show pesticide residues in cotton products. Therefore, it is recommended to continuously monitor the use of this pesticide in the study areas.

INTRODUCTION

Agriculture accounts for 18 % of India's gross domestic product and provides employment to 50% of the country's workforce. India is the world's largest producer of pulses, rice, wheat, spices and spice products. India has emerged as the second largest producer of fruits and vegetables in the world. The industrialization of agriculture has favoured the use of plenty of agrochemicals including fertilizers, pesticides, micro-nutrients and plant growth regulators in the agricultural fields. Pesticides are the integral part of modern agriculture. As India is a tropical country, it suffers severe losses in agriculture due to pests. This requires the use of pesticides in agriculture to check or control pests, diseases, weeds and other plant pathogens in an effort to reduce or eliminate yield losses and preserve high product quality. In the context of current farming practices, if pesticide use is prohibited, the agriculture production will decrease significantly and food prices would sky-rocket. In such circumstances, it would be impossible to feed the world's growing population sustainably. Therefore, use of pesticides has become imminent to increased protection and crop production. Application of pesticides is considered an economic and efficient defence against pest attacks which helps to increased crop productivity. The use and development of pesticides to protect crops against insects, pests and diseases has steadily increased over the past three or four decades. Today, the development in pesticide sector has led to completely new forms of crop production and protection of crops, as well as the preservation of stored grains and their products in the godowns and warehouses.

Pesticide applications in crops and animals can leave residues in or on food if consumed and lead to the accumulation of pesticides in the environment. Although pesticides are produced on the basis of strict regulatory processes to operate with logical certainty and with minimal impact on human health and the environment, serious concerns have been raised about the health risks of residues in food. Research conducted over the last decade shows the presence of pesticide residues in various foods, such as watermelon, onion, cucumber, lettuce, cabbage, okra, peppers, tomatoes, spinach and eggplant. Furthermore, pesticide residues constitute a danger for micro and microflora of the soil and its toxic effects occur in humans when bioaccumulation occurs along the food chain after the initial plant uptake. Organophosphates (OP) are the most widely used

pesticide, due to its favourable characteristics, such as biodegradable and short persistence compared to organochlorines (Chen et al. 2010). OPs protect crops from pests by inhibiting acetylcholinesterase enzyme activity in insects. OP samples degrade rapidly by hydrolysis on exposure to light, air and soil, however small amounts are detected in food and drinking water. They are sprayed over crops or soils, causing residues to be found in water (Arain et al. 2018, Tariq et al. 2004), soil (Akan et al. 2013, Stoleru et al. 2015) fruits (Hayat et al. 2018, Mahmud et al. 2015), vegetables (Chilumuru et al. 2015, Jallow et al. 2017, Akan et al. 2013) and crops (Ogah et al. 2012). Attallah & Abdelwahed (2017) found that chlorpyrifos, malathion, profenofos and cypermethrin were the most frequently detected pesticide residues in the cotton product samples. The size of the residue depends on the exposure level (treatment rate), its dissipation rate, environmental factors, and its physical and chemical properties. The main use of pesticides in India is for cotton crops (45%), followed by paddy and wheat. Cotton is one of the most important cash and fibre crops of India and plays a dominant role in the country's industrial and agricultural economy. It provides the basic raw material (cotton fibre) to cotton textile industry. Cotton in India provides direct livelihood to 6 million farmers and about 40-50 million people are employed in cotton trade and its processing. The production of cotton in India is around 40 million bales (170 kg each) out of which 30 million bales are of local consumption and 10 million bales is exports (Bayer, India)

In India, there are ten major cotton growing states which are divided into three zones, viz. north zone, central zone and south zone. North zone consists of Punjab, Haryana and Rajasthan. Central zone includes Madhya Pradesh, Maharashtra and Gujarat. South zone comprises Andhra Pradesh, Telangana, Karnataka and Tamil Nadu. Besides these ten States, cotton cultivation has gained momentum in the Eastern State of Orissa. Cotton is also cultivated in small areas of non-traditional States such as Uttar Pradesh, West Bengal and Tripura.

Cotton is a Kharif crop in the major parts of the country viz. Punjab, Haryana, Rajasthan, Uttar Pradesh, Madhya Pradesh, Gujarat, Maharashtra and parts of Andhra Pradesh and Karnataka. In these areas, the irrigated crop is sown from March-May and the rain fed crop in June-July with the commencement of the monsoon.

Cotton and paddy are the major crops where pesticides consumption is 50 per cent and 18 per cent, respectively. Cotton covers only 5 per cent of the cropped area, but accounts for 50 per cent of pesticide use (Devi et al. 2017). Cotton crop is highly susceptible to diseases and pests. Most of the diseases that affect cotton cultivation occur at all stages of crop growth and throughout the year, which necessitates spraying of pesticides. Around 60% of all commercialized agrochemicals are insanely applied on cotton fields, so that cotton has become one of the most polluted and chemical-intensive agricultural crops in the world (Kranthi & Russell 2009).

MATERIALS AND METHODS

The study was conducted for the estimation of pesticide residue in cotton crop of Tijara tehsil of Alwar district. Tijara is located at 27°56'3" North latitude and 76°51'21" East longitude. A total of 150 samples were collected randomly from the cotton farm, 50 samples every year from 2016-2018. All the samples were harvested directly from the cotton farm, labelled in plastic bags and transported to laboratory for analysis

Sample Preparation

For the extraction of the samples, 15 g of sample + 15 g of water were taken in the polypropylene tube and left for 5 min. Further, 15 mL of 1% formic acid in acetonitrile were added and shaken well. Subsequently 6 g anhydrous magnesium sulphate + 1.5 g of sodium chloride were added, mixed in a vortex mixer for 3 minutes and centrifuged at 5000 rpm for 5 minutes. 1.5 mL of supernatant were pipetted from the mixture and added to the test tube already containing 150 mg of anhydrous magnesium sulphate and 50 mg of PSA (primary secondary amine). The solution was further mixed in a vortex mixer for 1 min and centrifuged at 5000 rpm for 5 minutes. Finally, 1 mL was pipetted and filtered in the 2 mL vial. The extracted solution was performed in GC-MS/LS.

RESULTS

The present study was undertaken to determine the concentration of different organophosphorus pesticides residue in cotton samples collected from agriculture fields of Tijara tehsil, Alwar. Organophosphates are known to be present in cotton due to extensive and intensive use of corresponding pesticides in cultivation of cotton crop. The results revealed that 38% of the total analysed samples were contaminated with different residues. Most of the contaminated samples were within MRL value by FSSAI. Only 10.66% of analysed samples were having the concentration of pesticide residue above the MRL.

The consumption of pesticides shows large fluctuations over the years, which may be due to their relation to weather parameters and market availability. The range of various pesticide (Table 1, Fig. 1) showed that cotton is highly contaminated with Monocrotophos (22%) followed

by Acephate (10%), Chlorpyrifos (7.33%) and Profenofos (5.33%). Monocrotophos is one of the oldest pesticides still in use and although it is known to be toxic (Jayakumar, Director of the Pesticide Action Network). It was banned in 2005 in India for use on vegetable. Currently, Monocrotophos is mostly used to grow cotton (Dileep Kumar, Program Coordinator Pesticide Action Network). It was found from the study that 6% of the Monocrotophos contaminated sample were exceeded MRL. In a similar study, Chlorpyrifos, Malathion, Profenofos and Cypermethrin were the most frequently detected pesticide residues in the cotton product samples (Attallah & Abdelwahed 2017)

In current study, it was observed that the mean and standard deviation of Monocrotophos was 0.048 ± 0.203 respectively. Similarly, the mean and standard deviation of Chlorpyrifos was 0.014 ± 0.124, for Acephate was 0.064 ± 0.328 and for Profenofos was 0.005 ± 0.037. Zhao et al. (2008) had also determined residual levels of Profenofos in cotton leaves, soil and cotton seed. According to WHO recommended classification of Pesticides by hazard and guidelines for classification 2009, the acute toxicity for Chlorpyrifos, Acephate and Profenofos were recorded to be moderate hazardous (Class II), while Monocrotophos came out to be highly hazardous (Class I).

Table 1: Prevailing scenario of various pesticides in cotton crop.

Studied year	Name of pesticides detected (Number of samples contaminated)	Acute toxicity	Total number of samples contaminated with different pesticides	% of samples contaminated with pesticides	Mean &SD of detected pesticide	Pesticides detected range mg/kg	MRL mg/kg	No. of samples exceeded MRL
2016	Monocrotophos (9)	High			0.031 ± 0.128	0.03-0.89	0.1	3
	Chlorpyrifos (3)	Moderate			0.004 ± 0.019	0.02-0.13	0.05	1
	Acephate (7)	Moderate			0.069 ± 0.220	0.04-1.02	2	Nil
	Profenofos (1)	Moderate	17	34%	0.005 ± 0.035	ND-0.25	0.05	1
2017	Monocrotophos (14)	High			0.07 ± 0.281	0.02-1.72	0.1	3
	Chlorpyrifos (3)	Moderate			0.036± 0.214	0.05-1.5	0.05	2
	Acephate (4)	Moderate			0.032± 0.136	0.05-0.82	2	Nil
	Profenofos (4)	Moderate	23	46%	0.003 ± 0.011	0.02-0.06	0.05	1
2018	Monocrotophos (10)	High			0.044 ± 0.171	0.02-1.05	0.1	3
	Chlorpyrifos (5)	Moderate			0.002 ± 0.009	0.01-0.05	0.05	Nil
	Acephate (4)	Moderate			0.093 ± 0.508	0.08-3.5	2	1
	Profenofos (3)	Moderate	17	34%	0.009 ± 0.054	0.04-0.38	0.05	1
2016-2018	Monocrotophos (33)	High			0.048 ± 0.203	0.02-1.72	0.1	9
	Chlorpyrifos (11)	Moderate			0.014 ± 0.124	0.01-1.5	0.05	3
	Acephate (15)	Moderate			0.064 ± 0.328	0.04-3.5	2	1
	Profenofos (8)	Moderate	57	38%	0.005 ± 0.037	0.02-0.38	0.05	3

MRL-Maximum residual limit, SD- Standard deviation

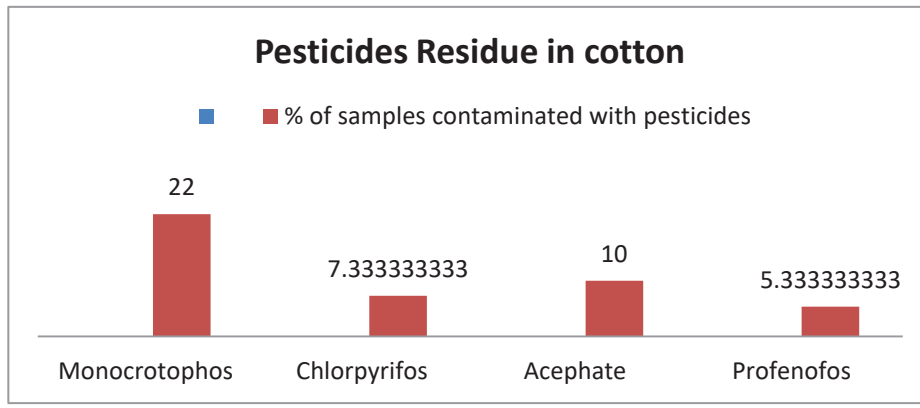

Fig. 1: Level of pesticide residue in cotton.

Fig. 2: Pesticide application on cotton crop in Tijara

There must be two possible reasons for high levels of pesticides in cotton. First, the pesticides are used to kill insects and other pests, to ensure the proper growth of cotton. Secondly, most of the farmers in the study area were not having enough scientific knowledge about the chemical nature of pesticides that have been used or the effects of pesticides on the environment and the exposure effects of pesticides on public health, when using them indiscriminately (Fig. 2).

CONCLUSION

It is recommended to periodically monitoring of cotton must be carried out to determine the predominant pesticide contamination scenario of cotton crop and to ensure safety. The present research will not only serve as reference document but also helpful in taking necessary and timely preventive measure to mitigate such problems.

REFERENCES

Ali, T., Ismail, M., Asad, F., Ashraf, A. and Khan, U.W.M. 2018. Pesticide genotoxicity in cotton picking women in Pakistan evaluated using comet assay. Drug and Chemical Toxicology, 41(2).

Attallah, E.R. and Abdelwahed, M. H. 2017. Monitoring of pesticide residues in some cotton products in Egypt using GC-MS/MS and LC-MS/MS. Middle East Journal of Applied Sciences, 7(1): 102-109.

Bayer, India. www.cropscience.bayer.in

Chawla, S., Gor, H.N., Patel, H.K., Parmer, K.D., Patel, A.R., Shukla, V., Ilyas, M., Parsai, S.K., Somashekar, Meena, R.S. and Shah, P.G. 2018. Validation, residue analysis, and risk assessment of fipronil and flonicamid in cotton (Gossypium sp.) samples and soil. Environmental Science and Pollution Research, 25(19): 19167-19178.

Devi, P. I., Thomas, J. and Raju, R.K. 2017. Pesticide consumption in India: A spatiotemporal analysis. Agricultural Economics Research Review, 30(1): 163-172.

Gutierrez, A.P., Herren, H.R., Ponti, L. and Baumgartner, J. 2015. Deconstructing Indian cotton: Weather, yields and suicides. Environmental Sciences Europe, 27:12.

Kranthi, K.R. and Russell, D.A. 2009. Changing trends in cotton pest management. Integrated Pest Management: Innovation-Development Process, 1: 499-541.

Ma, M., Dong, S., Jin, W., Zhang, C. and Zhou, W. 2019. Fate of the organophosphorus pesticide profenofos in cotton fiber. Journal of Environmental Science and Health, Part B, 54(1): 70-75.

Pandiselvi, S., Sathiyanarayanan, S. and Ramesh, A. 2010. Determination of spirotetramat and imidacloprid residues in cotton seed, lint, oil and soil by HPLC UV method and their dissipation in cotton plant. Pesticide Research Journal, 22(2): 168-173.

Rezaei, M., Shariatifar, N., Shoeibi, S., Ahmadi, M.A. and Khaniki, G.J. 2018. Simultaneous determination of residue from 58 pesticides in the wheat flour consumed in Tehran, Iran by GC/MS. Iran Journal of Pharmaceutical Research, 16(3): 1048-1058.

Rose, M.T., Sanchez-Bayo, F., Crossan, A.N. and Kennedy, I.R. 2006. Pesticide removal from cotton farm tailwater by a pilot-scale ponded wetland. Chemosphere, 63(11): 1849-1858.

Swarnam, T.P. and Velmurugan, A. 2013. Pesticide residues in vegetable samples from the Andaman Islands, India. Environmental Monitoring and Assessment, 185(7): 6119-612.

Taneja, S. 2017. Agriculture: Why India continues to use lethal pesticides. Down To Earth.

Ting-Ting, H.U., Chun-Mei, L.U., Han, L.I., Zhang Z.X., Zhao Y.H. and Juan, L.I. 2017. Determination of eleven organophosphorus pesticide residues in textiles by using HPLC-HRMS. Analytical Sciences, 33(9): 1027-1032.

Vig, K., Singh, D.K., Agarwal, H.C., Dhawan, A.K. and Dureja, P. 2001. Insecticide residues in cotton crop soil. Journal of Environmental Science and Health, Part B, Pesticides, Food Contaminants, and Agricultural Wastes, 36(4).

Zhang, H. 1996. Analytical method of profenofos residue in cotton seed, cotton foliage and soil. Pesticides, 4.

Zhao, W.Y., Shen, C.L., Ding, N., Jia, S.M and Fan, Z.X. 2008. Residual analysis of profenofos in cotton and soil. Journal of Qingdao University of Science & Technology (Natural Science edition), 4(6).

Nature Environment and Pollution Technology
An International Quarterly Scientific Journal

p-ISSN: 0972-6268
e-ISSN: 2395-3454

Vol. 18 | No. 4 | pp. 1459-1462 | 2019

Original Research Paper | Open Access

Metal Concentration of Water of Amaravathi and Thirumoorthy Reservoirs in Tamil Nadu, India

N. Natarajan†, V. Vivekk Velusamy, S. Nishar Ahamed, M. Imayaprakash and S. Dineshkumar
Department of Civil Engineering, Dr. Mahalingam College of Engineering and Technology, Pollachi-642003, Tamil Nadu, India
† Corresponding author: N. Natarajan

Nat. Env. & Poll. Tech.
Website: www.neptjournal.com

Received: 28-05-2019
Accepted: 21-06-2019

Key Words:
Metal concentration
Water quality
Water pollution
Amaravathi dam
Thirumoorthy dam

ABSTRACT

Reservoirs are the major source of water supply in many localities for meeting the water demand of the people, and hence it is important to monitor the metal concentration of the water stored in such reservoirs for the benefit of the people in terms of drinking water and irrigation. The main objective of this study is to monitor the metal concentrations of Arsenic (As), Boron (B), Cadmium (Cd), Chromium (Cr), Copper (Cu), Iron (Fe), Nickel (Ni), Lead (Pb), Selenium (Se), and Zinc (Zn) in the water of the Amaravathi and Thirumoorthy reservoirs located in the Tiruppur district of the state of Tamil Nadu, India. Results indicate that the water collected from the Thirumoorthy reservoir is free from metal contamination while that from the Amaravathi reservoir has a marginal contamination of Fe concentration. Thus, the water stored in these reservoirs is suitable for drinking and irrigation purpose.

INTRODUCTION

Surface water is one of the major sources of water supply used to meet the overall demand of the urban and rural population. Sources of water supply such as rivers, lakes, reservoirs, and groundwater are being directly or indirectly being polluted due to rapid industrialization as well as urbanization. Discharges from the municipal and industrial wastewaters are the main sources of water pollution since they contain organic pollutants, chemicals, metals (Goldar & Banerjee 2004). Metal pollution of water bodies is highly dangerous because of its toxicity, bioaccumulation, biomagnification of the food chain, prolonged persistence, and thus considered to be a worldwide problem. The metal concentration in aquatic ecosystems is generally monitored based on their concentrations in water and sediment samples (Ebrahimpour & Mushrifah 2008). Metal pollution in water bodies can severely affect the biotic communities (Badantoni et al. 2004). Moreover, the metal pollution also affects the health of human beings and disturbs the balance of the ecosystem, and social and economic development of the society (Milovanovic 2007). It is very essential to monitor the quality of the water resources keeping in view of the impact of human activities on the degradation of the water quality (Mansouri et al. 2011). The assessment of the water quality also plays a major role in developing an appropriate water quality management plan for a locality in order to reduce the effects of water pollution (Sanchez et al. 2007).

Several studies have been conducted in the past to illustrate the significance of monitoring the metal concentrations in the water bodies and sediments of various water sources. Rajaei et al. (2012) analysed the metal concentrations in the water of Chah Nimeh reservoirs in Zabol, Iran. They concluded that there were significant differences between Cr, Ni, Pb and Se in the water of Chah Nimeh reservoir. Hussein et al. (2014) monitored the monthly variations in the concentration of heavy metals (Pb, Ni and Fe) in Shatt Al-Hilla river water during November 2011-October 2012 to study the extent of contamination of the river with those metals. They observed a wide range of variations in the heavy metal concentration levels varying from high concentration of one of the metals at a certain site to low content at the other. Sayadi et al. (2015) studied the contribution of the natural and concentration factors of heavy metals such as Cd, Pb, and Cu in the sediments of six stations of Chah Nimeh reservoir, Sistan, Iran in 2013. They observed the highest concentrations of Cd and Pb in station one and maximum Cu concentration in station five. Bing et al. (2016) investigated the spatial distribution of the heavy metal concentration (Cu, Cd, Pb and Zn) in the sediments of the Three Gorges reservoir and also assessed their potential risk by multiple indices and metal fraction. They concluded that the sediments were moderate to highly contaminated by Cd, and slightly contaminated by other heavy metals.

Azadi et al. (2018) conducted a review on studies carried out on the contamination of lead in the coastal sediments of north and south Iran during 2006 to 2016. They observed that the variability in the Pb mean concentration was considerable and statistically significant.

Amaravathi and Thirumoorthy reservoirs are the major sources of water supply for drinking and irrigation for the Tiruppur district. Our study is aimed at investigation of the concentration of As, B, Cd, Cr, Cu, Fe, Ni, Pb, Se and Zn in the water of the Amaravathi and Thirumoorthy reservoirs so as: (1) to compare the concentration of various metals and (2) to assess its suitability for drinking by comparison of the results with IS: 10500:2012.

STUDY AREA

Tiruppur district is bounded by Karur district in the east, Coimbatore in the west, Erode in the north and Dindigul district in the south. The district lies between 11°14' N to 11°20' N latitude and 27°77'E to 77°56' E longitude with an area of 2296 sq. km. The study area consists of 13 blocks, 265 villages and 3597 habitations. The southern part of the district is covered by hill ranges of Western Ghats and the rest of the district consists of undulating plain sloping gradually from west to east. The major rivers flowing through the district are Noyyal and Amaravathi, which come under the Cauvery basin. Chinnar and Tenar are the main tributary of Amaravathi river, which is the main source of irrigation in the district. The average annual rainfall for the last six years, namely 2013, 2014, 2015, 2016, 2017 and 2018 are 703 mm, 360 mm, 278 mm, 411 mm, 680 mm and 618 mm respectively. The aquifers located in this region are semi-confined or unconfined aquifers and depth of water in these reservoirs can range from 7 m to 25 m. The water supply status as on 1.4.2017 indicates that out of 3597 inhabitants, 785 are partially covered (10-39 lpcd) and 2812 are fully covered (40 lpcd).

The Amaravathi dam is a dam constructed across the Amaravathi river in 1957. It is located at Amaravathinagar, 25 kilometers south of Udamalpet in the Indira Gandhi Wildlife sanctuary, Tiruppur district in the state of Tamil Nadu, India. The associated reservoir is 9.31 km^2 in area and 33.53 m deep. The dam was primarily built for irrigation and flood control and four megawatts of electricity generation capacity was installed in 2003-2004. The surface elevation is 427 m and the volumetric capacity is 3×10^9 cubic feet. Amaravathi dam is located south of the Thirumoorthy dam. Thirumoorthy dam is 20 km from Uduamlpet on the highway from Palani to Coimbatore. The dam has been constructed adjoining the Thirumoorthy hill. The dam is located close to a perennial stream and a waterfall. The dam is located amidst the rolling hills. The topographical location

Fig. 1: Location of Amaravathi dam and Thirumoorthy dam in the district of Tiruppur, Tamil Nadu, India.

of the dams in the Tiruppur district has been depicted in Fig. 1.

MATERIALS AND METHODS

Water samples were collected from four different site locations of each reservoir. The concentration of the metals was determined using the test method of IS 3025:1964 in NABL accredited laboratory. Table 1 provides the sections of IS 3025:1964 that was adopted for the determination of the metal concentration of various metals.

RESULTS AND DISCUSSION

The metal concentration of As, B, Cd, Cr, Cu, Fe, Ni, Pb, Se, and Zn in the water of Amaravathi and Thirumoorthy reservoirs were analysed in this study. The results obtained are given in Tables 2 and 3.

It is observed from Table 2 that the concentration for As, B. Cd, Ni, Se and Zn lies below the detectable limit of 0.001 ppm. The concentration of Cr is 0.01 ppm at site 1 but still within the standard limit of 0.05 ppm. The concentration of Cu (0.06 ppm) is marginally above the standard limit of 0.05 ppm at site 1 and within the prescribed limits at all other sites of the reservoir. The iron concentration was found to be 0.18 ppm, 0.16 ppm, 0.16 ppm and 0.12 ppm at the four sites, which is above the standard limit of 0.1 ppm. Since, the concentration is only marginally higher than the standard limit, it would not cause any serious health impacts for the people consuming this water. Chaturvedi & Dave (2012) indicated that iron intake has a positive effect on our health in moderate doses, since it is an essential nutrient. They have also mentioned that the recommended intake of iron can vary from 10 to 50 mg/L depending on age, sex, and physiological status. Even the concentration of lead (Pb) is within the limits prescribed by IS 10500:2012. Thus, the water from the Amaravathi reservoir was found to be suitable for drinking as well as irrigation purposes.

It is observed from Table 3 that the metal concentrations of As, B, Cd, Cr, Cu, Fe, Ni, Pb, Se and Zn are well below the detectable limit of 0.001 ppm as per the results obtained. Thus, the water from the Thirumoorthy dam is potable for the people of Tiruppur district.

CONCLUSION

The metal concentrations of As, B, Cd, Cr, Cu, Fe, Ni, Pb, Se and Zn were determined in the water of the reservoirs of Amaravathi and Thirumoorthy dams located in the Tiruppur district of the state of Tamil Nadu, India. The concentration of the metals was found to be well below the detectable limit of 0.001 ppm in the Thirumoorthy dam water. The concentration of Fe was found to be marginally higher than the limits prescribed by IS 10500: 2012 at the

Table 1: Sections of IS 3025: 1964 adopted for testing of metal concentration.

Sl. No.	Metal	Section
1	As	Part 37
2	B	Part 29
3	Cd	Part 41
4	Cr	Part 38
5	Cu	Part 36
6	Fe	Part 32
7	Ni	Part 54
8	Pb	Part 47
9	Se	Part 28
10	Zn	Part 39

Table 2: Metal concentration (ppm) at different site locations of Amaravathi dam.

S. No.	Metal	Concentration				Limits (IS 10500:2012)
		A1	A2	A3	A4	
1	As	<0.001	<0.001	<0.001	<0.001	0.05
2	B	<0.001	<0.001	<0.001	<0.001	5.0
3	Cd	<0.001	<0.001	<0.001	<0.001	0.01
4	Cr	0.01	<0.001	<0.001	<0.001	0.05
5	Cu	0.06	0.05	<0.001	0.02	0.05
6	Fe	0.18	0.16	0.16	0.12	0.1
7	Ni	<0.001	<0.001	<0.001	<0.001	0.02
8	Pb	0.01	<0.001	0.01	<0.001	0.01
9	Se	<0.001	<0.001	<0.001	<0.001	0.01
10	Zn	<0.001	<0.001	<0.001	<0.001	5.0

Table 3: Metal concentration in ppm at different site locations of Thirumoorthy dam.

S. No.	Metal	Concentration				Limits (IS 10500:2012)
		T1	T2	T3	T4	
1	As	<0.001	<0.001	<0.001	<0.001	0.05
2	B	<0.001	<0.001	<0.001	<0.001	5.0
3	Cd	<0.001	<0.001	<0.001	<0.001	0.01
4	Cr	<0.001	<0.001	<0.001	<0.001	0.05
5	Cu	<0.001	<0.001	<0.001	<0.001	0.05
6	Fe	<0.001	<0.001	<0.001	<0.001	0.1
7	Ni	<0.001	<0.001	<0.001	<0.001	0.02
8	Pb	<0.001	<0.001	<0.001	<0.001	0.01
9	Se	<0.001	<0.001	<0.001	<0.001	0.01
10	Zn	<0.001	<0.001	<0.001	<0.001	5.0

four sites from where water was collected but this would not have any major impact on the human health. Thus, the water from both the reservoirs is suitable for drinking and irrigation purposes.

REFERENCES

Azadi, N.A., Mansouri, B., Spada, L, Sinkakarimi, H.M., Hamesadeghi, Y. and Mansouri, A. 2018. Contamination of lead (Pb) in the coastal sediments of north and south Iran: a review study. Chemistry and Ecology, 34(9): 884-900.

Bing, H., Zhou, J., Wu, Y., Wang, X., Sun, H. and Li, R. 2016. Current state, sources and potential risk of heavy metals in sediments of Three Gorges Reservoir, China. Environmental Pollution, 214: 485-496.

Baldantoni. D., Alfani, A. and Tommasi, P.D. 2004. Assessment of macro and microelement accumulation capability of two aquatic plants. Environ. Pollut., 130: 149-156.

Chaturvedi, S. and Dave, P.N. 2012. Removal of iron for safe drinking water. Desalination, 303: 1-11.

Ebrahimpour, M. and Mushrifah, I. 2008. Heavy metal concentrations in water and sediments in Tasik Chini, a freshwater lake, Malaysia. Environ. Monit. Assess., 141: 297-307.

Goldar, B. and Banerjee, N. 2004. Impact of informal regulation of pollution on water quality in rivers in India. J. Environ. Manag., 73: 117-130.

Hussein, F., Baqir, S. and Karam, F. 2014. Seasonal variation in heavy metals contamination in surface water of Shatt Al-Hilla river, Babylon, Iraq. Asian Journal of Chemistry, 26: S207-S210.

Mansouri, B., Baramaki, R. and Ebrahimpour, M. 2011. Acute toxicity bioassay of mercury and silver on *Capoeta fusca* (black fish). Toxicol Ind. Health, 28: 393-398.

Milovanovic, M. 2007. Water quality assessment and determination of pollution sources along the Axios/Vardar River, Southeastern Europe. Desalination, 213: 159-173.

Rajaei, G., Mansouri, B., Jahantigh, H. and Hamidian, H. 2012. Metal concentrations in the water of Chah Nimeh reservoirs in Zabol, Iran. Bulletin of Environmental Contamination Toxicology, 89: 495-500.

Sanchez, E., Colmenarejo, M.F., Vicente, J., Rubio, A., Garcia, M.G., Travieso, L. and Borja, R. 2007. Use of the water quality index and dissolved oxygen deficit as simple indicators of watersheds pollution. Ecol. Indic., 7: 315-328.

Sayadi, M., Rezaei, M., Afsarim K. and PoorMollaeib, N. 2015. Natural and concentration factor distribution of heavy metals in sediments of Chah Nimeh reservoirs of Sistan, Iran. Ecopersia, 3(2): 1003-1012.

Nature Environment and Pollution Technology
An International Quarterly Scientific Journal

p-ISSN: 0972-6268
e-ISSN: 2395-3454

Vol. 18 | No. 4 | pp. 1463-1469 | 2019

Original Research Paper | Open Access

Mutagenicity of Bulk, Aqueous and Organic Partitions of Air Particulate Matter in Differentially Ventilated Wards in a Public Urban Hospital

Aurora S. Nakpil*, Emmanuel S. Bajaand Paul Mark B. Medina***†**

*College of Medicine, University of the Philippines Manila, 1610 Pedro Gil Street, Ermita, 1000, Manila, Philippines

**Institute of Clinical Epidemiology, National Institutes of Health, University of the Philippines Manila, 623 Pedro Gil Street, Ermita, 1000, Manila, Philippines

***Department of Biochemistry and Molecular Biology, College of Medicine, University of the Philippines Manila, 547 Pedro Gil Street, Ermita, 1000, Manila, Philippines

†Corresponding author: Paul Mark B. Medina

Nat. Env. & Poll. Tech.
Website: www.neptjournal.com

Received: 21-07-2018
Accepted: 21-09-2018

Key Words:
Mutagenicity
Mutagen
Ames test
Indoor air quality
S. cerevisae

ABSTRACT

The hospital environment requires indoor air quality conducive to the recovery of patients with poor health. Low indoor air quality is associated with an increased incidence of respiratory tract diseases and the development of cancer. This study investigated the mutagenicity of air particulate matter soluble in bulk, aqueous, and organic partitions collected from naturally and mechanically ventilated wards in the hospital environment through the Ames test and the mutagenicity testing with the D7 strain of *Saccharomyces cerevisae*. Bulk, aqueous, and organic fractions of air particulate matter at maximum (100% concentration), 10% concentration, and 1% were found to be mutagenic with both the Ames test ($p < 0.05$) and mutagenicity testing with D7 strain of *S. cerevisae* ($p < 0.05$). The Ames test suggested slight dominance of the aqueous phase-soluble mutagens in naturally ventilated wards ($p < 0.05$), and a more balanced mix of aqueous and organic phase mutagens in mechanically ventilated wards. Mutagenicity testing with the D7 strain of *S. cerevisae* showed no significant differences between the naturally and mechanically ventilated wards ($p > 0.05$), but showed the relative dominance of the organic phase-soluble mutagens over the other fractions ($p < 0.05$). Few other studies have compared naturally and mechanically ventilated wards through the lens of potential effect on the mutagenic activity of air particulate matter, but more understanding in this area is important in moving towards the development and implementation of policies to optimize ventilation systems for the health and safety of hospital staff and patients. Albeit coming from the study of concentrated air particulate matter samples, the mere presence of these mutagens in the air of the hospital highlights the importance of monitoring their quality and quantity such that they do not become concentrated enough to induce mutation-related etiologies of disease such as cancer.

INTRODUCTION

Poor indoor air quality is associated with an increased incidence of respiratory tract diseases, cardiovascular diseases, and cancer (Perez-Padilla et al. 2010). Indoor air pollution is split into two major categories: bioaerosols and volatile organic compounds. Air particulate matter that comes from living things such as pollen and seeds from plants, spores from fungi, bacteria and their endotoxins, animal dander, and even expelled breath or scattered latex from humans are considered bioaerosols. Volatile organic compounds usually refer to polycyclic aromatic hydrocarbons (PAHs), which can be found attached to air particulate matter, both indoors and outdoors, and are known to have mutagenic and carcinogenic effects (El-Sharkawy & Noweir 2014, Loh et al. 2007).

Generally, indoor air pollution comes from outdoor air, cigarette smoke, activities such as cooking and cleaning, and emissions from appliances such as air conditioners and fax machines (Apte & Salvi 2016). This means that how a space is ventilated determines the characteristics of the air particulate matter contained within it. Naturally ventilated spaces have the benefit of higher turnover rate of air in a room, quickly dispersing any existing pathogens and harmful particles, but exposing people to new pathogens and particles unfiltered. Mechanically ventilated spaces have the benefit of filtration of the air that enters the room, but with both a slow turnover rate and an added source of pollutant: the air conditioner and/or filter when contaminated (Hobday & Dancer 2013). Both the types of ventilation can be found in the hospital setting.

The hospital requires indoor air quality conducive to the recovery of patients with poor health. These vulnerable pop-

ulations are typically more susceptible to the development of diseases and potentially harmful effects of pollution in their environment. Studying the air quality and characteristics of the air particulate matter according to the type of ventilation has implications on the development of policies and practices that may improve the indoor air quality in the hospital, and thus, reduce any disease risks associated with poor air quality.

The Ames test in *Salmonella typhimurium* is the gold standard for mutagenicity testing. A variety of strains exist to test for the induction of different mutations with the repair systems for the genetic material removed. In the absence of S9 activation, substances are tested for their mutagenic activity in their entirety, not undergoing any sort of metabolism or fragmentation (Mortelmans & Zieger 2000). Mutagenicity testing using the D7 strain of *Saccharomyces cerevisae*, a strain developed and described by Zimmerman (1975), is less mainstream, but being a eukaryotic system, possesses the natural ability to metabolize substances without any additional enzymes to the media and with a single strain tests for three types of mutagenic activity alongside their respective DNA repair mechanisms. This model provides a good contrast to the prokaryotic, non-metabolizing, non-repairing *S. typhimurium* that is the most well-known and widely-used methodology in mutagenicity testing.

MATERIALS AND METHODS

Air Sample Collection and Processing

Air sampling was performed for seventy-two hours (72 hours) in four different hospital wards, 2 naturally ventilated and 2 mechanically ventilated, with roughly the same floor area per ward. During the collection period, both the wards were filled to capacity. The naturally ventilated wards contained about 70 people on average (30 beds for patients, all of whom had at least 1 companion with them constantly and 8-12 health professionals on duty). The mechanically ventilated wards were both ventilated by the same type of air conditioner set-ups and contained an average of about 30 people during the collection period (20 beds for patients, no patient companions as per hospital policy, and a team of 8-12 health professionals).

The air collection set-up was a chamber containing sterile phosphate buffer solution (PBS) attached to an air collection pump placed at a height of about 1.5 meters (average height at which humans breathe) inside each ward. Immediately following collection, the suspension was filtered through Whatman filter paper (pore size 0.45 μm), and fractionated into aqueous and organic phases. A portion of the bulk phase was also kept to be run alongside the fractionated components. Samples were stored at 4 degrees Celsius. For both, the Ames test and the mutagenicity testing with the D7 strain of *S. cerevisae*, samples were serially diluted prior to testing. Three concentrations of each fractionated sample were used: undiluted or 100% concentrated (100% conc.), 10% concentrated (10% conc.), and 1% concentrated (1% conc.).

Ames Test

Salmonella typhimurium strain TA100 was procured from Dr. Keichi Sugiyama of the Division of Genetics and Mutagenesis, National Institute of Hygienic Sciences (Tokyo, Japan). The TA100 strain detects base-pair substitutions on the *hisG* gene for histidine synthesis without the benefit of any type of repair system for DNA damage (Maron & Ames 1983). Ames test for mutagenicity traditional pour plate method was performed according to established protocols (Ames 1975, Maron & Ames 1983, Mortelmans & Zieger 2000). S9 activation was not used. Bacterial cells were incubated with shaking for 18 hours at 37 degrees Celsius in LB broth with ampicillin prior to their exposure to the air particulate matter samples to ensure that the bacteria were at the log phase during the exposure. Following a two hour period of exposure to samples at 37 degrees Celsius, sample was washed off. A positive control of sodium azide dissolved in sterile PBS (10 μg/mL) and negative control of sterile PBS alone were run alongside the samples. All the assays were run in triplicate.

Mutagenicity Testing in the D7 Strain of *S. cerevisae*

The D7 strain of *Saccharomyces cerevisae* was a gift from Dr. Pamela Marshall of the School of Mathematical and Natural Sciences, New College of Interdisciplinary Arts and Sciences, Arizona State University (West campus, Arizona, USA). Isolation and preparation of the D7 strain were performed according to previously validated and published protocol (Marshall 2007, Zimmerman 1975). Three types of media were used in this assay: yeast nitrogen base (YNB) agar, yeast nitrogen base agar without isoleucine (YNB-iso), and yeast nitrogen base agar without tryptophan (YNB-trp). Each type of media is used to test a different mutation at a different gene locus alongside the repair mechanism induced by mutagenesis: heteroallelic *ade2* causing a change in colony colour from white to pink on non-deficient media (YNB), *trp5* mutation causing inability to grow on tryptophan-deficient media (YNB-trp), and *ilv1* mutation causing inability to grow on isoleucine-deficient media (YNB-iso) (Marshall 2007, Zimmerman 1975).

Yeast cells were incubated in yeast nitrogen base broth at 28 degrees Celsius in a shaking incubator for 18 hours prior to exposure to the air particulate matter samples. Cells were exposed to the air particulate matter samples for 2

hours at 28 degrees Celsius, and sample was subsequently washed off. Cells were plated using the drop plate method optimized to yield countable colonies within a 48-hour growth period at 28 degrees Celsius. Controls of ethidium bromide (positive) at 10 µg/mL and sterile PBS (negative) were run together with the samples. All the assays were performed in triplicate.

Data Analysis

The Ames results and mutagenicity testing with the D7 strain of *S. cerevisae* results were run separately. With the Ames test plates, mutagenicity ratios were calculated by dividing each sample revertant colony count by the number of revertant colonies of the negative control. A mutagenicity ratio greater than or equal to 2.00 is a positive result according to the two-fold rule (Cariello & Piegorsch 1996, Mortelmans & Zieger 2000). This result implies that the spontaneous reversion rate has to at least be doubled by a substance in order to be considered mutagenic. Statistically significant differences between naturally and mechanically ventilated wards, as well as the bulk, aqueous, and organic fractions of the air particulate matter were calculated through a Two-Way Analysis of Variance (ANOVA) with a Tukey's post-hoc test using the means of the absolute colony counts (ACCs) at a significance level of $p < 0.05$.

For the mutagenicity testing with the D7 strain of *S. cerevisae*, absolute colony counts (ACCs) on the YNB-iso and YNB-trp plates were averaged, and compared using a Two-Way Analysis of Variance (ANOVA) with a Tukey's post hoc test. Substances were considered mutagenic if they were found to have significantly more colonies than the negative control at significance level of $p < 0.05$. Only single colonies were grown on the YNB media plates. Samples were considered mutagenic if the color of the single colony was pink instead of its typical white appearance, and were thus, qualitatively evaluated.

RESULTS

Ames Test

All the concentrations of bulk, aqueous, and organic fractions of air particulate matter collected from naturally and mechanically ventilated wards in a public urban hospital are mutagenic following the two-fold rule (Table 1). Within naturally ventilated wards, the aqueous fraction ACCs were significantly higher than the bulk and organic fractions ($p < 0.05$) (Fig. 1). Bulk fraction ACCs were the highest in mechanically ventilated wards, but this difference was not statistically significant ($p > 0.05$) (Fig. 2).

Mutagenicity Testing Using the D7 Strain of S. cerevisae

The D7 strain of *Saccharomyces cerevisae* can test for three different mutations: mitotic crossing over with recombinational repair, mitotic gene conversion with mismatch repair, and reverse point mutation (Marshall 2007). Mitotic crossing over with recombinational repair was not detected on

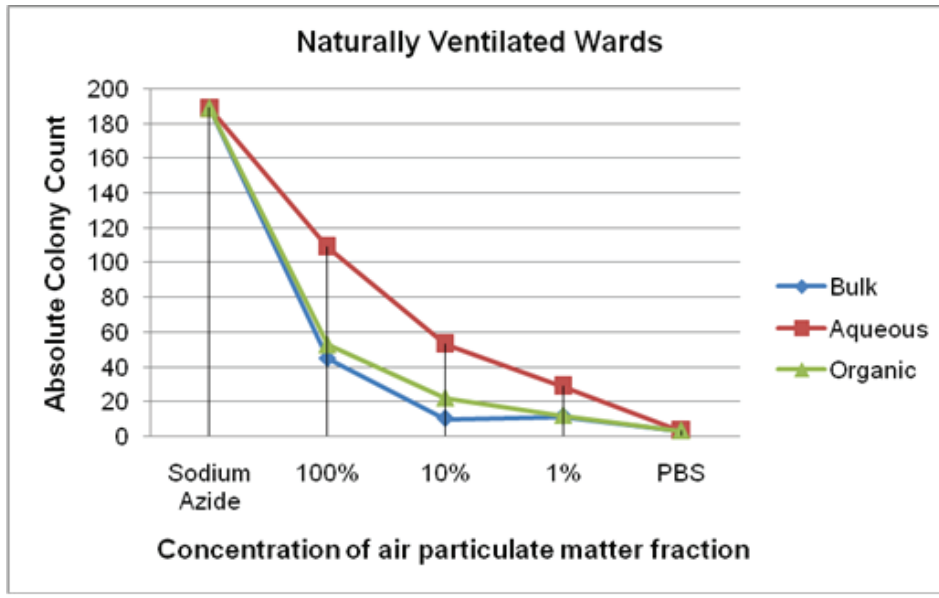

Fig. 1: Comparison of bulk, aqueous and organic fractions of air particulate matter absolute colony counts of *S typhimurium* TA 100 in naturally ventilated hospital wards.

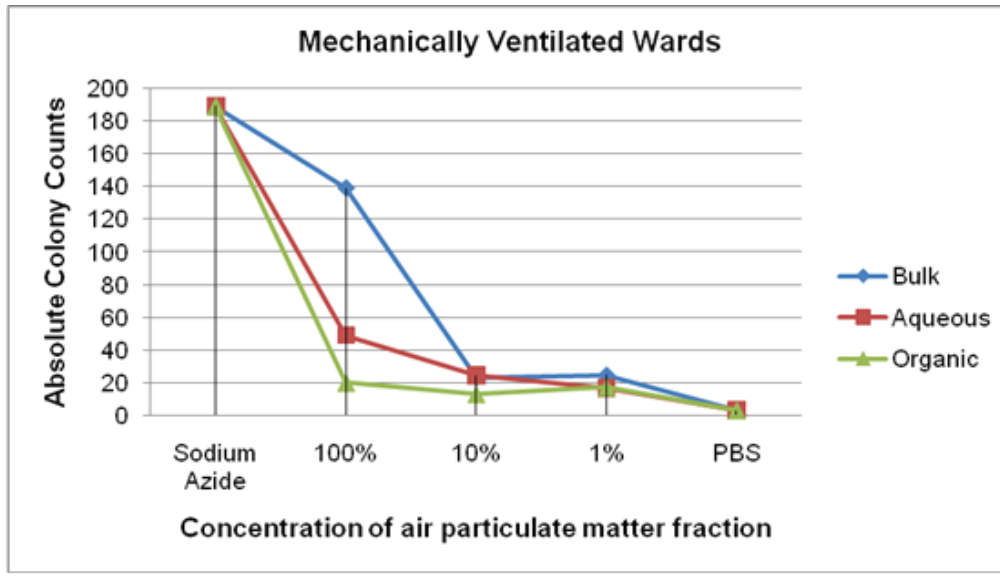

Fig. 2: Comparison of bulk, aqueous and organic fractions of air particulate matter absolute colony counts of *S typhimurium* TA 100 in mechanically ventilated hospital wards.

the YNB media (non-deficient media), as all of the colonies that grew were white in colour (Table 2).

Growth of yeast cell colonies was shown on both the YNB-trp and YNB-iso plates. Statistical significance testing of the absolute colony counts (ACCs) showed evidence of mitotic gene conversion with mismatch repair in that YNB-trp plates (tryptophan-deficient media) had significantly higher ACCs with all concentrations of the bulk, aqueous, and organic fractions of air particulate matter when compared against the negative control ($p < 0.05$) (Table 3). Reverse point mutation was also detected, as isoleucine-deficient media (YNB-iso) also showed statistically significant growth of colonies at all concentrations of all fractions ($p < 0.05$) (Table 4).

No significant differences were detected between naturally and mechanically ventilated wards ($p > 0.05$). For both the ventilation systems, the organic fraction produced significantly higher ACCs in both YNB-iso and YNB-trp media ($p < 0.05$) than bulk and aqueous fractions, especially at maximum, undiluted concentration (100% conc.) where it surpassed the positive control. Bulk and aqueous fractions were similar to one another ($p > 0.05$) with both fractions showing no significant differences among their various concentrations.

Table 1: Mutagenicity ratios (MR) of bulk, aqueous and organic fractions of air particulate matter from naturally and mechanically ventilated hospital wards with strain TA100 of *S. typhimurium.*

	Bulk				Aqueous				Organic			
	Natural	Result*	Mechanical	Result *	Natural	Result*	Mechanical	Result *	Natural	Result*	Mechanical	Result *
Sodium azide	56.78	+	56.78	+	56.78	+	56.78	+	56.78	+	56.78	+
100% conc.	13.46	+	41.79	+	32.78	+	14.77	+	15.86	+	6.06	+
10% conc.	3.10	+	7.01	+	16.02	+	7.41	+	6.66	+	5.20	+
1% conc.	3.45	+	7.46	+	8.71	+	5.16	+	3.65	+	3.95	+
PBS	1.00	-	1.00	-	1.00	-	1.00	-	1.00	-	1.00	-

*Positive result according to the 2-point rule (Cariello & Piegorsch 1996; Mortelmans & Zieger 2000)

Table 2: Presence of pink D7 *S. cerevisae* colonies on YNB (non-deficient media) plates.

	Bulk	Aqueous	Organic
	Result*	Result*	Result*
Ethidium bromide	+	+	+
100% conc.	-	-	-
10% conc.	-	-	-
1% conc.	-	-	-
PBS	-	-	-

*Positive result indicates pink color of single colony, while negative result indicates white

Table 3: Absolute colony count for YNB-trp plates.

	Bulk				Aqueous				Organic			
	Natural	Result*	Mechanical	Result *	Natural	Result*	Mechanical	Result*	Natural	Result*	Mechanical	Result*
Ethidium bromide	6	+	6	+	6	+	6	+	6	+	6	+
100% conc.	3.67	+	2.83	+	7	+	4	+	12.65	+	7.67	+
10% conc.	8.5	+	3.17	+	8.83	+	4	+	6.83	+	3	+
1% conc.	9	+	1	+	6.5	+	3.67	+	5.17	+	4	+
PBS	0.33	-	0.33	-	0.33	-	0.33	-	0.33	-	0.33	-

*Positive result indicates statistically significant difference from the negative control (PBS) at $p < 0.05$

DISCUSSION

Air particulate matter was collected from naturally and mechanically ventilated hospital wards and fractionated into bulk, aqueous, and organic partitions. Two different methods were used to test the mutagenicity of the air particulate matter fractions: the Ames test and mutagenicity testing with the D7 strain of *S. cerevisae*.

When subject to the Ames test, all fractions at all the concentrations were found to be mutagenic, yielding a broad range of mutagenicity ratios (3.45-41.79). Mutagenic activity was shown to be dose-related with higher concentrations of air particulate matter fractions alongside higher absolute colony counts, resulting in higher mutagenicity ratios. These results suggest that the air particulate matter collected from these hospital wards are able to increase the spontaneous reversion rate of the TA 100 strain of *Salmonella typhimurium*, and thus, have mutagenic activity.

Variations in absolute colony counts (ACCs) among the different fractions hinted towards a more dominant aqueous component in naturally ventilated wards. Higher levels of non-organic indoor air pollutants such as soluble salts, heavy metals, and bioaerosols (air particulate matter from living organisms such as bacterial endotoxins, fungal spores, and animal dander) are associated with more densely populated and naturally ventilated wards (El-Sharkawy & Noweir 2014). Thus, this more dominant aqueous phase may be related to how the naturally ventilated wards of this hospital are more densely populated and more exposed to biological organisms through windows open to the outside of the hospital.

With the mechanically ventilated wards, there was a more balanced combination of aqueous and organic components. Mechanical ventilation systems such as air conditioners can contribute to both emission and dilution/dispersion of potentially harmful chemicals and bioaerosols. Poorly cleaned air conditioning units tend to become a repository for dust and animal dander, and even breeding grounds for potentially harmful and infective fungi and bacteria (Apte & Salvi 2016). Chemical coolants used to control the temperature in rooms typically come in the form of organic chemicals, sometimes chlorofluorocarbons (CFCs) that are known to be mutagenic in particular doses (Benigni et al. 2009). Air conditioners and temperature control devices have also been found to emit certain levels of volatile organic compounds, again, known mutagens that may attach themselves to air particulate matter. Mechanical ventilation systems that are poorly maintained or make use of chemicals that can be mutagenic or toxic to humans thus contribute to and circulate these indoor air pollutants. On

Table 4: Number of revertant colonies for YNB-iso plates.

	Bulk				Aqueous				Organic			
	Natural	Result*	Mechanical	Result *	Natural	Result*	Mechanical	Result *	Natural	Result*	Mechanical	Result *
Ethidium bromide	11.67	+	11.67	+	11.67	+	11.67	+	11.67	+	11.67	+
100% conc.	4.17	+	5.83	+	4.67	+	9	+	26.33	+	17.67	+
10% conc.	4.83	+	9.83	+	9.33	+	10	+	5.33	+	9.33	+
1% conc.	7.83	+	13.83	+	5.67	+	7.83	+	5.17	+	4	+
PBS	0.33	-	0.33	-	0.33	-	0.33	-	0.33	-	0.33	-

*Positive result indicates statistically significant difference from the negative control (PBS) at $p < 0.05$

the other hand, a filtration system within the mechanical ventilation system can contribute to removing any hazardous components from the circulation and air mechanical ventilation set-ups that do not make use of harmful organic chemicals and thus, would not introduce these into the air circulation of the hospital are currently available market options (Hodgson et al. 1994, Xu et al. 2015). The mechanical ventilation systems of the hospital currently have no filtration mechanisms, and there is the potential that they are contributing more to the indoor air pollution than working towards its dilution or dispersion.

While the nature of the air particulate matter with mutagenic activity in the differentially ventilated wards is hinted at by the Ames test, the manner in which it may be received and processed by the human body is reflected in the mutagenicity testing with the D7 strain of *S. cerevisae*. This is because this model is eukaryotic system with the natural capacity for metabolizing substances that are taken in and intact DNA repair mechanisms for when damage is incurred. Results showed that regardless of ventilation system, the organic fraction produced the greatest mutagenic activity with absolute colony counts (ACCs) greater than even the positive control for both types of media, representing mitotic gene conversion (YNB-trp) and reverse point mutation (YNB-iso). Mitotic crossing over, on the other hand, was not detected on the YNB media. Polycyclic aromatic hydrocarbons (PAHs) tend to display levels of toxicity prior to break down, but their toxic and mutagenic effects, and thus, their harmfulness can increase following metabolism into their simpler chemical constituents (Balbo et al. 2014). Previous work has shown that even at low levels, these volatile and semi-volatile organic compounds can display notable levels of toxicity and mutagenicity (Hodgson et al. 1994).

The results of both the assays support one another in that the sampled air particulate matter is mutagenic. The YNB-iso plates test for a reverse point mutation to the *ilv1* locus on *Saccharomyces cerevisae*, that corrects the induced isoleucine auxotrophy on the strain similar to how the TA 100 strain is designed to test for the back-mutation of the induced histidine auxotrophy at the *hisG46* locus of *Salmonella typhimurium*. Positive results in both assays at all concentrations of all fractions support the presence of an increased rate of reverse point mutations in the presence of the air particulate matter fractions.

CONCLUSION AND FUTURE DIRECTIONS

In summary, the air particulate matter in the public urban hospital sampled has mutagenic activity according to both the Ames test and mutagenicity testing with the D7 strain of *S. cerevisae*. Although the nature of the dominant components of the mutagen may vary according to the ventilation system applied to the ward, it appears that intake and processing of the mutagen in eukaryotic systems is fairly constant across ventilation type. This may then suggest that policies and practices to improve the air quality of the hospital should be applied to wards of both types of ventilation systems, and move towards minimizing the concentrations of organic pollutants.

It must be noted that these significant results were detected using samples that concentrated 3 days'-worth of air particulate matter into small volume containers. This may not necessarily reflect the air being breathed in larger volume hospital wards, and thus, the study should cause any kind of panic about the harmfulness of the air in the hospital. In-depth fractionation and analysis of the different of the components of the indoor air, as well as monitoring the quality of the air alongside relevant practices and policies geared towards improving the air quality would lead to a more complete understanding, and thus, a more detailed action plan for improving hospital air quality at the administrative level.

ACKNOWLEDGEMENT

This project was supported by the Biological Models Laboratory based in the Department of Biochemistry and Molecular Biology, College of Medicine, University of the Philippines Manila, and the Institute of Clinical Epidemiology, National Institutes of Health, University of the Philippines Manila. Special thanks are given to Jeremiah Valencia Reyes, Cristine Joy Devilles, Lordom Grecia, Jared Dela Rosa, Maria Katrina Diana Cruz, and Jermaine Catherine Ramos. Thanks are also given to the Philippine Council for Health and Development Research.

REFERENCES

Apte, K. and Salvi, S. 2016. Household air pollution and its effects on health. F1000Res., 5: 2593.

Balbo, S., Turesky, R. J. and Villalta, P. W. 2014. DNA adductomics. Chem. Res. Tox., 27(3): 356-366.

Benigni, R., Cotta-Ramusino, M. and Andreoli, C. 1991. Relationship between chlorofluoro-carbon chemical structure and their Salmonella mutagenicity. J. Tox. Env. Health, 34(3): 397-407.

Błaszczyk, E., Rogula-Kozłowska, W., Klejnowski, K., Fulara, I. and Mielżyńska-Švach, D. 2016. Polycyclic aromatic hydrocarbons bound to outdoor and indoor airborne particles (PM2.5) and their mutagenicity and carcinogenicity in Silesian kindergartens, Poland. Air Qual. Atmosphere Health, 10(3): 389-400.

Cariello, N. F. and Piegorsch, W. W. 1996. The Ames test: The two-fold rule revisited. Mut. Res. Gen. Tox., 369(1-2): 23-31.

El-Sharkawy, M. and Noweir, M. H. 2014. Indoor air quality levels in a university hospital in the eastern province of Saudi Arabia. J. Fam. Comm. Med., 21(1): 39.

Hobday, R. and Dancer, S. 2013. Roles of sunlight and natural ventilation for controlling infection: Historical and current perspectives. J. Hospital Infection, 84(4): 271-282.

Hodgson, M., Levin, H. and Volkoff, P. 1994. Volatile organic compounds and indoor air. J. Allergy ClinImmuno., 94(2): 296-303.

Loh, M. M., Levy, J. I., Spengler, J. D., Houseman, E. A. and Bennett, D. H. 2007. Ranking cancer risks of organic hazardous air pollutants in the United States. Env. Health Perspectives, 115(8): 1160-1168.

Maron, D. M. and Ames, B. N. 1983. Revised methods for the Salmonella mutagenicity test. Mut. Res. Env. Mut. Rel. Subj., 113(3-4): 173-215.

Marshall, P. A. 2007. Using Saccharomyces cerevisiae to test the mutagenicity of household compounds: An open ended hypothesis-driven teaching lab. CBE-Life Sci. Ed., 6(4): 307-315.

Mortelmans, K. and Zeiger, E. 2000. The Ames Salmonella/microsome mutagenicity assay. Mut. Research Fund Mol. Mech. Mut., 455(1-2): 29-60.

Perez-Padilla, R., Schilmann, A. and Riojoas-Rodriguez, H. 2010. Respiratory health effects of indoor air pollution. Int. J. of Tuberculosis Lung Disease, 14(9): 1079-1086.

Xu, Y., Liang, Y., Urquidi, J. R. and Siegel, J. A. 2014. Semi-volatile organic compounds in heating, ventilation, and air-conditioning filter dust in retail stores. Indoor Air, 25(1): 79-92.

Zimmermann, F. 1975. A yeast strain for simultaneous detection of induced mitotic crossing over, mitotic gene conversion and reverse mutation. Mut. Res. Gen. Tox., 28(3): 381-388.

Nature Environment and Pollution Technology
An International Quarterly Scientific Journal

p-ISSN: 0972-6268
e-ISSN: 2395-3454

Vol. 18 | No. 4 | pp. 1471-1478 | 2019

Original Research Paper | Open Access

Assessment of Annual Effective Dose from the Indoor Radon in Bathinda District of Punjab in India

Amit Arora*†, Rohit Mehra, Rajeev Kumar Garg* and Anand K. Tyagi*****

*Department of Chemical Engineering, Shaheed Bhagat Singh State Technical Campus, Ferozepur, Punjab, India
**Department of Physics, Dr. B R Ambedkar National Institute of Technology, Jalandhar, Punjab, India
***Department of Applied Sciences, Shaheed Bhagat Singh State Technical Campus, Ferozepur, Punjab, India
†Corresponding author: Amit Arora

Nat. Env. & Poll. Tech.
Website: www.neptjournal.com

Received: 05-06-2019
Accepted: 22-06-2019

Key Words:
Radon
Dwellings
LR-115 type II films
BTD-7-BTD-8
Annual effective dose

ABSTRACT

Carrying out of indoor radon studies have been done in the 50 dwellings of Bathinda district (Punjab), India using LR-115 type II cellulose nitrate films in the bare mode. The films were exposed into four consecutive trimesters, i.e. from March 2010 to February 2011. The work has been undertaken for health risk assessment. The calibration constant of 1 track $cm^{-2}day^{-1}$ equal to 50 Bqm^{-3} (Becquerel/m^3) was used. In the present study average radon values vary from 83.15 (BTD-7) to 124.35 (BTD-8) Bqm^{-3} in different villages, which are higher than the word average value of 40 Bqm^{-3}. The inhabitants of the area of study receive average annual radiation dose varying from 1.41 (BTD-7) - 2.12 (BTD-8) mSv (millisievert). The effective dose is found to be less than lower limit of the recommended action level (3-10 mSv). The value of radon for the first floor portion of the same dwelling is lower in comparison to the ground floor. The values in the cemented floors are lower than in the dwellings with the un-cemented floors. The indoor radon values are more in very poorly ventilated dwellings in comparison to the very well-ventilated dwellings.

INTRODUCTION

UNSCEAR (1994) has revealed that a radioactive inert gas Radon (^{222}Rn) is a decay product of radium occurring naturally in the uranium series and almost half of the radiation dose received by common residents is from Radon (^{222}Rn). Kitto et al. (2009) found that 15,000-20,000 lung cancer deaths per year are related to Radon. As of 2005 in USA 90139 men and 69078 women died of lung cancer. The studies have been conducted in U.S.A., Canada, Australia, china and Europe, which have consistently shown an increase in lung cancer with exposure to radon decay products. Radon is a noble radioactive, invisible, odourless, tasteless and natural occurring gas which cannot be detected with the human senses. In 1923, the International Committee for Chemical Elements and International Union of Pure and Applied Chemistry (IUPAC) choose its name to be radon. Archer et al. (2004) has found that being single atom gas, it can penetrate many materials like paper, low density plastic, gypsum and concrete. When radon is condensed, it starts glowing because of the intense radiations it produces. Auxier et al. (1973) revealed that the concentration of radium (^{226}Ra) in alum shale varies from 125-43000 $Bq.kg^{-1}$, from 1-60 $Bqkg^{-1}$ in sand stone, and from 5-40 $Bqkg^{-1}$ in lime stone, which decays into radon by emitting α-particle. The natural concentration of radon in ambient outdoor air is about 10 Bqm^{-3}. Radon gets dissolved into groundwater and can be released into the air when the water is used. Radon is present in almost all the air. Every one of us breathes radon everyday but its concentration varies. Radon is significant contaminant, which affects indoor air quality worldwide. Radon gas levels vary with one location to another and with the composition of the underlying soil and rocks. Lide (1963) found that radon entry rate from subjacent earth and outdoor air is 56%and 20% respectively. Transport of radon is carried out by molecular diffusion or by forced transport. Henshaw et al. (1990) claimed that indoor radon exposure is associated with the risk of leukaemia and certain other cancers, such as cancers and melanoma of the prostate and kidney. Large temporal and local fluctuations are shown by the concentration of radon and its decay products in the indoor atmosphere due to variation in nature of building materials pressure, temperature, wind speed and ventilation conditions, etc.

Indoor Radon Sources

Radon is a problem in all types of dwellings, i.e. cold, new, draftee, insulated, etc. In outdoors radon is diluted to low concentration in the air, hence, it possesses less risk than indoors. The two major factors which can help in magnifying the radon concentration indoor are building materials and underlying soil. Few important sources (Fig. 1) are shown in the house as per following:

- Cracks in solid floors
- Construction joints
- Drainage hole
- Water supply
- Cavities inside walls
- Fractures in walls
- Gaps around service pipes

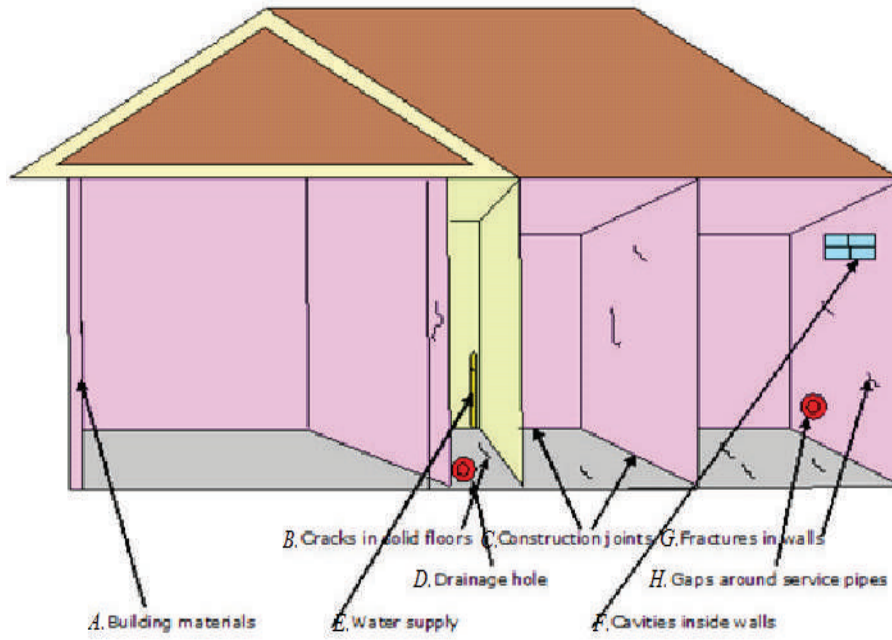

Fig. 1: Sources of radon in a house.

Radon and Lung Carcinoma

In 1597, the high incidence of lung disease was first noted by Agricola. There is association between indoor radon exposure and lung carcinoma as claimed. The mechanism of lung cancer due to radon exposure is explained below:

An unusual high mortality from lung disease was observed among the miners in Schneeberg Region of Germany in early 16th century. The occurrence of this lung disease increased manifolds in 17th and 18th century when mining was increased and later on this disease was identified as lung cancer by Harting & Hesse in 1879. About 15 years later, Ludewig and Lorenzer purposed that high lung cancer occurred among the Schneeberg miners because of high radon concentration of the order of 1000 Bqm^{-3} or higher Porstendorfer et al. (1994) . Bale et al. (1956) the real cause for the lung cancer is not the inhalation of Radon (^{222}Rn) the short lived daughters like ^{218}Po, ^{214}Pb, ^{214}Bi and ^{214}Po).

Types of Lung Cancer

Of all lung cancers, small cell (oat cell carcinoma) accounts for 10-15% and non-small cell accounts for 85-90% of are lung cancer type's small cell carcinoma. This is divided further as follows:

- Adeno carcinoma - 40%
- Squamous cell carcinoma - 25-30%
- Large cell carcinoma - 10-15%

Sun et al. (2007) revealed that the most common type of lung cancer is Adeno carcinoma in never smokers.

Mechanism of Lung Cancer Due to Radon Exposure and its Progeny

As per the American Cancer Society (2008) Radon-222 (^{222}Rn) is carcinogenic to human beings. Radon is claimed to be second leading cause of lung cancer. Evidence shows that generally cancers are of monoclonal origin, i.e. their origination from damage to a single cell. Cytoplasm and nuclei of the secretary cells and basal cells in the bronchioles are presumed to be regarded as sensitive targets, both of whose location is in the epithelial lining of the bronchial tree. For tumour growth, minimum estimated time is 5 years from initial cells transformation to clinical detection. A multiplicative interaction is there from exposure to radon

progeny and cigarette smoking. Before the age of 40 years lung cancer is rare. Occurrence of radon related deaths have not been there if the victims would have not smoked. After inhalation, some of the radon progeny are deposited and attached to bronchiolar epithelium; this deposited progeny will irradiate the cells with alpha particles, the basal cells in the bronchiolar epithelium are attacked and some of the deposited activity is spread by the body fluids to other organs. Unattached progeny is filtered by the nose. The ionization radiation emitted by radon can cause genetic mutation which depends upon:

- Type of radiation
- Dose rate
- Part of the body exposed
- Age and health of the person exposed

Lung cancer epidemiological studies on underground miners have shown that inhalation of radon progeny is related with risk of lung cancer. Rerichal et al. (2006) and Smith et al. (2007) found that there is sufficient evidence available that lung tumours in miners exposed to radon progeny have a characteristic mutation pattern in the p-53 tumour suppressor, but these kinds of data further need conformation. Even the human foetuses are affected by radiations. Radon is an inert gas because of which, it has low solubility in body fluid. The majority of lung cancers are caused by the isotopes ^{214}Po and ^{218}Po. Research has revealed in experiments on animals that lung cancer may be induced by exposure to radon progeny as low as 20 WLM (working level month) corresponding to a life time 70-year exposure of about 60 Bqm^{-3}. Radon decay products ^{218}Po and ^{214}Po get attached to aerosols or dust particles; if inhaled then they get trapped in the lungs where mucous membranes cells, bronchi and other pulmonary tissues are affected. The ionising radiation energy affecting the bronchial epithelial cells actually is believed to start off the process of carcinoma genesis. The fat content of organ is the determining factor of concentration of Radon as of because compared to blood radon is 16 times more soluble in fat. Miles et al. (1992) study has shown a yearly dose of 16 µSv to soft tissue consisting of 1% fat arise from exposure at 20 Bqm^{-3} in dwellings. Risk of leukaemia induction is present due to high fat content in bone marrow, from indoor radon exposure. 40% fats are contained by the red bone marrow, applying the speculations that the fat is dissolved constantly in bone marrow, and the yearly dose rising from exposure at 20 Bqm^{-3} can be calculated as 96 µSv (Richardson et al. 1991), but distribution of fat is not uniform, therefore, the sensitive cells are delivered with the maximum delivery dose in the bone marrow Miles et al. (1992), so the value of 96 µSv is likely to overestimate the annual dose. The action level of 200-600 µSv suggested by ICRP (1993) is likely not to increase further from 0.1-0.3 mSv for irradiation of red bone marrow, hence from radon exposure rise in lung cancer is the major health risk. Electrically charged daughter products get attached to minute dust particles, water, oxygen present in indoor air, vapours inhalation and solid surfaces of these aerosols into the lungs make it get attached to the epithelial lining of the lungs which may irradiate the tissue. These daughter products are decayed by emitting alpha particles, beta particles and gamma radiations, but out of them beta particles and gamma radiations have lower biological effects, so the doses from these are negligible. Alpha radiation may mutate the DNA of lung cells, which may initiate few events leading to cancer. Health hazard from radon is smaller than from its progeny due to their long half-life. Alpha radiations can damage DNA and induce mutation which may defect once genes, this may result in neoplasm formation. When inhaled these radioactive particles can damage cells that line the lungs which lead to lung cancer. Since, penetration of alpha particles is not more than a fraction of a millimetre into the tissues, hence the damages confined to the lung tissue in the immediate area. There is no well-known organisation at present that recommends screening for early detection of lung cancer (Collins et al. 2007), but Henschke et al. (2008) in their study in a new England General of medicine particle, have revealed that lung cancer can be detected in 85% of patients in their early stage by the use of annual low dose CT screening.

Cancer Other Than Lung Due to Radon Exposure

A study claimed that indoor exposure is associated with the risk of leukaemia and cancers of kidney and prostate. There have been studies showing correlations between domestic radon levels and cancer of specific sites, cancer of stomach and liver are found to have co-relation with radon exposure. There is relationship between radon and leukaemia as supported by studies. The radon progeny can attach itself to the smoke of cigarette, which is lodged with in the lungs. Radon is considered to be a known human carcinogen (classified by IARC as Group 1).

Geography of Bathinda Area

Bhatinda is located in the southern part of Punjab State, the heart of Malwa region. Faridkot Revenue Commissioner's Division, a newly created division is also consisted by this district and is located between north latitude (29^{o}33' & 30^{o}36') and east longitude (74^{o}38' & 75^{o}46'). The region is enclosed with places of Haryana State like Sirsa and Fatehabad in south, Sangrur in east and Mansa district from north-east Moga and Muktsar and Faridkot in the north-west. Bathinda is regarded as cotton fabricating belt of Punjab.

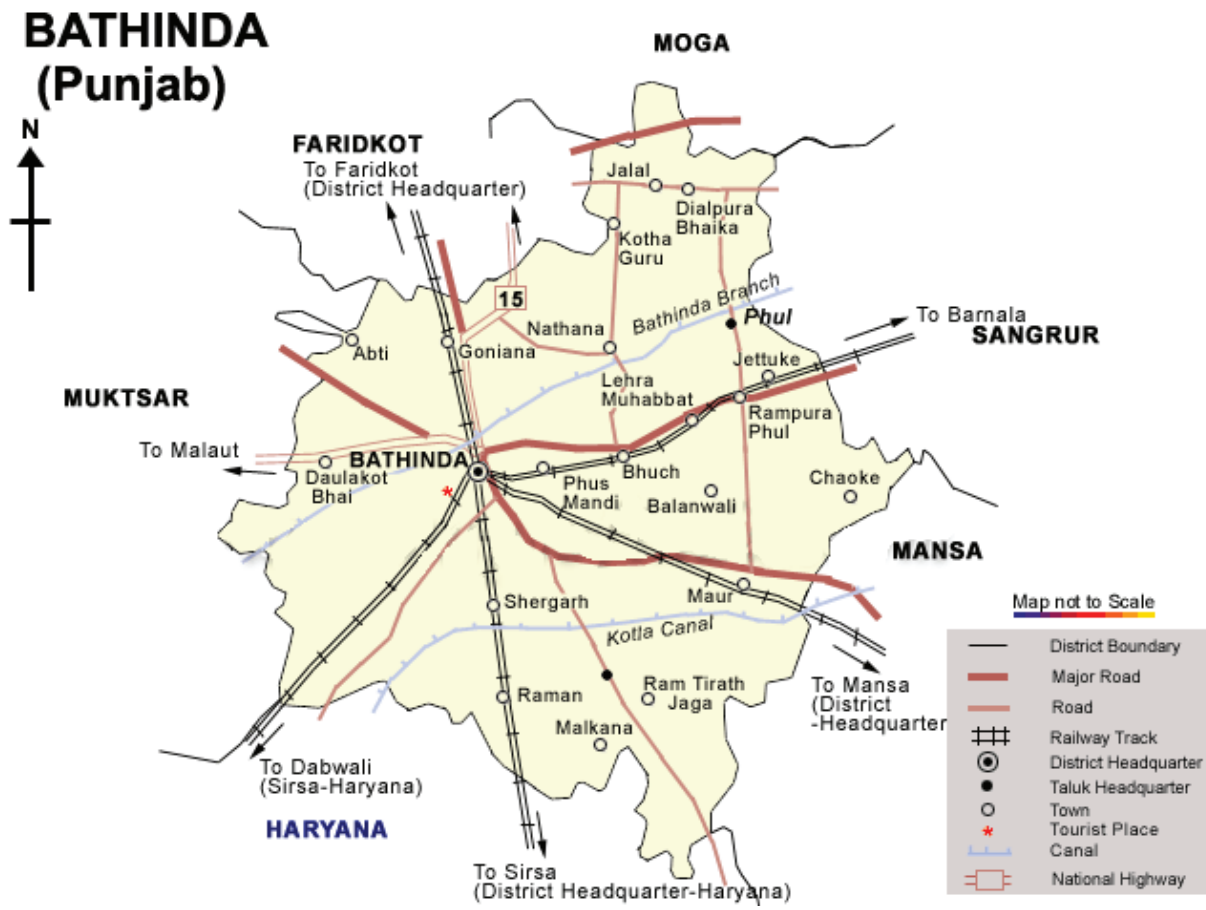

Fig. 2: Location of the study area.

The district encompass an area of 3,344 square kilometres as shown in the map. The location and the geography of the study area is shown in Fig. 2.

MATERIALS AND METHODS

LR-115 Type 2 (pelliculable) plastic track detectors of size approximately 1.3 cm × 1.5 cm were fixed on micro glass slides that were suspended at the centre of room in the bare mode for the annual duration, i.e. March 2010 to February 2011 in order to estimate the indoor concentration levels of radon by breaking it into four successive trimesters. To avoid any disturbance in the reactors due to the resident's movements, the detectors were suspended in the rooms at a height of more than 2 meter above from the ground level and 1 meter below the ceilings of the room so that direct α-particle from the building materials of the ceiling does not reach the detectors. LR-115 type-II has a property that it can register alpha particles with energy ranging between 1.7 MeV and 4.8 MeV (Mega electron volt). The radon daughter products ranging from ^{218}PO to ^{214}PO will not be registered on LR-115 because their alpha particle energies are 6.0 and 7.68 MeV respectively, which is more than its upper threshold energy, which can be tracked by LR-115. The detection efficiency as determined by Nakhara et al. (1980), Deamkjare (1986) and Ramola et al. (1987) is about 50% of energies between 1.5 MeV and 4.8 MeV at a normal incidence. The films of LR-115 in the electromagnetic resonance are not affected by radiations or by electrons. The LR-115 type II detectors (1.3 cm × 1.5 cm) are washed in triple distilled water and deionised water in succession. We can use IR lamp and hot air blowers also for quick drying of detectors. Afterwards, the detectors are stored carefully for future use. Etching recovers the path of particle, which is being travelled during the exposure. Etching is carried under controlled temperature approximately 70°C for 90 minutes. The detectors were etched using 2.5N NaOH solution. The tracks can be enlarged by chemical etching, hence they become visible under the optical microscope. The etching of samples was conducted in a constant temperature bath.

The tracks are counted manually through an optical microscope at a magnification of 400X. Calibration factor used is 0.02 tracks $Cm^{-2}day^{-1}$ = 1.Bqm^{-3}. In the current study, the calibration factor adopted from the study of Eappen et al. (2001) for LR-115 type-II was taken after the inter-laboratory comparison exercise carried out at the national level by the Environmental Assessment Division of Bhabha Atomic Research Centre (BARC), Mumbai and is also being used by other researchers.

RESULTS AND DISCUSSION

The effect of dose received by residents annually and their life time fatality risks were estimated as per the guidelines laid down by ICRP (1993). In the present study, annual average radon values vary from 83.15 (BTD-7) to 124.35 (BTD-8) Bqm^{-3} in different villages, which are higher than the global average value of 40 Bqm^{-3} (UNSCEAR 2000). These values are less than the lower limit of action level (200 to 300 Bqm^{-3}) recommended by ICRP (1993) safeguarding work and home from radon radiations. Different works have also been reported to calculate average radon values by different workers. The inhabitants of the area of study receive an average annual dose received ranging from 1.41 (BTD-7)-2.12 (BTD-8) mSv (Table 1). The effective dose is found to be less than lower limit of the recommended action level (3-10 mSv). The annual average of radon concentration for 10 villages comes out to be 100.43 Bqm^{-3} for the present study of dwellings of Bathinda District of Punjab, for the period March 2010-February 2011 with different floor and ventilation conditions. The lifetime casualty hazard of the inhabitants of the area of study varies from 1.09×10^{-4} (BTD-7) to 1.64×10^{-4} (BTD-8) (Table1) with an average value of 1.32×10^{-4} which is 0.01% and comparatively a smaller segment as compared to 4% of the life time hazard of lung cancer due to chewing of tobacco and smoking of cigarette (Evans et al. 1981). Un-cemented floor and poor ventilated dwellings have high radon concentration levels as compared to dwellings with cemented floor with well ventilation. The reason for the former is due to the high contribution of radon from soil which enters in the room along with the less dispersion of radon and the reason for the later is due to the prevention of radon from the underlying soil to enter in the room. Also, radon concentration values for limited number of dwellings having ground floor as well as first floor have been presented. The frequency distribution of annual average radon concentration (Bqm^{-3}) in different dwellings is given in Fig. 3. The radon concentration in the above dwellings is well below the recommended level. The Fig. 4 shows the distribution of life time fatality risk and annual average dose because of radon concentration in (Bqm-3) in the dwellings of different villages Bathinda district of Punjab from March 2010-February 2011. The Fig. 5 shows the frequency distribution of annual average radon concentration (Bqm^{-3}) for 50 dwellings of different villages of Bathinda District of Punjab for the period of March 2010 to February 2011. Fig. 6 shows

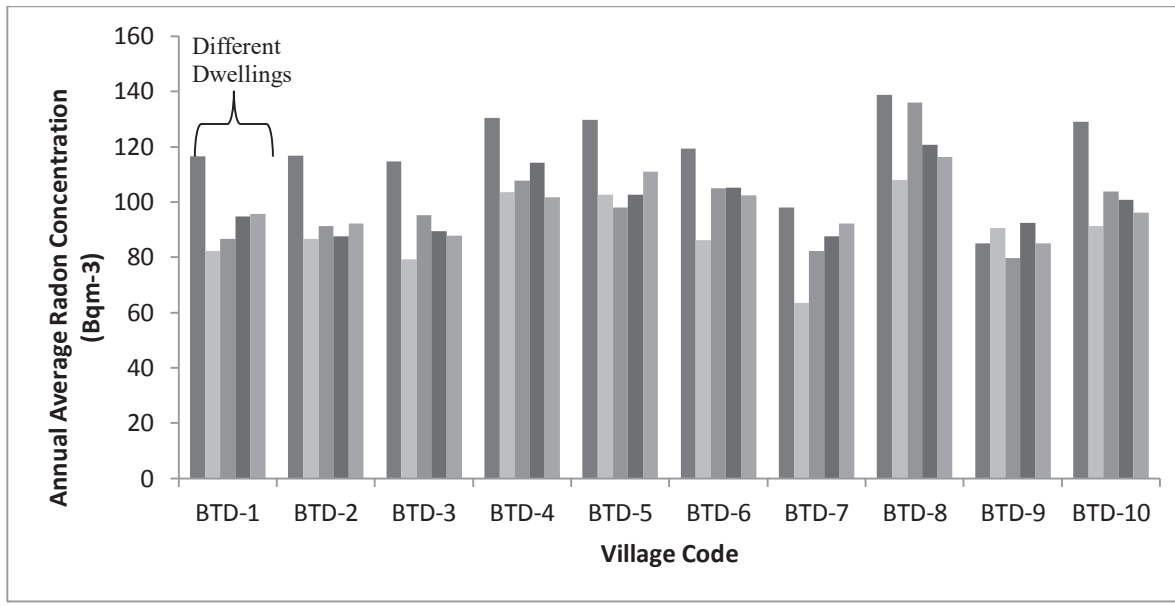

Fig. 3: Annual Average Distribution of Radon Concentration (Bqm^{-3}) level in the dwellings of different villages of Bathinda district of Punjab from March 2010-February 2011.

Table 1: Annual Average Indoor radon levels in the dwelling of Bathinda District of Punjab, corresponding Annual Average Dose and their Life Time Fatality Risk estimates for the period from March 2010 to February 2011.

Sr. No.	Village code	Villages studied	No. of dwellings studied	Radon concentration (Bqm^{-3}) from March 2010-February 2011			Geometric Mean (GM)	Geometric standard deviation (GSD)	Annual average concentraion ($Bq\ m^{-3}$)	Exposure in Working level month	Exposure ($mJ\ h\ m^{-3}$)	Life time fatality risk $\times 10^{-4}$	Annual average dose (mSv)
				Max.	Min.	Average value with ± (SD)							
1	BTD-1	Bhucho Mandi	5	163	55	95.2 ± 12.69	94.51	1.62	95.2	.418	1.47	1.25	1.62
2	BTD-2	Guniana	5	163	53	93.7 ±14.6	94.3	1.62	93.7	.412	1.45	1.23	1.59
3	BTD-3	Lehra Mohabat	5	142	59	93.3 ±12.8	92.58	1.64	93.3	.410	1.45	1.23	1.59
4	BTD-4	Rampura Phull	5	160	81	11.5 ±10.35	111.06	1.59	111.5	.490	1.73	1.47	1.90
5	BTD-5	Thermal Plant	5	182	77	108.85 ±14.79	108.30	1.62	108.85	.478	1.69	1.43	1.85
6	BTD-6	Bhagta	5	191	53	103.65 ±12.07	103.1	1.6	103.65	.456	1.61	1.36	1.76
7	BTD-7	Kotshmir	5	117	50	83.15 ±12.77	83.79`	1.63	83.15	.365	1.29	1.09	1.41
8	BTD-8	Bajakhan	5	196	78	124.35 ±14.1	123.39	1.63	124.35	.547	1.93	1.64	2.12
9	BTD-9	Pithu	5	141	43	86.35 ±10.89	86.43	1.35	86.35	.379	1.34	1.13	1.47
10	BTD-10	Nathana	5	158	73	104.2 ±14.87	103.44	1.67	104.2	.458	1.62	1.37	1.77

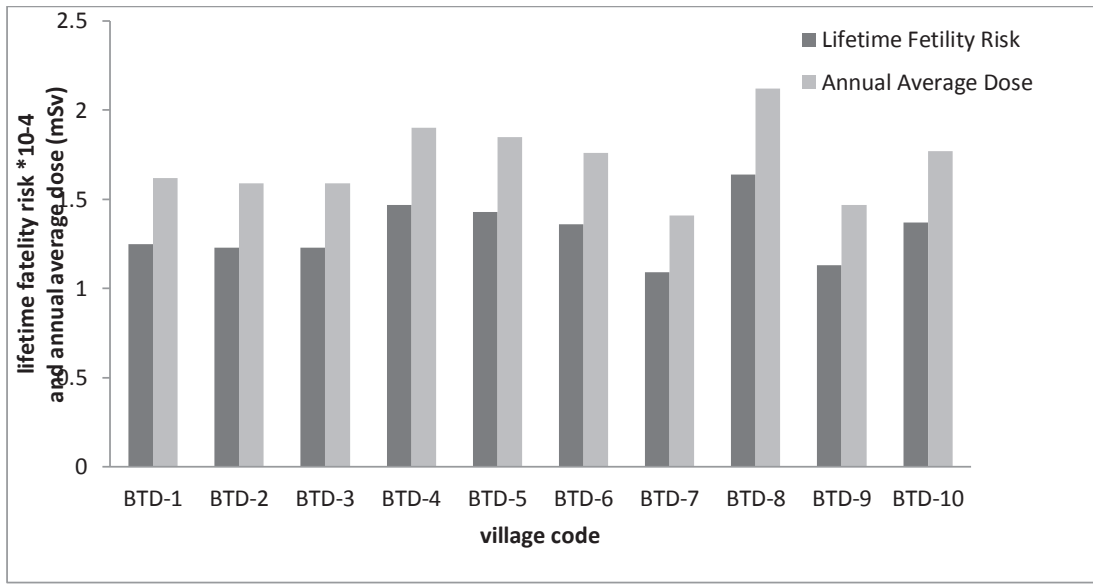

Fig. 4: Distribution of Life Time Fatality Risk and Annual Average Dose because of radon concentration (Bqm^{-3}) in the dwellings of different villages of Bathinda district of Punjab from March 2010-February 2011.

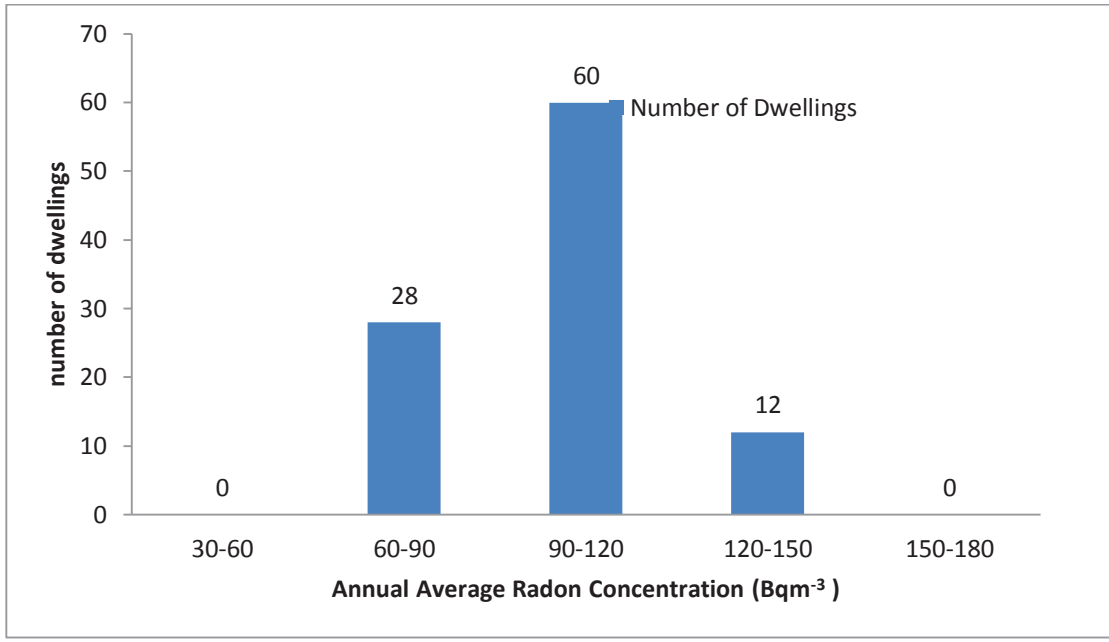

Fig. 5: Frequency distribution of Annual Average Radon Concentration (Bqm^{-3}) for 50 dwellings of different villages of Bathinda district of Punjab for the period of March 2010 to February 2011.

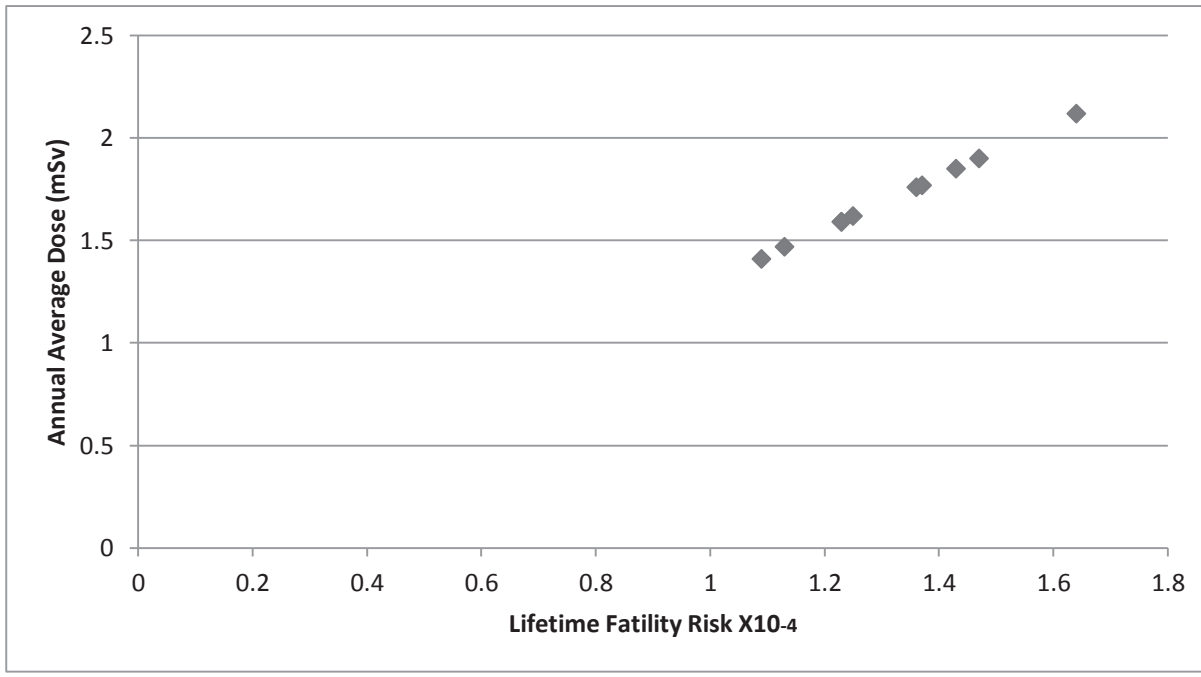

Fig. 6: Lifetime Fatality Risk vs Annual Average Dose for dwellings of Bathinda district of Punjab for the period of March 2010 to February 2011.

the life time fatality risk vs annual average dose for dwellings of Bathinda District of Punjab for the period of March 2010 to February 2011. The present work deviates from Singh et al. (2005) in Malwa region of Punjab and the minimum value reported in present work is more by 6.9 Bqm^{-3} and maximum value in the present study is less by 21.15 Bqm^{-3} than their work. The recent study deviates from the study of Mehra et al. (2009) in Hisar District of Haryana and the minimum value in the present study is more by amount of 19.55 Bqm^{-3} and maximum value in recent study is more by an amount of 3.95 Bqm^{-3} than their work. The recent calculated value deviating from the high content of the radon can be explained because of the uranium mineralization in the concerned area.

CONCLUSIONS

The value of radon for the first floor portion of the same dwelling is lower in comparison to the ground floor because of its more distance from the underlying soil.

The values in the cemented floors are lower than in the dwellings with the un-cemented floors because of the fact that the cement provides the shielding for the underlying soil. The indoor radon values are more in very poorly ventilated dwellings in comparison to the very well ventilated dwellings because radon and its progeny get accumulated in very poorly ventilated dwellings.

The area under the study is safe as per as health hazard affects due to radon on human beings are concerned for the above-said period. The desired outcome of this study was a recommendation to the residents of the survey area to alter the ventilation conditions, to reduce the cracks in the floor and wherever feasible to make the cemented floor, in order to reduce the indoor radon concentration in the dwellings which were studied.

ACKNOWLEDGEMENT

The support from Dr. B. R. Ambedkar National Institute of Technology, Jalandhar and Shaheed Bhagat Singh State Technical Campus, Ferozepur is gratefully acknowledged.

REFERENCES

American Cancer Society, Known and Probable Carcinogens 2008. http://www.cancer.org/docroot/PED/content/PED_1_3x Known and Probable Carcinogens.asp.

Archer, V.E., Coons, T., Saccomanno, G. and Hong, D.Y. 2004. Latency and the Lung Cancer Epidemic among United State Uranium Miners. Health Physics, 87(5): 480-489.

Auxier, J.A., Christian, D.J., Jones, T.D., Kerr, G.D., Perdue, P.T., Shinpaugh, W.H. and Thorngate, J.H. 1973. Contribution of Natural Terrestrial Sources to the Total Radiation Dose to Man. Oak Ridge National Laboratory, ORNL-TM-4323.

Bale, W.F. and Shapiro, J.V. 1956. Radiation dosage to lungs from radon and its daughter products. Proceeding of First International Conference on Peaceful Uses of Atomic Energy, Geneva, pp. 233-236.

Collins, L.G., Haines, C., Perkel, R. and Enck, R.E. 2007. Lung cancer diagnosis and management. American Family Physician, 75(1): 56-63.

Damkjare, A. 1986. The efficiency of cellulose nitrate LR-115 type 11 for alpha particle detection. Nucl. Tracks Radiat. Meas, 12: 295.

Eappen, K.P., Ramachandran, T.V., Shaikh, A.N. and Mayya, Y.S. 2001. Calibration factor for SSNTD-based radon/thoron dosimeter. Radiation Protection and Environment, 24(1-2) : 410-414.

Evans, R.D., Harley, J.H., Jacobi, W., Maclean, A.S., Mills, W.A. and Stewart, C.G. 1981. Estimation of risk from environmental exposure to Radon-222 and its decay products. Nature, 290: 98-100.

Henschke, C.I., Yankelevitz, D.F., Libby, D.M., Pasmantier, M.W., Smith, J.P. and Miettinen, O.S. 2008. Survival of patients with Stage I lung cancer detected on CT screening. New England Journal of Medicine, 355(17): 1763-1771.

Henshaw, D.L., Eatough, J.P. and Richardson, R.B. 1990. Radon as a causative factor in induction of myeloid leukemia and other cancers. Lancet, 355: 1008-1015.

ICRP 1993. Protection against Radon at home and work. Ann ICRP: 65

Kitto, M. E. and Menia, T. A. 2009. Can cat litter be a source of indoor Radon. International Radon Symposium, St. Louis.

Lide, D.R. 1963. Handbook of Chemistry and Physics. 74th edition. CRC Press, Florida.

Mehra, R., Singh, S. and Kumar, S. 2009. Passive integration Radon studies for environmental monitoring in Sirsa District, Haryana, India using solid state nuclear track detectors. Indian J. Phys., 83:1191-1196.

Miles, L.C. and Cliff, K.D. 1992. Dose of the lung and other organs from radon and thoron as a function of age. Radiate. Prot. Deism., 41: 251-253.

Nakhara, H., Kudo, H., Akiba, F. and Murakami, Y. 1980. Some basic studies on the absolute determination of radon concentration in the air by cellulose nitrate track detector, Nucl. Instr. Meth., 171.

Porstendorfer, J. 1994. Properties and behaviour of radon and thoron and their decay products in the air. Journal of Aerosol Science, 25(2): 219-263.

Ramola, R.C., Singh, M., Singh, S. and Virk, H.S. 1987. Measurement of indoor radon concentration using LR-115 plastic track detector. Ind. J. Pure and Appl. Phys., 25: 127-129.

Rericha, V., Kulich, M., Rericha, R., Shore, D.L. and Sandler, D.P. 2006. Incidence of leukaemia, lymphoma and multiple myeloma in Czech uranium miners: A case-cohort study. Environmental Health Perspectives, 114(6): 818-822.

Richardson, R.B., Eatough J.P. and Henshaw, D.L. 1991. Dose to red bone marrow from natural radon and thoron exposure. Br. J. Radiol, 64: 608-624.

Singh, S., Kumar, M. and Mahajan, R. K. 2005. The study of indoor radon in dwellings of Bathinda Dist., Punjab, India and its correlation with uranium and radon exhalation rate in soil. Radiation Measurements, 39(5): 535-542.

Smith, B.J., Zhang, L. and Field, W.R. 2007. Iowa radon leukaemia study: A hierarchical population risk model for spatially correlated exposure measured with error. Statistical Medicine, 26(25): 4619.

Sun, S., Schiller, J.H. and Gazdar, A.F. 2007. Lung Cancer in never smokers - A different disease. Nature Reviews, 7(10): 778-790.

UNSCEAR 1994. Sources Effects of Ionizing Radiation. United Nations Scientific Committee on the Effects of Atomic Radiation , New York: United Nations..

UNSCEAR 2000. Sources and Effects of Ionizing Radiations. United Nations Scientific Committee on the Effects of Atomic Radiation, New York: United Nations.

... Continued from inner front cover

- The text of the manuscript should run into **Abstract, Introduction, Materials & Methods, Results, Discussion, Acknowledgement** (if any) and **References** or other suitable headings in case of reviews and theoretically oriented papers. However, short communication can be submitted in running with **Abstract and References.** The references should be in full with the title of the paper.
- The figures should preferably be made on a computer with high resolution and should be capable of withstanding a reasonable reduction with the legends provided separately outside the figures. Photographs may be black and white or colour.
- Tables should be typed separately bearing a short title, preferably in vertical form. They should be of a size, which could easily be accommodated in the page of the Journal.
- References in the text should be cited by the authors' surname and year. In case of more than one reference of the same author in the same year, add suffix a,b,c,.... to the year. For example: (Thomas 1969, Mass 1973a, 1973b, Madony et al. 1990, Abasi & Soni 1991).

List of References

The references cited in the text should be arranged alphabetically by authors' surname in the following manner: (Note: The titles of the papers should be in running 'sentence case', while the titles of the books, reports, theses, journals, etc. should be in 'title case' with all words starting with CAPITAL letter.)

Dutta, A. and Chaudhury, M. 1991. Removal of arsenic from groundwater by lime softening with powdered coal additive. J. Water Supply Res. Techno. Aqua., 40(1) : 25-29.

Hammer, D.A. (ed.) 1989. Constructed Wetlands for Wastewater Treatment-Municipal, Industrial and Agricultural. Lewis Publishers Inc., pp. 831.

Haynes, R. J. 1986. Surface mining and wetland reclamation. In: Harper, J. and Plass, B. (eds.) New Horizons for Mined Land Reclamation. Proceedings of a National Meeting of the American Society for Surface Reclamation, Princeton, W.V.

Submission of Papers

- The paper can be submitted by e-mail as an attachment in a single WORD file at **contact@neptjournal.com**
- The paper can also be submitted online in a single WORD file through the journal's website: **www.neptjournal.com**

Attention

1. Any change in the authors' affiliation may please be notified at the earliest.
2. Please make all the correspondence by e-mail, and authors should always quote the manuscript ID (number).

Note: In order to speed up the publication, authors are requested to send the publication charges as soon as they get the 'initial acceptance' letter, and also correct the galley proof immediately after receipt. The galley proof must be checked with utmost care, as publishers owe no responsibility for mistakes. The papers will be put on priority for publication only after receiving the processing and publication charges.

Nature Environment and Pollution Technology

(Abbreviation: Nat. Env. Poll. Tech.)

(An International Quarterly Scientific Journal)

Published by

Technoscience Publications

A-504, Bliss Avenue, Opp. SKP Campus
Balewadi, Pune-411 045, Maharashtra, India

In association with

Technoscience Knowledge Communications

Mira Road, Mumbai, India

For further details of the Journal please visit the website. All the papers published on a particular subject/topic or by any particular author in the journal can be searched and accessed by typing a keyword or name of the author in the 'Search' option on the Home page of the website. All the papers containing that keyword or author will be shown on the home page from where they can be directly downloaded.

www.neptjournal.com

Published for Proprietor, Printer and Publisher: Mrs. T. P. Goel, B-34, Dev Nagar, Tonk Road, Jaipur, Rajasthan, India; Editors: Dr. P. K. Goel and Prof. K. P. Sharma